



ISSN 1580-3155

Pages 733–947 ■ Year 2022, Vol. 69, No. 4

Slovensko kemijsko društvo
Slovenian Chemical Society

ActaChimicaSlo ActaChimicaSlo SlovenicaActaC

4

69/2022



EDITOR-IN-CHIEF

KSENIJA KOGEJ

University of Ljubljana, Faculty of Chemistry and Chemical Technology, Večna pot 113, SI-1000 Ljubljana, Slovenija

E-mail: ACSi@fkk.uni-lj.si, Telephone: (+386)-1-479-8538

ASSOCIATE EDITORS

Alen Albreht, National Institute of Chemistry, Slovenia

Aleš Berlec, Jožef Stefan Institute, Slovenia

Janez Cerkovnik, University of Ljubljana, Slovenia

Mirela Dragomir, Jožef Stefan Institute, Slovenia

Ksenija Kogej, University of Ljubljana, Slovenia

Krištof Kranjc, University of Ljubljana, Slovenia

Matjaž Kristl, University of Maribor, Slovenia

Franč Perdih, University of Ljubljana, Slovenia

Aleš Ručigaj, University of Ljubljana, Slovenia

Helena Prosen, University of Ljubljana, Slovenia

Irena Vovk, National Institute of Chemistry, Slovenia

ADMINISTRATIVE ASSISTANT

Marjana Gantar Albreht, National Institute of Chemistry, Slovenia

Eva Mihalinec, Slovenian Chemical Society, Slovenia

EDITORIAL BOARD

Wolfgang Buchberger, Johannes Kepler University, Austria

Alojz Demšar, University of Ljubljana, Slovenia

Stanislav Gobec, University of Ljubljana, Slovenia

Marko Goličnik, University of Ljubljana, Slovenia

Günter Grampp, Graz University of Technology, Austria

Wojciech Grochala, University of Warsaw, Poland

Danijel Kikelj, University of Ljubljana

Janez Košmrlj, University of Ljubljana, Slovenia

Blaž Likozar, National Institute of Chemistry, Slovenia

Mahesh K. Lakshman, The City College and

The City University of New York, USA

Janez Mavri, National Institute of Chemistry, Slovenia

Friedrich Sreenc, University of Minnesota, USA

Walter Steiner, Graz University of Technology, Austria

Jurij Svete, University of Ljubljana, Slovenia

David Šarlah, University of Illinois at Urbana-Champaign, USA;
Università degli Studi di Pavia, Italy

Ivan Švancara, University of Pardubice, Czech Republic

Jiri Pinkas, Masaryk University Brno, Czech Republic

Gašper Tavčar, Jožef Stefan Institute, Slovenia

Ennio Zangrando, University of Trieste, Italy

ADVISORY EDITORIAL BOARD

Chairman

Branko Stanovnik, Slovenia

Members

Udo A. Th. Brinkman, The Netherlands

Attilio Cesaro, Italy

Vida Hudnik, Slovenia

Venc̃eslav Kaučič, Slovenia

Željko Knez, Slovenia

Radovan Komel, Slovenia

Stane Pejovnik, Slovenia

Anton Perdih, Slovenia

Slavko Pečar, Slovenia

Andrej Petrič, Slovenia

Boris Pihlar, Slovenia

Milan Randić, Des Moines, USA

Jože Škerjanc, Slovenia

Đurđa Vasić-Rački, Croatia

Marjan Veber, Slovenia

Gorazd Vesnaver, Slovenia

Jure Zupan, Slovenia

Boris Žemva, Slovenia

Majda Žigon, Slovenia

Acta Chimica Slovenica is indexed in: Academic Search Complete, Central & Eastern European Academic Source, Chemical Abstracts Plus, Chemical Engineering Collection (India), Chemistry Citation Index Expanded, Current Contents (Physical, Chemical and Earth Sciences), Digitalna knjižnica Slovenije (dLib.si), DOAJ, ISI Alerting Services, PubMed, Science Citation Index Expanded, SciFinder (CAS), Scopus and Web of Science. Impact factor for 2021 is IF = 1.524.



Articles in this journal are published under the
Creative Commons Attribution 4.0 International License

Izdaja – Published by:

SLOVENSKO KEMIJSKO DRUŠTVO – SLOVENIAN CHEMICAL SOCIETY

Naslov redakcije in uprave – Address of the Editorial Board and Administration

Hajdrihova 19, SI-1000 Ljubljana, Slovenija

Tel.: (+386)-1-476-0252; Fax: (+386)-1-476-0300; E-mail: chem.soc@ki.si

Izdajanje sofinancirajo – Financially supported by:

National Institute of Chemistry, Ljubljana, Slovenia

Jožef Stefan Institute, Ljubljana, Slovenia

Faculty of Chemistry and Chemical Technology, University of Ljubljana, Slovenia

Faculty of Chemistry and Chemical Engineering, University of Maribor, Slovenia

University of Nova Gorica, Slovenia

Slovensko kemijsko društvo
Slovenian Chemical Society



Acta Chimica Slovenica izhaja štirikrat letno v elektronski obliki na spletni strani <http://acta.chem-soc.si>. V primeru posvečenih števil izhaja revija tudi v tiskani obliki v omejenem številu izvodov.

Acta Chimica Slovenica appears quarterly in electronic form on the web site <http://acta.chem-soc.si>. In case of dedicated issues, a limited number of printed copies are issued as well.

Transakcijski račun: 02053-0013322846 Bank Account No.: SI56020530013322846-Nova Ljubljanska banka d. d., Trg republike 2, SI-1520 Ljubljana, Slovenia, SWIFT Code: LJBA SI 2X

Oblikovanje ovitka – Design cover: KULT, oblikovalski studio, Simon KAJTNA, s. p. Grafična priprava za tisk: OSITO, Laura Jankovič, s.p.

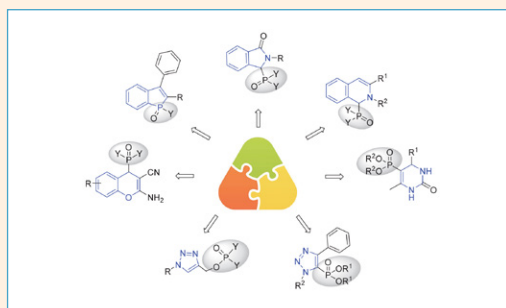


FEATURE ARTICLE

735–755 Feature Article

Multicomponent Synthesis of Potentially Biologically Active Heterocycles Containing a Phosphonate or a Phosphine Oxide Moiety

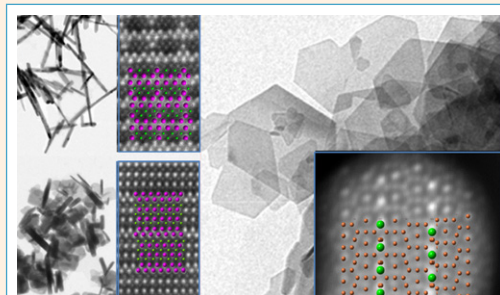
Nóra Popovics-Tóth and Erika Bálint



756–771 Feature Article

Adaptation of the Crystal Structure to the Confined Size of Mixed-oxide Nanoparticles

Darko Makovec

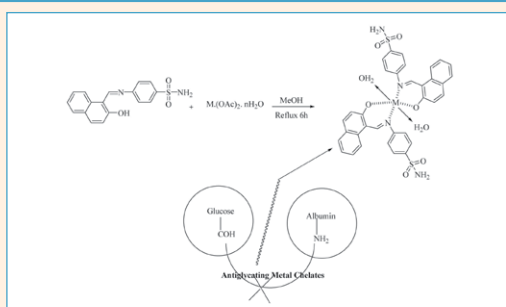


SCIENTIFIC PAPER

772–778 Organic chemistry

Synthesis, Characterization, Anti-Glycation, and Anti-Oxidant Activities of Sulfanilamide Schiff Base Metal Chelates

Muhammad Yaqoob, Waqas Jamil, Muhammad Taha and Sorath Solangi

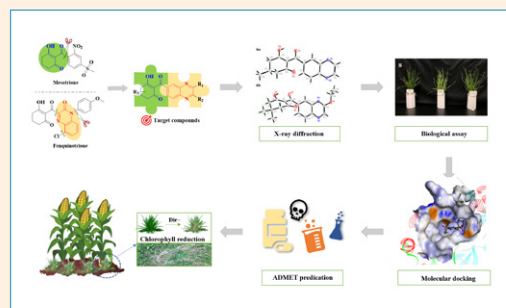


779–786

Organic chemistry

Synthesis, Crystal Structure and Biological Activity of Two Triketone-Containing Quinoxalines as HPPD Inhibitors

Xinyu Leng, Chengguo Liu and Fei Ye

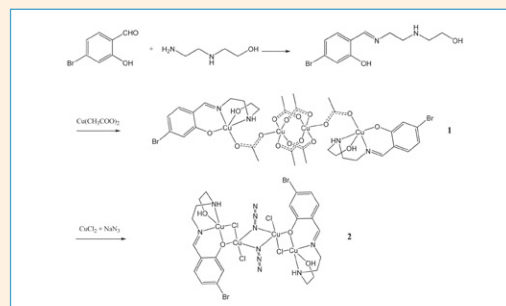


787–795

Inorganic chemistry

Tetranuclear Copper(II) Complexes Derived from 5-Bromo-2-((2-(2-hydroxyethylamino)ethylimino)methyl)phenol: Synthesis, Characterization, Crystal Structures and Catalytic Oxidation of Olefins

Xiao-Jun Zhao, Su-Zhen Bai and Ling-Wei Xue

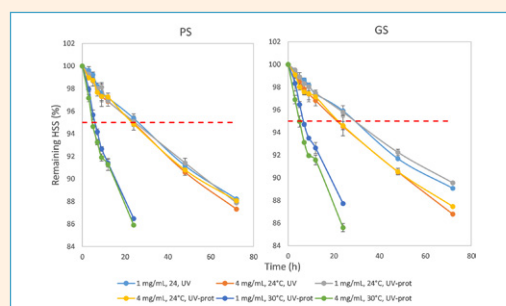


796–802

Biomedical applications

Evaluation of the Stability of Hydrocortisone Sodium Succinate in Solutions for Parenteral Use by a Validated HPLC-UV Method

Katja Mihovec, Žane Temova Rakuša, Enikő Éva Gaál and Robert Roškar

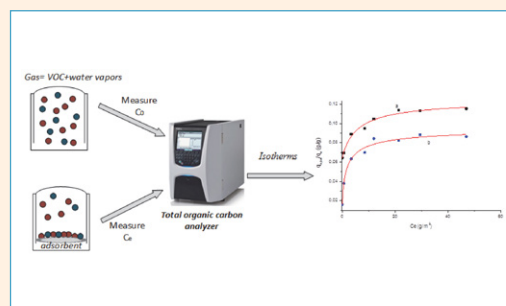


803–810

Applied chemistry

Use of Total Organic Carbon Analyzer in Isotherm Measurements of Co-Adsorption of VOCs and Water Vapor from the Air

Dragana Kešelj, Dragica Lazić and Zoran Petrović

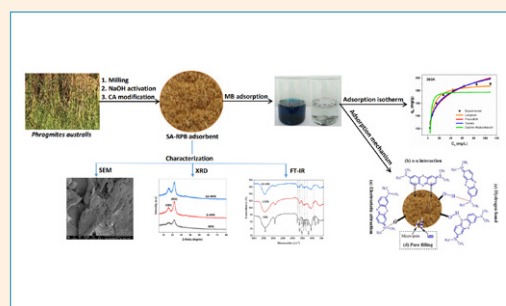


811–825

Chemical, biochemical and environmental engineering

Enhanced Adsorption of Methylene Blue by Chemically Modified Materials Derived from *Phragmites australis* Stems

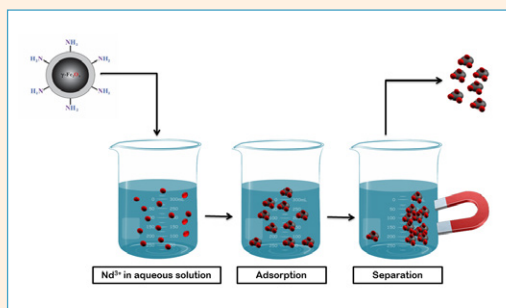
Bui Thi Minh Nguyet, Nguyen Huu Nghi, Nguyen Anh Tien, Dinh Quang Khieu, Ha Danh Duc and Nguyen Van Hung



826–836 Chemical, biochemical and environmental engineering

Assessment of the Capability of Magnetic Nanoparticles to Recover Neodymium Ions from Aqueous Solution

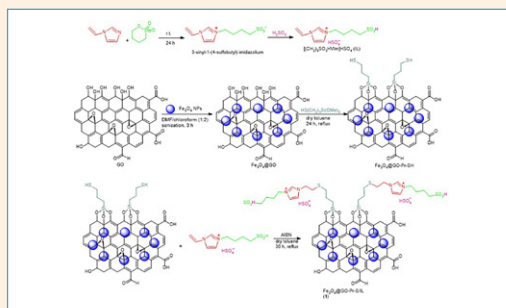
Ana Ambrož, Irena Ban and Thomas Luxbacher



837–847 Organic chemistry

Ionic Liquid Supported on Magnetic Graphene Oxide as a Highly Efficient and Stable Catalyst for the Synthesis of Triazolopyrimidines

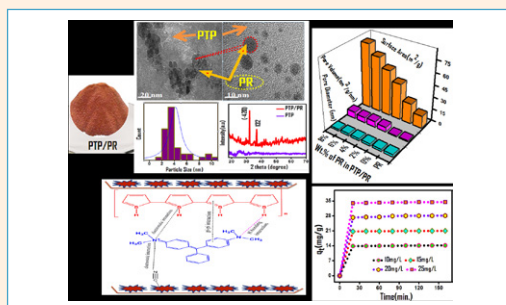
Azar Jahanbakhshi, Mahnaz Farahi and Yeganeh Aghajani



848–862 Chemical, biochemical and environmental engineering

Hybrid Polymer Composite of Prussian Red Doped Polythiophene for Adsorptive Wastewater Treatment Application

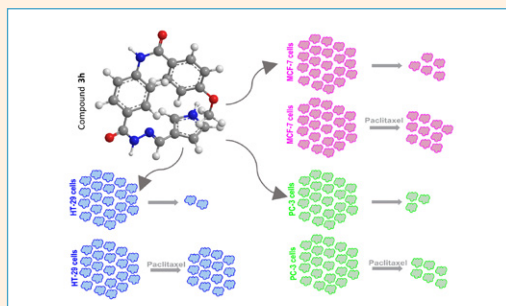
Mohd Mustafa, Shabnum Bashir, Syed Kazim Moosvi, Mohd. Hanief Najar, Mubashir Hussain Masoodi and Masood Ahmad Rizvi



863–875 Biochemistry and molecular biology

Synthesis and Biological Evaluation of Some Hydrazone-Hydrazone Derivatives as Anticancer Agents

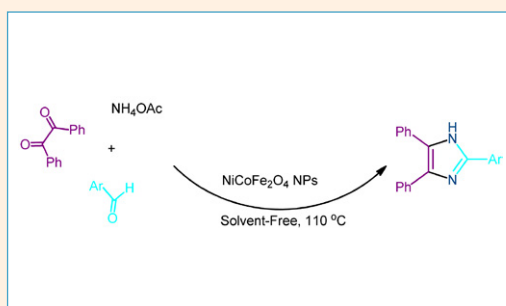
Kadriye Akdağ, Fatih Tok, Sevgi Karakuş, Ömer Erdoğan, Özge Çevik and Bedia Kaymakçıoğlu



876–883 Organic chemistry

Preparation and Characterization of NiCoFe₂O₄ Nanoparticles as an Effective Catalyst for the Synthesis of Trisubstituted Imidazole Derivatives Under Solvent-free Conditions

Leila Hemmesi and Hossein Naeimi

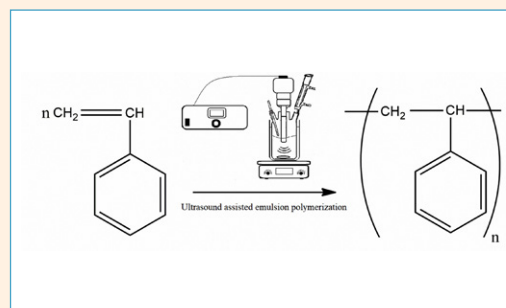


884–895

Chemical, biochemical and environmental engineering

Cost-Effective Control of Molecular Weight in Ultrasound-Assisted Emulsion Polymerization of Styrene

Ibrahim Korkut, Fuat Erden and Salih Ozbay

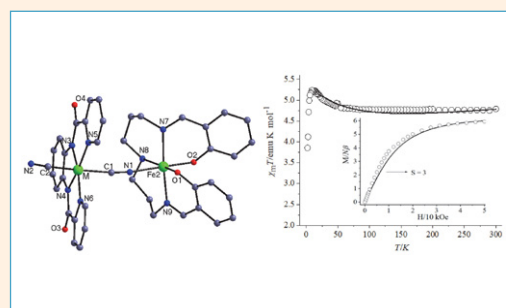


896–904

Inorganic chemistry

The Paramagnetic or Spin Crossover Iron(III) Complexes Based-on Pentadentate Schiff Base Ligand: Crystal Structure, and Magnetic Property Investigation

Zhijie Xu, Shuo Meng, Tong Cao, Yu Xin, Mingjian Zhang, Xiaoyi Duan, Zhen Zhou and Daopeng Zhang

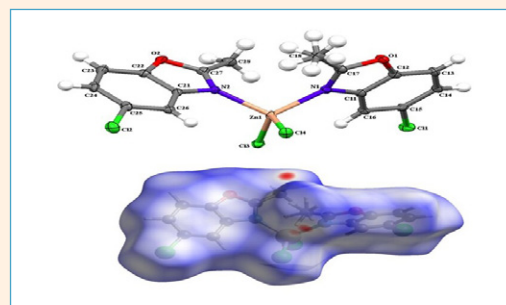


905–912

Inorganic chemistry

Zinc(II) Complex Containing Oxazole Ring: Synthesis, Crystal Structure, Characterization, DFT Calculations, and Hirshfeld Surface Analysis

Karwan Omer Ali, Hikmat Ali Mohamad, Thomas Gerber and Eric Hosten

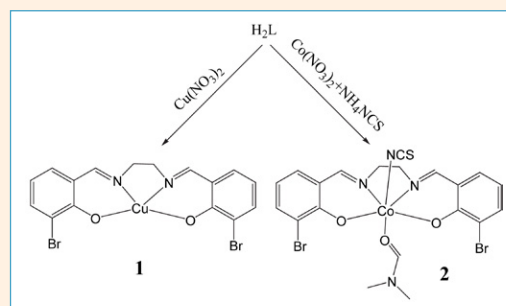


913–919

Inorganic chemistry

Synthesis, Crystal Structures and Antibacterial Activities of *N,N'*-Ethylene-bis(3-bromosalicylalimine) and Its Copper(II) and Cobalt(III) Complexes

Xue-Song Lin, Yong-Gang Huang, Rui-Fa Jin and Ya-Li Sang

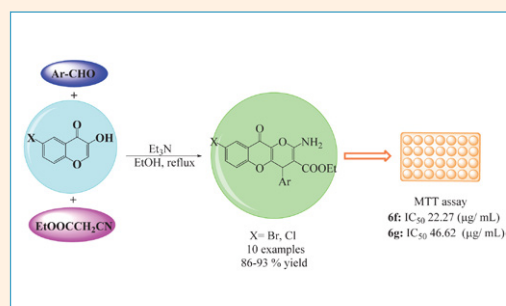


920–927

Biochemistry and molecular biology

Synthesis and *In Vitro* Cytotoxicity of Novel Halogenated Dihydropyrano[3,2-*b*]Chromene Derivatives

Salehe Sabouri, Ehsan Faghih-Mirzaei and Mehdi Abaszadeh

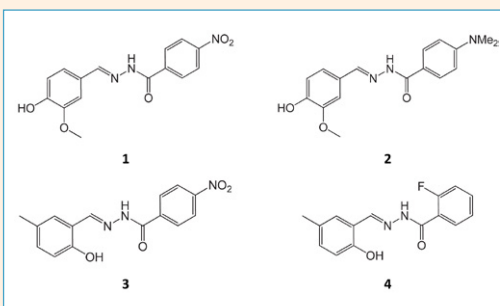


928–936

Organic chemistry

Syntheses, Crystal Structures and Xanthine Oxidase Inhibitory Activity of Aroylhydrazones

Yong-Jun Han, Xue-Yao Guo and Ling-Wei Xue

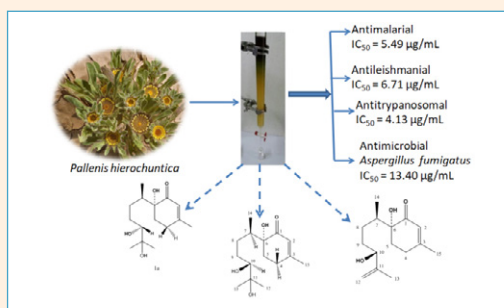


837–943

Organic chemistry

In vitro Assessment of Antiprotozoal and Antimicrobial Activities of Fractions and Isolated Compounds from *Pallenis hierochuntica*

Vincent O. Imieje, Abiodun Falodun and Ahmed A. Zaki



944–947

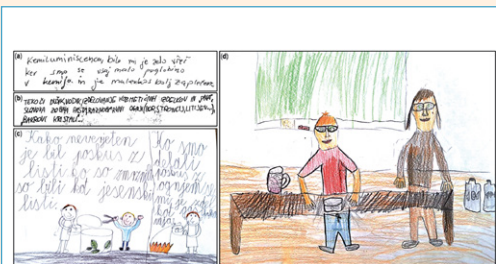
AUTHOR INDEX

DRUŠTVENE VESTI

S95–S97

Trideset let delovanja Šole eksperimentalne kemije na Institutu »Jožef Stefan«: trideset let motiviranja mladih generacij in utrjevanja poti naravoslovnega izobraževanja

Melita Tramšek, Evelin Gruden in Marko Jeran



S98–S106

Slavnostna akademija ob 70-letnici Slovenskega kemijskega društva



Multicomponent Synthesis of Potentially Biologically Active Heterocycles Containing a Phosphonate or a Phosphine Oxide Moiety

Nóra Popovics-Tóth and Erika Bálint*

Department of Organic Chemistry and Technology, Budapest University of Technology and Economics, Műegyetem rkp. 3., H-1111 Budapest, Hungary

* Corresponding author: E-mail: balint.erika@vbk.bme.hu
Tel.: +36-1-463-1111/5886

Received: 07-05-2022

Abstract

Several multicomponent synthetic approaches were elaborated for plenty of novel nitrogen or oxygen heterocycles containing a phosphonate or a phosphine oxide moiety. All multicomponent reactions were optimized through a model reaction in respect of the heating mode, molar ratio of the starting materials, atmosphere, catalyst, temperature, reaction time and solvent applied, and then, the extended preparation of small libraries of structurally-related compounds was performed. Most of the reactions could be considered as “green syntheses”, as they were carried out in the absence of any catalyst and/or solvent using microwave (MW) irradiation or even at ambient temperature. The scaling-up of a MW-assisted synthesis was also elaborated in a continuous flow MW system. Altogether more than 150 heterocyclic organophosphorus compounds were synthesized, among them several derivatives showed moderate or promising activity against the HL-60 cell line and *Bacillus subtilis* bacteria.

Keywords: Multicomponent reactions, Heterocycles, Organophosphorus compounds, Microwave chemistry, Biological activity

1. Introduction

In modern synthetic chemistry, the application of efficient and simple reaction routes for the preparation of organic compounds has become more and more important. Therefore, multicomponent reactions (MCRs) attract growing interest. In MCRs, the components react with each other in a “one-pot” manner without isolation of any intermediates, which may save time and energy.^{1,2} They can be considered as ideal synthetic methods due to their features, such as the quick and simple procedure, as well as energy saving and high atom efficiency.^{3–5} In general, complex structures can be easily formed from inexpensive and simple starting materials by these transformations.^{6–9} In addition, these properties make them suitable to create large libraries of structurally-related compounds.^{10–12} MCRs especially show their importance in the synthesis of heterocycles.

Heterocycles are present in human and animal organisms, as well as in plants as components of nucleic acids, sugars, enzymes, hormones, vitamins, pigments and

hemoglobin.^{13–17} In addition, their importance is further enhanced by many synthetic members, such as drugs, pesticides, fine chemicals and cosmetics.^{18–22} In the last few decades, the multicomponent synthesis of heterocycles containing phosphonate moieties has become more and more important, due to their promising biological properties.^{23,24}

The aim of our research work was to synthesize potentially biologically active nitrogen heterocycles bearing a phosphonate or a phosphine oxide moiety, such as oxoisoindolyl)phosphonates and -phosphine oxides **1**, (1,2-dihydroisoquinolyl)phosphonates and -phosphine oxides **2**, (dihydropyrimidinone)phosphonates **3**, (1,2,3-triazol-5-yl)phosphonates **4**, as well as ((1,2,3-triazol-4-yl)methyl)phosphinates and -phosphates **5** (Figure 1). In addition, oxygen heterocycles containing a phosphonate or a phosphine oxide moiety, such as (aminochromenyl)phosphonates and -phosphine oxides **6**, as well as 1-alkyl- and 1-alkoxy-1*H*-phosphindole-1-oxides **7** were also aimed to be investigated.

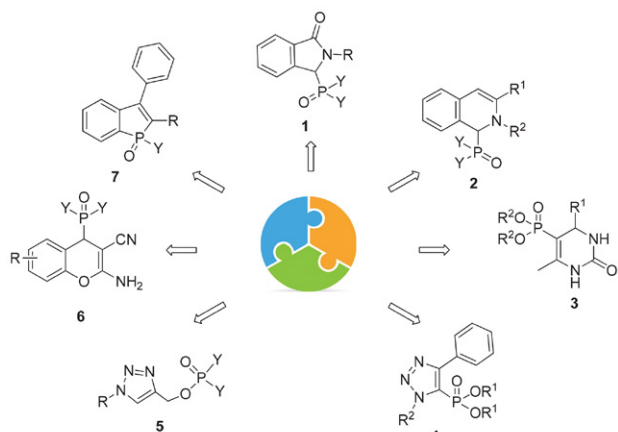
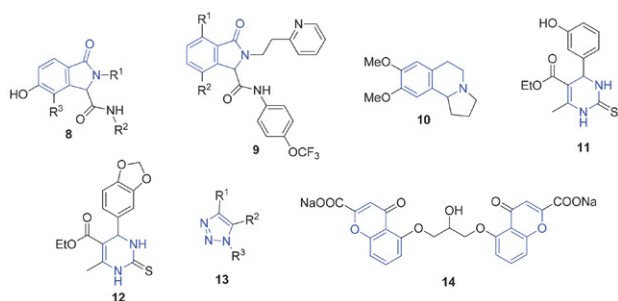


Figure 1. Target molecules

Several derivatives containing the above-mentioned target backbones have biological effects in a wide variety of indications (Figure 2). Some oxoisoindoline carboxylic acid **8** or carboxylic amide derivatives **9** can be found in the literature, which are anticancer or analgesic agents.^{25,26} Dihydroisoquinolines are effective in a variety of indications, such as antidepressants, sedatives, antitumor (e.g., Crispine A (**10**)) or as antibacterial drugs.^{27–30} Several 3,4-dihydropyrimidin-2(1H)-one carboxylates are applied as antitumor (e.g., Monastrol (**11**) or Piperastrol (**12**)), antihypertensive, anti-inflammatory, antibacterial, antiviral or antifungal agents.^{31–33} The 1,2,3-triazole derivatives **13** may have antibacterial, antiviral, antifungal, anticancer or anti-inflammatory effect.^{34–36} From among *O*-heterocycles, 4*H*-chromenes have various utilizations, especially in pharmaceutical industry, such as the antiallergic and antiasthmatic sodium chromoglycate (**14**), or in the cosmetic and dye industry, as well as in the agriculture.^{37–39}

Figure 2. Biologically active *N*- and *O*-heterocyclic derivatives

The biological activity of the phosphorylated heterocyclic compounds is less investigated; however, a few important examples can also be found (Figure 3). For example, 3,4-dihydropyrimidin-2(1*H*)-one phosphonates **15** have anti-inflammatory effect.⁴⁰ The 1,2,3-triazolyl phosphonate derivative **16** showed anti-HIV effect.⁴¹

Some 2-amino-4*H*-chromenylphosphonate derivatives **17** have antioxidant and anticancer activity,^{42,43} and a few (chromonylaminoethyl)phosphonates **18** also showed antitumor effect.⁴⁴ While benzo[*b*]phospholoxide **19** is used in the optoelectronic industry, e.g. in OLEDs.⁴⁵

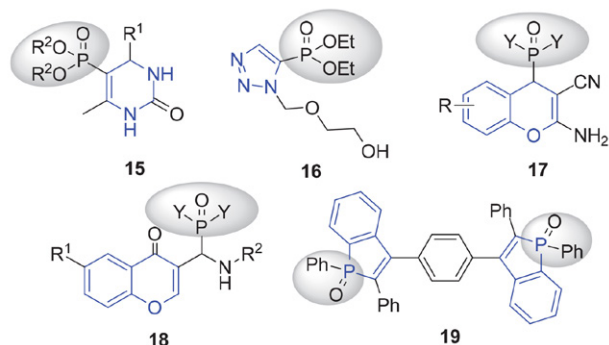


Figure 3. Biologically active phosphorylated heterocyclic compounds

Our main aim was to develop effective and simple methods for the preparation of phosphorylated *N*- and *O*-heterocyclic derivatives *via* multicomponent reactions, as far as possible, in the absence of any solvent and/or catalyst. We aimed at providing comprehensive study on the reactions, and the formation of diverse molecular libraries. We also investigated the *in vitro* cytotoxicity and antibacterial activity of the compounds synthesized. Furthermore, a phosphine oxide derivative was aimed to be utilized as a precursor of a phosphine ligand in the synthesis of a transition metal complex.

2. Multicomponent Synthesis of *N*-Heterocycles

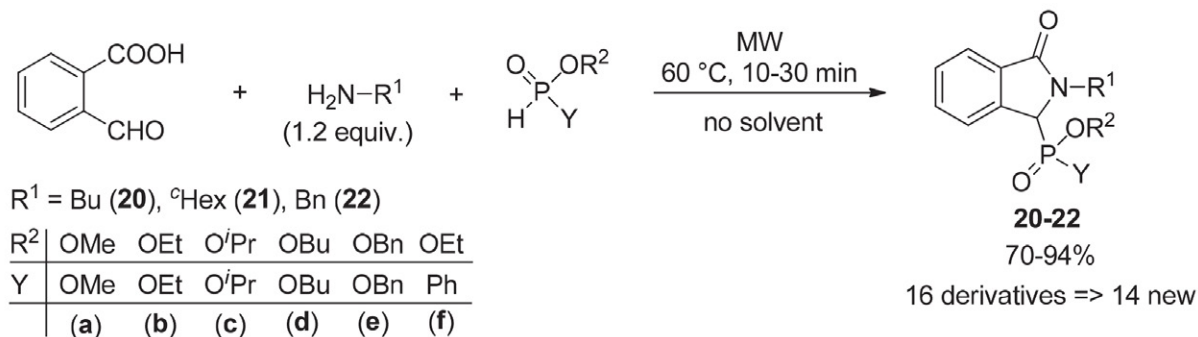
2. 1. Synthesis of (Oxoisoindolin-1-yl) phosphonates

A solvent- and catalyst-free MW-assisted method was developed for the synthesis of (oxoisoindolinyl) phosphonates by the Kabachnik–Fields reaction followed by intramolecular cyclization of 2-formylbenzoic acid, aliphatic primary amines and dialkyl phosphites. In the literature, only a few examples can be found for the condensation of 2-formylbenzoic acid, aromatic amines, amino alcohols or phenylethylamine derivatives and dialkyl phosphites. The reactions were carried out under thermal heating or under MW conditions usually for long reaction times (1–5 h) and in a solvent (methanol, ethyl acetate).^{46–49} In a few cases, the transformations were performed in the presence of a catalyst or an additive, such as NaH,⁵⁰ T₃P⁵¹ or OSU-6.⁵²

In the first step, the reaction of 2-formylbenzoic acid, butyl-, cyclohexyl- or benzylamine and diethyl phosphite was studied and optimized in respect of the heating mode, the molar ratio of starting materials, the temperature and the reaction time.⁵³ After the optimization, the model reaction was extended for the preparation of further (oxoisindolinyl)phosphonate derivatives **20–22** (Scheme 1). Carrying out the catalyst- and solvent-free MW-assisted condensation of 2-formylbenzoic acid, butylamine and dimethyl-, diethyl-, diisopropyl-, dibutyl- or dibenzyl phosphite at 60 °C for 10 min, the corresponding dialkyl (2-butyl-3-oxo-2,3-dihydro-2*H*-isindol-1-yl) phosphonates **20a–e** were synthesized in high yields (81–94%). Starting from cyclohexylamine and various dialkyl phosphites (dimethyl-, diethyl-, diisopropyl-, dibutyl- or dibenzyl phosphite), under the optimized conditions (60 °C, 30 min) five new (oxoisindolinyl)phosphonates **21a–e** were formed in yields of 70–84%. After that, the reaction was also performed applying benzylamine as the amine component, and five (oxoisindolin-1-yl)phosphonates **22a–e** were synthesized with high yields (80–90%) at 60 °C for 20 min.

Finally, the three-component reaction of 2-formylbenzoic acid, butylamine and ethyl phenyl-*H*-phosphinate as the *P*-reagent was also performed at 60 °C, for 10 min. The desired (oxoisindolin-1-yl)phosphinate **20f** was obtained in a yield of 78%, as a mixture of diastereomers in a ratio of almost 1:1.

The mechanism of the condensation was also investigated by *in situ* Fourier transform infrared (FT-IR) spectroscopy by the model reaction of 2-formylbenzoic acid (**FBA**), butylamine (**BA**) and diethyl phosphite (**DEP**) in ethanol. At first, the signal of the solvent (ethanol) was recorded, then the starting materials were added in ten-minute intervals. In the next step, the mixture was heated to 60 °C with an oil bath, and the IR spectrum of the mixture was measured continuously. In the time-dependent IR spectrum, the characteristic absorptions of the reaction components (**FBA**, **DEP**, **BA** and **20b**) can be seen (Figure 4). The lactone form of **FBA** had a strong absorption band at $\nu_{C=O} = 1756\text{ cm}^{-1}$. In the case of **DEP**, signals at 964 cm^{-1} (ν_{P-O-C}) and 1254 cm^{-1} ($\nu_{P=O}$) could be seen. **BA** was identified by the δ_{C-H} (1381 cm^{-1}) and δ_{N-H} (1605 cm^{-1}) absorptions. Diethyl (2-butyl-3-oxo-2,3-dihydro-2*H*-



Scheme 1. The reaction of 2-formylbenzoic acid, alkyl amines and dialkyl phosphites or ethyl phenyl-*H*-phosphinate

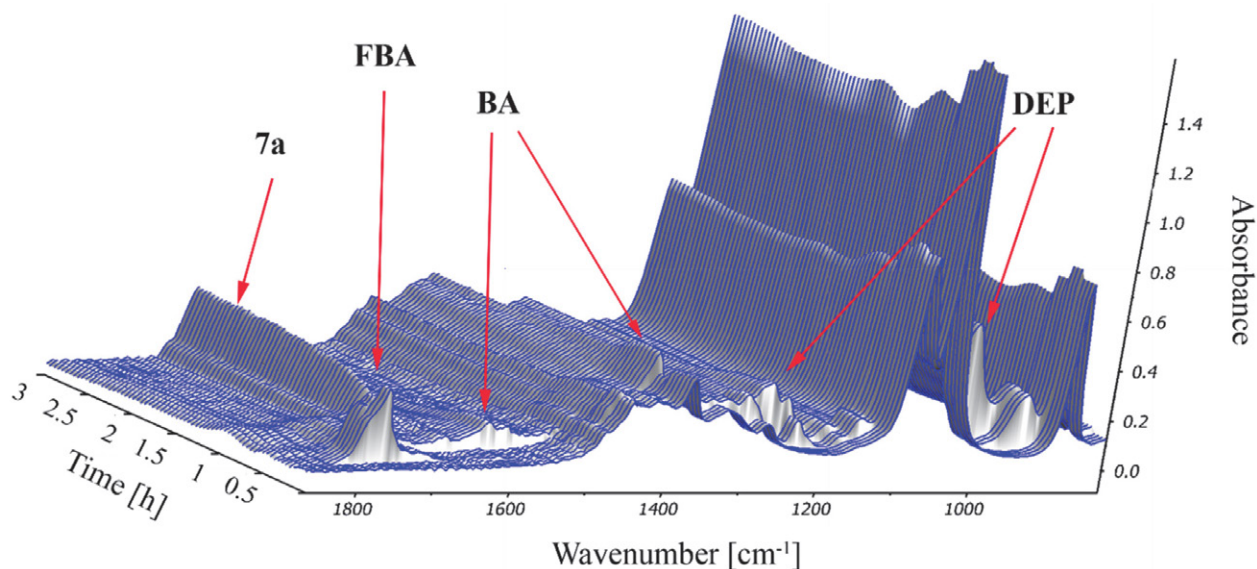


Figure 4. The time-dependent IR spectrum of the reaction of 2-formylbenzoic acid (**FBA**), butylamine (**BA**) and diethyl phosphite (**DEP**) in ethanol

isindol-1-yl)phosphonate (**20b**) had a $\nu_{\text{C=O}}$ characteristic absorption at 1690 cm^{-1} .

During the measurement, the signals of the starting materials decreased, while the signal of product **20b** increased, as it was expected. The signal of **FBA** decreased after the addition of **BA**, however, no signal of an intermediate, for instance an imine, appeared. The reason for the decrease of the signal of **FBA** is the change of IR properties of **FBA** in the reaction mixture.

Furthermore, to increase the productivity, the synthesis of some (oxoisindolyl)phosphonates (**20b**, **21b**, **22b**) was elaborated in a continuous flow MW system. The equipment contained a dual HPLC pump and CEM® MW reactor with a commercially available CEM® continuous flow cell. The **FBA** in ethanol (pump A) and the mixture of amines and **DEP** in ethanol (pump B) were fed separately. The temperature was monitored and controlled by the IR sensor of the MW reactor. The leaving mixture was cooled down to 25°C and was passed through a back-pressure regulator operating at 250 psi (17 bar).

At first, the continuous flow reaction of **FBA**, **BA** and **DEP** was carried out, and it was complete with 1.5 equivalents of both amine and dialkyl phosphite, at 60°C under a residence time of 30 min (at a flow rate of 0.25 mL/min) (Table 1, Entry 1). Starting from cyclohexylamine, a longer residence time of 45 min (at a flow rate of 0.15 mL/min) was needed to obtain a complete conversion (Table 1, Entry 2). While in the case of benzylamine, a residence time of 40 min (a flow rate of 0.18 mL/min) was applied, and the ratio of the (oxoisindolyl)phosphonate derivative **22b** was 100% (Table 1, Entry 3).

The productivity of the flow method was 2.3 g/h , 1.4 g/h and 1.8 g/h in the case of compounds **20b**, **21b**, **22b**, which were 1.5–2 times higher as compared to the batch method (1.8 g/h , 0.6 g/h and 1.0 g/h , respectively). The

productivity of the batch process was calculated for one h, based on the net reaction time of several consecutive reactions.

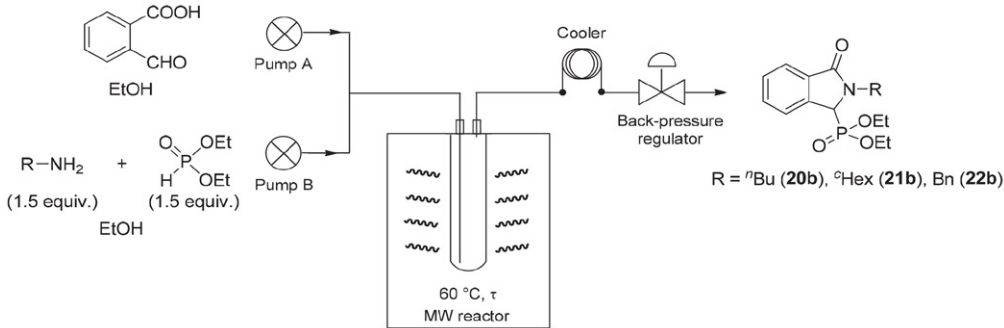
In all, 16 (oxoisindolin-1-yl)phosphonate derivatives **20–22** were synthesized, among them, 14 were new compounds. By the catalyst- and solvent-free MW-assisted method, good results were obtained at a lower temperature for shorter reaction times compared with the literature procedures. The mechanism of the condensation was studied by *in situ* FT-IR spectroscopy, and experiments were successfully performed in a continuous flow MW system to increase the productivity.

2. 2. Synthesis of (Oxoisindolin-1-yl) phosphine Oxides

Our aim was to carry out the special Kabachnik–Fields reaction of **FBA**, primary amines and secondary phosphine oxides, which is a new method for the synthesis of (oxoisindolyl)phosphine oxides. In the literature examples, the desired compounds were formed by multistep reactions, applying special reagents and conditions and in most cases, low yields were obtained.^{54–61}

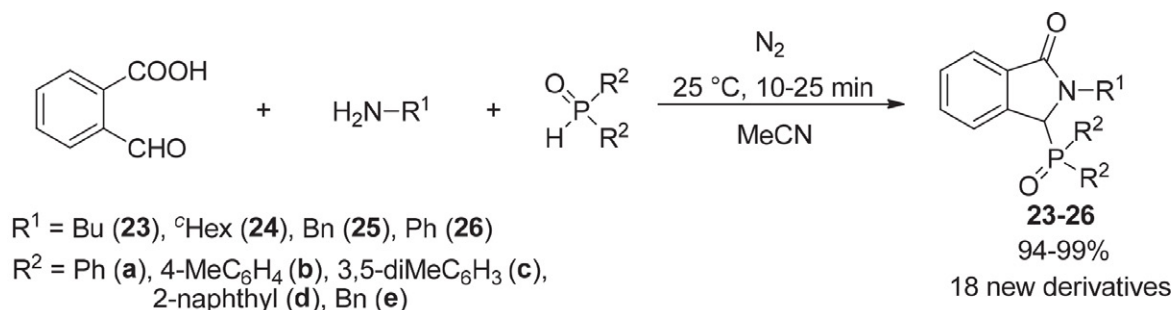
In our research work, the three-component condensation of **FBA**, butyl-, cyclohexyl-, benzylamine or aniline and diphenylphosphine oxide was studied.⁶² An efficient method was elaborated by us, where complete conversion was obtained in the absence of any catalyst, at room temperature, after short reaction times (10–20 min) in acetonitrile. The condensation was extended to various secondary phosphine oxides, such as bis(*p*-tolyl)-, bis(3,5-dimethylphenyl)-, bis(2-naphthyl)- or dibenzylphosphine oxides (Scheme 2). In the case of dibenzylphosphine oxide, a longer reaction time of 25 min was necessary to obtain full conversion. Altogether, 18 new (oxoisindolyl)

Table 1. Condensation of **FBA**, primary amines and diethyl phosphite (**DEP**) under continuous flow MW conditions



Entry	R	Flow rate [mL/min]	τ [min]	Conversion ^a [%]	Yield ^b [%]	Productivity [g/h]	
						Batch method	Flow method
1	ⁿ Bu	0.25	30	100	95 (20b)	1.8	2.3
2	^c Hex	0.15	45	100	86 (21b)	0.6	1.4
3	Bn	0.18	40	100	91 (22b)	1.0	1.8

^aBased on GC. ^bIsolated yield.



Scheme 2. The reaction of FBA, primary amines and secondary phosphine oxides

phosphine oxides **23–26** were isolated in excellent yields (94–99%).

After that, the Kabachnik–Fields reaction of FBA, butylamine and various *P*-stereogenic phosphine oxides (*tert*-butyl(phenyl)phosphine oxide, 2-methylphenyl(phenyl)phosphine oxide, 2-methoxyphenyl(phenyl)phosphine oxide, 2-, 3- or 4-trifluoromethylphenyl(phenyl)phosphine oxide, biphenyl(phenyl)phosphine oxide or 1-naphthyl(phenyl)phosphine oxide) was carried out (Scheme 3). Applying the optimized conditions (no catalyst, at 25°C , for 10–20 min in acetonitrile), eight (3-oxoisindolin-1-yl)phosphine oxides **27–34** were synthesized in high yields (94–98%). Due to the *P*-stereogenic centre on the phosphorus atom, the products **27–34** were formed as a mixture of two diastereomers. The diastereomeric ratio (*dr*) was close to 50:50 for most of the compounds **27–34** synthesized. 2-Trifluoromethylphenyl(phenyl)phosphine oxide as the *P*-reagent was an exception, in that case, the diastereomeric ratio was 35:65. It should be noted that the diastereomers of 1-naphthyl(phenyl) (2-butyl-3-oxo-2,3-dihydro-2*H*-isindol-1-yl)phosphine oxide (**34**) could be separated by column chromatography because of the bigger difference of the size of the functional groups on the phosphorus atom (phenyl and naphthyl groups).

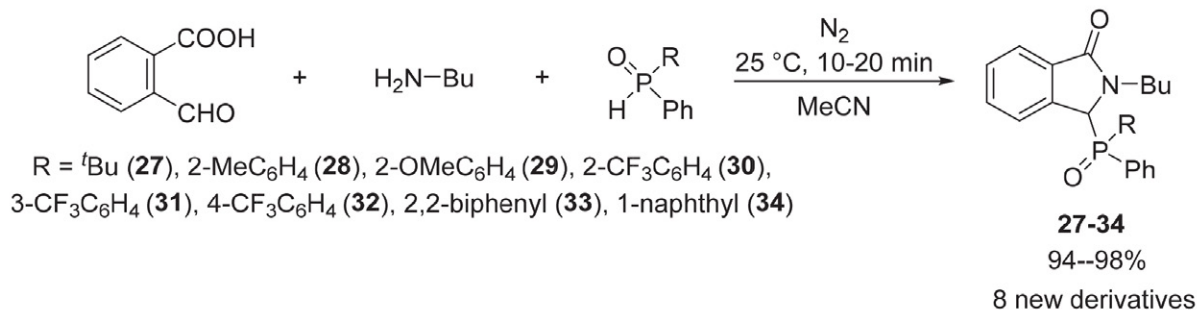
One of the (oxoisindolinyl)phosphine oxide (**23a**) was reduced to an (oxoisindolinyl)phosphine **35**, which was utilized as a phosphine ligand in the synthesis of a platinum(II) complex **36** (Scheme 4). In the first step, the de-

oxygenation of diphenyl (2-butyl-3-oxo-2,3-dihydro-2*H*-isindol-1-yl)phosphine oxide (**23a**) was performed with phenyl silane (PhSiH_3) as the reducing agent. The reaction was carried out under inert atmosphere, applying MW irradiation at 140°C for 6 h. The phosphine derivative **35** was not isolated, but it was further reacted with 0.5 equiv. of dichlorodibenzonitrile platinum(II) ($\text{Pt}(\text{PhCN})_2\text{Cl}_2$) precursor at 25°C in dichloromethane. The monodentate platinum(II) complex **36** was isolated by column chromatography in a yield of 80%.

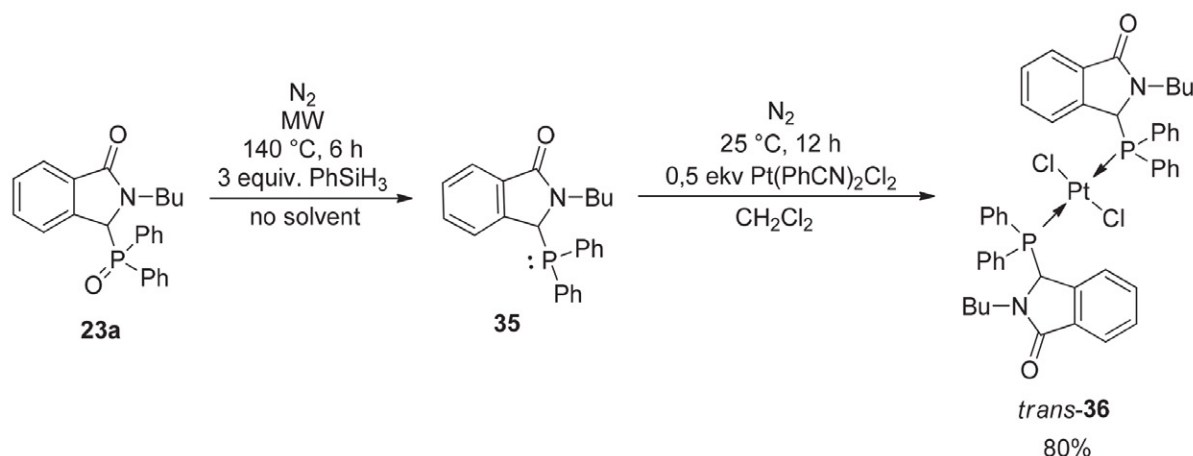
The complex **36** was formed in a relative configuration of *trans*, based on platinum-phosphorus coupling constant ($^1J_{\text{Pt-P}}$) in the ^{31}P NMR spectra. It is known in the literature that the $^1J_{\text{Pt-P}}$ between 3400 to 3600 Hz suggests *cis* complexes, while the $^1J_{\text{Pt-P}}$ coupling constant is 2500–3000 Hz in the case of *trans* arrangements.⁶³ In our case, the $^1J_{\text{Pt-P}}$ coupling constant was 2519 Hz. The relative orientation of the *trans*-**36** platinum(II) complex was also confirmed by X-ray diffraction measurements.

In addition, it was observed in the ^{31}P NMR spectrum that the central signal consisted of two very close peaks in a ratio of nearly 1:1. This can be explained by the chirality centre on the oxoisindoline ring, which caused the formation of the complex *trans*-**36** as a mixture of homo- and heterochiral diastereomers.

To conclude, an efficient, simple, one-pot method was developed for the synthesis of (oxoisindolinyl)phosphine oxides by the Kabachnik–Fields reaction followed



Scheme 3. The reaction of 2-formylbenzoic acid, butylamine and *P*-stereogenic secondary phosphine oxides



Scheme 4. Deoxygenation of (oxoisoindolyl)phosphine oxide (**23a**) and formation of platinum(II) complex *trans*-**36**

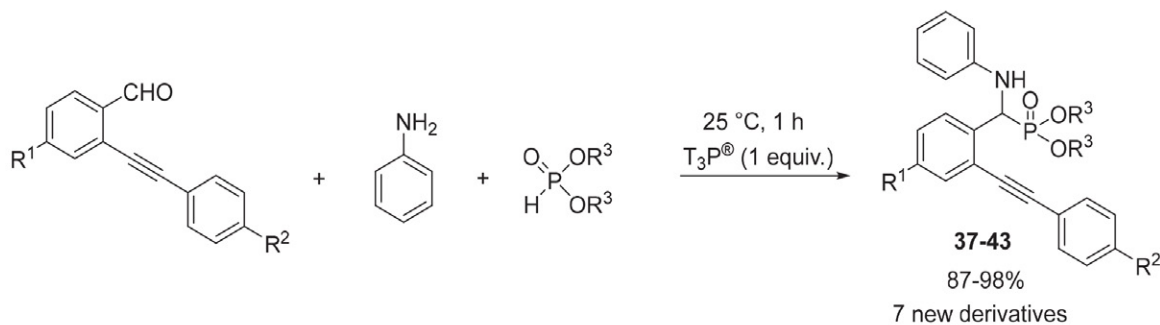
by intramolecular cyclization of **FBA**, primary amines and secondary phosphine oxides. The condensation was extended to *P*-stereogenic secondary phosphine oxides as well. In all, 26 (3-oxoisoindolin-1-yl)phosphine oxide derivatives **23–34** could be synthesized in excellent yields at room temperature after short reaction times (10–60 min). After deoxygenation, diphenyl (2-butyl-3-oxo-2,3-dihydro-2*H*-isoindol-1-yl)phosphine oxide (**23a**) was utilized in the synthesis of a platinum(II) complex *trans*-**36**.

2.3. Synthesis of (Dihydroisoquinolin-1-yl)phosphonates and α -Amino-(2-alkynylphenyl)-methylphosphonates

In the literature, the Kabachnik–Fields reaction of 2-alkynylbenzaldehydes, primary amines and dialkyl phosphites was carried out in the presence of various catalysts. α -Amino-(2-alkynylphenyl)-methylphosphonates were prepared at room temperature or at 60 °C after 4 h in 1,2-dichloroethane, using magnesium perchlorate ($\text{Mg}(\text{OCl}_4)_2$) or Lewis acids (FeCl_3 , $\text{In}(\text{OTf})_3$, $\text{Bi}(\text{OTf})_3$,

$\text{Yb}(\text{OTf})_3$) as the catalysts.^{64,65} However, (1,2-dihydroisoquinolin-1-yl)phosphonates were obtained in the presence of a silver or a copper salt (AgOTf or CuI) in ethanol or in 1,2-dichloroethane at 60 °C for 4–6 h.^{64,65} Under ultrasonic conditions, a surfactant-type copper catalyst ($\text{C}_{12}\text{H}_{25}\text{SO}_3\text{Na}$ and CuSO_4) was used in water.⁶⁶ In another example, the condensation was performed applying a chiral spirocyclic phosphonic acid as a chiral additive, and the optically active (dihydroisoquinolinyl)phosphonates were obtained at -10 °C after 3 days.⁶⁷ (Dihydroisoquinolinyl)phosphonates were also synthesized by a ring-closure method, starting from α -amino-(2-alkynylphenyl)-methylphosphonates in the presence of silver triflate (AgOTf).⁶⁸

In our research work, the Kabachnik–Fields reaction of 2-alkynylbenzaldehydes, aniline and dialkyl phosphites was studied and optimized in respect of the molar ratio of the starting materials, the temperature, the reaction time, the additive or catalyst and the solvent.⁶⁹ Based on our results, depending on the conditions, α -amino-(2-alkynylphenyl)-methylphosphonates **37–43** or (1,2-dihydroisoquinolin-1-yl)phosphonates **44–50** could be syn-



Scheme 5. $\text{T}_3\text{P}^{\text{®}}$ -mediated Kabachnik–Fields reaction of 2-alkynylbenzaldehydes, aniline and dialkyl phosphites

thesized selectively. An efficient procedure was developed for the preparation of α -amino-(2-alkynylphenyl)-methylphosphonates **37–43** at room temperature for 1 h in the presence of T_3P^* (propylphosphonic anhydride) as an additive (Scheme 5). Then, the model reaction was extended to different alkynylbenzaldehydes (2-(phenylethynyl)-, 2-(*p*-tolylethynyl)-, 4-fluoro-2-(*p*-tolylethynyl)-, 2-((4-methoxyphenyl)ethynyl)- and 2-((4-chlorophenyl)ethynyl)-benzaldehyde), as well as dialkyl phosphites (diethyl-, dibutyl- and dibenzyl phosphite), and seven new derivatives **37–43** were prepared in yields of 87–98%.

The condensation may take place through an imine intermediate, which may form by the reaction of 2-alkynylbenzaldehyde and aniline. The role of the T_3P^* is promoting dehydration. After the addition of the phosphorus reagent to the double bond of the intermediate, the α -amino-(2-alkynylphenyl)-methylphosphonates **37–43** are formed.

Performing the three-component reaction at 60 °C for 1 h, in the presence of 5 mol% of copper chloride (CuCl) as the catalyst, and using 2-alkynylbenzaldehyde and aniline in a small excess (1.2 equiv.), (1,2-dihydroisoquinolin-1-yl)phosphonates **44–50** were synthesized selectively (Scheme 6). After the optimization, by changing the 2-alkynylbenzaldehydes and dialkyl phosphites, seven new (dihydroisoquinolin-1-yl)phosphonates **44–50** were prepared in good to high yields (79–86%). In contrast to the literature, in our method, we applied a cheaper catalyst and shorter reaction time.

The first step of the formation of (1,2-dihydroisoquinoline)phosphonates **44–50** is the CuCl-catalyzed Kabachnik–Fields reaction of 2-alkynylbenzaldehydes, aniline and dialkyl phosphites. After that, the catalyst interacts with the triple bond of the α -amino-(2-alkynylphenyl)-methylphosphonates **37–43**, which makes the intramolecular nucleophile attack possible by the amino group, causing the ring closure step.

Altogether seven new α -amino-(2-alkynylphenyl)-methylphosphonates **37–43** were prepared in a short-

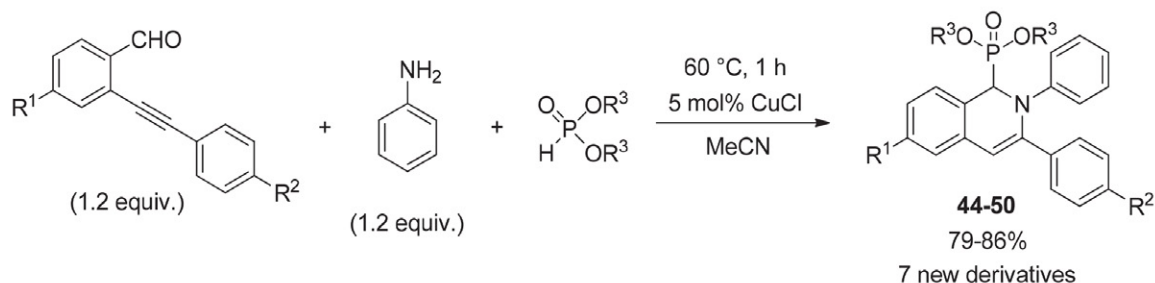
er reaction time (1 h) under milder conditions (25 °C) by the T_3P^* -mediated process developed by us as compared to the literature methods, which were carried out in the presence of $Mg(OCl_4)_2$ or Lewis acids for long reaction times. Furthermore, seven new (1,2-dihydroisoquinolin-1-yl) phosphonates **44–50** were also synthesized using a small excess (1.2 equiv.) of alkynylbenzaldehyde and amine, in acetonitrile instead of a halogenated solvent (1,2-dichloroethane) in a shorter reaction time (1 h instead of 4–6 h) using a cheaper catalyst (CuCl), than in the literature.

2. 4. Synthesis of (Dihydroisoquinolin-1-yl) phosphine Oxides

The Reissert-type reaction of isoquinoline, different acetylenes and secondary phosphine oxides or phosphine sulfides for the synthesis of (1,2-dihydroisoquinolin-1-yl) phosphine oxide derivatives was studied in the literature, however, only in two cases.^{70,71} The condensations were performed at high temperature (70–72 °C) for long reaction times (1.5–12 h), applying 1.1–1.5 equiv. excess of isoquinoline and acetylenes. However, starting from acylphenylacetylenes, longer reaction times (45–72 h) were used.⁷¹

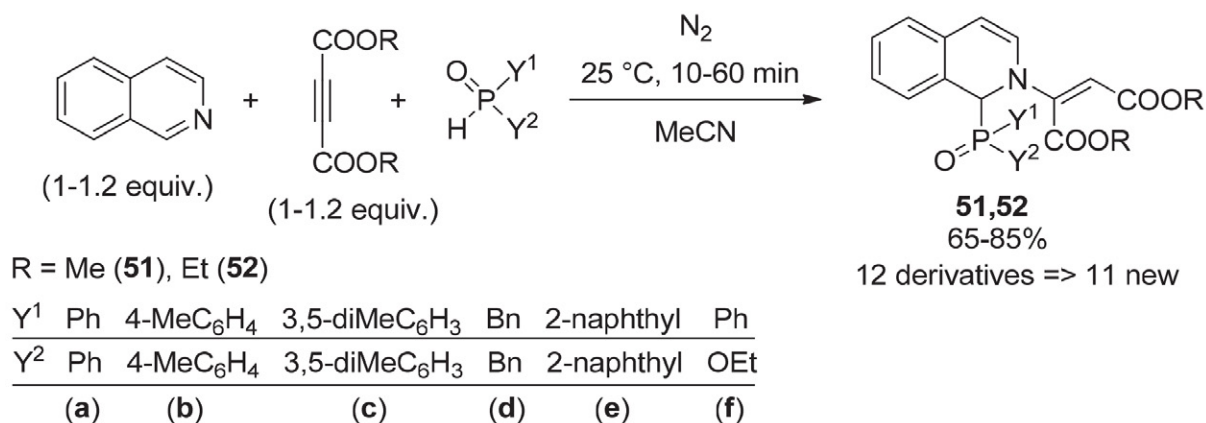
In two other examples, the Reissert-type reaction was performed with dialkyl phosphites in the absence of any catalyst and solvent at room temperature for 2–4 h.^{72,73} The (1,2-dihydroisoquinolin-1-yl)phosphonates were obtained in yields of 52–90%.

The Reissert-type reaction of isoquinoline, diethyl acetylenedicarboxylate and diphenylphosphine oxide was investigated, and the effect of the solvent, catalyst, temperature and reaction time was investigated.⁷⁴ A complete conversion was obtained using equivalent amount of the starting materials in acetonitrile, at room temperature after 10 min. Under the optimized conditions, the condensation of isoquinoline, dimethyl or diethyl acetylenedicarboxylate and diphenyl-, bis(*p*-tolyl)-, bis(3,5-dimethylphenyl)phosphine oxide or ethyl phenyl-*H*-phosphinate



Scheme 6. CuCl-catalyzed Kabachnik–Fields reaction of 2-alkynylbenzaldehydes, aniline and dialkyl phosphites

R ¹	H	H	H	F	H	H	H
R ²	Me	Me	Me	Me	OMe	Cl	H
R ³	Bu	Me	Et	Bu	Bu	Bu	Bu
	(44)	(45)	(46)	(47)	(48)	(49)	(50)



Scheme 7. Reissert-type reaction of isoquinoline, dialkyl acetylenedicarboxylates, and secondary phosphine oxides or ethyl phenyl-*H*-phosphinate

was performed, and eight (1,2-dihydroisoquinolin-1-yl) phosphine oxide derivatives (**51** and **52**) were formed in yields of 65–85% (Scheme 7). In the case of ethyl phenyl-*H*-phosphinate, the desired dialkyl (*E*)-2-[1-(ethoxy(phenyl)phosphoryl)isoquinolin-2(1*H*)-yl]maleate derivatives (**51f** and **52f**) were obtained as a mixture of diastereomers in a ratio of 60:40.

Starting from dibenzyl-, or di(2-naphthyl)phosphine oxides as the *P*-reagent, a small excess (1.2 equiv.) of isoquinoline and dialkyl acetylenedicarboxylate, as well as somewhat longer reaction time (1 h) were applied to obtain complete conversion. Thus, further four new (1,2-dihydroisoquinolin-1-yl)phosphine oxides (**51d,e** and **52d,e**) were synthesized in yields of 70–73%.

The mechanism of the formation of (1,2-dihydroisoquinolin-1-yl)phosphine oxides **51** and **52** can be explained by the nucleophile addition of isoquinoline to dialkyl acetylenedicarboxylates, forming a zwitterion intermediate. Then the products **51** and **52** are formed after the reaction of the intermediate with the *P*-reagent.

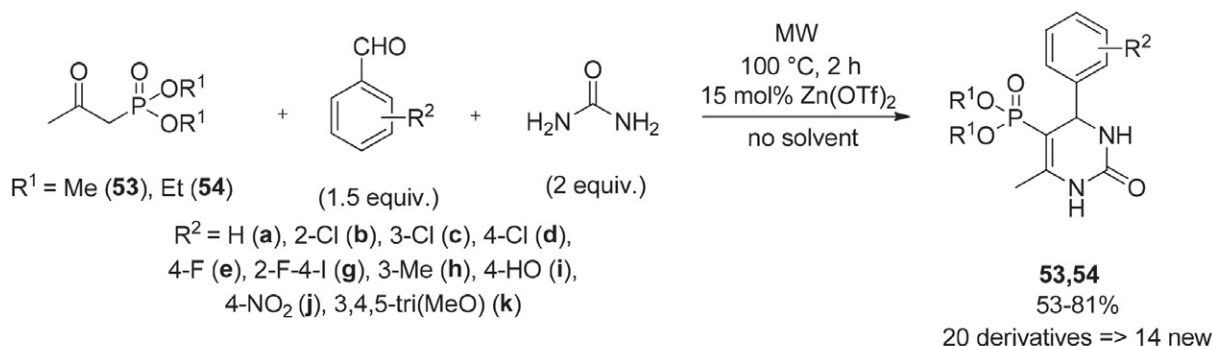
In summary, an efficient, rapid process was developed for the synthesis of (dihydroisoquinoline)phosphine oxides **51** and **52** by the Reissert-type reaction of isoquinoline, dialkyl acetylenedicarboxylates and secondary phosphine oxides or ethyl phenyl-*H*-phosphinate. As compared to the literature, a complete conversion was obtained in shorter reaction time (10 min instead of 1.5–72 h) and in most cases, without the excess (1.1–1.5 equivalents) of isoquinoline and acetylene. In all, 12 dialkyl (*E*)-2-[1-(phosphoryl)isoquinolin-2(1*H*)-yl]maleate derivatives **51** and **52** were synthesized, among them 11 compounds were new.

2. 5. Synthesis of (Dihydropyrimidinone) phosphonates

Only a few examples can be found in the literature for the Biginelli reaction of β -ketophosphonates, aldehydes and urea. In one example, the condensation was

performed in the presence of 15 mol% of zinc triflate (Zn(OTf)₂) in toluene, at high temperature (110 °C) for 3 h.⁴⁰ In another case, 50 mol% of *p*-toluenesulfonic acid (PTSA) was used as a catalyst in boiling acetonitrile for longer reaction time (24 h).⁷⁵ Finally, the condensation was performed with ytterbium triflate (Yb(OTf)₃) in toluene, at reflux temperature for 12 h.⁷⁶ In all cases, urea was used in excess. Based on the literature data, the Biginelli reaction of β -ketophosphonates does not take place starting from aliphatic aldehydes.

The Biginelli reaction of diethyl (2-oxopropyl)phosphonate, benzaldehyde and urea was studied by us.⁷⁷ The conditions (heating mode, temperature, reaction time, molar ratio of the starting materials, catalyst and solvent) were changed to maximize the conversion. Based on our results, a new solvent-free MW-assisted method was developed for the synthesis of (dihydropyrimidinone) phosphonates **53–57** by the Zn(OTf)₂-catalyzed Biginelli reaction. During optimization it was found that besides starting materials and the desired (dihydropyrimidinone) phosphonate **53a**, a by-product containing a styryl group at position six was also in the reaction mixture, which could be formed by the aldol condensation of the product **53a** and benzaldehyde. The optimal parameters for the MW-assisted synthesis of (dihydropyrimidinone) phosphonates were applying 1.5 equiv. of benzaldehyde and 2 equiv. of urea, in the presence of 15 mol% of Zn(OTf)₂ at 100 °C for 2 h. After that, the condensation was carried out with different β -ketophosphonates (dimethyl or diethyl (2-oxopropyl)phosphonate), substituted benzaldehydes (benzaldehyde, 2-chlorobenzaldehyde, 3-chlorobenzaldehyde, 4-chlorobenzaldehyde, 4-fluorobenzaldehyde, 2-fluoro-4-iodobenzaldehyde, 3-methylbenzaldehyde, 4-hydroxybenzaldehyde, 4-nitrobenzaldehyde, 3,4,5-trimethoxybenzaldehyde) and urea derivatives (urea or *N*-methylurea) (Scheme 8). In all 20 (dihydropyrimidinone)phosphonates **53** and **54** were obtained in yields of 53–81% after column chromatography, and among them, 14 were new derivatives, not yet described in the literature.



Scheme 8. Biginelli reaction of β -ketophosphonates, substituted benzaldehydes and urea

Starting from *N*-methylurea, dimethyl or diethyl (2-oxopropyl)phosphonate and benzaldehyde, further two new compounds were prepared in slightly lower yields (Scheme 9).

In contrast with the literature procedures, our method was also suitable when using aliphatic aldehydes in the Biginelli reaction of β -ketophosphonates (Scheme 10). The condensation of dimethyl or diethyl (2-oxopropyl)phosphonate, butyraldehyde or isovaleraldehyde and urea was accomplished successfully, and further four new compounds **56** and **57** were isolated in yields of 41–43%.

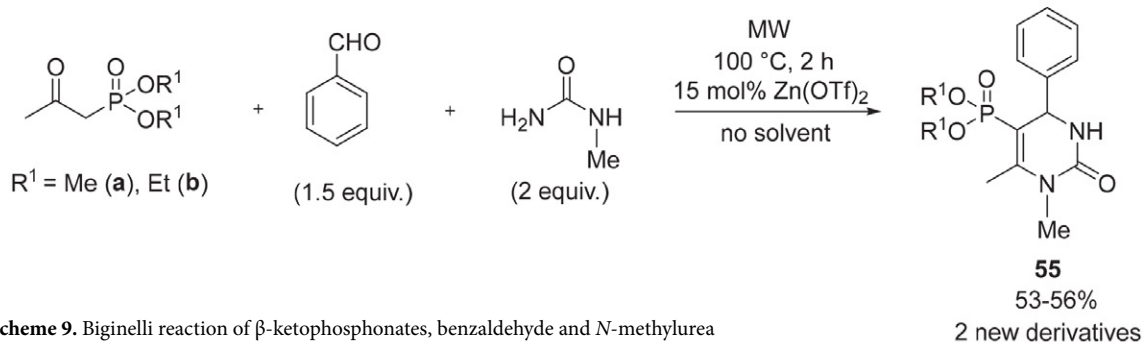
In conclusion, a new solvent-free MW-assisted process was elaborated for the preparation of (3,4-dihydropyrimidin-2-(1*H*)-one)phosphonates **53–57** by the Biginelli reaction of β -ketophosphonates, substituted benzaldehydes and urea derivatives. As compared to the literature examples, the desired compounds **53–57** could be obtained in shorter reaction time (2 h instead of 3–24

h) without solvent. The condensation was also successfully performed starting from aliphatic aldehydes. In our research work, a molecular library of 26 (dihydropyrimidinone)phosphonate derivatives **53–57** was created, of which 20 compounds were new.

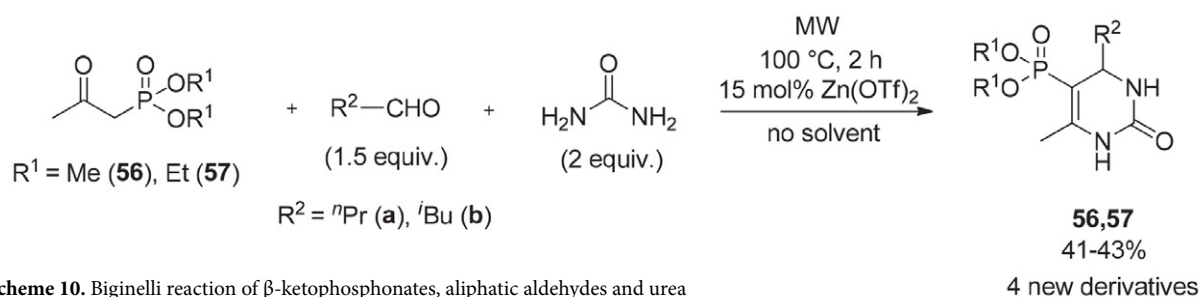
2. 6. Synthesis of (1,2,3-Triazol-5-yl) phosphonates

In the literature, the 1,3-dipolar cycloaddition of azides and alkynyl phosphonates is the most common way for the synthesis of (1,2,3-triazol-5-yl)phosphonates, however, in most cases, the reaction was not selective, since (1,2,3-triazol-4-yl)phosphonates were also obtained besides (1,2,3-triazol-5-yl)phosphonates.

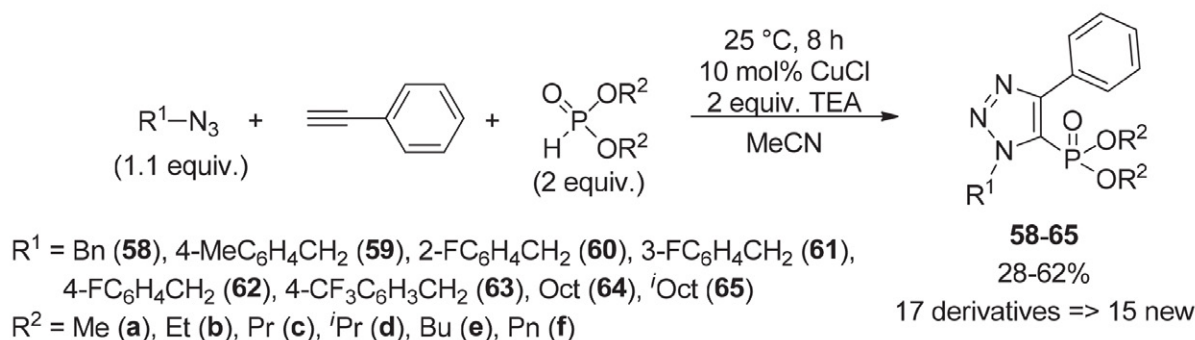
In three cases, the reactions were carried out in the absence of any catalyst, in different solvents, such as toluene,⁷⁸ diethyl ether⁷⁹ or water.⁸⁰ In refluxing toluene, the cy-



Scheme 9. Biginelli reaction of β -ketophosphonates, benzaldehyde and *N*-methylurea



Scheme 10. Biginelli reaction of β -ketophosphonates, aliphatic aldehydes and urea



Scheme 11. Synthesis of (1,2,3-triazol-5-yl)phosphonates **58–65** by CuCl-catalyzed domino reaction

click reaction of benzyl azide and diethyl ethynylphosphonate derivatives was performed applying copper(II) sulfate pentahydrate ($\text{CuSO}_4 \cdot 5\text{H}_2\text{O}$) and sodium ascorbate as a catalyst in DMF at $170\text{ }^\circ\text{C}$ for 12 h.⁸¹ The desired (1,2,3-triazol-5-yl)phosphonates were formed selectively, and were obtained in good to high yields (83–92%). Finally, a MW-assisted solvent- and catalyst-free method was also published, where the ratio of the (1,2,3-triazol-4-yl)phosphonate and the (1,2,3-triazol-5-yl)phosphonate derivative was 34:66.⁸²

In the literature, there is only one example regarding the domino synthesis of (1,2,3-triazol-5-yl)phosphonates.⁸³ The condensation of azides, terminal alkynes, and various dialkyl phosphites was performed using CuCl as a catalyst in acetonitrile at room temperature for 20 h under air atmosphere.

In our work, the synthesis of (1,2,3-triazol-5-yl)phosphonates **58–65** was optimized through the three-component reaction of phenylacetylene, benzyl azide and dibutyl phosphite in respect of the catalyst, base, solvent, molar ratio of the starting materials, atmosphere, temperature, as well as the reaction time.⁸⁴ The best result was obtained using 1.1 equiv. of the azide derivative, 2 equiv. of dialkyl phosphite in the presence of 10 mol% of CuCl and 2 equiv. of triethylamine (TEA) in acetonitrile at room temperature after 8 h, using continuous air bubbling. During the optimization, the reaction mixtures contained two triazole derivatives. One of them was the desired (1,2,3-triazol-5-yl)phosphonate and the other compound was the product of the click reaction of phenylacetylene and benzyl azide.

After the optimization, the CuCl-catalyzed domino reaction of phenylacetylene, benzyl azide and dibutyl

phosphite was extended to various benzyl azides (benzyl-, 4-methylbenzyl-, 2-fluorobenzyl-, 3-fluorobenzyl-, 4-fluorobenzyl- or 4-(trifluoromethyl)benzyl azide) and dialkyl phosphites (dimethyl-, diethyl-, dipropyl-, diisopropyl-, dibutyl- or dipentyl phosphite) (Scheme 11). After column chromatography, 13 (1,2,3-triazol-5-yl)phosphonate derivatives **58–63** were obtained in yields of 30–62%, of which 11 were new compounds.

Next, the domino reaction was also carried out starting from aliphatic azides (octyl or isooctyl azide), phenylacetylene and different dialkyl phosphites (dimethyl-, diethyl- or dibutyl phosphite) under the optimized conditions (with 10 mol% of CuCl and 2 equiv. of TEA at room temperature for 8 h, in acetonitrile). Further four new (1,2,3-triazol-5-yl)phosphonates **64** and **65** were synthesized in yields of 58% and 28%, respectively.

The synthesis of (1,2,3-triazol-5-yl)phosphonates **58–65** was efficiently performed by the three-component domino reaction of phenylacetylene, various azides and dialkyl phosphites in the presence of CuCl and TEA. In all, 17 (1,2,3-triazol-5-yl)phosphonate **58–65** derivatives were synthesized in good yields, among them 15 were new compounds.

2.7. Synthesis of [(1,2,3-Triazol-4-yl)methyl]phosphinates and [(1,2,3-Triazol-4-yl)methyl]phosphates

The synthesis of (1,2,3-triazol-4-yl)phosphonates can be performed by the Cu(I)-catalyzed 1,3-dipolar (Huisgen) cycloaddition—also known as the click reaction—of azides and phosphorylated alkynes.^{85,86}

By the click reaction of benzyl azide and ethyl ethynylphosphonate, 1,2,3-triazol-4-ylphosphonate and 1,2,3-triazol-5-ylphosphonate were synthesized without catalyst in toluene at reflux temperature.⁸⁷ In two cases, triazoles containing bisphosphonate unit were obtained by the 1,3-dipolar cycloaddition of organic azides and propargyl-substituted bisphosphonates at room temperature after long reaction times (24–68 h).^{88,89} In one case, the reaction was carried out in the presence of copper iodide (CuI) as a catalyst and *N,N*-diisopropylethylamine

(DIPEA) as a base, in THF.⁸⁸ In another example, $\text{CuSO}_4 \cdot 5 \text{H}_2\text{O}$ and sodium ascorbate was used as a catalyst, and the solvent was the mixture of *tert*-butyl alcohol and water.⁸⁹ The click reaction of azides and ethynyl- or propargyl-substituted phosphonates was carried out with $\text{CuSO}_4 \cdot 5 \text{H}_2\text{O}$ and sodium ascorbate and $\alpha\text{-CF}_3\text{-}\alpha\text{-aminophosphonates}$ containing triazole unit were formed in yields of 38–92%.⁹⁰ A triazole-functionalized phosphate flame-retardant monomer was synthesized by the cycloaddition of 2-azidoethanol and triprop-2-ynyl phosphate at 85 °C for 12 h in toluene.⁹¹

In our research work, we aimed at the study of the Cu(I)-catalyzed click reaction of propynyl phosphinates, propynyl phosphates—which were prepared by esterification of the corresponding phosphinic acid—and organic azides.⁹² At first, the parameters (heating mode, temperature, reaction time and load of the catalyst) of the click reaction of benzyl azide and prop-2-ynyl diphenylphosphinate were investigated in the presence of $\text{CuSO}_4 \cdot 5 \text{H}_2\text{O}$ and sodium ascorbate in the mixture of *tert*-butyl alcohol and water (4:1). The optimal conditions were 3 mol% of $\text{CuSO}_4 \cdot 5 \text{H}_2\text{O}$, 5 mol% of sodium ascorbate and 60 °C for 10 min. In the next step, the cycloaddition of benzyl-, 4-methylbenzyl-, 2-fluorobenzyl-, 3-fluorobenzyl-, 4-fluorobenzyl- or 4-(trifluoromethyl)benzyl-, octyl-, isooctyl-, cyclohexyl- or phenyl azide and prop-2-ynyl diphenylphosphinate were performed, and 10 new (1,2,3-triazol-4-yl)methyl diphenylphosphinate derivatives **66a–j** were isolated in yields of 63–91% (Scheme 12).

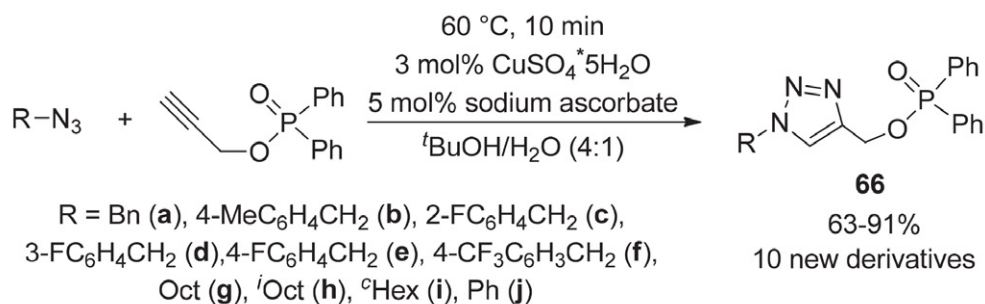
Carrying out the click reaction of azides mentioned above with diethyl prop-2-ynyl phosphate, the conversion was not complete under the optimized conditions found earlier (60 °C, after 10 min) (Scheme 13). In this case, a slightly longer reaction time (30 min) had to be used. In all, 10 new (1*H*-1,2,3-triazol-4-yl)methyl diethyl phosphates **67a–j** were synthesized in yields of 51–75%.

To sum up, a simple, fast and efficient method was developed for the synthesis of (1*H*-1,2,3-triazol-4-yl)methyl phosphinates **66a–j** and (1*H*-1,2,3-triazol-4-yl)methyl diethyl phosphates **67a–j** by the cycloaddition of azides and prop-2-ynyl phosphinate or diethyl prop-2-ynyl phosphate. The target compounds were prepared in the presence of $\text{CuSO}_4 \cdot 5 \text{H}_2\text{O}$ and sodium ascorbate under mild conditions (60 °C) after short reaction times (10–30 min). In all, 20 novel derivatives **66** and **67** were synthesized.

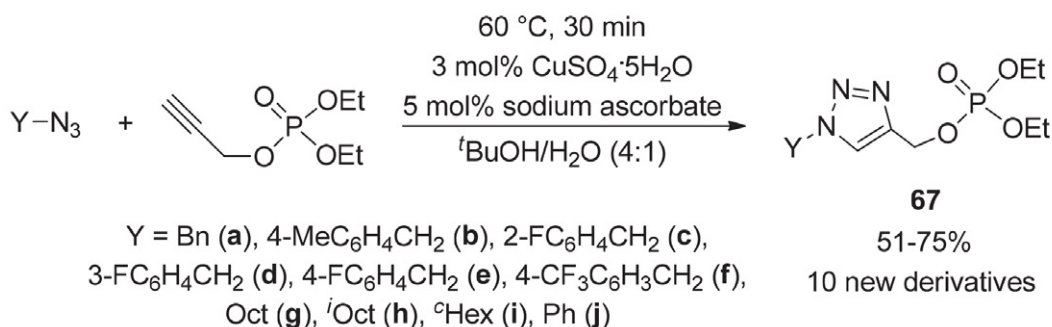
3. Synthesis of O-Heterocycles

3. 1. Synthesis of (2-Amino-3-cyano-4*H*-chromen-4-yl)phosphonates and -phosphine Oxides

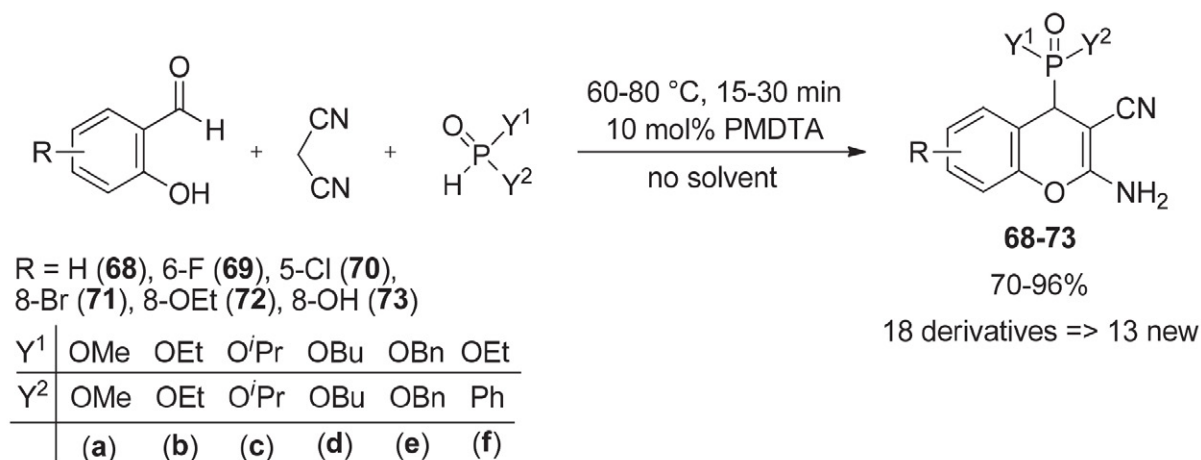
A few publications can be found for the three-component synthesis of (2-amino-3-cyano-4*H*-chromen-4-yl) phosphonates starting from salicylaldehydes, malononitrile and dialkyl phosphites or trialkyl phosphites. In most



Scheme 12. Synthesis of (1,2,3-triazol-4-yl)methyl diphenylphosphinates **66a–j** by click reaction



Scheme 13. Synthesis of (1,2,3-triazol-4-yl)methyl diethyl phosphates **67a–j** by click reaction



Scheme 14. PMDTA-catalyzed reaction of salicylaldehydes, malononitrile and dialkyl phosphites

cases, the reactions were performed in the presence of a basic catalyst and solvent. The condensations were carried out with diethylamine,⁹³ dibutylamine,⁴³ triethylamine,⁹⁴ dimethylaminopyridine,⁹⁵ imidazole,⁹⁶ ethylenediamine diacetate,⁹⁷ lithium hydroxide,⁹⁶ potassium phosphate,⁹⁸ magnesium oxide⁹⁹ or indium chloride¹⁰⁰ in ethanol, or with iron oxide,¹⁰¹ iodine⁴² or β -cyclodextrin¹⁰² in water. A few examples can be found for the use of special solvents, such as polyethylene glycol,¹⁰³ ionic liquids¹⁰⁴ or the mixture of urea and choline chloride.¹⁰⁵ In four cases, the reactions were carried out without solvents, however, special catalysts (silica-bonded 2-HEAA-3 catalyst,¹⁰⁶ ZnO nano-rods,¹⁰⁷ iodine¹⁰⁸) or a simple catalyst in a large excess (3.5 equiv. of tetramethylguanidine)¹⁰⁹ were needed. In the literature, there is no example for the condensation

of salicylaldehydes, malononitrile and secondary phosphine oxides.

The condensation of salicylaldehydes, malononitrile and dialkyl phosphites was studied through a model reaction.¹¹⁰ The effect of various basic catalysts, solvent, temperature and reaction time was investigated. Based on our results, pentamethyldiethylenetriamine (PMDTA) was the most effective among the bases. A complete conversion was achieved with 10 mol% PMDTA in the absence of any solvent at 60–80 °C after 15–30 min (Scheme 14). A total of 18 (2-amino-3-cyano-4*H*-chromen-4-yl)phosphonate derivatives **68–73** were synthesized in yields of 70–96%, of which 13 were new compounds. The products were isolated from the reaction mixture by a simple filtration. Starting from ethyl phenyl-*H*-phosphinate as the phosphorus

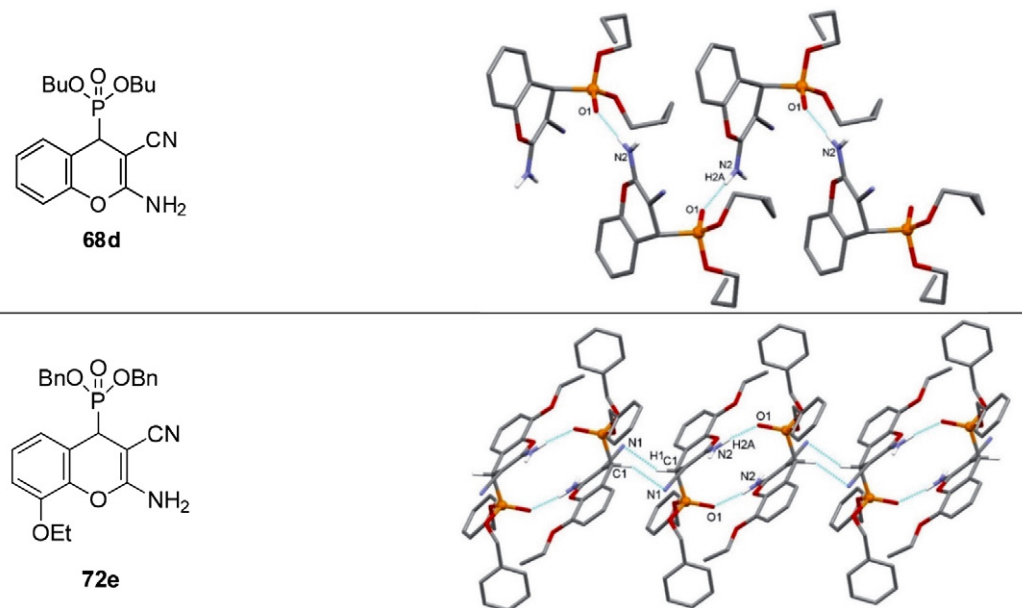
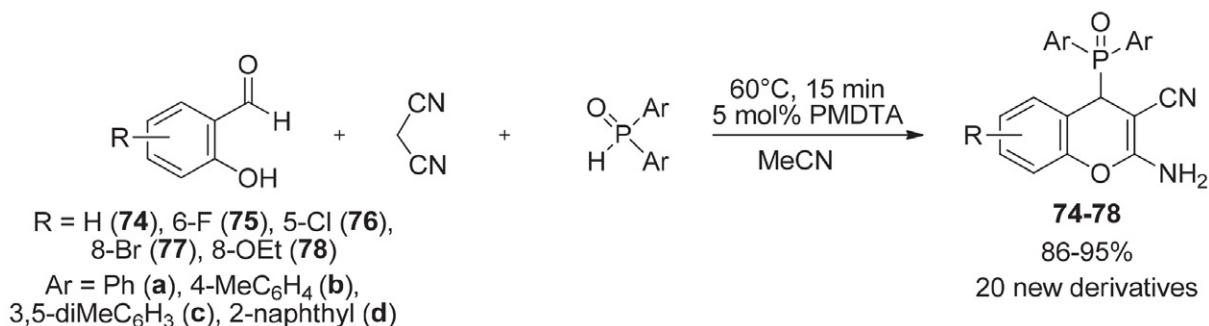


Figure 5. The crystal structure of **68d** and **72e** (2-amino-3-cyano-4*H*-chromen-4-yl)phosphonates



Scheme 15. PMDTA-catalyzed reaction of salicylaldehydes, malononitrile and secondary phosphine oxides

reagent, the desired (aminochromenyl)phosphinate **68f** was obtained in a yield of 86%, as a mixture of diastereomers in a ratio of 1:1.

The crystal structures of dibutyl (2-amino-3-cyano-4*H*-chromen-4-yl)phosphonate (**68d**) and dibenzyl

(2-amino-3-cyano-8-ethoxy-4*H*-chromen-4-yl)phosphonate (**72e**) were determined by X-ray diffraction (XRD), as well (Figure 5). In both derivatives (**68d** and **72e**), an intermolecular N–H...O=P hydrogen bonding between the amino group and the phosphonate oxygen atom was

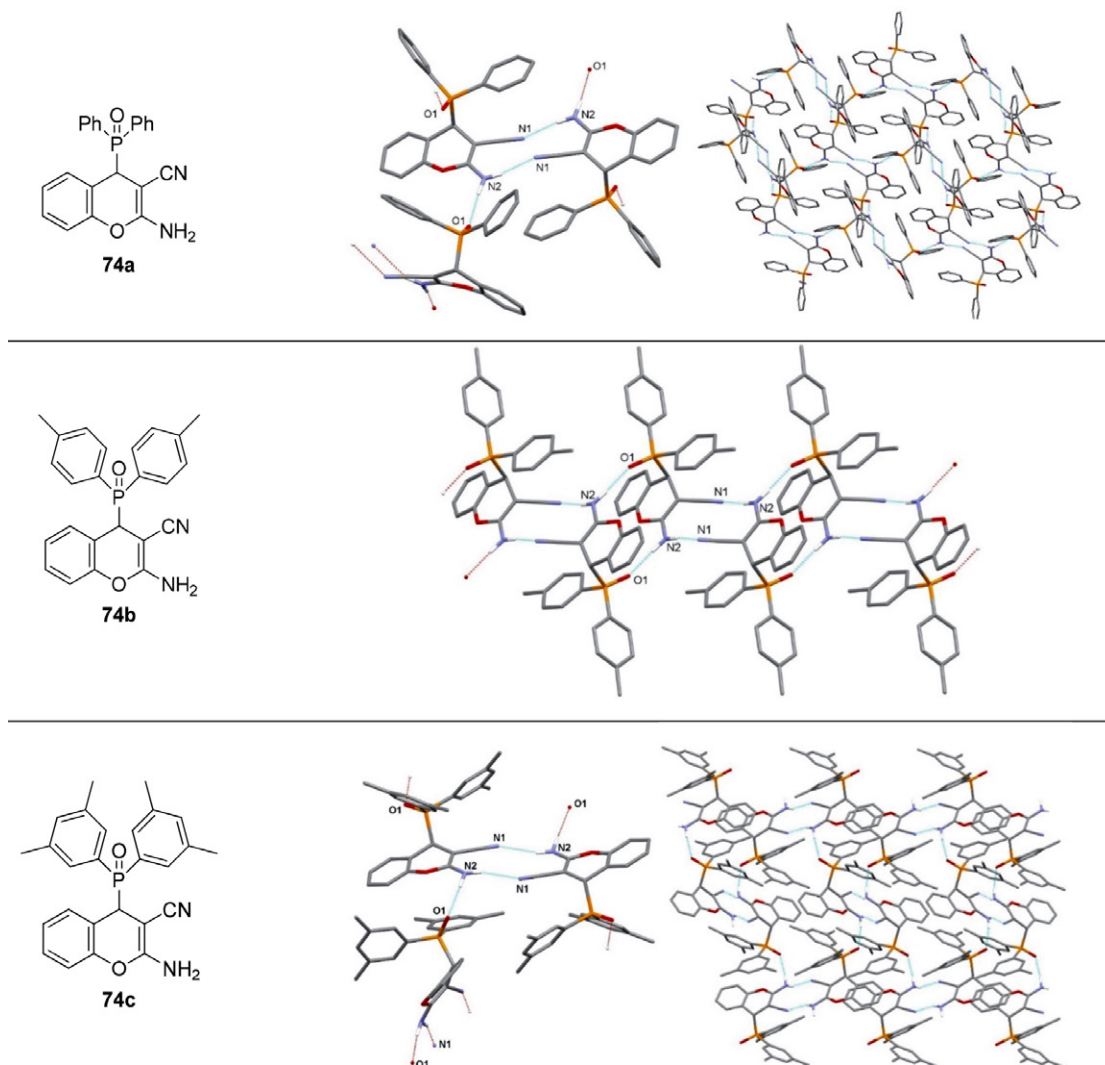


Figure 6. The crystal structure of **74a–c** (2-amino-3-cyano-4*H*-chromen-4-yl)phosphine oxides

found. However, the amino group as a hydrogen bond donor was observed to be involved in the formation of two interactions in the case of the butyl ester (**68d**). The other interaction was a centrosymmetric N–H...N hydrogen bond with the cyano group. Due to these interactions, hydrogen-bonded layers were formed. In the benzyl ester (**72e**), besides the centrosymmetric N–H...O=P interactions, centrosymmetric C–H...N interactions between the chromenyl ring and the cyano group of two adjacent molecules are present, resulting in the hydrogen-bonded chain.

According to the proposed mechanism of the formation of (2-amino-3-cyano-4*H*-chromen-4-yl)phosphonates **68–73**, at first, the Knoevenagel condensation of the salicylaldehyde and malononitrile takes place. Next, iminocoumarine is formed by the intramolecular Pinner-like reaction from the 2-(2-hydroxybenzylidene)malononitrile intermediate. Finally, the phospho-Michael addition of dialkyl phosphites leads to (2-amino-3-cyano-4*H*-chromen-4-yl)phosphonates **68–73**.

The PMDTA-catalyzed condensation of salicylaldehydes (salicylaldehyde or 5-fluoro-, 2-chloro-, 3-bromo-, or 3-ethoxysalicylaldehyde), malononitrile and *P*-reagents was extended to secondary phosphine oxides (such as diphenyl-, bis(*p*-tolyl)-, bis(3,5-dimethylphenyl)- or bis(2-naphthyl)phosphine oxides), as well. A new family of compounds, (2-amino-3-cyano-4*H*-chromen-4-yl)phosphine oxides **74–78** were formed with 5 mol% PMDTA at 60 °C after 15 min, in acetonitrile (Scheme 15). In our work, 20 new (aminochrome-nyl)phosphine oxides **74–78** were synthesized in excellent (86–95%) yields.

Single crystals were also grown from three derivatives **74a–c** in acetonitrile and their structures were investigated by XRD (Figure 6). Based on our results, an intermolecular N–H...O=P hydrogen bond is formed between the amino group and the phosphine oxide side chain. Furthermore, the amino group is involved in a centrosymmetric N–H...N interaction with the cyano group of the adjacent molecule. In the case of (diphenyl) (2-amino-3-cyano-4*H*-chromen-4-yl)phosphine oxide

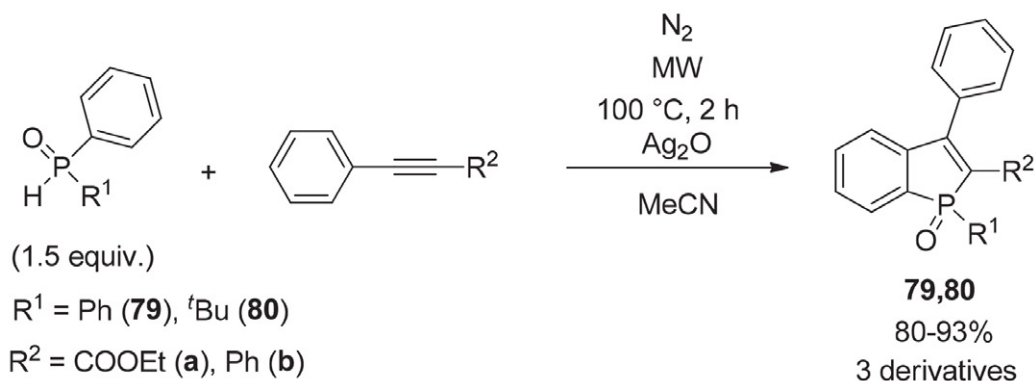
(**74a**) and [bis(3,5-dimethylphenyl)](2-amino-3-cyano-4*H*-chromen-4-yl)phosphine oxide (**74c**), N–H...O=P interactions lead to the formation of layers. A difference can be observed in the crystal structure of [bis(*p*-tolyl)] (2-amino-3-cyano-4*H*-chromen-4-yl)phosphine oxide (**74b**), where a centrosymmetric N–H...N interactions (between the amino and the cyano groups) and centrosymmetric N–H...O=P hydrogen bonds led to the formation of hydrogen-bonded chains.

Summarizing our results, the model reaction of salicylaldehyde, malononitrile and dialkyl phosphites was studied and optimized. By our solvent-free PMDTA-catalyzed method, 18 (2-amino-3-cyano-4*H*-chromen-4-yl) phosphonate derivatives **68–73** were prepared in good to high yields (70–96%). Our method was also suitable for the domino Knoevenagel-phospho-Michael reaction of secondary phosphine oxides, and 20 new (2-amino-3-cyano-4*H*-chromen-4-yl)phosphine oxides **74–78** were synthesized, which are members of a new family of compounds in the literature.

4. Synthesis of *P*-Heterocycles

4. 1. Synthesis of 1-Alkyl-1*H*-phoshindole-1-oxides and 1-Alkoxy-1*H*-phoshindole-1-oxides

In the literature, phoshindole-1-oxide derivatives were prepared by the intermolecular radical cycloaddition of secondary phosphine oxides or phosphinates and internal alkynes.¹¹¹ In the examples, several oxidizing agents were used, and in general, a long reaction time (8–24 h) was applied to obtain complete conversion, for example: Ag₂O (8–10 h),^{112,113} AgOAc (4–18 h),^{114–116} Mn(OAc)₂/MnO₂ (4 h),¹¹⁷ K₂S₂O₈ (24 h)¹¹⁸ or *N*-etoxy-2-methylpyridinium tetrafluoroborate (48 h).¹¹⁹ In one case, a shorter reaction time of 30 min was enough, however, beside the oxidant (*tert*-butyl hydroperoxide), a catalyst (CuSO₄) and a base (NH₃) were necessary.¹²⁰ Our aim was to find a fast and simple method for the synthesis of phoshindole-1-oxides.



Scheme 16. Cycloaddition of secondary phosphine oxides and ethyl phenylpropiolate or diphenylacetylene

The first step of our work was the study and optimization of the MW-assisted cycloaddition of diphenylphosphine oxide and ethyl phenylpropiolate in respect of the oxidant, temperature and reaction time in acetonitrile as the solvent.¹²¹ It was found that complete conversion could be obtained under MW conditions, applying 1.5 equivalents of diphenylphosphine oxide, 2 equivalents of Ag₂O as the oxidizing agent, at 100 °C for 2 h in acetonitrile (Scheme 16). Using the optimal conditions, the reaction of diphenyl acetylene and diphenylphosphine oxide or *tert*-butyl(phenyl)phosphine oxide was performed. The three benzophosphole oxide derivatives **79a**, **79b** and **80b** were obtained after column chromatography, in yields of 80–93%.

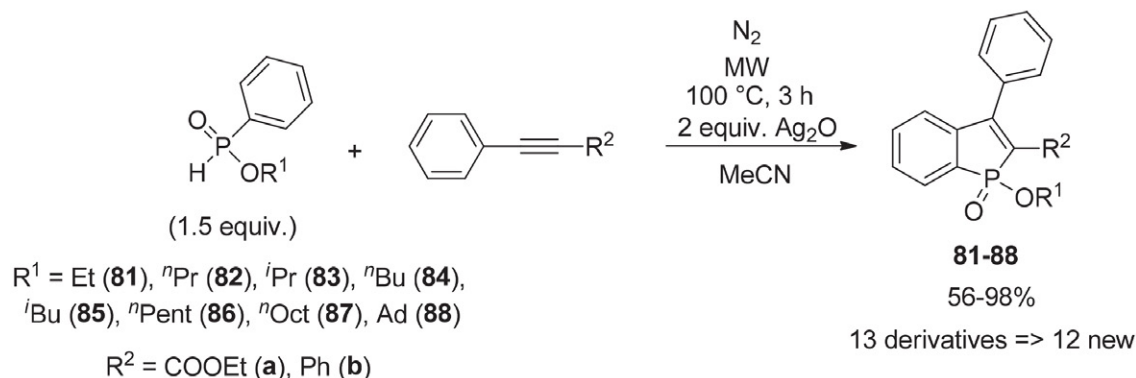
In the next series of experiments, the cycloaddition was extended to alkyl phenyl-*H*-phosphinates and different acetylenes in the presence of Ag₂O (Scheme 17). The MW-assisted reaction of ethyl phenyl-*H*-phosphinate and ethyl phenylpropiolate was optimized in respect of temperature and reaction time. Based on our results, the reaction was complete after a slightly longer (3 h) reaction time as compared to the reactions carried out with secondary phosphine oxides. Then, the cycloaddition was performed starting from further alkyl phenyl-*H*-phosphinates (*n*-propyl-, isopropyl-, *n*-butyl-, isobutyl-, *n*-pentyl-, *n*-octyl- and adamantyl phenyl-*H*-phosphinate) and ethyl phenylpropiolate or diphenyl acetylene. In all, 13 1-alkoxy-1*H*-phosphindole-

1-oxides were synthesized in yields of 56–98%. Slightly lower yields (56–68%) were obtained starting from *n*-pentyl-, *n*-octyl- and adamantyl phenyl-*H*-phosphinate, due to the steric hindrance.

A single crystal was grown of 1-isopropoxy-2,3-diphenylphosphindole 1-oxide (**83b**) and the structure was analyzed by XRD (Figure 8). The analysis showed the formation of hydrogen-bonded wavy layer through two intermolecular C–H...O=P hydrogen bonds between two phenyl rings and the O=P group. The layers formed a 3D network *via* C–H... π interactions between the phenyl groups of adjacent molecules.

In order to investigate the efficiency of our MW-assisted method, two scaled-up reactions were also performed at a “gram-scale”. The condensation of diphenylphosphine oxide or ethyl phenyl-*H*-phosphinate and diphenyl acetylene was carried out on a 25-times-bigger scale. The desired 1,2,3-triphenylphosphindole 1-oxide (**79b**) and 1-ethoxy-2,3-diphenylphosphindole 1-oxide (**81b**) were obtained in yields of 94% and 70%.

To sum up, a MW-assisted, fast (2–3 h instead of 8–24 h) and efficient approach for the synthesis of benzo[*b*]phosphole oxides **79–88** by the oxidative cycloaddition of secondary phosphine oxides or alkyl phenyl-*H*-phosphinates with acetylenes (diphenylacetylene or ethyl phenylpropiolate) was developed. Altogether 16 derivatives **79–88** were prepared, among them 12 were new.



Scheme 17. Condensation of alkyl phenyl-*H*-phosphinate and ethyl phenylpropiolate or diphenylacetylene

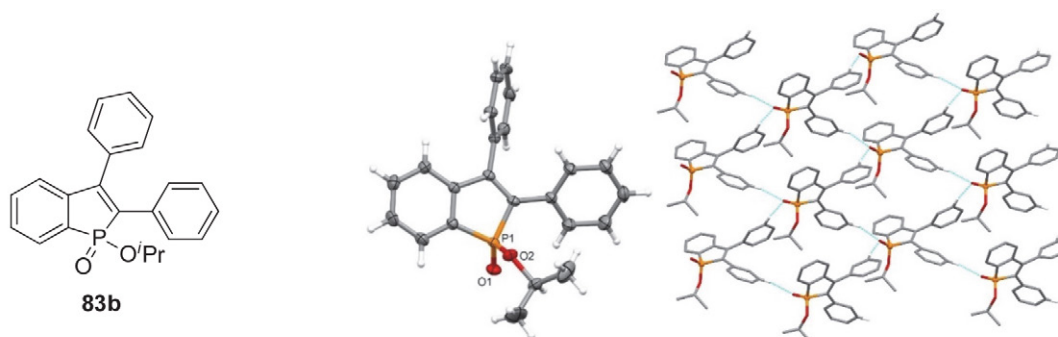


Figure 8. The crystal structure of 1-isopropoxy-2,3-diphenylphosphindole 1-oxide (**83b**)

5. Biological Activity Investigations

The *in vitro* cytotoxicity and antibacterial activity of all compounds synthesized was also investigated. In Table 2 only the most active derivatives are shown.

The cytotoxicity evaluations were performed on three different cell lines, such as human lung adenocarcinoma (A549), mouse fibroblast (NIH/3T3) as healthy cell line and human promyelocytic leukemia (HL-60) using the fluorescent Resazurin assay as described previously.¹²² Positive controls were doxorubicin for A549 and NIH/3T3 ($IC_{50} = 0.31 \pm 0.24 \mu\text{M}$ and $5.65 \pm 0.81 \mu\text{M}$, respectively) and bortezomib for HL60 ($IC_{50} = 7.42 \pm 2.60 \text{ nM}$). The antibacterial activity of the compounds was tested on green fluorescent protein (GFP) producing *Bacillus subtilis* (Gram-positive) and *Escherichia coli* (Gram-negative) bacterial cells. The GFP producing bacteria are effective tools for screening for the antibacterial activity, since the GFP signal measured by fluorimetry is proportional to the number of the bacterial cells. Active compounds kill bacterial cells, which results in the decrease in the GFP fluorescence signal, therefore it is suitable for evaluating the antimicrobial effect of different agents. Positive controls were doxycycline and gentamicin for *Bacillus subtilis* ($IC_{50} = 0.04 \pm 0.01 \mu\text{M}$ and $0.49 \pm 0.14 \mu\text{M}$) and for *Escherichia coli* ($IC_{50} = 0.10 \pm 0.02 \mu\text{M}$ and $4.23 \pm 0.99 \mu\text{M}$) bacterial cells. The IC_{50} values (50% inhibiting concentration) determined are shown in Table 2.

Among (3-oxo-2,3-dihydro-2*H*-isoindol-1-yl)phosphine oxides **23–34**, derivatives containing 3,5-dimethylphenyl- or naphthyl groups on the phosphorus atom showed activity.⁶² The *N*-butyl and *N*-benzyl bis(3,5-dimethylphenyl) (3-oxo-2,3-dihydro-2*H*-isoindol-1-yl) phosphine oxides **23c** and **25c** were slightly active in HL-60 cell line. However, against Grampositive bacteria (*B. subtilis*), the same derivatives (**23c** and **25c**) showed promising activity, as their IC_{50} values ($4.60 \pm 1.13 \mu\text{M}$ and $3.61 \pm 1.25 \mu\text{M}$) were close to the reference value. In the case of bis(2-naphthyl) (2-butyl-3-oxo-2,3-dihydro-2*H*-isoindol-1-yl)-phosphine oxide (**23d**), no antibacterial activity was shown, but against all the three investigated cell lines (A549, NIH/3T3 and HL-60) modest cytotoxicity was observed. The IC_{50} value was the smallest against HL-60 cells ($12.26 \pm 1.02 \mu\text{M}$).

The biological activity of the α -amino-(2-alkynylphenyl)methylphosphonates **37–43** was investigated, as well. According to our results, some butyl esters showed modest activity against HL-60 cells. The IC_{50} value of the chloro (**41**) or the unsubstituted derivatives (**42**) were in the range of 13–15 μM .

The results of the bioactivity tests of the (1,2-dihydroisoquinoline)phosphonates **44–50** also showed that the butyl esters were more active as compared to the other derivatives. Compounds containing methyl (**47**), meth-

oxy (**48**), or chloro group (**49**) on the *para* position of the phenyl group, showed *in vitro* cytotoxicity. The (1,2-dihydroisoquinoline)phosphonate **47** was effective in A549, NIH/3T3 and HL-60 cell lines. In addition, the IC_{50} value was close to the reference against human promyelocytic leukemia cells ($4.36 \pm 1.31 \mu\text{M}$).

The (1,2-dihydroisoquinoline)phosphine oxides containing 3,5-dimethylphenyl (**51c** and **52c**) or naphthyl groups (**51e**) on the phosphorus atom showed *in vitro* cytotoxicity and antibacterial activity.⁷⁴ Dimethyl and diethyl (*E*)-2-[1-[bis(3,5-dimethylphenyl)phosphoryl]isoquinolin-2(1*H*)-yl]maleates (**51c** and **52c**) were slightly active in HL-60 cell line, however the IC_{50} value was closer to the reference in the case of the methyl ester **51c** ($IC_{50} = 4.58 \pm 1.08 \mu\text{M}$ vs. $12.59 \pm 1.18 \mu\text{M}$). Compound **52c** also showed modest activity against *B. subtilis* ($IC_{50} = 9.06 \pm 1.01 \mu\text{M}$). Among the (1,2-dihydroisoquinoline)phosphine oxides, dimethyl (*E*)-2-[1-[di(naphthalen-2-yl)phosphoryl]isoquinolin-2(1*H*)-yl]maleate (**51e**) had the most significant *in vitro* cytotoxicity against HL-60 cells ($IC_{50} = 3.58 \pm 1.16 \text{ mM}$).

Based on the IC_{50} values of (1,2,3-triazolyl)phosphonates, some derivatives were active against HL-60 cells.⁸⁴ The dimethyl [1-(4-methylbenzyl)-4-phenyl-1,2,3-triazol-5-yl]phosphonate (**59a**), dipropyl (1-benzyl-4-phenyl-1,2,3-triazol-5-yl)phosphonate (**58c**), dibutyl [1-(2-fluorobenzyl)-4-phenyl-1,2,3-triazol-5-yl]phosphonate (**60e**) and dibutyl [1-(4-trifluoromethyl)-4-phenyl-1,2,3-triazol-5-yl]phosphonate (**62e**) showed activity in the range of 9–13 μM .

Among chromenylphosphonates, the dibenzyl (2-amino-3-cyano-4*H*-chromen-4-yl)phosphonates **68e**, **69e**, **70e**, **71e** and **72e** were the best candidates.¹¹⁰ The anti-cancer activity in NIH/3T3 cell line was close to the reference in the case of the unsubstituted (**68e**) or the 8-bromo derivatives (**71e**) ($IC_{50} = 8.73 \pm 1.17 \mu\text{M}$ or $9.33 \pm 1.18 \mu\text{M}$, respectively). In addition, all benzyl esters synthesized (**68e**, **69e**, **70e**, **71e** and **72e**) showed good or moderate activities against HL-60 cells. The IC_{50} value obtained was the smallest in the case of the 6-fluoro (**69e**) or 8-bromo (**71e**) substituted (2-amino-3-cyano-4*H*-chromen-4-yl) phosphonates ($IC_{50} = 3.62 \pm 1.38 \mu\text{M}$ or $4.79 \pm 1.08 \mu\text{M}$, respectively).

The biological activity investigations showed that the [bis(3,5-dimethylphenyl)](2-amino-3-cyano-4*H*-chromen-4-yl)phosphine oxides were effective against human promyelocytic leukemia cells and Gram-positive bacteria.¹¹⁰ The IC_{50} values of the 6-fluoro (**69e**) and 8-bromo derivatives (**71e**) were in the range of 10 μM in HL-60 cell line. The growth of *B. subtilis* was reduced the most by the unsubstituted, 6-fluoro and 5-chloro [bis(3,5-dimethylphenyl)](2-amino-3-cyano-4*H*-chromen-4-yl)phosphine oxides (**74c**, **75c** and **76c**) ($IC_{50} = 8.92 \pm 1.21 \mu\text{M}$, $5.03 \pm 1.28 \mu\text{M}$ and $5.29 \pm 1.38 \mu\text{M}$, respectively).

Table 2. *In vitro* cytotoxicity and antibacterial activity of the compounds synthesized.^a

Compound	R ¹	R ²	In vitro Cytotoxicity]			Antibacterial Activity	
			A549	[IC ₅₀ , μM NIH/3T3	HL-60	IC ₅₀ , μM] <i>B. subtilis</i>	<i>E. coli</i>
	3,5-diMeC ₆ H ₃	ⁿ Bu (23c)	>30	>30	17.55±1.70	4.60±1.13	>10
	3,5-diMeC ₆ H ₃	Bn (25c)	>30	>30	18.31±1.33	3.61±1.25	>10
	2-naphthyl	ⁿ Bu (23d)	28.2±1.05	25.94±1.06	12.26±1.02	>10	>10
	Bu	Cl (41)	>30	>30	13.66±1.08	>10	>10
	Bu	H (42)	>30	>30	15.09±1.17	>10	>10
	F	Me (47)	11.64±1.11	14.17±1.38	4.36±1.31	>10	>10
	H	OMe (48)	>30	>30	13.16±1.22	>10	>10
	H	Cl (49)	>30	13.58±1.09	13.33±1.14	>10	>10
	3,5-diMeC ₆ H ₃	Me (51c)	>30	>30	4.58±1.08	>10	>10
	3,5-diMeC ₆ H ₃	Et (52c)	>30	>30	12.59±1.18	9.06±1.01	>10
	2-naphthyl	Me (51e)	>30	>30	3.58±1.16	>10	>10
	Me	4-MeC ₆ H ₄ CH ₂ (59a)	>30	19.8±1.2	11.0±1.2	>10	>10
	ⁿ Pr	Bn (58c)	>30	>30	12.6±1.7	>10	>10
	ⁿ Bu	2-FC ₆ H ₄ CH ₂ (60e)	>30	27.5±1.1	11.7±1.2	>10	>10
	ⁿ Bu	4-CF ₃ C ₆ H ₄ CH ₂ (62e)	>30	23.1±1.2	9.7±1.1	>10	>10
	OBn	H (68e)	26.46±1.02	8.73±1.17	6.25±1.06	>10	>10
	OBn	6-F (69e)	>30	21.2±1.71	3.62±1.38	>10	>10
	OBn	5-Cl (70e)	>30	23.49±1.09	7.51±1.02	>10	>10
	OBn	8-Br (71e)	28.65±1.22	9.33±1.18	4.79±1.08	>10	>10
	OBn	8-OEt (72e)	>30	27.99±1.06	14.37±1.24	>10	>10
	3,5-diMeC ₆ H ₃	H (74c)	>30	>30	>30	8.92±1.21	>10
	3,5-diMeC ₆ H ₃	6-F (75c)	>30	>30	10.06±1.25	5.03±1.28	>10
	3,5-diMeC ₆ H ₃	5-Cl (76c)	>30	>30	>30	5.29±1.38	>10
	3,5-diMeC ₆ H ₃	8-Br (77c)	>30	>30	9.80±1.33	>10	>10
	Doxorubicin		0.31±0.24	5.65±0.81	–	–	–
	Bortezomib		–	–	7.42×10 ⁻³ ± 2.60×10 ⁻³	–	–
	Doxycycline		–	–	–	0.126±0.029	0.10±0.02
	Gentamicin		–	–	–	0.115±0.001	4.23±0.99

^a Data were expressed as mean ± standard deviation.

Summarizing the results of the biological activity investigations, heterocyclic phosphonates (butyl, benzyl) or phosphine oxides (3,5-dimethylphenyl, naphthyl) containing larger groups on the phosphorus atom showed promising activity against human promyelocytic leukemia (HL-60) cells and *B. subtilis* Gram-positive bacteria.

6. Conclusions

In conclusion, the multicomponent synthesis of the target *N*- and *O*-heterocycles containing a phosphonate or a phosphine oxide moiety and the synthesis of *P*-heterocyclic derivatives was elaborated successfully. The procedures developed are more effective and accept-

able according to the principles of “green chemistry” as compared to the literature data. Altogether more than 150 derivatives were synthesized and fully characterized, and most of them were new compounds. According to the biological activity investigations, it was found that in the case of phosphonates butyl- and benzyl esters of α -amino-(2-alkynylphenyl)-methylphosphonates, (1,2-dihydroisoquinolyl)phosphonates, (1,2,3-triazol-5-yl)phosphonates and (aminochromenyl)phosphonates were effective, however, from among phosphine oxides, those derivatives showed promising antibacterial and/or anticancer effects, which contained large groups (3,5-dimethylphenyl or 2-naphtyl) on the phosphorus atom, especially (oxoisindolyl)phosphine oxides, (1,2-dihydroisoquinolyl)phosphine oxides, and (aminochromenyl)phosphine oxides.

The development of highly convergent syntheses is an ongoing evergreen of heterocyclic chemistry. Multicomponent reactions are significant for this diversity-oriented chemistry, they are an excellent tool for exploring the chemical molecular space. Multicomponent chemistry is now more active than ever, and new approaches are being developed every day to address the challenges of contemporary organic chemistry.

Acknowledgement

This research was funded by the Hungarian Research Development and Innovation Office (FK123961) and was supported by the Servier-Beregi PhD Research Fellowship.

7. References

1. W. Jieping, Zhu, Qian, Wang, Mei-Xiang, *Multicomponent Reactions in Organic Synthesis*, Wiley-VCH, Weinheim, **2014**.
2. S. E. John, S. Gulati, N. Shankaraiah, *Org. Chem. Front.* **2021**, 8, 4237–4287. DOI:10.1039/D0QO01480J
3. E. Ruijter, R. Scheffelaar, R. V. A. Orru, *Angew. Chemie* **2011**, 50, 6234–6246. DOI:10.1002/anie.201006515
4. R. C. Cioc, E. Ruijter, R. V. A. Orru, *Green Chem.* **2014**, 16, 2958–2975. DOI:10.1039/C4GC00013G
5. E. Schaumann, M. J. Arévalo, M. Ayaz, L. Banfi, A. Basso, L. Bernardi, F. Berrée, B. Carboni, V. A. Chebanov, F. De Moliner, A. Dömling, N. Yu. Gorobets, Y. Huang, C. Hulme, G. N. Kaluđerović, R. Lavilla, E. Le Gall, G. Lemanski, C.-J. Li, E. D. Matveeva, A. Mayence, R. S. Menon, G. A. Morales, M. C. Morejon, T. J. J. Müller, V. Nair, R. A. W. Neves Filho, A. Ricci, R. Riva, Y. V. Sedash, M. V. Shuvalov, J. J. Vanden Eynde, L. A. Wessjohann, W.-J. Yoo, N. S. Zefirov, L. Zhao, T. Ziegler, *Multicomponent Reactions, Volume 1*, Georg Thieme Verlag, Stuttgart, **2014**.
6. S. Zhi, X. Ma, W. Zhang, *Org. Biomol. Chem.* **2019**, 17, 7632–7650. DOI:10.1039/C9OB00772E
7. C. Lambruschini, L. Moni, A. Basso, in *Multicomponent React. Toward Heterocycles Concepts Appl.* (Eds.: E. van der Eycken, U.K. Sharma), Wiley-VCH, Weinheim, **2021**, p. 211. DOI:10.1002/9783527832439.ch6
8. V. G. Nenajdenko, *Russ. Chem. Rev.* **2020**, 89, 1274–1336. DOI:10.1070/RCR5010
9. B. H. Rotstein, S. Zaretsky, V. Rai, A. K. Yudin, *Chem. Rev.* **2014**, 114, 8323–8359. DOI:10.1021/cr400615v
10. H. Malinakova, *Reports Org. Chem.* **2015**, 5, 75–90. DOI:10.2147/ROC.S65115
11. C. E. Arcadia, E. Kennedy, J. Geiser, A. Dombroski, K. Oakley, S.-L. Chen, L. Sprague, M. Ozmen, J. Sello, P. M. Weber, S. Reda, C. Rose, E. Kim, B. M. Rubenstein, J. K. Rosenstein, *Nat. Commun.* **2020**, 11, 691–699. DOI:10.1038/s41467-020-14455-1
12. K. L. Ameta, D. Anshu, *Multicomponent Reactions: Synthesis of Bioactive Heterocycles*, CRC Press, Boca Raton, **2017**. DOI:10.1201/9781315369754
13. J. A. T. Louis D. Quin, *Fundamentals of Heterocyclic Chemistry: Importance in Nature and in the Synthesis of Pharmaceuticals*, Wiley, Weinheim, **2010**.
14. N. Kerru, L. Gummidi, S. Maddila, K. K. Gangu, S. B. Jonnalagadda, *Molecules* **2020**, 25, 1909–1951. DOI:10.3390/molecules25081909
15. M. M. Heravi, V. Zadsirjan, *RSC Adv.* **2020**, 10, 44247–44311. DOI:10.1039/D0RA09198G
16. J. Zhou, in *Vol. 7 O-Heterocycles Aromat.*, De Gruyter, **2019**, pp. 1–80.
17. P. Levy, Daniel E., Fügedi, Ed., *The Organic Chemistry of Sugars*, CRC Press, Boca Raton, **2005**. DOI:10.1201/9781420027952
18. E. Vitaku, D. T. Smith, J. T. Njardarson, *J. Med. Chem.* **2014**, 57, 10257–10274. DOI:10.1021/jm501100b
19. M. Asif, *Int. J. Bioorg. Chem.* **2017**, 2, 146–152.
20. S. Arunkumar, *Int. J. PharmTech Res.* **2015**, 8, 170–179.
21. P. Singh, O. Silakari, *ChemMedChem* **2018**, 13, 1071–1087. DOI:10.1002/cmdc.201800119
22. V. Hillemane, N. Anil, in *Heterocycles - Synth. Biol. Act.*, IntechOpen, **2019**.
23. M. Haji, *Beilstein J. Org. Chem.* **2016**, 12, 1269–1301. DOI:10.3762/bjoc.12.121
24. T. E. Ali, *Arkivoc* **2013**, (i), 2014, 21–91. DOI:10.3998/ark.5550190.p008.189
25. C. P. Gordon, N. Byrne, A. McCluskey, *Green Chem.* **2010**, 12, 1000–1006. DOI:10.1039/b924835h
26. I. Macsari, Y. Besidski, G. Csajnyik, L. I. Nilsson, L. Sandberg, U. Yngve, K. Åhlin, T. Bueters, A. B. Eriksson, P.-E. Lund, E. Venyike, S. Oerther, K. Hygge Blakeman, L. Luo, P. I. Arvidsson, *J. Med. Chem.* **2012**, 55, 6866–6880. DOI:10.1021/jm300623u
27. B. E. Maryanoff, D. F. McComsey, J. F. Gardocki, R. P. Shank, M. J. Costanzo, S. O. Nortey, C. R. Schneider, P. E. Setler, *J. Med. Chem.* **1987**, 30, 1433–1454. DOI:10.1021/jm00391a028
28. H. J. Knolker, S. Agarwal, *Tetrahedron Lett.* **2005**, 46, 1173–1175. DOI:10.1016/j.tetlet.2004.12.066
29. L. F. Tietze, N. Rackelmann, I. Müller, *Chem. – A Eur. J.* **2004**, 10, 2722–2731. DOI:10.1002/chem.200306039
30. L. Edmunds, S. Izolda, Z. Alla, G. Skaidrite, *Molecules* **1997**,

- 2, 180–185. DOI:10.3390/21200180
31. Á. de Fátima, T. C. Braga, L. da S. Neto, B. S. Terra, B. G. F. Oliveira, D. L. da Silva, L. V. Modolo, *J. Adv. Res.* **2015**, *6*, 363–373. DOI:10.1016/j.jare.2014.10.006
32. T. U. Mayer, T. M. Kapoor, S. J. Haggarty, R. W. King, S. L. Schreiber, T. J. Mitchison, *Science* **1999**, *286*, 971–974. DOI:10.1126/science.286.5441.971
33. D. Russowsky, R. F. S. Canto, S. A. A. Sanches, M. G. M. D'Oca, A. de Fátima, R. A. Pilli, L. K. Kohn, M. A. Antônio, J. E. de Carvalho, *Bioorg. Chem.* **2006**, *34*, 173–182. DOI:10.1016/j.bioorg.2006.04.003
34. E. Bonandi, M. S. Christodoulou, G. Fumagalli, D. Perdicchia, G. Rastelli, D. Passarella, *Drug Discov. Today* **2017**, *22*, 1572–1581. DOI:10.1016/j.drudis.2017.05.014
35. D. Dheer, V. Singh, R. Shankar, *Bioorg. Chem.* **2017**, *71*, 30–54. DOI:10.1016/j.bioorg.2017.01.010
36. A. Rani, G. Singh, A. Singh, U. Maqbool, G. Kaur, J. Singh, *RSC Adv.* **2020**, *10*, 5610–5635. DOI:10.1039/C9RA09510A
37. R. N. Brogden, T. M. Speight, G. S. Avery, *Drugs* **1974**, *7*, 164–282. DOI:10.2165/00003495-197407030-00002
38. N. Thomas, S. M. Zachariah, *Asian J. Pharm. Clin. Res.* **2013**, *6*, 11–15.
39. V. Raj, J. Lee, *Front. Chem.* **2020**, *8*, 623–646. DOI:10.3389/fchem.2020.00623
40. I. Essid, K. Lahbib, W. Kaminsky, C. Ben Nasr, S. Touil, *J. Mol. Struct.* **2017**, *1142*, 130–138. DOI:10.1016/j.molstruc.2017.04.054
41. S. Radi, H. B. Lazrek, *J. Chem. Res.* **2002**, *2002*, 264–266. DOI:10.3184/030823402103172149
42. M. Rajasekhar, K. U. Maheswara Rao, C. S. Sundar, N. B. Reddy, S. K. Nayak, C. S. Reddy, *Chem. Pharm. Bull.* **2012**, *60*, 854–858. DOI:10.1248/cpb.c12-00160
43. R. M. N. Kalla, J.-S. Choi, J.-W. Yoo, S. J. Byeon, M. S. Heo, I. Kim, *Eur. J. Med. Chem.* **2014**, *76*, 61–66. DOI:10.1016/j.ejmech.2014.02.025
44. M. A. Assiri, T. E. Ali, M. M. Ali, I. S. Yahia, *Phosphorus Sulfur Silicon Relat. Elem.* **2018**, *193*, 668–674. DOI:10.1080/10426507.2018.1487969
45. H. Tsuji, K. Sato, L. Ilies, Y. Itoh, Y. Sato, E. Nakamura, *Org. Lett.* **2008**, *10*, 2263–2265. DOI:10.1021/ol800684x
46. M. Ordóñez, G. D. Tibhe, A. Zamudio-Medina, J. L. Viveros-Ceballos, *Synthesis* **2012**, *44*, 569–574. DOI:10.1055/s-0031-1289680
47. M. A. Reyes-González, A. Zamudio-Medina, M. Ordóñez, *Tetrahedron Lett.* **2012**, *53*, 5756–5758. DOI:10.1016/j.tetlet.2012.08.040
48. J. L. Viveros-Ceballos, C. Cativiela, M. Ordóñez, *Tetrahedron: Asymmetry* **2011**, *22*, 1479–1484. DOI:10.1016/j.tetasy.2011.08.003
49. M. Reyes, A. Zamudio-Medina, O. Ramírez, M. Ordóñez, *Monatsh. Chem.* **2014**, *145*, 1001–1007.
50. S. Failla, P. Finocchiaro, *Phosphorus Sulfur Silicon Relat. Elem.* **1995**, *105*, 195–203. DOI:10.1080/10426509508042063
51. M. Milen, A. Dancsó, T. Földesi, P. Slégel, B. Volk, *Tetrahedron* **2016**, *72*, 5091–5099. DOI:10.1016/j.tet.2016.06.074
52. N. P. Muddala, B. Nammalwar, R. A. Bunce, *RSC Adv.* **2015**, *5*, 28389–28393. DOI:10.1039/C5RA02307F
53. Á. Tajti, N. Tóth, B. Rávai, I. Csontos, P. Szabó, E. Bálint, *Molecules* **2020**, *25*, 3307–3323. DOI:10.3390/molecules25143307
54. A. Couture, E. Deniau, P. Grandclaudon, H. Rybalko-Rosen, S. Léonce, B. Pfeiffer, P. Renard, *Bioorg. Med. Chem. Lett.* **2002**, *12*, 3557–3559. DOI:10.1016/S0960-894X(02)00794-1
55. V. Rys, A. Couture, E. Deniau, P. Grandclaudon, *Tetrahedron* **2003**, *59*, 6615–6619. DOI:10.1016/S0040-4020(03)01067-6
56. A. Couture, E. Deniau, P. Grandclaudon, S. Lebrun, *Synlett.* **1998**, *29*, 1475–1477.
57. A. Couture, E. Deniau, P. Grandclaudon, C. Hoarau, *J. Org. Chem.* **1998**, *63*, 3128–3132. DOI:10.1021/jo972247t
58. E. Deniau, D. Enders, A. Couture, P. Grandclaudon, *Tetrahedron: Asymmetry* **2005**, *16*, 875–881. DOI:10.1016/j.tetasy.2005.01.012
59. A. Couture, E. Deniau, P. Woisel, P. Grandclaudon, *Synthesis* **1998**, *29*, 1439–1445. DOI:10.1055/s-1997-1370
60. A. Couture, E. Deniau, P. Grandclaudon, C. Hoarau, *Tetrahedron* **2000**, *56*, 1491–1499. DOI:10.1016/S0040-4020(00)00067-3
61. A. Moreau, A. Couture, E. Deniau, P. Grandclaudon, *J. Org. Chem.* **2004**, *69*, 4527–4530. DOI:10.1021/jo049869g
62. N. Popovics-Tóth, B. Rávai, Á. Tajti, B. Varga, P. Bagi, F. Perdihi, P. Szabó, L. Hackler, L. Puskás, E. Bálint, *Org. Biomol. Chem.* **2021**, *19*, 8754–8760. DOI:10.1039/D1OB01610E
63. L. Kollár, G. Szalontai, *J. Organomet. Chem.* **1991**, *421*, 341–345. DOI:10.1016/0022-328X(91)86419-Q
64. Q. Ding, B. Wang, J. Wu, *Tetrahedron* **2007**, *63*, 12166–12171. DOI:10.1016/j.tet.2007.09.044
65. W. Sun, Q. Ding, X. Sun, R. Fan, J. Wu, *J. Comb. Chem.* **2007**, *9*, 690–694. DOI:10.1021/cc070030z
66. Y. Ye, Q. Ding, J. Wu, *Tetrahedron* **2008**, *64*, 1378–1382. DOI:10.1016/j.tet.2007.11.055
67. L. Zou, J. Huang, N. Liao, Y. Liu, Q. Guo, Y. Peng, *Org. Lett.* **2020**, *22*, 6932–6937. DOI:10.1021/acs.orglett.0c02487
68. Q. Ding, Y. Ye, R. Fan, J. Wu, *J. Org. Chem.* **2007**, *72*, 5439–5442. DOI:10.1021/jo070716d
69. N. Popovics-Tóth, K. Szabó, E. Bálint, *Materials* **2021**, *14*, 6015–6027. DOI:10.3390/ma14206015
70. N. K. Gusarova, P. A. Volkov, N. I. Ivanova, K. O. Khrapova, A. I. Albanov, A. V. Afonin, T. N. Borodina, B. A. Trofimov, *Tetrahedron Lett.* **2016**, *57*, 3776–3780. DOI:10.1016/j.tetlet.2016.07.024
71. B. A. Trofimov, P. A. Volkov, K. O. Khrapova, A. A. Telezhkin, N. I. Ivanova, A. I. Albanov, N. K. Gusarova, A. M. Belogolova, A. B. Trofimov, *J. Org. Chem.* **2019**, *84*, 6244–6257. DOI:10.1021/acs.joc.9b00519
72. I. Yavari, A. Mirzaei, L. Moradi, *Synth. Commun.* **2010**, *40*, 2407–2414. DOI:10.1080/00397910903249598
73. A. Shaabani, A. Sarvary, S. Mousavi-Faraz, S. W. Ng, *Monatsh. Chem.* **2012**, *143*, 1061–1065. DOI:10.1007/s00706-011-0686-0
74. N. Popovics-Tóth, M. Turpanova, K. Németh, L. Hackler, L. Puskás, E. Bálint, *Tetrahedron* **2022**, *111*, 132720–132728. DOI:10.1016/j.tet.2022.132720

75. I. Essid, S. Touil, *Arxivoc* **2013**, (iv), 2013, 98–106. DOI:10.3998/ark.5550190.p007.871
76. D. Gong, L. Zhang, C. Yuan, *Heteroat. Chem.* **2003**, *14*, 13–17. DOI:10.1002/hc.10058
77. N. Popovics-Tóth, Á. Tajti, E. Hümpfner, E. Bálint, *Catalysts* **2020**, *11*, 45–59. DOI:10.3390/catal11010045
78. R. G. Hall, S. Trippett, *Tetrahedron Lett.* **1982**, *23*, 2603–2604. DOI:10.1016/S0040-4039(00)87407-9
79. Y. Shen, J. Zheng, Y. Xin, Y. Lin, M. Qi, *J. Chem. Soc.* **1995**, 997–999. DOI:10.1039/p19950000997
80. O. Artyushin, E. Matveeva, I. Bushmarinov, I. Odinets, *Arxivoc* **2012**, (iv), 2012, 252–263. DOI:10.3998/ark.5550190.0013.419
81. P. Huang, Q. Su, W. Dong, Y. Zhang, D. An, *Tetrahedron* **2017**, *73*, 4275–4284. DOI:10.1016/j.tet.2017.05.076
82. F. Louërât, K. Bougrin, A. Loupy, A. M. O. de Retana, J. Pagalday, F. Palacios, *Heterocycles* **1998**, *48*, 161–170. DOI:10.3987/COM-97-7997
83. L. Li, G. Hao, A. Zhu, X. Fan, G. Zhang, L. Zhang, *Chemistry* **2013**, *19*, 14403–14406. DOI:10.1002/chem.201303324
84. A. Tripolszky, E. Tóth, P. T. Szabó, L. Hackler, B. Kari, L. G. Puskás, E. Bálint, *Molecules* **2020**, *25*, 2643–2658. DOI:10.3390/molecules25112643
85. V. V. Rostovtsev, L. G. Green, V. V. Fokin, K. B. Sharpless, *Angew. Chemie Int. Ed.* **2002**, *41*, 2596–2599. DOI:10.1002/1521-3773(20020715)41:14<2596::AID-ANIE2596>3.0.CO;2-4
86. C. W. Tornøe, C. Christensen, M. Meldal, *J. Org. Chem.* **2002**, *67*, 3057–3064. DOI:10.1021/jo011148j
87. E. Thiery, V. You, A.-S. Mora, M. Abarbri, *Eur. J. Org. Chem.* **2015**, *2016*, n/a–n/a.
88. H. Skarpos, S. N. Osipov, D. V. Vorob'eva, I. L. Odinets, E. Lork, G.-V. Röschenhaler, *Org. Biomol. Chem.* **2007**, *5*, 2361–2367. DOI:10.1039/B705510B
89. X. Zhou, S. V. Hartman, E. J. Born, J. P. Smits, S. A. Holstein, D. F. Wiemer, *Bioorg. Med. Chem. Lett.* **2013**, *23*, 764–766. DOI:10.1016/j.bmcl.2012.11.089
90. D. V. Vorobyeva, N. M. Karimova, T. P. Vasilyeva, S. N. Osipov, G. T. Shchetnikov, I. L. Odinets, G.-V. Röschenhaler, *J. Fluor. Chem.* **2010**, *131*, 378–383. DOI:10.1016/j.jfluchem.2009.12.003
91. K. Sykam, K. K. R. Meka, S. Donempudi, *ACS Omega* **2019**, *4*, 1086–1094. DOI:10.1021/acsomega.8b02968
92. A. Tripolszky, K. Németh, P. T. Szabó, E. Bálint, *Molecules* **2019**, *24*, 2085–2102. DOI:10.3390/molecules24112085
93. M. A. Kulkarni, V. R. Pandurangi, U. V. Desai, P. P. Wadgaonkar, *Comptes Rendus Chim.* **2012**, *15*, 745–752. DOI:10.1016/j.crci.2012.07.001
94. P. Kour, A. Kumar, R. Sharma, R. Chib, I. Khan, V. Rai, *Res. Chem. Intermed.* **2017**, *43*, 1–11.
95. P. Kour, A. Kumar, V. K. Rai, *Comptes Rendus Chim.* **2017**, *20*, 140–145. DOI:10.1016/j.crci.2016.05.013
96. F. Darvish, A. Abdollahzade, D. Saravani, *Res. Chem. Intermed.* **2017**, *43*, 1487–1494. DOI:10.1007/s11164-016-2710-9
97. S. R. Kolla, Y. R. Lee, *Tetrahedron* **2012**, *68*, 226–237. DOI:10.1016/j.tet.2011.10.060
98. D. Gaikwad, K. Undale, T. Shaikh, D. Pore, C. R. Chim. **2011**, *14*, 865–868. DOI:10.1016/j.crci.2011.03.001
99. G. Brahmachari, S. Laskar, *Phosphorus Sulfur Silicon Relat. Elem.* **2014**, *189*, 873–888. DOI:10.1080/10426507.2014.903484
100. P. Jayashree, G. Shanthi, P. T. Perumal, *Synlett* **2009**, *2009*, 917–920. DOI:10.1055/s-0028-1087960
101. R. Mohammadi, M. Z. Kassae, *J. Mol. Catal. A Chem.* **2013**, *380*, 152–158. DOI:10.1016/j.molcata.2013.09.027
102. S. N. Murthy, B. Madhav, V. P. Reddy, Y. V. D. Nageswar, *Tetrahedron Lett.* **2010**, *51*, 3649–3653. DOI:10.1016/j.tetlet.2010.05.028
103. B. Das, P. Balasubramanyam, G. Chinna Reddy, N. Salvanna, *Helv. Chim. Acta* **2011**, *94*, 1347–1350. DOI:10.1002/hlca.201000461
104. W. Yuanyuan, *Chim. J. Chem.* **2012**, *30*, 1709–1714. DOI:10.1002/cjoc.201200181
105. S. K. Krishnammagari, B. G. Cho, Y. T. Jeong, *Phosphorus Sulfur Silicon Relat. Elem.* **2018**, *193*, 306–316. DOI:10.1080/10426507.2017.1417296
106. S. Sobhani, M. Honarmand, *Catal. Lett.* **2013**, *143*, 476–485. DOI:10.1007/s10562-013-0968-8
107. M. Hosseini-Sarvari, A. Roosta, *Comb. Chem. High Throughput Screen.* **2014**, *17*, 47–52. DOI:10.2174/13862073113166660064
108. S. Sobhani, R. Jahanshahi, *Synth. Commun.* **2013**, *43*, 3247–3257. DOI:10.1080/00397911.2013.768670
109. R. M. N. Kalla, S. J. Byeon, M. S. Heo, I. Kim, *Tetrahedron* **2013**, *69*, 10544–10551. DOI:10.1016/j.tet.2013.10.052
110. Á. Tajti, K. Szabó, N. Popovics-Tóth, J. Iskandarov, F. Perdih, L. Hackler, B. Kari, L. Puskás, E. Bálint, *Org. Biomol. Chem.* **2021**, *19*, 6883–6891. DOI:10.1039/D1OB01204E
111. Y. H. Budnikova, *Chem. Heterocycl. Compd.* **2018**, *54*, 269–279. DOI:10.1007/s10593-018-2261-7
112. Y.-R. Chen, W.-L. Duan, *J. Am. Chem. Soc.* **2013**, *135*, 16754–16757. DOI:10.1021/ja407373g
113. F. Bu, E. Wang, Q. Peng, R. Hu, A. Qin, Z. Zhao, B. Z. Tang, *Eur. J. Chem.* **2015**, *21*, 4440–4449. DOI:10.1002/chem.201405902
114. Y. Unoh, K. Hirano, T. Satoh, M. Miura, *Angew. Chem.* **2013**, *52*, 12975–12979. DOI:10.1002/anie.201307211
115. W. Ma, L. Ackermann, *Synthesis* **2014**, *46*, 2297–2304. DOI:10.1055/s-0033-1338630
116. G. Hu, Y. Zhang, J. Su, Z. Li, Y. Gao, Y. Zhao, *Org. Biomol. Chem.* **2015**, *13*, 8221–8231. DOI:10.1039/C5OB00959F
117. O. Berger, J.-L. Montchamp, *J. Org. Chem.* **2019**, *84*, 9239–9256. DOI:10.1021/acs.joc.9b01239
118. K. Fourmy, D. H. Nguyen, O. Dechy-Cabaret, M. Gouygou, *Catal. Sci. Technol.* **2015**, *5*, 4289–4323. DOI:10.1039/C4CY01701C
119. V. Quint, F. Morlet-Savary, J.-F. Lohier, J. Lalevée, A.-C. Gaumont, S. Lakhdar, *J. Am. Chem. Soc.* **2016**, *138*, 7436–7441. DOI:10.1021/jacs.6b04069
120. P. Zhang, Y. Gao, L. Zhang, Z. Li, Y. Liu, G. Tang, Y. Zhao, *Adv. Synth. Catal.* **2016**, *358*, 138–142. DOI:10.1002/adsc.201500667

121. Á. Tajti, B. Kovács, N. Popovics-Tóth, F. Perdih, E. Bálint, *Tetrahedron* **2021**, *102*, 132527–132533.
DOI:10.1016/j.tet.2021.132527
122. G. J. Szebeni, Á. Balázs, I. Madarász, G. Pócz, F. Ayaydin, I. Kanizsai, R. Fajka-Boja, R. Alföldi, L. Hackler Jr., L. G. Puskás, *Int. J. Mol. Sci.* **2017**, *18*, 2105–2121.
DOI:10.3390/ijms18102105

Povzetek

Razvili smo več multikomponentnih sinteznih pristopov do množice novih dušikovih in kisikovih heterociklov, ki vsebujejo fosfonatne ali fosfin oksidne skupine. Za vse multikomponentne reakcije smo na primerih modelnih reakcij optimizirali reakcijske parametre: način segrevanja, množinsko razmerje izhodnih spojin, atmosfero, katalizatorje, temperaturo, reakcijske čase in topila. Na tak način dobljeni reakcijski parametri so bili uporabljeni za priprave majhnih knjižnic strukturno sorodnih spojin. Večino reakcij lahko smatramo kot skladnih s principi »zelene kemije«, saj so potekale brez prisotnosti katalizatorjev in/ali topil ter pod pogoji obsevanja z mikrovalovi (MW) ali celo že pri sobni temperaturi. S pomočjo pretočnega MW sistema smo nekatere mikrovalovne sinteze izvedli tudi na večji skali. Skupno smo pripravili več kot 150 heterocikličnih organofosforjevih spojin; nekateri izmed pripravljenih derivatov so izkazali zmerne do obetavne aktivnosti na HL-60 celično linijo ter na bakterije *Bacillus subtilis*.



Except when otherwise noted, articles in this journal are published under the terms and conditions of the Creative Commons Attribution 4.0 International License

Adaptation of the Crystal Structure to the Confined Size of Mixed-oxide Nanoparticles

Darko Makovec

Department for Materials Synthesis, Jožef Stefan Institute, Jamova ulica 39, SI-1000 Ljubljana, Slovenia.

* Corresponding author: E-mail: darko.makovec@ijs.si

Received: 08-29-2022

Abstract

Chemical composition and crystal structure are central to defining the functional properties of materials. But when a material is prepared in the form of nanoparticles, the structure and, as a consequence, the composition will also frequently change. Understanding these changes in the crystal structure at the nanoscale is therefore essential not only for expanding fundamental knowledge, but also for designing novel nanostructures for diverse technological and medical applications. The changes can originate from two thermodynamically driven phenomena: (i) a crystal structure will adapt to the restricted size of the nanoparticles, and (ii) metastable structural polymorphs that form during the synthesis due to a lower nucleation barrier (compared to the equilibrium phase) can be stabilized at the nanoscale. The changes to the crystal structure at the nanoscale are especially pronounced for inorganic materials with a complex structure and composition, such as mixed oxides with a structure built from alternating layers of several structural blocks. In this article the complex structure of nanoparticles will be presented based on two examples of well-known and technologically important materials with layered structures: magnetic hexaferrites ($\text{BaFe}_{12}\text{O}_{19}$ and $\text{SrFe}_{12}\text{O}_{19}$) and ferroelectric Aurivillius layered-perovskite bismuth titanate ($\text{Bi}_4\text{Ti}_3\text{O}_{12}$).

Keywords: Nanoparticles; crystal structure; hexaferrites; Aurivillius structure; layered perovskites; polymorphs

1. Introduction

The functional properties of materials change significantly when they are prepared in the form of nanoparticles. In the scientific literature these changes are usually associated with one of two fundamental reasons. The size effect can simply originate from the large surface-to-volume ratio of nanoparticles. The properties, which are defined by processes occurring on the surfaces (e.g., adsorption capacity, catalytic activity, the rate of solid-state chemical reactions, etc.) will generally improve as the particle size becomes smaller. With the explosion in research devoted to nanoscience at the beginning of this millennium, an especially large amount of attention was given to the direct effects of the confined size on some functional properties. Well-known examples are the quantum-confinement effect observed in semiconducting nanoparticles (i.e., quantum dots) and the superparamagnetism of magnetic nanoparticles. Much less attention has been given to the changes in properties that are an indirect consequence of the changes in crystal structure that are due to the restricted size of nanomaterials. This is because when the size is restricted to such an extent, the crystal structure of nanoparticles can also change significantly.

The influence of the confined size on the structure of nanoparticles can range from minor changes in atomic positions to the stabilization of diverse structural variations and metastable structural polymorphs. At the very large surface-to-volume ratios of nanoparticles, the structural changes can simply be related to the relaxation and reorganization of the atoms at the surfaces. However, the adaptation of the structure to the small size frequently cannot be explained merely by the increased surface area as it clearly affects the whole particle, including its interior.

The adaptation of the crystal structure generally involves systematic displacements of the atoms from their ordered positions and deviations in the occupation of different lattice sites. The extent of the changes in the crystalline structure that can be accommodated with the small size depends on the complexity of the composition and the crystal structure. In simple oxides the changes in the occupation of different lattice sites can be restricted to an increased content of vacancies. Classical thermodynamic calculations indicate that the size-dependent vacancy-formation energy and entropy result in an increase in the vacancy concentration at a reduced crystallite size.¹ In mixed oxides comprising different cationic lattice sites (e.g., in

cubic ferrites with a spinel structure) an additional adaptation mechanism is possible based on the changes in the distribution of constituting cations over different lattice sites.^{2–6} Finally, in mixed oxides with a complex structure built from alternating layers of several structural blocks, e.g., a structure of hexagonal ferrites (hexaferrites) and the Aurivillius structures of layered perovskites, the adaptation of the crystal structure to the constricted size of the nanoparticles is dominated by the termination of the particle at its surfaces with a specific, low-energy atomic layer.⁷ That can enable the synthesis of nanoparticles with a specific structure, which can be referred to as a specific structural variation of the bulk structure, stabilized at the nanoscale.⁸ In addition, the changes in the crystal structure due to the confined size of the nanoparticles can lead to a deviation from the bulk composition,^{5,7} or at least to an increased flexibility of the composition, i.e., the composition of the nanoparticles can change to a much larger extent without any precipitation of secondary phases when compared to the corresponding bulk.⁵ Also, the solid solubility of the foreign atoms in the host crystal usually increases with a decreasing size of the nanoparticles.¹

In addition to the above-mentioned changes in the crystal structure due to the restricted size of the nanoparticles, various metastable structural polymorphs can be stabilized at the nanoscale. Polymorphs are defined as substances that are chemically identical but exist in more than one crystal form. For example, iron(III) oxide appears in five different polymorphs: α (hematite), β , γ (maghemite), ϵ , and ξ .⁹ The metastable polymorphs are formed during the initial stages of crystallization, because they have a lower nucleation barrier than the stable phase.^{10,11} With the particle growth, a metastable polymorph usually transforms in an energetically cascading series of polymorphic stages to the equilibrium polymorph. This phenomenon is known as the Ostwald step rule.¹¹ However, if the metastable polymorph has a lower surface energy than the equilibrium polymorph it can remain stable while in the form of small particles with a large surface area.¹⁰ For example, with the confined growth of iron(III) oxide nanoparticles dispersed in a silica matrix, the γ , ϵ , and sometimes β polymorphs appear in sequence before the transformation to the thermodynamically stable α polymorph in the larger particles resembling the bulk.^{12,13} Even though the polymorphs stabilized on the nanoscale are usually referred to as “metastable”, their stability can be thermodynamically explained by taking into consideration their large surface area related to their small size.^{12,13} Strictly speaking, the metastable polymorphs are not a consequence of the adaptation of the crystal structure to the restricted size; however, as they only appear at the nanoscale they can be considered in the context of the size effect.

Metastable polymorphs stabilized at the nanoscale are abundant among simple oxides. Well-known examples of polymorphs for which the stability changes with the nanoparticle size include titania (anatase→brookite→rutile),

zirconia (monoclinic→tetragonal), alumina (γ → α), silica (tridymite→cristobalite→quartz), and many others. The polymorphism is technologically very important, as different polymorphs of the same stoichiometry can have vastly different functional properties, and many metastable polymorphs represent very important functional nanomaterials. Iron(III) oxide can be used as a good illustration of the diversity of magnetic properties for different polymorphs.⁹ The thermodynamically stable phase hematite (α -Fe₂O₃) is only weakly magnetic. The metastable maghemite (γ -Fe₂O₃) is soft magnetic with a relatively high saturation magnetization, and maghemite nanoparticles are actually the most frequently used magnetic nanoparticles, especially in medicine.¹⁴ In contrast, ϵ -Fe₂O₃ is hard magnetic as it exhibits the largest coercive field among all the oxides. The β -Fe₂O₃ and ξ -Fe₂O₃ phases are antiferromagnetic.⁹

Even though the Ostwald step rule should not be restricted to simple oxides, reports of polymorphs stabilized at the nanoscale are very scarce for inorganic materials with a complex composition and crystal structure, such as mixed oxides with several constituting ions distributed over many non-equivalent lattice sites within a large unit cell. Such complex materials include mixed oxides with a layered structure, which are the topic of this article.

Finally, in contrast to the thermodynamically driven adaptations of the structure to the small size mentioned so far, nanomaterials can exhibit a specific crystal structure because of the reaction kinetics during their synthesis. Usually, mild synthesis conditions, e.g., a low temperature, are used during the synthesis of the nanoparticles to limit the particle growth. Such specific, non-equilibrium synthesis conditions can also contribute to deviations from the regular, bulk structure when the material is synthesized in the form of nanoparticles.

In this feature, article the thermodynamically driven adaptations of the crystal structure to the small size of the nanoparticles will be presented using two examples of mixed-oxide nanoparticles with a structure built from alternating layers of two structural blocks: a hexaferrite (BaFe₁₂O₁₉ and SrFe₁₂O₁₉) and an Aurivillius layered-perovskite bismuth titanate (Bi₄Ti₃O₁₂). The mixed oxides with a layered structure represent technologically important materials. The hexaferrites exhibit extraordinary magnetic properties dominated by a very large magnetocrystalline anisotropy constant. As ceramics they represent the most abundant materials (by volume) used today for permanent magnets and are also used in microwave devices and absorbers.¹⁵ In the form of nanoparticles, hexaferrites enabled the development of some entirely new types of materials, including the first ferromagnetic fluids (i.e., liquid magnets),^{16,17} and novel magneto-responsive suspensions^{18,19} and polymer composites.²⁰ Hexaferrite nanoparticles were also tested in novel applications, e.g., in novel spin-memory devices^{21,22} and in medical applications.^{23,24} Layered-perovskite phases of the Aurivillius family ((Bi₂O₂)(A_{n-1}B_nO_{3n+1}), where A is a large

12-coordinated cation, and B is a small 6-coordinated cation), the Ruddlesden-Popper family ($A'_{n-1}A''_2B_nO_{3n+1}$, where A' and A'' are alkali, alkaline earth or rare-earth ions) and the Dion-Jacobson family ($A''(A'_{n-1}B_nO_{3n+1})$) possess interesting properties such as ferroelectricity, colossal magnetoresistance, catalytic activity and superconductivity. The Aurivillius $\text{Bi}_4\text{Ti}_3\text{O}_{12}$ ceramics are promising materials for ferroelectric random-access-memory devices and lead-free, high-temperature piezoelectric and pyroelectric devices.²⁵ $\text{Bi}_4\text{Ti}_3\text{O}_{12}$ nanoparticles were tested for biomechanical energy harvesting,²⁶ sensing,^{27,28} visible-light photocatalysis,^{29,30} electrocatalysis,²⁸ and piezocatalysis.^{31,32} Technologically important families of layered mixed oxides further include high-temperature superconducting cuprates,³³ and lithium and sodium transition-metal layered oxides (LiMO_2 and Na_xMO_2 , M = transition metal), which are used as the cathode materials in batteries.^{34,35} In all these materials we can expect that similar mechanisms will govern the adaptation of the crystal structure to the nanoscale.

Attempts to study the adaptation of such complex crystal structures to the restricted sizes of nanoparticles have seldom been reported in the scientific literature. To the best of our knowledge also, the metastable polymorphs of layered mixed oxides stabilized at the nanoscale were not reported prior to our work. The reason is primarily related to the difficult synthesis of such complex materials in the form of small nanoparticles, which usually involves high temperatures that lead to the rapid growth of particles and favour thermodynamically stable phases. The hydrothermal method is one of the few methods enabling the direct synthesis (without a calcination stage) of layered mixed oxides, such as hexaferrites and bismuth titanate. The method involves the precipitation of the constituting cations from the aqueous solutions with a strong hydroxide, usually NaOH, followed by a hydrothermal treatment, i.e., the alkaline aqueous suspension of the precipitated hydroxides is heated in a closed autoclave at an elevated temperature (typically around 200 °C) and an equilibrium water pressure.³⁶

On the other hand, the characterization of small nanoparticles with a complex structure is very challenging. Conventional methods based on x-ray diffraction (XRD) are not efficient for the characterization of small nanoparticles. In our research we combined direct atomic-resolution high-angle annular dark-field (HAADF) imaging with a probe spherical-aberration corrected scanning-transmission electron microscope (STEM) with other microscopy techniques (energy-dispersive X-ray spectroscopy (EDXS), electron-energy-loss spectroscopy (EELS)) and XRD to examine the nanoparticle structures. HAADF imaging enables “Z-contrast”, as the intensity of the spots representing individual atomic columns in the atomic resolution images of the crystal depends on the column’s average atomic number Z ($\sim Z^a$ with a slightly lower than 2).³⁷ Thus, the columns occupied by the heavy cations

(Ba^{2+} , Sr^{2+} , Bi^{3+}) can be clearly resolved from the columns of the lighter cations (Fe^{3+} , Ti^{4+}) (the O^{2-} columns are too light to be visible in HAADF images).

2. Structure of Barium and Strontium Hexaferrite Nanoplatelets

2.1. Magnetoplumbite Structure

Barium hexaferrite ($\text{BaFe}_{12}\text{O}_{19}$, or BHF) and strontium hexaferrite ($\text{SrFe}_{12}\text{O}_{19}$, or SHF) are the simplest members of a large family of hexagonal ferrites (i.e., hexaferrites) that can be formed by repeatedly stacking layers of three structural building blocks: the “S” block (MeFe_4O_8 , where Me denotes either a divalent (e.g., Zn^{2+} , Co^{2+}) or trivalent (Fe^{3+}) ion), the “R” block ($\text{AFe}_6\text{O}_{11}$, where A denotes a large divalent ion Ba^{2+} , Sr^{2+} , or Pb^{2+}), and the “T” block ($\text{A}_2\text{Fe}_8\text{O}_{14}$), along the c -axis of the hexagonal structure. The BHF and SHF are also known as M-type hexaferrites. They represent the simplest members of the hexaferrite family with a magnetoplumbite structure composed of only $\text{Ba}^{2+}/\text{Sr}^{2+}$ ions and Fe^{3+} ions arranged in the hexagonal “R” block ($(\text{BaFe}_6\text{O}_{11})^{2-}$) and the cubic “S” block ($(\text{Fe}_6\text{O}_8)^{2+}$) (Note that the magnetoplumbite structure is frequently simply referred to as the “hexaferrite” structure). The unit cell (S.G.: $P6_3/mmc$, $a = 5.88$ Å, $c = 23.18$ Å) can be illustrated by the RSR^*S^* stacking sequence, where the asterisk denotes the rotation of the block by 180° around the hexagonal c -axis. Within the structure, the Fe^{3+} ions occupy five different lattice sites, i.e., one tetrahedral ($4f_1$), three octahedral ($12k$, $2a$, $4f_2$), and one trigonal ($2b$) (see Figure 2(a)).¹⁵ Due to the anisotropic, layered structure, the growth of the hexaferrite crystals is limited in the c -direction, resulting in nanoparticles growing in the form of thin hexagonal platelets, i.e., nanoplatelets (NPL).¹⁶

2.2. Hydrothermal Synthesis of Hexaferrite Nanoplatelets

Hexaferrite nanoplatelets can be efficiently synthesized using a simple and scalable hydrothermal method.^{7,18,39–45} This method is based on the hydrothermal treatment of an aqueous suspension of the corresponding hydroxides in the presence of a high concentration of hydroxyl ions. An excess of $\text{Ba}^{2+}/\text{Sr}^{2+}$ ions is used to avoid the parallel formation of hematite. After the hydrothermal treatment the product is washed with a dilute acid to dissolve any Ba/Sr-rich compounds that formed due to the excess Ba/Sr. Ba- and Sr-rich compounds (e.g., $\text{BaCO}_3(\text{s})$, $\text{SrCO}_3(\text{s})$) are all very soluble, whereas the hexaferrite is completely insoluble.^{7,39–42,45}

The evolution of the morphology of the formed NPLs during hydrothermal synthesis is very similar for the two hexaferrites: BHF and SHF. The primary, ultraf-

ine discoid NPLs, around 10 nm wide and less than 3 nm thick, already form at temperatures below 100 °C (given a sufficient time for the hydrothermal treatment) (Figure 1). The ultrafine NPLs exhibit weak magnetic properties. With an increased temperature of the hydrothermal treatment, the size of the NPLs remains almost constant up to approximately 150 °C, when individual NPLs start to grow with the mechanism of Ostwald ripening (Figure 1). With Ostwald ripening the NPLs obtain their characteristic shape of hexagonal platelets, which reflects their hexagonal structure. And only after the Ostwald ripening do the NPLs obtain their hard-magnetic properties with a sizable saturation magnetization, characteristic for hexaferrites. The Ostwald ripening (sometimes also referred to as a secondary recrystallization) is a special mechanism, where individual particles grow very rapidly at the expense of other particles, which dissolve. Because of this

very rapid growth, the phenomenon is also referred to as anomalous or exaggerated growth. The size of particles that grow exaggeratedly is very difficult to control. Hexaferrite NPLs with a size below 100 nm can only be obtained if the hydrothermal treatment is stopped immediately after the start of the exaggerated growth. If the exaggerated growth is allowed to proceed, the widths of the platelets rapidly exceed 1 µm, while their thickness increases much more gradually (Figure 1).^{7,39} The exaggerated growth can be regulated to some extent with chemical substitutions. For example, if the Fe^{3+} in the composition of the BHF is partially substituted with Sc^{3+} , the exaggerated growth is suppressed to some extent, enabling the controlled synthesis of NPLs with a relatively narrow distribution of widths centred around 50 nm.^{42,44} Alternatively, the growth of NPLs can be mediated with appropriate surfactants, such as oleic acid.³⁹

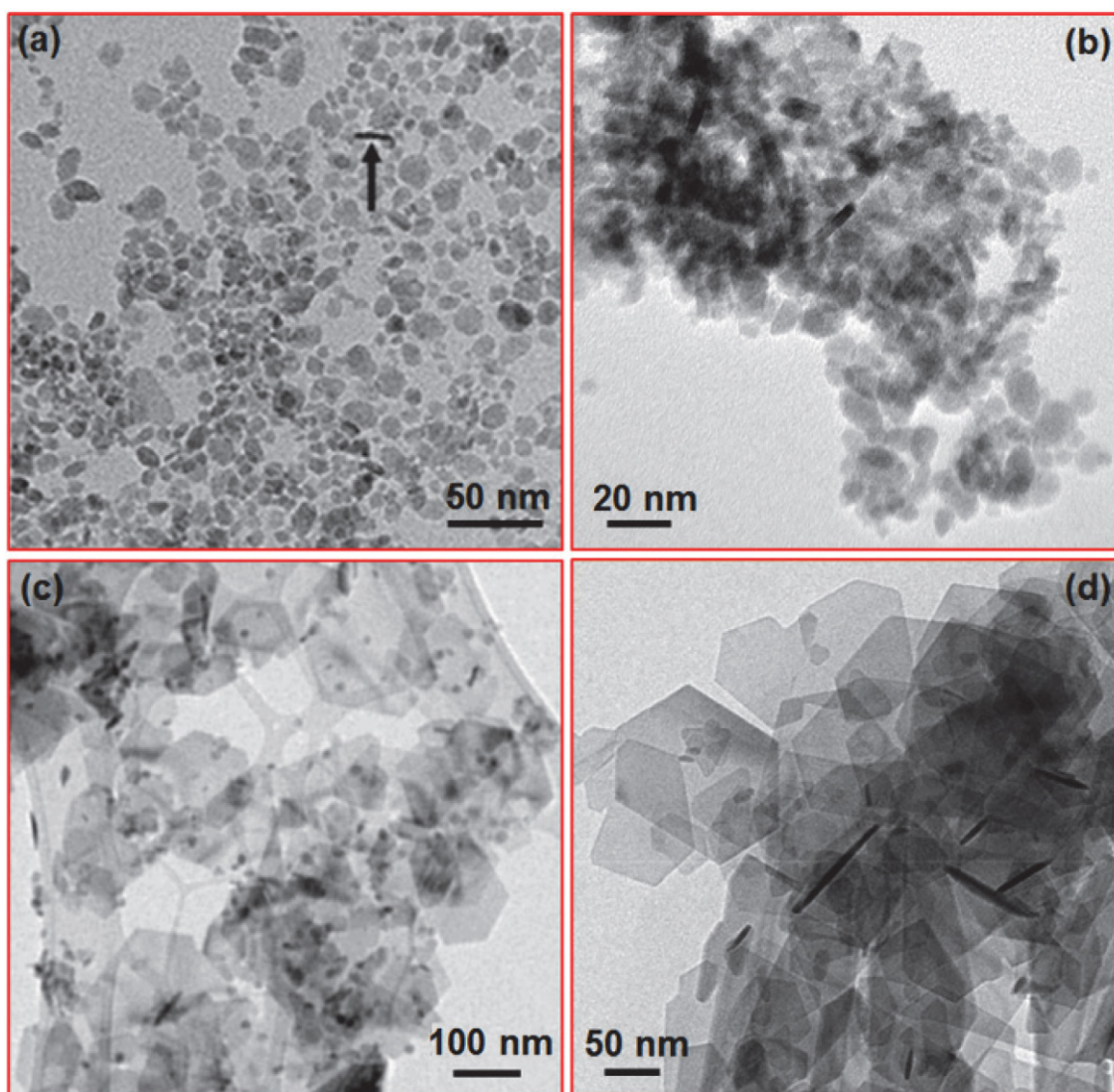


Figure 1. TEM micrographs of the BHF NPLs hydrothermally synthesized for 24 hours at 80 °C (a), and by heating the autoclave to 150 °C (b), 160 °C (c), and 200 °C (d).

2. 3. Structure of Hexaferrite Nanoparticles Obtained by Exaggerated Growth

For the hydrothermal synthesis of hexaferrite NPLs with applicable magnetic properties the exaggerated growth is necessary; however, it must be stopped before the NPLs grow too large. Usually, the NPLs with widths below 100 nm are required for various applications.^{42,44} For widths around 100 nm, the hexaferrite NPLs remain very thin, i.e., their thickness remains less than two unit-cell parameters of their hexagonal structure in the corresponding c -direction ($c = 23.18 \text{ \AA}$). Already after analyses of the first successfully synthesized NPLs with a high-resolution transmission electron microscope (HRTEM) they appear to exhibit a specific structure. For the small thickness it seemed logical that their layered structure will be terminated at the basal surfaces always at the same, low-energy crystal plane. In the layered structure, such a specific structure should also result in a deviation from the bulk composition. For example, if the hexaferrite NPLs were to terminate at the basal surfaces with the Ba-containing planes, their composition would be Ba-rich, and vice versa. However, our analyses of the BHF NPLs' structure with a combination of XRD, X-ray absorption fine structure (XAFS), Mössbauer spectroscopy, HRTEM, and EDXS could not unambiguously confirm this hypothesis.⁴⁶ The structure of the BHF NPLs was revealed later, when we applied HAADF imaging with a STEM.⁸

Figure 2 (b) shows a HAADF STEM image of an exaggeratedly grown BHF NPL oriented edge-on, i.e., with the basal surfaces parallel to the electron beam. The Ba-containing columns can be clearly resolved from the lighter Fe columns. The positions of the cations in the projected magnetoplumbite structural model are super-

imposed over the experimental image of Figure 2 (b) to reveal the NPL structure. The NPL in Figure 2 (b) contains only two Ba-containing R structural blocks and its cationic sublattice terminates at the basal surfaces with a layer of Fe ions at the octahedral Fe(12k) sites, i.e., with the complete S structural block. It should be noted that the oxygen columns are not visible on the HAADF images. However, it is expected that the NPLs' structure is terminated with an oxygen-terminating layer in the air.

An analysis of a large number of NPLs showed that the NPLs with widths below 100 nm usually contained only two R blocks. Only seldom did the BHF nanoplatelets contained three or four R blocks. However, the cationic sublattice of the NPLs' structure always terminated at the basal surfaces with the same, Fe(12k) lattice plane. The content of the R blocks and the specific termination of the NPLs' structure determine their thickness: the NPL containing two R blocks is $\sim 3.1 \text{ nm}$ thick. Moreover, all the NPLs of equal thickness have basically the same structure across the NPL. The structure of a NPL containing two R structural blocks can be represented by the $\text{SRS}^*\text{R}^*\text{S}$ stacking sequence across the NPL. With growth, the thickness of the NPLs cannot increase continuously, but in a discrete, stepwise manner, by gradually adding the SR segments.^{7,8} The structure of exaggeratedly grown SHF NPLs was similar to that of the BHF NPLs.⁴⁵

Due to the specific structure the hexaferrite NPLs display a different composition than the $\text{BaFe}_{12}\text{O}_{19}$ bulk. The composition of a NPL containing the two R blocks ($\text{SRS}^*\text{R}^*\text{S}$ stacking) corresponds to the theoretical composition $\text{BaFe}_{15}\text{O}_{23}$. This theoretical composition was confirmed by a quantitative EDXS analysis. With increasing thickness, the nanoplatelet composition gradually approaches that of the bulk.^{7,8,45} Note that although the the-

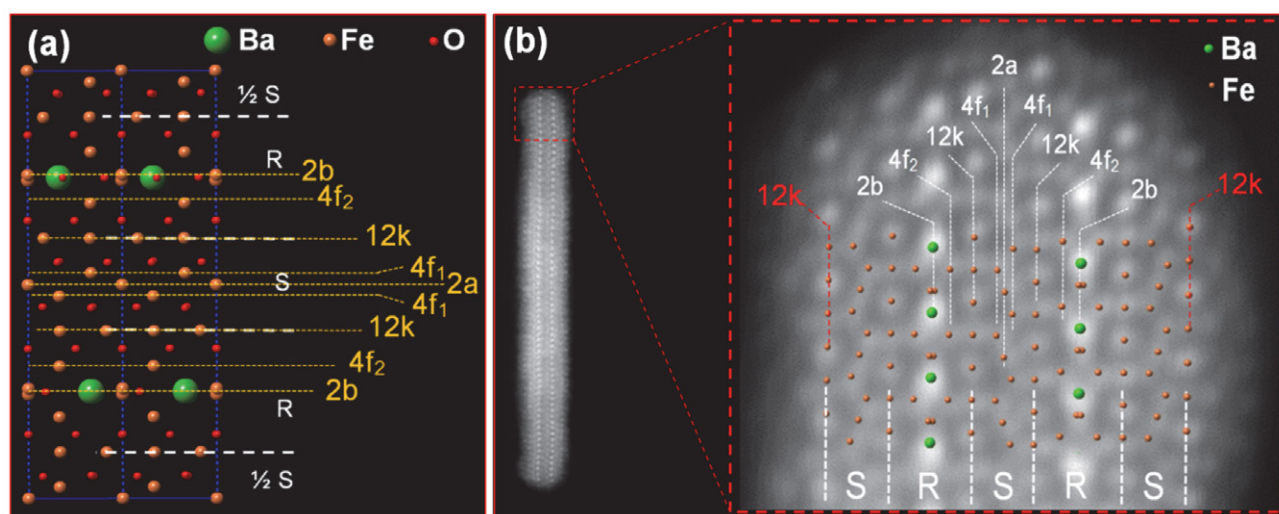


Figure 2. A schematic representation of the magnetoplumbite structure (a) and HAADF STEM image of a hexaferrite nanoplatelet oriented along the $\langle 10\bar{1}0 \rangle$ direction of its magnetoplumbite structure (b). In image (b) the projected magnetoplumbite structure is superimposed to illustrate the positions of the Ba^{2+} and Fe^{3+} columns. Different Fe lattice sites (trigonal 2b, tetrahedral $4f_1$, octahedral 12k, 2a, and $4f_2$) are marked. (Reproduced from the publication⁴⁴ by D. Makovec, M. Komelj, G. Dražič, B. Belec, T. Goršak, S. Gyergyek, D. Lisjak, *Acta Mater.* 2019, 172, 84–91 under the terms of CC BY 4.0 license).

oretical composition of the nanoplatelets containing two R blocks is equal to the composition of the Fe^{2+} -containing X-type hexaferrite $\text{Ba}_2\text{Fe}^{2+}_2\text{Fe}^{3+}_{28}\text{O}_{46}$, the stacking of the structural blocks in the X-type hexaferrite is different ($\text{RSRSS}^*\text{S}^*\text{R}^*\text{S}^*$) and its unit cell is much larger ($c = 84.1 \text{ \AA}$) than the thickness of the nanoplatelet.⁴⁷ Moreover, the specific composition of the thin NPLs is not related to the change in the oxidation state of Fe ions. The experimental determination of Fe valence state of the NPLs using an analysis of the EELS spectra showed the Fe valence to be close to $3+$.⁷

The termination of the NPLs' structure at the basal surfaces was found to depend on the conditions applied during their preparation. The S-block-terminated structure was actually only found in the NPLs washed with diluted acid after the hydrothermal synthesis (Figure 3

(b)).^{7,8} If the nanoplatelets were extracted from the reaction mixture before the washing step, they were terminated at the basal surfaces with the Ba/O/Fe(2b) mixed planes (Figures 3 (a) and (c)). Interestingly, during the washing not only was the top Ba-containing plane dissolved, but also the first Fe plane beneath ($\text{Fe}(4f_2)$) was dissolved from the surface to reveal the S-terminated structure (Figure 3 (a)).⁷

Experimental observations of the NPLs' structure termination were supported with *ab initio* calculations of the relative stability of different terminations of the BHF performed using the density functional theory (DFT). The first calculations of a periodic structure resembling the bulk were performed by Matej Komelj from the Jožef Stefan Institute, Ljubljana, Slovenia. These calculations suggested that in energy terms the most stable surface lay-

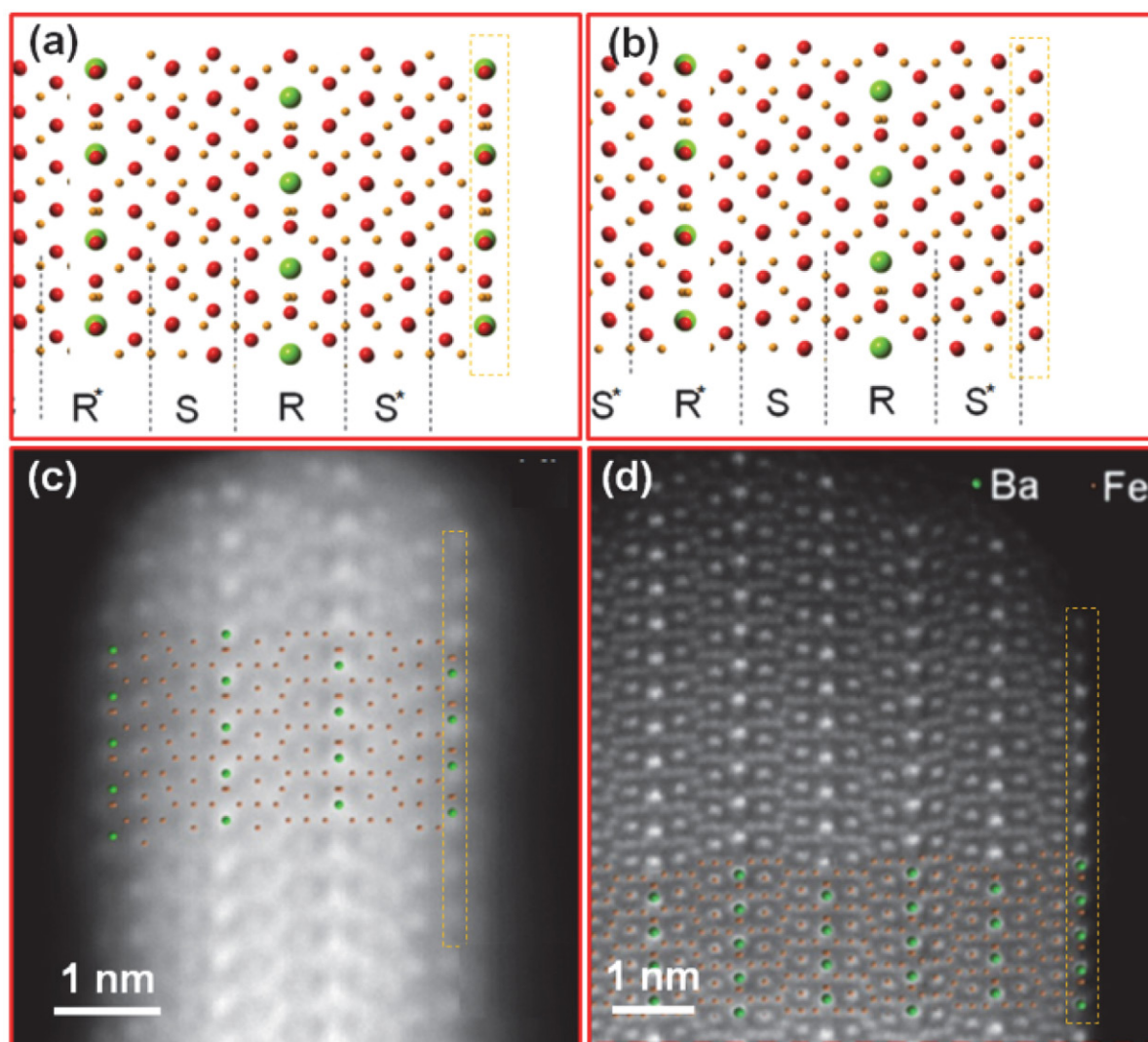


Figure 3. Two structural models schematically representing the structure across the hexaferrite NPL before (a) and after (b) washing with dilute nitric acid. Figures (c) and (d) show HAADF STEM images of BHF NPLs after washing with diluted acid (c) and after annealing for 2 hours at 700 °C. The projected magnetoplumbite structure is superimposed over the images (c) and (d) to illustrate the positions of the Ba^{2+} and Fe^{3+} columns. The termination layer at the basal surfaces of the NPLs is marked with a yellow rectangle. (Adapted from the publication by D. Makovec, B. Belec T. Goršak, D. Lisjak, M. Komelj, G. Dražić, S. Gyergyek, *Nanoscale* 2018, 10, 14480–14491 with permission from The Royal Society of Chemistry.⁷)

er is obtained with a termination of mixed Ba/O/Fe(2b) planes.⁸ Such a structure was observed experimentally when the NPLs were annealed at high temperatures. Figure 3(d) shows an atomic-resolution HAADF STEM image of the platelet crystal obtained by annealing the BHF NPLs at 700 °C. At that high temperature the NPLs grew to larger, plate-like crystals resembling the bulk. At their flat, basal surfaces they were clearly terminated with the Ba-containing planes.⁷ The difference in the termination of the structure between the NPLs and the larger crystals after annealing highlights the crucial role of the chemical environment, which was not taken into the consideration during the calculations. We must bear in mind that the NPLs after the hydrothermal synthesis are suspended in an aqueous solution containing high concentrations of different ions, mainly originating from an excess amount of Ba²⁺ ions and a high concentration of NaOH, hydrating the surfaces.

Later, the *ab initio* calculations were extended to thin structures, which resembled the structure of the primary nanoplatelets.⁷ The calculations of the relative stability of thin structures symmetrically terminating at both basal surfaces at different lattice planes showed the highest stability for a structure terminated with the O layers above the Fe(4f₁) of the S block; however, its stability was just slightly higher than the termination at the O-only layers above the Fe(12k) layers, experimentally determined as the termination layers for the washed BHF nanoplatelets.

Recently, detailed DFT calculations were performed by the group from Scuola Internazionale Superiore di Studi Avanzati (SISSA), Trieste, Italy, led by Layla Martin-Samos. Their calculations clearly demonstrated the influence of the chemical environment on the equilibrium structure of BHF NPLs. In the absence of water (and other

species), the calculations showed that the structure terminating with the mixed Ba/O/Fe(2b) planes is the most stable. The same surface is also the most stable in oxygen/iron-poor (Ba-rich) conditions, whereas the fully hydroxylated 12k-O surface is the most stable in oxygen/iron-rich conditions, in line with the experimental observations.⁴⁸

In conclusion, the BHF and SHF NPLs synthesized via exaggerated growth (i.e., Ostwald ripening) during the hydrothermal treatment show specific structures and compositions, defined by the termination of the particle at its surfaces with a specific, low-energy atomic layer. The termination layer depends on the chemical environment. As the structure and composition of hexaferrite NPLs are significantly different from the bulk, they can be considered as a novel structural variation of the hexaferrites stabilized on the nanoscale. An equivalent adaptation mechanism can also be expected for other mixed oxides with a layered structure when they are synthesized in the form of thin NPLs.

2. 4. Structure of Primary Hexaferrite Nanoplatelets

The NPLs that grow exaggeratedly during the hydrothermal synthesis exhibit the same crystal structure for both the hexaferrite analogues: BHF and SHF. In contrast, the primary NPLs, i.e., the nanoparticles that appeared as the first product in the initial stage of the hydrothermal synthesis, exhibit a completely different structure for the two hexaferrite analogues, even though they had a similar discoid morphology. Atomic-resolution HAADF STEM imaging showed that the washed primary BHF NPLs exhibit a specific variation of the magnetoplumbite structure – the smallest possible structural segment still maintaining the hexaferrite motif. Figure 4 shows a HAADF STEM im-

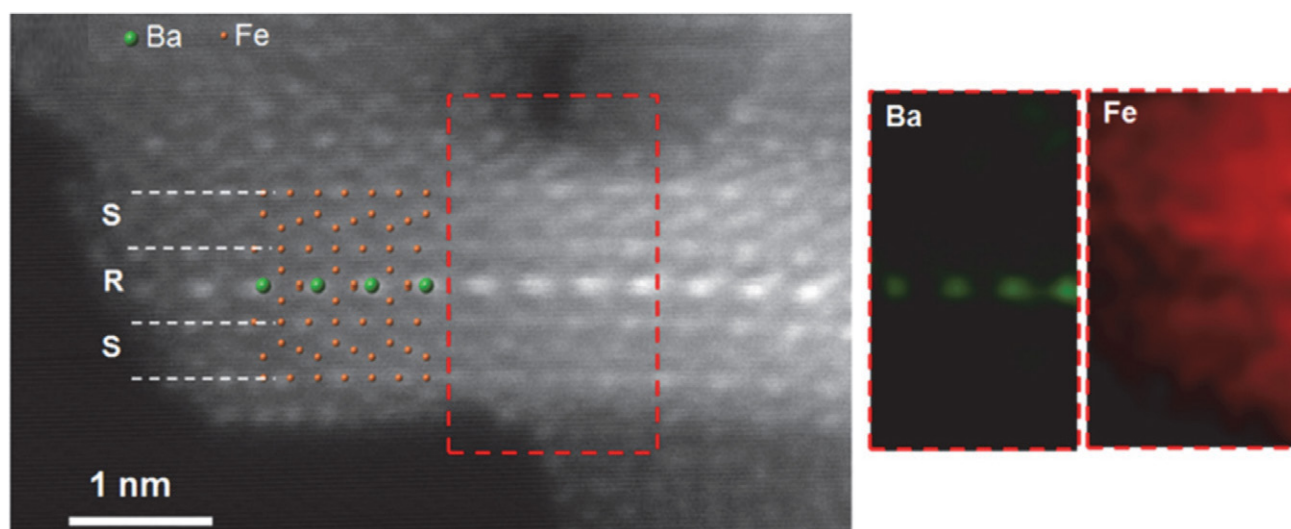


Figure 4. HAADF STEM images of a primary BHF NPL with corresponding EELS elemental maps for Ba and Fe (the area of the analysis is marked on the image with a red rectangle). An SRS⁺ segment of the hexaferrite structure projected along the <10 $\bar{1}$ 0> direction is superimposed over the image to illustrate the positions of the Ba²⁺ and Fe³⁺ ions. (Adapted from the publication by D. Makovec, B. Belec T. Goršak, D. Lisjak, M. Komelj, G. Dražić, S. Gyergyek, *Nanoscale* 2018, 10, 14480–14491 with permission from The Royal Society of Chemistry.⁷)

age of a primary BHF NPL oriented edge-on. Even though the NPL is not perfectly oriented along the zone axis and an additional layer of adsorbed atoms is visible on its surfaces, its structure is composed of only one Ba-containing R structural block sandwiched between the two S blocks. The thickness of the SRS⁺-structured NPLs is therefore less than the dimension of one magnetoplumbite SRS⁺R⁺ unit cell. Their composition is significantly enriched in Fe compared with the theoretical composition corresponding to the chemical formula BaFe₁₈O₂₈.⁷ Note, that the theoretical composition of the SRS⁺-structured primary BHF nanoplatelets is equal to the composition of the Fe²⁺-containing W-type hexaferrite (BaFe₂²⁺₂Fe₁₆³⁺O₂₇) with different stacking of the structural blocks (SSRS⁺S⁺R⁺).⁴⁷

Even though the structure and composition of the primary BHF NPLs strongly deviates from the bulk, their structure remains a specific variation of the hexaferrites. Their structure can therefore be understood in the context of the adaptation of the magnetoplumbite structure to the restricted size.

In contrast to the primary BHF NPLs, the primary SHF NPLs display an entirely different structure. Already during our first study devoted to the hydrothermal synthesis of SHF NPLs we noticed that the structure of the primary SHF NPLs deviates from the magnetoplumbite structure. HRTEM images showed a dominant periodicity across the primary SHF NPLs that was considerably smaller (~ 9 Å) than that for the magnetoplumbite (11.5 Å corresponding

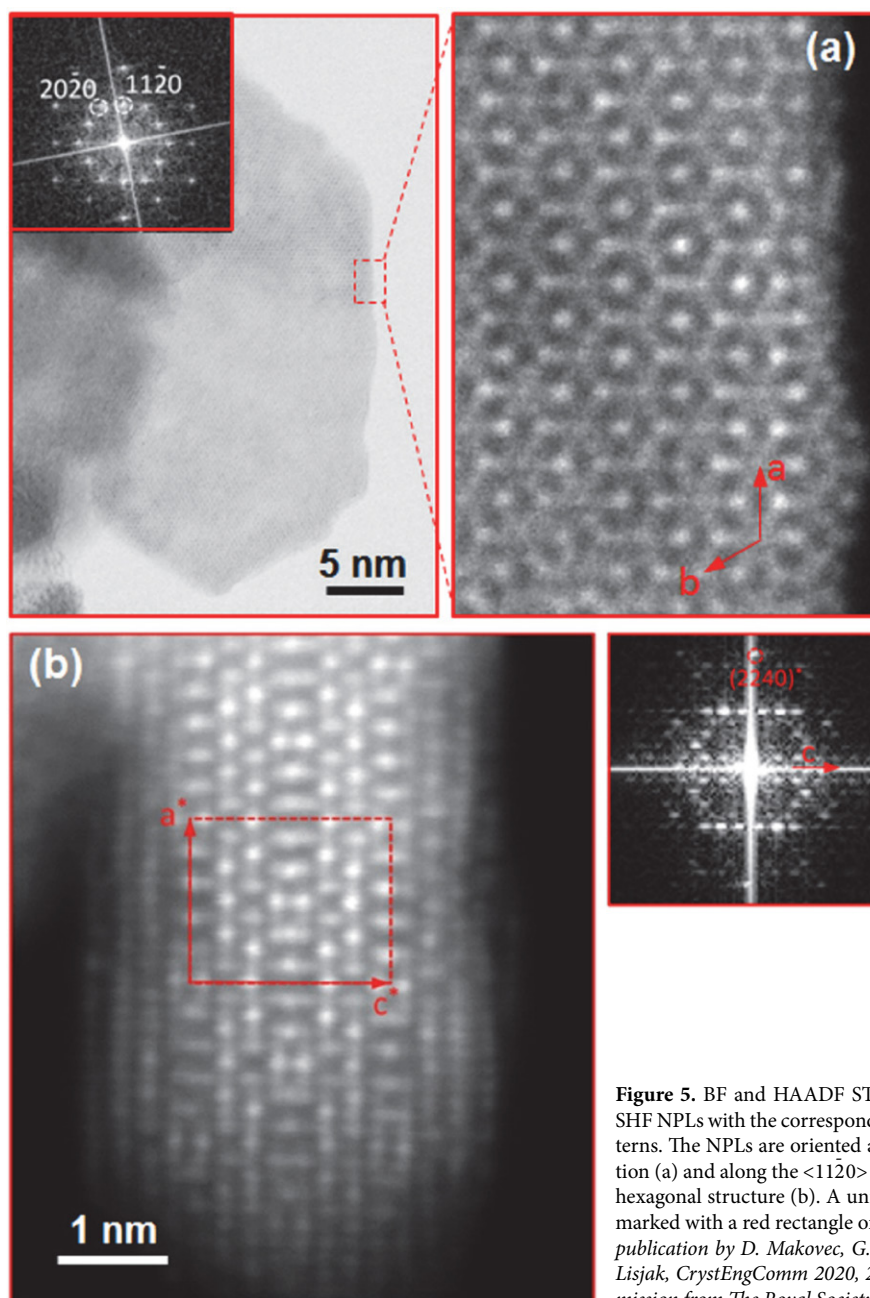


Figure 5. BF and HAADF STEM images of primary SHF NPLs with the corresponding calculated FFT patterns. The NPLs are oriented along the $\langle 0001 \rangle$ direction (a) and along the $\langle 1120 \rangle$ direction of its complex hexagonal structure (b). A unit cell of the structure is marked with a red rectangle on (b). (Adapted from the publication by D. Makovec, G. Dražić, S. Gyergyek, D. Lisjak, *CrystEngComm* 2020, 22, 7113–7122 with permission from The Royal Society of Chemistry.⁴⁵)

to (0002)).⁴¹ However, the NPLs were too small for any reliable structural analysis with conventional methods (e.g. XRD). Later, direct atomic-resolution HAADF STEM imaging showed that the primary SHF NPLs exhibit an exotic layered hexagonal structure, not reported before (Figure 5).⁴⁵ Due to the severe complexity of the new structure and the small thickness of the NPLs, we were not able to propose a specific structural model. However, it was evident that the new layered structure is not a variation of the hexaferrite structure. The structure was described with HAADF STEM images having an unusually large unit cell. A basic periodicity unit cell with $a^* \approx 28.3$ Å, $c^* \approx 18.0$ Å is marked on the atomic-resolution HAADF image taken along the $\langle 11\bar{2}0 \rangle$ direction (Figure 5(b)), however the atomic-resolution images along the $\langle 10\bar{1}0 \rangle$ direction suggested doubling of the unit cell in the a -direction.⁴⁵ Along the c -direction, the structure is composed of five layers of cations: three neighbouring layers containing Fe^{3+} and Sr^{2+} ions are separated by two Fe^{3+} -only layers. The structure of the discoid NPLs always terminates at the basal surfaces with an Fe^{3+} -only layer. The EDXS analysis showed an Fe-rich composition when compared to the $\text{SrFe}_{12}\text{O}_{19}$ bulk. When the primary SHF NPLs were annealed above 500 °C they grew and transformed into the magnetoplumbite structure.⁴⁵

The complex structure of primary SHF NPLs cannot be formed because of the adaptation of the magnetoplumbite structure to the restricted size. It is clearly a metastable polymorph of the SHF stabilized at the nano-scale. It can, therefore, be explained in the context of the Ostwald step rule, where the phases with a lower thermodynamic stability form in the initial stages of the synthesis because of the lower nucleation barrier. With the growth of the nanoparticles at high temperatures the metastable polymorph transforms into the thermodynamically stable magnetoplumbite structure.

In conclusion, the primary NPLs, which appear as the first crystalline products of the hydrothermal synthesis, exhibit different structures for the two hexaferrites. The structure of the primary BHF NPLs is an SRS^* variation of the SRS^*R^* magnetoplumbite structure, whereas the primary SHF NPLs exhibit a different, complex layered structure, which is a metastable polymorph of the SHF. The striking difference in the structure of the primary NPLs can be related to the thermodynamic stability of the two hexaferrites. The stability of the $\text{AFe}_{12}\text{O}_{19}$ hexaferrites decreases with the decreasing size of the A ion in the series: $\text{Ba}^{2+} > \text{Sr}^{2+} > \text{Ca}^{2+}$.¹⁵

3. Structure of Bismuth Titanate Nanoplatelets and Nanowires

3. 1. Aurivillius Structure

Bismuth titanate ($\text{Bi}_4\text{Ti}_3\text{O}_{12}$, or BIT) belongs to an Aurivillius ($(\text{Bi}_2\text{O}_2)(\text{A}_{n-1}\text{B}_n\text{O}_{3n+1})$) family of layered per-

ovskites. Its layered structure derives from the high-temperature paraelectric phase of tetragonal $I4/mmm$ symmetry, composed of two alternating layers: a $(\text{Bi}_2\text{O}_2)^{2+}$ layer and a perovskite $(\text{Bi}_2\text{Ti}_3\text{O}_{10})^{2-}$ layer stacked along the pseudo-tetragonal c -axis (see Figure 7(a)). With the onset of ferroelectricity below the Curie temperature ($T_C \sim 675$ °C the BIT structure is slightly distorted to monoclinic symmetry $P1a1$ with parameters $a = 5.411$ Å, $b = 5.448$ Å, $c = 32.83$ Å.⁴⁹

3. 2. Hydrothermal Synthesis of Bismuth-Titanate Nanoplatelets and Nanowires

BIT can be successfully synthesized with the hydrothermal treatment of an aqueous suspension of precipitated Bi^{3+} and Ti^{4+} ions in mineralizer hydroxide (NaOH or KOH) with a moderate concentration.^{27,28,30–32,50–53} The synthesized BIT nanoparticles appear in a wide variety of different nano-morphologies, including 2-D platelet crystals, (i.e., rectangular nanoplatelets and nanosheets),^{27,28,32,50,52,53} 1-D crystals (e.g., nanowires, nanobelts, nanobundles, nanorods),^{27,28,51–53} and 3-D nanostructures assembled from 1-D or 2-D nanoparticles.^{30,31,51} Our research showed that the morphologies of the product particles crucially depend on the concentration of the mineralizer hydroxide.⁵² The nanowires (NWs) formed when the precipitated ions were hydrothermally treated in aqueous solutions of NaOH with lower concentrations, whereas the nanoplatelets (NPLs) were obtained at higher NaOH concentrations. For example, the hydrothermal treatment for 38 hours at 200 °C produced NWs (from 15 nm to 35 nm wide and from several hundreds of nm to several μm long) in 0.5 mol/L NaOH, whereas the rectangular NPLs (approximately 10 nm thick and from 50 nm to 200 nm wide) were synthesized in 2-mol/L NaOH (Figure 6 (a) and (b)). The NWs formed as the first crystalline BIT phase in the initial stages of the hydrothermal treatment independently of the NaOH concentration. Initially, the BIT NWs appeared together with globular aggregates of nanocrystallites with a highly defected perovskite structure. The subsequent morphology evolution depended on the concentration of the hydroxide, which influences the stability of the different phases and the kinetics of the hydrothermal reactions. At lower NaOH concentrations the NWs grew with the treatment temperature/time, while the perovskite aggregates dissolved. At the higher NaOH concentrations, the nanowires dissolved, while the NPLs grew epitaxially on the surfaces of the aggregated perovskite nanocrystallites (Figure 6 (c)).⁵²

3. 3. Structure of Bismuth-Titanate Nanoplatelets

The plate-like shape of the hydrothermally synthesized BIT rectangular NPLs is consistent with their pseudo-tetragonal layered Aurivillius-type structure. Figure 7

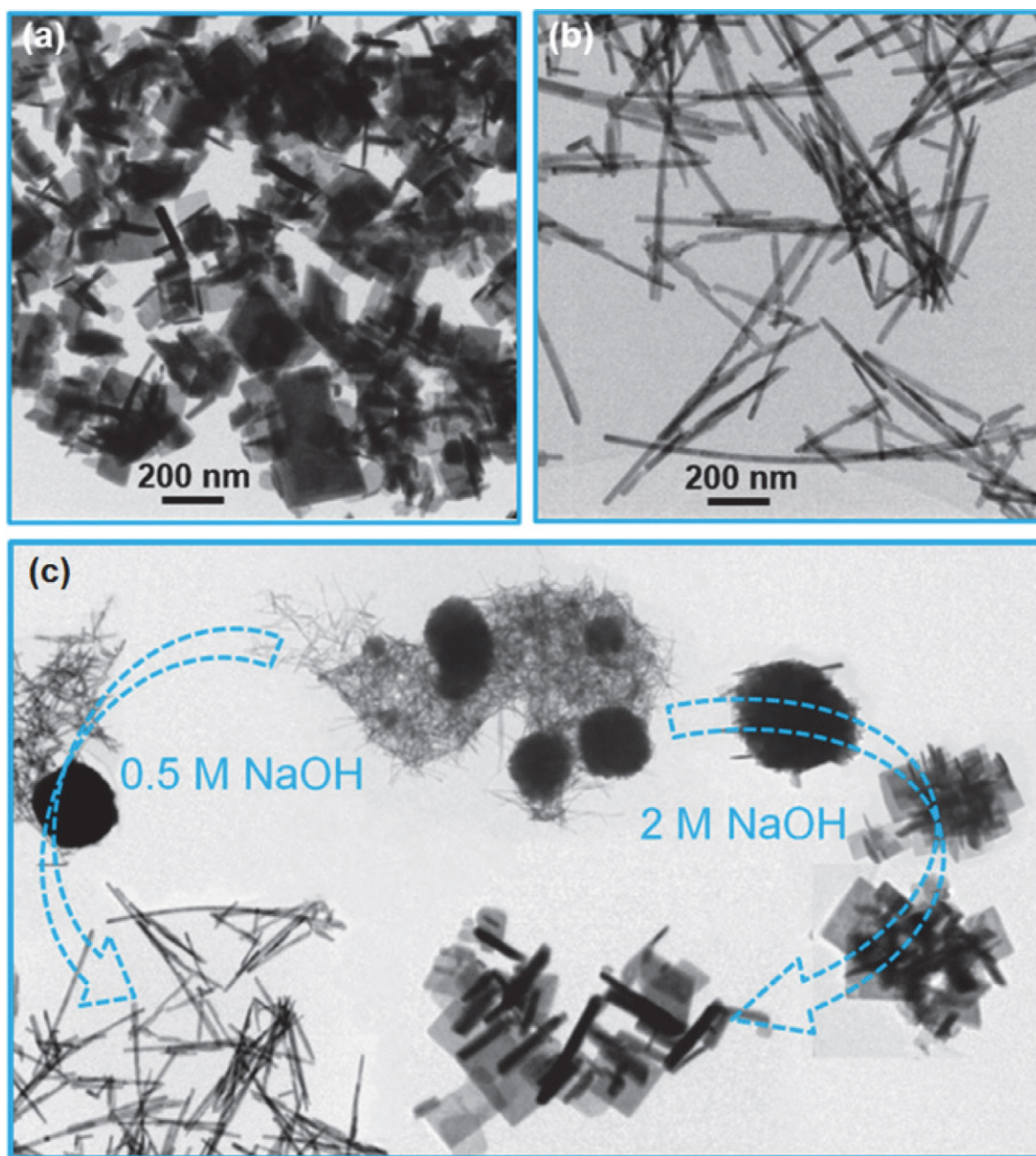


Figure 6. TEM images of bismuth-titanate NPLs (a) and NWs (b) synthesized with hydrothermal treatment of the precipitated Bi and Ti ions for 38 hours at 200 °C in the aqueous solution of NaOH with the concentration of 2 mol/L and 0.5 mol/L, respectively. (c) A schematic presentation of the morphology evolution during hydrothermal synthesis. Independently of the NaOH concentration, a mixture of NWs and globular nanocrystalline particles with a defected perovskite structure forms first. With temperature/time of the treatment in NaOH with a lower concentration, the perovskite aggregates dissolve, while the NWs grow. At a higher NaOH concentration, the NWs dissolve, while on the surfaces of the perovskite aggregates the NPLs grow epitaxially. ((a) and (b) are reproduced from the publication by D. Makovec, N. Križaj, A. Meden, G. Dražić, H. Uršič, R. Kostanjšek, M. Šala, S. Gyergyek, *Nanoscale* 2022, 14, 3537–3544,⁵² (c) adapted from the publication by D. Makovec, N. Križaj, S. Gyergyek, *CrystEngComm* 2022, 24, 3972–398, with permission from The Royal Society of Chemistry.⁵²)

(b) shows the HAADF STEM image of a small BIT NPL, oriented edge-on along the [110] direction of its pseudo-tetragonal structure. The two layers of the Aurivillius structure, i.e., a $(\text{Bi}_2\text{O}_2)^{2+}$ layer and a $(\text{Bi}_2\text{Ti}_3\text{O}_{10})^{2-}$ perovskite-like layer, can be clearly distinguished. The NPL structure always terminates at the large {001} surfaces

with the $(\text{Bi}_2\text{O}_2)^{2+}$ layers. Thus, it is expected that the thin BIT NPLs will be Bi-rich compared to the $\text{Bi}_4\text{Ti}_3\text{O}_{12}$ bulk. However, the BIT NPLs were generally much thicker than the hexaferrite NPLs presented above, usually more than 10 nm thick, so that their actual composition approached to the bulk composition.

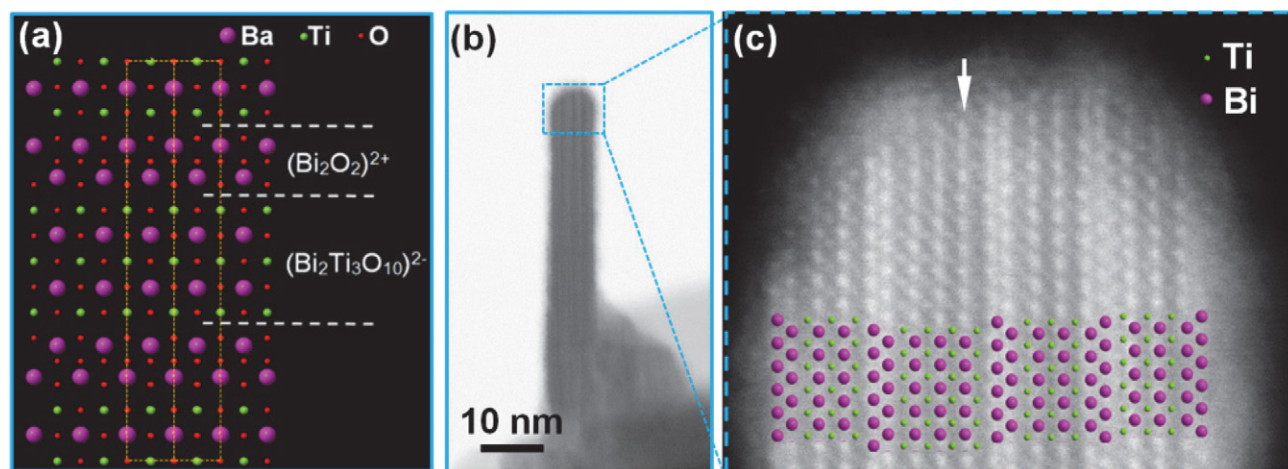


Figure 7. Schematic representation of the magnetoplumbite structure (a), and BF (b) and HAADF (c) STEM images of BIT NPL oriented along [110] direction of the pseudo-tetragonal Aurivillius structure (b). The projected structural models are superimposed over the image (c) to illustrate the positions of the Bi^{3+} and Ti^{4+} ions. The arrow marks a defected perovskite block (Adapted from the publication by D. Makovec, N. Križaj, S. Gyergyek, *CrystEngComm* 2022, 24, 3972 – 398, with permission from The Royal Society of Chemistry.⁵²)

3. 4. Structure of Bismuth-Titanate Nanowires

The 1-D shape of the NWs, which always form in the initial stages of the hydrothermal synthesis, is not consistent with the layered Aurivillius structure (the pseudo-tetragonal layered structure will tend to form rectangular platelet crystals). Indeed, the XRD of the BIT NWs suggested a new structure, entirely different to the Aurivillius structure characteristic for the BIT.⁵² (As explained below, the NW structure does not contain any perovskite-like layers). EDXS analyses showed the same composition for the two BIT morphologies within the uncertainty of the method. The chemical ICP-OES analysis further confirmed the EDXS analyses and showed that sodium from the NaOH used as the mineralizer hydroxide for the synthesis was not incorporated into the NW structure in a significant concentration. Electron diffraction in the TEM suggested an orthorhombic unit cell. Based on the orthorhombic cell and the cell parameters obtained from the electron diffraction it was possible to find a unit cell that gave a satisfactory LeBail fit to the experimental powder XRD pattern with the refined unit-cell parameters: $a = 3.804(1) \text{ \AA}$, $b = 11.816(3) \text{ \AA}$, and $c = 9.704(1) \text{ \AA}$.⁵³

Atomic-resolution STEM imaging confirmed that the NWs exhibit a different structure to that of the NPLs. Figure 8 shows HAADF STEM images of NWs oriented normal to the electron beam (in the [010] zone axis) and along the beam (in the [100] zone axis). Based on the HAADF STEM imaging and the analysis of the XRD pattern, a tentative arrangement of the cations in the structure was proposed (Figure 8 (a)). The structure of the NWs is composed of two layers stacked along the c -direction of the orthorhombic unit cell: a layer composed of two parallel rows of Bi atoms in a zig-zag arrangement (marked with “B” in Figure 8 (c)) and a layer of two rows of Ti atoms in a zig-zag arrangement, where every sixth Ti is ex-

changed with Bi (marked with “T”). The B layer resembles the $(\text{Bi}_2\text{O}_2)^{2+}$ layer of the Aurivillius structure, while the T layer is much thinner than the perovskite $(\text{Bi}_2\text{Ti}_3\text{O}_{10})^{2-}$ layer of the Aurivillius structure. The arrangement of the Ti atoms in the T layer is consistent with two layers of edge-sharing $(\text{TiO}_6)^{2-}$ octahedra, as opposed to the corner-sharing $(\text{TiO}_6)^{2-}$ octahedra of the perovskite layers. The proposed cation arrangement in the NW structure predicts a Bi:Ti ratio of 7:5, which deviates from the BIT composition (Bi:Ti = 4:3). The excess Bi, predicted by the model, is most probably compensated by a random partial insertion of the Ti layers parallel to the (010) planes, visible along the [100] direction (Figure 8 (e)).⁵³

If the BIT NWs were annealed at high temperature, they transformed to the Aurivillius structure. In the powder obtained by annealing the NWs for 2 hours at 525 °C some nanoparticles were just partially transformed. A HAADF STEM analysis (Figure 9) showed that the transformation of the NW structure to the Aurivillius (AU) structure is topotactic $((100)_{\text{NW}} \parallel (110)_{\text{AU}}, (001)_{\text{NW}} \parallel (001)_{\text{AU}}, (010)_{\text{NW}} \parallel (\bar{1}10)_{\text{AU}})$.⁵³ The analysis also strongly suggested that the transformation does not involve any changes to the composition (the precipitation of secondary phases was not detected). This is a strong indication that the NWs are actually a metastable polymorph of BIT stabilized at the nanoscale. With growth at high temperatures the metastable NW structure transforms to the thermodynamically stable Aurivillius structure.

4. Final Remarks and Future Directions

The chemical composition and the crystal structure of materials tend to define their functional properties. Nowadays, discoveries of entirely new crystal structures of

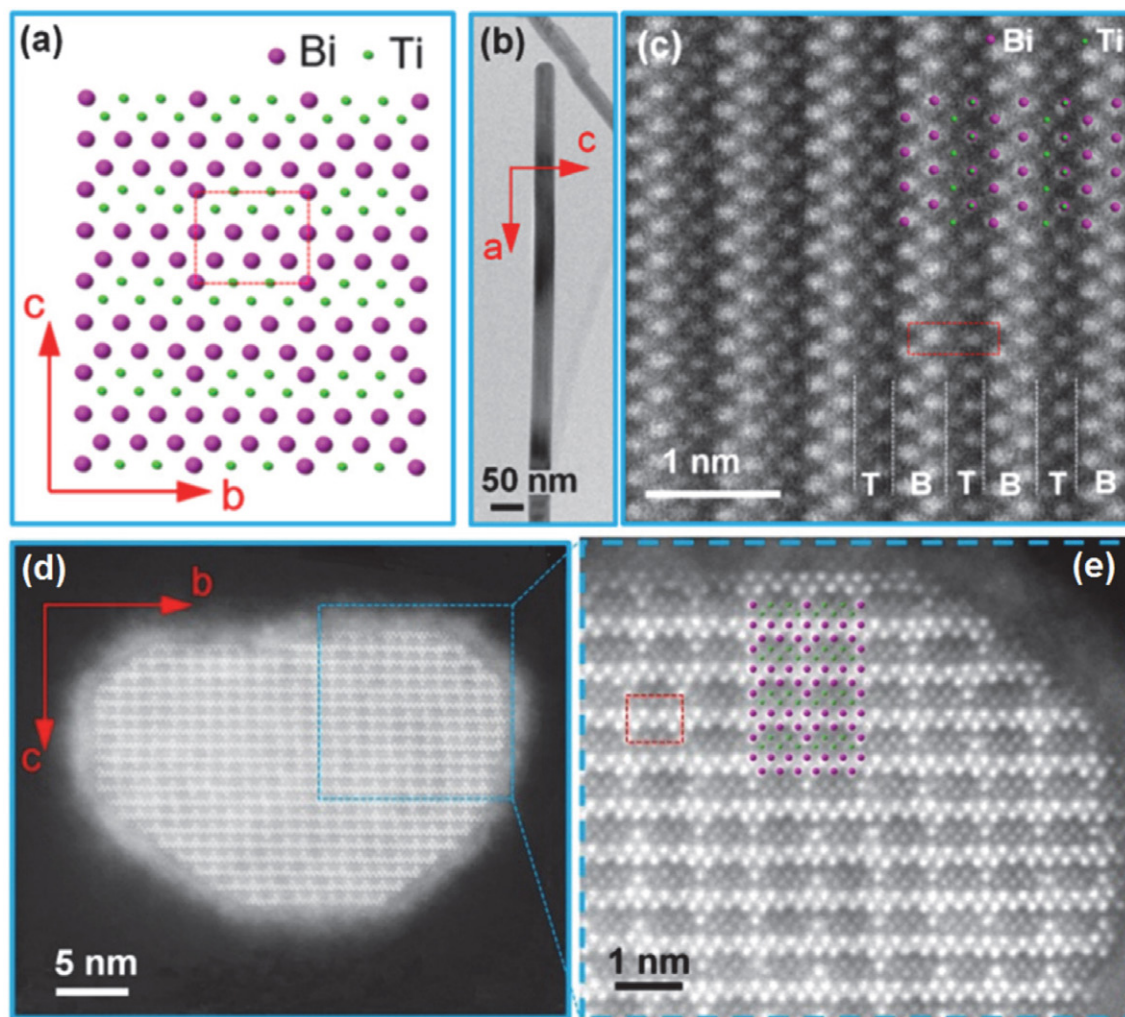


Figure 8. Cation arrangement in a tentative model of an orthorhombic structure of BIT NW (a), TEM (b) and HAADF STEM (c) images of NW oriented along the [010] direction, and HAADF STEM images ((d) and (e)) of NW oriented along the [100] direction of the orthorhombic structure. The projected model proposed for the NW structure is also superimposed over the images (c) and (e) to illustrate the positions of the Bi^{3+} and Ti^{4+} ions. The unit cell of the NW structure is marked with a red rectangle on the HAADF image. (Adapted from the publication by D. Makovec, N. Križaj, A. Meden, G. Dražić, H. Uršič, R. Kostanjšek, M. Šala, S. Gyergyek, *Nanoscale* 2022, 14, 3537–3544 with permission from The Royal Society of Chemistry.⁵³)

inorganic materials are seldom. However, when materials are synthesized in the form of nanoparticles, their crystal structure can change significantly because of its adaptation to the restricted size. The extent of these structural changes increases with the increasing complexity of the structure. In this article, research at the Department for Materials Synthesis, Jožef Stefan Institute, devoted to the adaptation of complex structures built from alternating layers of two structural blocks to the restricted size of nanoparticles was presented based on two examples of well-known and technologically very important materials, the hexaferrites BHF and SHE, and the Aurivillius layered perovskite, BIT. Both examples confirmed that the nanoparticles with layered structures will normally adopt a plate-like shape and a specific structure defined by a termination at surfaces with a specific, low-energy atomic layer. For a small thickness of the platelet crystal, the structure can significantly deviate from the ordered bulk structure. Moreover, the adaptation

of the crystal structure to the restricted size will result in a deviation from the bulk composition. With the defined structure and composition, which are different to those of the bulk, the NPLs can even be considered as new compounds or at least variations of the bulk structures.

The adaptation of the structure to the restricted size will certainly contribute to changed material properties when compared to the bulk properties. This aspect of the size effect has seldom been studied. Since the size has a large effect on the properties per se, it is difficult to estimate the extent of the size effect, which is specifically related to the changed structure. However, there are some indications of positive effects of the structural adaptation on the functional properties of nanoparticles. For example, we can speculate that the $\text{SRS}^*\text{R}^*\text{S}$ -structured hexaferrite NPLs exhibit increased magnetization due to the surface termination with the S block, because the S block has a larger theoretical saturation magnetization

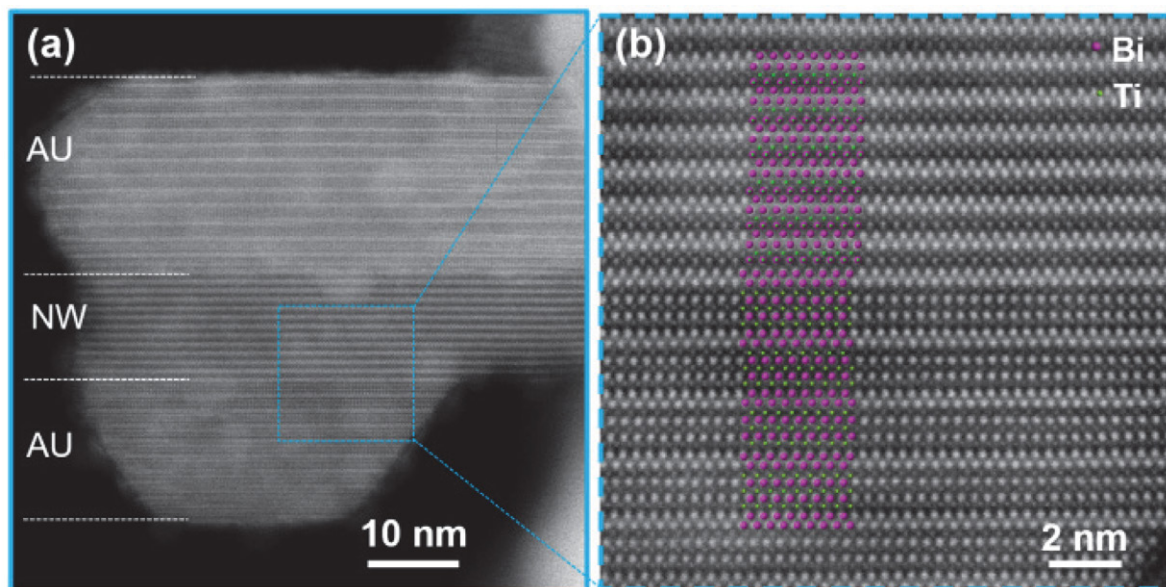


Figure 9. HAADF STEM images of a BIT particle from the NW sample annealed for 2 hours at 525 °C. The particle is composed of a NW sandwiched between two lamellas with the Aurivillius (AU) structure ($[010]_{\text{NW}}||[110]_{\text{AU}}$). Projected models of the AU structure and the NW structure are superimposed over (b) to illustrate the positions of the Bi^{2+} and Ti^{4+} ions. (Reproduced from the publication by D. Makovec, N. Križaj, A. Meden, G. Dražić, H. Uršič, R. Kostanjšek, M. Šala, S. Gyergyek, *Nanoscale* 2022, 14, 3537–3544 with permission from The Royal Society of Chemistry.⁵³)

than the R block.⁸ We also found one example where the BHF nanoplatelets behave completely differently than the bulk. A partial substitution of Fe^{3+} ions in BHF with Sc^{3+} ions greatly improves the saturation magnetization of the NPLs. The effect was surprising since the substitution of diamagnetic Sc strongly decreases the saturation magnetization of bulk BHF. Ab-initio calculations pointed to a specific, two-dimensional magnetic ordering in the NPLs as the most probable reason for the opposite effect of the Sc substitution in the NPLs to that in the bulk.⁴⁴

The metastable polymorphs, which are frequently obtained because they have a lower nucleation barrier compared to the thermodynamically stable phase, have seldom been considered in the context of size effect, even though they remain stable only while in the form of small particles, i.e., at the nanoscale. Many well-known and technologically very important nanomaterials, e.g., magnetic maghemite nanoparticles and catalytic anatase nanoparticles, are actually metastable polymorphs stabilized on the nanoscale. Interestingly, metastable polymorphs were not reported for complex materials such as mixed oxides with a layered structure. To the best of our knowledge the structure of primary SHF NPLs represented the first reported inorganic metastable polymorph with a complex, layered structure, stabilized at the nanoscale. The NPLs with the newly discovered SHF structure exhibit weak magnetic properties, comparable to those of the SRS^+ -structured BHF NPLs. Other functional properties, e.g., catalytic, electronic, etc., were not compared. To show that the discovery of a new structure is not only a special case specific for the SHF, we looked for new metastable polymorphs in other well-known materials

with a layered structure. The discovery of the new BIT polymorph clearly demonstrated that the metastable polymorphs can generally also be expected to form in mixed oxides with a layered structure. Observations of the ferroelectric domains with TEM and piezo-response force microscopy indicated the ferroelectric nature of the BIT NWs polymorph;⁵³ however, their functional properties remain to be studied. Nevertheless, the discovery of new polymorphs demonstrated the immense potential of the stabilization of new metastable polymorphs of complex functional materials for the discovery of new nanomaterials. It is possible that a metastable polymorph of a known complex functional material, which will exhibit improved or even entirely new functional properties, could be discovered.

Both aspects of the influence of the size effect on the crystal structure of nanoparticles, i.e., the adaptation of the structure to the restricted size and the stabilization of metastable polymorphs on the nanoscale, are also important in the context of materials synthesis. For example, the adaptation of the hexaferrite structure to the small size of hydrothermally synthesized nanoplatelets will influence the final composition of hexaferrite ceramics after sintering.⁵⁴ Moreover, we showed that the metastable polymorphs have an important role in the hydrothermal synthesis of BIT nanoparticles.⁵²

Advances in controlled synthesis enabling the synthesis of small nanoparticles of inorganic materials with a complex structure, on the one hand, and the advances in structural characterization based on advanced electron microscopy, on the other, will pave the way to further discoveries of nanoparticles with new and interesting crystal

structures. And with new structures, new properties of the nanoparticles can be expected.

Acknowledgements

I would like to thank my colleagues at the Department for Materials Synthesis, Jožef Stefan Institute, Prof. Dr. Darja Lisjak and Asst. Prof. Dr. Sašo Gyergyek for a fruitful collaboration. The research contribution and experimental help of former and current Ph.D. students and coworkers is also acknowledged: Dr. Darinka Primc, Dr. Blaž Belec, Tanja Goršak, Nina Križaj, and Bernarda Anželak. I am particularly grateful to Prof. Dr. Goran Dražić and other colleague microscopists from the National Institute of Chemistry and Jožef Stefan Institute for their help with the microscopy. I also have to acknowledge Prof. Dr. Matej Komelj from the Department for Nanostructured Materials, Jožef Stefan Institute, Prof. Dr. Layla Martin-Samos, Dr. Matic Poberžnik, and Dr. Gabriela Herrero-Saboya from SISSA, Trieste, for the theoretical considerations, Prof. Dr. Anton Meden from Faculty of Chemistry and Chemical Technology, University of Ljubljana for the XRD analyses of the BIT nanoparticles, Prof. Dr. Rok Kostanjšek from the Biotechnical Faculty, University of Ljubljana, for the help with TEM specimen preparation using microtome, and Dr. Martin Šala from the National Institute of Chemistry for the ICP chemical analyses. The financial support from the Slovenian Research Agency (ARRS) within research core funding No. P2-0089 is greatly appreciated.

5. References

1. G. Guisbiers, *J. Phys. Chem. C* **2011**, 115, 2616–2621. DOI:10.1021/jp108041q
2. T. Kamiyama, K. Haneda, T. Sato, S. Ikeda, H. Asano, *Solid State Commun.* **1992**, 81, 563–566. DOI:10.1016/0038-1098(92)90412-3
3. S. Calvin, E. E. Carpenter, B. Ravel, V. G. Harris, S. A. Morrison, *Phys. Rev.* **2002**, B66, 224405-1–13. DOI:10.1016/0038-1098(92)90412-3
4. D. Makovec, A. Kodre, I. Arčon, M. Drofenik, *J. Nanoparticle Res.* **2008**, 11, 1145–1158. DOI:10.1007/s11051-008-9510-0
5. D. Makovec, M. Drofenik, *J. Nanoparticle Res.* **2008**, 10, 131–141. DOI:10.1007/s11051-008-9400-5
6. D. Makovec, A. Kodre, I. Arčon, M. Drofenik, *J. Nanoparticle Res.* **2011**, 13, 1781–1790. DOI:10.1007/s11051-010-9929-y
7. D. Makovec, B. Belec, T. Goršak, D. Lisjak, M. Komelj, G. Dražić, S. Gyergyek, *Nanoscale* **2018**, 10, 14480–14491. DOI:10.1039/C8NR03815E
8. B. Belec, G. Dražić, S. Gyergyek, B. Podmiljšak, T. Goršak, M. Komelj, J. Nogués, D. Makovec, *Nanoscale* **2017**, 9, 17551–17560. DOI:10.1039/C7NR05894B
9. R. M. Cornell, U. Schwertmann, *The Iron Oxides: Structure, Properties, Reactions, Occurrences and Uses*, Wiley-VCH, Weinheim, 2003. DOI:10.1002/3527602097
10. I. N. Stranski, D. Totomanow, *Z. Phys. Chem.* **1933**, 163, 399–408. DOI:10.1515/zpch-1933-16335
11. A. Navrotsky, *Proc. Natl. Acad. Sci. USA* **2004**, 101, 12096–12101. DOI:10.1073/pnas.0404778101
12. S. Sakurai, A. Namai, K. Hashimoto, S. Ohkoshi, *J. Am. Chem. Soc.* **2009**, 131, 18299–18303. DOI:10.1021/ja9046069
13. M. Tadić, I. Milosevic, S. Kralj, D. Hanzel, T. Barudžija, L. Motte, D. Makovec, *Acta Mater.* **2020**, 188, 16–22. DOI:10.1016/j.actamat.2020.01.058
14. N.T.K. Thanh, *Magnetic Nanoparticles From Fabrication to Clinical Applications*, CRC Press, Boca Raton, 2012.
15. R. Pullar, *Prog. Mat. Sci.* **2012**, 57, 1191–1334. DOI:10.1016/j.pmatsci.2012.04.001
16. A. Mertelj, D. Lisjak, M. Drofenik, M. Čopič, *Nature* **2013**, 504, 237–241. DOI:10.1038/nature12863
17. M. Shuai, A. Klitnick, Y. Shen, G.P. Smith, M.R. Tuchband, C. Zhu, R.G. Petschek, A. Mertelj, D. Lisjak, M. Čopič, J.E. MacLennan, M.A. Glaser, N.A. Clark, *Nat. Commun.* **2016**, 7, 10394-1–8. DOI:10.1038/ncomms10394
18. S.E. Kushnir, A.I. Gavrilov, P.E. Kazin, A.V. Grigorieva, Y.D. Tretyakova, M. Jansen, *J. Mater. Chem.* **2012**, 22, 18893–18901. DOI:10.1039/c2jm33874b
19. A.A. Eliseev, A.A. Eliseev, L.A. Trusov, A.P. Chumakov, P. Boesecke, E.O. Anokhin, A.V. Vasiliev, A.E. Sleptsova, E.A. Gorbachev, V.V. Korolev, P.E. Kazin, *Appl. Phys. Lett.* **2018**, 113, 13106-1–5. DOI:10.1063/1.5044728
20. G. Ferik, P. Kranjc, A. Hamler, A. Mertelj, F. Cebollada, M. Drofenik, D. Lisjak, *Sci. Rep.* **2015**, 5, 11395-1–8. DOI:10.1038/srep11395
21. H. Al-Bustami, G. Koplovitz, D. Primc, S. Yochelis, E. Capua, D. Porath, R. Naaman, Y. Paltiel, *Small* **2018**, 14, 1801249-1–6. DOI:10.1002/sml.201801249
22. G. Koplovitz, D. Primc, O. B. Dor, Shira Y., D. Rotem, D. Porath, Y. Paltiel, *Adv. Mater.* **2017**, 29, 1606748-1–6. DOI:10.1002/adma.201606748
23. J. Hu, T. Gorsak, E. Martín Rodríguez, D. Calle, T. Muñoz-Ortiz, D. Jaque, N. Fernández, L. Cussó, F. Rivero, R. Aguilar Torres, J. García Solé, A. Mertelj, D. Makovec, M. Desco, D. Lisjak, F. Alfonso, F. Sanz-Rodríguez, D. H. Ortgies, *ChemPhotoChem* **2019**, 3, 1–12. DOI:10.1002/cptc.201900071
24. T. Goršak, M. Drab, D. Križaj, M. Jeran, J. Genova, S. Kralj, D. Lisjak, V. Kralj-Iglič, A. Iglič, D. Makovec, *J. Colloid Interface Sci.* **2020**, 579, 508–519. DOI:10.1016/j.jcis.2020.06.079
25. T. Jardiell, A.C. Caballero, M. Villegas, *J. Ceram. Soc. JAPAN* **2008**, 116, 511–518. DOI:10.2109/jcersj2.116.511
26. H. Li, L. Su, S. Kuang, Y. Fan, Y. Wu, Z. L. Wang, G. Zhu, *Nano Res.* **2017**, 10, 785–793. DOI:10.1007/s12274-016-1331-3
27. J. Hu, Y. Yu, H. Guo, Z. Chen, A. Li, X. Feng, B. Xi, G. Hu, *J. Mater. Chem.* **2011**, 21, 5352–5359. DOI:10.1039/c0jm03010d
28. Z. Chen, Y. Yu, H. Guo, J. Hu, *J. Phys. D: Appl. Phys.* **2009**, 42, 125307-1–9. DOI:10.1088/0022-3727/42/12/125307
29. T. Xiao, C. Guo, H. Wanga, R. Zhang, Y. Li, W. Shao, Y.

- Zhang, X. Wu, J. Tan, W. Ye, *Mater. Lett.* **2020**, 269, 127679–127679–4. DOI:10.1016/j.matlet.2020.127679
30. S. Tu, H. Huang, T. Zhang, Y. Zhang, *Appl. Catal.*, 2017, 219, 550–562. DOI:10.1016/j.apcatb.2017.08.001
31. J. Wu, N. Qin, E. Lin, B. Yuan, Z. Kang, D. Bao, *Nanoscale* **2019**, 11, 21128–21136. DOI:10.1039/C9NR07544E
32. Q. Yang, Y. Li, Q. Yin, P. Wang, Y.-B. Cheng, *J. Eur. Ceram. Soc.* **2003**, 23, 161–166. DOI:10.1016/S0955-2219(02)00087-0
33. N. Plakida, *High-Temperature Cuprate Superconductors: Experiment, Theory, and Applications*, Springer, Berlin, Heidelberg, 2012.
34. M. Zhang, D.A. Kitchaev, Z. Lebens-Higgins, J. Vinckeviciute, M. Zuba, P.J. Reeves, C.P. Grey, M.S. Whittingham, L.F.J. Piper, A. Van der Ven, Y.S. Meng, *Nat. Rev. Mater.* **2022**, 7, 522–540. DOI:10.1038/s41578-022-00416-1
35. C. Zhao, Z. Yao, Q. Wang, H. Li, J. Wang, M. Liu, S. Ganapathy, Y. Lu, J. Cabana, B. Li, X. Bai, A. Aspuru-Guzik, M. Wagemaker, L. Chen, Y.-S. Hu, *J. Am. Chem. Soc.* **2020**, 142, 5742–5750. DOI:10.1021/jacs.9b13572
36. Y.X. Gan, A.H. Jayatissa, Z. Yu, X. Chen, M. Li, *J. Nanomater.* **2020**, 8917013–1–3. DOI:10.1155/2020/8917013
37. A.C.T. Koch, Determination of Core Structure Periodicity and Point Defect Density along Dislocations. Ph.D. Thesis, Arizona State University, 2002.
38. D. Lisjak, A. Mertelj, *Prog. Mater. Sci.* **2018**, 95, 286–328. DOI:10.1016/j.pmatsci.2018.03.003
39. D. Primc, D. Makovec, D. Lisjak, M. Drofenik, *Nanotechnology* **2009**, 20, 315605–1–9. DOI:10.1088/0957-4484/20/31/315605
40. M. Drofenik, I. Ban, G. Ferik, D. Makovec, A. Žnidaršič, Z. Jagličić, D. Lisjak, *J. Am. Ceram. Soc.* **2010**, 93, 1602–1607. DOI:10.1111/j.1551-2916.2010.03620.x
41. D. Primc, M. Drofenik, D. Makovec, *European J. Inorg. Chem.* **2011**, 2011, 3802–3809. DOI:10.1002/ejic.201100326
42. D. Lisjak, M. Drofenik, *Cryst. Growth Des.* **2012**, 12, 5174–5179. DOI:10.1021/cg301227r
43. C. Granados-Miralles, M. Saura-Múzquiz, E. D. Bøjesen, K. M. Ø. Jensen, H. L. Andersen, M. Christensen, *J. Mater. Chem. C* **2016**, 4, 10903–10913. DOI:10.1039/C6TC03803D
44. D. Makovec, M. Komelj, G. Dražić, B. Belec, T. Goršak, S. Gyergyek, D. Lisjak, *Acta Mater.* **2019**, 172, 84–91. DOI:10.1016/j.actamat.2019.04.050
45. D. Makovec, G. Dražić, S. Gyergyek, D. Lisjak, *CrystEngComm* **2020**, 22, 7113–7122. DOI:10.1039/D0CE01111H
46. D. Makovec, D. Primc, S. Šturm, A. Kodre, D. Hanzel, M. Drofenik, *J. Sol. State Chem.* **2012**, 196, 63–71. DOI:10.1016/j.jssc.2012.07.043
47. J. A. Kohn, D. W. Eckart, Jr. F. C. Charles, *Science*, **1971**, 172, 519–525. DOI:10.1126/science.172.3983.519
48. M. Poberžnik, G. Herrero-Saboya, D. Lisjak, A. Mertelj, D. Makovec, L. Martin-Samos, Book of Abstracts, SCS Annual Meeting 2022, Portorož, 21–23.9.2022, Slovenian Chemical Society.
49. D. Urushihara, M. Komabuchi, N. Ishizawa, M. Iwata, K. Fukuda, T. Asaka, *J. Appl. Phys.*, **2016**, 120, 142117–1–5. DOI:10.1063/1.4961719
50. H. Gu, Z. Hu, Y. Hu, Y. Yuan, J. You, W. Zou, *Colloids Surf. A Physicochem. Eng.* **2008**, 315, 294–298. DOI:10.1016/j.colsurfa.2007.08.010
51. F. Wang, J. Wang, X. Zhong, B. Li, J. Liu, D. Wu, D. Mo, D. Guo, S. Yuan, K. Zhang, Y. Zhou, *CrystEngComm* **2013**, 15, 1397–1403. DOI:10.1039/c2ce26330k
52. D. Makovec, N. Križaj, S. Gyergyek, *CrystEngComm* **2022**, 24, 3972–3981. DOI:10.1039/D2CE00491G
53. D. Makovec, N. Križaj, A. Meden, G. Dražić, H. Uršič, R. Kostanjšek, M. Šala, S. Gyergyek, *Nanoscale* **2022**, 14, 3537–3544. DOI:10.1039/D2NR00307D
54. D. Makovec, S. Gyergyek, T. Goršak, B. Belec, D. Lisjak, *J. Eur. Ceram. Soc.* **2019**, 39, 4831–4841. DOI:10.1016/j.jeurceramsoc.2019.07.016
55. G. Guisbiers, *J. Phys. Chem. C* **2011**, 115, 2616–2621. DOI:10.1021/jp108041q
56. T. Kamiyama, K. Haneda, T. Sato, S. Ikeda, H. Asano, *Solid State Commun.* **1992**, 81, 563–566. DOI:10.1016/0038-1098(92)90412-3
57. S. Calvin, E. E. Carpenter, B. Ravel, V. G. Harris, S. A. Morrison, *Phys. Rev.* **2002**, B66, 224405–1–13. DOI:10.1016/0038-1098(92)90412-3
58. D. Makovec, A. Kodre, I. Arčon, M. Drofenik, *J. Nanoparticle Res.* **2008**, 11, 1145–1158. DOI:10.1007/s11051-008-9510-0
59. D. Makovec, M. Drofenik, *J. Nanoparticle Res.* **2008**, 10, 131–141. DOI:10.1007/s11051-008-9400-5
60. D. Makovec, A. Kodre, I. Arčon, M. Drofenik, *J. Nanoparticle Res.* **2011**, 13, 1781–1790. DOI:10.1007/s11051-010-9929-y
61. D. Makovec, B. Belec, T. Goršak, D. Lisjak, M. Komelj, G. Dražić, S. Gyergyek, *Nanoscale* **2018**, 10, 14480–14491. DOI:10.1039/C8NR03815E
62. B. Belec, G. Dražić, S. Gyergyek, B. Podmiljšak, T. Goršak, M. Komelj, J. Nogués, D. Makovec, *Nanoscale* **2017**, 9, 17551–17560. DOI:10.1039/C7NR05894B
63. R. M. Cornell, U. Schwertmann, *The Iron Oxides: Structure, Properties, Reactions, Occurrences and Uses*, Wiley-VCH, Weinheim, 2003. DOI:10.1002/3527602097
64. I. N. Stranski, D. Totomanow, *Z. Phys. Chem.* **1933**, 163, 399–408. DOI:10.1515/zpch-1933-16335
65. A. Navrotsky, *Proc. Natl. Acad. Sci. USA* **2004**, 101, 12096–12101. DOI:10.1073/pnas.0404778101
66. S. Sakurai, A. Namai, K. Hashimoto, S. Ohkoshi, *J. Am. Chem. Soc.* **2009**, 131, 18299–18303. DOI:10.1021/ja9046069
67. M. Tadić, I. Milosevic, S. Kralj, D. Hanzel, T. Barudžija, L. Motte, D. Makovec, *Acta Mater.* **2020**, 188, 16–22. DOI:10.1016/j.actamat.2020.01.058
68. N.T.K. Thanh, *Magnetic Nanoparticles From Fabrication to Clinical Applications*, CRC Press, Boca Raton, 2012.
69. R. Pullar, *Prog. Mat. Sci.* **2012**, 57, 1191–1334. DOI:10.1016/j.pmatsci.2012.04.001
70. A. Mertelj, D. Lisjak, M. Drofenik, M. Čopič, *Nature* **2013**, 504, 237–241. DOI:10.1038/nature12863
71. M. Shuai, A. Klitnick, Y. Shen, G.P. Smith, M.R. Tuchband, C. Zhu, R.G. Petschek, A. Mertelj, D. Lisjak, M. Čopič, J.E. MacLennan, M.A. Glaser, N.A. Clark, *Nat. Commun.* **2016**, 7, 10394–1–8. DOI:10.1038/ncomms10394

72. S.E. Kushnir, A.I. Gavrilov, P.E. Kazin, A.V. Grigorieva, Y.D. Tretyakova, M. Jansen, *J. Mater. Chem.* **2012**, *22*, 18893–18901. DOI:10.1039/c2jm33874b
73. A.A. Eliseev, A.A. Eliseev, L.A. Trusov, A.P. Chumakov, P. Boesecke, E.O. Anokhin, A.V. Vasiliev, A.E. Sleptsova, E.A. Gorbachev, V.V. Korolev, P.E. Kazin, *Appl. Phys. Lett.* **2018**, *113*, 13106-1–5. DOI:10.1063/1.5044728
74. G. Ferk, P. Kranjc, A. Hamler, A. Mertelj, F. Cebollada, M. Drofenik, D. Lisjak, *Sci. Rep.* **2015**, *5*, 11395-1–8. DOI:10.1038/srep11395
75. H. Al-Bustami, G. Koplovitz, D. Primc, S. Yochelis, E. Capua, D. Porath, R. Naaman, Y. Paltiel, *Small* **2018**, *14*, 1801249-1–6. DOI:10.1002/smll.201801249
76. G. Koplovitz, D. Primc, O. B. Dor, Shira Y., D. Rotem, D. Porath, Y. Paltiel, *Adv. Mater.* **2017**, *29*, 1606748-1–6. DOI:10.1002/adma.201606748
77. J. Hu, T. Gorsak, E. Martín Rodríguez, D. Calle, T. Muñoz-Ortiz, D. Jaque, N. Fernández, L. Cussó, F. Rivero, R. Aguilar Torres, J. García Solé, A. Mertelj, D. Makovec, M. Desco, D. Lisjak, F. Alfonso, F. Sanz-Rodríguez, D. H. Ortgies, *ChemPhotoChem* **2019**, *3*, 1–12. DOI:10.1002/cptc.201900071
78. T. Goršak, M. Drab, D. Križaj, M. Jeran, J. Genova, S. Kralj, D. Lisjak, V. Kralj-Iglič, A. Iglič, D. Makovec, *J. Colloid Interface Sci.* **2020**, *579*, 508–519. DOI:10.1016/j.jcis.2020.06.079
79. T. Jardiell, A.C. Caballero, M. Villegas, *J. Ceram. Soc. JAPAN* **2008**, *116*, 511–518. DOI:10.2109/jcersj2.116.511
80. H. Li, L. Su, S. Kuang, Y. Fan, Y. Wu, Z. L. Wang, G. Zhu, *Nano Res.* **2017**, *10*, 785–793. DOI:10.1007/s12274-016-1331-3
81. J. Hu, Y. Yu, H. Guo, Z. Chen, A. Li, X. Feng, B. Xi, G. Hu, *J. Mater. Chem.* **2011**, *21*, 5352–5359. DOI:10.1039/c0jm03010d
82. Z. Chen, Y. Yu, H. Guo, J. Hu, *J. Phys. D: Appl. Phys.* **2009**, *42*, 125307-1–9. DOI:10.1088/0022-3727/42/12/125307
83. T. Xiao, C. Guo, H. Wanga, R. Zhang, Y. Li, W. Shao, Y. Zhang, X. Wu, J. Tan, W. Ye, *Mater. Lett.* **2020**, *269*, 127679-1 – 127679-4. DOI:10.1016/j.matlet.2020.127679
84. S. Tu, H. Huang, T. Zhang, Y. Zhang, *Appl. Catal.*, **2017**, *219*, 550–562. DOI:10.1016/j.apcatb.2017.08.001
85. J. Wu, N. Qin, E. Lin, B. Yuan, Z. Kang, D. Bao, *Nanoscale* **2019**, *11*, 21128–21136. DOI:10.1039/C9NR07544E
86. Q. Yang, Y. Li, Q. Yin, P. Wang, Y.-B. Cheng, *J. Eur. Ceram. Soc.* **2003**, *23*, 161–166. DOI:10.1016/S0955-2219(02)00087-0
87. N. Plakida, *High-Temperature Cuprate Superconductors: Experiment, Theory, and Applications*, Springer, Berlin, Heidelberg, 2012.
88. M. Zhang, D. A. Kitchaev, Z. Lebens-Higgins, J. Vinckeviciute, M. Zuba, P.J. Reeves, C.P. Grey, M. S. Whittingham, L. F. J. Piper, A. Van der Ven, Y. S. Meng, *Nat. Rev. Mater.* **2022**, *7*, 522–540. DOI:10.1038/s41578-022-00416-1
89. C. Zhao, Z. Yao, Q. Wang, H. Li, J. Wang, M. Liu, S. Ganapathy, Y. Lu, J. Cabana, B. Li, X. Bai, A. Aspuru-Guzik, M. Wagemaker, L. Chen, Y.-S. Hu, *J. Am. Chem. Soc.* **2020**, *142*, 5742–5750. DOI:10.1021/jacs.9b13572
90. Y. X. Gan, A. H. Jayatissa, Z. Yu, X. Chen, M. Li, *J. Nanomater.* **2020**, 8917013-1–3. DOI:10.1155/2020/8917013
91. A.C.T. Koch, Determination of Core Structure Periodicity and Point Defect Density along Dislocations. Ph.D. Thesis, Arizona State University, 2002.
92. D. Lisjak, A. Mertelj, *Prog. Mater. Sci.* **2018**, *95*, 286–328. DOI:10.1016/j.pmatsci.2018.03.003

Povzetek

Uporabne lastnosti materialov so v veliki meri določene s sestavo in kristalno strukturo materialov. Struktura materiala in posledično tudi njegova sestava se lahko znatno spremenita, če material pripravimo v obliki nanodelcev. Poznavanje sprememb v kristalni strukturi zaradi končne dimenzije nanomaterialov je torej pomembno tako s stališča širjenja osnovnega znanja, kot tudi za načrtovanje novih nanomaterialov za uporabo v tehnologiji in medicini. Spremembe v strukturi so lahko posledica dveh različnih pojavov: (i) kristalna struktura se prilagodi končni velikosti nanodelcev, in (ii) z majhno velikostjo delcev lahko stabiliziramo različne metastabilne strukturne polimorfe, ki nastanejo med sintezo v tekočem zaradi nižje energijske pregrade za nukleacijo v primerjavi z energijsko pregrado potrebno za nukleacijo ravnotežnih faz. Omenjene spremembe v kristalni strukturi so posebej pogoste pri anorganskih materialih s kompleksno strukturo in sestavo, kot so zmesni oksidi s plastovito strukturo sestavljeno iz več strukturnih blokov. Pričujoči članek pojasnjuje kompleksno strukturo nanodelcev na primerih dveh dobro znanih in tehnološko zelo pomembnih materialov s plastovito strukturo: magnetnih heksaferitov ($\text{BaFe}_{12}\text{O}_{19}$ in $\text{SrFe}_{12}\text{O}_{19}$) in feroelektričnega bizmutovega titanata ($\text{Bi}_4\text{Ti}_3\text{O}_{12}$) s plastovito perovskitno strukturo Aurivilliusovega tipa.



Except when otherwise noted, articles in this journal are published under the terms and conditions of the Creative Commons Attribution 4.0 International License

Synthesis, Characterization, Anti-Glycation, and Anti-Oxidant Activities of Sulfanilamide Schiff Base Metal Chelates

Muhammad Yaqoob,¹ Waqas Jamil,^{1,*} Muhammad Taha² and Sorath Solangi¹

¹ Institute of Advanced Research Studies in Chemical Sciences, University of Sindh, Jamshoro, Pakistan

² Institute for Research and Medical Consultations (IRMC), Imam Abdulrahman Bin Faisal University, Dammam, Saudi Arabia

* Corresponding author: E-mail: waqas.jamil@usindh.edu.pk

Received: 02-21-2022

Abstract

The current study reports synthesis, structure establishment, anti-glycation, and anti-oxidant activities of ligand 4-[(2-hydroxynaphthalene-1-ylmethylene)-amino]-benzenesulfonamide (L) and its coordination compounds with Mn(II), Co(II), Ni(II), Cu(II), and Zn(II) metal ions. The analytical techniques used (UV-Vis, FT-IR, CHN/S) confirmed the bidentate nature of the ligand, coordinating *via* O and N atoms in 2:1 ligand-to-metal ratio. The TG/DTA analysis displayed that these compounds are thermally stable. Furthermore, the synthesized compounds were evaluated for their anti-glycation and antioxidant potential and showed significant activities with IC₅₀ values range 184.11–386.34 μM and 37.05–126.27 μM, respectively. The Mn (IC₅₀ = 184.11 ± 2.11 μM), Ni (IC₅₀ = 211.26 ± 1.46 μM), Cu (IC₅₀ = 254.56 ± 1.16 μM), and Zn (IC₅₀ = 276.43 ± 2.14 μM) metal complexes exhibited substantial anti-glycation activity and comparatively better activity than the standard rutin (IC₅₀ = 294.4 ± 1.50 μM), whereas Zn complex (IC₅₀ = 37.05 ± 1.53 μM) also showed better DPPH radical scavenging activity than the standard *tert*-butyl-4-hydroxyanisole (IC₅₀ = 44.7 ± 1.21 μM).

Keywords: 4-[(2-Hydroxynaphthalene-1-ylmethylene)amino]benzenesulfonamide (L), Coordination Compounds, Anti-oxidant activity, Anti-glycation activity

1. Introduction

Coordination chemistry deals with the study of coordination compounds or metal complexes. The group of ten elements (*i.e.* V, Cr, Fe, Mn, Co, Cu, Ni, Mo, Zn, and Cd) form many complexes with various biomolecules to execute different biological functions.^{1,2} These metal complexes are required for our bodies in very small quantities, but their excess or deficiency can cause many serious diseases.^{3,4} The clinical and commercial importance of metal complexes as medicinal drugs is increasing day by day for the treatment of various diseases.^{5,6} The synthesis of metal complexes as chemotherapeutic agents in clinical application has shown significant progress in medicinal chemistry to fight against several human diseases, such as to treat different types of cancers, tumors, diabetes mellitus, anti-inflammation, possessing antifungal activity and acting against a wide range of bacterial diseases.^{7–9} Recently, the metal complexes of transition elements have shown great importance in materials synthesis, catalysis and photo-

chemistry.^{10,11} The platinum metal complexes including cisplatin, carboplatin and nedaplatin are widely used drugs for cancer chemotherapy.¹² Copper(II), zinc(II), vanadium(V) and oxidovanadium(V) metal complexes have been reported for their excellent antibacterial urease enzyme inhibition and catalytic properties.^{13–17}

According to the literature, sulfonamides have a variety of bioactivities, including antitumor, antimalarial, antimicrobial, antithyroid, antidiabetic, anti-HIV/AIDS, anti-parasitic, antiepileptic, and dihydropteroate synthetase inhibitors activities.^{18–21} Sulfonamide metal chelates derivatives have also been reported for their anti-inflammatory, antidiabetic, anti-HIV, anticancer, anti-carbonic anhydrase, diuretic, hypoglycemic, antithyroid, antimalarial, antitumor, anti-angiogenic, anti-tubercular, antibacterial, and antifungal activities.^{22–25} Moreover, gold sulfonamide chelates were also found to have applications for the treatment of skin disorders and rheumatoid arthritis.²⁶

Schiff bases are widely studied compounds due to their structural resemblance with the natural bioactive molecules and ease of synthesis of diverse structures.^{27,28} The importance of Schiff base complexes in supramolecular chemistry, catalysis and material science, separation and encapsulation processes, biomedical applications and formation of compounds with unusual properties and structures has been well recognized and reviewed.^{29–31} Sulfonamides Schiff base complexes with cobalt(II), copper(II), nickel(II) and zinc(II) have shown significant *in vitro* antibacterial, antifungal, and cytotoxic properties. The *N,N*-chelating half-sandwich ruthenium(II) *para*-cymene complexes containing sulfonamide moieties also showed a broad range of therapeutic applications, which include the inhibition of various isoforms of carbonic anhydrases (CAs).³²

Glycation is a reaction of blood sugar with the proteins like collagen; when this reaction occurs in a great extent advanced glycation products (AGEs) are formed which may further degrade protein and cause oxidative stress that damage cell membranes and produce diabetic complications such as neuropathy and diabetes retinopathy which further increase the rate of the aging processes.

Oxidative stress is the main aspect of all living systems which occurs due to the excess of free radicals. Due to oxidative stress, biochemical energy is converted into adenosine triphosphate with the help of oxygen, this biochemical reaction generates reactive oxygenated species (ROS). These ROS can damage lipids, proteins, and DNA by oxidation and cause many diseases such as cancer, brain disorders, rheumatoid arthritis, atherosclerosis, obesity, aging, diabetes and skin disease.³³ Antioxidant compounds are used as health-protecting factors in food playing an important role in preventing many diseases. The antioxidant compounds obtained from plants such as carotenes, phenolic acids, vitamin C and E, phytate, and phytoestrogens were found to be very helpful in decreasing the risks of many diseases. A number of synthetic compounds have also been reported having remarkable anti-oxidant properties.³⁴ The cosmetic and food industries are funded by several companies to promote the research of the synthesis of glycation-inhibiting ingredients and anti-oxidants in order to discover new anti-aging compounds for keeping skin youthful for a prolonged period. The latest research focuses on finding the ways for the inhibition of AGEs formation, and on reducing oxidative stress with the objective

of promoting health by treating degenerative changes and mitigating the effect of lifestyle-related diseases.³⁵

Earlier, we have reported anti-glycation and anti-oxidant properties of isatin containing hydrazone Schiff base metal complexes.³⁶ In the continuation of exploring metal complexes for bioactivities, herein we have synthesized 4-[(2-hydroxynaphthalen-1-ylmethylene)amino]benzenesulfonamide Schiff base ligand (L) and its metal (Mn, Co, Ni, Cu, Zn) complexes for the evaluation of anti-glycation and anti-oxidant activities.

2. Experimental

2.1. Physical Parameters

Elemental (CHN/S), TG/DTA, and UV-Vis and metal content analyses were done on Perkin Elmer's 2400 Series II and Diamond TG/DTA, Lambda 35 UV-Vis spectrophotometer, and Analyst 800 atomic absorption spectrophotometer, respectively. FT-IR were performed by Thermoscientific iS10 IR spectrophotometer in the region 4000–600 cm⁻¹. Bruker 300 MHz spectrometer was used for ¹H NMR experiments. EI-MS were measured on Finnigan MAT-311A (Germany) mass spectrometer. Molar conductance was measured on Thermoscientific Orian 5 Star meter.

2.2. Materials and Methods

Analytical grade chemicals (Sigma-Aldrich) sulfanilamide, 2-hydroxynaphthaldehyde, acetic acid, ammonium acetate and metal salts *viz* MnSO₄·H₂O, Co(CH₃COO)₂·4H₂O, Ni(CH₃COO)₂·4H₂O, CuCl₂·2H₂O, and Zn(CH₃COO)₂·2H₂O were used for synthesis. Bovine serum albumin (BSA) was obtained from Research Organics (Cleveland, USA).

2.3. Synthesis of 4-[(2-Hydroxynaphthalen-1-ylmethylene)amino]benzenesulfonamide ligand (L)

0.5 mol of 2-hydroxynaphthaldehyde was added to 50 mL methanol with 2 to 3 drops of acetic acid and then added equimolar amount of sulfanilamide and refluxed for about 8 hours. The solvent was evaporated, precipitate obtained, dried and recrystallized from ethanol (Figure 1).

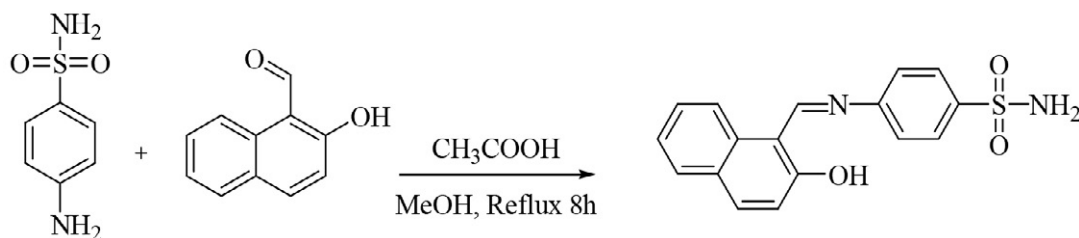


Figure 1. Synthesis of 4-[(2-hydroxynaphthalen-1-ylmethylene)amino]benzenesulfonamide ligand (L)

Yield 80%, m.p. 278 °C. FT-IR ν_{\max} 3290 (-OH, NH), 1622 (-C=N-), 1347 (O=S=O), 1586 (-C=C-) cm^{-1} . ^1H NMR (DMSO- d_6 , 300 MHz) δ 6.87 (s, 1H, OH), 9.68 (s, 1H, CH=N), 8.52 (d, 2H, Ar, J = 8.7 Hz), 7.97 (d, 2H, Ar, J = 8.3 Hz), 6.88 (d, 1H, J = 7.4 Hz), 7.02 (d, 1H, J = 7.4 Hz), 7.58 (d, 2H, Ar, J = 7.6 Hz), 7.44 (m, 2H). EI-MS m/z 326 (M^+) 310, 246, 170, 157, 153, 77. Anal. Calcd for $\text{C}_{17}\text{H}_{14}\text{N}_2\text{O}_3\text{S}$: C, 62.56; H, 4.32; N, 8.85; S, 9.82. Found: C, 62.51; H, 4.30; N, 8.79; S, 9.80.

2. 4. Synthesis of 4-[(2-Hydroxynaphthalene-1-ylmethylene)amino]benzenesulfonamide Ligand Metal Chelates

$\text{MnSO}_4 \cdot \text{H}_2\text{O}$, $\text{Co}(\text{CH}_3\text{COO})_2 \cdot 4\text{H}_2\text{O}$, $\text{Ni}(\text{CH}_3\text{COO})_2 \cdot 4\text{H}_2\text{O}$, $\text{CuCl}_2 \cdot 2\text{H}_2\text{O}$, and $\text{Zn}(\text{CH}_3\text{COO})_2 \cdot 2\text{H}_2\text{O}$ metal salts were refluxed with the ethanolic solution of 4-[(2-hydroxynaphthalene-1-ylmethylene)amino]benzenesulfonamide ligand (L) and ammonium acetate for 6 h. Then, the solvent was evaporated and the obtained precipitates were isolated and washed with water. The structures of these compounds were confirmed by UV/Vis, FT-IR spectroscopy and CHN/S analysis, while thermal stability was measured by TG/DTA analysis.

Mn(L) $_2$ · 2H $_2$ O. Yield 83%, m.p. 235 °C. FT-IR ν_{\max} 3480 (H_2O), 3278 (-OH, NH), 1615 (-C=N-), 1348 (O=S=O), 1587 (-C=C-) cm^{-1} . Anal. Calcd for $\text{C}_{34}\text{H}_{26}\text{N}_4\text{O}_6\text{S}_2\text{Mn}$: C, 55.06; H, 4.08; N, 7.55; S, 8.65. Found: C, 55.01; H, 4.01; N, 7.51; S, 8.60. Electrical conductance (DMF, μScm^{-1}): 5.22.

Co(L) $_2$ · 2H $_2$ O. Yield 84%, m.p. 170 °C. FT-IR ν_{\max} 3480 (H_2O), 3278 (-OH, NH), 1615 (-C=N-), 1348 (O=S=O), 1587 (-C=C-) cm^{-1} . Anal. Calcd for $\text{C}_{34}\text{H}_{30}\text{N}_4\text{O}_8\text{S}_2\text{Co}$: C, 54.76; H, 4.06; N, 7.51; S, 8.60. Found: C, 54.73; H, 4.01; N, 7.47; S, 8.51. Electrical conductance (DMF, μScm^{-1}): 9.53.

Ni(L) $_2$ · 2H $_2$ O. Yield 87%, m.p. 250 °C. FT-IR ν_{\max} 3480 (H_2O), 3278 (-OH, NH), 1615 (-C=N-), 1348 (O=S=O), 1587 (-C=C-) cm^{-1} . Anal. Calcd for $\text{C}_{34}\text{H}_{30}\text{N}_4\text{O}_8\text{S}_2\text{Ni}$: C, 54.78; H, 4.06; N, 7.52; S, 8.60. Found: C, 54.70; H, 4.02; N, 7.46; S, 8.64. Electrical conductance (DMF, μScm^{-1}): 0.25.

Cu(L) $_2$ · 2H $_2$ O. Yield 85%, m.p. 210 °C. FT-IR ν_{\max} 3480 (H_2O), 3278 (-OH, NH), 1615 (-C=N-), 1348 (O=S=O), 1587 (-C=C-) cm^{-1} . Anal. Calcd for $\text{C}_{34}\text{H}_{30}\text{N}_4\text{O}_8\text{S}_2\text{Cu}$: C, 54.43; H, 4.03; N, 7.47; S, 8.55. Found: C, 54.40; H, 4.01; N, 7.41; S, 8.49. Electrical conductance (DMF, μScm^{-1}): 53.9.

Zn(L) $_2$ · 2H $_2$ O. Yield 81%, m.p. 250 °C. FT-IR ν_{\max} 3480 (H_2O), 3278 (-OH, NH), 1615 (-C=N-), 1348 (O=S=O), 1587 (-C=C-) cm^{-1} . Anal. Calcd $\text{C}_{34}\text{H}_{30}\text{N}_4\text{O}_8\text{S}_2\text{Zn}$: C, 54.29; H, 4.02; N, 7.45; S, 8.53. Found: C, 54.25; H, 4.01; N, 7.38; S, 8.44. Electrical conductance (DMF, μScm^{-1}): 2.02.

2. 5. Anti-Oxidant (DPPH Radical Scavenging) Protocol

1,1-Diphenyl-2-picrylhydrazyl (DPPH) free radical was used to measure the scavenging activity of ligand and metal complexes by using literature protocols. The reaction matrix consists of 5 μL test sample (1 mM in DMSO) and 300 μM DPPH (95 μL) and ethanol as the solvent. After 30 min of incubation at 37 °C, the absorbance of test samples was measured at 515 nm. All the samples were tested in triplicate. The following formula was used to calculate percent radical scavenging activity, whereas DMSO was used as a control.

$$\% \text{ inhibition} = \frac{1 - \text{Absorbance of analyte}}{\text{Absorbance of the control group}} \cdot 100$$

50% of DPPH scavenge radicals represented by IC_{50} values. *tert*-Butyl-4-hydroxyanisole was used as the control. The anti-oxidant activities with IC_{50} values were measured according to the reported procedures.³⁷

2. 6. Anti-Glycation Activity

Bovine Serum Albumin (10 mg/mL), anhydrous D-glucose (14 mM), and 0.1 M phosphate buffer (pH 7.4) containing sodium azide (30 mM) and various concentrations of the tested compounds in DMSO were incubated at 37 °C for 9 days. After 9 days, fluorescence (excitation, 330 nm; emission, 440 nm) was measured against blank. Rutin was taken as the standard anti-glycation agent. The AGE % inhibition was calculated by given formula:

$$\% \text{ inhibition} = \frac{1 - \text{Fluorescence of analyte}}{\text{Fluorescence of the control}} \cdot 100$$

The anti-glycation activities with IC_{50} values were measured according to the reported procedures.³⁸

3 Result and Discussion

3. 1. Chemistry

The literature revealed that metal complexes may be useful candidates in drug development process, therefore these compounds were synthesized and evaluated for their various physical parameters as well as bioactivities.

The ligand and its metal chelates were coloured, non-hygroscopic in nature, stable in air, have sharp melting points and were obtained with good yield. All metal chelates including the ligand were insoluble in hexane, chloroform, water, and ethanol although they were found to be soluble in dimethyl sulfoxide (DMSO) and dimethyl formamide (DMF). The electrical conductance values for metal chelates in DMF solvent were found to be 0.25 to 53.9 $\mu\text{S}/\text{cm}^{-1}$. These values indicate the non-electrolytic

nature of metal chelates and the ligand are shown in Table S.1 (see Supp. data).

3. 2. Molecular Formula of the Ligand and Metal Complexes

The CHN/S elemental micro-analysis data agree well with the proposed formulae for 4-[(2-hydroxynaphthalene-1-ylmethylene)amino]benzenesulfonamide ligand (L) and also confirm the composition of all synthesized metal chelates (Figure 2). The elemental analysis results show that calculated values are in close agreement with the values found. Elemental analysis confirmed the formula of the ligand and its metal complexes with 1:2 metal ligand ratio indicating the bidentate nature of the ligand as shown in Table S.2 (see Supp. data).

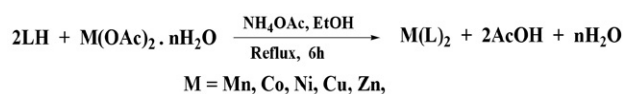


Figure 2. Proposed reaction for the synthesis of metal chelates

3. 3. Electronic Spectra

The UV-Vis spectra (see Supp. data Figures S.3–S.8) of 4-[(2-hydroxynaphthalene-1-ylmethylene)amino]benzenesulfonamide (L) and its metal chelates were determined in DMSO solutions and show absorption bands at a longer wavelength with increasing intensity as shown in Table S.3 (see Supp. data). The ligand showed characteristic absorption bands at 315 and 364 nm. These bands were assigned to $\pi \rightarrow \pi^*$ intra ligand transitions. The UV-Vis spectra of all metal complexes showed bathochromic shifts [$\text{Mn}(\text{L})_2$, 467 nm], [$\text{Co}(\text{L})_2$, 471 nm], [$\text{Ni}(\text{L})_2$, 473 nm], [$\text{Cu}(\text{L})_2$, 470 nm], [$\text{Zn}(\text{L})_2$, 472 nm] that were taken as an indication for metal complexation. These shifts might be attributed to the d-d-transitions. There were characteristic electronic transitions within the range of 260 nm to approximately 380 nm, that were also observed; these bands being unique for the electronic inter-ligand $\pi \rightarrow \pi^*$ transitions. Ligand to metal charge transfer (LMCT) peaks were also observed in a distinct region, *i.e.* within the range of 412 nm onwards, and these are a characteristic feature of nitrogen and oxygen atoms charge transfer to the central metal atoms.

3. 4. IR Spectroscopy

The data obtained from FT-IR spectra (see Supp. data Figures S.9–S.14) of some important functional groups of 4-[(2-hydroxynaphthalene-1-ylmethylene)amino]benzenesulfonamide (L) and its metal chelates are presented in Table S.4 (see Supp. material). The IR spectrum of the ligand showed strong absorption bands at 1622 and 3290 cm^{-1} , which were attributed to the characteristic

band of the $\nu(\text{-C=N-})$ and $\nu(\text{-OH})$ or -NH groups respectively. The sharp bands observed at 1347 cm^{-1} are due to -S=O stretching vibration. FT-IR spectral calculation revealed that for the ligand, which may act as a bidentate according to its structure, is expected that FT-IR measurements will be highly indicative with respect to the complexation behavior with various metal ions. Peaks in 3400 to 3500 cm^{-1} region support the observation of water molecules participating in the complex formation; this being further confirmed by CHN/S and thermogravimetric data. In the case of metal complexes, the peaks for azomethine group (-C=N-) were shifted from 1622 cm^{-1} to 1615, 1612, 1610, 1609, 1608 cm^{-1} and hydroxy group (-OH) peaks were shifted from 3290 cm^{-1} to 3278, 3260, 3248, 3240, 3237 cm^{-1} for $\text{Mn}(\text{L})_2$, $\text{Co}(\text{L})_2$, $\text{Ni}(\text{L})_2$, $\text{Cu}(\text{L})_2$ and $\text{Zn}(\text{L})_2$ complexes, respectively. The changes in the frequency of the peaks indicated that these two groups are involved in coordination. Only spectra of metal complexes showed these new bands, which were thus established as those participating in these donor groups. The band at 1347 cm^{-1} for the -SO_2 group remains almost unaltered in the chelates, demonstrating that -SO_2 group is not contributing to the coordination.

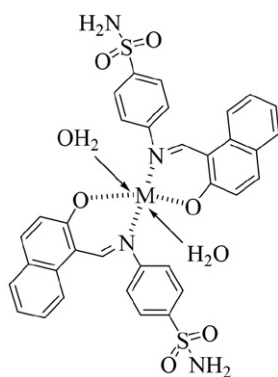
3. 5. Thermogravimetric Analysis of Ligand and Its Metal Chelates

The ligand 4-[(2-hydroxynaphthalene-1-ylmethylene)amino]benzenesulfonamide and its metal chelates were subjected for thermal stability profile. According to the TGA thermograms (see Supp. data Figures S.15–S.20) the ligand showed no weight loss upon heating till 250 °C. The further TGA process of the ligand was carried out which showed thermal decomposition in two stages. In the first stage the TGA curve of thermal decomposition was observed between 250–300 °C with weight loss of 1.85%, while the second stage was observed between 300–350 °C with weight loss of 39.5%. DTA thermogram showed one exothermic peak at 328 °C, while two endothermic peaks appeared at 69.42 °C and 270 °C, these may be due to some physical or chemical change phenomenon occurring during weight loss, such as melting, phase change, chemisorptions etc. The TGA of $\text{Mn}(\text{L})_2$ complex showed thermal decomposition in three stages. In the first stage the TGA curve of thermal decomposition was observed between 150–200 °C with weight loss of 5.78%, this might be due to the dehydration process. The second and the third stages were observed between 200–250 °C (13.7%), and 250–350 °C (28.1%). These stages correspond to the decomposition of organic part of metal complex. The DTA thermogram showed three endothermic peaks which were observed at 172 °C, 219 °C, and 326 °C. The TGA of $\text{Co}(\text{L})_2$ complex showed thermal decomposition in two stages. In the first stage the TGA curve of thermal decomposition was observed between 150–200 °C with weight loss of 3.6%, the second stage was observed within the temperature range

200–350 °C with weight loss of 59.04%. These weight losses are linked with the loss of water molecules and disintegration of the ligand molecule. The two endothermic peaks were spotted at 115 °C and 225 °C in DTA. The TGA of Ni(L)_2 complex showed thermal decomposition in three stages, *i.e.* 150–250 °C, 250–350 °C and 350–410 °C with weight loss of 39.9%, 11.79%, and 16.05%, respectively. These weight losses are due to the dehydration breakdown of ligand. In the DTA thermogram three endothermic peaks appeared at 127 °C, 325 °C, and 388 °C. The TGA of Cu(L)_2 complex showed thermal decomposition in two stages. In the first stage the TGA curve of thermal decomposition was observed between 150–200 °C with weight loss of 4.14% (dehydration), while the second thermal putrefaction chelating molecule was observed at 200–350 °C with weight loss of 28.07%. Three endothermic peaks were marked in DTA thermogram at 91 °C, 246 °C, and 300 °C. The thermal disintegration of Zn(L)_2 complex was observed in three stages. In the first stage the thermal decomposition was observed at 150–270 °C with weight loss of 4.23%, possibly due to the dehydration; the second at 270–370 °C (28.7%), while the third stage was observed at 400–460 °C with weight loss of 10.89%. The DTA thermogram showed five endothermic peaks which were observed at 108 °C, 148 °C, 251 °C, 346 °C, and 441 °C. These values are closely related to the calculated values. The metal chelates total weight loss thermal stability was found to be as $\text{Cu} > \text{Zn} > \text{Mn} > \text{Co} > \text{Ni}$ (Table S.5, see Supp. data).

3. 6. Structural Interpretation

The data of spectroscopic, elemental and thermal analyses revealed that metals are coordinated *via* N and O atoms of ligand molecules in 1:2 M/L ratio (Figure 3). It is reported in the literature that copper can form the octahedral coordinated metal complexes such as $[\text{Cu}(\text{Hmbm})_2(\text{OAc})_2]$, which was reported as an octahedral complex. Hmbm is bonded to the Cu(II) ion in a chelating mode through its nitrogen and oxygen atoms, and two carboxylic oxygen atoms complete the octahedral coordi-



M = Mn, Co, Ni, Cu, Zn,

Figure 3. The proposed structures for metal chelates

nation. The coordination of a water molecule was confirmed by FT-IR and XRD data.⁴⁰ For the same cause, the synthesized complexes have the octahedral geometry.

4. Biological Screening

4. 1. Anti-Glycation Activity

4-[(2-Hydroxynaphthalene-1-ylmethylene)amino] benzenesulfonamide ligand (L) and its metal chelates were tested for their anti-glycation activity, using rutin ($\text{IC}_{50} = 294.4 \pm 1.50 \mu\text{M}$) as the standard (Table 1). They showed excellent anti-glycation activity. The ligand ($\text{IC}_{50} = 265.11 \pm 1.86 \mu\text{M}$) and its metal chelates including Mn(L)_2 ($\text{IC}_{50} = 184.11 \pm 2.11 \mu\text{M}$), Zn(L)_2 ($\text{IC}_{50} = 211.26 \pm 2.14 \mu\text{M}$), Ni(L)_2 ($\text{IC}_{50} = 254.56 \pm 1.73 \mu\text{M}$), Cu(L)_2 ($\text{IC}_{50} = 276.43 \pm 1.16 \mu\text{M}$) showed outstanding anti-glycation activity, whereas, Co(L)_2 ($\text{IC}_{50} = 386.34 \pm 1.46 \mu\text{M}$) was observed as a weak anti-glycating agent. Among them, Mn(L)_2 complex showed the highest activity and it was found to be many fold more active than the standard rutin. However, Zn(L)_2 , Ni(L)_2 , and Cu(L)_2 are comparatively less active than Mn(L)_2 complex, although they were also found to have better activities than the standard. The activity pattern of these complexes can therefore be depicted as: $\text{Mn(L)}_2 > \text{Zn(L)}_2 > \text{Ni(L)}_2 > \text{Cu(L)}_2 > \text{Co(L)}_2$ (see Supp. data S.21–S.24). It was found that these chelates have capability to interact with proteins or glucose in a great extent and can obstruct the advancement of glycation. The active compounds may insert into hydrophobic cavities of BSA followed by the inhibition of advance glycation. Mn(L)_2 has elevated level of insertion into the slots of BSA protein.

Table 1. Anti-glycation Activity of Ligand and Respective Chelates

S#	Compounds	Anti-Glycation IC_{50} ($\mu\text{M} \pm \text{SEM}^a$)
1.	Ligand	265.11 ± 1.86
2.	$\text{Mn(L)}_2 \cdot 2\text{H}_2\text{O}$	184.11 ± 2.11
3.	$\text{Co(L)}_2 \cdot 2\text{H}_2\text{O}$	386.34 ± 1.46
4.	$\text{Ni(L)}_2 \cdot 2\text{H}_2\text{O}$	254.56 ± 1.73
5.	$\text{Cu(L)}_2 \cdot 2\text{H}_2\text{O}$	276.43 ± 1.16
6.	$\text{Zn(L)}_2 \cdot 2\text{H}_2\text{O}$	211.26 ± 2.14
7.	Rutin	294.4 ± 1.50

^a SEM is the standard error of the mean; ^b rutin is standard inhibitor for anti-glycation activity

4. 2. Antioxidant Assay

4-[(2-Hydroxynaphthalene-1-ylmethylene)amino] benzenesulfonamide ligand (L) and its metal chelates were assessed for DPPH radical scavenging activity (Table 2). Ligand ($\text{IC}_{50} = 65.58 \pm 1.29 \mu\text{M}$) itself was found to be weakly active, while its metal complex Zn(L)_2 ($\text{IC}_{50} = 37.05 \pm 1.53 \mu\text{M}$) showed excellent antioxidant activity as com-

pared to the standard *tert*-butyl-4-hydroxyanisole ($IC_{50} = 44.7 \pm 1.21 \mu M$). The metal complexes such as $Mn(L)_2$ ($IC_{50} = 76.1 \pm 1.44 \mu M$), $Cu(L)_2$ ($IC_{50} = 86.11 \pm 1.12 \mu M$), $Co(L)_2$ ($IC_{50} = 112.14 \pm 1.11 \mu M$), and $Ni(L)_2$ ($IC_{50} = 126.27 \pm 1.54 \mu M$) were found to be less active than the standard. The order of anti-oxidant potential of these chelates is $Zn(L)_2 > Mn(L)_2 > Cu(L)_2 > Co(L)_2 > Ni(L)_2$.

Table 2. Antioxidant Activity of Ligand and Respective Chelates

S#	Compounds	DPPH Radical Scavenging Activity IC_{50} ($\mu M \pm SEM^a$)
1.	Ligand	65.58 ± 1.29
2.	$Mn(L)_2 \cdot 2H_2O$	76.1 ± 1.44
3.	$Co(L)_2 \cdot 2H_2O$	112.14 ± 1.11
4.	$Ni(L)_2 \cdot 2H_2O$	126.27 ± 1.54
5.	$Cu(L)_2 \cdot 2H_2O$	86.11 ± 1.12
6.	$Zn(L)_2 \cdot 2H_2O$	37.05 ± 1.53
7.	<i>tert</i> -butyl-4-hydroxyanisole ^b	44.7 ± 1.21

^a SEM is the standard error of the mean; ^b *tert*-butyl-4-hydroxyanisole is standard inhibitor for antioxidant activity

5. Conclusion

4-[(2-Hydroxynaphthalene-1-ylmethylene)amino]benzenesulfonamide ligand (L) and its $Mn(L)_2$, $Co(L)_2$, $Ni(L)_2$, $Cu(L)_2$, $Zn(L)_2$ chelates were investigated for anti-glycation and DPPH radical scavenging activity. Among these chelates $Mn(L)_2$ ($IC_{50} = 184.11 \pm 2.11 \mu M$), $Zn(L)_2$ ($IC_{50} = 211.26 \pm 2.14 \mu M$), $Ni(L)_2$ ($IC_{50} = 254.56 \pm 1.73 \mu M$), and $Cu(L)_2$ ($IC_{50} = 276.43 \pm 1.16 \mu M$) showed notable anti-glycation potential while $Zn(L)_2$ ($IC_{50} = 37.05 \pm 1.53 \mu M$) showed excellent DPPH radical scavenging activity. The results show that these complexes have excellent potential towards anti-glycation activity. So, it is concluded that these complexes may serve as organometallic lead compounds in the drug development process to cure diabetic complications. However, further studies on the mechanisms of antioxidation and anti-glycation are required.

Acknowledgement

The authors are thankful to the University of Sindh, Jamshoro and Imam Abdulrahman Bin Faisal University, Dammam, Saudi Arabia to support this research work.

Conflict of Interest

There is no conflict of interest

Supplementary Data

Tables S.1–S.5 and figures S.1–S.24 (proton NMR and mass spectrum of the ligand; UV-Vis, FT-IR and

TGA/DTA spectra of the ligand and complexes; structure of complexes).

5. References

1. T. E. Brown, H. E. LeMay, B. E. Bursten, C. Murphy, P. Woodward, *Chemistry: The Central Science*, 12th edition. Pearson Education, Inc., publishing as Pearson Prentice Hall, 2012.
2. V. U. Rani, G. Jyothi, G. N. Rao, B. B. V. Sailaja, *Acta Chim. Slov.* **2010**, 57, 916–921.
3. B. Nagy, A. Maicaneanu, C. Indolean, S. Burca, L. S. Dumitrescu, C. Majdik, *Acta Chim. Slov.* **2013**, 60, 263–273.
4. M. Strlič, J. Kolar, V.-S. Šelih, D. Kočar, B. Pihlar, *Acta Chim. Slov.* **2003**, 50, 619–632.
5. I. Ott, *Coord. Chem. Rev.* **2009**, 253, 1670–1681. DOI:10.1016/j.ccr.2009.02.019
6. C. X. Zhang, S. J. Lippard, *Curr. Opin. Chem. Biol.* **2003**, 7, 481–489. DOI:10.1016/S1367-5931(03)00081-4
7. P. Ghanghas, A. Choudhary, D. Kumar, K. Poonia, *Inorg. Chem. Commun.* **2021**, 130, 108710. DOI:10.1016/j.inoche.2021.108710
8. J. Karges, R.W. Stokes, S. M. Cohen, *Trends Chem.* **2021**, 3, 7523–7534. DOI:10.1016/j.trechm.2021.03.006
9. G. Benchamas, G. Huang, S. Huang, H. Huang, *Trends Food Sci Technol.* **2021**, 107, 38–44. DOI:10.1016/j.tifs.2020.11.027
10. A. A. Warra, *J. Chem. Pharm. Res.* **2011**, 3, 951–958.
11. B. Yin, Z. Luo, *Coord. Chem. Rev.* **2021**, 429, 213643. DOI:10.1016/j.ccr.2020.213643
12. A. Khoury, K. M. Deo, J. R. Aldrich-Wright, *J. Inorg. Biochem.* **2020**, 207, 111070. DOI:10.1016/j.jinorgbio.2020.111070
13. C. Liu, *Acta Chim. Slov.* **2022**, 69, 157–166. DOI:10.17344/acsi.2021.7167
14. Y. Lei, *Acta Chim. Slov.* **2022**, 69, 235–242. DOI:10.17344/acsi.2021.7296
15. W. G. Zhang, J.H. Liang, *Acta Chim. Slov.* **2021**, 68, 921–929. DOI:10.17344/acsi.2021.6902
16. Y. Yuan, X. K. Lu, G. Q. Zhou, X. Y. Qiu, *Acta Chim. Slov.* **2021**, 68, 1008–1015. DOI:10.17344/acsi.2021.7070
17. H. Zhao, X. R. Liu, X. Wang, J. Hu, Y. J. Cai, Q. A. Peng, *Acta Chim. Slov.* **2021**, 68, 804–810. DOI:10.17344/acsi.2021.6781
18. S. A. Dalia, F. Afsan, M. S. Hossain, M. N. Khan, C. Zakaria, M. K. Zahan, M. M. Ali, *Int. J. Chem. Stud.* **2018**, 6, 2859–2866.
19. S. Rafique, M. Idrees, A. Nasim, H. Akbar, A. Athar, *Biotechnol. Mol. Biol. Rev.* **2010**, 5, 38–45.
20. X. Liu, C. Manzur, N. Novoa, S. Celedón, D. Carrillo, J. Hamon, *Coord. Chem. Rev.* **2018**, 357, 144–172. DOI:10.1016/j.ccr.2017.11.030
21. M. A. Abbasi, S. Ahmad, Aziz-ur-Rehman, S. Rasool, M. K. Khan, M. Ashraf, R. Nasar, T. Ismail, *Trop. J. Pharm.* **2014**, 13, 739–745. DOI:10.4314/tjpr.v13i5.13
22. N. Al-Mohammed, Y. Alias, Z. Abdullah, R. M. Shakir, R. M. Taha, A. Hamid, *Molecules.* **2013**, 18, 11978–11995. DOI:10.3390/molecules181011978
23. A. Pareek, P. Rani, D. Kishore, *Int. J. Pharma Bio Sci.* **2013**, 4,

- 812–820.
24. M. Pervaiz, A. Riaz, A. Munir, Z. Saeed, S. Huassain, A. Rashid, U. Younas, A. Adnan. *J. Mol. Struct.* **2020**, *1202*, 127284. DOI:10.1016/j.molstruc.2019.127284
 25. T. Narasaiah, D. S. Rao, K. V. Ramana, S. Adamb, C. N. Rajua, *Der Pharma Chemica*. **2012**, *4*, 1582–1590.
 26. S. A. Abu-Khadra, R. S. Farag, A. Abdel-Hady, *Am. J. Anal. Chem.* **2016**, *7*, 233–245. DOI:10.4236/ajac.2016.73020
 27. M. A. Neelakantan, M. Esakkiammal, S. S. Mariappan, J. Dharmaraja, T. Jeya kumar, *Indian J. Pharm. Sci.* **2010**, *72*, 216–222. DOI:10.4103/0250-474X.65015
 28. F. P. Andrew, J. A. Woods, A. Akinterinwa, H. Mukhtar, J. A. Ndahi, *Pharm. Chem. J.* **2016**, *3*, 99–104.
 29. M. Nasir-Uddin, S. S. Ahmed, S. M. R. Alam, *J. Coord. Chem.* **2020**, *73*, 3109–3149. DOI:10.1080/00958972.2020.1854745
 30. W. A. Zoubi, *Int. J. Org. Chem.* **2013**, *3*, 73–95. DOI:10.4236/ijoc.2013.33A008
 31. M. S. More, P. G. Joshi, Y. K. Mishra, P. K. Khanna, *Mater. Today Chem.* **2019**, *14*, 100195. DOI:10.1016/j.mtchem.2019.100195
 32. M. Maji, S. Acharya, I. Bhattachary, A. Gupta, A. Mukherjee *Inorg. Chem.* **2021**, *60*, 4744–4754. DOI:10.1021/acs.inorgchem.0c03706
 33. F. Cacciapuoti, *J. Cardiovasc. Med.* **2016**, *3*, 1–6. DOI:10.23937/jiacvd-2017/1710001
 34. T. C. Shekhar, G. Anju, *Am. J. Ethnomed.* **2014**, *1*, 244–249.
 35. L. Parengkuan, M. Yagi, M. Matsushima, M. Ogura, U. Hamada, Y. Yonei, *J. Anti-Aging Med.* **2013**, *10*, 70–76.
 36. W. Jamil, S. Solangi, M. Ali, K. M. Khan, M. Taha, M. Y. Khuhawar, *Arab. J. Chem.* **2019**, *12*, 2262–2269. DOI:10.1016/j.arabjc.2015.02.015
 37. K. M. Khan, A. Karim, N. Ambreen, S. Saied, S. Rasheed, S. Perveen, M. I. Choudhary, *J. Pharm. Res.* **2012**, *5*, 664–665.
 38. N. Pise, K. Jena, D. Maharana, D. Gaikwad, T. Jagtap, *J. Algal Biomass Util.* **2010**, *1*, 29–42.
 39. A. Benhassine, H. Boulebd, B. Anak, A. Bouraiou, S. Bouacida, M. Bencharif, A. Belfaitah, *J. Mol. Struct.* **2018**, *1160*, 406–414. DOI:10.1016/j.molstruc.2018.02.033
 40. S. S. Batool, S. R. Gilani, S. S. Zainab, M. N. Tahir, W. T. A. Harrison, *Polyhedron* **2020**, *178*, 114346. DOI:10.1016/j.poly.2020.114346

Povzetek

Predstavljena raziskava opisuje sintezo, določitev strukture ter anti-glikacijske in antioksidativne lastnosti liganda 4-[(2-hidroksinaftalen-1-ilmetilen)amino]benzensulfonamida (L) ter njegovih koordinacijskih spojin z Mn(II), Co(II), Ni(II), Cu(II) ter Zn(II) kovinskimi ioni. Uporabljene analizne tehnike (UV-Vis, FT-IR, CHN/S) so potrdile bidentatno naravo liganda, ki se koordinira preko O in N atomov v razmerju liganda proti kovini 2:1. TG/DTA analiza je pokazala, da so te spojine termično stabilne. Za sintetizirane spojine smo določili tudi anti-glikacijske aktivnosti (IC_{50} vrednosti v območju 184.11–386.34 μ M) ter antioksidativne lastnosti (IC_{50} vrednosti v območju 37.05–126.27 μ M). Kovinski kompleksi Mn ($IC_{50} = 184.11 \pm 2.11 \mu$ M), Ni ($IC_{50} = 211.26 \pm 1.46 \mu$ M), Cu ($IC_{50} = 254.56 \pm 1.16 \mu$ M) in Zn ($IC_{50} = 276.43 \pm 2.14 \mu$ M) so izkazali precej boljše anti-glikacijske aktivnosti kot standard rutin ($IC_{50} = 294.4 \pm 1.50 \mu$ M). Kompleks s Zn ($IC_{50} = 37.05 \pm 1.53 \mu$ M) pa je pokazal boljšo sposobnost lovljenja radikalov na DPPH testu kot standard *terc*-butil-4-hidroksianizol ($IC_{50} = 44.7 \pm 1.21 \mu$ M).



Except when otherwise noted, articles in this journal are published under the terms and conditions of the Creative Commons Attribution 4.0 International License

Synthesis, Crystal Structure and Biological Activity of Two Triketone-Containing Quinoxalines as HPPD Inhibitors

Xinyu Leng,¹ Chengguo Liu² and Fei Ye^{1,*}

¹ Department of Chemistry, College of Arts and Sciences, Northeast Agricultural University, Harbin 150030, China

² Department of State Assets Management, Northeast Agricultural University, Harbin 150030, China

* Corresponding author: E-mail: yefei@neau.edu.cn

Tel: +86-451-55190070

Received: 04-03-2022

Abstract

Two new triketone-containing quinoxaline derivatives were designed by fragment splicing strategy and synthesized using 3,4-diaminobenzoic acid and substituted cyclohexanedione as starting materials. Both compounds were characterized by IR, ¹H and ¹³C NMR, HRMS and X-ray diffraction. 3-Hydroxy-5-methyl-2-(quinoxaline-6-carbonyl)cyclohex-2-en-1-one (**6a**) crystallized in the triclinic system, space group *P*₁, *a* = 7.9829(2) Å, *b* = 8.1462(2) Å, *c* = 10.7057(3) Å, α = 84.3590(10)°, β = 89.7760(10)°, γ = 87.4190(10)°, *Z* = 2, *V* = 692.12(3) Å³, *F*(000) = 296, *D*_c = 1.335 Mg/m³, μ (MoK α) = 0.095 mm⁻¹, *R* = 0.0683 and *wR* = 0.1983. 3-Hydroxy-5,5-dimethyl-2-(3-ethoxyquinoxaline-6-carbonyl)cyclohex-2-en-1-one (**6b**) crystallized in the monoclinic system, space group *P*2₁/*c*, *a* = 10.1554(6) Å, *b* = 9.6491(6) Å, *c* = 17.7645(10) Å, β = 90.784(2)°, *Z* = 4, *V* = 1740.59(18) Å³, *F*(000) = 720, *D*_c = 1.299 Mg/m³, μ (MoK α) = 0.092 mm⁻¹, *R* = 0.0462 and *wR* = 0.1235. Physicochemical property comparison and ADMET prediction showed that compound **6a** had similar properties to the commercial herbicide mesotrione. Molecular docking results showed that the interactions between **6a** and AtHPPD were similar to mesotrione. Moreover, the extended aromatic ring system and the additional alkyl form more interactions with the surrounding residues. Examination of AtHPPD inhibition and herbicidal activity showed that **6a** had similar inhibition values to mesotrione and had a superior inhibitory effect on *Echinochloa crus-galli*.

Keywords: Triketone-containing quinoxaline derivatives; Synthesis; Single-crystal structure; Molecular structure information; Herbicidal activity

1. Introduction

Herbicides that inhibit 4-hydroxyphenylpyruvate dioxygenase (EC 1.13.11.27, HPPD) have been used in agriculture for weed control since the 1970s.¹ HPPD is one of the α -keto acid-dependent, non-heme, Fe(II)-dependent enzymes belonging to the 2-His-1-carboxylate facial triad family, and is involved in tyrosine catabolism, which is necessary for most aerobic organisms.^{1–3} *L*-tyrosine is converted to 4-hydroxyphenylpyruvic acid (HPPA) by a transamination catalyzed by tyrosine aminotransferase (TAT). Subsequently, HPPA is converted to homogentisic acid (HGA) by a complex biochemical reaction catalyzed by HPPD. In plants, HGA is converted to plastoquinone and tocopherol,^{4–7} and its absence leads to bleaching symptoms, necrosis, and plant death.^{8,9} Therefore, HPPD is an important enzyme class discovered in recent years that targets herbicides. HPPD inhibitor herbicides are characterized by broad spectrum weed control, flexibility, remarkable plant selectivity, good environmental com-

patibility, low toxicity, and high efficiency.^{9–11} Based on their structure, they can be classified into three categories: Triketones, isoxazoles, and pyrazoles.^{12,13} Triketone derivatives are among the best-studied herbicides and generally contain both triketone and aromatic ring components.^{14,15} Unfortunately, with the widespread use of HPPD herbicides recently, more and more weeds have developed resistance to these active ingredients, which is not limited to the target site.^{16,17} This highlights the importance of developing new HPPD herbicides to effectively manage weed resistance and improve weed control efficiency. Inspired by our previous reports and interest in HPPD herbicides,^{18–22} two novel triketone-containing quinoxaline derivatives were designed and synthesized (Figure 1). Comparisons of physical and chemical properties, ADMET parameters (absorption, distribution, metabolism, excretion, and toxicity), and molecular docking were performed. The biological results showed that compound **6a** had similar inhibition values to the commercial herbicide mesotrione.



Figure 1. Design of the target compounds.

2. Experimental

2. 1. Materials and Characterization

All reagents were purchased from Shanghai Aladdin Biochemical Technology Co. and were of analytical grade that could be used without any purification. Melting points were measured using a Shanghai INESA melting point instrument (WRS-3) and were uncorrected. The IR spectrum was recorded in KBr pellets using a Bruker ALPHA -T instrument. The NMR spectrum was recorded with a Bruker AV -400 MHz spectrometer (Bruker Company, DEU) using CDCl_3 as solvent and tetramethylsilane (TMS) as internal standard. High-resolution mass spectrometry (HRMS) data were obtained using a Bruker micrOTOF-Q II 10410 spectrometer. X-ray diffraction data were obtained using a RAPID-AUTO area detector diffractometer.

2. 2. Preparation of the Quinoxaline-6-carboxylic acid (2)

In a three-neck flask (100 mL), 3,4-diaminobenzoic acid (10 mmol) was stirred in distilled water, 10% sodium dioctyl sulfosuccinate (SDOSS, 10 mmol) and substituted diketones (**1**, 12 mmol) were added, and the mixture was stirred at room temperature for 4 h.²³ After the reaction, the mixture was filtered under vacuum, the filter cake was dried and recrystallized with EtOH/water to give quinoxaline-6-carboxylic acid (**2**).

2. 3. Preparation of the Acid Chloride (3)

Compound **1** (2 mmol) was dissolved in CH_2Cl_2 (40 mL) in a three-neck flask (100 mL), to which sulfoxide chloride (3 mmol) and DMF (0.1 mL) were added and refluxed for 2 hours.²⁴ Compound **3** was isolated by removing the solvent.

2. 4. Preparation of Enol Ester Compounds (5)

Compound **3** (2.4 mmol) and substituted 1,3-cyclohexanedione (2.1 mmol) were dissolved in CH_2Cl_2 (30 mL), and triethylamine (Et_3N , 2.3 mol) was added dropwise and reacted at 0 °C for 6 h.²⁵ After completion of the

reaction, the mixture was washed three times with aqueous HCl (50 mL, 1 M), followed by washing with saturated sodium chloride solution (50 mL), drying with anhydrous MgSO_4 , and then removing the solvent by filtration under reduced pressure, leaving a solid residue. Compound **5** was obtained by purifying the crude product by silica gel column chromatography (ethyl acetate : petroleum ether = 1:3).

2. 5. Preparation of Triketone-Containing Quinoxalines (6)

The synthetic pathway of **6a** and **6b** is shown in Figure 2. Compound **5** (1 mmol), Et_3N (12 mmol), CH_3CN (13 mmol), and acetone cyanohydrin (AC, 5 mmol) were mixed in CH_2Cl_2 (30 mL) and the reaction was carried out at 25 °C for 6 h.²⁶ After completion of the reaction, the solution was washed three times with aqueous HCl (30 mL, 1 M), followed by washing with saturated aqueous NaCl (30 mL), drying with anhydrous MgSO_4 , and evaporation of the solvent. Compound **6** was obtained by purifying the crude product by silica gel column chromatography (ethyl acetate : petroleum ether = 4:1). Supporting information includes IR, ^1H NMR, ^{13}C NMR, and HRMS information for compounds **6** (Figures S1-S8).

3-Hydroxy-5-methyl-2-(quinoxaline-6-carbonyl)cyclohex-2-en-1-one (6a), Yellow solid; yield: 58%; m.p. 132.5–133.5 °C, IR (KBr, cm^{-1}) 3063–2847 ($-\text{CH}_2-$, $=\text{CH}$), 1651–1608 ($\text{C}=\text{O}$), 1578–1543 ($\text{C}=\text{C}$), ^1H NMR (400 MHz, CDCl_3 , ppm) δ 16.81 (s, 1H, OH), 8.90 (s, 2H, Ar-H), 8.26–7.81 (m, 3H, Ar-H), 2.83 (s, 1H, CH), 2.67–2.29 (m, 4H, $2\times\text{CH}_2$), 1.17 (d, $J = 6.1$ Hz, 3H, CH_3). ^{13}C NMR (100 MHz, CDCl_3 , ppm) δ 197.82, 196.18, 193.95, 146.02, 145.53, 144.16, 142.17, 140.08, 129.59, 129.08, 128.79, 112.95, 26.74, 20.82. HRMS (ESI): calculated for $\text{C}_{16}\text{H}_{14}\text{N}_2\text{O}_3$ $[\text{M}+\text{H}]^+$ 283.1077, found 283.1080.

3-Hydroxy-5,5-dimethyl-2-(3-ethoxyquinoxaline-6-carbonyl)cyclohex-2-en-1-one (6b) Yellow solid; yield: 42%; m.p. 162.7–163.5 °C; IR (KBr, cm^{-1}) ν 3039–2904 ($-\text{CH}_2-$, $=\text{CH}$), 1670–1661 ($\text{C}=\text{O}$), 1550 ($\text{C}=\text{C}$), ^1H NMR (400 MHz, CDCl_3 , ppm) δ 17.01 (s, 1H, OH), 8.49–7.58 (m, 4H, Ar-H), 4.51–4.45 (m, 2H, CH_2), 2.77–2.60 (m, 2H,

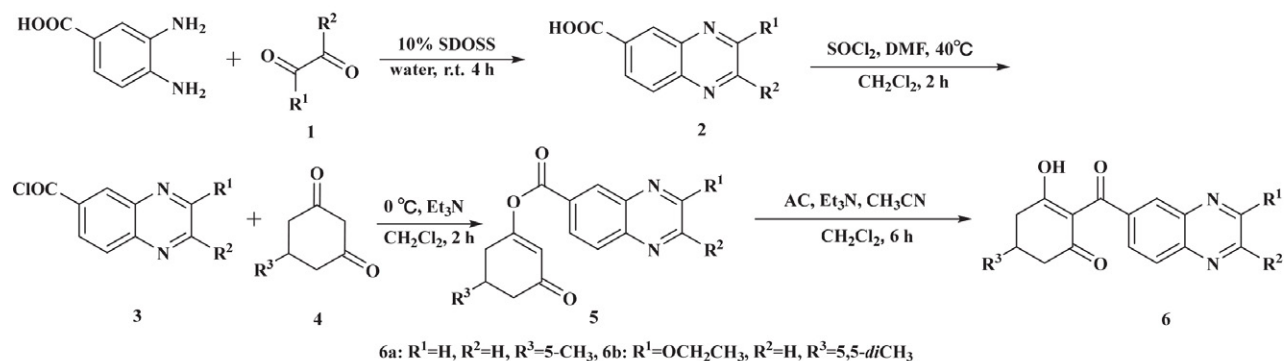


Figure 2. The synthetic route for the compounds 6.

CH_2CO), 2.42 (s, 2H, CH_2), 1.48 (t, $J = 7.1$ Hz, 3H, CH_3), 1.18 (s, 6H, $2\times\text{CH}_3$). ^{13}C NMR (100 MHz, CDCl_3 , ppm) δ 197.14, 196.11, 194.02, 157.78, 148.05, 146.13, 142.02, 139.80, 129.13, 128.64, 128.42, 112.37, 77.37, 76.74, 74.66, 51.96, 45.97, 31.13, 28.33. HRMS (ESI): calculated for $\text{C}_{19}\text{H}_{20}\text{N}_2\text{O}_4$ $[\text{M}+\text{H}]^+$ 341.1500, found 341.1496.

2. 6. Crystal Structure Determination

Compound **6** was dissolved in EtOAc to form a nearly saturated solution. The crystals grew during the volatilization of the solvent at room temperature in the dark. The crystal was mounted on a RAPID-AUTO area detector diffractometer with MoK α radiation ($\lambda = 0.71073$ Å) at 293(2) K. The crystal structures were solved by direct methods and refined using SHELXS-97 and SHELXL-97.^{27,28} The symmetric equivalent reflectance was used to optimize the shape and size of the crystal. The H atom was then constrained to an ideal geometry with a C–H distance of 0.93–0.98 Å. The $U_{\text{iso}}(\text{H})$ value for the methyl H atoms was set to 1.5 $U_{\text{eq}}(\text{C})$ and 1.2 $U_{\text{eq}}(\text{C})$ for the other H atoms. Crystal packing diagrams were prepared using the xp software. Cambridge Crystallographic Data Center under supplemental publication numbers CCDC 2150405 (**6a**) and 2150406 (**6b**). Copies of the data are available free of charge on request from CCDC, 12 Union Road, Cambridge CB21EZ, UK [www.ccdc.cam.ac.uk/data_request/cif].

2. 7. AtHPPD Inhibitory Experiments in Vitro

Homogentisate 1,2-dioxygenase (HGD) and *Arabidopsis thaliana* HPPD (*AtHPPD*) were prepared and purified according to methods described in the literature.²⁹ Mesotrione, compounds **6**, and *AtHPPD* were preincubated for 25 minutes, then a mixture of appropriate amounts of HGD, HPPA, FeCl_2 (1 mM), ascorbic acid (20 mM), and 4-(2-hydroxyethyl)-1-piperazineethanesulfonic acid (HEPES, 20 mM) buffer (pH 7.0) was added sequentially.^{9,30} An initial screening of the inhibitory effect of each compound was performed at a concentration of 10 μM to determine the final concentration range of the IC_{50} . The

test compounds were dissolved in DMSO and diluted with buffer to various concentrations before use. The IC_{50} of residual activity was calculated by fitting the curves for different concentrations of the compounds at specific substrate concentrations.

2.8. Herbicidal Activity Assay

All test weeds were purchased from the seed market in Harbin, China. Mesotrione and compounds **6** were tested against the weeds *Echinochloa crus-galli* (EC), *Setaria faberi* (SF), *Digitaria sanguinalis* (DS), Amaranthaceae *Amaranthus retroflexus* (AR), and broadleaf *Abutilon juncea* (AJ) by post-emergence application.¹⁰ Mesotrione and compounds **6** were prepared using DMSO as solvent and Tween 80 (0.1 g/mL) as emulsifier. These solutions were diluted with distilled water to the required concentration and then sprayed on the test plants in the greenhouse. The clay soil was Mollisols-Cryolls clay loam with a pH of 7.3. Approximately 15 weed seeds from EC, SF, DS, AR, and AJ were planted in paper cups, covered with 1.5 cm of soil, and grown in a greenhouse at 18–28 °C and 78% humidity. Broadleaf weeds and monocotyledonous weeds were treated at the two-leaf stage and one-leaf stage, respectively. Once weeds reached the appropriate stage, they were treated with the inhibitors at doses of 0.045 and 0.090 mmol/m² (approximately 150 and 300 g ai/ha). Seeds of the positive control group were treated with the commercial herbicide mesotrione. After 10 days of treatment with these compounds, herbicide activity was measured visually, with each treatment repeated three times.¹²

2. 9. Computational Chemistry

Physical and chemical property comparison, ADMET prediction, and molecular docking were performed using Discovery Studio 2019 (DS, Biovia Inc., CA, USA), and electronegativity was calculated using SYBYL-X 2.0. The 3D structure of mesotrione, compounds **6a** and **6b** was created using Chem3D 15.1, and the molecular structures were further optimized using the MM₂ minimization module. The crystal structure of the protein was down-

loaded from Protein Data Bank (PDB ID: 5YY6, <http://www.rcsb.org/pdb>). 5YY6 was processed before molecular docking, all hydrogen atoms were added, all heteroatoms, ligands and water molecules were removed. Then, the Clean Protein Tool in DS was used to complete incomplete residues, remove excess protein conformations, hydrogenate, and assign the associated charges. The active site was defined using a binding sphere of the native ligand. Molecular docking was performed using the CDOCKER module, and parameters were set to default values. The crystal structure of 5YY6 contained the native ligand 94L, and the ligand molecules at the active site of the complex were abstracted and redocked into the binding pocket. The root mean square deviation (RMSD) was calculated.³

3. Results and Discussion

3. 1. Description of the Crystal Structures and Hydrogen Bonding

The crystallographic data and structural refinement details for **6a** and **6b** are given in Table S1. **6a** crystallized in triclinic $P\bar{1}$ -space group with a unit cell volume of 692.12(3) Å³, the cell dimensions are: $a = 7.9829(2)$ Å, $b = 8.1462(2)$ Å, $c = 10.7057(3)$ Å, $\alpha = 84.3590(10)^\circ$, $\beta = 89.7760(10)^\circ$, $\gamma = 87.4190(10)^\circ$, and $Z = 2$. **6b** crystallizes in monoclinic $P2_1/c$ space group with a unit cell volume of 1740.59(18) Å³, the cell dimensions are: $a = 10.1554(6)$ Å, $b = 9.6491(6)$ Å, $c = 17.7645(10)$ Å, $\beta = 90.784(2)^\circ$, and $Z = 4$.

The molecular structures of compounds **6a** and **6b** with the numbering of the atoms are shown in Figure 3. Selected bond lengths and bond angles of **6a** and **6b** are listed in Table S2. The molecule is not coplanar; both crystal structures of compounds **6a** and **6b** consist of two aro-

matic moieties: a cyclohexanedione (A) and a quinoxaline (B). In compound **6a**, for example, the C-C bond length was entirely within the range of the typical C-C bond length (1.54 Å).³⁰ The bond length of C(15)-O(3) was 1.3162(15), which was shorter than the typical C-O length (1.42 Å); the bond length of C(10)=C(15) (1.3841(16) Å) and C(9)-O(1) (1.2490(15) Å) was also longer than the typical C=C length (1.34 Å) and C=O length (1.21 Å).^{31–33} These results suggest a conjugative effect between carbonyl, hydroxyl, and C=C bond. In addition, the C(6)-C(9) bond length (1.4892(16) Å) was shorter than the typical C-C length, which could be due to a π - π conjugation between carbonyl and benzene of quinoxaline. The dihedral angles of part A and part B in compound **6a** and **6b** were 50.32° and 53.80°, respectively. And the cyclohexanedione in both compounds belongs to the half-chair conformation.

The presence of π - π packing interactions, hydrogen bonding, and van der Waals forces resulted in an ordered

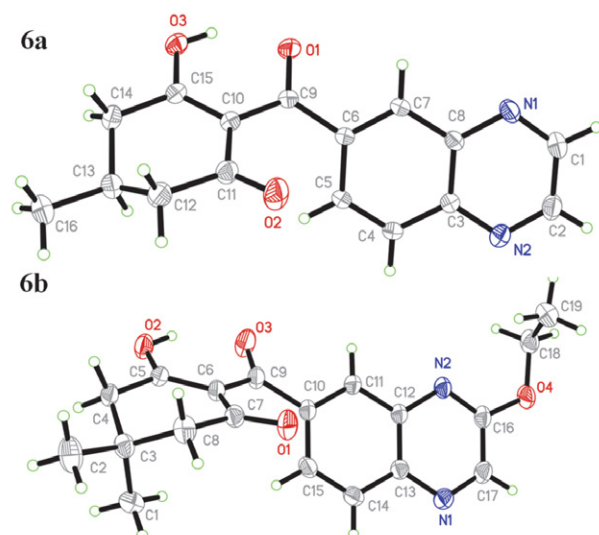


Figure 3. Molecular structures of compounds **6a** and **6b**.

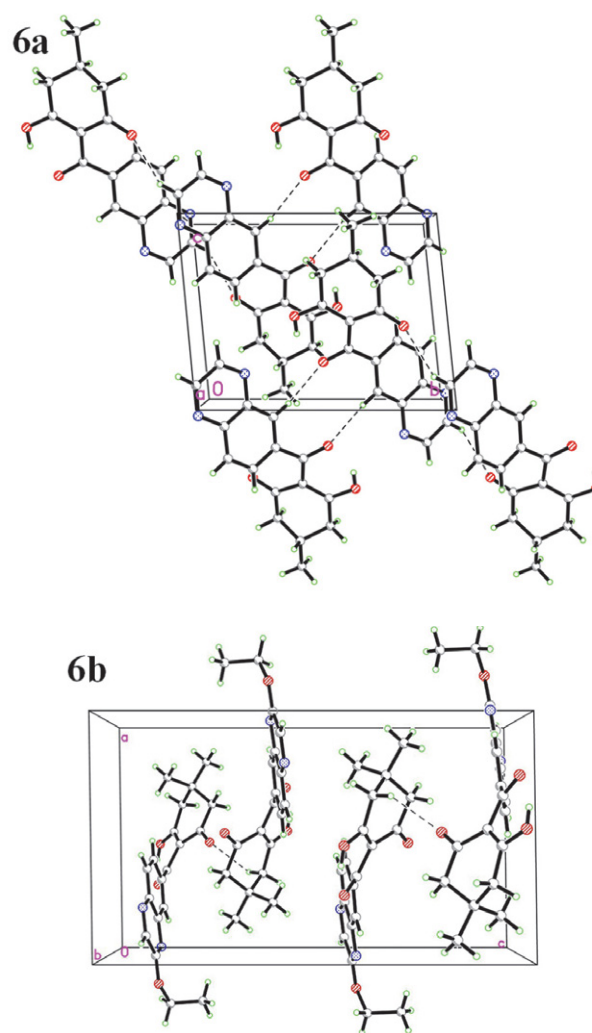
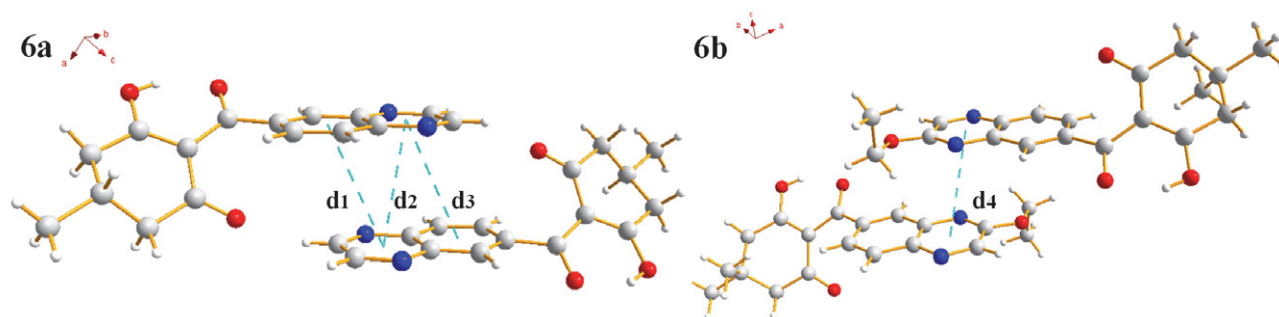


Figure 4. Molecular packing diagram of **6a** and **6b**, hydrogen bonds are shown as dashed lines.

Table 1. Hydrogen bonding parameters in the structures of **6a** and **6b**.

	D-H...A	d(D-H)	d(H...A)	d(D...A)	Symmetry codes	∠DHA
6a	C(7)–H(7)...O(1) ^a	0.9302(11)	2.514(1)	3.2713(15)	1–x, –y, 1–z	138.754(75)
	C(2)–H(2)...O(2) ^b	0.9295(17)	2.4973(13)	3.1763(21)	1–x, –y, –z	130.071(103)
	C(12)–H(12B)...N(2) ^c	0.9699(16)	2.7456(13)	3.5689(20)	1–x, 1–y, –z	143.073(99)
6b	C(4)–H(4B)...O(1) ^d	0.9703(14)	2.5100(11)	3.3190(18)	1–x, –0.5+y, 0.5–z	140.789(86)

**Figure 5.** π - π packing interactions between two molecules.

crystal arrangement with high symmetry and regularity (Figure 4). Compound **6a** formed the packing through the hydrogen bonds C(7)–H(7)...O(1), C(2)–H(2)...O(2), and C(12)–H(12B)...N(2). Compound **6b** formed the packing through hydrogen bonds C(4)–H(4B)...O(1). The hydrogen bonding data are shown in Table 1. As shown in Figure 5, the distance between aromatic rings is within the limited range of typical π - π packing interaction ($d_1 = 3.8537(1)$ Å, $d_2 = 3.6850(1)$ Å, $d_3 = 3.8537(1)$ Å, $d_4 = 3.7647(2)$ Å).

3. 2. Spectroscopic Studies

Compounds **6** were confirmed by IR, ^1H and ^{13}C NMR, and HRMS. Let us take compound **6a** as an example. The IR analysis confirmed the presence of methylene and =CH- group at 3063–2847 cm^{-1} , carbonyl at 1651–1608 cm^{-1} , and C=C bond at 1578–1543 cm^{-1} . The NMR data indicated the possible structure of the compound. The ^1H NMR signals at δ 16.81 ppm are associated with the hydroxyl group of enol. The signals at δ 7.81–8.90 ppm are associated with the five Ar-H of the pyrazine and benzene rings. The signal at δ 2.83 ppm is associated with the hydrogen on the tertiary carbon. The signals at δ 2.37–2.68 ppm and 1.17 ppm are associated with the methylene and methyl groups, respectively. The ^{13}C NMR data at δ 193.95–197.82 ppm show the presence of the carbon atom of enol. The signals at δ 128.79–146.02 ppm relate to the pyrazine and benzene rings and signals at δ 112.95 ppm refer to the carbon between three enols. The signals at δ 20.82–20.74 are characteristic of the remaining saturated carbon atoms. The $[\text{M}+\text{H}]^+$ ion of **6a** was calculated with Chemdraw 15.1 as 283.1007; the actual signal found was 283.1080.

3. 3. AtHPPD Inhibition and Herbicidal Activities

The IC_{50} values against AtHPPD in vitro of mesotrione and target compounds **6** are shown in Table 2. The IC_{50} values of mesotrione, **6a**, and **6b** were 0.23, 0.46, and 6.41 μM , respectively. Compound **6a** showed similar inhibition values as mesotrione, possibly because they share the same skeletal structure. The herbicidal effects of mesotrione and compounds **6** against EC, SF, AJ, DS, and AR are listed in Table 2. Weeds treated with compounds **6a** and **6b** showed similar symptoms to mesotrione, suggesting that these target compounds are potential HPPD inhibitors. All compounds tested showed no inhibition in monocotyledonous weeds (AG, DS, and AR). Compound **6a** showed similar inhibitory activity against EC and SF as mesotrione. Notably, **6a** had the superior EC inhibitory activity, suggesting that the scaffold of compounds **6** could be further modified as herbicides.

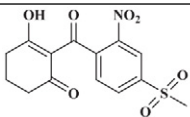
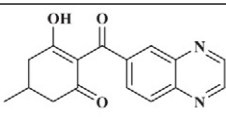
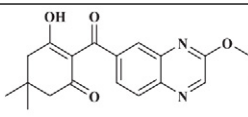
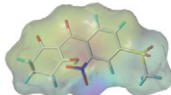
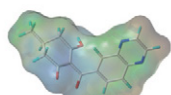
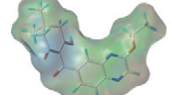
Table 2. Inhibitory activities and post-emergence herbicidal activities (inhibition rating 0–100) of compounds **6a** and **6b** (150 g ai/ha).

compounds	IC_{50} (μM)	Inhibition (%) ^a				
		EC	SF	AJ	DS	AR
Mesotrione	0.23	B	A	G	E	G
6a	0.46	A	B	G	G	G
6b	6.41	F	F	G	G	G

^a Rating scale of inhibition percentage in relation to the untreated control: A, 100%; B, 99–90%; C, 89–70%; D, 69–50%; E, 49–30%; F, 29–20%; G, 0–19%.

The comparisons of physical and chemical properties were studied and are shown in Table 3. Certain sim-

Table 3. Comparison of physical and chemical properties of mesotrione, **6a** and **6b**.

	Mesotrione	6a	6b
Structure			
MW ^a	340.33	282.29	340.37
Log p^a	0.26	1.68	2.78
HBAs ^a	7	5	6
HBDs ^a	2	1	1
RBs ^a	4	2	4
ARs ^a	1	2	2
SA ^a	317.34	280.81	362.96
electronegativity ^b			

ilarities of these compounds at the molecular level were confirmed by the hydrogen bond acceptors (HBAs), hydrogen bond donors (HBDs), rotatable bonds (RBs), aromatic rings (ARs), and electronegativity. When comparing the log p of **6a** and **6b**, it was found that **6a** has a relatively low value that favors herbene transfer and absorption,³⁴ and that compound **6a** has a similar surface area (SA) to mesotrione, which is advantageous for compound **6a** to enter the active pocket. In addition, experiments on AtH-PPD inhibition and herbicide activity showed that compound **6a** had a stronger inhibitory effect than compound **6b**. This is likely due to the p- π conjugation between pyrazine and ethoxy, with ethoxy acting as an electron donor and enhancing the inhibitory effect.

3. 4. ADMET Prediction

ADMET prediction has received special attention in drug development. The predicted parameters of mesotrione, **6a** and **6b** are shown in Table 4. Both compounds **6a** and mesotrione were similar in terms of solubility degree, cytochrome P450 2D6 (CYP2D6) prediction, and plasma protein binding ability (PPB). Apparently, compound **6a** was better absorbed than mesotrione. CYP2D6 prediction showed that these two compounds could successfully pass through the first stage of metabolism. The PPB prediction values of the two compounds were not correct, which could lead to low bioavailability because they do not attach to the carrier protein.^{35,36} On the other hand, in the case of compound **6b**, although it has good CYP2D6 prediction and absorption degree, its solubility degree and PPB prediction value are unsatisfactory, leading to a decrease in its activity. In conclusion, compound **6a** has similar pharmacokinetic properties to the commercial herbicide mesotrione, confirming that it has some prospect of weed control.

Table 4. The ADMET prediction of mesotrione, **6a** and **6b**.

	Mesotrione	6a	6b
Solubility Level ^a	4	3	2
Absorption Level ^b	1	0	0
CYP2D6 Prediction ^c	false	false	false
AlogP98 ^d	0.093	1.698	2.776
PPB# prediction ^e	false	false	True

^a Solubility Level: Categorical solubility level. 2: Yes, low.

^b Absorption Level: Absorption Level. 0: Good absorption.

^c CYP2D6: cytochrome P450 2D6. <0.161: false, non-inhibitor; >0.161: true, inhibitor.

^d AlogP98: the logarithm of the partition coefficient between n-octanol and water. <4.0: Binding is <90%; >4.0: Binding is >90% and Binding is <95%

^e PPB: Plasma Protein Binding ability. <-2.209: $\geq 90\%$, false; >-2.209: $\leq 90\%$, true.

3. 5. Molecular Docking

Molecular docking was an essential tool for computer-aided drug design (CADD), which correctly predicted

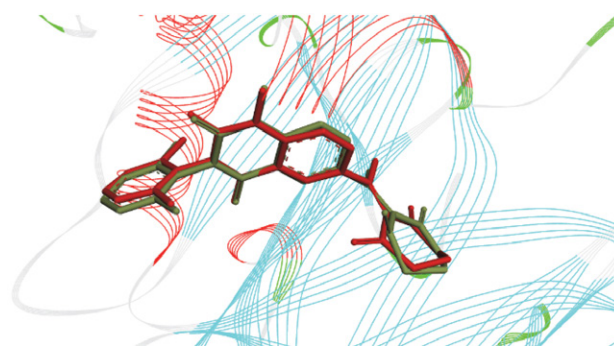


Figure 6. The ligand compared using the CDOCKER docking method (the newly docked ligand was red and the native ligand was green).

the interaction between the inhibitor and herbicide target enzymes.³⁷ To verify the feasibility of molecular docking, the native ligand 94L was redocked to the target protein. The superposition of the conformation of the native ligand with the newly docked conformation is shown in Figure 6. The conformation of the native and redocked ligand 94L was almost completely overlapping with an RMSD value of 0.5549 Å (< 2 Å), confirming the accuracy of the CDOCK-ER docking procedure.³

The mesotrione, **6a** and **6b** were selected for the molecular docking experiments to predict the binding pattern with 5YY6. Compounds **6a** and **6b** hardly differed from mesotrione in terms of geometric complementarity of the binding position in the active pocket. Mesotrione and **6a** occupied the active pocket almost completely, whereas **6b** occupied only part of the pocket (Figure S9 in the Supporting Information). The enol structure and carbonyl groups in these compounds all coordinate with Co²⁺. In compound **6a**, the distances between the Co²⁺ and O atoms were 2.02 Å and 1.86 Å, respectively, similar to mesotrione. The benzene moiety of compound **6a** formed a π - π -stacked interaction with PHE424, similar to that of mesotrione, and HIS226 formed a new interaction with the O atom, further improving the binding ability of the ligand. The additional interactions of compound **6a** with PRO280 and VAL269 resulted in strong binding to the receptor, which may explain the similarity of the AtHPPD inhibitory activity of compound **6a** with mesotrione.

4. Conclusion

In summary, two new triketone-containing quinoxaline derivatives were developed and synthesized as novel HPPD herbicides. Both compounds exhibited certain HPPD inhibitory activities. In particular, compound **6a** showed similar AtHPPD inhibition and herbicidal activity to the commercial herbicide mesotrione, as demonstrated by physical and chemical property comparisons, ADMET prediction, and molecular docking study.

Acknowledgements

This work was supported by the National Nature Science Foundation of China (grant number 22077014) and the Under-graduate SIPT Program of Northeast Agricultural University (grant number 202110224014).

Supporting information includes the crystallographic data and structure refinement details for compounds **6** (Table S1), selected bond lengths and bond angles for crystals of compounds **6** (Table S2), the IR, ¹H, ¹³C NMR and HRMS spectra of compounds **6** (Figures S1–S8), the receptor-ligand interaction, and coordination patterns of mesotrione and compounds **6** with AtHPPD (Figure S9).

5. References

1. E. Rocaboy-Faquet, L. Barthelmebs, C. Calas-Blanchard, T. Noguer, *Talanta*, **2016**, *146*, 510–516. DOI:10.1016/j.talanta.2015.09.030
2. L. Serre, A. Sailland, D. Sy, P. Boudec, A. Rolland, E. Pebay-Peyroula, C. Cohen-Addad, *Structure*, **1999**, *8*, 977–988. DOI:10.1016/S0969-2126(99)80124-5
3. Y. Fu, S. Q. Zhang, Y. X. Liu, J. Y. Wang, S. Gao, L. X. Zhao, F. Ye, *Ind. Crops Prod.*, **2019**, *137*, 566–575. DOI:10.1016/j.indcrop.2019.05.070
4. S. O. Duke, *Pest Manag. Sci.*, **2012**, *68*, 505–512. DOI:10.1002/ps.2333
5. K. Lei, X. W. Hua, Y. Y. Tao, Y. Liu, N. Liu, Y. Ma, Y. H. Li, X. H. Xu, C. H. Kong, *Bioorg. Med. Chem.*, **2016**, *24*, 92–103. DOI:10.1016/j.bmc.2015.11.032
6. R. Beaudegnies, A. J. F. Edmunds, T. E. M. Fraser, R. G. Hall, T. R. Hawkes, G. Mitchell, J. Schaetzer, S. Wendeborn, J. Wiley, *Bioorg. Med. Chem.*, **2009**, *17*, 4134–4152. DOI:10.1016/j.bmc.2009.03.015
7. P. S. Garcia, A. L. D. Moreau, J. C. M. Ierich, A. C. A. Vig, A. M. Higa, G. S. Oliveira, F. C. Abdalla, M. Hausen, F. L. Leite, *IEEE Sens. J.*, **2015**, *15*, 2106–2113. DOI:10.1109/JSEN.2014.2371773
8. L. X. Zhao, J. F. Peng, F. Y. Liu, Y. L. Zou, S. Gao, Y. Fu, F. Ye, *J. Agric. Food Chem.*, **2022**, *70*, 1003–1018. DOI: 10.1021/acs.jafc.1c05210 DOI:10.1021/acs.jafc.1c05210
9. F. Ndikuryayo, B. Moosavi, W. C. Yang, G. F. Yang, *J. Agric. Food Chem.*, **2017**, *65*, 8523–8537. DOI:10.1021/acs.jafc.7b03851
10. D. W. Wang, H. Y. Lin, R. J. Cao, T. Chen, F. X. Wu, G. F. Hao, Q. Chen, W. C. Yang, G. F. Yang, *J. Agric. Food Chem.*, **2015**, *63*, 5587–5596. DOI:10.1021/acs.jafc.5b01530
11. Y. Fu, M. Wang, L. X. Zhao, S. Q. Zhang, Y. X. Liu, Y. Y. Guo, D. Zhang, S. Gao, F. Ye, *Pest. Biochem. Physiol.*, **2021**, *174*, 104811. DOI:10.1016/j.pestbp.2021.104811
12. Y. Fu, D. Zhang, S. Q. Zhang, Y. X. Liu, Y. Y. Guo, M. X. Wang, S. Gao, L. X. Zhao, F. Ye, *J. Agric. Food Chem.*, **2019**, *67*, 11839–11847. DOI:10.1021/acs.jafc.9b01412
13. H. Huang, M. M. Wang, L. Shu, Y. L. Yan, J. Q. Zhang, J. M. Liu, X. H. Zhan, D. Y. Zhang, *Pest Manag. Sci.*, **2020**, *76*, 4112–4122. DOI:10.1002/ps.5967
14. A. Santucci, G. Bernardini, D. Braconi, E. Petricci, F. Manetti, *J. Med. Chem.*, **2017**, *60*, 4101–4125. DOI:10.1021/acs.jmedchem.6b01395
15. M. Baalouch, A. D. Mesmaeker, R. Beaudegnies, *Tetrahedron Lett.*, **2013**, *54*, 557–561. DOI:10.1016/j.tetlet.2012.11.081
16. N. E. Hausman, S. Singh, P. J. Tranel, D. E. Riechers, S. S. Kaundun, N. D. Polge, D. A. Thomas, A. G. Hager, *Pest Manag. Sci.*, **2011**, *67*, 258–261. DOI:10.1002/ps.2100
17. P. M. McMullan, J. M. Green, *Weed Technol.*, **2011**, *25*, 514–518. DOI:10.1614/WT-D-10-00150.1
18. W. Hu, S. Gao, L. X. Zhao, K. L. Guo, J. Y. Wang, Y. C. Gao, Y. Fu, F. Ye, *Pest Manag. Sci.*, **2022**, *78*, 938–946. DOI:10.1002/ps.6703
19. H. M. Song, L. X. Zhao, S. Q. Zhang, T. Ye, Y. Fu, F. Ye, *J. Agric.*

- Food Chem.*, **2021**, 69, 12621–12633. DOI:10.1021/acs.jafc.1c04621
20. L. Jia, S. Gao, Y. Y. Zhang, L. X. Zhao, Y. Fu, F. Ye, *J. Agric. Food Chem.*, **2021**, 69, 8366–8379. DOI:10.1021/acs.jafc.1c02221
 21. Z. W. Wang, L. X. Zhao, P. Ma, T. Ye, Y. Fu, F. Ye, *Pest Manag. Sci.*, **2021**, 77, 1724–1738. DOI:10.1002/ps.6193
 22. L. Jia, X. Y. Jin, L. X. Zhao, Y. Fu, F. Ye, *J. Agric. Food Chem.*, **2022**, 70, 5499–5515. DOI:10.1021/acs.jafc.2c01565
 23. L. Cuesta, I. Maluenda, T. Soler, R. Navarro, E. P. Urriolabeitia, *Inorg. Chem.*, **2011**, 50, 37–45. DOI:10.1021/ic101946n
 24. F. Ye, Y. Zhai, T. Kang, S. L. Wu, J. J. Li, S. Gao, Y. Fu, *Pest. Biochem. Physiol.*, **2019**, 157, 60–68. DOI:10.1016/j.pestbp.2019.03.003
 25. B. He, J. Dong, H. Y. Lin, M. Y. Wang, X. K. Li, B. F. Zheng, Q. Chen, G. F. Hao, W. C. Yang, G. F. Yang, *J. Agric. Food Chem.*, **2019**, 67, 10844–10852. DOI:10.1021/acs.jafc.9b04917
 26. D. W. Wang, H. Y. Lin, R. J. Cao, Z. Z. Ming, T. Chen, G. F. Hao, W. C. Yang, G. F. Yang, *Pest Manag. Sci.*, **2015**, 71, 1122–1132. DOI:10.1002/ps.3894
 27. G. M. Sheldrick, SHELXS-97, Program for X-ray Crystal Structure Solution. University of Göttingen, Göttingen, Germany, **1997**.
 28. G. M. Sheldrick, SHELXL-97, Program for X-ray Crystal Structure Refinement. University of Göttingen, Göttingen, Germany, **1997**.
 29. H. Huang, J. Q. Zhang, J. M. Liu, M. M. Wang, L. Shu, Y. L. Yan, X. H. Zhang, P. Wang, X. T. Huan, D. Y. Zhang, *Pest Manag. Sci.*, **2020**, 77, 1409–1421. DOI:10.1002/ps.6159
 30. F. B. Rudolph, B. B. Baugher, R. B. Beissner, *Methods Enzymol.*, **1979**, 63, 22–42. DOI:10.1016/0076-6879(79)63004-5
 31. T. Topal, *Acta Chim. Slov.*, **2021**, 68, 88–101. DOI:10.17344/acsi.2020.6183
 32. Z. H. Yang, X. Li, H. K. Ma, J. Y. Zheng, X. C. Zhen, X. H. Zhang, *Bioorg. Med. Chem.*, **2014**, 24, 152–155. DOI:10.1016/j.bmcl.2013.11.051
 33. M. Y. Huang, W. Xu, J. J. Huang, Y. J. Huang, M. Yuan, *Chinese J. Struct. Chem.*, **2015**, 34, 497–502. DOI:10.4028/www.scientific.net/KEM.671.497
 34. M. A. Ezeokonkwo, O. N. Ogbonna, S. N. Okafor, E. U. Godwin-Nwakwasi, F. N. Ibeanu, U. C. Okoro, *Front. Chem.*, **2017**, 5, 107. DOI:10.3389/fchem.2017.00107
 35. Z. W. Wang, L. X. Zhao, S. Gao, X. Y. Leng, Y. Yu, Y. Fu, F. Ye, *Pest. Biochem. Physiol.*, **2021**, 179, 104958. DOI:10.1016/j.pestbp.2021.104958
 36. L. Jia, L. X. Zhao, F. Sun, J. Y. Wang, X. Y. Leng, S. Gao, Y. Fu, F. Ye, *Pest. Biochem. Physiol.*, **2022**, 187, 105185. DOI:10.1016/j.pestbp.2022.105185
 37. S. Sakkiath, S. Thangapandian, S. John, Y. J. Kwon, K. W. Lee, *Eur. J. Med. Chem.*, **2010**, 45, 2132–2140. DOI:10.1016/j.ejmech.2010.01.016

Povzetek

V prispevku je opisana priprava dveh novih triketonskih kinoksalinskih derivatov, ki vsebujeta triketone, s strategijo spajanja posameznih fragmentov, sintetiziranih iz 3,4-diaminobenzojske kisline in substituiranega cikloheksandiona kot izhodnih molekul. Oba kinoksalinska derivata so okarakterizirali z IR, ^1H in ^{13}C NMR, HRMS in rentgensko difrakcijo. 3-Hidroksi-5-metil-2-(kinoksalin-6-karbonil)cikloheks-2-en-1-on (**6a**) kristalizira v triklnskem kristalnem sistemu, v prostorski skupini $P\bar{1}$, $a = 7.9829(2) \text{ \AA}$, $b = 8.1462(2) \text{ \AA}$, $c = 10.7057(3) \text{ \AA}$, $\alpha = 84.3590(10)^\circ$, $\beta = 89.7760(10)^\circ$, $\gamma = 87.4190(10)^\circ$, $Z = 2$, $V = 692.12(3) \text{ \AA}^3$, $F(000) = 296$, $D_c = 1.335 \text{ Mg/m}^3$, $\mu(\text{MoK}\alpha) = 0.095 \text{ mm}^{-1}$, $R = 0.0683$ and $wR = 0.1983$. 3-Hidroksi-5,5-dimetil-2-(3-ethoxyquinoxaline-6-carbonyl)cyclohex-2-en-1-one (**6b**) crystallized in the monoclinic system, space group $P2_1/c$, $a = 10.1554(6) \text{ \AA}$, $b = 9.6491(6) \text{ \AA}$, $c = 17.7645(10) \text{ \AA}$, $\beta = 90.784(2)^\circ$, $Z = 4$, $V = 1740.59(18) \text{ \AA}^3$, $F(000) = 720$, $D_c = 1.299 \text{ Mg/m}^3$, $\mu(\text{MoK}\alpha) = 0.092 \text{ mm}^{-1}$, $R = 0.0462$ and $wR = 0.1235$. Primerjava fizikalno-kemijskih lastnosti in ADMET napovedi so pokazale, da ima spojina **6a** podobne lastnosti kot komercialni herbicid mezotrion. Rezultati molekulskega modeliranja so pokazali, da so interakcije med **6a** in AtHPPD podobne tistim pri mezotrionu. Poleg tega razširjeni aromatski obročni sistem in dodatne alkilne skupine povečajo interakcije z okolico. Raziskave inhibicije AtHPPD in herbicidnega delovanja so pokazale, da ima kinoksalin **6a** podobne vrednosti inhibicije kot mezotrion in boljši inhibični učinek na *Echinochloa crus-galli*.



Except when otherwise noted, articles in this journal are published under the terms and conditions of the Creative Commons Attribution 4.0 International License

Tetranuclear Copper(II) Complexes Derived from 5-Bromo-2-((2-(2-hydroxyethylamino)ethylimino)methyl)phenol: Synthesis, Characterization, Crystal Structures and Catalytic Oxidation of Olefins

Xiao-Jun Zhao, Su-Zhen Bai and Ling-Wei Xue*

School of Chemical and Environmental Engineering, Pingdingshan University, Pingdingshan Henan 467000, P. R. China

* Corresponding author: E-mail: pdsuchemistry@163.com

Received: 04-14-2022

Abstract

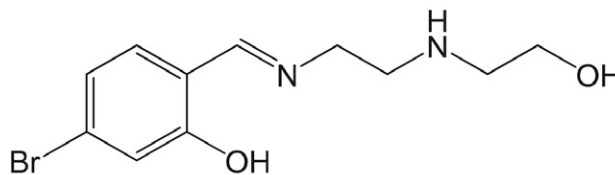
An acetate bridged tetranuclear copper(II) complex, $[\text{Cu}_4\text{L}_2(\mu_2\text{-}\eta^1\text{-}\eta^1\text{-CH}_3\text{COO})_6(\text{CH}_3\text{OH})_2]$ (**1**), and a chloride, phenolate and azide co-bridged tetranuclear copper(II) complex, $[\text{Cu}_4\text{L}_2\text{Cl}_2(\mu\text{-Cl})_2(\mu_{1,1}\text{-N}_3)_2]2\text{CH}_3\text{OH}$ (**2**), where L is the deprotonated form of the Schiff base 5-bromo-2-((2-(2-hydroxyethylamino)ethylimino)methyl)phenol (HL), have been synthesized and characterized by elemental analysis, IR and UV spectra, and single crystal X-ray diffraction. Single crystal X-ray analysis revealed that the Cu atoms in both complexes are in square pyramidal geometry. In complex **1**, two $[\text{CuL}]$ units and $[\text{Cu}_2(\mu_2\text{-}\eta^1\text{-}\eta^1\text{-CH}_3\text{COO})_4]$ core are linked through two acetate ligands. In complex **2**, $[\text{Cu}_2\text{LCl}(\mu\text{-Cl})]$ units are linked together by two end-on azido ligands. The Schiff base ligand coordinates to the Cu atoms through four N and O donor atoms. The molecules of both complexes are linked through hydrogen bonds to generate three dimensional networks. The catalytic property of the complexes for epoxidation reactions of some alkenes was studied using *tert*-butylhydroperoxide as the terminal oxidant under mild conditions in acetonitrile.

Keywords: Schiff base; copper complex; crystal structure; tetranuclear complex; catalytic property.

1. Introduction

Transition metal complexes with Schiff bases as ligands have received much attention for their structures, biological, pharmaceutical, magnetic and catalytic properties.¹ The complexes have been widely studied on the catalytic processes in many fundamentally and industrially important reactions.² Among the catalytic reactions, the epoxidation of olefins is of remarkable interest, because the products are necessary precursors for the production of fine chemicals. Copper complexes with Schiff base ligands are of particular interest due to their versatile structures and catalytic properties.³ Some copper complexes have been used as catalysts for the epoxidation reactions. Among them, those with Schiff base ligands have received particular attention.⁴ A number of reports used hydrogen peroxide as oxidant in the catalytic reactions. However, due to the explosive nature of hydrogen peroxide, industrial processes prefer to use *tert*-butylhydroperoxide (TBHP) as the oxidant.⁵ Although the catalytic properties of Schiff base copper(II) complexes toward oxidation re-

actions both in homogeneous and heterogeneous conditions are well documented, catalytic oxidation of alkenes involving tetranuclear Schiff base copper(II) complexes has rarely reported. Notably, TBHP has seldom been used as an oxidant in the catalytic oxidation reactions by copper(II) complexes as homogeneous catalysts.⁶ In this work, two new tetranuclear copper(II) complexes, namely $[\text{Cu}_4\text{L}_2(\mu_2\text{-}\eta^1\text{-}\eta^1\text{-CH}_3\text{COO})_6(\text{CH}_3\text{OH})_2]$ (**1**) and $[\text{Cu}_4\text{L}_2\text{Cl}_2(\mu\text{-Cl})_2(\mu_{1,1}\text{-N}_3)_2]2\text{CH}_3\text{OH}$ (**2**), where L is the deprotonated Schiff base 5-bromo-2-((2-(2-hydroxyethylamino)ethylimino)methyl)phenol (HL; Scheme 1), have been synthesized, characterized and studied on their catalytic epoxidation efficacy towards some alkenes.



Scheme 1. The Schiff base HL.

2. Experimental

2. 1. Materials and Methods

All solvents used were of AR grade and used as received. 4-Bromosalicylaldehyde, 2-(2-aminoethylamino) ethanol, copper acetate monohydrate, copper chloride dihydrate and sodium azide were purchased from Aladin Chemical Co. Ltd. and were used as received. Styrene, cyclooctene, cyclohexene and TBHP were purchased from Aldrich and were used as received. Infrared spectra (4000–400 cm^{-1}) were recorded as KBr discs with a FTS-40 Bio-Rad FT-IR spectrophotometer. The electronic spectra were recorded on a Lambda 35 spectrometer. Microanalyses (C, H, N) of the complex were carried out on a Carlo-Erba 1106 elemental analyzer. Solution electrical conductivity was measured at 298K using a DDS-11 conductivity meter. GC analyses were performed on a Shimadzu GC-2010 gas chromatograph. Crystallographic data of the complexes were collected on a Bruker SMART 1000 CCD area diffractometer with graphite monochromated Mo-K α radiation ($\lambda = 0.71073 \text{ \AA}$) at 298(2) K.

Caution! Transition metal azido complexes are potentially explosive especially in the presence of organic ligands. Although we have not encountered any problem during our study, yet a small quantity of materials should be prepared and it should be handled with care.

2. 2. X-Ray Crystallography

Absorption corrections were applied by using the SADABS program.⁷ Structures of the complexes were solved by direct methods and successive Fourier difference syntheses, and anisotropic thermal parameters for all non-hydrogen atoms were refined by full-matrix least-squares procedure against F^2 using SHELXTL and SHELXL-97

packages.⁸ All non-hydrogen atoms were refined anisotropically. The amino and hydroxyl H atoms of the Schiff base ligands in both complexes were located from difference Fourier maps and refined isotropically. The N–H and O–H distances were restrained to 0.90(1) and 0.85(1) \AA , respectively. The crystallographic data and experimental details for the structural analysis are summarized in Table 1, and selected bond lengths and angles are listed in Table 2.

2. 3. Synthesis of $[\text{Cu}_4\text{L}_2(\mu_2\text{-}\eta^1\text{-}\eta^1\text{-CH}_3\text{COO})_6(\text{CH}_3\text{OH})_2]$ (1)

4-Bromosalicylaldehyde (1.0 mmol, 0.20 g) and 2-(2-aminoethylamino)ethanol (1.0 mmol, 0.10 g) were mixed and stirred in methanol (30 mL) for 30 min at 25 $^\circ\text{C}$. Then, copper acetate monohydrate (2.0 mmol, 0.40 g) was added. The final mixture was further stirred for 30 min. The deep blue solution was evaporated to remove three quarters of the solvents under reduced pressure, yielding deep blue solid product of the complex. Yield: 0.41 g (69%). Well-shaped single crystals suitable for X-ray diffraction were obtained by re-crystallization of the solid from methanol. Anal. calcd for $\text{C}_{34}\text{H}_{46}\text{Br}_2\text{Cu}_4\text{N}_4\text{O}_{16}$ (%): C 34.59, H 3.93, N 4.75. Found (%): C 34.37, H 4.02, N 4.83. IR data (KBr, cm^{-1}): 3285, 3067, 2929, 2873, 1632, 1565, 1512, 1431, 1418, 1349, 1299, 1248, 1207, 1193, 1138, 1097, 1056, 1020, 995, 930, 911, 875, 803, 682, 623, 468, 443. UV-Vis data in acetonitrile [λ_{max} (nm), ϵ ($\text{L mol}^{-1} \text{cm}^{-1}$)]: 227, 6.89×10^3 ; 249, 6.91×10^3 ; 270, 4.57×10^3 ; 365, 1.51×10^3 ; 640, 83.

2. 4. Synthesis of $[\text{Cu}_4\text{L}_2\text{Cl}_2(\mu\text{-Cl})_2(\mu_{1,1}\text{-N}_3)_2]2\text{CH}_3\text{OH}$ (2)

4-Bromosalicylaldehyde (1.0 mmol, 0.20 g) and 2-(2-aminoethylamino)ethanol (1.0 mmol, 0.10 g) were

Table 1. Crystallographic data for the single crystal of the complexes

	1	2
Empirical formula	$\text{C}_{34}\text{H}_{46}\text{Br}_2\text{Cu}_4\text{N}_4\text{O}_{16}$	$\text{C}_{24}\text{H}_{36}\text{Br}_2\text{Cl}_4\text{Cu}_4\text{N}_{10}\text{O}_6$
Formula weight	1180.73	1116.41
Crystal system	Triclinic	Monoclinic
Space group	$P\bar{1}$	$C2/c$
a , \AA	8.1594(11)	21.6461(16)
b , \AA	10.4407(13)	9.7999(15)
c , \AA	12.9744(12)	18.9698(17)
α , $^\circ$	88.6530(10)	90
β , $^\circ$	84.1000(10)	116.908(2)
γ , $^\circ$	77.3890(10)	90
V , \AA^3	1072.9(2)	3588.4(7)
Z	1	4
$F(000)$	592	2208
Data/restraints/parameters	3960/2/280	3341/2/234
Goodness-of-fit on F^2	1.070	1.032
R indices [$I > 2\sigma(I)$]	$R_1 = 0.0299$, $wR_2 = 0.0808$	$R_1 = 0.0281$, $wR_2 = 0.0645$
R indices (all data)	$R_1 = 0.0360$, $wR_2 = 0.0838$	$R_1 = 0.0376$, $wR_2 = 0.0679$

Table 2. Selected bond distances (Å) and bond angles (°) for the complexes

1			
Cu(1)–O(1)	1.894(2)	Cu(1)–N(1)	1.950(2)
Cu(1)–O(3)	1.9801(19)	Cu(1)–N(2)	2.028(2)
Cu(1)–O(2)	2.348(2)	Cu(2)–O(5)	1.962(2)
Cu(2)–O(7)	1.964(2)	Cu(2)–O(6A)	1.970(2)
Cu(2)–O(8A)	1.977(2)	Cu(2)–O(4)	2.143(2)
O(1)–Cu(1)–N(1)	92.95(10)	O(1)–Cu(1)–O(3)	87.61(9)
N(1)–Cu(1)–O(3)	164.84(10)	O(1)–Cu(1)–N(2)	176.83(10)
N(1)–Cu(1)–N(2)	84.18(10)	O(3)–Cu(1)–N(2)	95.51(9)
O(1)–Cu(1)–O(2)	101.13(10)	N(1)–Cu(1)–O(2)	105.97(10)
O(3)–Cu(1)–O(2)	88.75(9)	N(2)–Cu(1)–O(2)	78.46(9)
O(5)–Cu(2)–O(7)	89.25(10)	O(5)–Cu(2)–O(6A)	168.40(9)
O(7)–Cu(2)–O(6A)	90.03(9)	O(5)–Cu(2)–O(8A)	90.00(10)
O(7)–Cu(2)–O(8A)	168.33(9)	O(5)–Cu(2)–O(4)	94.32(9)
O(7)–Cu(2)–O(4)	101.00(9)	O(6)–Cu(2)–O(4A)	97.18(9)
O8–Cu(2)–O(4A)	90.67(9)		
2			
Cu(1)–N(1)	1.882(3)	Cu(1)–O(1)	1.891(2)
Cu(1)–N(2)	1.936(3)	Cu(1)–Cl(1)	2.2248(8)
Cu(1)–O(2)	2.280(2)	Cu(2)–O(1)	1.9344(18)
Cu(2)–N(3)	1.947(3)	Cu(2)–N(3B)	1.955(3)
Cu(2)–Cl(2)	2.1834(9)	Cu(2)–Cl(1)	2.4889(9)
N(1)–Cu(1)–O(1)	92.33(10)	N(1)–Cu(1)–N(2)	85.05(12)
O(1)–Cu(1)–N(2)	172.71(10)	N(1)–Cu(1)–Cl(1)	156.24(8)
O(1)–Cu(1)–Cl(1)	88.77(6)	N(2)–Cu(1)–Cl(1)	96.37(8)
N(1)–Cu(1)–O(2)	110.16(10)	O(1)–Cu(1)–O(2)	95.45(9)
N(2)–Cu(1)–O(2)	79.14(11)	Cl(1)–Cu(1)–O(2)	93.35(6)
O(1)–Cu(2)–N(3)	169.70(11)	O(1)–Cu(2)–N(3B)	94.55(10)
N(3)–Cu(2)–N(3B)	76.96(15)	O(1)–Cu(2)–Cl(2)	95.16(7)
N(3)–Cu(2)–Cl(2)	95.13(9)	N(3)–Cu(2)–Cl(2B)	147.00(10)
O(1)–Cu(2)–Cl(1)	80.48(6)	N(3)–Cu(2)–Cl(1)	96.78(10)
N(3)–Cu(2)–Cl(1B)	109.98(9)	Cl(2)–Cu(2)–Cl(1)	102.71(3)

Symmetry codes: A: 1 – x, 1 – y, 2 – z; B: 1/2 – x, 3/2 – y, 1 – z.

mixed and stirred in methanol (30 mL) for 30 min at 25 °C. Then, copper chloride dihydrate (2.00 mmol, 0.34 g) and sodium azide (2.00 mmol, 0.13 g) were added. The final mixture was further stirred for 30 min. The deep blue solution was evaporated to remove three quarters of the solvents under reduced pressure, yielding deep blue solid product of the complex. Yield: 0.43 g (77%). Well-shaped single crystals suitable for X-ray diffraction were obtained by re-crystallization of the solid from methanol. Anal. calcd for $C_{34}H_{46}Br_2Cu_4N_4O_{16}$ (%): C 25.82, H 3.25, N 12.55. Found (%): C 43.75, H 4.31, N 15.56. IR data (KBr, cm^{-1}): 3415, 3243, 2962, 2083, 1658, 1585, 1538, 1470, 1445, 1420, 1383, 1293, 1265, 1207, 1138, 1086, 1065, 1021, 989, 930, 910, 846, 805, 725, 686, 626, 608, 591, 556, 463. UV-Vis data in acetonitrile [λ_{max} (nm), ϵ ($L\ mol^{-1}\ cm^{-1}$)]: 226, 1.45×10^4 ; 245, 1.14×10^4 ; 275, 7.27×10^3 ; 367, 2.60×10^3 ; 640, 74.

2. 5. Catalytic Reactions

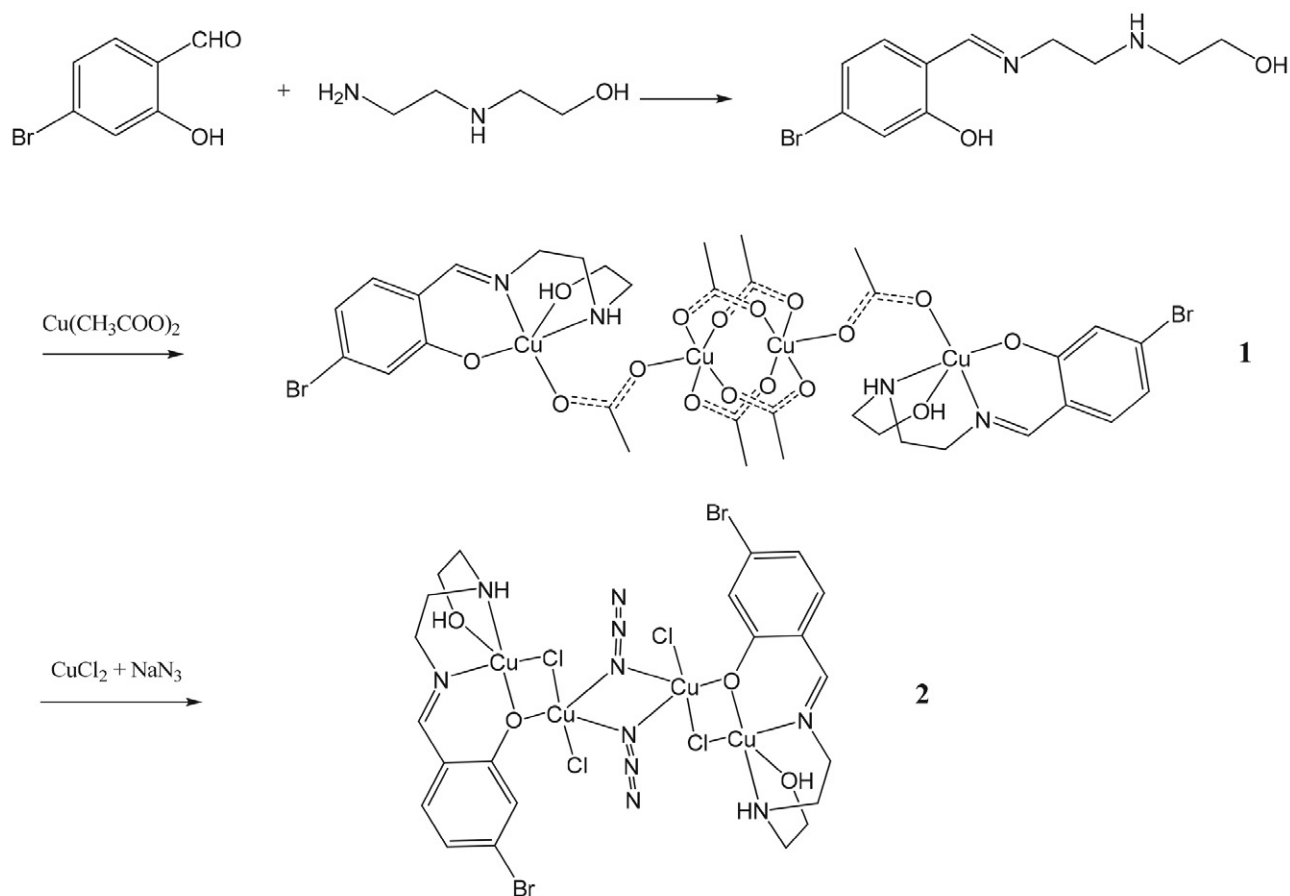
The catalytic reactions were performed according to the procedure described as follows. Substrate (10 mmol),

solvent (8 mL) and the complex as catalyst (0.005 mmol) were mixed in a flask. The mixture was equilibrated to 65 °C. Then, TBHP (20 mmol) was added to the mixture. The final mixture was further stirred for 24 h. The products of the oxidation reactions at different time intervals were collected and identified by gas chromatograph.

3. Results and Discussion

3. 1. Chemistry

The synthetic procedure of the complexes is shown in Scheme 2. The Schiff base 5-bromo-2-((2-(2-hydroxyethylamino)ethylimino)methyl)phenol was formed by reaction of 4-bromosalicylaldehyde and 2-(2-aminoethylamino)ethanol in methanol, which was not isolated and used directly to prepare the complexes. Complex **1** was synthesized by reaction of the Schiff base with copper acetate monohydrate, and complex **2** was synthesized by reaction of the Schiff base with copper chloride dihydrate and sodium azide. The reaction progresses are accompanied by



Scheme 2. The preparation of the complexes.

an immediate color change of the solution from yellow to deep blue. The elemental analyses are in good agreement with the general formulae determined by single crystal X-ray determination. The molar conductivities ($\Lambda_M = 27 \Omega^{-1} \text{ cm}^2 \text{ mol}^{-1}$ for **1** and $35 \Omega^{-1} \text{ cm}^2 \text{ mol}^{-1}$ for **2**) measured in methanol are consistent with the values expected for non-electrolyte.⁹

3. 2. Structure Descripiton of Complex 1

The ORTEP plot of complex **1** is shown in Fig. 1. The molecule of the complex possesses crystallographic inversion center symmetry. The two [CuL] units and the central $[\text{Cu}_2(\mu_2\text{-}\eta^1\text{:}\eta^1\text{-CH}_3\text{COO})_4]$ core are linked through two $\mu_2\text{-}\eta^1\text{:}\eta^1\text{-acetate}$ ligands. In the central $[\text{Cu}_2(\mu_2\text{-}\eta^1\text{:}\eta^1\text{-CH}_3\text{COO})_4]$ core (tetraacetatodicopper(II)), the two Cu atoms has a distance of 2.627(1) Å. The central Cu atom is coordinated by five acetate oxygen atoms, forming a wonderful square pyramidal geometry. The *cis* and *trans* angles in the basal plane are in the ranges of 88.36(9)–90.03(9)° and 168.33(9)–168.40(9)°, respectively. The bond angles among the apical and basal donor atoms are in the range of 90.67(9)–101.00(9)°. The Cu–O bond lengths are comparable to those observed in acetate bridged copper complexes.¹⁰ The Cu atom in [CuL] unit is coordinated in a square

pyramidal geometry, with the phenolate oxygen (O(1)), imino nitrogen (N(1)) and amino nitrogen (N(2)) of the Schiff base ligand, and the acetate oxygen (O(3)) defining the basal plane, and with the hydroxyl oxygen (O(2)) of the Schiff base ligand occupying the apical position. The Cu(1) atom deviates from the basal plane by 0.122(2) Å. The square pyramidal coordination is distorted from ideal model, as evidenced by the bond angles. The *cis* and *trans* angles in the basal plane are in the ranges of 84.18(10)–105.97(10)° and 164.84(10)–176.83(10)°, respectively. The bond angles among the apical and basal donor atoms are in the range of 78.46(9)–105.97(10)°. The distortion is mainly caused by the strain created by the five-membered chelate

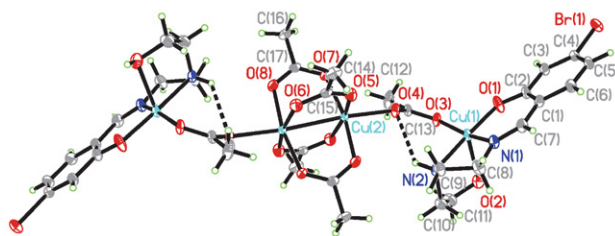


Fig. 1. ORTEP diagram of complex **1** with 30% thermal ellipsoid. Unlabeled atoms are related to the symmetry operation $1 - x, 1 - y, 2 - z$. Hydrogen bonds are shown as dashed lines.

rings Cu(1)-N(1)-C(8)-C(9)-N(2) and Cu(1)-N(2)-C(10)-C(11)-O(2). The Cu(1)-O and Cu(1)-N bond lengths are comparable to those observed in Schiff base copper complexes.¹¹ The intramolecular hydrogen bond between N(2) and O(4) locks the conformation of the Schiff base ligand.

In the crystal structure of the complex, the molecules are linked through O-H...O and C-H...Br hydrogen bonds (Table 3), to form three-dimensional network (Fig. 2).

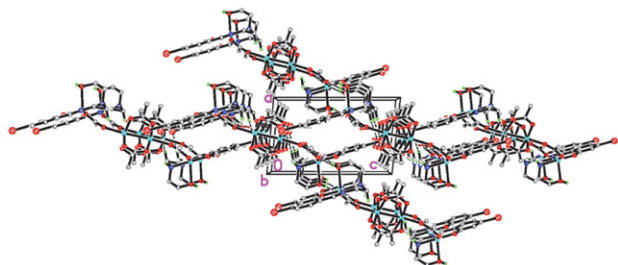


Fig. 2. Molecular packing structure of complex 1 linked by hydrogen bonds.

3. 3. Structure Descripton of Complex 2

The ORTEP plot of complex 2 is shown in Fig. 3. The molecule of the complex possesses crystallographic inversion center symmetry. The two $[\text{Cu}_2\text{LCl}(\mu\text{-Cl})]$ units are linked together by two end-on azido ligands. The Cu atom in the $[\text{Cu}_2\text{LCl}(\mu\text{-Cl})]$ unit is coordinated in a square pyramidal geometry, with the phenolate oxygen (O(1)), imino nitrogen (N(1)) and amino nitrogen (N(2)) of the Schiff base ligand, and the bridging chloride atom (Cl(1)) defining the basal plane, and with the hydroxyl oxygen (O(2)) of the Schiff base ligand occupying the apical position. The Cu(1) atom deviates from the basal plane by 0.159(2) Å. The square pyramidal coordination is distort-

ed from ideal model, as evidenced by the bond angles. The *cis* and *trans* angles in the basal plane are in the ranges of 85.05(12)–96.37(8)° and 156.24(8)–172.71(10)°, respectively. The bond angles among the apical and basal donor atoms are in the range of 79.14(11)–110.16(10)°. The distortion is mainly caused by the strain created by the five-membered chelate rings Cu(1)-N(1)-C(8)-C(9)-N(2) and Cu(1)-N(2)-C(10)-C(11)-O(2), and the four-membered chelate ring Cu(1)-O(1)-Cu(2)-Cl(1). The Cu(1)-O and Cu(1)-N bond lengths are comparable to those observed in Schiff base copper complexes.¹⁰ In the central azido bridged $[\text{Cu}_2(\mu_{1,1}\text{-N}_3)_2]$ core, the two Cu atoms has a distance of 3.054(1) Å. The central Cu atom is coordinated in a square pyramidal geometry, with the phenolate oxygen (O(1)) of the Schiff base ligand, the terminal chloride ligand (Cl(2)), and two azido nitrogen (N(3) and N(3A)) defining the basal plane, and with the bridging chloride ligand (Cl(1)) occupying the apical position. The Cu(2) atom deviates from the basal plane by 0.255(2) Å. The square pyramidal coordination is distorted from ideal model, as evidenced by the bond angles. The *cis* and *trans* angles in the basal plane are in the ranges of 76.96(15)–95.16(7)° and 147.00(10)–169.70(11)°, respectively. The bond angles among the apical and basal donor atoms are

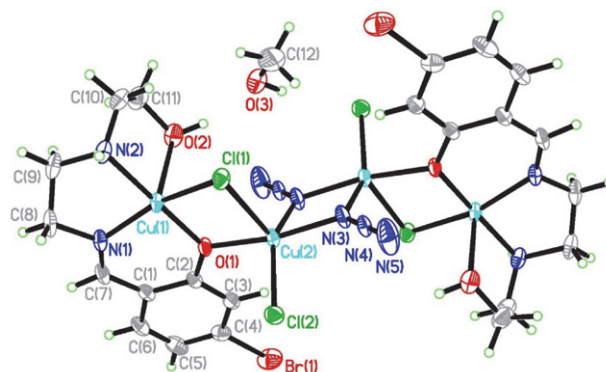


Fig. 3. ORTEP diagram of complex 2 with 30% thermal ellipsoid. Unlabeled atoms are related to the symmetry operation $1/2 - x, 3/2 - y, 1 - z$.

Table 3. Hydrogen bond distances (Å) and bond angles (°) for the complexes

D-H...A	d(D-H)	d(H...A)	d(D...A)	Angle (D-H...A)
1				
O(2)–H(2)···O(3) ^{#1}	0.84	1.90	2.7318	168
C(9)–H9B···Br(1) ^{#2}	0.97	2.93	3.6688	134
2				
N(2)–H(2)···Cl2 ^{#3}	0.89	2.51	3.2061	135
O(2)–H(2)A···O(3) ^{#4}	0.84	1.82	2.6347	164
O(3)–H(3)···Cl2 ^{#5}	0.82	2.28	3.0680	162
C(5)–H(5)···Cl2 ^{#6}	0.93	2.76	3.4815	136
C(8)–H8A···Cl1 ^{#3}	0.97	2.68	3.4459	137
C(8)–H8B···O(2) ^{#7}	0.97	2.50	3.4587	171
C(9)–H(9A)···N(6) ^{#5}	0.97	2.52	3.2450	132

Symmetry codes: #1: $1 - x, -y, 1 - z$; #2: $-x, 1 - y, 1 - z$; #3: $1/2 - x, 1/2 - y, 1 - z$; #4: $1/2 - x, 1/2 + y, 1/2 - z$; #5: $2 - x, 1 - y, 1 - z$; #6: $1 - x, 1 - y, 1 - z$; #7: $1/2 - x, -1/2 + y, 1/2 - z$.

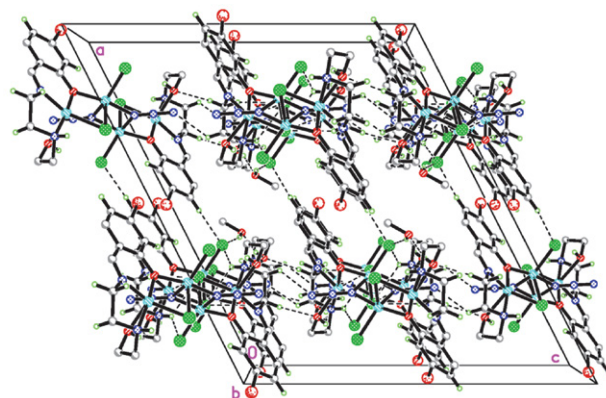


Fig. 4. Molecular packing structure of complex 2 linked by hydrogen bonds.

in the range of 80.48(6)–109.98(9)°. The Cu–Cl and Cu–N bond lengths are comparable to those observed in chlorido and azido coordinated copper complexes.¹²

There are two independent methanol molecules of crystallization. In the crystal structure of the complex, the methanol molecules and the coordination moieties are linked through O–H...O, N–H...Cl, O–H...Cl, C–H...Cl, C–H...O and C–H...N hydrogen bonds (Table 3), to form three-dimensional network (Fig. 4).

3. 4. Infrared and Electronic Spectra

The infrared spectra of the complexes were recorded in the region of 4000–400 cm^{−1} using KBr pellets. The sharp absorptions at 3285 cm^{−1} for **1** and 3243 cm^{−1} for **2** are attributed to the N–H bonds of the Schiff base ligands. Peaks at 3400–3500 cm^{−1} are attributable to O–H stretching vibrations of solvent or hydroxyl group of the Schiff base ligand. Several weak peaks observed in the range 3100–2870 cm^{−1} likely to be due to C–H stretches. Complex **1** displays peak at 1632 cm^{−1}, and complex **2** displays peak at 1658 cm^{−1}, which are assigned to the C=N stretches of the Schiff base ligands.¹³ The different frequencies are in accordance with the bond lengths of C=N, viz. 1.279(4) Å for **1**, and 1.230(4) Å for **2**. The Ar–O stretching bands are observed at 1248 cm^{−1} for **1** and 1265 cm^{−1} for **2**. The asymmetric and symmetric stretching vibrations of the acetate groups in **1** appear at 1565 and 1418 cm^{−1}, respectively. The difference between $\nu_{\text{asym}}(\text{COO})$ and $\nu_{\text{sym}}(\text{COO})$ ($\Delta\nu = 147 \text{ cm}^{-1}$), which is smaller than 164 cm^{−1} observed in ionic acetate, reflects the bidentate bridging coordination mode.¹⁴ The occurrence of medium and sharp intensity peaks at 2083 cm^{−1}, suggests the presence of N=N stretching frequency of the end-on azide group.¹⁵ In addition, new bands observed in the region of 440–600 cm^{−1} for the complexes due to $\nu(\text{Cu–O})$, $\nu(\text{Cu–N})$ and $\nu(\text{Cu–Cl})$.¹⁶

In the UV-Vis spectra of the complexes, the bands at 245–250 nm and 270–275 nm are attributed to the $\pi\text{--}\pi^*$ and $n\text{--}\pi^*$ transitions of the aromatic rings and the C=N groups.¹⁷ The bands at about 365 nm can be attributed to the ligand to Cu(II) charge transfer transition (LMCT).^{15b}

The visible spectra of complexes display weak single broad *d-d* bands centered at about 640 nm, which are consistent with the five-coordinate geometry of the Cu(II) complex.^{15b}

3. 5. Catalytic Property

Some aromatic and aliphatic alkenes reacted with TBHP to produce the corresponding oxides and epoxides in good yields and selectivity in acetonitrile when catalyzed by the two complexes (Figs. 5 and 6). The results are summarized in Table 4. The oxidation of styrene with TBHP gave styrene epoxide in 43% yield for **1** and 45% yield for **2** (selectivity 48–49%) under the homogeneous conditions. Besides, benzaldehyde with yields of 44–48% was produced. The oxidation of cyclohexene and cyclooctene with TBHP catalyzed by the complexes gave good conversion of 95–98% and 82–85%, respectively. The epoxide yields are about 32–38% for both complexes, while the other oxides like cyclohex-2-en-1-ol, cyclohex-2-en-1-one and cyclooctane-1,2-diol were produced in high yields (49–61%).

The solvent effects on the oxidation reactions of cyclohexene catalyzed by the complexes have been studied (Table 5). It is clear that acetonitrile is a preferred solvent for this reaction.

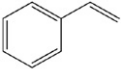
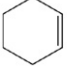

The proposed mechanism for the catalytic reaction is depicted in Scheme 3. Both copper complexes contain unsaturated penta-coordinated Cu spheres, which can be used as Lewis acidic catalysts under homogeneous conditions. The peroxo group of TBHP coordinates to the Cu atoms of both complexes to form the pre-catalysts containing LCu–OOH units. The oxo-functionality transferred to the olefins to produce the oxidized products.

Table 5. The catalytic results^a

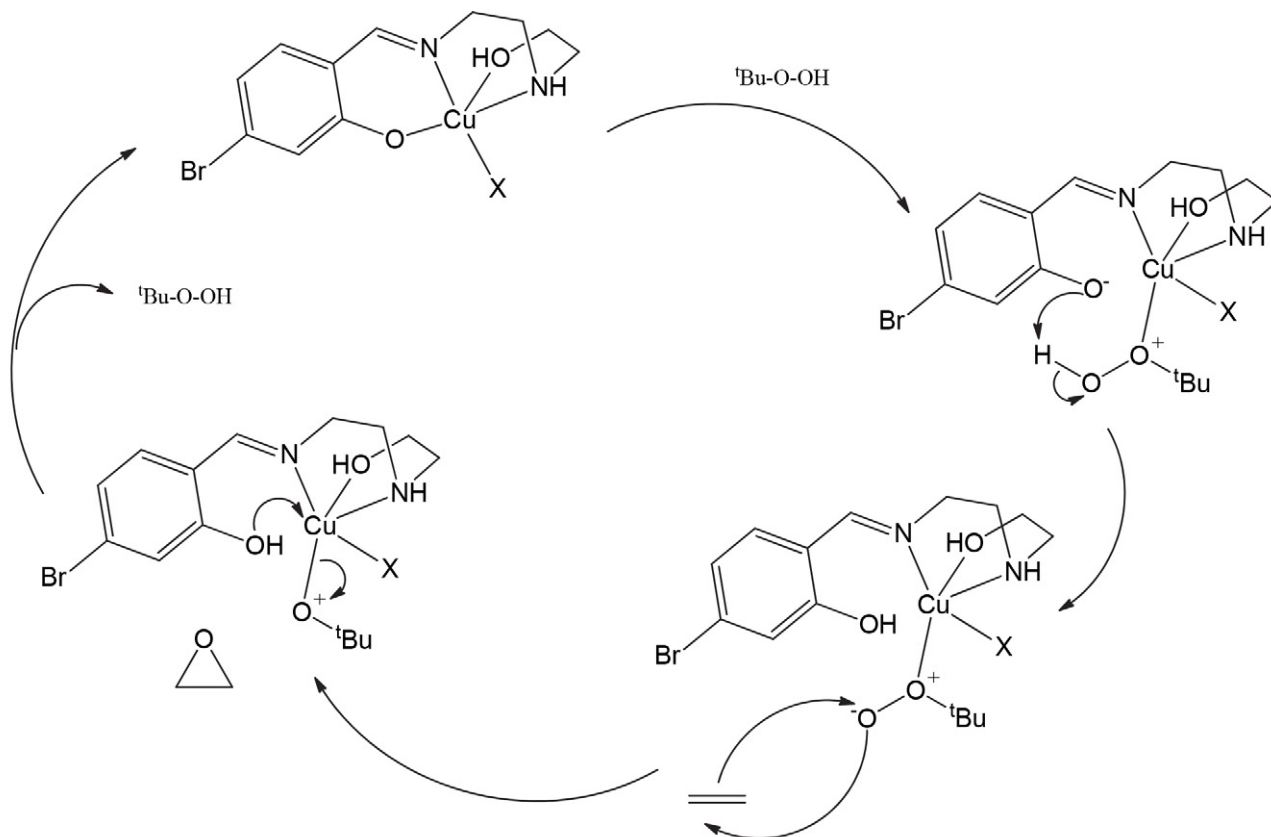
Complex	MeCN	MeOH	CH ₂ Cl ₂	CHCl ₃
1	95	63	85	82
2	98	57	81	78

^a The reaction time is 24 h, and the temperature is 70 °C.

Table 4. The catalytic results^a

Substrate	Complex	Conversion (wt%)	Yield of products	
			Epoxide	Others
	1	87	43	44
	2	93	45	48
	1	95	38	57
	2	98	37	61
	1	82	32	50
	2	85	36	49

^a The reaction time is 24h, and the temperature is 70 °C.



Scheme 3. The proposed mechanism of the catalytic reactions by the complexes as catalysts.

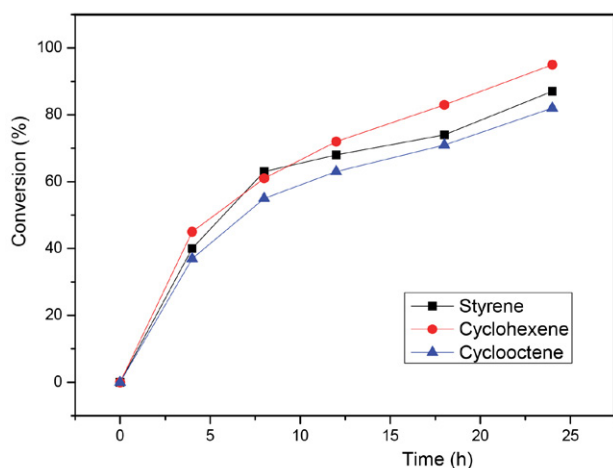


Fig. 5. The conversion plot for the oxidation reactions with complex 1 as the catalyst.

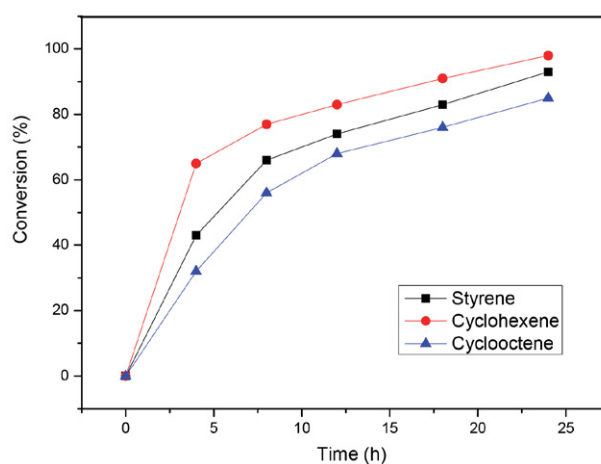


Fig. 6. The conversion plot for the oxidation reactions with complex 2 as the catalyst.

4. Conclusion

Two new tetranuclear copper(II) complexes derived from the Schiff base 5-bromo-2-((2-(2-hydroxyethylamino)ethylimino)methyl)phenol were prepared and characterized. All Cu atoms in the complexes are in square pyramidal coordination. The μ_2 - η^1 : η^1 -acetate, chloride and

end-on azide bridging ligands play important role in the formation of these polynuclear complexes. Both complexes have good catalytic property for the industrially important epoxidation reactions of styrene, cyclohexene and cyclooctene under homogeneous condition in acetonitrile with TBHP as the oxidant.

Supplementary Material

CCDC 2059783 (1) and 2059784 (2) contain the supplementary crystallographic data for this paper. These data can be obtained free of charge via <http://www.ccdc.cam.ac.uk/conts/retrieving.html>, or from the Cambridge Crystallographic Data Centre, 12 Union Road, Cambridge CB2 1EZ, UK; fax: (+44) 1223-336-033; or e-mail: deposit@ccdc.cam.ac.uk.

6. References

- (a) S. H. Sumrra, W. Zafar, S.A. Malik, K. Mahmood, S. S. Shafqat, S. Arif, *Acta Chim. Slov.* **2022**, *69*, 200–216; DOI:10.17344/acsi.2022.7842
(b) M. Abdi, A.F. Shojaei, M. Ghadermazi, Z. Moradi-Shoeili, *Acta Chim. Slov.* **2020**, *67*, 476–486; DOI:10.17344/acsi.2019.5466
(c) S. Dasgupta, S. Paul, D. Samanta, S. Hansda, E. Zangrando, D. Das, *Inorg. Chim. Acta* **2020**, *501*, 119336; DOI:10.1016/j.ica.2019.119336
(d) C. Spinu, A. Kriza, *Acta Chim. Slov.* **2000**, *47*, 179–185; DOI:10.1023/A:1014014631732
(e) S. Rayati, E. Khodaei, P. Nafarieh, M. Jafarian, B. Elmi, A. Woitczak, *RSC Advances* **2020**, *10*, 17026–17036; DOI:10.1039/D0RA02728F
(f) P. K. Mudi, N. Bandopadhyay, M. Joshi, M. Shit, S. Paul, A. R. Choudhury, B. Biswas, *Inorg. Chim. Acta* **2020**, *505*, 119468. DOI:10.1016/j.ica.2020.119468
- (a) V. Thamilarasan, P. Revathi, A. Praveena, J. Kim, V. Chandramohan, N. Sengottuvelan, *Inorg. Chim. Acta* **2020**, *508*, 119626; DOI:10.1016/j.ica.2020.119626
(b) S. Parveen, H. H. Nguyen, T. Premkumar, H. Puschmann, S. Govindarajan, *New J. Chem.* **2020**, *44*, 12729–12740; DOI:10.1039/D0NJ01016B
(c) A. Mandal, A. Sarkar, A. Adhikary, D. Samanta, *Dalton Trans.* **2020**, *49*, 15461–15472; DOI:10.1039/D0DT02784G
(d) B. Rezazadeh, A. R. Pourali, A. Banaei, H. Behniafar, *J. Coord. Chem.* **2019**, *72*, 3401–3416; DOI:10.1080/00958972.2019.1691724
(e) N. C. Jana, M. Patra, P. Brandao, A. Panja, *Inorg. Chim. Acta* **2019**, *490*, 163–172; DOI:10.1016/j.ica.2019.03.017
(f) N. C. Jana, M. Patra, P. Brandao, A. Panja, *Polyhedron* **2019**, *164*, 23–34. DOI:10.1016/j.poly.2019.02.024
- (a) S. Esmaielzadeh, E. Zarenezhad, *Acta Chim. Slov.* **2018**, *65*, 416–428; DOI:10.17344/acsi.2018.4159
(b) Y. Soberanes, K. A. Lopez-Gastelum, J. Moreno-Urbalejo, A. J. Salazar-Medina, M. D. Estrada-Montoya, R. Sugich-Miranda, J. Hernandez-Paredes, A. F. Gonzalez-Cordova, B. Vallejo-Cordoba, R. R. Sotelo-Mundo, E. F. Velazquez-Contreras, F. Rocha-Alonzo, *Inorg. Chem. Commun.* **2018**, *94*, 139–141; DOI:10.1016/j.inoche.2018.06.010
(c) B. K. Kundu, V. Chhabra, N. Malviya, R. Ganguly, G. S. Mishra, S. Mukhopadhyay, *Microporous Mesoporous Mater.* **2018**, *271*, 100–117; DOI:10.1016/j.micromeso.2018.05.046
(d) R. Vafazadeh, M. Alinaghi, A.C. Willis, A. Benvidi, *Acta Chim. Slov.* **2014**, *61*, 121–125;
(e) I. Demir, M. Bayrakci, K. Mutlu, A. I. Pekacar, *Acta Chim. Slov.* **2008**, *55*, 120–124;
(f) A. A. Alemi, B. Shaabani, *Acta Chim. Slov.* **2000**, *47*, 363–369. DOI:10.1353/dss.2008.0061
- (a) M. Karman, G. Romanowski, *Inorg. Chim. Acta* **2020**, *511*, 119832; DOI:10.1016/j.ica.2020.119832
(b) S. S. Hosseinyzade, F. M. Zonoz, B. Bahramian, *Catal. Lett.* **2018**, *148*, 1324–1335; DOI:10.1007/s10562-018-2354-z
(c) S. R. Pour, A. Abdolmaleki, M. Dinari, *J. Mater. Sci.* **2019**, *54*, 2885–2896; DOI:10.1007/s10853-018-3035-4
(d) K. Moghe, A. K. Sutar, I. K. Kang, K. C. Gupta, *RSC Advances* **2019**, *9*, 30823–30834. DOI:10.1039/C9RA05811G
- L. F. Veiros, A. Prazeres, P. J. Costa, C. C. Romao, F. E. Kuhn, M. J. Calhorda, *J. Chem. Soc. Dalton Trans.* **2006**, *11*, 1383–1389. DOI:10.1039/b515484g
- C. Adhikary, R. Bera, B. Dutta, S. Jana, G. Bocelli, A. Cantoni, S. Chaudhuri, S. Koner, *Polyhedron* **2008**, *27*, 1556–1562. DOI:10.1016/j.poly.2008.01.030
- Bruker, SMART (Version 5.625) and SAINT (Version 6.01). Bruker AXS Inc., Madison, Wisconsin, USA, **2007**.
- (a) G. M. Sheldrick, *Acta Crystallogr.* **2015**, *A71*, 3–8; DOI:10.1107/S2053273314026370
(b) G.M. Sheldrick, *Acta Crystallogr.* **2015**, *C71*, 3–8.
- W. J. Geary, *Coord. Chem. Rev.* **1971**, *7*, 81–122. DOI:10.1016/S0010-8545(00)80009-0
- (a) B. Sarkar, M. G. B. Drew, M. Estrader, C. Diaz, A. Ghosh, *Polyhedron* **2008**, *27*, 2625–2633; DOI:10.1016/j.poly.2008.05.004
(b) R. N. Patel, D.K. Patel, V. P. Sondhiya, K. K. Shukla, Y. Singh, A. Kumar, *Inorg. Chim. Acta* **2013**, *405*, 209–217. DOI:10.1016/j.ica.2013.05.024
- (a) S. Khan, S. Sproules, L. S. Natrajan, K. Harms, S. Chattopadhyay, *New J. Chem.* **2018**, *42*, 1634–1641; DOI:10.1039/C7NJ03990E
(b) I. Buta, L. Cseh, C. Cretu, D. Aparaschivei, C. Maxim, P. Lonneck, E. Hey-Hawkins, N. Stanica, E. Ohler, E. Rentschler, M. Andruh, O. Costisor, *Inorg. Chim. Acta* **2018**, *475*, 133–141. DOI:10.1016/j.ica.2017.10.024
- (a) A. Pradhan, S. Halder, K. B. Mallik, M. Ghosh, M. Bera, N. Sepay, D. Schollmeyer, S.K. Ghatak, S. Roy, S. Saha, *Inorg. Chim. Acta* **2019**, *484*, 197–205; DOI:10.1016/j.ica.2018.09.026
(b) H. Chowdhury, R. Bera, C. Rizzoli, C. Adhikary, *J. Coord. Chem.* **2020**, *73*, 3062–3078. DOI:10.1080/00958972.2020.1836360
- X. M. Chen, Y. X. Tong, T. C. W. Mak, *Inorg. Chem.* **1994**, *33*, 4586–4588. DOI:10.1021/ic00098a029
- (a) U. Kumar, J. Thomas, N. Thirupathi, *Inorg. Chem.* **2010**, *49*, 62–72; DOI:10.1021/ic901100z
(b) H. Grove, M. Julve, F. Lloret, P. E. Kruger, K. W. Tornroos, J. Sletten, *Inorg. Chim. Acta* **2001**, *325*, 115–124. DOI:10.1016/S0020-1693(01)00642-9
- (a) S. Shit, P. Talukder, J. Chakraborty, G. Pilet, M. S. El Fallah, J. Ribas, S. Mitra, *Polyhedron* **2007**, *26*, 1357–1363;

DOI:10.1016/j.poly.2006.11.013

(b) A. Ray, D. Sadhukhan, G.M. Rosair, C.J. Gomez-Garcia, S. Mitra, *Polyhedron* **2009**, 28, 3542–3550.

DOI:10.1016/j.poly.2009.07.017

16. A. Jayamani, M. Sethupathi, S.O. Ojwach, *Inorg. Chem. Commun.* **2017**, 84, 144–149. DOI:10.1016/j.inoche.2017.08.01317. H. Chowdhury, R. Bera, C. Rizzoli, C. Adhikary, *Transition Met. Chem.* **2020**, 45, 605–612.

DOI:10.1007/s11243-020-00415-7

Povzetek

Sintetizirali smo štirijedrni kompleks bakra(II) z mostovnimi acetatnimi ligandi, $[\text{Cu}_4\text{L}_2(\mu_2\text{-}\eta^1\text{-CH}_3\text{COO})_6(\text{CH}_3\text{OH})_2]$ (**1**), in štirijedrni kompleks bakra(II) s kloridnimi, fenolatnimi in azidnimi mostovnimi ligandi, $[\text{Cu}_4\text{L}_2\text{Cl}_2(\mu\text{-Cl})_2(\mu_{1,1}\text{-N}_3)_2]2\text{CH}_3\text{OH}$ (**2**), pri čemer je L deprotonirana oblika Schiffove baze 5-bromo-2-((2-(2-hidroksietilamino)etylimino)metil)fenol (HL). Produkta smo karakterizirali z elementno analizo, IR in UV spektroskopijo ter rentgensko monokristalno difrakcijo. Strukturna analiza na monokristalu je v obeh spojinah pokazala kvadratno planarno geometrijo okoli bakrovih atomov. V kompleksu **1** dva acetatna liganda povezujeta dve enoti $[\text{CuL}]$ z jedrom $[\text{Cu}_2(\mu_2\text{-}\eta^1\text{-CH}_3\text{COO})_4]$. V kompleksu **2** so enote $[\text{Cu}_2\text{LCl}(\mu\text{-Cl})]$ povezane z azido ligandi. Schiffova baza kot ligand je koordinirana na bakrov atom preko štirih N in O donorskih atomov. Vodikove vezi povezujejo molekule obeh kompleksov v tridimenzionalno mrežo. Katalitske lastnosti kompleksov smo preučevali v reakcijah epoksidacije alkenov s tert-butilhidroperoksidom kot terminalnim oksidantom pod blagimi pogoji v acetonitrilu.



Except when otherwise noted, articles in this journal are published under the terms and conditions of the Creative Commons Attribution 4.0 International License

Evaluation of the Stability of Hydrocortisone Sodium Succinate in Solutions for Parenteral Use by a Validated HPLC-UV Method

Katja Mihovec,¹ Žane Temova Rakuša,² Enikő Éva Gaál² and Robert Roškar²

¹ University Medical Centre Ljubljana, Slovenia

² University of Ljubljana, Faculty of Pharmacy, Ljubljana, Slovenia

* Corresponding author: E-mail: robert.roskar@ffa.uni-lj.si

Tel: +386 1 4769 655

Received: 06-30-2022

Abstract

This study aimed to determine the in-use stability ($t_{95\%}$) of hydrocortisone sodium succinate (HSS) infusion solutions and provide evidence-based guidelines on their usability.

HSS infusion solutions were prepared and stored as recommended by the manufacturer and under common conditions in our hospital. The effects of HSS concentration (1 and 4 mg/mL), solvent (isotonic saline and glucose), temperature (ambient and 30 °C), and light on its stability were evaluated using a validated stability-indicating HPLC-UV method.

HSS degradation followed first-order kinetics. No significant difference in its stability was observed between the two evaluated concentrations, solvents and light exposure ($t_{95\%}$ between 25 and 30 h). Elevated temperature (30 °C) affected HSS stability and significantly reduced the $t_{95\%}$ (4.6–6.3 h).

HSS infusion solutions are physically and chemically stable (<5% degradation) for at least 6 h if stored below 30 °C. The in-use stability may be extended up to 24 h if stored below 24 °C.

Keywords: Forced degradation study; in-use stability; infusion; injection; Solu-Cortef.

1. Introduction

Cortisone is a glucocorticoid hormone synthesized endogenously in the adrenal gland cortex, as a response to stress.¹ Its synthetic form – hydrocortisone, mostly as hydrocortisone sodium succinate (HSS), is used in medicines for various conditions, requiring rapid and intense corticosteroid effects, such as acute or chronic adrenal insufficiency, various autoimmune and allergic diseases, and septic shock, unresponsive to fluid resuscitation and treatment with vasopressors.^{2,3} Thus, the use of HSS as a continuous infusion is associated with more stable cortisol plasma concentrations and reduced fluctuation in blood glucose levels compared to intermittent boluses.⁴ This is particularly important in patients with diabetes, as hyperglycaemia is one of the most common glucocorticoid side effects.^{4,5} The application of continuous HSS infusion is also well-established practice for critically ill patients in hospital intensive care units (ICUs), also including the ICU of our hospital. For such purposes, commercially

available medicinal products, in the form of vials containing freeze-dried powder for solution for injection/infusion, are used. Thus, an intravenous infusion is prepared as recommended by the manufacturer – by reconstituting the powder with 2 mL of sterile water for injection and addition of this solution to 100–1000 mL of 5% glucose in water or isotonic saline solution or 5% glucose in isotonic saline solution under aseptic conditions.² While the manufacturer recommends immediate use after reconstitution with sterile water for injection and disposal of any remainder, no information is provided on the in-use stability of the diluted HSS solution for infusion.² HSS is an ester, susceptible to hydrolysis and other degradation reactions (oxidation and transesterification) in aqueous solutions.^{6–8} In a broader sense, data on HSS stability can be found in the literature, as HSS stability studies in oral solutions and suspensions,^{9,10} solutions for infusion,^{11,12} or as compatibility studies with other drugs.^{13–15} Focusing on stability studies of HSS individually in solutions for infusion, which are limited to isotonic saline solutions, we identified a need for

a stability study under clinically relevant real-life conditions, since the type of media, temperature, and HSS concentration may affect its stability.^{8–10} As medical personnel deal with these issues on daily basis, our primary objective within this study was to evaluate the stability of HSS under common real-life conditions and thus provide evidence-based guidelines. For such purpose, we investigated the stability of HSS in solutions for infusion, as commonly prepared in our hospital, by using a stability-indicating HPLC-UV method. We thus evaluated the effect of clinically relevant HSS concentration (1 mg/mL and 4 mg/mL), type of reconstitution solvent (isotonic saline and glucose solutions), temperature (24 °C and 30 °C), and light (protected and exposed to daylight) on its stability in infusion solutions.

2. Experimental

2.1. Chemicals and Preparations

HPLC grade acetonitrile (ACN) was purchased from Sigma-Aldrich (Steinheim, Germany). Hydrochloric acid (HCl) and sodium hydroxide (NaOH) solutions (Titrisol®) as well as phosphoric acid (H_3PO_4) (85%) were purchased from Merck (Darmstadt, Germany). H_2O_2 solution (30%) was purchased from Honeywell Fluka™ (Seelze, Germany). High purity water was obtained using a Milli-Q A10 Advantage water purification system (Millipore Corporation, Bedford, MA, USA). Solu-Cortef 100 mg powder for solution for injection or infusion (Pfizer, Luxembourg, Luxembourg), and solutions for infusion: 0.9% sodium chloride (S) in 50 mL infusion bags (Baxter, Deerfield, Illinois, USA), and 5% glucose (G) in 100 mL intravenous (IV) containers (B. Braun, Melsungen, Germany) were used. Due to the lack of an HSS reference standard, its calibration and quality control (QC) solutions, as well as samples for the forced degradation study, were prepared by dissolving a portion of the powder of the medicinal product Solu-Cortef in Milli-Q water. The total powder was initially weighted to calculate the share of HSS, according to the reported HSS content in the product.

2.2. Instrumentation and Chromatographic Conditions

The analysis was performed on an Agilent 1100/1200 series HPLC system (Agilent Technologies, Santa Clara, CA, USA) equipped with a UV-VIS detector and a ChemStation data acquisition system. A reversed-phase Luna C18 250 × 4.6 mm, 5 µm particle size column (Phenomenex, Torrance, CA, USA) at 40 °C using 1% (v/v) H_3PO_4 (mobile phase A), and ACN (mobile phase B) in isocratic mode (33% A, 67% B), at a flow-rate of 1.5 mL/min was utilized for the analysis. Detection was performed at 254 nm. The injection volume was 2 µL. The retention time (t_r) of HSS was 10.8 min and the total runtime was 13 min.

2.3. Preparation of Samples for Forced Degradation Study

The forced degradation study was performed according to the ICH guidelines Q1A (R2).¹⁶ A stock HSS solution (5 mg/mL) was initially prepared and diluted 5-fold, to obtain samples containing 0.1 M HCl, 0.1 M NaOH, 3% H_2O_2 , or Milli-Q water. Samples with Milli-Q water were used as controls (ambient temperature and protected from light) and to assess the effect of temperature (60 °C) and light (exposure to daylight). All samples, except those for thermal degradation, were stored at ambient temperature (24 °C) and protected from light (except those for the photostability testing). The samples were exposed to stress conditions for 24 hours. The samples were neutralized with HCl or NaOH (when required) or cooled to ambient temperature (thermal stress samples) before analysis.

2.4. Preparation of Calibration Standards and QC Solutions

A stock solution containing 5 mg/mL HSS was initially prepared and further diluted with Milli-Q water to obtain calibration standards with the following HSS concentrations: 0.05 mg/mL, 0.5 mg/mL, 2.0 mg/mL, 3.0 mg/mL and 5.0 mg/mL. QC samples containing 0.1 mg/mL, 1.0 mg/mL, and 4.0 mg/mL HSS were prepared from the initially prepared HSS stock solution in triplicate in the same manner. The calibration and QC solutions were prepared and analysed on three consecutive days of the validation.

2.4. Method Validation

The utilized HPLC-UV method was validated following the ICH guidelines Q2(R1) in terms of specificity, linearity, precision, accuracy, quantitation limit (LOQ), detection limit (LOD), and sample stability.¹⁷

Specificity was evaluated in chromatograms of the used solvents (Milli-Q water, 0.9% sodium chloride solution, 5% glucose solution, and the solvent in the vial of the medicinal product Solu-Cortef, which contains benzyl alcohol as a preservative), which were compared with the chromatogram of HSS solution. Specificity was also assessed in forced degradation HSS samples, which were evaluated for chromatographic interferences.

Linearity was assessed by linear regression analysis of calibration standards, covering expected HSS concentrations in solutions for infusion (0.05–5.0 mg/mL). The determination coefficient (R^2) > 0.999 was considered acceptable.

The QC solutions, prepared at three concentration levels on each day of the validation, were used to evaluate the accuracy, precision, and injection repeatability. Intra- and inter-day accuracy was determined as the ratio between the HSS concentration calculated from the regres-

sion line and its actual concentration. Intra- and inter-day precision was determined by calculating the relative standard deviation (RSD) of the QC solutions in triplicate and injection repeatability was determined as the RSD of six consecutive injections of a QC solution. The acceptance criteria were $100 \pm 5\%$ for accuracy, $\leq 5\%$ RSD for precision, and $\leq 2\%$ RSD for injection repeatability.

The LOD and LOQ were calculated using the equations $\text{LOD} = (3.3 \times \sigma)/S$ and $\text{LOQ} = (10 \times \sigma)/S$, where σ is the standard deviation of the intercepts and S is the average slope of the three regression lines.

HSS stability was determined by storing the QC solutions at all three concentration levels in the autosampler (6°C) and analysing them within 24 h. HSS stability, expressed as a share of the initial response, was set at $100 \pm 5\%$.

2. 6. Sample Preparation and HSS in-use Stability Study in Solutions for Infusion

The stability of HSS was studied in solutions for infusion prepared according to the manufacturer's instructions, and as prepared in our hospital. A 50 mg/mL HSS solution was initially prepared by adding 2 mL of sterile water for injection to the content of a vial of Solu-Cortef, followed by manual shaking. Half of this solution (1 mL) was withdrawn and diluted up to 50 mL with S or G in the original IV containers to an HSS concentration of 1 mg/mL. The 4 mg/mL HSS solutions in S or G were prepared in the same way, using two vials of Solu-Cortef (2×2 mL diluted with 50 mL of S or G). The pH values of the prepared solutions were measured using a pH meter MP 220 (Mettler Toledo, Switzerland).

The effects of different HSS concentrations (1 mg/mL and 4 mg/mL), solvent (S and G), temperature (controlled

ambient ($24 \pm 1^\circ\text{C}$) and elevated ($30 \pm 1^\circ\text{C}$), and light exposure (protected (UV-prot) and unprotected (UV)) on HSS stability in solutions for infusion were studied (Table 1). All samples were prepared and stored in the original S and G IV containers in triplicate and analyzed at regular time points within 72 hours. All samples were also visually examined for potential physical changes.

2. 7. In-use Stability Determination and Statistical Analysis

The results are expressed as the mean of three parallels of the samples along with the standard error of the mean. Zero ($c = c_0 - kt$), first ($\ln c = \ln c_0 - kt$), and second-order ($1/c = 1/c_0 + kt$) kinetics, where t is time, c is the HSS concentration at time t , c_0 is the initial HSS concentration, and k is the reaction rate constant, were fitted to the HSS degradation using the least square regression function. Among them, the model with the highest R-square was selected and applied for in-use stability determination, which was defined as HSS content $\geq 95\%$ of the initial content. The determined rate constants and in-use stability were compared by 95% confidence intervals. Statistical analyses using a two-sample t-test assuming variances, as previously determined by the F-test for two sets of data, which differ in only one parameter (e.g., different storage temperature, light, HSS concentration, or type of solvent) were performed using MS Excel 2019. Differences with p values < 0.05 were considered significant.

3. Results

3. 1. HSS Forced Degradation Study

Among the conditions tested within the forced degradation study, HSS proved most susceptible to hydrolytic degradation with only 2% remaining in 0.1 M NaOH and 20% in 0.1 M HCl after 24 hours. HSS was also susceptible to oxidation (56% remaining after 24 hours in 3% H_2O_2), thermal degradation (63% remaining after 24 hours of storage at 60°C), and photolytic degradation to a lesser extent (96% remaining after 24 hours). The HSS main degradation products (t_r 4.0, 5.7, and 6.5 min) formed during the forced degradation study did not interfere with its chromatographic evaluation (t_r 10.9 min) (Figures S1, S2, and S3).

3. 2. Method Validation

The specificity of the method was confirmed as all solvents recommended by the manufacturer for dissolution and dilution of the medicinal product Solu-Cortef, did not contain interfering peaks at HSS retention time. Also, no interfering degradation product peaks were formed during the HSS forced degradation study (Figure S2). In addition, the linearity, intra- and inter-day accuracy and precision,

Table 1. Conditions during hydrocortisone sodium succinate (HSS) stability study in isotonic saline (S) and 5% glucose (G) solutions for infusion.

Sample	HSS concentration [mg/mL]	Solvent	Storage temperature [$^\circ\text{C}$]	Light exposure
1	1	S	24	UV-prot
4	4	S	24	UV-prot
1	1	G	24	UV-prot
4	4	G	24	UV-prot
1	1	S	24	UV
4	4	S	24	UV
1	1	G	24	UV
4	4	G	24	UV
1	1	S	30	UV-prot
4	4	S	30	UV-prot
1	1	G	30	UV-prot
4	4	G	30	UV-prot

S – isotonic saline (0.9% sodium chloride); G – 5% glucose solution; UV – exposed to daylight; UV-prot – light protected.

Table 2. Validation data of the analytical method for hydrocortisone sodium succinate (HSS) quantification.

HSS calibration samples	Range [mg/mL]	R ²		LOD [mg/L]		LOQ [mg/L]		
	0.05-5.00	1.0000		12.6		39.2		
QC samples	Intra-day accuracy and precision			Inter-day accuracy and precision				
HSS conc. [mg/mL]	Found conc. [mg/mL]	Accuracy (%)	RSD (%)	Found conc. [mg/mL]	Accuracy (%)	RSD (%)	Inj. rep.	Stability (%)
0.1	0.0981	98.1	1.29	0.0997	99.7	3.30	0.52	100.5
1.0	1.0054	100.5	0.02	1.0087	100.9	0.29	0.20	99.2
4.0	3.9901	99.8	0.46	3.9956	99.9	0.55	0.29	99.2

LOD – detection limit; LOQ – quantitation limit; QC – quality control; conc. – concentration; RSD – relative standard deviation; Inj. rep. – injection repeatability.

and injection repeatability of the method were confirmed (Table 2), as all results were within the acceptance criteria. The method was found sufficiently sensitive for HSS evaluation within the stability study (LOQ ≤ 3.9% of the expected HSS content). HSS also proved proper stability in the QC solutions, with a < 1% change in its response after 24 hours (Table 2).

3. 3. HSS in-use Stability Study in Solutions for Infusion

The determined pH values of the simulated solutions for infusion with different HSS concentrations

were as follows: 7.04 in S containing 1 mg/mL HSS; 7.26 in S containing 4 mg/mL HSS; 7.42 in G containing 1 mg/mL HSS and 7.52 in G containing 4 mg/mL HSS and were within the pH range, specified by the manufacturer.² The obtained results on HSS stability in the simulated solutions for infusion are shown in Figure 1. The increase in temperature (from 24 °C to 30 °C) significantly increased HSS degradation, while the other tested conditions – different HSS concentrations (1 mg/mL and 4 mg/mL), media (S or G), and light exposure only slightly affected HSS stability. No changes in colour, odour or precipitations were detected in the samples during the stability study.

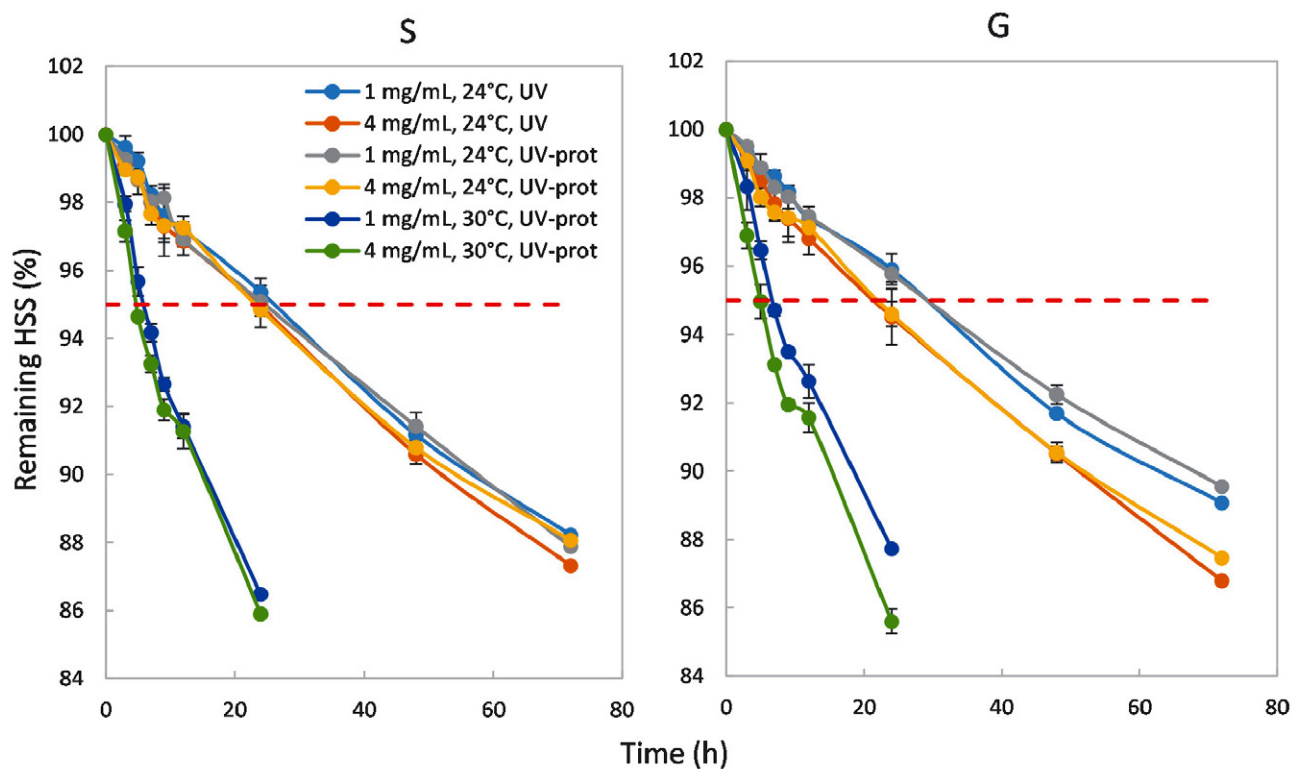


Figure 1. Hydrocortisone sodium succinate (HSS) stability in the simulated solutions for infusion in isotonic saline (0.9% sodium chloride) (S) and 5% glucose solution (G) under different storage conditions. The results are presented as an average ± standard error of the mean, n = 3.

Table 3. First-order rate constants (k_1) and in-use stability ($t_{95\%}$) for hydrocortisone sodium succinate (HSS) at two concentrations (1 mg/mL and 4 mg/mL) in the simulated solutions for infusion under different storage conditions.

Simulated solutions for infusion	k_1 [h^{-1}] (CI)			In-use stability [h] (CI)		
	24 °C, UV-prot	24 °C, UV	30 °C, UV-prot	24 °C, UV-prot	24 °C, UV	30 °C, UV-prot
1 mg/mL HSS in S	1.84×10^{-3} ($1.86 \times 10^{-3} - 2.01 \times 10^{-3}$)	1.92×10^{-3} ($1.90 \times 10^{-3} - 1.93 \times 10^{-3}$)	8.79×10^{-3} ($7.84 \times 10^{-3} - 9.74 \times 10^{-3}$)	28.0 (26.6 – 29.3)	26.7 (26.5 – 27.0)	5.9 (5.2 – 6.5)
4 mg/mL HSS in S	1.94×10^{-3} ($1.86 \times 10^{-3} - 2.01 \times 10^{-3}$)	1.99×10^{-3} ($1.91 \times 10^{-3} - 2.07 \times 10^{-3}$)	1.03×10^{-2} ($9.46 \times 10^{-3} - 1.10 \times 10^{-2}$)	26.5 (25.4 – 27.5)	25.8 (24.7 – 26.8)	5.0 (4.6 – 5.4)
1 mg/mL HSS in G	1.64×10^{-3} ($1.55 \times 10^{-3} - 1.73 \times 10^{-3}$)	1.76×10^{-3} ($1.71 \times 10^{-3} - 1.81 \times 10^{-3}$)	7.81×10^{-3} ($7.46 \times 10^{-3} - 8.17 \times 10^{-3}$)	31.2 (29.6 – 32.9)	29.1 (28.2 – 29.9)	6.6 (6.3 – 6.9)
4 mg/mL HSS in G	1.98×10^{-3} ($1.91 \times 10^{-3} - 2.05 \times 10^{-3}$)	2.00×10^{-3} ($2.00 \times 10^{-3} - 2.05 \times 10^{-3}$)	1.10×10^{-2} ($9.88 \times 10^{-3} - 1.05 \times 10^{-2}$)	25.9 (25.0 – 26.9)	25.4 (25.0 – 25.7)	5.0 (4.9 – 5.2)

CI – 95% confidence interval; S – isotonic saline (0.9% sodium chloride); G – 5% glucose solution; UV – exposed to daylight; UV-prot – light protected.

The fitting of zero, first, and second-order kinetic models showed that HSS degradation in aqueous solutions follows first-order kinetics, which was applied to its stability evaluation. First-order reaction rate constants were calculated for HSS degradation in each tested solution and used for the determination of its in-use stability (Section In-use stability determination and statistical analysis) (Table 3).

4. Discussion

The main objective of our study was to determine the chemical and physical stability of HSS at two concentrations (1 mg/mL and 4 mg/mL) at ambient temperature after reconstitution with the solvent in the vial of the medicinal product and dilution with 0.9% sodium chloride or 5% glucose solution. Although the HSS concentration of 4 mg/mL exceeds the highest HSS concentration in infusions, prepared according to the manufacturer's instructions, it is a clinically relevant concentration in the treatment of ICU patients, for whom a reduction in the infusion volume is very desirable. These two HSS concentrations represent the most common circumstances, when preparing an HSS infusion, in our hospital and were therefore selected for the study. HSS stability evaluation was performed by utilizing a stability-indicating HPLC-UV method, based on the method proposed in the European pharmacopeia HSS monograph,¹⁸ which was further optimized and properly validated following the ICH Q2(R1) guidelines.¹⁷ The stability-indicating nature of the method was confirmed by forced degradation studies, as the chromatographic peak of HSS was chromatographically separated from its degradation products, as can be seen in Figure S2, yet the peak purity was not assessed due to limitations of the analytical equipment (variable wavelength UV detector). Forced degradation studies also revealed the

susceptibility of HSS to degradation under hydrolytic, oxidative, and thermal conditions. However, these stability issues are not addressed by the manufacturer of the medicinal product Solu-Cortef, who does not specify the in-use stability of the HSS solution for infusion. Specified in-use stability would be valuable information for the medical personnel with implications for the patients, as HSS is commonly applied as a continuous infusion. However, it is also unaccounted for in the accessible literature. Therefore, the in-use stability of HSS in solutions for infusion was determined within this study, together with the effects of real-life conditions and situations (use of different types and volumes of solution for dilution, temperature variations, and exposure to light).

The main conclusion from the performed in-use stability study is that HSS stability is mostly affected by temperature, as the increase in temperature (from 24 °C to 30 °C) significantly increased HSS degradation (reaction rate constants in Table 3) and resulted in significantly shorter in-use stability of ≤ 6.3 hours (in-use stability in Table 3) (t-test, $p < 0.001$). The destabilizing effect of higher storage temperature on HSS in S was also demonstrated by Gupta and Ling.¹⁶ The determined in-use stability, considering the 95% confidence interval was higher in the samples protected from light (Table 3). However, these differences were typically not statistically significant (t-test, $p > 0.05$), which is in line with the findings from the performed forced degradation study (Section HSS forced degradation study). Analogously, the differences between the stability of HSS at different concentrations in S were not significant (t-test, $p > 0.05$), whereas G containing a higher HSS concentration (4 mg/mL) was significantly less stable than the 1 mg/mL solution (t-test, $p < 0.03$) under all three evaluated conditions (24 °C, protected from light; 24 °C, exposed to daylight; and 30 °C, protected from light) (Table 3). Comparing the HSS stability in solution with the same concentration and stored under the same conditions

(Table 3), we concluded that the use of different dilution solvents (S or G) does not significantly affect the HSS stability (t-test, $p > 0.05$), which was expected as they are both recommended as dilution solvents by the manufacturer.² The determined in-use stability of 24 hours under controlled room temperature provides the medical personnel reliable evidence on the usability of the infusion solution, during the application of the infusion. During this time period, all evaluated HSS solutions remained physically stable, as no changes in the organoleptic properties were observed. The microbiological stability was not evaluated within this study. The results of this stability study, performed in clinically relevant conditions on the medicinal product, represent a step forward in providing high-quality patient care, which is primarily ensured by the quality of the medicinal product itself, guaranteed by its manufacturer and the competent regulatory bodies.

5. Conclusion

The chemical and physical stability of HSS in solutions for infusion under different conditions, which simulate the conditions in hospitals, was assessed within this study. The results, obtained using a stability-indicating HPLC-UV method, revealed HSS degradation in these solutions, which followed first-order kinetics. Based on the stability data, in-use stability ($t_{95\%}$) of at least 24 hours was confirmed at ambient temperature and a significantly lower in-use stability (≤ 6 hours) at 30 °C. Other evaluated conditions (HSS concentration, light exposure, and use of different dilution solvents), did not significantly affect the stability of HSS in the examined solutions for infusion. All evaluated solutions were physically stable within the determined in-use stability. The significant temperature effect on the stability of HSS in solutions for infusion should be considered in hospitals with uncontrolled temperatures and especially during summertime.

Acknowledgements

This research was financially supported by the Slovenian Research Agency (ARRS) [P1-0189].

Competing interest: None declared.

6. References

1. M. Q. Almeida, B. B. Mendonca, *Clinics (Sao Paulo)* **2020**, 75, e2022–e2022. DOI:10.6061/clinics/2020/e2022
2. 'Solu-Cortef – Summary of Product Characteristics (SmPC)' – <https://www.medicines.org.uk/emc/medicine/7833#gref>, (assessed: July 21, 2021).
3. R. H. Straub, M. Cutolo, *Rheumatology* **2016**, 55, ii6–ii14. DOI:10.1093/rheumatology/kew348
4. H. Hoang, S. Wang, S. Islam, A. Hanna, A. Axelrad, C. Brathwaite, *P T* **2017**, 42, 252–255.
5. H. E. Tamez-Pérez, D. L. Quintanilla-Flores, R. Rodríguez-Gutiérrez, J. G. González-González, A. L. Tamez-Peña, *World J Diabetes* **2015**, 6, 1073–1081. DOI: 10.4239/wjd.v6.i8.1073
6. E. R. Garrett, *J Pharm Sci* **1962**, 51, 445–450. DOI:10.1002/jps.2600510511
7. L. Solomun, S. Ibric, V. Pejanovic, J. Djuris, J. Jockovic, P. Stankovic, Z. Vujic, *Hem Ind* **2012**, 66, 647–657. DOI:10.2298/HEMIND120207023S
8. V. Das Gupta, *J Pharm Sci* **1978**, 67, 299–302. DOI:10.1002/jps.2600670305
9. J. Chappe, N. Osman, S. Cisternino, J.-E. Fontan, J. Schlatter, *J Pediatr Pharmacol Ther* **2015**, 20, 197–202. DOI:10.5863/1551-6776-20.3.197
10. A. Manchanda, M. Laracy, T. Savji, R. H. Bogner, *Int J Pharm Compd* **2018**, 22, 66–75.
11. V. D. Gupta, J. Ling, *Int J Pharm Compd* **2000**, 4, 396–397.
12. D. C. Rigge, M. F. Jones, *J Pharm and Biomed* **2005**, 38, 332–336. DOI:10.1016/j.jpba.2004.12.026
13. J. C. Craddock, L. M. Kleinman, A. Rahman, *Am J Hosp Pharm* **1978**, 35, 402–406. DOI:10.1093/ajhp/35.4.402
14. L. A. Trissel, K. M. King, Y. Zhang, A. M. Wood, *J Oncol Pharm Pract* **2002**, 8, 27–32. DOI:10.1191/1078155202jp087oa
15. Y. W. Cheung, B. R. Vishnuvajjala, K. P. Flora, *Am J Hosp Pharm* **1984**, 41, 1802–1806. DOI:10.1093/ajhp/41.9.1802
16. International Council for Harmonisation. ICH Harmonised Tripartite Guideline. Stability Testing of New Drug Substances and Products Q1A(R2). Geneva, Switzerland, 2003.
17. International Council for Harmonisation. ICH Harmonised Tripartite Guideline. Validation of Analytical Procedures: Text and Methodology Q2(R1). Geneva, Switzerland, 2005.
18. Hydrocortisone Hydrogen Succinate. In: European Pharmacopoeia 10ed. Strasbourg: Council of Europe. 2020:2888-9.

Povzetek

Namen te študije je opredelitev stabilnosti in določitev roka uporabnosti med uporabo ($t_{95\%}$) raztopin za infundiranje z natrijevim hidrokortizonsukcinatom (HSS) ter zagotovitev na dokazih podprtih priporočil o njihovi uporabnosti.

Infuzijske raztopine HSS smo pripravili in shranjevali v skladu s priporočili proizvajalca in pri običajnih pogojih v naši bolnišnici. Z validirano stabilnostno indikativno HPLC-UV metodo smo ugotavljali vpliv koncentracije HSS (1 in 4 mg/mL), topila (izotonična fiziološka raztopina in raztopina glukoze), temperature (sobna in 30 °C) in svetlobe na njegovo stabilnost.

Razgradnja HSS je sledila kinetiki prvega reda. Ugotovili smo, da različni preiskovani koncentraciji HSS, obe topili in izpostavljenost svetlobi niso značilno vplivali na stabilnost HSS ($t_{95\%}$ med 25 in 30 urami), medtem ko je povišana temperatura (30 °C) značilno skrajšala $t_{95\%}$ (4,6–6,3 ur).

Infuzijske raztopine HSS so fizikalno in kemično stabilne (<5 % razgradnja) vsaj 6 ur pri temperaturi do 30 °C in najdlje 24 ur pri temperaturi do 24 °C.



Except when otherwise noted, articles in this journal are published under the terms and conditions of the Creative Commons Attribution 4.0 International License

Scientific paper

Use of Total Organic Carbon Analyzer in Isotherm Measurements of Co-Adsorption of VOCs and Water Vapor from the Air

Dragana Kešelj,^{1,*} Dragica Lazić¹ and Zoran Petrović¹

¹ Faculty of Technology, University of East Sarajevo, Karakaj 34A, 75400 Zvornik, BiH

* Corresponding author: E-mail: dragana.keselj@tfzv.ues.rs.ba; draganakeselj@yahoo.com;
Tel.: +38766253256

Received: 04-05-2022

Abstract

The binary adsorption isotherms of volatile organic compounds (VOCs), and water vapor from the air have been the focus of much research in recent years. The content of adsorbed VOCs in the presence of water vapor can be determined by the volumetric or gravimetric method, in a static or dynamic mode. This study focuses on the adsorption technique in a static mode for isotherm measurement of the co-adsorption of VOCs and water vapor from the air using the gravimetric method. The content of VOCs is determined using a total organic carbon analyzer, while the amount of the adsorbed water was calculated from the difference between total adsorption (VOCs and water) and the adsorbed VOCs. This paper presents several adsorption isotherms with different VOCs (toluene, benzene, methanol, ethanol and isopropyl alcohol) and adsorbents (ZSM-5 zeolite, silica gel and Na-Form mordernite) in the presence of water vapor. The well-known adsorption isotherm models (Langmuir, extended Langmuir, Freundlich, extended Freundlich and Hill) were used to treat experimental results. The adjusted R-Squared (adj. R^2) values obtained for those non-linear models for isotherms (total adsorption ($q_{e,tot}$) as a function of equilibrium concentration of VOC (C_e) and the adsorbed VOC (q_e) as a function of equilibrium concentration of VOC (C_e) are used to determine the best-fit isotherm model. The modeling results showed that the 3-parameter models could fit the data better than the 2-parameter model, with relatively higher adj. R^2 . Experimental results demonstrate that the presented adsorption technique can be used for isotherm measurement of the co-adsorption of VOCs and water vapor from the air.

Keywords: Adsorption, adsorption isotherms, VOCs, water vapor

1. Introduction

The binary adsorption isotherms of VOCs and water vapor from the air have been the focus of much research in recent years.^{1–7} Much research is also dedicated to the adsorption of VOCs on zeolites or activated charcoal in the absence of moisture. Under real conditions, water vapor is always present, and its content may sometimes vary and even exceed that of VOCs. The influence of relative humidity on VOCs diffusion and adsorption is still not well understood. Research in the past couple of years has shown that the presence of water vapor (moisture) affects the adsorption of gases and volatile compounds.^{8–10} For example, investigations into the adsorption of dichloroethane, ethyl acetate and benzene on metal–organic frameworks (MOFs) show that the adsorption of these volatile organic

compounds decreases in the presence of humidity.¹¹ Very limited experimental research has been done on the effect of humidity on the diffusion coefficient.¹² The attraction between water molecules and methanol molecules may weaken the interaction forces between the solid surface and the methanol molecule and reduce the total adsorption capacity of methanol.^{2,11} A piece of equipment that may be quicker and more effective at measuring pure CO₂ adsorption, pure H₂O adsorption, and co-adsorption is the DVS Vacuum.¹² This has previously been used by Su et al. to measure CO₂ and H₂O isotherms on an amine-functionalised Mg-MOF-74.¹³ The DVS Vacuum uses a microbalance to measure the weight change of a sample subjected to various conditions. The temperature, pressure, and composition in the sorption chamber can be controlled

very accurately.^{12,13} Today there are different devices which can perform adsorption of a variety of vapors (H_2O , MeOH , EtOH , C_6H_6 and other non-corrosive vapors). A unique principle of the DVS Vacuum is the ability to control and measure sorbate entry and exit flows simultaneously while recording changes in sample mass.¹²

The determination of adsorption capacity can be done by volumetric or gravimetric method, in a static or dynamic mode. This study sets out to show how co-adsorption isotherms can be performed in a static mode, using a total organic carbon analyzer for gravimetric determination of the amount (mass) of adsorbed VOCs. The total adsorption of VOCs and water vapor was determined gravimetrically, from the difference in the mass of the adsorbent after and before the adsorption, while the amount of adsorbed water is calculated from the difference between total adsorption and the adsorbed VOCs.

2. Materials and Methods

2.1. Materials

Zeolites, porous polymers, composites, aluminophosphates (AlPOs) and silica aluminophosphates (SAPOs), silica gels, activated carbons and metal organic frameworks (MOFs) are important classes of materials used in various sorption-based technologies. In order to obtain representative experimental data for the purpose of the analysis, the study included adsorbents of different physical and chemical properties.

The following adsorbents were used for the purpose of this study: highly silicate ZSM-5 zeolite – two samples with different molar ratio $\text{SiO}_2/\text{Al}_2\text{O}_3$ (*Adsorbent 1*- $\text{SiO}_2/\text{Al}_2\text{O}_3 = 394$ and *Adsorbent 2*- $\text{SiO}_2/\text{Al}_2\text{O}_3 = 926$), Na-Form mordenite (*Adsorbent 3*), and silica gel (*Adsorbent 4*) (Table 1). Molar ratio $\text{SiO}_2/\text{Al}_2\text{O}_3$ for adsorbents 1–3 is calculated based on their chemical analysis (mass percentages of SiO_2 and Al_2O_3), and refers to the ratio between the content of SiO_2 and Al_2O_3 expressed in mass per cent multiplied by the ratio between the molar masses of Al_2O_3 and SiO_2 . For these adsorbents, apart from the content of SiO_2 and Al_2O_3 , the analysis also included determining the content of Na in mass per cent. Loss of annealing for adsorbents 1–3 was calculated in the form of the percentage of the shrinkage in mass after heating at 950 °C, whereas *Adsorbent 4* was analyzed for water residue, which also represents the loss of mass in percentages, but after drying at 160 °C. A low-temperature N_2 adsorption for the adsorbents used was employed to determine the pore size as well as the specific surface area using the BET method. The adsorbents were analyzed for the mean diameter of 50% of the particles ($d(50)$) and the mean diameter of 10% of the particles ($d(10)$) (Table 1) using a laser diffraction particle size analyzer (Mastersizer 3000).

The adsorbents were pre-dried to remove moisture before the experiments.

The chemicals used as adsorbates were toluene, benzene, methanol, ethanol and isopropyl alcohol. The physical properties of the five VOCs used as adsorbates are listed in Table 2.

Table 1. Physical and chemical characteristics of *Adsorbent 1*, *2*, *3* and *4*

Parameter	<i>Adsorbent 1</i>	<i>Adsorbent 2</i>	<i>Adsorbent 3</i>	<i>Adsorbent 4</i>
Loss of annealing, w %	2.5	3.1	6.9	–
$d(10)$, μm	1.3	–	2.3	–
$d(50)$, μm	2.5	< 10	8.8	15–35
Molar ratio $\text{SiO}_2/\text{Al}_2\text{O}_3$	384	926	13.5	–
Na content, w %	1.2	1.32	4.9	–
BET, m^2/g	355	434	420	450–550
Water residue, w %	–	–	–	< 10
pH (5%)	–	–	–	6–8
Pore size, nm	–	–	–	4.7–8

Table 2. Physicochemical properties of adsorbates

Chemical	Chemical formula	Density (g/cm^3)	Molecular weight (g/mol)	Boiling point (°C)	Vapor pressure (kPa)
Methanol	CH_3OH	0.792	32.04	64.7	13.02 (20 °C)
Ethanol	$\text{C}_2\text{H}_5\text{OH}$	0.7893	46.07	78.4	5.95 (20 °C)
Isopropyl alcohol	$(\text{CH}_3)_2\text{CHOH}$	0.7855	60.10	82.4	4.4 (20 °C)
Benzene	C_6H_6	0.8765	78.114	80.1	12.7 (25 °C)
Toluene	$\text{C}_6\text{H}_5\text{CH}_3$	0.866	92.14	110.6	2.8 (20 °C)

2. 2. Experimental Method and Analysis

The adsorbents were pre-dried to remove moisture before the experiments. A mass of 0.5 g of adsorbent is weighed into nine small glass jars with lids. The closed glass jars with adsorbents are placed in the adsorption chambers (2.5 L). Adsorption chambers (2.5 L) with closed glass jars were put in a climate chamber, where they were thermostated and filled with humid air at atmospheric pressure. Then the adsorption chambers were closed. A known volume of VOCs in the range of 10–250 μL is injected into the adsorption chambers. After allowing all the VOCs to evaporate for an hour, a portion of the gas phase was taken and analyzed using a total organic carbon analyzer (Shimadzu TOC high sensitivity). It represents the concentration of the gas-phase VOCs (C_0).

For the purpose of the analysis, the manual injection kit is installed on the total organic carbon analyzer (Shimadzu TOC high sensitivity) (Figure 1).

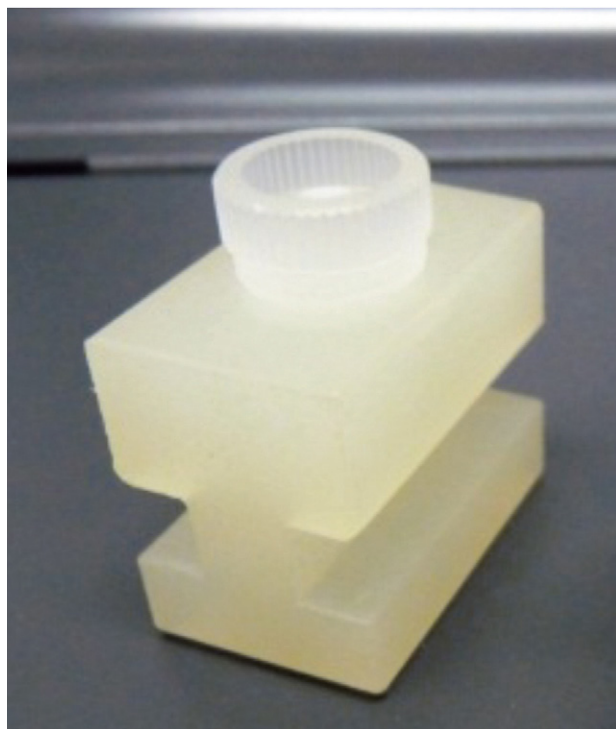


Figure 1. The manual injection kit

After determining the initial VOC concentration, the lids on the adsorbent jars are opened and the co-adsorption of VOC and water is performed. Part of the gaseous phase is taken again after equilibration and analyzed on a total organic carbon analyzer; this represents the equilibrium concentration of VOC (C_e). The amount of adsorbed VOC is calculated using the following equation (1):

$$q_e = \frac{(C_0 - C_e)V}{m_1} \quad (1)$$

where:

q_e – the amount of the adsorbed VOC per gram of adsorbent (g/g)

C_0 – VOC concentration at the beginning of adsorption (g/m³)

C_e – equilibrium concentration of VOC (g/m³)

V – adsorption chamber volume (m³)

m_1 – mass of the adsorbent (g)

The total adsorption of VOCs and water vapor ($m_{e,tot}$) was determined gravimetrically, from the difference in the mass of the adsorbent before and after the adsorption.

$$m_{e,tot} = m_2 - m_1 \quad (2)$$

$$q_{e,tot} = \frac{m_{e,tot}}{m_1} \quad (3)$$

$q_{e,tot}$ – total mass of adsorbed VOC and water per gram of adsorbent (g/g)

m_2 – mass of the adsorbent after co-adsorption of VOC and water (g).

The mass of water adsorbed per gram of the adsorbent ($q_{e,w}$) was determined from the difference between the total mass of VOC and water adsorbed per gram of the adsorbent ($q_{e,tot}$) and the mass of VOC adsorbed per gram of the adsorbent (q_e):

$$q_{e,w} = q_{e,tot} - q_e \quad (4)$$

Freundlich and Langmuir isotherm models are used to discuss the equilibrium behavior of single-component adsorption. The Langmuir isotherm can be written as

$$q_e = \frac{q_0 K_L C_e}{1 + K_L C_e} \quad (5)$$

where:

q_0 – is the maximum amount of adsorbed adsorbate (g/g),

C_e – is the equilibrium concentration of the adsorbate (g/m³) and

K_L – is the Langmuir constant (m³/g).

The Freundlich isotherm model mathematically is expressed as:

$$q_e = K_F \cdot C_e^{\frac{1}{n}} \quad (6)$$

where:

K_F – is adsorption capacity (m³/g) and

$1/n$ – is adsorption intensity.

Freundlich and Langmuir models were used to discuss the equilibrium behavior of single-component adsorption.¹⁵

The models used for a single-component system are not always suitable for a multicomponent system.^{15–19} Therefore, the single-component isotherm models were modified to suit a multicomponent system. There are

many models for analyzing adsorption equilibrium data, and in this study, apart from the non-linear Langmuir and Freundlich, we also used the extended Langmuir, extended Freundlich and Hill defined models in Origin software. Extended Langmuir and extended Freundlich are hybrid, three-parameter isotherm models, with another constant C added as the third parameter, apart from the constant B. A Hill isotherm model is a three-parameter isotherm model which refers to a modified Langmuir model with constants K and n ,^{20–22} introduced. An indicator of isotherm model suitability used in this study is adjusted R-Squared (adj. R^2), which is calculated as a function of Origin software by the following equation²³:

$$Adj. R^2 = \left\{ 1 - \left[\frac{(1-R^2)(n-1)}{(n-k-1)} \right] \right\} \quad (7)$$

here,

n – represents the number of data points in our dataset,

k – represents the number of independent variables, and

R – represents the R-squared values determined by the model.

The coefficient of determination (R^2) is defined by the following equation:²¹

$$R^2 = \frac{\sum (q_e - q_{mexp})^2 - \sum (q_e - q_{cal})^2}{\sum (q_e - q_{mexp})^2} \quad (8)$$

where:

q_e – is the amount of the adsorbate adsorbed by the adsorbent during the experiment (g/g),

q_{cal} – is the amount of the adsorbate obtained by isotherm models (g/g), and

q_{mexp} – is the average value of q_e (g/g).

The advantage of the non-linear method is that the error distribution does not get altered as in the linear regression approach.

3. Results and Discussion

The adsorbents used in the study had different characteristics. *Adsorbents 1* and *2* are hydrophobic, with different specific surface areas (355 and 434 m²/g, respectively) determined by low-temperature nitrogen adsorption. *Adsorbents 3* and *4* are hydrophilic. The adsorbates used in adsorption also had different characteristics: polar (methanol, ethanol), semi-polar (isopropyl alcohol) and non-polar (toluene, benzene).

The adsorbates were adsorbed on the adsorbents at atmospheric pressure, defined temperature (t) and relative humidity (rH). Based on the results obtained, we were able to obtain six isotherms

- co-adsorption of isopropyl alcohol -H₂O on *Adsorbent 1* ($rH = 65\%$, $t = 25\text{ }^\circ\text{C}$) (Figure 2);
- co-adsorption of methanol - H₂O on *Adsorbent 2* ($rH = 60\%$, $t = 25\text{ }^\circ\text{C}$) (Figure 3);

- co-adsorption of methanol-H₂O on *Adsorbent 3* ($rH = 55\%$, $t = 25\text{ }^\circ\text{C}$) (Figure 4);
- co-adsorption of ethanol - H₂O on *Adsorbent 3* ($rH = 46\%$, $t = 25\text{ }^\circ\text{C}$) (Figure 5);
- co-adsorption of toluene - H₂O on *Adsorbent 4* ($rH = 70\%$, $t = 22\text{ }^\circ\text{C}$) (Figure 6) and
- co-adsorption of benzene - H₂O on *Adsorbent 4* ($rH = 50\%$, $t = 26\text{ }^\circ\text{C}$) (Figure 7).

The obtained results show that co-adsorption of adsorbate (VOC) and water vapor occurred on all adsorbents. The shape of all isotherms indicates that there is a resemblance to type I or the lowest concentration part of type IV isotherm.

Analyzing the adsorption equilibrium data using a curve fitting tool (user-defined non-linear Langmuir and Freundlich, extended Langmuir, extended Freundlich and Hill models) in Origin software, adjusted R-Squared (R^2) and parameters of models were obtained and presented in Table 3.

The values of corresponding isotherm parameters obtained by fitting of experimental data on the co-adsorption of isopropyl alcohol -H₂O on *Adsorbent 1* based on the chosen isotherm models, shows a high value of adj. R^2 . The highest value of adj. R^2 (adj. $R^2 = 0.9688$) for the total adsorbed isopropyl and water vapor and water ($q_{e,tot} = f(C_e)$) was for the extended Freundlich. The model which gives the best description of adsorption of isopropyl alcohol from the water vapor- isopropyl alcohol binary system ($q_e = f(C_e)$) is the Freundlich model with adj. $R^2 = 0.9566$. Very close adj. R^2 was obtained for the extended Freundlich model for $q_e = f(C_e)$ (adj. $R^2 = 0.9495$). The order of the isotherm models which best fits the experimental data of co-adsorption of isopropyl alcohol -H₂O on *Adsorbent 1* for co-adsorption of isopropyl alcohol –water vapor on *Adsorbent 1* for $q_{e,tot} = f(C_e)$ is the extended Freundlich >Hill> Freundlich> extended Langmuir> Langmuir (adj. R^2 values were 0.9688; 0.9479; 0.9191; 0.90259; 0.4420). On the other hand, for $q_e = f(C_e)$ the best fitting non-linear model for adsorption isotherms is Freundlich > Langmuir > extended Freundlich > Hill > extended Langmuir (adj. R^2 values were 0.9566; 0.9536; 0.9439; 0.9495; 0.94792).

The order of the isotherm models which best fit the adsorption of methanol and water vapor on *Adsorbent 2* $q_{e,tot} = f(C_e)$ is extended Langmuir = Hill > extended Freundlich > Langmuir > Freundlich (adj. R^2 were 0.99656; 0.99656; 0.9965; 0.9956; 0.93556). Whereas the order of the isotherm models that offers the best representation of measured data for methanol in the methanol-water vapor binary system is extended Langmuir = Hill > extended Freundlich> Langmuir> Freundlich (adj. R^2 values were 0.99228; 0.99228; 0.98899; 0.9345; 0.85256).

The values of corresponding isotherm parameters obtained by fitting the experimental data of co-adsorption of methanol and water vapor on *Adsorbent 3* shows the following order of models Langmuir > extended Langmuir

= Hill > extended Freundlich > Freundlich (adj. R^2 were 0.9523; 0.94712; 0.94712; 0.9273; 0.77091). The order of the isotherm models that describe the adsorption of methanol from the binary system of methanol-water vapor on Adsorbent 3 ($q_e = f(C_e)$) is extended Freundlich > Fre-

undlich > extended Langmuir > Hill > Langmuir (adj. R^2 values were 0.94633; 0.94362; 0.93194; 0.9298; 0.4100).

The order of the isotherm models which best fit the adsorption of toluene and water vapor on Adsorbent 4 $q_{e,tot} = f(C_e)$ is Hill > extended Freundlich > Freundlich > ex-

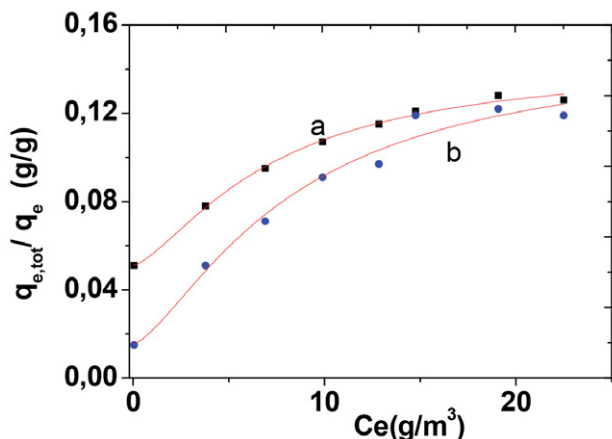


Figure 2. Adsorption Isotherms a- co-adsorption of isopropyl alcohol -H₂O; b- isopropyl alcohol on Adsorbent 1 (rH = 65%, t = 25 °C)

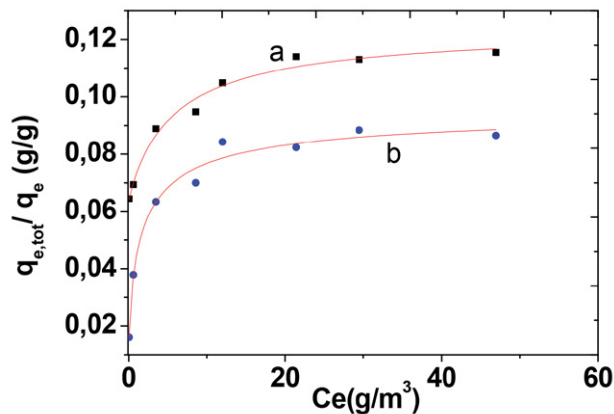


Figure 5. Adsorption Isotherms a- co-adsorption of ethanol - H₂O; b- ethanol on Adsorbent 3 (rH = 46%, t = 25 °C)

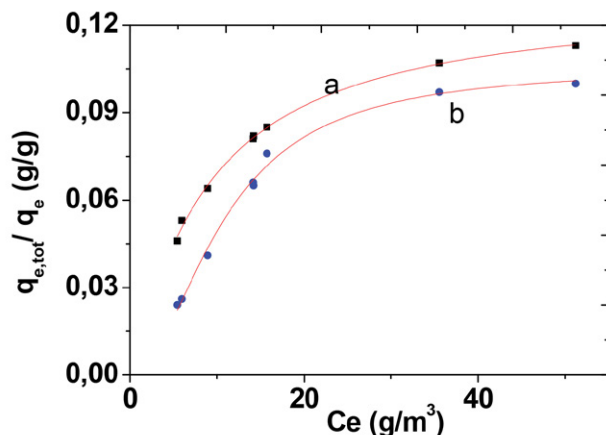


Figure 3. Adsorption Isotherms a-co-adsorption of methanol -H₂O; b- methanol on Adsorbent 2 (rH = 60%, t = 25 °C)

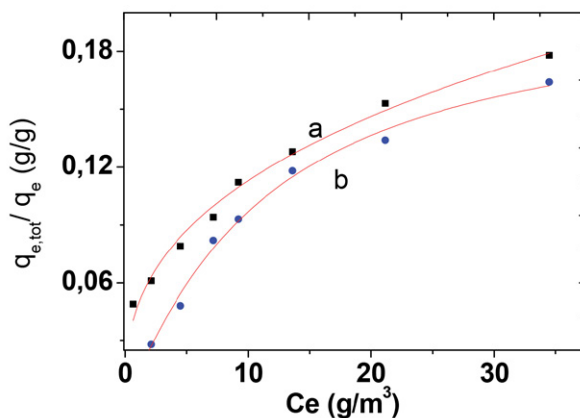


Figure 6. Adsorption Isotherms a-co-adsorption of toluene -H₂O; b-toluene on Adsorbent 4 (rH = 70%, t = 22 °C)

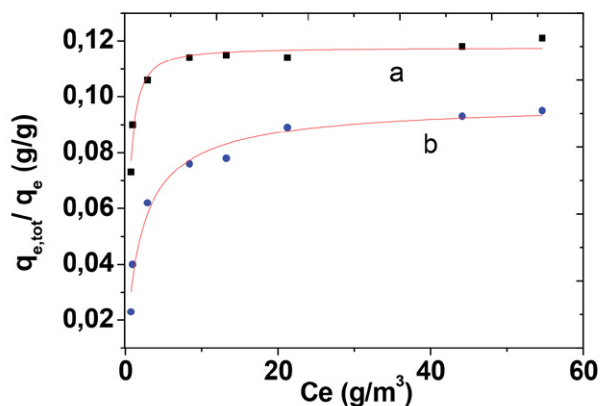


Figure 4. Adsorption Isotherms a- co-adsorption of methanol-H₂O; b- methanol on Adsorbent 3 (rH = 55%, t = 25 °C)

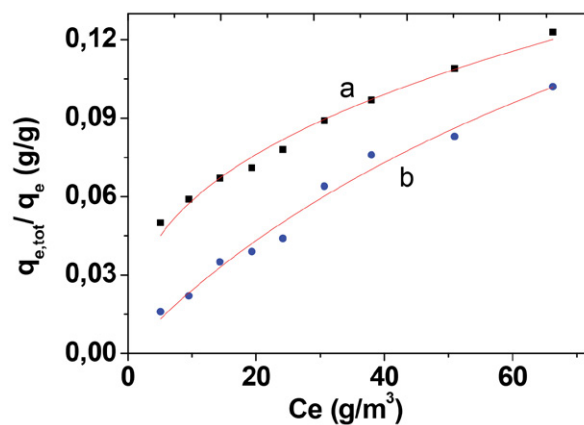


Figure 7. Adsorption Isotherms a-co-adsorption of benzene -H₂O; b- benzene on Adsorbent 4 (rH = 50%, t = 26 °C)

Table 4. Langmuir, Freundlich, extended Langmuir, extended Freundlich and Hill isotherm parameters obtained by non-linear fitting for co-adsorption of VOC (isopropyl alcohol, methanol, ethanol, toluene, benzene) on adsorbents (*Adsorbents 1-4*)

Adsorbate / Adsorbent			Isopropyl Alcohol/ Adsorbent 1	Methanol/ Adsorbent 2	Methanol/ Adsorbent 3	Ethanol/ Adsorbent 3	Toluene/ Adsorbent 4	Benzene/ Adsorbent 4
Model								
Langmuir	$q_{e,tot}$	$K_L(m^3/g)$	0.3114	0.103	2.608	29.12	0.1554	0.06855
		$q_o(g/g)$	0.1448	0.1358	0.1192	0.1018	0.1989	0.1379
		Adj. R^2	0.4420	0.9956	0.9523	0.4100	0.8835	0.8800
	q_e	$K_L(m^3/g)$	0.1044	0.05112	0.592	1.17	0.0707	0.01073
		$q_o(g/g)$	0.1786	0.1466	0.0948	0.0859	0.2309	0.2444
		Adj. R^2	0.9536	0.9345	0.9665	0.9309	0.9924	0.9804
Extended Langmuir	$q_{e,tot}$	$A(g/g)$	21.2227	0.12882	0.11757	5.91215	17.70209	13.862
		$B(m^3/g)^{1/1-C}$	0.00335	0.08734	2.81094	0.01368	0.00271	0.00175
		C	0.81494	-0.12337	-0.25522	0.89807	0.62488	0.61706
		Adj. R^2	0.90259	0.99656	0.94712	0.93194	0.98435	0.98037
	q_e	$A(g/g)$	1.423	0.10571	0.09826	0.1045	0.2083	0.28798
		$B(m^3/g)^{1/1-C}$	0.0248	0.00973	0.57812	0.7981	0.06503	0.01038
		C	0.5645	-0.9534	0.12835	0.4779	-0.12623	0.05433
		Adj. R^2	0.9439	0.99228	0.96259	0.9769	0.99217	0.97732
Freundlich	$q_{e,tot}$	$1/n$	0.18441	0.34577	0.08446	0.10043	0.37272	0.38071
		$K_F(g/g)^n$	0.07084	0.03052	0.08891	0.07979	0.04787	0.02433
		Adj. R^2	0.9191	0.93556	0.77091	0.94362	0.98705	0.98337
	q_e	$1/n$	0.44875	0.49811	0.21789	0.19472	0.53652	0.73792
		$K_F(g/g)^n$	0.03162	0.01551	0.0425	0.04533	0.02587	0.0047
		Adj. R^2	0.9566	0.85256	0.86869	0.92199	0.96059	0.97764
Extended Freundlich	$q_{e,tot}$	$A(g/g)$	0.0664	0.12972	0.0858	0.07834	0.0507	0.36699
		B	0.1458	-5.05901	0.2511	0.09095	0.3091	-3.16602
		C	-0.1341	1.26742	0.2901	-0.05036	-0.04299	0.59346
		Adj. R^2	0.9688	0.9965	0.9273	0.94633	0.9874	0.99296
	q_e	$A(g/g)$	0.0334	0.11086	0.0362	0.07912	0.0108	0.32614
		B	0.3911	-16.4310	0.5556	0.01	1.415	-6.34167
		C	-0.03276	1.67984	0.2124	9.65401	0.1731	0.74606
		Adj. R^2	0.9495	0.98899	0.9636	0.77668	0.9900	0.97957
Hill	$q_{e,tot}$	$V_{max}(g/g)$	6.69483	0.12882	0.11757	1.03324	16.18856	16.65986
		K	$3.49 \cdot 10^{10}$	8.75983	0.43895	$6.341 \cdot 10^9$	$5.439 \cdot 10^6$	$2.577 \cdot 10^7$
		n	0.1869	1.12337	1.25522	0.10983	0.37542	0.38267
		Adj. R^2	0.9479	0.99656	0.94712	0.9298	0.99217	0.98041
	q_e	$V_{max}(g/g)$	4.26917	0.10571	0.09826	0.1045	0.2083	0.28798
		K	44168.7	10.71157	1.87509	1.54257	11.32094	125.2708
		n	0.45875	1.9534	0.87165	0.52191	1.12623	0.94567
		Adj. R^2	0.94792	0.99228	0.96259	0.97687	0.98434	0.97732

tended Langmuir > Langmuir (adj. R^2 values were 0.99217; 0.9874; 0.98705; 0.98435; 0.8835), whereas for $q_e = f(C_e)$ the order is Langmuir > extended Langmuir > extended Freundlich > Hill > Freundlich (adj. R^2 : 0.9924; 0.99217; 0.9900; 0.98434; 0.96059).

For the data obtained for co-adsorption of benzene-water vapor on *Adsorbent 4*, the order of the isotherm best fits for $q_{e,tot} = f(C_e)$ is extended Freundlich > Freundlich > Hill > extended Langmuir > Langmuir (adj. R^2 values were 0.99296; 0.98337; 0.98041; 0.98037; 0.8800), and for

$q_e = f(C_e)$ the order is Langmuir > extended Freundlich > Freundlich > extended Langmuir = Hill (adj. R^2 0.9804; 0.97957; 0.97764; 0.97732; 0.97732).

Figures 2–7 show the best fitting non-linear models for adsorption isotherms of VOC-water vapor co-adsorption.

The values of Adjusted R- Squared (R^2), which is an indicator of isotherm model suitability, obtained for all six adsorption isotherms for co-adsorption of VOC and water vapor, were lower for the two-parameter models

(Langmuir and Freundlich) than for the three-parameter models (extended Langmuir are, extended Freundlich and Hill). This paper confirms that three-parameter models are more suitable for describing the isotherm measurements of VOC-water co-adsorption, i.e., multicomponent adsorptions. This can be explained by the fact that another constant is added to a two-parameter model, which allows additional factors characteristic for multicomponent systems to be introduced and quantified (such as the content of particular gaseous components, their molar mass, the surface area occupied by each of these components, etc.).

4. Conclusions

The adsorption equilibrium data of co-adsorption of VOC and water vapor from the air on the test adsorbents included the total adsorbed VOC and water vapor, adsorbed VOC, initial and equilibrium concentrations of VOC. The initial and equilibrium concentrations of VOC were determined using a total organic carbon analyzer. The experimental data for six co-adsorption isotherms of VOC-water vapor were analyzed. The analysis was performed using nonlinear models, which are considered to be a better tool for calculating isothermal parameters, and adj. R^2 was also used to determinate the best fitting isotherm to the experimental data. The values obtained for adj. R^2 indicate a good fit to isotherm models, which clearly demonstrates that the technique used in the present work is suitable for studying the co-adsorption of VOCs and water vapor from the air.

Acknowledgments

The authors would like to acknowledge the support provided by “Zeochem” doo, Zvornik for funding this work through the project “Adsorption isotherms of volatile organic compounds (VOC) on products of the company “Zeochem” d.o.o.”

5. References

1. C. Gebald, J. A. Wurzbacher, A. Borgschulte, T. Zimmermann, *Environ. Sci. Technol.*, **2014**, 48, 2497–2504. DOI:10.1021/es404430g
2. S. Xian, Y. Yu, J. Xiao, Z. Zhang, Q. Xia, H. Wang, Z. Li, *RSC Adv.*, **2015**, 5, 1827–1834. DOI:10.1039/C4RA10463C
3. R. Veneman, N. Frigka, W. Zhao, Z. Li, S. Kersten, W. Brilman, *Int. J. Greenh. Gas Control*, **2015**, 41, 268–275. DOI:10.1016/j.ijggc.2015.07.014
4. J. A. Thompson, S. I. Zones, *Ind. Eng. Chem. Res.*, **2020**, 59, 18151–18159. DOI:10.1021/acs.iecr.0c03480
5. E. P. Hessou, L. A. Bédé, H. Jabraoui, A. Semmeq, M. Badawi, V. Valtchev, **2021**, *Molecules*, 26, 5486. DOI:10.3390/molecules26185486
6. J. Rodri'guez-Mirasol, J. Bedia, T. Cordero, J. J. Rodri'guez, *Separation Science and Technology*, **2005**, 40, 3113–3135. DOI:10.1080/01496390500385277
7. U. Sager, F. Schmid, *Chem. Eng. Technol.*, **2010**, 33, 1203–1207. DOI:10.1002/ceat.201000086
8. S.B. Bal'zhinimaev, A. E. Paukshtis, V. A. Toktarev, V. E. Kovalyov, A. M. Yaranova, E.A. Smirnov, S. Stompel, *Microporous Mesoporous Mater.*, **2019**, 277, 70–77. DOI:10.1016/j.micromeso.2018.10.023
9. N. Astrath, J. Shen, D. Song, J. H. Rohling, F. B. G. Astrath, J. Zhou, T. Navessin, Z. S. Liu, C. Gu, X. Zhao, *J. Phys. Chem. B* **2009**, 113, 8369–8374. DOI:10.1021/jp900796w
10. M. Kraus, U. Trommler, F. Holzer, F. D. Kopinke, U. Roland, **2018**, *Chem. Eng. J.*, 351, 356–363, DOI:10.1016/j.cej.2018.06.128
11. K. Vellingiri, P. Kumar, A. Deep, K.H. Kim, *Chem. Eng. J.*, **2017**, 307, 1116–1126. DOI:10.1016/j.cej.2016.09.012
12. J. Xu, J. S. Zhang, *Building and Environment*, **2011**, 46, 1785–1796 DOI:10.1016/j.buildenv.2011.02.007
13. Surface Measurement Systems, “DVS Vacuum Dynamic Vacuum Vapor & Gas Gravimetric Sorption Analyzer.” 2020. <https://www.microtrac.com/products/gas-adsorption-measurement/surface-area-pore-size-distribution/belsorp-max-ii/>
14. J. P. Young, V. Martis, S. Garcia, M. van der Spek, CO-Adsorption And Pure-Component Isotherm Measurements On Direct Air Capture Adsorbents Using The Dvs VacuUM, TCCS-11 – Trondheim Conference on CO2 Capture, Transport and Storage Trondheim, Norway – June 21–23, **2021**, pp45–50
15. S. Kalam, S.A. Abu-Khamsin, M. S. Kamal, S. Patil, *ACS Omega*, **2021**, 6, 32342–32348. DOI:10.1021/acsomega.1c04661
16. L. J. Dunne, G. Manos, *Phil. Trans. R. Soc. A*, **2018**, 376: 20170151. DOI:10.1098/rsta.2017.0151
17. C. R. Girish, *International Journal of Civil Engineering and Technology*, **2017**, 8, 80–86. <http://www.iaeme.com/ijciyet/issues.asp?JType=IJCIET&VType=8&ITType=10>
18. S. Divekar, A. Nanoti, S. Dasgupta, Aarti, R. Chauhan, P. Gupta, M. O. Garg, S.P. Singh, I. M. Mishra, *J. Chem. Eng. Data*, **2016**, 61, 2629–2637 DOI:10.1021/acs.jced.6b00294
19. CM. Simon, E. Braun, C. Carraro, B. Smit, *PNAS*, **2017**, 114, 287–296. DOI:10.1073/pnas.1613874114
20. X. Chen, *Information*, **2015**, 6, 14–22. DOI:10.3390/info6010014
21. N. Ayawei, A. N.Ebelegi, D. Wankasi, *Journal of Chemistry*, **2017**, 2017, 1–11 DOI:10.1155/2017/3039817
22. T. A. Osmari, R. Gallon, M. Schwaab, E. Barbosa-Coutinho, J. Baptista Severo Jr., J. C. Pinto, *Adsorption Science & Technology*, **2013**, 31, 433–458. DOI:10.1260/0263-6174.31.5.433
23. S. Dubey, D. Gusain, Y. C. Sharma, *Journal of Molecular Liquids*, **2016**, 219, 1–8. DOI:10.1016/j.molliq.2016.01.021

Povzetek

V zadnjih letih je fokus raziskovanja na binarnih adsorpcijskih izotermah hlapne organske komponente (VOC) in vodne pare iz zraka. Količino adsorbirane VOC v prisotnosti vodne pare lahko določimo volumetrično ali gravimetrično, v statičnem ali dinamičnem načinu. Ta študija je osredotočena na adsorpcijsko tehniko v statičnem načinu za izotermne meritve koadsorpcije VOC in vodne pare iz zraka z uporabo gravimetrične metode. Količino VOC smo določili s pomočjo analizatorja celotnega dušika, medtem ko smo količino vode izračunali iz razlike med celotno adsorpcijo (VOC in voda) in količino absorbirane VOC. V članku predstavljamo nekaj adsorpcijskih izoterm za različne VOC (toluen, benzen, metanol, etanol in izopropilalkohol) in različne adsorbente (zeolite ZSM-5, silikagel in natrijevo obliko mordenita) v prisotnosti vodne pare. Za obravnavo eksperimentalnih podatkov smo uporabili dobro znane adsorpcijske modele (Langmuir, razširjeni Langmuir, Freundlich, razširjeni Freundlich in Hill). Za določitev najboljše prilagajočih izotermnih modelov smo uporabili prilagojene vrednosti R^2 , ki smo jih dobili iz teh nelinearnih modelov (to je krivulj celotne količine adsorbiranih plinov ($q_{e,tot}$) v odvisnosti od ravnotežne koncentracije VOC (C_e)). Rezultati so pokazali, da dajo modeli s tremi parametri boljše rezultate za prileganje k meritvam kot modeli z dvema parametroma, torej z višjimi vrednostmi R^2 . Eksperimentalni rezultati kažejo, da to adsorpcijsko tehniko lahko uporabimo za izotermne meritve ko-adsorpcije VOC in vodnih par iz zraka.



Except when otherwise noted, articles in this journal are published under the terms and conditions of the Creative Commons Attribution 4.0 International License

Scientific paper

Enhanced Adsorption of Methylene Blue by Chemically Modified Materials Derived from *Phragmites australis* Stems

Bui Thi Minh Nguyet,¹ Nguyen Huu Nghi,¹ Nguyen Anh Tien,²
Dinh Quang Khieu,³ Ha Danh Duc¹ and Nguyen Van Hung^{1,*}

¹ Dong Thap University, Cao Lanh City, 81000, Vietnam

² Ho Chi Minh City University of Education, Ho Chi Minh City, 700000, Vietnam

³ University of Sciences, Hue University, 530000, Vietnam

* Corresponding author: E-mail: nguyenvanhung@dthu.edu.vn

Received: 05-05-2022

Abstract

In this study, the biomass of *Phragmites australis* was chemically modified using NaOH and subsequently citric acid to produce an effective adsorbent named SA-RPB. The adsorbent was characterized using XRD, SEM, BET, and FT-IR methods. The study's findings indicated that the adsorbent existed mainly as cellulose crystals, contained micropores with an average diameter of 15.97 nm, and had a large number of hydroxyl and carboxyl groups on the surface. The adsorption process of SA-RPB was evaluated through the adsorption of methylene blue (MB) dye in aqueous solution. Adsorption kinetics showed that the pseudo-second-order model well described the adsorption process. The adsorption isotherm process satisfactorily fitted with the Langmuir model with the maximum adsorption capacity of 191.49 mg/g at 303 K. These findings show that MB may be efficiently removed from aqueous solutions using the adsorbent made from the raw biomass of *Phragmites australis* treated with NaOH and then citric acid.

Keywords: Adsorbent; *Phragmites australis*; Methylene blue; Kinetics; Adsorption mechanism

1. Introduction

Dye has been extensively used in various industries such as textile, leather, cosmetics, tanning, paper, food technology, hair coloring, pulp mill, pharmaceuticals, and plastics.¹ Wastewater discharged from these industries has reportedly caused severe environmental pollution² and health problems. Specifically, methylene blue (MB), widely used for coloring cotton, wood, and silk³, can damage humans' and animals' eyes and trigger nausea, vomiting, profuse sweating, and mental instability when it passes through the mouth, causing rapid or difficult breathing within short periods of inhaling.⁴ Therefore, it is practically essential to remove MB from dye wastewater.

Many advanced techniques have been developed for removing MB, including the Fenton process and combined electrochemical treatments, electrochemical degradation, reverse osmosis, photodecomposition, coagulation/flocculation, membrane processing, oxidative degradation, electrocoagulation, and carbonaceous nanomaterials.^{5–13} In addition, activated carbon has been recognized to ef-

fectively remove different dye molecules.^{14–16} However, these methods are costly, owing to poor regeneration. In recent years, considerable efforts have been made in developing adsorbents derived from plant materials such as mango peels, pistachio shell, cladodes of *Opuntia ficus indica*, peach stone, carbonized watermelon, seed fibers, and potato peels.^{17–23}

Some recent studies have used raw materials or raw materials modified with NaOH to treat MB.^{26,27} For instance, plant materials modified with citric acid (CA) show good potential for wastewater treatment.^{20,28,29} Cellulose fibrils extracted from *P. australis* and treated by both NaOH and CA appear to be a better-modified material compared to being treated with only NaOH as described in the previous report.²⁶ *P. australis* is a type of reed that mainly grows around lakes, rivers, streams, and brackish water worldwide between 10° and 70° northern latitudes.²⁴ This plant type has a high tissue porosity formed by cellulose, hemicellulose, and lignin, which are vital constituents for developing adsorbents.²⁵ It wildly grows all year round throughout the country of Viet Nam, especially in

wetlands. In this study, the biomass of *P. australis* modified with NaOH and followed by esterification using citric acid (NaOH-then-CA treatment) was investigated in adsorbing MB from aqueous solutions. In addition, the effects of environmental parameters on MB adsorption by raw and modified adsorbents were evaluated.

2. Materials and Methods

2.1. Chemicals and Materials

Citric acid ($\text{HOC}(\text{COOH})(\text{CH}_2\text{COOH})_2$, $\geq 99.5\%$), sodium hypophosphite monohydrate ($\text{NaH}_2\text{PO}_2 \cdot \text{H}_2\text{O}$, $\geq 99.5\%$), sodium hydroxide (NaOH , $\geq 97\%$), hydrochloric acid (HCl , 37%), sodium chloride (NaCl , $\geq 99.5\%$), and MB ($\text{C}_{16}\text{H}_{18}\text{N}_3\text{SCL}$, 99.5%) were purchased from Sigma-Aldrich. Then, MB was diluted with double-distilled water to a range of 125–300 mg/L. The pH was adjusted using NaOH (0.1 M) and HCl (0.1 M).

P. australis samples were collected from a wetland in Dong Thap province, Vietnam and cleaned with tap water to remove dirt and other impurities adhered to their surfaces. The plant stems were dried under the sunlight for four days prior to being finely ground to approximately 1–2 mm sizes. The obtained biomass was rinsed with distilled water and dried in a vacuum oven at 70°C to a constant weight. The product was stored in a desiccator and used as raw *P. australis* biomass (RPB).

2.2. Chemical Modifications of *P. australis* Biomass

RPB (5 g) was added to a 250 mL glass beaker containing 100 mL NaOH (0.5 M). The solution was stirred at 60°C and 400 rpm using a magnetic bar for 5 h. After that, the biomass was collected and cleaned with distilled water until the pH of the solution was 7.0. The product was then dried in a vacuum oven at 60°C for 12 h until it yielded an adsorbent. The biomass modified with NaOH was designated as S-RPB, which was further denatured with a 50 mL (0.1 M) CA solution added to a 2.0 g S-RPB. Then, $\text{NaH}_2\text{PO}_2 \cdot \text{H}_2\text{O}$ (2.65 g), used as a catalyst, was added to the solution. The biomass was collected after stirring at 60°C and 400 rpm using a magnetic bar for 5 h. After that, it was soaked in 50 mL distilled water several times until the pH reached 7.0, and then was dried at 60°C for 12 h, and subsequently arriving at 140°C for 3 h. The second modified adsorbent was designated as SA-RPB.

2.3. Characterization of Materials

The lignocellulosic composition before and after being modified (as mentioned above) was determined according to the National Renewable Energy Laboratory (NREL) compositional analysis procedure.³⁰ The C, H, N, S, and O contents of the materials were analyzed using a

CHNS-O Elemental Analyzer (Thermo, Flash EA1112, USA). Also, the products' XRD was performed by a Mini-Flex 600 diffractometer (Rigaku, Japan) with a radiation source of Cu K α , $\lambda = 0.15406$ nm. The scanned angle (2θ values) ranged between 5° and 80° with a step size of 0.01° . The adsorbents' surface morphology was scanned under the scanning electron microscopy (SEM) technique (FEI-SEM NOVA NanoSEM 450-USA). Meanwhile, the samples' FTIR spectra were recorded by an Infrared Affinity-1S spectrophotometer (Shimadzu) and BET was determined by N_2 adsorption-desorption isotherms at liquid nitrogen temperature (77 K) using a Quantachrome TriStar 3000 V6.07A absorption instrument.

2.4. Determination of Point of Zero Charge (pH_{PZC})

The pH_{PZC} of the adsorbents was determined using the pH drift method described in a previous study.³¹ Forty-five milliliters of 0.5 M NaCl with pH values were adjusted from 2 to 12 by either 0.1 M NaOH or 0.1 M HCl solution. Then, distilled water (50 mL) was added, and the pH values were readjusted, closely noting the initial pH (pH_i). Next, an obtained adsorbent was added to each flask at 1.0 g/L, incubated at 180 rpm using a magnetic stir bar for 24 h at room temperature ($\sim 30^\circ\text{C}$). The differences in the pH (ΔpH) values between the initial pH and final pH (pH_f) ($\Delta\text{pH} = \text{pH}_i - \text{pH}_f$) were plotted against pH_i . The points of intersection of the curve with the abscissa at which ΔpH is equal to zero were presented as the pH_{PZC} .

2.5. Adsorption Tests

Adsorption tests were performed by adding an adsorbent into a 250 mL glass beaker containing 100 mL MB solution. For the effects of the adsorbent on adsorption, the MB was diluted to 125–300 mg/L, while SA-RPB was used from 0.4 to 1.4 g/L. The solution was stirred at 300 rpm, and liquid media were collected from 2 to 105 min. Liquid media samples were centrifuged at 3000 rpm for 5 min to remove solid particles. Also, MB concentrations were measured by an ultraviolet-visual spectrophotometer (Spectro UV-2650, Labomed, USA) at a wavelength of 665 nm. The percent removal (R) and adsorption capacity per unit mass (q_t) after a specific contact time (t) were calculated via Eqs. (1) and (2), respectively, as follows:

$$R(\%) = \frac{C_0 - C_t}{C_0} \times 100 \quad (1)$$

$$q_t = \frac{(C_0 - C_t) \times V}{m} \quad (2)$$

where C_0 (mg/L) and C_t (mg/L) are MB concentrations in liquid media at the initial and time t , respectively, and V is the volume of the solution (L).

2. 5. 1. Adsorption Kinetics

The adsorption kinetics were fitted to the pseudo-first-order and pseudo-second-order kinetic models, which are expressed by Eqs. (3) and (4), respectively^{32,22}, below:

$$q_t = q_e (1 - e^{-k_1 t}) \quad (3)$$

$$q_t = \frac{q_e^2 k_2 t}{1 + q_e k_2 t} \quad (4)$$

where k_1 (1/min) and k_2 (1/min) are rate constants of the pseudo-first-order and pseudo-second-order, respectively; and t (min) is the contact time.

2. 5. 2. Adsorption Mechanisms

The Weber–Morris intra-particle diffusion and Boyd models were applied in order to investigate diffusion mechanisms. The former model was derived from the Fick's second law of diffusion as expressed by Eqs. (5):^{1,4}

$$q_t = k_{pi} t^{1/2} + C_i \quad (5)$$

where k_{pi} (mg/gmin^{1/2}) means the diffusion rate constant at stage i , and C_i is the intercept which can be evaluated from the slope of the linear plot of q_t versus $t^{1/2}$. The q_t (mg/g) is adsorption capacity per unit weight of adsorbent per time, and $t^{1/2}$ (min^{1/2}) denotes half adsorption time. The intercept, C_i , relates to the extent of external mass transfer during the adsorption, acting as the rate-controlling step. When the linear plot of q_t versus $t^{1/2}$ passes through the origin, intra-particle diffusion is the sole rate-limiting step. However, if the linear plots at each concentration do not pass through the origin, when it indicates that the intra-particle diffusion was not only rate controlling step.¹

Meanwhile, the Boyd model was implemented to distinguish between film diffusion and intra-particle diffusion as expressed by Eqs. (6) and (7):^{15,16}

$$B_t = -0.4977 - \ln(1 - F) \quad (\text{for } F > 0.85) \quad (6)$$

$$B_t = \left(\sqrt{\pi} - \sqrt{\pi - \left(\frac{\pi^2 F}{3} \right)} \right)^2 \quad (\text{for } F < 0.85) \quad (7)$$

where B_t is a mathematical function of F representing the fractional attainment of equilibrium at any time t given by Eqs.(8):

$$F = \frac{q_t}{q_e} \quad (8)$$

The plot Bt versus time t (s) is used to anticipate the diffusion limit. If the plot is linear and passes through the origin, it indicates that the pore diffusion occurs. If the lines are linear and pass through the origin, the intra-particle diffusion takes place. However, if the lines are linear but do not pass through the origin or non-linear, the film diffusion controls the adsorption process.

2. 5. 3. Adsorption Isotherms

Four isotherm equations, namely the Langmuir, Freundlich, Temkin, and Dubinin–Radushkevich, were used to fit the experimental equilibrium isotherm data for MB adsorption on SA-RPB. Adsorption isotherm tests were performed by adding 0.1 g SA-RPB into 100 mL MB at a concentration range of 125–300 mg/L. The initial pH of the MB solution was 6.5, and the controlled temperatures were 30 °C (303 K). The Langmuir model assumes that adsorption is localized on a monolayer, and all adsorption sites on the adsorbent homogeneously possess the same adsorption capacity, as expressed by Eqs. (9)³⁵:

$$q_e = \frac{q_{max} K_L C_e}{1 + K_L C_e} \quad (9)$$

where C_e (mg/L) is the equilibrium concentration; q_e (mg/L) is the amount of adsorbed dye at equilibrium; q_{max} (mg/g) is the maximum adsorption capacity; and K_L (L/mg) is the Langmuir adsorption equilibrium constant. The equilibrium parameter (R_L) is a dimensionless constant of the Langmuir isotherm, expressed by Eqs. (10)³⁵:

$$R_L = \frac{1}{1 + K_L C_0} \quad (10)$$

where C_0 is the highest initial solute concentration. The Freundlich isotherm model assumes that multilayer adsorption processes occur on heterogeneous surfaces, expressed by Eqs. (11)³⁶:

$$q_e = K_F C_e^{1/n_F} \quad (11)$$

where K_F (mg/g.(L/mg)^{1/n}) and n are Freundlich constants related to the adsorption capacity and adsorption intensity, respectively. The adsorbate–adsorbate interactions can cause a decrease in the heat of adsorption of all the molecules in the layer. The Temkin isotherm reflects the effect of the adsorbate interaction on SA-RPB, expressed by Eqs. (12)³⁷:

$$q_e = (RT / b) \ln(A_T C_e) \quad (12)$$

$$B_T = RT / b \quad (13)$$

where A_T (L/g) and b (g.J/mg.mol) are Temkin's isotherm constants; R (8.314 J/mol.K) is the universal gas constant; T (K) is the absolute temperature. The Dubinin–Radushkevich isotherm model³⁸ was used to determine the mean free energy of biosorption, expressed by Eqs. (14)–(16):

$$q_e = q_{DR} e^{-K_{DR} \varepsilon^2} \quad (14)$$

$$E = 1 / \sqrt{2 K_{DR}} \quad (15)$$

$$\varepsilon = RT \ln \left(1 + \frac{1}{C_e} \right) \quad (16)$$

where K_{DR} is a constant related to the adsorption energy (mol²/kJ²); q_{DR} (mg/g) is the Dubinin–Radushkevich iso-

therm adsorption capacity; ϵ (kJ/mol) is the Polanyi potential; R is the ideal gas constant; and T (K) is the temperature. The free energy of adsorption (E) is considered as either chemical adsorption ($E = 8\text{--}16$ kJ/mol) or physical adsorption ($E < 8$ kJ/mol).

2. 5. 4. Adsorption Thermodynamics

The thermodynamic parameters for MB adsorption onto SA-RPB were evaluated at 303, 313, and 323 K. The Gibbs free energy change (ΔG°), enthalpy (ΔH°), and entropy (ΔS°) were calculated using Eqs. (17)–(19).

$$\Delta G^\circ = -RT \ln K_L \quad (17)$$

$$\Delta G^\circ = \Delta H^\circ - T\Delta S^\circ \quad (18)$$

Adding Eqs. (17) and (18) amounts to Eq. (19):

$$\ln K_L = -\frac{\Delta H^\circ}{RT} + \frac{\Delta S^\circ}{R} \quad (19)$$

where R (8.314 J/mol K) is the universal gas constant; T (K) the absolute temperature, and K_L the Langmuir equilibrium constant. The values of ΔH° and ΔS° can be calculated from the slope and intercept, respectively, of the linear plot of $\ln K_L$ versus $1/T$.

2. 6. Reusability

After each cycle of batch experiment, the SA-RPB was collected through centrifugation at 5000 rpm for 10 min. The adsorbent was first washed with absolute ethanol and then rinsed with double-distilled water three times. The adsorbent (0.1 mg) was transferred into 100 mL of the rinse media, stirred at 300 rpm for 6 hours, and collected through centrifugation at 5000 rpm for 10 min, followed by being dried for 24 h at 100 °C until its weight stayed constant.

3. Results and Discussion

3. 1. Characterization of Materials

The biomass components of *P. australis* are listed in Table 1. The components of the raw RPB were also determined in previous studies^{39,40}. The cellulose content significantly increased, whereas hemicellulose and lignin contents comparatively decreased after the NaOH treatment (S-RPB) and the NaOH-then-CA treatment (SA-RPB) (Table 1). The C content in RPB (46.42%) decreased slightly, whereas the O content (45.82%) and the ratio of O to C increased slightly after NaOH-then-CA treatment (Table 1) was done. Moreover, the percentages of N, S, Si, K, and Mg significantly decreased after the treatment. Acidic and basic solutions are typically used for modifying and/or removing lignin and hemicellulose from plant biomass.⁴¹

The treatment with NaOH resulted in the formation of hydroxyl groups on the S-RPB, which then reacted with citric acid, forming an ester linkage to introduce carboxyl groups into SA-RPB.²⁰

Table 1. Chemical compositions of RPB, S-RPB, and SA-RPB

Parameter	RPB	S-RPB	SA-RPB
<i>Lignocellulosic analysis (dry weight basis), wt%</i>			
Cellulose (%)	43.31	66.32	71.21
Hemicellulose (%)	30.82	15.17	13.28
Lignin (%)	20.37	12.30	9.19
<i>Elemental analysis (dry weight basis), wt%</i>			
C (%)	46.42	45.71	45.23
O (%)	45.82	47.72	48.83
H (%)	5.910	5.610	5.720
N (%)	0.232	0.111	0.021
S (%)	0.313	0.222	0.107
O/C (mol/mol)	0.7403	0.7830	0.8097
Si (%)	1.050	0.021	–
K (%)	0.454	0.284	0.182
Mg (%)	0.601	0.322	0.110

SEM micrograph images of *P. australis* biomass before and after the NaOH-then-CA treatment were captured (Fig. 1). The raw material had a surface composed of fibrous rods (Fig. 1(a)). The surface morphology was found to transform, being affected by NaOH. The S-RPB sample retained its tubular structure, but the surface turned out to be more porous and uneven (Fig. 1(b)). The texture was also rough and irregular after being treated with CA (Fig. 1(c)). The treatment with citric acid reduces the cavities on the adsorbent surface. Citric acid clogged the carbon surface, which explains for a spotted reduction in the surface area and pore volume of the adsorbent.⁴²

Table 2. Porous textural parameters of RPB, S-RPB, and SA-RPB samples

Sample	Surface area (m ² /g)	Pore volume (dm ³ /g)	Average pore diameter (nm)
RPB	1.01	2.626	16.64
S-RPB	0.87	2.052	16.86
SA-RPB	0.74	1.935	15.97

The crystallographic structures of the RPB, S-RPB, and SA-RPB were analyzed using the XRD technique (Fig. 1(d)). The results indicated that all samples had two diffraction peaks at angles 2θ of 15.7° and 22.3°, corresponding to (101) and (002) planes of cellulose crystals.⁴³ The diffraction intensities were in the order of SA-RPB > S-RPB > RPB (Fig. 1(d)), indicating that NaOH-then-

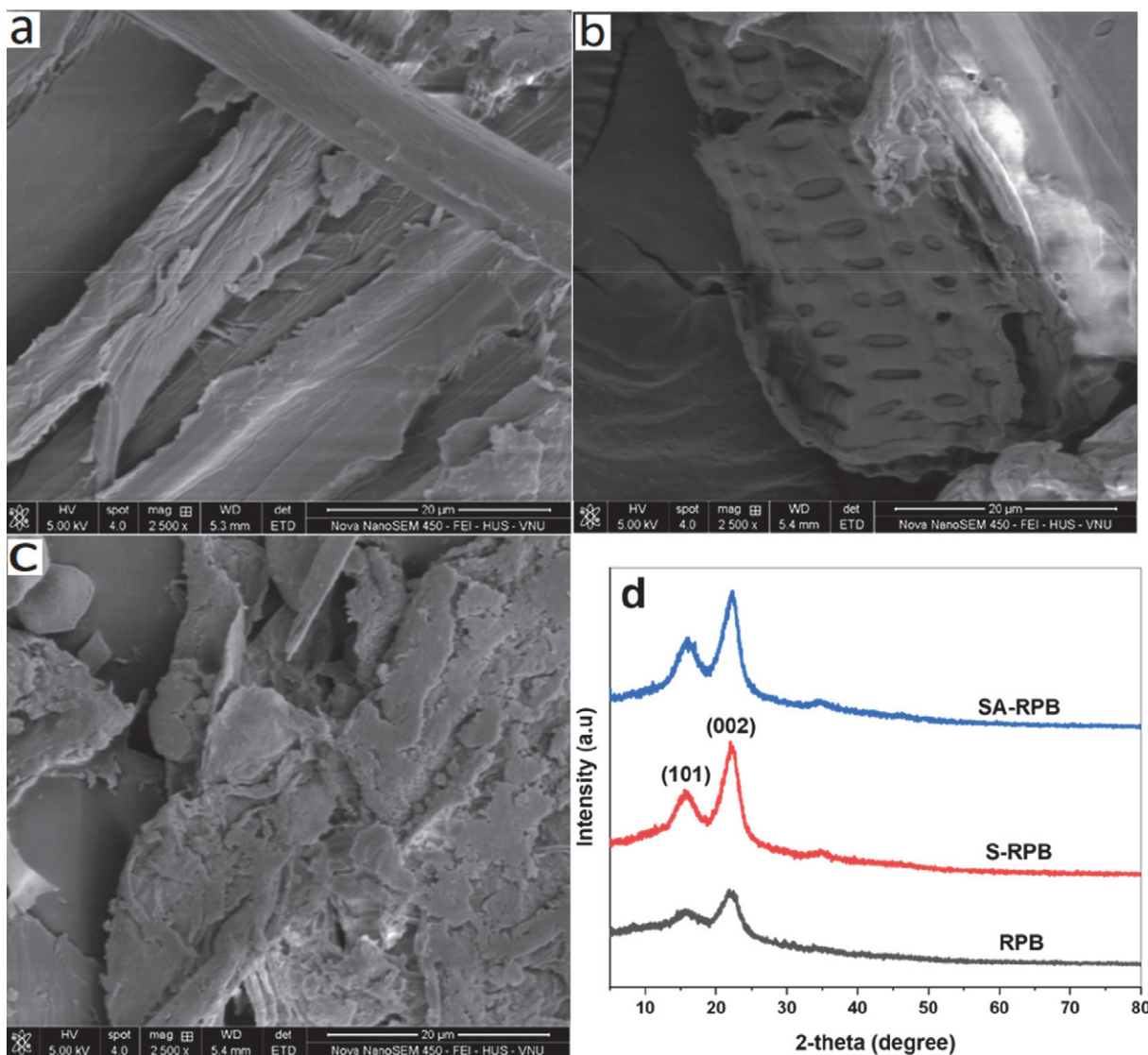


Fig. 1. Morphology and crystallization of samples; SEM images of (a) RPB, (b) S-RPB, and (c) SA-RPB; (d) XRD patterns of RPB, S-RPB, and SA-RPB samples

CA treatment enhanced the cellulose crystallinity. The increased crystallization attributed to the partial removal of amorphous polymers (hemicellulose and lignin) from plant structures has also been reported.^{26,44} The specific surface area and porous texture of the obtained samples were evaluated using the nitrogen adsorption–desorption isotherms at 77 K (Table 2). The RRB sample had a specific surface area of 1.01 m²/g, a common property of raw plant biomasses.⁴⁵ The surface areas decreased by 13.9% after the NaOH treatment and went down to 26.7%, resulting from that of the NaOH-then-CA treatment, while the pore volumes decreased by 21.8% and 26.3%. Besides, the average pore diameter slightly decreased after the treatment. Citric acid can easily penetrate the pore structure because of its small molecular size, causing the pore block of the adsorbent.⁴² These results indicate that the dye adsorption

capacity can be boosted due to the formation of hydroxyl and carboxyl groups on the surface of *P. australis* biomass, and the functional groups might play a more important role than the surface area in MB adsorption.

The functional groups on the adsorbent surfaces with differing intensities of the observed peaks during *P. australis* biomass modification were analyzed via FTIR (Fig. 2). Adsorption bands corresponding to functional groups were determined according to Reddy.⁴⁶ A broad peak of approximately 3321 cm^{−1} corresponded to the stretching vibration of the hydroxyl groups (–OH) for cellulose, hemicellulose, and lignin, whereas the 2918 cm^{−1} band indicated the presence of C–H stretching vibrations of methyl and methylene. After the raw material was modified with NaOH and NaOH-then-CA, the stretching vibration bands of OH shifted to 3443 and 3438 cm^{−1}, respective-

ly. The band at 1734 cm^{-1} could be attributed to the C=O bond stretching of acetyl ester groups in hemicellulose, lignin, or both.

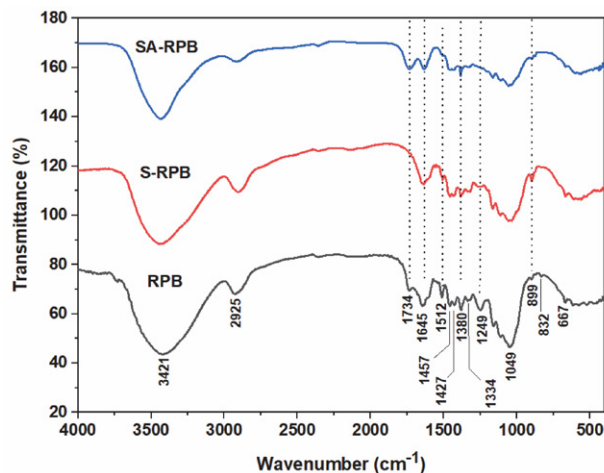


Fig. 2. FTIR spectra of RPB, S-RPB and SA-RPB samples

This adsorption peak was absent from the FTIR spectrum of the S-RPB sample (Fig. 2) after the alkaline treatment because of the removal of hemicellulose and lignin through a process called de-esterification. Moreover, C=O bond stretching was observed after the NaOH-then-CA treatment, owing to the esterification reaction. The band at 1645 cm^{-1} could be attributed to COO^- stretching of carboxylate groups with the aromatic ring. The band at approximately 1512 cm^{-1} was associated with C=C stretching vibrations in aromatic rings of lignin, whereas the band at 1427 cm^{-1} was attributed to the C-H bond deformation of lignin. The peak intensities at 1457 and 1380 cm^{-1} reflected C-H symmetric and asymmetric deformations of cellulose, respectively. The appearance of peaks at 1334 and 1327 cm^{-1} could be attributed to the -OH bending

vibration in C-OH and C1-O vibrations in S derivative vibrations of cellulose, respectively. The signal at 1249 cm^{-1} corresponded to the COO^- vibration of acetyl groups in hemicellulose and lignin.^{20,47} The adsorption peaks at 1159 and 1111 cm^{-1} were attributed to C-O-C antisymmetric and anhydroglucose ring vibrations, respectively, whereas the band at 1049 cm^{-1} corresponded to C-O stretching vibrations of cellulose, hemicellulose, and lignin.⁴⁸ A band at 899 cm^{-1} corresponds to C-H rocking vibrations of cellulose.⁴⁹ The intensities of these parts of S-RPB and SA-RPB decreased, owing to the removal of lignin. The weak adsorption peaks of $832\text{--}400\text{ cm}^{-1}$ were probably related to C-H and C=C bending in aromatic rings, C-H bending, and C-O stretching.^{40,50} The FTIR results indicated abundant functional groups of -OH, -COOH, and COO^- on the adsorbent surfaces.

3. 2. pH_{PZC} determination

The differences in the pH_{PZC} of RPB, S-RPB, and SA-RPB are shown in Fig. 3(a). The raw *P. australis* biomass had a pH_{PZC} of 6.72, also obtained in a previous study.²⁷ The pH_{PZC} levels of S-RPB and SA-RPB were 6.17 and 3.10, respectively.

The pH_{PZC} level slightly decreased after the NaOH treatment, possibly because of de-esterification and the removal of a part of hemicellulose and lignin.⁵¹ The pH_{PZC} value of the SA-RPB was significantly lower than those of RPB and S-RPB, which could be attributed to the esterification reaction of hydroxyl on the raw material surface with the carboxyl group of citric acid to increase the carboxyl group on its surface.^{20,52} Absorbents with pH values lower than pH_{PZC} absorb compounds with a positive surface charge.⁵³ The MB dye with a molecular diameter of 0.8 nm ⁵⁴ was smaller than the pore diameter of SA-RPB (15.97 nm , Table 2); hence, MB could easily penetrate the SA-RPB pore structure. The batch adsorption test results

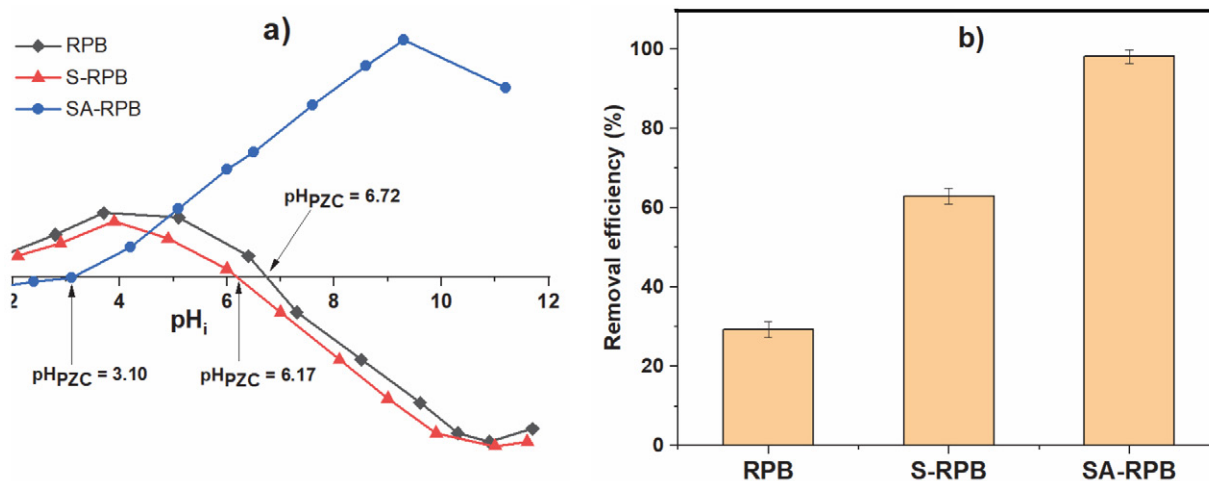


Fig. 3. (a) Plots of point of zero charges of RPB, S-RPB, and SA-RPB (1.0 g/L adsorbent at different pH values); (b) percentage removal efficiency values for MB on RPB, S-RPB, and SA-RPB samples (150 mg/L MB at 6.5 pH value)

showed that the removal efficiency by SA-RPB adsorbent was $98.11 \pm 1.76\%$, about 68.8 and 35.1% higher than that of RPB and S-RPB, respectively (Fig. 3(b)). The increase in removal efficiency by SA-RPB was due to both NaOH and CA modified to the raw material. Therefore, SA-RPB was used for other experiments.

3. 3. Batch Adsorption

3. 3. 1. Effect of Adsorbent Dosage

In this experiment, the effects of the adsorbent dose (SA-RPB) on MB adsorption were examined. As seen in Fig. 4, an increase in the adsorbent mass from 0.4 to 1.0 g/L improved the MB removal rate because of the increased sites available for adsorption. However, the adsorption did not statistically differ at adsorbent doses higher than 1.0 g/L. The adsorption appeared to be in equilibrium when the adsorbent mass reached a particular value, possibly because the number of MB dye molecules available in the solution was insufficient to combine with all effective adsorption sites on the adsorbent.

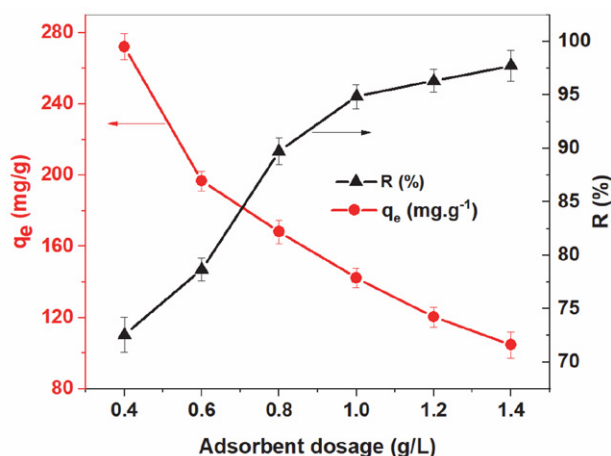


Fig. 4. SA-RPB dosage effects on equilibrium adsorption capacity (q_e , mg/g) and removal efficiency of MB (R , %) (The tests conducted for 105 min by 150 mg/L MB at 6.5 pH)

3. 3. 2. Effects of Contact Time, Temperature, and Adsorption Kinetics

The effect of contact time on MB removal via the SA-RPB adsorbent is depicted in Fig. 5. The adsorption sharply increased within 20 min at the initial stage and then attained equilibrium after 60 min at all temperatures, followed by a maximum removal. About 89.98% of equilibrium adsorption capacity was achieved within 10 min. The fast adsorption at the initial stage was probably caused by available vacant active sites of the adsorbent (with functional groups of $-OH$, $-COOH$, and $-COO^-$) and a higher driving force between MB ions and the surface. However, adsorption isotherms at three temperatures were not statistically different. This phenomenon is due to available

active sites for adsorption, which previous studies used to modify plant materials for MB removal^{55,56}. Meanwhile, decreased vacant sites and insufficient active sites of the adsorbent slowed down the adsorption rate and equilibrium.⁵⁶

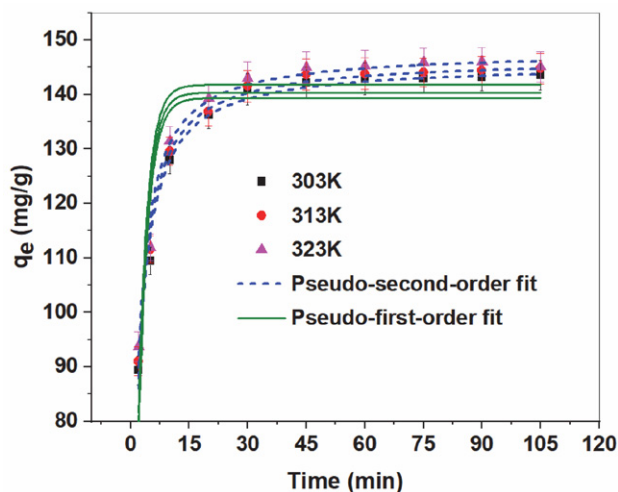


Fig. 5. Pseudo-first and pseudo-second-order kinetics for MB adsorption by SA-RPB at different temperatures. The experiments were conducted by 1.0 g/L SA-RPB and 150 mg/L MB at 6.5 pH

Two kinetic models (pseudo-first-order and pseudo-second-order) were used to determine adsorption rate and analyze kinetic data. The calculated correlation coefficients (R^2) and other data are listed in Table 3. The $q_{e,cal}$ and $q_{e,exp}$ values for each model at different temperatures slightly rose, whereas (and) k_1 and k_2 tended to increase at higher temperatures, indicating that adsorption kinetics was faster at higher temperatures. This shows that the adsorption is the endothermic, in which higher temperature is more favorable for dye adsorption.

Regarding the second-order kinetic model as seen in Table 3, it fitted well with high correlation coefficients ($R^2 > 0.98$). Moreover, slight differences between calculated data ($q_{e,cal}$) and experimental data ($q_{e,exp}$) and its low χ^2 values indicated the optimum adsorption at the equilibrium. Therefore, the model better described experimental data indicating the adsorption highly depended on available active sites more than MB concentrations. Thus, it satisfactorily simulates MB adsorption onto modified cellulose fibers of *P. australis*.^{26,27}

3. 3. 3. Intra-particle Diffusion and Film Diffusion Models

Intra-particle diffusion was used to analyze kinetic adsorption at different MB concentrations. The multi-linear (Fig. 6) shows three phases of the adsorption process. The first phase occurred within first 10 min, probably due to the adsorption on external surface of the adsorbent, or

Table 3. Kinetic parameters for MB adsorption by SA-RPB at different temperatures

Temp. (K)	$q_{e,exp}$ (mg/g)	First-order kinetic model				Second-order kinetic model			
		k_1 (1/min)	$q_{e,cal}$ (mg/g)	R^2	χ^2	k_2 (1/min)	$q_{e,cal}$ (mg/g)	R^2	χ^2
303	143.56	0.4047	139.36	0.807	4.084	0.0049	145.64	0.987	0.340
313	144.75	0.4192	140.35	0.849	3.841	0.0051	146.58	0.989	0.281
323	145.11	0.4275	141.79	0.828	4.241	0.0052	147.93	0.981	0.467

boundary layer diffusion of solute molecules (film diffusion).^{1,12} The electrostatic attraction between MB and the adsorbent might involve in this phase. The second phase was intra-particle diffusion at a gradual adsorption stage. The last one was equilibrium phase during which intra-particle diffusion occurred when MB concentration was reduced.

Non-zero C_i intercepts (Table 4) showed that the intra-particle diffusion was not the only rate limiting step. Moreover, the fact that the first and second phases did not pass through the origin signifies the intra-particle diffusion. C_i enhanced when the temperature increased (Table 4), indicating that temperature promoted the boundary layer diffusion effect.¹

The boundary layer diffusion rate constants of the first phase (k_{p1}) were significantly higher than those of

the second and third ones (Table 4). These results signify that mass transfer from bulk solution to exterior surface of SA-RPB was higher than that from exterior surface into its pores. Moreover, k_p value at 313 K was higher than at 303 K, boosting MB diffusion rate.

As shown in Fig. 8, calculated Bt values were plotted adsorption against time t (min). It denotes that linear lines for all MB initial concentrations did not pass through the origin. This indicates that MB adsorption on prepared SA-RPB is mainly governed by external mass transport, where particle diffusion is the rate limiting step.

Boyd model was used to distinguish between film and intra-particle diffusions. Accordingly, Bt values plotted against time can be used to determine diffusion processes. If the lines are linear and pass through the origin, then intra-particle diffusion occurs. However, if they are

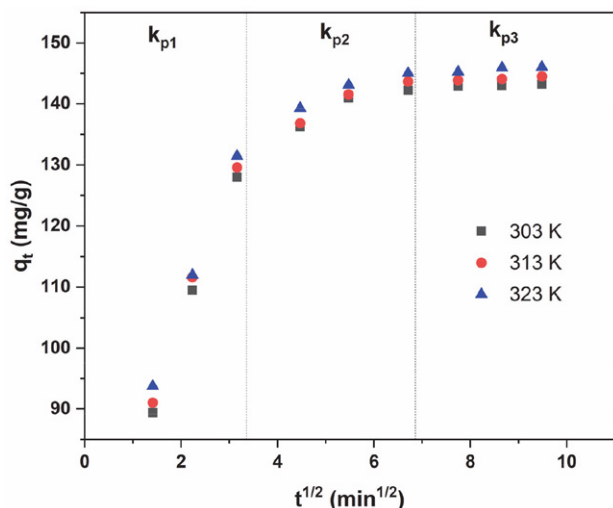


Fig. 6. Plots of intra-particle diffusion model for the adsorption of MB dye onto SA-RPB at 303; 313 and 323 K

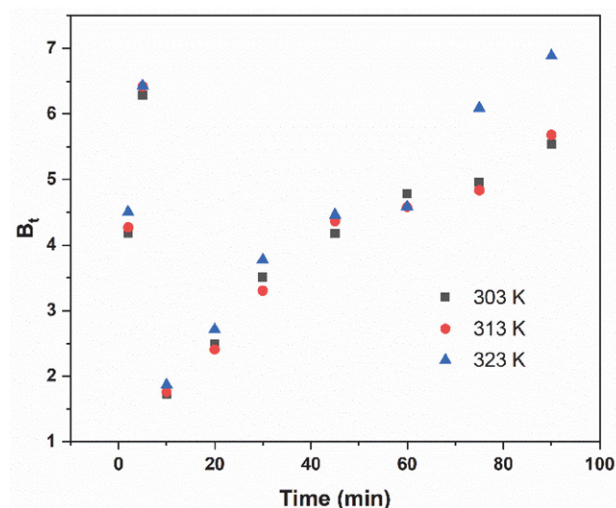


Fig. 7. Boyd plots for MB adsorption by SA-RPB at 303, 313, and 323 K

Table 4. Intra-particle diffusion model constant for MB adsorption by SA-RPB at different temperatures

Temp. (K)	Intra-particle diffusion model								
	k_{p1} (mg/gmin ^{1/2})	k_{p2} (mg/gmin ^{1/2})	k_{p3} (mg/gmin ^{1/2})	C_1	C_2	C_3	$(R_1)^2$	$(R_2)^2$	$(R_3)^2$
303	22.065	2.607	0.220	58.823	125.330	141.099	0.996	0.862	0.939
313	22.114	3.000	0.342	60.732	123.992	141.161	0.994	0.926	0.953
323	21.584	2.520	0.470	63.361	128.449	141.652	0.999	0.940	0.870

linear but do not pass through the origin, or non-linear, then film diffusion controls the adsorption process.^{15,16} Fig. 7 shows that the Boyd plots at all temperatures are non-linear, indicating the film diffusion occurred. This probably resulted from a mass transfer difference in the first and second phases.

3. 3. 4. Effects of Initial MB Concentration and Adsorption Isotherms

The effects of initial MB concentration (from 125 to 300 mg/L) on adsorption were determined by 0.1 g/L SA-RPB, at pH 6.5 and 303 K. Adsorption isotherms were analyzed at different initial MB concentrations, reflecting MB removal by SA-RPB (Fig. 8(a)). It clearly displays that the removal rate rapidly went up from 125 to 250 mg/L MB concentrations and gradually increased at higher concentrations. More than 94% MB was absorbed at 125 and 150 mg/L concentrations, and the MB equilibrium adsorption capacity (q_e) increased with higher initial dye concentrations (Fig. 8(a)). However, the initial MB concentration (from 125 to 300 mg/L) resulted in a decreased MB removal from 96.93% to 63.64% at 303 K (Fig. 8(a)). The lack of available active sites required for high initial MB concentrations accounted for these reductions. The adsorption isotherms, which revealed the interactive behaviors between the adsorbate and adsorbent at liquid–solid interfaces, were analyzed.

The obtained results show that Langmuir, Freundlich, Dubinin–Radushkevitch, and Temkin models simulated MB adsorption on SA-RPB. The nonlinear plots at different concentrations are evident in Fig. 8(b), while Table 4 depicts their corresponding parameters. R^2 and χ^2 were used as indicators to analyze adsorption at equilibrium. Langmuir model appeared to yield the best fit because of its higher R^2 and lower χ^2 than those of other models. The Langmuir isotherm model showed the homogeneous

nature of the adsorbent surface and the monolayer cover of dye molecules formed on the outer surface of SA-RPB. Also, its isotherm R_L values indicate that the fundamental features were higher than 0 and less than 1.0; thus, the adsorption was favorable within the evaluated concentration range.⁵⁷ For the Freundlich model, the $1/n$ values (Table 5) were within the range of $0.1 < 1/n < 1.0$, signifying physisorption mechanism, and the adsorption process was considered favorable, rapid, and effective.⁵⁸ The equilibrium models provide insights on the adsorbent's adsorption mechanism, surface properties, and affinity.

Non-linear regression of the Temkin model fitted well with the experimental data with high $R^2(T)$ and low $\chi^2(T)$ (Table 5). B_T was 21.47 J/mol at 303K, reflecting the endothermic nature of adsorption. The $R^2(DR)$ value generated by Dubinin–Radushkevitch isotherm (Table 5) was significantly lower than those of other isotherms mentioned above. This result shows that the MB adsorption by SA-RPB was not well-aligned with the Dubinin–Radushkevitch isotherm. Moreover, mean energy of sorption (E) calculated from this model was 0.615 kJ/mol at 303 K, which proved the endothermic nature of adsorption.¹⁵

The NaOH-then-CA adsorbent exhibited its effective MB removal with a maximum adsorption capacity of 191.49 mg/g at 150 mg/L MB concentration. This value is higher than those obtained in other studies using modified *P. australis* biomass and other modified plant materials listed in Table 6. For example, Kankılıç *et al.* reported that the maximum adsorption capacity of cellulose microfibrils of *P. australis* modified with NaOH was 54.9 mg/g at 400 mg/L.⁵⁸ The treatment with citric acid increased the absorption ability in our study.

3. 3. 5. Adsorption Thermodynamics

Determining thermodynamic parameters is also conducted to better understand temperature effects on

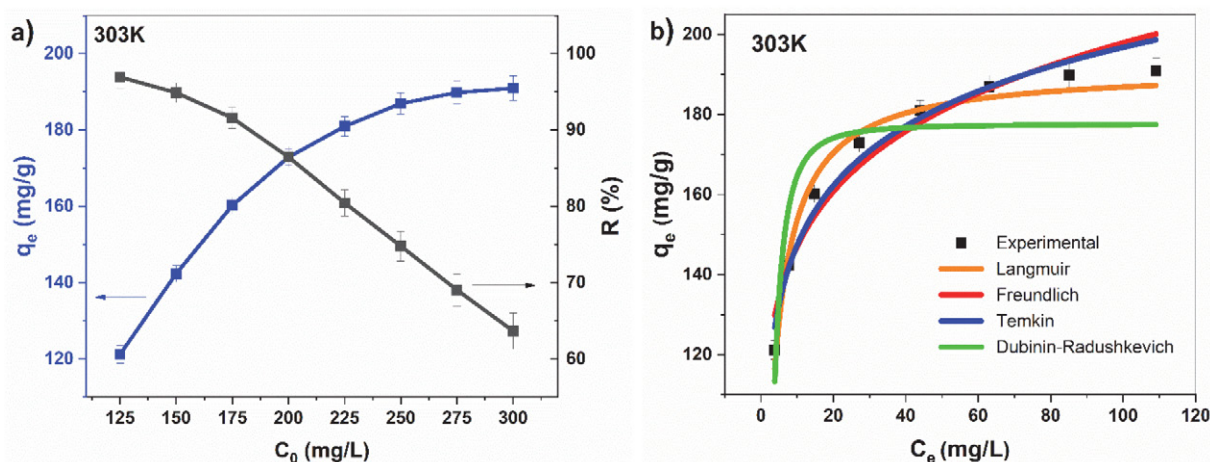


Fig. 8. (a) Effect of initial MB concentration on MB removal efficiency and adsorption capacity by SA-RPB at 303 K; (b) MB adsorption isotherm by SA-RPB based on Langmuir, Freundlich, Temkin, and Dubinin–Radushkevich isotherm models at 303 K. The experiments were conducted using 1.0 g/L SA-RPB at different initial MB concentrations and 6.5 pH value

Table 5. Isotherm parameters for MB adsorption by SA-RPB at 303K

Temp. (K)	$q_{e,exp}$ (mg/g)	Langmuir isotherm			$R^2(L)$	$\chi^2(L)$	Freundlich isotherm		$R^2(F)$	$\chi^2(F)$
		q_{max} (mg/g)	K_L (L/mg)	R_L			K_F (mg/g·(L/mg) ^{1/n})	n_F		
303	190.94	191.49	0.404	0.0082	0.981	0.548	109.15	7.739	0.946	99.505
Temp. (K)	$q_{e,exp}$ (mg/g)	Dubinin–Radushkevitch isotherm			$R^2(DR)$	$\chi^2(DR)$	Temkin isotherm		$R^2(T)$	$\chi^2(T)$
		q_{DR} (mg/g)	E (kJ/mol)	K_{DR} (mol ² /kJ ²)			A_T (L/mg)	B_T (J/mol)		
303	190.94	177.62	0.615	-1.32×10^{-6}	0.817	5.135	95.66	21.47	0.970	0.867

Table 6. MB adsorbents' capacities in comparison

Absorbent	Temperature (K)	pH	q_{max} (mg/g)
<i>P. australis</i> treated with NaOH and citric acid	303	6.5	191.49
<i>P. australis</i> treated with NaOH ²⁶	298	7.0	54.9
Raw <i>P. australis</i> ⁵⁸	298	6.5	22.7
<i>P. australis</i> treated with organic compounds ⁵⁸	298	6.5	46.8
Raw Tunisian <i>P. australis</i> ²⁷	298	8.0	41.2
Peach stones modified with citric acid ²⁰	303	6.0	178.25
Lawny grass treated with citric acid ²⁸	298	5.7	301.1
Peanut shell modified with citric acid ²⁹	303	10.0	120.48
Activated carbon ¹⁵	303	7	81.20

adsorption processes, applying Arrhenius equation (Eqs. (20)). Accordingly, a chemical reaction velocity is used for all predictive expressions of reaction-rate constants.

$$\ln k_2 = \ln A - \frac{E_a}{RT} \quad (20)$$

In Eqs. (20), A (g/mg·min) is the pre-exponential factor; E_a (kJ/mol) is the activation energy of absorption; R (8.314 J/mol K) is the gas constant, and T (K) is absolute temperature.

Plots of $\ln K_2$ versus $1/T$ and $\ln K_L$ versus $1/T$ were straight lines with R^2 values of 0.99 and 0.98, respectively, from which E_a and A values were calculated (Table 7). The low values of activation energy (< 42 kJ/mol) obtained in this study indicated a diffusion-controlled process and a physisorption mechanism.⁵⁹ The negative values of ΔG° at all temperatures reveal that the adsorption process was feasible and spontaneous. The obtained ΔS° was positive, showing the endothermic nature of adsorption, while the positive ΔS° spotted an increased randomness of the solid-liquid and adsorption medium interface over the process. The positive ΔS° value also indicated the adsorbent's affinity and some structural changes in adsorbate and adsorbent.⁶⁰

3. 3. 6. Effect of Initial pH

An increase in pH from 1.0 to 6.5 significantly enhanced adsorption, but adsorption rates stayed almost constant at a higher pH value (Fig. 9). The adsorbent surface got more positively charged at low pH values, reducing the attraction between the adsorbent and MB. A more negatively charged surface is available when pH increases, facilitating greater MB uptake.⁵¹ The pH effect on MB removal efficiency could be attributed to functional groups' features on the surface and isoelectric point pH_{PZC} of the SA-RPB adsorbent. The isoelectric point pH_{PZC} value of SA-RPB (determined by the drift pH method) was 3.1 (as seen in Fig. 3(a) above). The hydroxyl (–OH) and carboxyl (–COOH) groups were dominant on SA-RPB surface, which was deprotonated and became less charged, i.e. $pH_{PZC} < 3.1$.⁶¹ When initial pH (pH_{in}) was lower than pH_{PZC} (3.1), the adsorbent surface was protonated and became more positive.⁶¹ In this case, the SA-RPB surface exhibited an electrostatic repulsion between SA-RPB surface and the MB–N⁺ cation in the solution, leading to poor adsorption efficiency.⁶² In contrast, when pH value was lower than pH_{PZC} , functional groups on SA-RPB surface were depro-

Table 7. Thermodynamic parameters for MB adsorption by SA-RPB

E_a (kJ/mol)	A (g/mg min)	Temperature (K)	ΔG° (kJ/mol)	ΔH° (kJ/mol)	ΔS° (kJ/mol K)
2.242	0.012	303	–28.63	16.82	0.155
		313	–30.18		
		323	–31.73		

tonated and became more negative, inducing electrostatic attraction to MB–N⁺ and boosting the removal efficiency.⁶²

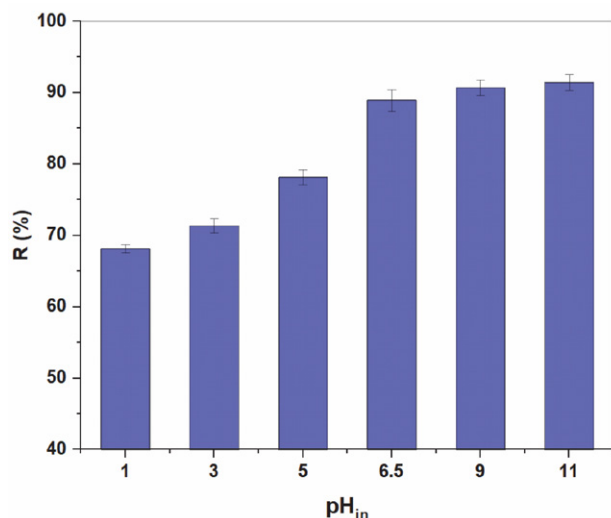


Fig. 9. Initial pH effects on MB adsorption by SA-RPB (The tests performed using 1.0 g/L SA-RPB at 150 mg/L MB concentration)

3. 3. 7. Possible Mechanism of MB Adsorption onto SA-RPB

Dye adsorption involves adsorbent-adsorbate interactions in the solution. Based on the result ($\Delta H^\circ = 16.82$ kJ/mol), adsorption was mainly induced by electrostatic and/or hydrogen bond forces.⁶³ At a pH < 3.1 (pH_{PZC} of SA-RPB), the protonated adsorbent surface became positively charged (Fig. 3(a)). Therefore, the MB–N⁺ adsorption was mainly attributed to physical interaction caused by capillary diffusion and weak hydrogen bonds. The surface of negatively charged adsorbent electrostatically interacted with MB–N⁺ at pH > 3.1, improving MB adsorption efficiency by SA-RPB, which reached a maximum value at the initial pH of the MB solution (6.5); hence, this pH value was selected to evaluate the adsorption mechanism.

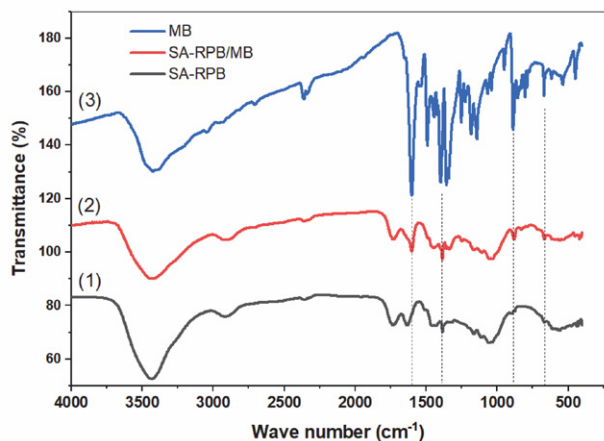


Fig. 10. FTIR spectra of SA-RPB (1) before and (2) after MB adsorption, and (3) pure MB

The FTIR analysis plots showed the spectra of MB, SA-RPB, and SA-RPB after MB adsorption and were used to describe their adsorption mechanisms. From the spectral peaks (Fig. 10), vibrations were revealed (Table 8). Based on the wavenumbers, it implies that pure MB had functional groups, that is, –OH, C=C, C=N, C=N⁺, C–N, C=S, C–S, and C–H.^{64,65} Variations in functional groups' peak positions and the strength of SA-RPB dye complex indicate MB adsorption onto the SA-RPB surface. Differences in the wavenumbers for C–H deformation in the benzene ring, C–N in the heterocycle, and C–N bonds connected with the benzene ring in the MB, C–H aromatic rings, C=C stretching vibrations in aromatic rings, and C–H asymmetric deformation in SA-RPB and SA-RPB dye complex (Table 8) corresponded to MB attachment to the adsorbent surface by π – π stacking between the aromatic backbone of MB and SA-RPB.^{50,64} This interaction was evidently reflected by adsorption peaks of MB and SA-RPB at 1599 and 1506 cm^{–1}, respectively, disappearing in SA-RPB dye complex. Furthermore, SA-RPB peak at 897 cm^{–1} after MB adsorption (Fig. 10), attributed to the bending vibration of C–H in the aromatic ring, moved up to a higher intensity than the SA-RPB sample before MB adsorption.

The peak ranges of 1340–1000 cm^{–1} of SA-RPB with oxygen-rich functional groups shifted, suggesting hydrogen bonds created between SA-RPB and MB molecules. The band shifts occurred as N–CH₃ stretching, Ar–N deformation vibration, C=S stretching vibration, and C–S stretching vibration. These phenomena signify that N in the –N(CH₃)₂ and Ar–N groups and S in the C=S and C–S groups might have been used as the hydrogen-bonding acceptor and formed intramolecular hydrogen bonding with the hydrogen atom of the –OH and –COOH groups on the adsorbent surface.⁶⁴ Hydrogen atoms in SA-RPB functional groups could also generate hydrogen bonds with N and S in MB functional groups. In addition, SA-RPB dye complex had a new adsorption peak at 1249 cm^{–1}, owing to the Ar–N deformation vibration of the MB molecule; this verified MB adsorption onto the SA-RPB surface.

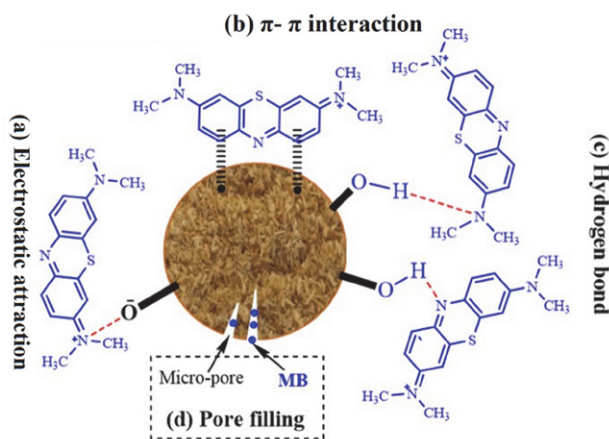


Fig. 11. Possible adsorption mechanism of MB onto SA-RPB

Table 8. FTIR spectral features of MB and SA-RPB before and after MB adsorption

MB		SA-RPB	
Vibration (cm ⁻¹)	Wavenumber (cm ⁻¹)	Vibration	Wavenumber
		Before ads.	After ads.
O–H or N–H stretching	3424	–OH stretching	3438
–CH ₃ stretching	2939	C–H stretching vibration	2917
C=N–C group	2360	–COOH stretching vibration	1735
=N ⁺ (CH ₃) ₂ stretching	1661	–COO [–] stretching of carboxylate groups with an aromatic ring	1633
C=N (and C=C) stretching in heterocycle	1599	C=C stretching vibrations in aromatic rings	1506
C–H deformation in benzene ring	1492	C–H deformation in aromatic rings	1456
C–N in heterocycle	1396	C=C stretching vibrations in aromatic rings	1431
C–N bonds connected with benzene ring	1356	C–H asymmetric deformation	1384
N–CH ₃ stretching	1340	–OH bending vibration in C–OH	1334
		C1–O vibrations in S derivatives	1321
Ar–N deformation vibration	1252	–	1249
C=S stretching vibration	1183	C–O–C antisymmetric vibrations	1165
C–S stretching vibration	1142	Anhydroglucose ring vibration	1111
C–N stretching vibration	1066; 1038	C–O stretching vibration in cellulose, hemicellulose, and lignin	1057; 1035
C–H axial deformation in aromatic rings	950–669	C–H rocking vibrations	898
C–S and C–N stretching	616–449	C–H bending in aromatic rings	875–500

These obtained results clearly show that MB adsorption by SA-RPB was attributed to four possible adsorption mechanisms: electrostatic interaction, hydrogen bonding, π – π stacking interaction, and pores filling between MB and SA-RPB (Fig. 11) (i.e., adsorbent-adsorbate interactions).

3. 4. Reusability

The reusable efficiency of adsorbents for wastewater treatment is economically and environmentally critical.

The regeneration results showed that the adsorption efficiency decreased by approximately 11.69% after six desorption–adsorption cycles compared with the first batch experiment (Fig. 12(a)). Ethanol was used to desorption MB from adsorbents in some previous reports.^{66,67} Additionally, FTIR spectra of adsorbents showed similar spectra after six cycles (Fig. 12(b)), indicating the adsorbent stability during the adsorption process. This result suggests that the adsorbent is practically useful for treating real-time industrial effluent.

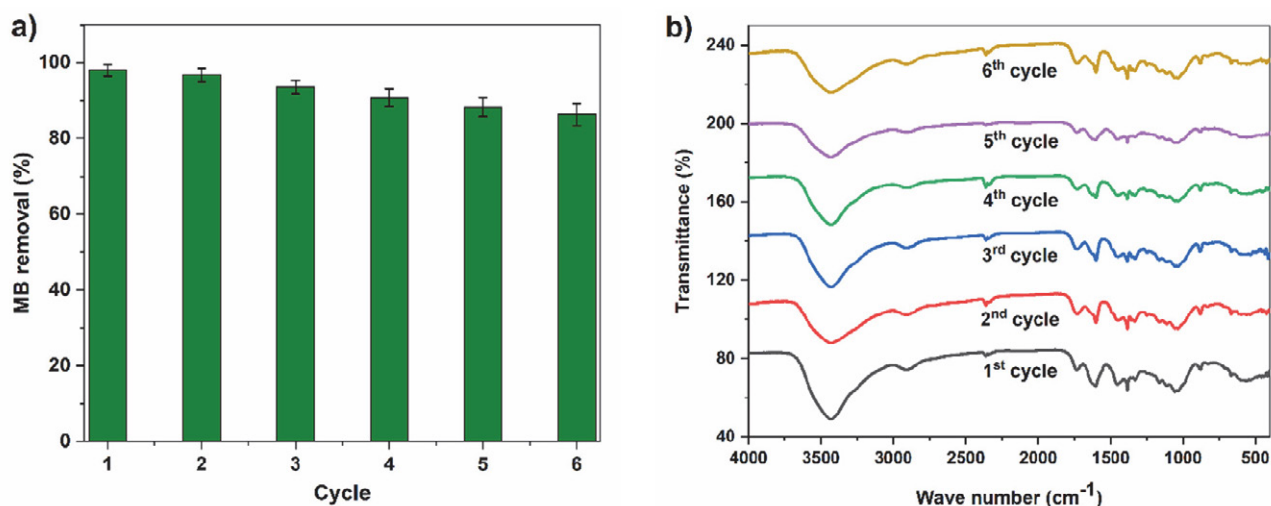


Fig. 12. (a) Removal efficiency of MB onto SA-RPB in successive desorption–adsorption cycles; (b) FTIR spectra of SA-RPB after six desorption–adsorption cycles. The tests were done using 1.0 g/L SA-RPB at 150 mg/L MB concentration and 6.5 pH

4. Conclusion

This study demonstrates that chemically modified *P. australis* biomass can be used as an effective adsorbent for removing MB dye from aqueous solutions. Batch adsorption test results show that materials treated with NaOH followed by citric acid boosted the removal compared with raw materials or those modified with only NaOH. The initial pH of the solution, the adsorbent dosage, contact time, and initial MB concentrations significantly influenced the adsorption rates of SA-RPB. All SEM, FTIR, and BET analyses indicate significant modifications in the structure after chemical treatments. Moreover, calculated adsorption energy denotes that MB adsorption by SA-RPB occurred through physical interactions at different temperatures when the removal process was endothermic and spontaneous. The maximum MB adsorption capacity of SA-RPB was 191.49 mg/g, which was slightly decreased after four desorption–adsorption cycles. Four possible adsorption mechanisms (i.e., electrostatic interaction, hydrogen bonding, π – π stacking interaction, and pores filling between MB and SA-RPB) were spotted to functionally take place. This study shows that modified materials derived from reeds are expected to be highly economical and efficient for removing synthetic dyes in wastewater treatment. For practical uses, column experiments are underway for viable industrial scales and will be presented in the future.

Acknowledgements

This research is supported by the project SPD2020.01.05. The authors are thankful to Dong Thap University for providing the instrumental facility and financial support.

Competing interests

The authors declare that no conflict of interest would prejudice the impartiality of this scientific work.

5. References

1. Y. Yao, F. Xu, M. Chen, Z. Xu, Z. Zhu, *Bioresour. Technol.* **2010**, *101*(9), 3040–3046. DOI:10.1016/j.biortech.2009.12.042
2. L. Meili, P. V. S. Lins, M. T. Costa, R. L. Almeida, A. K. S. Abud, J. I. Soletti, G. L. Dotto, E. H. Tanabe, L. Sellaoui, S. H. V. Carvalho, A. Erto, *Prog. Biophys. Mol. Biol.* **2019**, *141*, 60–71. DOI:10.1016/j.pbiomolbio.2018.07.011
3. N. Nasuha, B. H. Hameed, A. T. Din, *J. Hazard. Mater.* **2010**, *175*(1–3), 126–132. DOI:10.1016/j.jhazmat.2009.09.138
4. M. J. Ahmed, S. K. Dhedan, *Fluid Phase Equilibria* **2012**, *317*, 9–14. DOI:10.1016/j.fluid.2011.12.026
5. A. Lahkimi, M. A. Oturan, N. Oturan, M. Chaouch, *Environ. Chem. Lett.* **2006**, *5*(1), 35–39. DOI:10.1007/s10311-006-0058-x
6. M. Panizza, A. Barbucci, R. Ricotti, G. Cerisola, *Sep. Purif. Technol.* **2007**, *54*(3), 382–387. DOI:10.1016/j.seppur.2006.10.010
7. S. K. Nataraj, K. M. Hosamani, T. M. Aminabhavi, *Desalination* **2009**, *249*(1), 12–17. DOI:10.1016/j.desal.2009.06.008
8. F. Gulshan, S. Yanagida, Y. Kameshima, T. Isobe, A. Nakajima, K. Okada, *Water Res.* **2010**, *44*(9), 2876–2884. DOI:10.1016/j.watres.2010.01.040
9. K. L. Yeap, T. T. Teng, B. T. Poh, N. Morad, K. E. Lee, *Chem. Eng. Sci.* **2014**, *243*, 305–314. DOI:10.1016/j.ces.2014.01.004
10. M. Soniya, G. Muthuraman, *Ind. Eng. Chem.* **2015**, *30*, 266–273. DOI:10.1016/j.jiec.2015.05.032
11. M. Khaksar, D. M. Boghaei, M. Amini, *Comptes. Rendus. Chimie.* **2015**, *18*(2), 199–203. DOI:10.1016/j.crci.2014.04.004
12. M. K. Mbacké, C. Kane, N. O. Diallo, C. M. Diop, F. Chauvet, M. Comtat, T. Tzedakis, *J. Environ. Chem. Eng.* **2016**, *4*(4), 4001–4011. DOI:10.1016/j.jece.2016.09.002
13. W. Ahlawat, N. Kataria, N. Dilbaghi, A. A. Hassan, S. Kumar, K. H. Kim, *Environ. Res.* **2020**, *181*, 108904. DOI:10.1016/j.envres.2019.108904
14. N. H. Thang, D. S. Khang, T. D. Hai, D. T. Nga, P. D. Tuan, *RSC Advances* **2021**, *11*(43), 26563–26570. DOI:10.1039/D1RA04672A
15. M. F. M. Yusop, M. A. Ahmad, N. A. Rosli, M. E. A. Manaf, *Arab. J. Chem.* **2021**, *14*(6), 103122. DOI:10.1016/j.arabjc.2021.103122
16. F. Marrakchi, M. J. Ahmed, W. A. Khanday, M. Asif, B. H. Hameed, *Int. J. Biol. Macromol.* **2017**, *98*, 233–239. DOI:10.1016/j.ijbiomac.2017.01.119
17. A. H. Jawad, N. F. Hanani Mamat, M. Fauzi Abdullah, K. Ismail, *Desalin. Water Treat.* **2016**, *59*, 210–219. DOI:10.5004/dwt.2017.0097
18. İ. Şentürk and M. Alzein, *Acta Chim. Slov.* **2020**, *67*, 55–69. DOI:10.17344/acsi.2019.5195
19. B. Djobbi, G. L. B. Miled, H. Raddadi and R. B. Hassen, Alzein, *Acta Chim. Slov.* **2021**, *68*, 548–561. DOI:10.17344/acsi.2020.6248
20. J. Yan, G. Lan, H. Qiu, C. Chen, Y. Liu, G. Du, J. Zhang, *Sep. Sci. Technol.* **2018**, *53*(11), 1678–1688. DOI:10.1080/01496395.2018.1439064
21. A. H. Jawad, R. Razuan, J. N. Appaturi, L. D. Wilson, *Surf. Interfaces* **2019**, *16*, 76–84. DOI:10.1016/j.surf.2019.04.012
22. N. Sebeia, M. Jabli, A. Ghith, Y. El Ghoul, F. M. Alminderej, *Int. J. Biol. Macromol.* **2019**, *121*, 655–665. DOI:10.1016/j.ijbiomac.2018.10.070
23. K. Ben Jeddou, F. Bouaziz, F. Ben Taheur, O. Nouri-Ellouz, R. Ellouz-Ghorbel, S. Ellouz-Chaououni, *Water Sci. Technol.* **2021**, *83*(6), 1384–1398. DOI:10.2166/wst.2021.075
24. A. I. Engloner, *Morphol.* **2009**, *204*(5), 331–346. DOI:10.1016/j.flora.2008.05.001
25. T. Březinová, J. Vymazal, *Ecol. Eng.* **2014**, *73*, 53–57. DOI:10.1016/j.ecoleng.2014.09.022
26. G. B. Kankılıç, A. Ü. Metin, *J. Mol. Liq.* **2020**, *312*, 113313. DOI:10.1016/j.molliq.2020.113313
27. R. Dallel, A. Kesraoui, M. Seffen, *J. Environ. Chem. Eng.* **2018**,

- 6(6), 7247–7256. DOI:10.1016/j.jece.2018.10.024
28. L. Chen, A. Ramadan, L. Lü, W. Shao, F. Luo, J. Chen, *J. Chem. Eng. Data*. **2011**, 56(8), 3392–3399. DOI:10.1021/je200366n
 29. P. Wang, Q. Ma, D. Hu, L. Wang, *Water Treat.* **2015**, 57(22), 10261–10269. DOI:10.1080/19443994.2015.1033651
 30. A. Sluiter, B. Hames, R. Ruiz, C. Scarlata, J. Sluiter, D. Templeton, D. Crocker, National Renewable Energy Laboratory Golden Co., **2008**.
 31. M. Danish, T. Ahmad, S. Majeed, M. Ahmad, L. Ziyang, Z. Pin, S. M. Shakeel Iqbal *Bioresour. Technol. Rep.* **2018**, 3, 127–137. DOI:10.1016/j.biteb.2018.07.007
 32. S. Lagergren, *Handlingar Band*, **1898**, 24(4), 1–39.
 33. Y. S. Ho, G. McKay, *Process Biochem.* **1999**, 34, 451–465. DOI:10.1016/S0032-9592(98)00112-5
 34. L. Mouni, L. Belkhir, J.-C. Bollinger, A. Bouzaza, A. Assadi, A. Tirri, F. Dahmoune, K. Madani, H. Reminie, *Appl. Clay Sci.* **2018**, 153, 38–45. DOI:10.1016/j.clay.2017.11.034
 35. K. R. Hall, L. C. Eagleton, A. Acrivos, T. Vermeulen, *Ind. Eng. Chem. Fundam.* **1966**, 5(2), 212–223. DOI:10.1021/i160018a011
 36. H. M. Freundlich, *J. Phys. Chem. A*. **1906**, 57, 385–470. DOI:10.1515/zpch-1907-5723
 37. M. J. Temkin, V. Pyzhev, *URSS*. **1940**, 12, 217–225.
 38. M. M. Dubinin, L. V. Radushkevich, *Proceedings of the Academy of Sciences of the USSR*. **1947**, 55, 331–337.
 39. H. Zhao, H. Yan, C. Zhang, X. Liu, Y. Xue, Y. Qiao, Y. Tian, S. Qin, *Evid. Based Complement Alternat. Med.* **2011**, 408973. DOI:10.1155/2011/408973
 40. A. El Shahawy, G. Heikal, *Ecol. Eng.* **2018**, 122, 207–218. DOI:10.1016/j.ecoleng.2018.08.004
 41. D. D. Q. Melo, V. D. O. S. Neto, F. C. D. F. Barros, G. S. C. Raulino, C. B. Vidal, R. F. do Nascimento, *J. Appl. Polym. Sci.* **2016**, 133(15), 43286. DOI:10.1002/app.43286
 42. J. P. Chen, S. Wu, K.-H. Chong, *Carbon*. **2003**, 41(10), 1979–1986. DOI:10.1016/S0008-6223(03)00197-0
 43. P. Lu, Y. L. Hsieh, *ACS Appl. Mater. Interfaces*. **2010**, 2(8), 2413–2420. DOI:10.1021/am1004128
 44. D.-Y. Kim, B. -M. Lee, D. H. Koo, P. -H. Kang, J. -P. Jeun, *Cel-lulose* **2016**, 23(5), 3039–3049. DOI:10.1007/s10570-016-1037-4
 45. A. Barakat, C. Mayer-Laigle, A. Solhy, R. A. D. Arancon, H. de Vries, R. Luque, *RSC Adv.* **2014**, 4(89), 48109–48127. DOI:10.1039/C4RA07568D
 46. K. O. Reddy, B. R. Guduri, A. V. Rajulu, *J. Appl. Polym. Sci.* **2009**, 114(1), 603–611. DOI:10.1002/app.30584
 47. C. Uma Maheswari, K. Obi Reddy, E. Muzenda, B. R. Guduri, A. Varada Rajulu, *Biomass and Bioenergy* **2012**, 46, 555–563. DOI:10.1016/j.biombioe.2012.06.039
 48. C. Pappas, P. A. Tarantilis, I. Daliani, T. Mavromustakos, M. Polissiou, *Ultrason. Sonochem.* **2002**, 9(1), 19–23. DOI:10.1016/S1350-4177(01)00095-5
 49. A. Alemdar, M. Sain, *Bioresour. Technol.* **2008**, 99(6), 1664–1671. DOI:10.1016/j.biortech.2007.04.029
 50. L. Hevira, Zilfa, Rahmayeni, J. O. Ighalo, H. Aziz, R. Zein, *J. Ind. Eng. Chem.* **2021**, 97, 188–199. DOI:10.1016/j.jiec.2021.01.028
 51. D. H. K. Reddy, Y. Harinath, K. Seshiah, A. V. R. Reddy, *Chem. Eng. Sci.* **2010**, 162, 626–634. DOI:10.1016/j.ces.2010.06.010
 52. H. Nazir, M. Salman, M. Athar, U. Farooq, A. Wahab, M. Akram, *Water Air Soil Pollut.* **2019**, 230, 303. DOI:10.1007/s11270-019-4360-1
 53. E. C. Lima, B. Royer, J. C. Vaggetti, N. M. Simon, B. M. da Cunha, F. A. Pavan, *J. Hazard. Mater.* **2008**, 155(3), 536–550. DOI:10.1016/j.jhazmat.2007.11.101
 54. B. H. Hameed, A. A. Ahmad, *J. Hazard. Mater.* **2009**, 164(2–3), 870–875. DOI:10.1016/j.jhazmat.2008.08.084
 55. M. M. Abd El- Latif, A. M. Ibrahim, *Desalin. Water Treat.* **2012**, 6(1–3), 252–268. DOI:10.5004/dwt.2009.501
 56. D. Pathania, S. Sharma, P. Singh, *Arab. J. Chem.* **2017**, 10(1), S1445–S1451. DOI:10.1016/j.arabjc.2013.04.021
 57. V. Vilar, C. Botelho, R. Boaventura, *J. Hazard. Mater.* **2007**, 147(1–2), 120–132. DOI:10.1016/j.jhazmat.2006.12.055
 58. G. B. Kankılıç, A. Ü. Metin, İ. Tüzün, *Ecol. Eng.* **2016**, 86, 85–94. DOI:10.1016/j.ecoleng.2015.10.024
 59. M. Al-Ghouti, M. A. Khraisheh, M. N. Ahmad, S. Allen, *J. Colloid Interface Sci.* **2005**, 287(1), 6–13. DOI:10.1016/j.jcis.2005.02.002
 60. Y. Bulut, H. Aydın, *Desalination* **2006**, 194(1–3), 259–267. DOI:10.1016/j.desal.2005.10.032
 61. T. Maneerung, J. Liew, Y. Dai, S. Kawi, C. Chong, C. H. Wang, *Bioresour. Technol.* **2016**, 200, 350–359. DOI:10.1016/j.biortech.2015.10.047
 62. X. Liu, C. He, X. Yu, Y. Bai, L. Ye, B. Wang, L. Zhang, *Powder Technol.* **2018**, 326, 181–189. DOI:10.1016/j.powtec.2017.12.034
 63. J. Mattson, H. Mark, Marcel Dekker, Ins., New York. **1971**.
 64. J. Gong, J. Liu, Z. Jiang, X. Wen, E. Mijowska, T. Tang, X. Chen, *J. Colloid Interface Sci.* **2015**, 445, 195–204. DOI:10.1016/j.jcis.2014.12.078
 65. M. Danish, T. Ahmad, S. Majeed, M. Ahmad, L. Ziyang, Z. Pin, S. S. M. Iqbal, *Bioresour. Technol. Rep.* **2018**, 3, 127–137. DOI:10.1016/j.biteb.2018.07.007
 66. T. Benhalima, H. Ferfera-Harrar, *Int. J. Biol. Macromol.* **2019**, 132, 126–141. DOI:10.1016/j.ijbiomac.2019.03.164
 67. S. Lapwanit, T. Sooksimuang, T. Trakulsujaritchok, *J. Environ. Chem. Eng.* **2018**, 6(5), 6221–6230. DOI:10.1016/j.jece.2018.09.050

Povzetek

V raziskavi je bila biomasa iz vrste *Phragmites australis* kemično modificirana z NaOH in za tem še s citronsko kislino, da bi proizvedli učinkovit adsorbent, imenovan SA-RPB. Adsorbent je bil karakteriziran z metodami XRD, SEM, BET in FT-IR. Dokazano je bilo, da adsorbent obstaja predvsem v obliki kristalov celuloze, vsebuje mikropore s povprečnim premerom 15,97 nm in ima veliko število hidroksilnih in karboksilnih skupin na površini. Adsorpcijski proces SA-RPB smo ovrednotili z adsorpcijo barvila metilen modrega (MB) v vodni raztopini. Kinetika adsorpcije je bila opisana z modelom psevdo-drugega reda. Adsorpcijska izoterma je skladna z Langmuirjevim modelom z največjo adsorpcijsko zmogljivostjo 191,49 mg/g pri 303 K. Ugotovitve kažejo, da je MB mogoče učinkovito odstraniti iz vodnih raztopin z uporabo adsorbenta, izdelanega iz surove biomase *Phragmites australis*, obdelane z NaOH in nato s citronsko kislino.



Except when otherwise noted, articles in this journal are published under the terms and conditions of the Creative Commons Attribution 4.0 International License

Scientific paper

Assessment of the Capability of Magnetic Nanoparticles to Recover Neodymium Ions from Aqueous Solution

Ana Ambrož,¹ Irena Ban² and Thomas Luxbacher^{1,3,*}

¹ University of Maribor, Faculty of Chemistry and Chemical Engineering, Laboratory for Water Biophysics and Membrane Processes, Smetanova 17, 2000 Maribor, Slovenia

² University of Maribor, Faculty of Chemistry and Chemical Engineering, Laboratory for Inorganic Chemistry, Smetanova 17, 2000 Maribor, Slovenia

³ Anton Paar GmbH, Anton-Paar-Strasse 20, 8054 Graz, Austria

* Corresponding author: E-mail: thomas.luxbacher@anton-paar.com

Received: 10-03-2022

Abstract

Magnetic nanoparticles (MNPs) have received increasing attention for various applications due to their fast synthesis, versatile functionalization, and recyclability by the application of a magnetic field. The high surface-to-volume ratio of MNP dispersions has suggested their use as an adsorbent for the removal of heavy metal ions. We investigated the applicability of MNPs composed of a maghemite core surrounded by a silica shell functionalized with aminopropylsilane, $\gamma\text{-Fe}_2\text{O}_3\text{-NH}_4\text{OH@SiO}_2(\text{APTMS})$, for the removal of neodymium ions (Nd^{3+}) from aqueous solution. The MNPs were characterized for their size, composition, surface functionality and charge. Despite the promising properties of MNPs, their removal from the aqueous dispersion with an external magnet was not sufficient to reliably quantify the adsorption of Nd^{3+} by UV-Vis spectroscopy.

Keywords: Rare earth elements; Maghemite; Nanoparticles; UV-Vis spectroscopy, Adsorption

1. Introduction

The rare earth elements (REEs) are a group of 17 strongly related heavy elements that comprise scandium (Sc), yttrium (Y), lanthanum (La) and the f-block elements known as the lanthanide group, cerium (Ce) through lutetium (Lu). In addition to being of great value to general geochemistry investigations, the REEs also have high commercial value and a wide scope of applications. They are used worldwide in various electronic and optical products, in advanced technologies, medical devices, military defence systems, as well as in the field of clean energy.^{1,2} REEs have been on the list of critical raw materials since 2010, and pressure on already limited resources is still increasing with the growth of the global population, industrialization, and digitalization. With regard to high economic importance and high supply risk, neodymium (Nd), europium (Eu), terbium (Tb), dysprosium (Dy), and yttrium (Y) are considered most critical.³ With increasing demand and production, the amount of electronic waste containing REEs in various concentrations is also expanding. Sustain-

ability in REE supply and proper treatment of end-of-life electrical and electronic compounds are crucial to achieving climate neutrality.³ However, recycling of REEs presents many challenges. Firstly, REEs are usually present in small amounts in tiny electronic parts of gadgets like mobile phones. In some materials like touch screens, these metals are evenly distributed making them much more difficult to extract.⁴ Secondly, due to the low yield and high cost of recycling processes, REEs are not recycled in large quantities, regardless of the end use. However, if REEs' prices rise, recycling may become feasible.^{4,5} At present, the main focus is on the direct recycling of scrap and the urban mining, and subsequent recycling of end-of-life REE-containing products.⁶

The conventional processes for the separation and recovery of REEs mainly include precipitation, ion exchange, coagulation, flocculation, liquid-liquid extraction, biosorption, and adsorption. Among these methods, adsorption offers an efficient, environmentally friendly, and economical procedure for the removal of rare earth ions.^{7,8} Among different adsorbents, magnetic nanoparti-

cles show a significant potential due to their high surface area and their response to an external magnetic field, which eases separation from a supernatant solution after completing the adsorption process.^{9–11} The chemical and physical stability, biocompatibility, ease of surface modification, low toxicity, straightforward synthesis, and low cost of iron oxide nanoparticles (IONPs) make them ideal for a variety of applications.^{12–15}

Preparation methods and surface coating play a key role in determining the size distribution, morphology, magnetic properties, and surface chemistry of MNPs.¹⁶ Co-precipitation is the most widely used method for the synthesis of MNPs of controlled size and magnetic properties. It is extensively used for biomedical applications of MNPs, because of the ease of preparation and the avoidance of harmful materials and procedures.¹⁶ Common problems in the preparation of magnetic nanoparticle dispersions are agglomeration and oxidation, which may result in the loss of dispersibility and magnetism. An additional coating of the magnetic core helps to prevent particle agglomeration and aggregation.¹² The coating method not only prevents agglomeration and oxidation of the particle, but also provides physical and chemical stability. The coating provides an interface between the magnetic nanoparticle and the surrounding environment and offers the possibility for further functionalization. The properties of the coating may markedly differ from those of the nanoparticle core.^{15,17,18} Magnetic nanoparticles are commonly coated with organic (polymers or surfactants such as polyethylene glycol and dextran) or inorganic layers (gold, platinum, cobalt oxide, aluminium oxide, silica, activated carbon, etc.).¹⁹ The coating helps to obtain a specific affinity to target molecules, to increase dispersion stability, and to improve other physicochemical properties.^{9,20}

The adsorption of heavy metal ions on MNPs combined with magnetic separation has been used extensively in water treatment and environmental clean-up.^{14,21} Functionalized magnetic nanoparticles act towards metal ions as a kind of “nano-sponges” and can easily be retrieved from solution with a magnet, thus they are excellent for the selective extraction of metal traces from wastewater or industrial effluents. After the adsorbed ions are stripped, the nanoparticles can be reused, making this procedure a promising sustainable green technology.^{22,23} Core@shell MNPs composed of a maghemite core ($\gamma\text{-Fe}_2\text{O}_3$), and a functionalized silica coating have recently been applied for the adsorptive removal of Cu^{2+} and the rare earth ions Tb^{3+} and Dy^{3+} .^{24,25}

For the adsorption of Nd^{3+} from aqueous solutions, various magnetic nanoparticles have been synthesized. Ashour et al. synthesized magnetite nanoparticles functionalized with citric acid ($\text{CA@Fe}_3\text{O}_4$ NPs) or l-cysteine ($\text{Cys@Fe}_3\text{O}_4$ NPs) for the adsorption of La^{3+} , Nd^{3+} , Gd^{3+} and Y^{3+} from aqueous solution.²⁶ Dupont et al. synthesized $\text{Fe}_3\text{O}_4\text{@SiO}_2(\text{TMS-EDTA})$ nanoparticles for the extraction and separation of different rare-earth ions.²⁷ Gal-

houm et al. used Cysteine-functionalized chitosan magnetic nanoparticles for the sorption of La^{3+} , Nd^{3+} and Yb^{3+} and hybrid chitosan magnetic nanoparticles functionalized by diethylenetriamine (DETA) for the recovery of Yb^{3+} , Dy^{3+} and Nd^{3+} .^{28,29} Gok investigated batch adsorption method as a green technology for removal and recovery of Nd and Sm using magnetic nano-hydroxyapatite adsorbent (MNHA).³⁰ Li et al. prepared mesoporous magnetic $\text{Fe}_3\text{O}_4\text{@mSiO}_2\text{-DODGA}$ nanomaterials for adsorption and recycling of REEs. The surface of mesoporous Fe_3O_4 particles was modified with a diglycolamide ligand.³¹ Liu et al. worked with magnetic bio-adsorbent $\text{Fe}_3\text{O}_4\text{-C}_{18}\text{-chitosan-DETA}$ (FCCD) composite to test the adsorption capacity of Dy^{3+} , Nd^{3+} , and Er^{3+} .³² Miraoui et al. studied the sorption capacities of Nd^{3+} on magnetic nanoparticles grafted by poly(aminoethylene N-methyl 1-formic acid, 1-phosphonic acid) (PAEMFP).³³ Molina et al. synthesized adsorbents based on functionalized magnetite nanoparticles for the uptake of La^{3+} , Pr^{3+} and Nd^{3+} from aqueous solutions.³⁴

In this paper we extend the application of $\gamma\text{-Fe}_2\text{O}_3\text{-NH}_4\text{OH@SiO}_2$ nanoparticles functionalized with aminopropyl trimethyl silane (APTMS) towards the adsorption of Nd^{3+} ions from dilute aqueous solutions. To the best of our knowledge, $\gamma\text{-Fe}_2\text{O}_3\text{-NH}_4\text{OH@SiO}_2(\text{APTMS})$ magnetic nanoparticles have not been previously used for the removal of Nd^{3+} from aqueous solutions.

The monitoring of the adsorption process of dissolved heavy metal and rare-earth ions on MNPs requires the analytical detection of either the adsorbed ion concentration or the depletion of ions in solution. Aqueous solutions of Nd^{3+} appear strongly coloured and suggest the use of UV-Vis spectroscopy as a simple and reliable method for the determination of Nd^{3+} ion concentration in solution. After separation of the MNPs with an external magnet the remaining, Nd^{3+} ion concentration in the supernatant is expected to reveal the REE removal efficiency at different adsorption time. Upon a re-dispersion of the MNPs, the adsorption process may continue thereby giving fast and easy access to the characterization of the kinetics and the optimization of the adsorption process. However, the polydisperse size distribution and the stabilization of the core@shell MNPs compete with the magnetic force applied for their separation. We demonstrate that the additional separation processes of centrifugation and filtration are required for a complete removal of MNPs in order to obtain reliable information on the Nd^{3+} ion adsorption efficiency. These additional steps for MNP separation add complexity to the process and reduce the apparent benefits of REE recovery by the adsorption on MNPs.

2. Materials and Methods

Iron(II) chloride tetrahydrate ($\text{FeCl}_2\cdot 4\text{H}_2\text{O}$), iron(II) chloride hexahydrate ($\text{FeCl}_3\cdot 6\text{H}_2\text{O}$), and tetraethyl or-

thosilicate (TEOS) were obtained from Merck. (3-aminopropyl)trimethoxysilane (APTMS, 97%) and 2-propanol ($(\text{CH}_3)_2\text{CHOH}$, $\geq 99.8\%$) were obtained from Sigma Aldrich. Ethanol ($\text{C}_2\text{H}_5\text{OH}$) was obtained from Carlo Erba Reagents, ammonia solution (NH_4OH , 25%) from Alkaloid AD, Skopje. Potassium chloride (KCl) and nitric acid (HNO_3 , $\geq 65\%$) were obtained from Kemika. All chemicals were used as received, without any further purification. Deionized water (dH_2O) supplied by a water purification unit (MilliporeSigma, Burlington, USA) was used throughout the experiments. Neodymium(III) oxide (Nd_2O_3) obtained from Sigma Aldrich was used for the synthesis of neodymium(III) nitrate hexahydrate ($\text{Nd}(\text{NO}_3)_3 \cdot 6\text{H}_2\text{O}$).

2. 1. Synthesis of $\gamma\text{-Fe}_2\text{O}_3\text{-NH}_4\text{OH@SiO}_2(\text{APTMS})$

For the preparation of the maghemite-silica core@shell MNPs the protocol described by Kegl et al. was used.³⁵ In brief, the $\gamma\text{-Fe}_2\text{O}_3$ magnetic nanoparticles were obtained by a co-precipitation method. To prepare 50 mL of 0.5 M $\text{Fe}^{2+}/\text{Fe}^{3+}$ solution in dH_2O , $\text{FeCl}_2 \cdot 4\text{H}_2\text{O}$ and $\text{FeCl}_3 \cdot 6\text{H}_2\text{O}$ were used in molar ratio 1:2. 25% ammonia solution (150 mL) was added to a round-bottomed flask and heated under reflux and constant stirring at 300 rpm. The temperature was maintained at 87 °C. Prepared 0.5 M $\text{Fe}^{2+}/\text{Fe}^{3+}$ solution (50 mL) was added instantaneously to the reaction mixture and kept for 1 h at 87 °C and pH 10.6. The obtained black coloured precipitate was then thoroughly rinsed with dH_2O and separated from the supernatant using a permanent magnet. Rinsed $\gamma\text{-Fe}_2\text{O}_3$ particles were stabilized in 25 mL of 25% ammonia solution at 50 °C under constant stirring at 300 rpm for 24 h. The obtained particles were precipitated from the reaction mixture by a permanent magnet.

The $\gamma\text{-Fe}_2\text{O}_3\text{-NH}_4\text{OH}$ particles were functionalized by SiO_2 and APTMS. 2-propanol (66 mL), dH_2O (15.42 mL), ammonia solution (1.7 mL, 25%), TEOS (0.324 mL, 99%) and APTMS (0.518 mL) were added to 4.93 mL aqueous dispersion of $\gamma\text{-Fe}_2\text{O}_3\text{-NH}_4\text{OH}$. The reaction was carried out for 24 h in a closed vessel at room temperature and stirring at 500 rpm. The $\gamma\text{-Fe}_2\text{O}_3\text{-NH}_4\text{OH@SiO}_2(\text{APTMS})$ particles were precipitated from the reaction mixture by a permanent magnet and washed two times with ethanol and dH_2O , respectively.

2. 2. Synthesis of $\text{Nd}(\text{NO}_3)_3 \cdot 6\text{H}_2\text{O}$

Neodymium nitrate hexahydrate ($\text{Nd}(\text{NO}_3)_3 \cdot 6\text{H}_2\text{O}$) was synthesised from neodymium oxide (Nd_2O_3) powder. First, a small quantity of dH_2O was added to cover the Nd_2O_3 powder, followed by HNO_3 ($\geq 65\%$). Nd_2O_3 and HNO_3 were used in molar ratio 1:2. The solution was heated to 90 °C and mixed in a closed beaker to achieve a clear solution. When Nd_2O_3 was completely dissolved and the solution was clear, the liquid content of the mixture was

evaporated at 110 °C. The collected light purple crystals were dried at room temperature.

2. 3. Adsorption Protocol

Stock solutions of 0.05 M, 0.025 M and 0.01 M $\text{Nd}(\text{NO}_3)_3 \cdot 6\text{H}_2\text{O}$ were prepared by dissolving an appropriate amount of obtained salt in dH_2O . Adsorption experiments were conducted by mixing 5 mL of the stock solution with 12 mg of magnetic nanoparticles ($\gamma\text{-Fe}_2\text{O}_3\text{-NH}_4\text{OH@SiO}_2(\text{APTMS})$). Functionalized magnetic nanoparticles were dispersed in the stock solution by placing the sample in an ultrasonic bath (Iskra PIO, Sonis 10) for 3 hours. After the reaction time, the adsorbent was separated from the solution by an external magnet, centrifugation at 11000 rpm for 5 min (Eppendorf, centrifuge 5804 R), and filtration with 200 nm and/or 20 nm pore-size filters (Whatman, Anotop 25), to remove the remaining nano-adsorbent.

2. 4. Characterization

The thermal behaviour and stability of the magnetic nanoparticle samples was studied using a Mettler Toledo TGA/DSC1 thermogravimetric analyser in air and N_2 atmosphere, respectively, at a gas flow rate of 100 mL/min. The TGA curves with the weight pattern and heat flow were recorded as a function of temperature in the range of 25–600 °C with a heating rate of 10 °C/min, using alumina crucibles. The used MNPs were pre-dried for 24 hours at 80 °C.

The presence of 6 mol of water in $\text{Nd}(\text{NO}_3)_3 \cdot 6\text{H}_2\text{O}$ was confirmed using the same thermogravimetric analyser by direct heating in the range of 25–700 °C at a heating rate of 10 °C/min in N_2 , O_2 and air atmosphere with 50 mL/min flow rate.

To confirm the formation of Nd_2O_3 , X-ray diffraction (XRD) analysis was conducted after TGA analysis using an X'Pert PRO (PANalytical) X-ray diffractometer coupled with $\text{Cu K}\alpha$ radiation with a wavelength of 0.15406 nm. The measurement was performed at room temperature with a time step of 100 s in the angular range of 10° to 70° with a step size of 0.034°. Fully open (2.122) X'Celerator detector was used in the measuring protocol.

The Brunauer, Emmet and Teller (BET) theory was used to determine the specific surface area of the nanoparticles by using the Micromeritics Tristar II 3020 Surface Area and Porosity system. The samples were degassed at 40 °C for 24 hours prior to each measurement by using the Micromeritics FlowPrep 060 Gas Adsorption Sample Preparation Device. Specific surface area was determined in the relative pressure range of 0.05–0.3 in nitrogen gas and temperature of –195.8 °C.

A Perkin Elmer Spectrum GX ATR-FTIR spectrometer was used to confirm the grafting of the organic ligands to the surface of the MNPs. Spectra were recorded over the

range of 4000 cm^{-1} to 400 cm^{-1} in transmission mode at a resolution of 4 cm^{-1} . Samples were dried for 24 h at $80\text{ }^{\circ}\text{C}$, ground into a fine powder, placed on the ATR crystal, and pressed into a thick film.

Transmission electron microscopy (TEM) images were obtained to analyse the morphology and size distribution of the nanoparticles. TEM analyses were performed with a JEOL 2010F model transmission electron microscope operating at 200 kV. The sample was prepared in a water solution, dropped onto a carbon-copper grid, and dried at room temperature. Digital Micrograph and OriginPro 2015 software were used for image analysis.

Zeta potential and size of the MNPs were measured using a Malvern Zetasizer Nano ZS with automatically chosen settings. Size characterization of the samples was made by dynamic light scattering (DLS) measurements with a 4 mW He–Ne laser operating at a wavelength of 633 nm, and a detection angle of 173° (backward scattering). A disposable cuvette was filled up to 1 cm with the particle dispersion. The zeta potential was measured using a combination of electrophoresis and laser Doppler velocimetry. For all measurements, a voltage of 50 V was applied. The attenuator index and measurement position are automatically adjusted by the software. For zeta potential measurements a folded capillary cell was used. Nanoparticle titration was performed using the Malvern MPT-2 Autotitrator in parallel with the Zetasizer Nano ZS. A titration from neutral to high pH using 0.1 M NaOH was performed to determine the isoelectric point (IEP). A subsequent titration from high to low pH with 0.1 M HCl was performed to determine the reversibility of the zeta potential. The concentration of MNPs in dH_2O was 0.01% V/V.

UV-Vis absorption spectra of Nd^{3+} solutions were recorded in the range of 200–800 nm using a Varian Cary 1 UV-Vis spectrophotometer and a quartz cuvette. For the preparation of the reference sample, magnetic nanoparticles (12 mg) were added to 1 mM KCl (5 mL). After 3 hours the MNPs were separated from the solution by an external magnet, centrifugation (11000 rpm, 5 min), and filtration with 200 nm and/or 20 nm pore-size filters. As samples, 5 mL of $\text{Nd}(\text{NO}_3)_3 \cdot 6\text{H}_2\text{O}$ stock solution of different concentrations (0.05, 0.025, 0.01 M, respectively) and MNPs (12 mg) were used.

3. Results and Discussion

The results of TGA of MNPs in air (blue curve) and nitrogen (red curve) atmosphere are displayed in Fig. 1, where the mass loss in percentages of $\gamma\text{-Fe}_2\text{O}_3\text{-NH}_4\text{OH@SiO}_2(\text{APTMS})$ NPs by heating up to $600\text{ }^{\circ}\text{C}$ is presented. The TGA curves show that the mass loss in both atmospheres occurs in one major step. In the range from $30\text{ }^{\circ}\text{C}$ to $180\text{ }^{\circ}\text{C}$ absorbed alcohol and water molecules evaporate from the MNPs surface. The interval from $280\text{ }^{\circ}\text{C}$ to $600\text{ }^{\circ}\text{C}$ is associated with the thermal decomposition of amino

groups (NH_2) and the removal of the alkyl chains of silanes from the silica coating.^{11,35,36} Around $550\text{ }^{\circ}\text{C}$ the transition of maghemite to hematite occurs without any mass change.³⁷

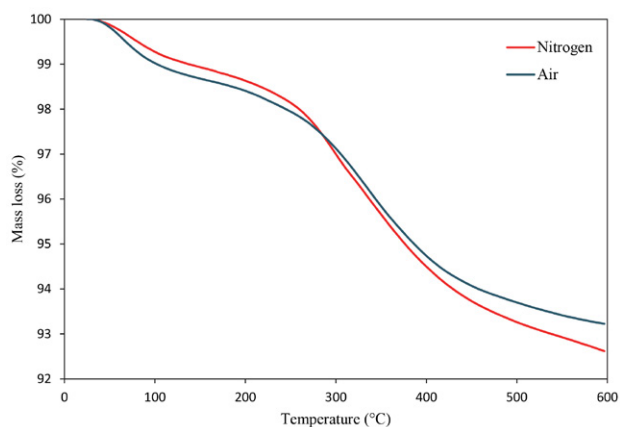


Figure 1: Mass loss of $\gamma\text{-Fe}_2\text{O}_3\text{-NH}_4\text{OH@SiO}_2(\text{APTMS})$ in N_2 and air atmosphere

The mass loss in air atmosphere corresponds to 6.7% of the sample weight. In N_2 atmosphere the mass loss presents 7.3% of the sample weight. The difference in mass loss between both atmospheres is 0.6%. Both curves show the same trend for the evolution of the mass loss with temperature. We cannot see any additional effect of oxygen on MNPs and therefore no significant sign of oxidation.

The thermal decomposition of $\text{Nd}(\text{NO}_3)_3 \cdot 6\text{H}_2\text{O}$ is a complex step-wise process, which starts with the simultaneous condensation of 6 mol of the initial monomer $\text{Nd}(\text{NO}_3)_3 \cdot 6\text{H}_2\text{O}$ into the complex $[\text{Nd}(\text{NO}_3)_3 \cdot 6\text{H}_2\text{O}]_6$. The main volatile products of the thermal decomposition are water, nitric acid, the azeotrope of 68% HNO_3 and 32% H_2O , nitrogen dioxide and oxygen.³⁸ The results of TGA in air (blue curve), nitrogen (red curve) and oxygen (green curve) atmosphere are displayed in Fig. 2, where the mass loss in percentages of $\text{Nd}(\text{NO}_3)_3 \cdot 6\text{H}_2\text{O}$ by heating up to $700\text{ }^{\circ}\text{C}$ is presented.

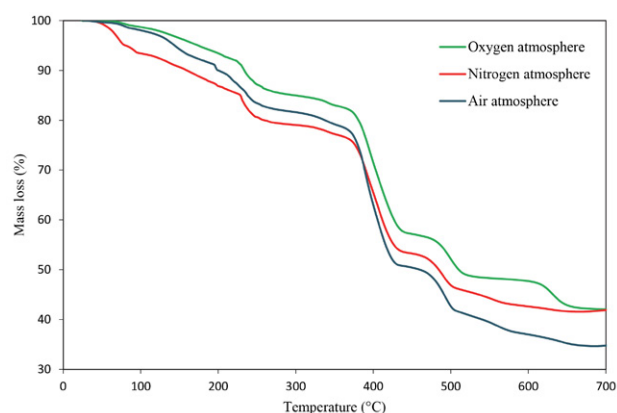


Figure 2: Mass loss of $\text{Nd}(\text{NO}_3)_3 \cdot 6\text{H}_2\text{O}$ in N_2 , O_2 and air atmosphere

The thermal decomposition of samples resulted in a mass loss of 58.4% in N₂, 58.1% in O₂ and 65.2% in air atmosphere. The formation of Nd₂O₃ as the final product of TGA was confirmed with XRD analysis.

The theoretical mass loss for the thermal decomposition of Nd(NO₃)₃·6H₂O is 61.6%.³⁸

There are no significant changes between oxidizing and inert atmospheres. All three curves have similar trends for the evolution of mass loss with temperature. The decomposition occurs in multiple steps, regardless of the atmosphere.

The stepwise mass loss in N₂ atmosphere is explained in accordance with the experimental results.³⁸ The first mass loss up to 62 °C reflects the evaporation of water during melting of the hexahydrate. It constitutes 2%, that corresponds to 3 mol of water out of 6 mol available at the beginning of the decomposition process, which are eliminated during evaporation. In the 62–358 °C range, the mass loss is 21.1%, representing the removal of 14 mol of H₂O and 5 mol of HNO₃. The next mass loss is 23.3% and it takes place in the range of 358–436 °C with the removal of 1 mol HNO₃, 5 mol of H₂O and 10 mol of NO₂. In the range of 436–513 °C 6 mol of H₂O and 2 mol of NO₂ are removed, constituting the mass loss of 7.6%. The final mass loss equals 4.4% and takes place in the range of 513–660 °C where 5 mol of H₂O and 1 mol of O₂ are removed. The remaining mass becomes constant at around 660 °C. The sum of the partial losses yields 58.4% and the presence of 6 mol of water in Nd(NO₃)₃·6H₂O was confirmed.

The BET analysis gave specific surface area of 78.27 m²/g for γ-Fe₂O₃-NH₄OH@SiO₂(APTMS). BJH adsorption average pore width for γ-Fe₂O₃-NH₄OH@SiO₂(APTMS) is 14.07 nm and desorption average pore width is 13.85 nm with total pore volume of 0.32 cm³/g.

Infrared spectra of synthesized nanoparticles γ-Fe₂O₃-NH₄OH (black spectrum), γ-Fe₂O₃-NH₄OH@

SiO₂(APTMS) (blue spectrum) and Nd³⁺/ γ-Fe₂O₃-NH₄OH@SiO₂(APTMS) (green spectrum) are shown in Fig. 3.

The absorption peak at 3380.21 cm⁻¹, attributed to N-H and O-H bonds, is observed in all spectra and it is the broadest band. By comparing the spectra of the coated and the uncoated MNPs, it is observed that the band at 3380.21 cm⁻¹ is less pronounced and shallower for the coated nanoparticles than for the γ-Fe₂O₃-NH₄OH nanoparticles, indicating the presence of the SiO₂ shell. The presence of Nd³⁺ on coated MNPs is visible by an even reduced intensity of the peak at 3380.21 cm⁻¹, which indicates a successful adsorption of Nd³⁺ ions on MNPs. The absorption band observed at 1627.39 cm⁻¹ is found in all three samples and corresponds to the N-H bending vibration. The peak found at 1020.92 cm⁻¹ corresponds to the asymmetric stretching vibration of the Si-O-Si bond and confirms the silanol functional groups grafted on the surface of γ-Fe₂O₃-NH₄OH particles. The peak observed at 542.16 cm⁻¹ belongs to the stretching vibration of Fe-O, which confirms the presence of the magnetic core. When comparing uncoated and coated MNPs this peak shifts from 540.46 cm⁻¹ to 542.16 cm⁻¹.

When Nd³⁺ is complexed with γ-Fe₂O₃-NH₄OH@SiO₂(APTMS) nanoparticles, a new peak at 1307.39 cm⁻¹ could be observed in the spectrum. Due to the adsorption of Nd³⁺ two peaks shift to a higher wavenumber. The peak at 542.16 cm⁻¹, which corresponds to the stretching vibration of Fe-O, is shifted to 548.99 cm⁻¹. The peak at 1020.92 cm⁻¹, which corresponds to the asymmetric stretching vibration of the Si-O-Si bond, is shifted to 1022.44 cm⁻¹. The ATR-FTIR absorption spectra confirm the composition of the synthesised magnetic nanoparticles, the successful coating with SiO₂(APTMS), and the adsorption of Nd³⁺.

The TEM photos in Fig. 4 A-C display the morphology of the MNPs with increasing magnification.

The magnetic nanoparticles have a diameter ranging between 2.5 nm and 22.5 nm, with an average particle size of 9.5 ± 1.9 nm (Fig. 4 D). This value is an estimate of size, analysed from 81 particles, as it is difficult to determine the real size of individual particles due to agglomerates and blurred boundaries between particles. Aggregation of particles results in wider size variation. None of the crystalline particles are ideally spherical, as their surface ends with a crystal plane, which is not curved. If nanoparticles are formed in a way that they can achieve an equilibrium structure, they will assume an octahedral form. But since the precipitation is an instantaneous process, we usually get incomplete shapes, which are somewhere in between a sphere and an octahedron. As shown in Fig. 4 C the particle is octahedral, but because of orientation and 2D projection of TEM images it looks like a hexagon. In Fig. 4 B and C a surface layer of amorphous SiO₂ is visible surrounding the Fe₂O₃ core, which confirms the successful coating of the MNPs.

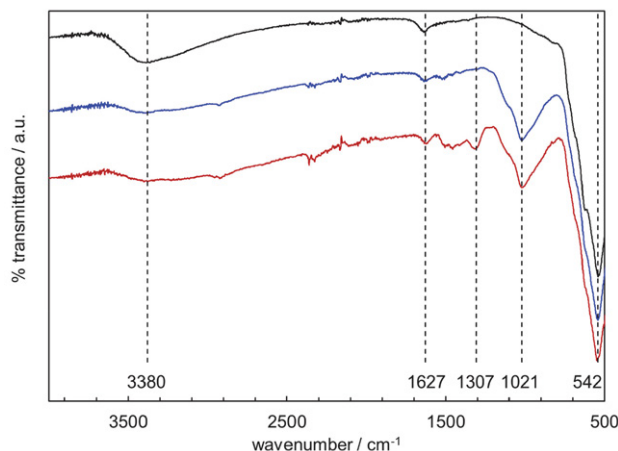


Figure 3: ATR-FTIR spectra of γ-Fe₂O₃-NH₄OH (top curve, black), γ-Fe₂O₃-NH₄OH@SiO₂(APTMS) (middle curve, blue) and Nd³⁺/γ-Fe₂O₃-NH₄OH@SiO₂(APTMS) (bottom curve, green)

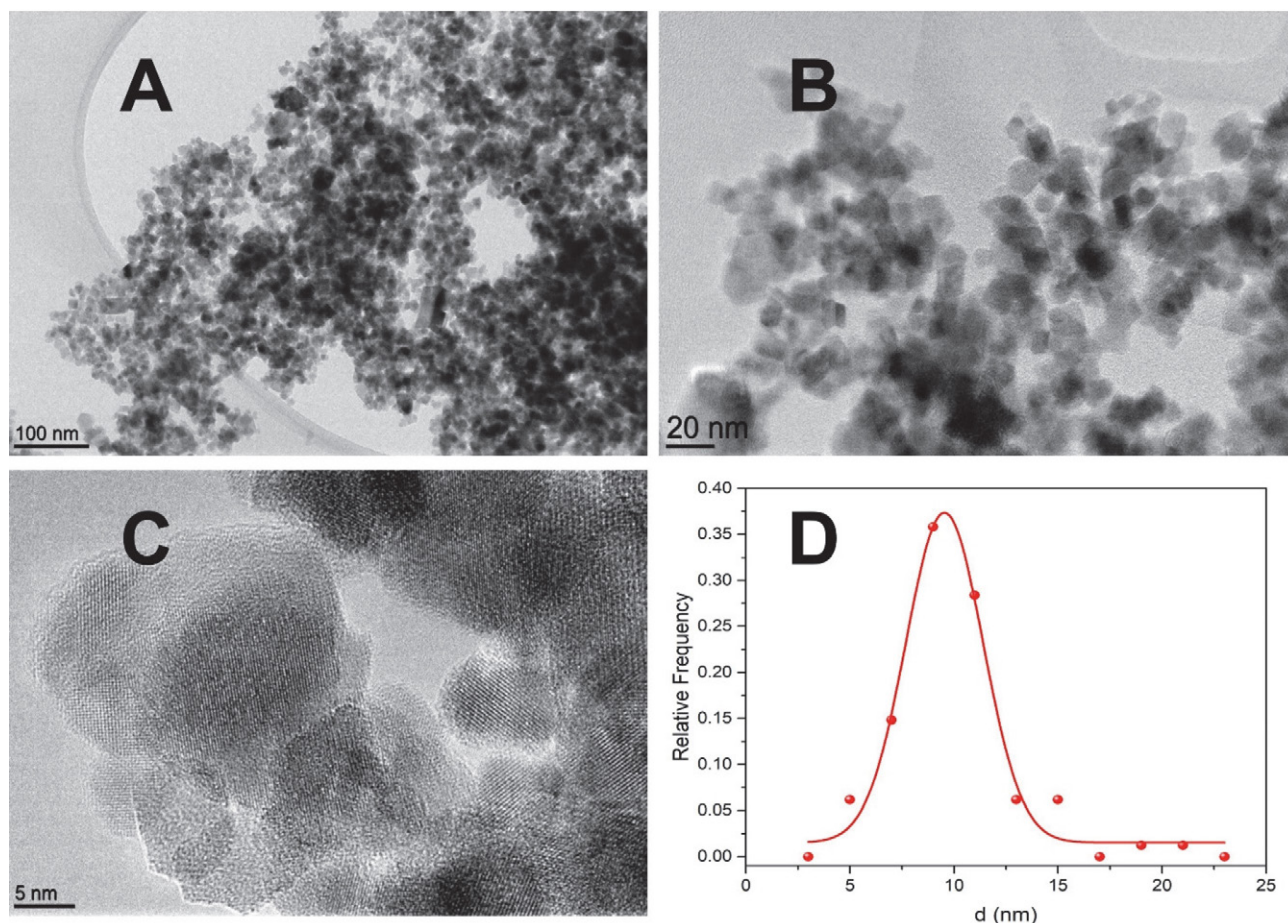


Figure 4: TEM images of $\gamma\text{-Fe}_2\text{O}_3\text{-NH}_4\text{OH@SiO}_2(\text{APTMS})$ with increasing magnification (A: scale bar 100 nm, B: 20 nm, C: 5 nm) and size distribution of MNPs (D).

The measuring parameters and the specificity of each measurement technique often result in different sizes for the same sample. Dynamic light scattering (DLS) is compared with transmission electron microscopy (TEM) for the characterization of the size distribution of magnetic nanoparticles. TEM measures the geometric size of dry MNPs deposited on a support surface under ultrahigh vacuum conditions. The DLS technique measures the hydrodynamic diameter that refers to how a particle diffuses within a liquid. Consequently, results obtained from DLS show a larger diameter than those from TEM. The significant difference in size between DLS and TEM results may be explained by an increased size in DLS due to the presence of the dispersant and the formation of hydrate layers. The presence of bigger particles and aggregates enhances light scattering and can also contribute to larger size values. Even though boundaries between particles in aggregates are not always obvious to recognize when analysing TEM images, the MNP size distribution observed by the TEM image-processing technique had a narrower range than that of DLS analysis.

Fig. 6 shows the pH dependence of the particle size and the zeta potential for 0.01% V/V MNPs in dH_2O . DLS

reveals a hydrodynamic diameter of 250 nm at the current pH 7 of the MNP dispersion in dH_2O . The TEM image in Fig. 4A already suggests larger aggregates of primary nanoparticles, which maintain their assembly when dispersed in water. A pH titration was first performed from the native pH 7 to pH 11 using 0.1 mol/L NaOH (measurement 1). Above pH 8, the particle size shows a sudden increase and approaches a steady diameter of 3 μm at pH 9. At higher pH we observe the onset of a trend towards smaller size, but the scatter of data disables a firm conclusion on a decreasing diameter. The direction of the pH change was then reversed by a titration towards the acidic range using 0.1 mol/L HCl. The diameter of 3 μm remains down to pH 8 followed by a sudden decrease and an approach of the initial diameter of 250 nm at pH 5. Below pH 3 we may assume again the onset of a trend towards a small growth of the particle aggregates. Although the changes in the hydrodynamic diameter of the MNPs is obviously fully reversible, we observe a hysteresis of the evolution of particle size with pH between the titrations to high and low pH, respectively.

To understand the pH dependence of the particle size, the zeta potential of the MNPs was recorded in paral-

lel. The zeta potential is the key parameter that controls electrostatic interactions in particle dispersions, provides information about surface functionality and determines the dispersion stability. The zeta potential for particle dispersions is calculated from the measurement of the electrophoretic mobility by electrophoretic light scattering (ELS). At pH 7 a positive zeta potential of $\zeta = +30$ mV was observed, which indicates a significant positive charge density at the nanoparticle-water interface and confirm the presence of the amine functional groups of the outermost APTMS coating of the core@shell maghemite nanoparticles. The amine groups get protonated in water and assume a positive charge.³⁹ When increasing the pH of the aqueous dispersion of the MNPs, the zeta potential decreases and approaches the isoelectric point (IEP) at pH 9.8. Beyond the IEP the zeta potential assumes a negative sign indicating the charge reversal of the MNPs. The IEP 9.8 is indicative for the moderately basic character of the aminosilane.⁴⁰ When continuing the pH titration from the alkaline to the acidic range, the zeta potential increases again and shows a charge reversal of the MNPs at a lower IEP 8.5. The electrokinetic charge density achieves a steady state indicated by the plateau value of the zeta potential of $\zeta = +35$ mV below pH 5. We observe the same hysteresis for the pH dependence of the zeta potential and of the particle size when repeating the titration from high to low pH.

As a rule of thumb, a zeta potential below $-25 \dots -30$ mV or above $+25 \dots +30$ mV describes a stable dispersion where the aggregation of nanoparticles is suppressed by the electrostatic repulsion of particles with alike charge.⁴¹ This empirical observation is confirmed by the correlation of the hydrodynamic diameter and the zeta potential of MNPs shown in Fig. 5.

As the initial zeta potential drops below $\zeta = +25$ mV, the size of the MNPs starts to increase indicating the onset of the formation of larger aggregates. As the zeta potential approaches the IEP, the electrostatic repulsion between MNPs becomes weaker, and the average size of the particle aggregates, which remain suspended in dH₂O, obtains its maximum diameter of 3 μm . Above the IEP 9.8, the negative zeta potential steadily increases thereby introducing repulsive electrostatic forces between MNPs, which are now negatively charged. Since the zeta potential at pH 11 does not exceed the empirical threshold of $\zeta = \pm 25$ mV, its effect on the disaggregation of particle assemblies remains rather small.

In the opposite direction of the pH titration, the threshold value of $\zeta = +25$ mV is observed at pH 6.5 where the hydrodynamic diameter returns to 250 nm, which is the average size of the MNP aggregates in dH₂O. At very low pH, the significant volume of acid (0.1 mol/L HCl) added to decrease pH introduces a simultaneous increase in the ionic strength of the aqueous solution. Although the scatter of results in the range of pH 2.5–4 does not allow a conclusion on a decrease in the zeta potential, the electric double layer at the MNP-water interface gets suppressed at

higher ionic strength, which again weakens the repulsive force between positively charged MNPs.

The hysteresis observed when repeating the analysis of the pH dependence of the zeta potential and the shift of the IEP from pH 9.8 (for the first titration) to pH 8.5 (for the second titration) indicate a decrease in the average basic strength of the functional coating of the MNPs. Obviously, the stability of the silane coating on the silica shell of the MNPs at higher pH is limited.

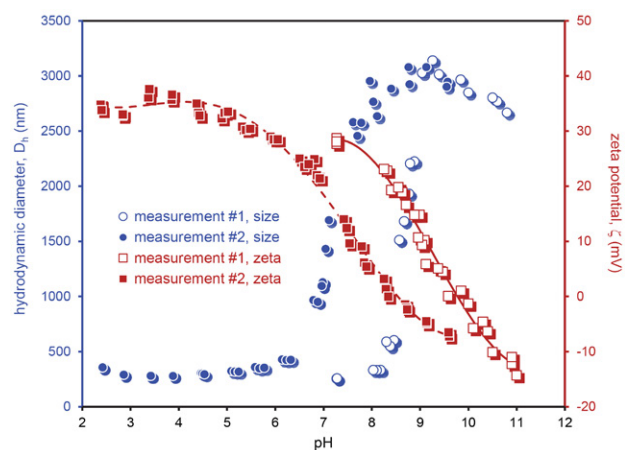


Figure 5: pH dependence of zeta potential and particle size for a dispersion of 0.01% V/V MNPs in dH₂O

3. 1. Adsorption of Nd³⁺ Ions

To elucidate the efficiency of Nd³⁺ ion adsorption on MNPs, an appropriate analytical method for quantification of the adsorption process was selected. The concentration of Nd³⁺ ions adsorbed on the MNP surface or the depletion of Nd³⁺ ion concentration in the aqueous solution may be determined. There have been many analytical techniques used for the determination of the REEs in solid and solution samples; flame or graphite furnace atomic absorption spectrometry, atomic absorption with chemical vapor generation, X-ray fluorescence spectrometry (XRF), inductively coupled plasma optical emission spectrometry (ICP-OES), inductively coupled plasma mass spectrometry (ICP-MS), high-performance liquid chromatography (HPLC) and neutron activation analysis (NAA).^{41–43} Among the methods presented above for the characterization of various properties of the MNPs (composition, functional groups, size, charge), ATR FTIR and ELS may be considered to exhibit changes in the IR spectrum and in the zeta potential, respectively, of MNPs before and after adsorption of Nd³⁺ ions.

As shown in Fig. 3, the ATR FTIR spectrum of the core@shell MNPs after adsorption of Nd³⁺ ions indicates the presence of neodymium by the additional peak at 1307 cm⁻¹. The intensity of this peak compares with the peak indicating the N-H bending vibration (at 1627 cm⁻¹) and is likely assigned to a vibration of the assumed Nd-NH

surface complex that shows responsible for the adsorption of Nd^{3+} ions on the positively charged $\gamma\text{-Fe}_2\text{O}_3\text{-NH}_4\text{OH@SiO}_2(\text{APTMS})$ nanoparticles. Since the intensity of the peak at 1307 cm^{-1} is rather weak and a calibration protocol is thus not feasible to correlate peak intensity with Nd surface concentration, ATR FTIR is only applicable to qualitatively confirm the presence of Nd.

The zeta potential is occasionally applied to describe and to study the adsorption process of dissolved compounds such as surfactants, polymers (polyelectrolytes, polysaccharides), or proteins on material surfaces.^{44–46} It is therefore feasible to investigate the capability of ELS for monitoring the adsorption of Nd^{3+} ions on MNPs although the same positive sign of the charge reduces the sensitivity of zeta potential analysis for the characterization of adsorption processes.

Table 1 shows the zeta potential of MNPs remaining in dispersion after an apparent separation by an external magnet followed by centrifugation and filtration with a 200 nm filter after adsorption of Nd^{3+} ions from aqueous solutions of $\text{Nd}(\text{NO}_3)_3$ with different bulk concentration (0.01, 0.025, 0.05 mol/L, respectively). The average zeta potential and the standard deviation were obtained from three repetitive measurements.

A steady decrease in the positive zeta potential was found from $\zeta = +47.7 \pm 4.2\text{ mV}$ after adsorption from a 0.01 mol/L Nd^{3+} to $\zeta = +23.4 \pm 2.4\text{ mV}$ when the initial concentration of Nd^{3+} ions was 0.05 mol/L. In the same series, the conductivity of the corresponding solutions increased from 406 mS/m to 1366 mS/m. The dependence of the zeta potential on the ionic strength is therefore dominating the decrease in the magnitude of the positive zeta potential of remaining MNPs in dispersion. Independent of the zeta potential and the ionic strength, the particle size remains at $D_h = 80.5 \pm 0.8\text{ nm}$. This hydrodynamic diameter is significantly smaller than the size of $D_h = 256\text{ nm}$ of the MNPs determined in the MNP stock solution in deionized water. The difference in the particle size is explained by the removal of the larger fraction of MNPs by filtration with a 200 nm filter. The zeta potential of the bulk dispersion of MNPs in dH_2O reads $\zeta = +28.2 \pm 0.5\text{ mV}$. This zeta potential is only 60% of the zeta potential determined in 0.01 mol/L $\text{Nd}(\text{NO}_3)_3$ (the lowest Nd^{3+} ion concentration used in the series of adsorption experiments) although the conductivity of the MNP bulk dispersion (18.4 mS/m) is much lower than the corresponding conductivity (406 mS/m) of 0.01 mol/L Nd^{3+} . If the diminishingly small ionic strength of deionized water is considered, the Hückel approach for the calculation of the zeta potential can be used, which transfers $\zeta = +28.2\text{ mV}$ determined in the Smoluchowski limit to $\zeta = +42.3\text{ mV}$ and therefore closer to the zeta potential obtained in the 0.01 mol/L Nd^{3+} solution. However, the conductivity of the bulk MNP dispersion of 18.4 mS/m is multiple times higher than the conductivity expected for

dH_2O (theoretically 0.006 mS/m) indicating a significant contribution of the charged MNPs to the electric conductance of the aqueous dispersion. A conductivity of 18.4 mS/m corresponds to an ionic strength of approx. 0.001 mol/L when considering a monovalent electrolyte such as NaCl or KCl. This ionic strength justifies the application of the Smoluchowski approach for the calculation of the zeta potential especially when considering the average particle diameter of 256 nm. It can be concluded that either the influence of the particle size and/or the high concentration of MNPs in the bulk dispersion affect the electrophoretic mobility and thus the zeta potential.

In conclusion, the strong dependence of the zeta potential on the ionic strength does not qualify this method for the estimation of the surface concentration of adsorbed Nd^{3+} ions on the MNPs.

Table 1: Zeta potential (ζ) and hydrodynamic diameter (D_h) of MNPs after adsorption of Nd^{3+} ions from aqueous solution with different bulk concentration of $\text{Nd}(\text{NO}_3)_3$.

Nd^{3+} bulk concentration (mol/L)	Conductivity (mS/m)	ζ (mV)	D_h (nm)
0 *	18.4	28.2 ± 0.5	256
0.01	406	47.7 ± 4.2	81.3
0.025	906	34.1 ± 3.4	80.3
0.05	1366	23.4 ± 2.4	79.8

* MNPs dispersed in dH_2O , i.e., without separation

For monitoring the depletion of Nd^{3+} ions in solution upon adsorption on MNPs, the optical properties of aqueous solutions of this REE suggest the application of UV-Vis spectroscopy. Fig. 6 shows the UV-Vis spectrum of aqueous solutions of $\text{Nd}(\text{NO}_3)_3$ at different concentration (0.01, 0.025, 0.05 mol/L, respectively) in the wavelength range of 540–780 nm. In this range we find two distinct absorption peaks at 575 nm and 740 nm, which may be assigned to the electronic f-f transitions $^4\text{I}_{9/2} \rightarrow ^2\text{G}(1)_{7/2}$ and $^4\text{G}_{5/2}$ (575 nm, 17391 cm^{-1}) and $^4\text{I}_{9/2} \rightarrow ^4\text{F}_{7/2}$ (740 nm, 13514 cm^{-1}).⁴⁷ The absorbance recorded at these peaks was used to establish calibration curves for the estimation of the Nd^{3+} ion concentration from the measured absorbance after completing the adsorption process on MNPs. The corresponding calibration curves are shown in the inset of Fig. 6. Coincidentally at a given Nd^{3+} concentration, the peaks at 575 nm and 740 nm show almost the same absorbance.

Fig. 6 also shows the UV-Vis spectra obtained after adsorption of Nd^{3+} on MNPs in solutions with the corresponding Nd^{3+} starting concentration (0.01, 0.025 and 0.05 mol/L, respectively) after separation of the MNPs by an external magnet, centrifugation and filtration using a

filter with 200 nm pores. We do not find any decrease in the absorbance for both f-f transition peaks, which suggests that adsorption of Nd^{3+} ions on $\gamma\text{-Fe}_2\text{O}_3\text{-NH}_4\text{OH@SiO}_2(\text{APTMS})$ nanoparticles did not occur. However, upon filtration of the supernatant obtained after centrifugation of the MNP dispersion, that is remaining after applying an external magnet, with a 20 nm filter, the absorbance decreases consistently for the peaks at both 575 nm and 740 nm. The evaluation of the depletion of Nd^{3+} from the stock solution using the UV-Vis calibration curves reveals a removal of 30% at pH 7 and after 3 h of interaction time. DLS and ELS measurements of the filtrate still show clear distributions of size and zeta potential with $D_h = 51$ nm and $\zeta = +17.8 \pm 1.8$ mV. We note that (i) small aggregates of primary MNPs pass the 20 nm filter and (ii) the filter shows a small rejection at the nominal threshold of 20 nm. The measured conductivity in the filtrate reads 1176 mS/m, which is 14% lower than the conductivity in the filtrate of the 200 nm filter. We may thus assume a larger zeta potential but observe the opposite. Obviously, the different size fractions of MNPs exhibit different effective charge density represented by the difference in the zeta potential. The presence of MNPs in the filtrate of the 20 nm filter suggests a contribution of Nd^{3+} adsorbed on these MNPs to the UV-Vis absorption spectrum. The removal efficiency is therefore expected slightly higher than the estimated 30%.

4. Conclusions

Magnetic nanoparticles with a $\gamma\text{-Fe}_2\text{O}_3$ core, coated with SiO_2 and functionalized with APTMS, were synthesized with the purpose of removing rare earth elements from aqueous solutions. The main reason for selecting Nd^{3+} as the source of REE is the fact that neodymium is one of the most important REE in terms of usage and applicability. Furthermore, neodymium is among those REEs that show a lot of absorption peaks in the visible spectrum, which makes UV-Vis absorption spectroscopy convenient for the determination of the Nd^{3+} concentration in solution. The synthesized MNPs were characterized in terms of size (TEM, DLS), charge (zeta potential; ELS), surface functionality (ATR-FTIR), and composition (TGA, XRD). The adsorption of Nd^{3+} on $\gamma\text{-Fe}_2\text{O}_3\text{-NH}_4\text{OH@SiO}_2(\text{APTMS})$ was performed in batch mode. The UV-Vis calibration curves revealed maximum adsorption to be 30% at pH 7, with use of 12 mg of MNPs in 0.05 mol/L of neodymium solution. Based on the results, an obvious decrease in neodymium concentration becomes visible only after a reaction time of 3 hours, which makes this process uneconomical for large-scale use. The removal of $\gamma\text{-Fe}_2\text{O}_3\text{-NH}_4\text{OH@SiO}_2(\text{APTMS})$ from dispersion after Nd^{3+} adsorption requires multiple steps (removal with a magnet, centrifugation, and filtration) in order to measure the absorbance spectrum without a significant interfer-

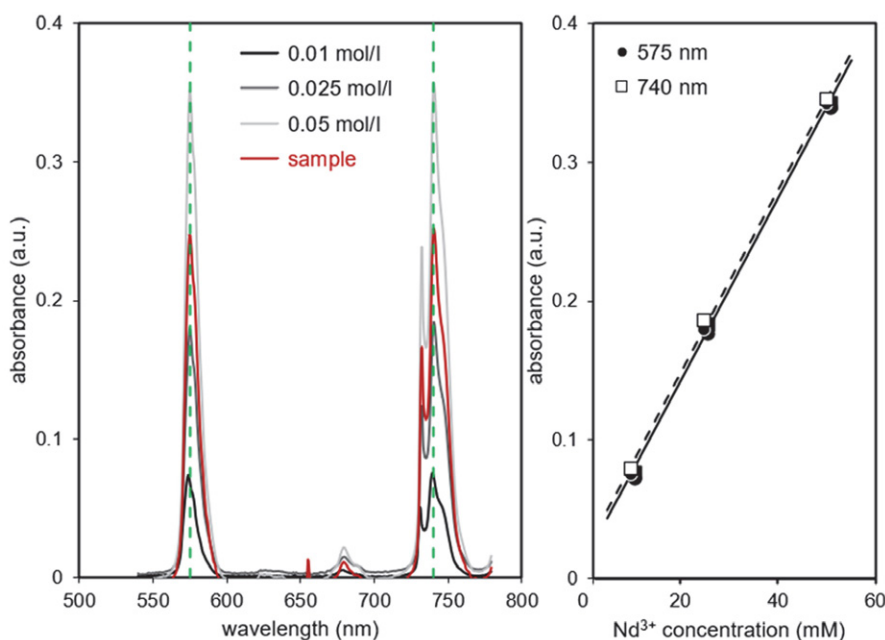


Figure 6: Absorbance spectra of Nd^{3+} before and after adsorption on MNPs. The labels of spectra recorded after adsorption indicate the filter used for removing MNPs (pore size 20 nm, 200 nm).

From the change in the absorbance for MNPs filtered with a 20 nm filter after adsorption of 0.05 M Nd^{3+} , we conclude that 0.035 M Nd^{3+} remain in solution. The adsorption efficiency after 3 hours is therefore 30%.

ence of MNPs remaining in the processed solution, which also requires time and adds additional steps to the process. Ban et al. reported the use of ultrafiltration to completely remove even the primary particles of MNPs.⁴⁸ The slow

adsorption of Nd^{3+} ions on $\gamma\text{-Fe}_2\text{O}_3\text{-NH}_4\text{OH@SiO}_2$ (APTMS) suggests a coating by different chelating compounds, such as polyethylenimine or negatively charged MNPs.³⁴

Acknowledgements

The authors acknowledge dr. Julija Volmajer Valh for her help with ATR-FTIR, dr. Sašo Gyergyek for TEM analysis, Edi Kranjc for XRD analysis, and dr. Karl Gatterer of Graz University of Technology for donating Nd_2O_3 .

5. References

1. D. A. Atwood: The rare earth elements: Fundamentals and Applications, John Wiley & Sons Ltd, **2012**, pp. 2–27.
2. J. H. L. Voncken: The Rare Earth Elements: An Introduction, Springer, **2016**, pp. 1–11. DOI:10.1007/978-3-319-26809-5
3. U.S. department of Energy, Critical Materials Strategy, https://www.energy.gov/sites/prod/files/DOE_CMS2011_FINAL_Full.pdf, (accessed: February 18, 2022)
4. V. Balaran, *Geosci. Front.*, **2019**, 10, 1285–1303. DOI:10.1016/j.gsf.2018.12.005
5. C. E. D. Cardoso, J. C. Almeida, C. B. Lopes, T. Trindade, C. Vale and E. Pereira, *Nanomater.*, **2019**, 9, 1–55. DOI:10.3390/nano9060814
6. K. Binnemans, P. T. Jones, B. Blanpain, T. Van Gerven and Y. Pontikes, *J. Clean. Prod.*, **2015**, 99, 17–38. DOI:10.1016/j.jclepro.2015.02.089
7. R. Ashour, R. Elsayed, A. F. Abdel-Magied, K. M. Forsberg, A. Uheida and M. Muhammed, *Chem. Eng. J.*, **2017**, 327, 286–296. DOI:10.1016/j.cej.2017.06.101
8. A. Negrea, A. Gabor, C. M. David, M. Ciopec, P. Negrea, N. Duteanu and A. Barbulescu, *Sci. Rep.*, **2018**, 8, 1–11. DOI:10.1038/s41598-017-18623-0
9. M. A. Agotegaray, V. L. Lassalle: Silica-coated Magnetic Nanoparticles: An Insight into Targeted Drug Delivery and Toxicology, Springer, **2017**, pp. 12–24. DOI:10.1007/978-3-319-50158-1
10. L. L. Vatta, R. D. Sanderson, K. R. Koch, *Pure Appl. Chem.*, **2006**, 78, 1793–1801. DOI:10.1351/pac200678091793
11. T. Kegl, A. Košak, A. Lobnik, I. Ban, Z. Novak and A. Kovač Kralj, *J. Hazard. Mater.*, **2019**, 386, 1–59. DOI:10.1016/j.jhazmat.2019.121632
12. S. Majidi, F. Zeinali Sehrig, S. Mussa Farkhani, M. Soleymani Goloujeh, A. Akbarzadeh, *Artif. Cells Nanomed. Biotechnol.*, **2016**, 44, 722–734. DOI:10.3109/21691401.2014.982802
13. Y. Bao, T. Wen, A. C. S. Samia, A. Khandhar, K. M. Krishnan, *J. Mater. Sci.*, **2016**, 51, 513–553. DOI:10.1007/s10853-015-9324-2
14. M. Sharma, P. Kalita, K. K. Senapati, A. Garg: Study on Magnetic Materials for Removal of Water Pollutants, **2018**, 61–78. DOI:10.5772/intechopen.75700
15. N. Zhu, H. Ji, P. Yu, J. Niu, M. U. Farooq, M. Waseem Akram, I. O. Udego, H. Li, X. Niu, *Nanomater.*, **2018**, 10, 1–27.
16. P. Xu, G. M. Zeng, D. L. Huang, C. L. Feng, S. Hu, M. H. Zhao, C. Lai, Z. Wei, C. Huang, G. Xin Xie and Z. Feng Liu, *Sci. Total Environ.*, **2012**, 424, 1–10. DOI:10.1016/j.scitotenv.2012.02.023
17. S. P. Gubin: Magnetic Nanoparticles, Wiley-VCH, **2009**, 25–58. DOI:10.1002/9783527627561
18. A. Jurgec, Funkcionalizirani magnetni nanodelci za odstranjevanje težkih kovin iz odpadnih vod, <https://dk.um.si/Izpis-Gradiva.php?id=74201&lang=slv>, (accessed: February 20, 2022)
19. I. Ali, C. Peng, I. Naz and M. A. Amjed: Magnetic Nanostructures, Springer, **2019**, 161–179.
20. J. Kudr, Y. Haddad, L. Richtera, Z. Heger, M. Cernak, V. Adam, O. Zitka, *Nanomater.*, **2017**, 9, 1–28.
21. A. M. Gutierrez, T. D. Dziubla, J. Z. Hilt, *Rev. Environ. Health*, **2017**, 32, 111–117. DOI:10.1515/reveh-2016-0063
22. O. Pereao, C. A. Bode-Aluko, O. Fatoba, K. Laatikainen, L. F. Petrik, *Desalination Water Treat.*, **2018**, 130, 71–86. DOI:10.5004/dwt.2018.22844
23. D. Dupont, W. Brullot, M. Bloemen, T. Verbiest and K. Binnemans, *ACS Appl. Mater. Interfaces.*, **2014**, 7, 4980–4988. DOI:10.1021/am406027y
24. O. Plohl, U. Ajdnik, S. Gyergyek, I. Ban, A. Vesel, T. Kraševac Glaser, L. Fras Zemljič, *J. Environ. Chem. Eng.*, **2019**, 7, 6777–6789. DOI:10.1016/j.jece.2019.102913
25. O. Plohl, M. Finšgar, S. Gyergyek, U. Ajdnik, I. Ban and L. Fras Zemljič, *Nanomater.*, **2019**, 209, 1–20. DOI:10.3390/nano9020209
26. R. M. Ashour, R. El-sayed, A. F. Abdel-Magued, A. A. Abdel-khalek, M. M. Ali, K. Forsberg, A. Uheida, M. Muhammed and J. Dutta, *J. Chem. Eng.*, **2017**, 327, 286–296. DOI:10.1016/j.cej.2017.06.101
27. D. Dupont, J. Luyten, M. Bloemen, T. Verbiest and K. Binnemans, *Ind. Eng. Chem. Res.*, **2014**, 53, 15222–15229. DOI:10.1021/ie502546c
28. A. A. Galhoum, M. G. Mafhouz, S. T. Abdel-Rehem, N. A. Gomaa, A. A. Atia, T. Vincent and E. Guibal, *Nanomater.*, **2015**, 5, 154–179. DOI:10.3390/nano5010154
29. A. A. Galhoum, M. G. Mafhouz, S. T. Abdel-Rehem, N. A. Gomaa, A. A. Atia, T. Vincent and E. Guibal, *Cellulose.*, **2015**, 22, 2589–2605. DOI:10.1007/s10570-015-0677-0
30. C. Gok, *J. Radioanal. Nucl. Chem.*, **2014**, 301, 641–651. DOI:10.1007/s10967-014-3193-z
31. J. Li, A. Gong, F. Li, L. Qiu, W. Zhang, G. Gao, Y. Liu and J. Li, *RSC Adv.*, **2018**, 68, 39149–39161.
32. E. Liu, X. Zheng, X. Xu, F. Zhang, E. Liu, Y. Wang, C. Li and Y. Yan, *NJC*, **2017**, 15, 7739–7750. DOI:10.1039/C7NJ02177A
33. A. Miraoui, M. A. Didi and D. Villemin, *JRNC*, **2016**, 307, 963–971. DOI:10.1007/s10967-015-4267-2
34. L. Molina, J. Gaete, I. Alfaro, V. Ide, F. Valenzuela, J. Parada and C. Basualto, *J. Mol. Liq.*, **2019**, 275, 178–191. DOI:10.1016/j.molliq.2018.11.074
35. S. D. Topel, E. Polido Legaria, C. Tiseanu, J. Rocha, J.-M. Nedelec, V. G. Kessler and G. A. Seisenbaeva, *J. Nanoparticle Res.*, **2014**, 2783.
36. V. Rocher, J. Manerova, M. Kinnear, D. J. Evans, *Dalton Trans.*, **2014**, 43, 2948–2952. DOI:10.1039/C3DT52386A

37. P. Melnikov, I. V. Arkhangelsky, V. A. Nascimento, L. C. S. de Oliveira, G. A. Wandekoken, D. Muniz de Albuquerque, *J. Therm. Anal. Calorim.*, **2019**, 1117–1121.
38. J. G. Smith: Organic Chemistry, McGraw-Hill, 3rd edition, **2011**, pp. 1075–1086.
39. P. Nygård, K. Grundke, E. Mäder, C. Bellmann, *J. Adhes. Sci. Technol.*, **2002**, 16, 1781–1808.
DOI:10.1163/156856102320396148
40. T. Luxbacher: The Zeta Potential for Solid Surface Analysis, Anton Paar GmbH, **2014**, pp. 10–138.
41. B. Zawisza, K. Pytlakowska, B. Feist, M. Polowniak, A. Kita, R. Sitko, *J. Anal. At. Spectrom.*, **2011**, 26, 2373–2390.
DOI:10.1039/c1ja10140d
42. A. Anggraeni, F. Arianto, A. Mutalib, U. Pratomo, H. H. Bah-ti: Mathematics, Science, and Computer Science Education (MSCEIS 2016): AIP Conf. Proc., **2017**.
43. E. Zolfonoun, S. R. Yousefi, *J. Braz. Chem. Soc.*, **2016**, 27, 1–6.
44. Z. Adamczyk, M. Nattich, M. Wasilewska, M. Zauha, *Adv. Colloid Interface Sci.*, **2011**, 168, 3–28.
DOI:10.1016/j.cis.2011.04.002
45. J. Ethève and P. Déjardin, *Langmuir*, **2002**, 18, 1777–1785.
DOI:10.1021/la011224d
46. C. Payerl, M. Bračić, A. Zankel, W. J. Fischer, M. Kaschowitz, E. Fröhlich, R. Kargl, F. Stelzer, S. Spirk, *Carbohydr. Polym.*, **2017**, 164, 49–56. DOI:10.1016/j.carbpol.2017.01.088
47. P. Caro, D. R. Svoronos, E. Antic, M. Quarton, *J. Chem. Phys.*, **1977**, 66, 215–220. DOI:10.1063/1.433910
48. I. Ban, S. Markuš, S. Gyergyek, M. Drofenik, J. Korenak, C. Helix-Nielsen, I. Petrinić, *J. Nanomater.*, **2019**, 9, 1–17.
DOI:10.3390/nano9091238

Povzetek

Magnetni nanodelci (MNP) so zaradi svoje hitre sinteze, vsestranske funkcionalizacije in možnosti recikliranja z uporabo magnetnega polja deležni vse večje pozornosti za različne aplikacije. Visoko razmerje med površino in prostornino disperzij MNP predstavlja zmožnost njihove uporabe kot adsorbenta za odstranjevanje ionov težkih kovin. Raziskali smo uporabnost MNP, sestavljenih iz maghemitnega jedra in obdanih s kremenčevo lupino, funkcionalizirano z amino-propilsilanom, $\gamma\text{-Fe}_2\text{O}_3\text{-NH}_4\text{OH@SiO}_2$ (APTMS), za odstranjevanje neodimovih ionov (Nd^{3+}) iz vodne raztopine. MNP so bili karakterizirani glede na velikost, sestavo, površinsko funkcionalnost in naboj. Kljub obetavnim lastnostim MNP pa njihova odstranitev iz vodne disperzije z zunanjim magnetom ni zadostovala za zanesljivo kvantificiranje adsorpcije Nd^{3+} z UV-Vis spektroskopijo.



Except when otherwise noted, articles in this journal are published under the terms and conditions of the Creative Commons Attribution 4.0 International License

Scientific paper

Ionic Liquid Supported on Magnetic Graphene Oxide as a Highly Efficient and Stable Catalyst for the Synthesis of Triazolopyrimidines

Azar Jahanbakhshi, Mahnaz Farahi* and Yeganeh Aghajani

Department of Chemistry, Yasouj University, Yasouj 75918-74831, Iran

* Corresponding author: E-mail: farahimb@yu.ac.ir

Received: 05-25-2022

Abstract

A novel sulfonic acid functionalized ionic liquid was prepared by anchoring 1-(propyl-3-sulfonate) vinylimidazolium hydrogen sulfate ($[(\text{CH}_2)_3\text{SO}_3\text{HVIm}]\text{HSO}_4$) on $\text{Fe}_3\text{O}_4@\text{GO}$. The prepared heterogeneous catalyst was characterized by XRD, FT-IR, EDX, SEM, VSM and TGA techniques. The results show that $[(\text{CH}_2)_3\text{SO}_3\text{HVIm}]\text{HSO}_4$ was successfully deposited on the surface of $\text{Fe}_3\text{O}_4@\text{GO}$ and the prepared ionic liquid catalyst exhibited good thermal stability. The activity of the prepared catalyst was investigated in the synthesis of triazolo[1,5-*a*]pyrimidine derivatives by a one-pot three-component reaction of active methylene compound (malononitrile or ethyl cyanoacetate), 3-amine-1*H*-1,2,4-triazole and aryl aldehydes under solvent-free conditions. This catalyst could be rapidly separated by an external magnet and recycled seven times without significant loss of catalytic activity.

Keywords: Ionic liquid; graphene oxide; triazolopyrimidines; Fe_3O_4

1. Introduction

Ionic liquids (ILs) are increasingly recognized as environmentally friendly materials, alternative reaction media, and promising catalysts due to their unique properties such as tunable acidity, selective solubility, negligible vapor pressure, wide liquid range, and high thermal stability.^{1,2} Ionic liquids have been developed for various specialty applications such as catalysts, fossil fuel desulfurization reagents, lubricants, and as monomers for the synthesis of ionic polymers. They are also known as “versatile chemicals” in various fields of synthetic chemistry.^{3,4} Among them, the acidic ionic liquids functionalized with sulfonic acid groups with a hydrogen sulfate counteranion have been intensively studied as a class of dual acid functionalized ILs because both the SO_3H functional groups and the hydrogen sulfate counteranion can increase their acidity. Despite the advantages of ionic liquids, their widespread use was still hindered by some disadvantages, such as intolerable viscosity, complex product isolation and catalyst recovery, high cost, and long reaction times.^{5,6} Immobilization of ionic liquids on various solid supports is one of the most efficient ways to overcome these problems. Ionic liquids on supports have the advantage of combining the properties of an ionic liquid with the typical advantages

of immobilization, such as easy recycling and improved selectivity in applications with catalytic activity.⁷ Heterogenization of ionic liquids on suitable porous supports,^{8–10} suitable magnetic nanoparticles,^{11–13} immobilized on solid supports, either by physical coating of the ionic liquids on Al_2O_3 ,^{14,15} SiO_2 ^{16,17} and TiO_2 ^{18,19} or by covalent bonding of the ionic liquids to the support surface, would be a feasible and attractive approach to prepare an efficient solid catalyst with superior activity and stability.²⁰ While reasonable reusability was observed in most cases, the dispersion of the ionic liquid on the solid support was poor, and leaching of the ionic liquid occurred, resulting in loss of activity.^{21,22} To overcome these drawbacks, graphene oxide (GO) can be used as a support material for immobilization of the ionic liquid with better dispersion, excellent activity, covalent bonding, and good reusability. In general, graphene oxide has some oxygen-containing functions (such as epoxy, carboxy and hydroxy groups). Therefore, it could be a promising candidate as an advantageous support for the immobilization of ILs.^{23–27} ILs on graphene oxide supports have advantages due to their physicochemical properties; nevertheless, it is the tedious and time-consuming separation procedures that limit their practical applications. In this context, the development of magnetic graphene oxide as a support material has shown promise.^{28–31}

In recent years, green chemistry has become one of the most important aspects of experimental and industrial efforts of chemists. Due to their high atomic efficiency and significant diversity, multicomponent reactions (MCRs) have occupied an essential place in the world of green chemistry.^{32–34} The multicomponent reaction is a powerful synthetic strategy in modern chemistry in which three or more simple components are involved as starting reagents in a one-pot system to obtain new complex molecules with lower processing costs compared to the stepwise method, which usually produces few byproducts. Multicomponent reactions are an advantageous tool for the synthesis of critical heterocyclic compounds that have many biological activities.^{35–37} The pyrimidine family is the most important nitrogen-containing heterocycle because it is found in many natural and biologically active products. It is known that the condensation of triazole and pyrimidine leads to the formation of bicyclic heterocycles known as triazolopyrimidines, which exhibit a wide range of biological properties.^{38–40} Triazolopyrimidines can be used in a variety of synthetic pharmacophores. In addition, they are valuable building blocks for the structure of many herbicides such as penoxsulam, diclosulam, flumetsulam, azafenidin, and floransulan.^{41–45} Furthermore, triazolopyrimidines are synthetic analogs of purines and nucleosides. Also, [1,2,4]triazolo[1,5-*a*]pyrimidines, a subtype of bioisosteric purine analogs, have been reported to possess potential antitumor activities, particularly those bearing functional groups at C-5, C-6, or C-7 positions.^{46,47} Several synthetic strategies have been described for the preparation of triazolopyrimidine derivatives, most of which are based on a modification of the classical Biginelli reaction.^{48,49} Although some of these procedures are efficient, some of them have limiting factors, including long reaction times, side reactions, rigid workup, high-temperature conditions, and nonrecyclable reagents.

Continuing our efforts to establish an environmentally friendly method for the synthesis of reusable catalysts,^{50–59} we report a novel magnetic graphene oxide supported by a doubly acidic ionic liquid and the catalytic activities in the synthesis of triazolo[1,5-*a*]pyrimidine derivatives.

2. Experimental

All solvents, reagents, and chemicals were purchased from Sigma-Aldrich, Merck, and Fluka chemical companies. X-ray diffraction analyzes were recorded using a Philips X Pert Pro X diffractometer operated with a Ni-filtered Cu-K α radiation source. XRD diffraction patterns were obtained from $2\theta = 10$ – 80° . The EDS was performed using the TESCAN-Vega model. Scanning electron micrographs were performed using a SEM: KYKY-EM3200 instrument. Thermogravimetric analysis was performed with a Perkin Elmer STA 6000 instrument in the temperature range 25–900 °C under air atmosphere. Vibration-

al sample magnetometry of magnetic materials was performed using a Kavr Magnet VSM. The IR spectrum was recorded in the range 400–4000 cm⁻¹ using a FT-IR JASCO 6300D instrument. ¹H and ¹³C NMR spectra were recorded with a Bruker Ultrashield spectrometer (400 MHz) using DMSO-*d*₆ as solvent.

Preparation of [(CH₂)₃SO₃H-VIm]HSO₄ (IL)

First, a mixture of 1-vinylimidazole (9.4 g) and 1,4-butanedisulfone (12.4 g) was stirred at room temperature for 24 hours. Then the obtained white solid was collected, washed with diethyl ether and dried at 50 °C. The prepared material was dissolved in H₂O (5 ml) in a 100-ml round bottom flask, and equimolar H₂SO₄ was added dropwise at 0 °C. After the addition was completed, the mixture was stirred at 50 °C for 12 h, during which the ionic liquid was formed. Finally, the ionic liquid was repeatedly washed with diethyl ether and dried in vacuo at 50 °C.²

Synthesis of graphene oxide (GO)

Graphene oxide was synthesized using graphite powders by the modified Hummer method. In a typical synthesis procedure, graphite powder (3 g) was added to a mixture of concentrated H₂SO₄ (12 ml), K₂S₂O₈ (2.5 g), and P₂O₅ (2.5 g) in a beaker containing 500 ml and stirred at 80 °C for 5 hours. The mixture was then cooled to room temperature, diluted with deionized water, and stirred at room temperature for 24 hours. The mixture was then filtered, washed with deionized water and ethanol, and dried. After drying, the resulting powder was dissolved in H₂SO₄ (120 ml) and KMnO₄ (15 g) in an ice bath and stirred until complete dissolution. Deionized water (250 ml) was added slowly with stirring and then heated at 35 °C for 2 hours. The reaction was then stopped by adding deionized water (250 ml) and finally hydrogen peroxide (20 ml, 30%). The resulting mixture was washed several times with aqueous HCl solution (1:10) in a centrifuge and then dried in an oven at 60 °C. Finally, the graphene oxide was sonicated in deionized water for 1 h to obtain graphene oxide nanosheets.⁶⁰

Preparation of magnetic Fe₃O₄ nanoparticles (MNPs)

To synthesize magnetic Fe₃O₄ nanoparticles, FeCl₃·6H₂O (2.7 g, 10 mmol) and FeCl₂·4H₂O (1 g, 5 mmol) were first dissolved in deionized water (45 ml) under N₂ atmosphere at 80 °C for 30 min. In the next step, NaOH solution (10 ml, 25%) was slowly added dropwise until the color darkened, and then stirred for 1 h. Finally, the black product of magnetic Fe₃O₄ nanoparticles was collected with an external magnet, washed with deionized water and ethanol, and dried.⁵²

Synthesis of Fe₃O₄@GO nanocomposite

The nanocomposite Fe₃O₄@GO was synthesized by the liquid self-assembly method. In a typical synthesis, GO (50 mg) was dispersed in DMF (5 ml) by ultrasonication

for two hours, and then Fe_3O_4 (40 mg) was slowly added dropwise in chloroform (10 ml). The mixture was sonicated for 4 hours at room temperature. The black colored $\text{Fe}_3\text{O}_4@\text{GO}$ nanocomposite was separated with an external magnet, washed with deionized water and ethanol, and finally dried.⁶¹

Preparation of $\text{Fe}_3\text{O}_4@\text{GO-Pr-SH}$

For the functionalization of $\text{Fe}_3\text{O}_4@\text{GO}$ nanocomposites, 3-mercaptopropyltrimethoxysilane (2 ml) was added to $\text{Fe}_3\text{O}_4@\text{GO}$ (1 g) in dry toluene (30 ml), and the mixture was stirred under N_2 atmosphere and refluxed for 24 h. The resulting product ($\text{Fe}_3\text{O}_4@\text{GO-Pr-SH}$) was separated by an external magnet, washed with distilled water and ethanol, and dried.

Synthesis $\text{Fe}_3\text{O}_4@\text{GO-Pr-S/IL}$ (1)

To prepare an acidic ionic liquid on modified GO (nanocatalyst 1), a mixture of $\text{Fe}_3\text{O}_4@\text{GO-Pr-SH}$ (1 g), $[(\text{CH}_2)_3\text{SO}_3\text{H-VIm}]\text{HSO}_4$ (5 ml), and azobisisobutyronitrile (AIBN) (5 mol%) was refluxed in toluene (100 mL) for 30 h under N_2 atmosphere. The catalyst was then separated with an external magnet, washed several times with diethyl ether, and then dried at 50 °C.

General procedure for the synthesis of triazolopyrimidines 5

To a mixture of aldehyde (1 mmol), ethyl cyanoacetate or malononitrile (1 mmol), and 3-amine-1*H*-1,2,4-triazole (1 mmol) was added catalyst 1 (0.004 g) under solvent-free conditions at 80 °C. The reaction progress was monitored by TLC (n-hexane/EtOAc). After completion of the process, EtOAc (10 ml) was added and the $\text{Fe}_3\text{O}_4@\text{GO-Pr-S/IL}$ -nanocatalyst was separated using an external magnet. Further purification of the product was performed by recrystallization from EtOH.

General procedure for the recovery of nanocatalyst 1

Recovery of $\text{Fe}_3\text{O}_4@\text{GO-Pr-S/IL}$ was carried out in the synthesis of pyrimidine derivatives. The mixture of benzaldehyde (1 mmol), ethyl cyanoacetate or malononitrile (1 mmol) and 3-amine-1*H*-1,2,4-triazole (1 mmol) was stirred in the presence of catalyst 1 (0.004 g) under optimum conditions. After completion of the reaction, hot EtOAc (10 ml) was added and the nanocatalyst was separated from the reaction mixture using an external magnet. Then, the recovered catalyst was washed several times with EtOAc (10 ml) and deionized water (10 ml) and dried. Finally, the recovered catalyst was reused seven times consecutively under the same conditions.

Selected spectral data

Ethyl 5-amino-7-phenyl-1,7-dihydro-[1,2,4]triazolo[1,5-*a*]pyrimidine-6-carboxylate (**5a**). FT-IR (KBr, cm^{-1}) ν 3396, 3375, 3326, 2746, 1687, 1565, 1490, 1110; ^1H NMR (400 MHz, $\text{DMSO}-d_6$) δ 9.25 (s, 1H), 8.08 (d, 1H, $J = 8$ Hz),

7.66 (s, 2H), 5.37 (s, 1H), 3.93 (q, 2H, $J = 8$ Hz), 0.84 (t, 3H, $J = 8$ Hz), 7.57–7.64 (m, 5H) ppm.

Ethyl 5-amino-7-(4-chlorophenyl)-4,7-dihydro-[1,2,4]triazolo[1,5-*a*]pyrimidine-6-carboxylate (**5b**). FT-IR (KBr, cm^{-1}) ν 3412, 3253, 3115, 2872, 1692, 1532, 1485, 1203; ^1H NMR (400 MHz, $\text{DMSO}-d_6$) δ 9.25 (s, 1H), 8.08 (d, 1H, $J = 8$ Hz), 7.65 (s, 2H), 5.41 (s, 1H), 4.38 (q, 2H, $J = 7$ Hz), 0.92 (t, 3H, $J = 7$ Hz), 7.45–7.58 (m, 5H); ^{13}C NMR (100 MHz, $\text{DMSO}-d_6$) δ 163.83, 160.63, 154.82, 134.82, 130.96, 129.87, 129.04, 110.16, 61.09, 57.01, 14.02.

Ethyl 5-amino-7-(4-bromophenyl)-4,7-dihydro-[1,2,4]triazolo[1,5-*a*]pyrimidine-6-carboxylate (**5c**). FT-IR (KBr, cm^{-1}) ν 3427, 3389, 3098, 2923, 1677, 1587, 1488, 1178; ^1H NMR (400 MHz, $\text{DMSO}-d_6$) δ 9.16 (s, 1H), 7.08 (d, 1H, $J = 3.6$ Hz), 8.39 (s, 2H), 5.21 (s, 1H), 3.98 (q, 2H, $J = 6.4$ Hz), 1.33 (t, 3H, $J = 6.6$ Hz), 7.41–7.43 (m, 5H); ^{13}C NMR (100 MHz, $\text{DMSO}-d_6$) δ = 169.6, 156, 146, 141.99, 132.5, 129, 126.8, 62.1, 40.6, 27.5.

Ethyl 5-amino-7-(4-nitrophenyl)-4,7-dihydro-[1,2,4]triazolo[1,5-*a*]pyrimidine-6-carboxylate (**5d**). FT-IR (KBr, cm^{-1}) ν 3480, 3430, 3198, 2917, 1680, 1604, 1504, 1054; ^1H NMR (400 MHz, $\text{DMSO}-d_6$) δ 13.99 (s, 1H), 8.10 (d, 1H, $J = 8$ Hz), 7.83–7.91 (m, 4 H), 5.99 (s, 1H), 4.43 (q, 2H, $J = 7.2$ Hz), 1.03 (t, 1H, $J = 3.2$ Hz); ^{13}C NMR (100 MHz, $\text{DMSO}-d_6$) δ 163.62, 154.95, 149.60, 144.21, 134.01, 131.06, 130.42, 124.86, 124.46, 114.11, 63.57, 59.84, 14.00.

Ethyl 5-amino-7-(3-nitrophenyl)-1,7-dihydro-[1,2,4]triazolo[1,5-*a*]pyrimidine-6-carboxylate (**5e**). FT-IR (KBr, cm^{-1}) ν 3444, 3328, 3097, 2888, 1697, 1623, 1531, 1272; ^1H NMR (400 MHz, $\text{DMSO}-d_6$) δ 6.41 (s, 1H), 8.09 (d, 1H, $J = 8$ Hz), 7.80–7.83 (m, 5H), 5.69 (s, 1H), 4.03 (q, 2H, $J = 8$ Hz), 0.92 (t, 3H, $J = 8$ Hz); ^{13}C NMR (100 MHz, $\text{DMSO}-d_6$) δ 163.63, 154.55, 150.36, 147.93, 134.84, 131.17, 130.83, 125.30, 123.78, 123.13, 113.63, 63.19, 59.06, 13.86.

Ethyl 5-amino-7-(2,4-dichlorophenyl)-1,7-dihydro-[1,2,4]triazolo[1,5-*a*]pyrimidine-6-carboxylate (**5f**). FT-IR (KBr, cm^{-1}) ν 3489, 3421, 3085, 2878, 1699, 1586, 1474, 1106; ^1H NMR (400 MHz, $\text{DMSO}-d_6$) δ 11.67 (s, 1H), 8.11 (d, 1H, $J = 8$ Hz), 7.87 (s, 2H), 4.16 (s, 1H), 2.48 (q, 2H, $J = 8$ Hz), 1.25 (t, 3H, $J = 7$ Hz), 7.26–7.77 (m, 5H); ^{13}C NMR (100 MHz, $\text{DMSO}-d_6$) δ 160.6, 153.6, 137.6, 130.2, 120.8, 127, 67.1, 40.4, 21.6.

Ethyl 5-amino-7-(4-methylphenyl)-7,8-dihydro-[1,2,4]-triazolo[4,3-*a*]pyrimidine-6-carbonitrile (**5g**). FT-IR (KBr, cm^{-1}) ν 3347, 3262, 3185, 3118, 2921, 2192, 1660, 1633, 1531, 1482, 1363, 1286, 1214, 1157; ^1H NMR (400 MHz, $\text{DMSO}-d_6$) δ 2.28 (s, 3H), 5.29 (d, 1H, $J = 2.4$ Hz), 7.18 (s, 4H), 7.21 (s, 2H), 7.71 (s, 1H), 8.75 (d, 1H, $J = 1.6$ Hz); ^{13}C NMR (100 MHz, $\text{DMSO}-d_6$) δ 20.64, 53.70, 56.06, 119.06, 126.00, 129.18, 137.26, 140.24, 146.93, 151.83, 153.92.

Ethyl 5-amino-7-(4-isopropylphenyl)-7,8-dihydro-[1,2,4]-triazolo[4,3-*a*]pyrimidine-6-carbonitrile (**5h**). FT-IR (KBr, cm^{-1}) ν 3378, 3295, 3181, 3118, 2964, 2186, 1656, 1627, 1523, 1479, 1367, 1284, 1211, 1151; ^1H NMR (400 MHz, $\text{DMSO}-d_6$) δ 1.23 (d, 6H, $J = 6.8$ Hz), 2.92 (s, 1H),

5.33 (d, 1H, $J = 2$ Hz), 7.24 (s, 4H), 7.31 (s, 2H), 7.76 (s, 1H), 8.80 (d, 1H, $J = 1.6$ Hz); ^{13}C NMR (100 MHz, $\text{DM-SO}-d_6$) δ 23.81, 33.11, 53.68, 55.97, 119.11, 125.99, 126.59, 140.71, 146.95, 148.21, 151.83, 153.91.

3. Results and Discussion

The procedure for preparing the nanocatalyst $\text{Fe}_3\text{O}_4@\text{GO-Pr-S/IL}$ (**1**) is shown in Scheme 1. Brønsted's acidic ionic liquid $[(\text{CH}_2)_3\text{SO}_3\text{HVIm}]\text{HSO}_4$ synthesized by the reaction of 1-vinylimidazole with 1,4-butanedisulfone followed by treatment with sulfuric acid. Subsequently, a $\text{Fe}_3\text{O}_4@\text{GO}$ -nanocomposite was prepared and functionalized with 3-mercaptopropyltrimethoxysilane (MPTMS) via covalent bonds to prepare $\text{Fe}_3\text{O}_4@\text{GO-Pr-SH}$. Finally, $\text{Fe}_3\text{O}_4@\text{GO-Pr-S/IL}$ nanocatalyst **1** was obtained by the reaction of $[(\text{CH}_2)_3\text{SO}_3\text{HVIm}]\text{HSO}_4$ and $\text{Fe}_3\text{O}_4@\text{GO-Pr-SH}$ in the presence of azobisisobutyronitrile (AIBN) in toluene under N_2 atmosphere. After successful synthesis of $\text{Fe}_3\text{O}_4@\text{GO-Pr-S/IL}$, the structure of this new nanocatalyst was characterized by XRD, EDS, FT-IR, VSM, SEM and TGA techniques.

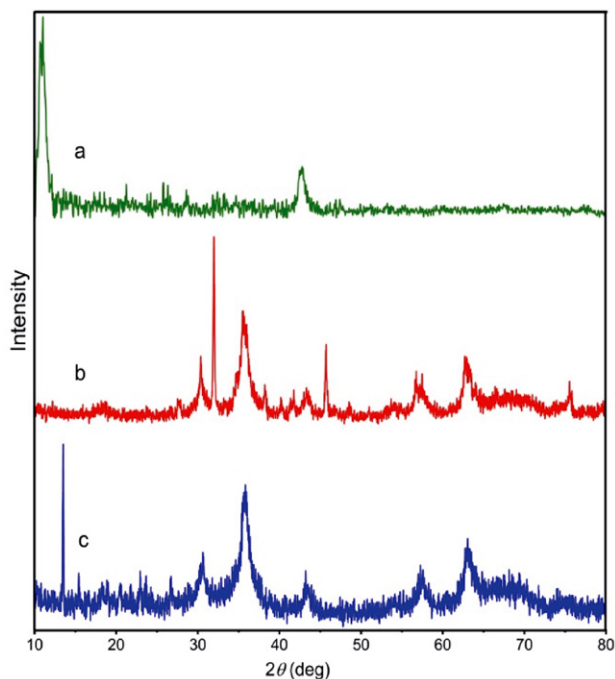
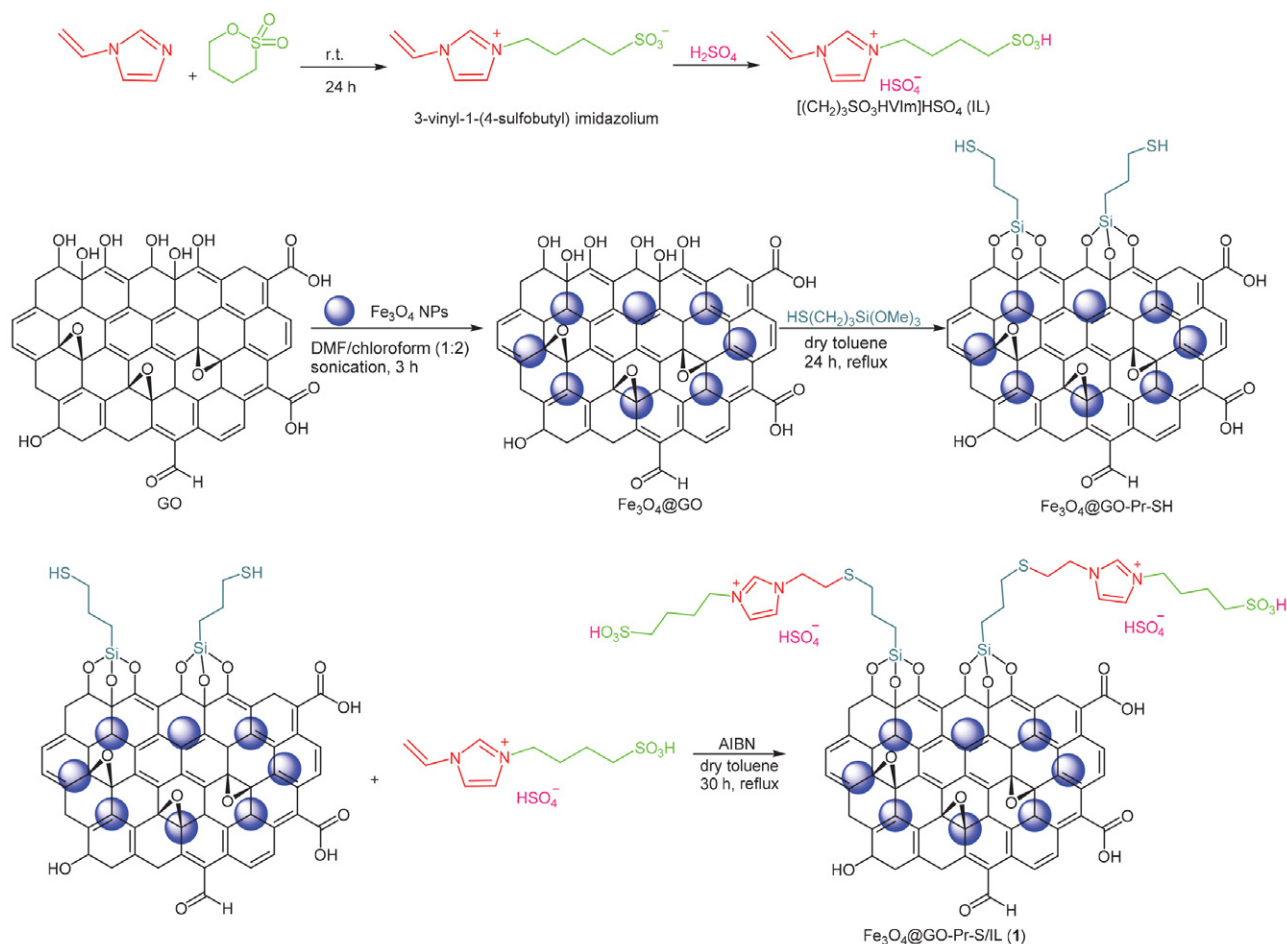


Figure 1. XRD patterns of a) GO, b) Fe_3O_4 , and c) $\text{Fe}_3\text{O}_4@\text{GO-Pr-S/IL}$.



Scheme 1. Preparation of $\text{Fe}_3\text{O}_4@\text{GO-Pr-S/IL}$ (**1**).

Figure 1 shows the X-ray diffraction spectroscopy patterns of GO, Fe_3O_4 , and $\text{Fe}_3\text{O}_4@\text{GO-Pr-S/IL}$. The peaks at $2\theta = 10.5^\circ$ and 43.5° could correspond to the (01) and (101) layers of GO, respectively.^{62,63} In Figure 1b, the peaks at 30.26° , 35.7° , 43.5° , 53.59° , 57.5° , and 63.26° relate to (220), (311), (400), (422), (511), and (440) free Fe_3O_4 , respectively, which agrees well with the pattern of Fe_3O_4 .^{64,65} After grafting various functional groups onto GO (Figure 1c), the 001 diffraction peak of GO completely disappeared, indicating complete exfoliation of GO and preventing the aggregation of GO after partial reduction. Moreover, the $\text{Fe}_3\text{O}_4@\text{GO-Pr-S/IL}$ nanocatalyst shows characteristic peaks at 2θ , which are consistent with the bare peaks of Fe_3O_4 .

Elemental analysis of $\text{Fe}_3\text{O}_4@\text{GO-Pr-S/IL}$ was performed by EDX analysis (Figure 2). The EDX spectrum proves the presence of the common elements C, O, Fe, N, Si and S in the catalyst structure as shown.

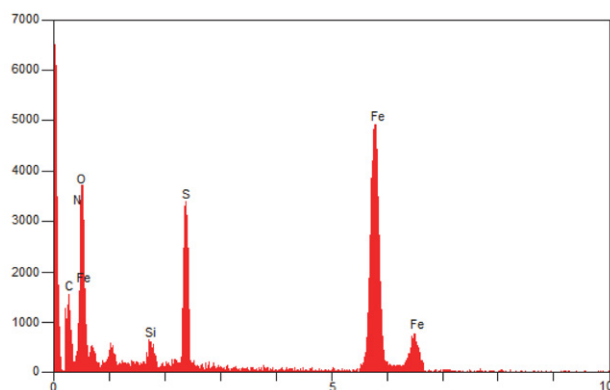


Fig. 2. EDS diagram of $\text{Fe}_3\text{O}_4@\text{GO-Pr-S/IL}$.

In Figure 3a, three absorption peaks at about 645, 1050, and 1135 cm^{-1} are associated with the vibrations of the S-O, SO_2 , and C-S bands, respectively. In addition, the characteristic peaks of the imidazolium ring at 1563 cm^{-1} were observed (Figure 3a).^{66–68} The FT-IR spectra of GO are shown in Figure 3b. The peak at 1227 cm^{-1} is assigned to the stretching vibration of C-O of the epoxide group, and the peak of C=O of the carboxyl and carbonyl groups is at 1724 cm^{-1} (Figure 3b).^{69,70} The strong peak in all spectra at 3400 cm^{-1} corresponds to the OH group (Figure 3b-f). In $\text{Fe}_3\text{O}_4@\text{GO-Pr-S/IL}$ this peak (OH group) is much more pronounced than in $\text{Fe}_3\text{O}_4@\text{GO-Pr-SH}$ due to the sulfonic acid groups. Moreover, the typical peak at 580 cm^{-1} in all spectra (Figure 3c-f) can be attributed to Fe-O stretching.⁷¹ In addition, symmetric and asymmetric vibrations of the Si-O bond occur at about 973 and 1140 cm^{-1} , confirming the presence of MPTMS (Figure 3d).⁷² The presence of all these peaks indicates the successful association of the Bronsted ionic acid liquid with the $\text{Fe}_3\text{O}_4@\text{GO-Pr-SH}$ via a radical reaction.

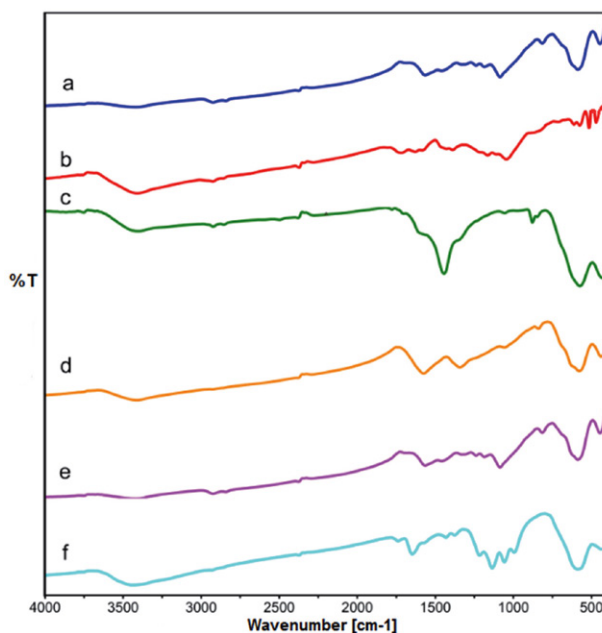


Figure 3. FT-IR spectra of a) IL, b) GO, c) Fe_3O_4 , d) $\text{Fe}_3\text{O}_4@\text{GO}$, e) $\text{Fe}_3\text{O}_4@\text{GO-Pr-SH}$, and f) $\text{Fe}_3\text{O}_4@\text{GO-Pr-S/IL}$.

The magnetic property of Fe_3O_4 and $\text{Fe}_3\text{O}_4@\text{GO-Pr-S/IL}$ nanocatalysts was determined by VSM at room temperature (Figure 4). The curves in Figure 4 show that the saturation magnetization values of $\text{Fe}_3\text{O}_4@\text{GO-Pr-S/IL}$ (20.55 emu/g) are lower than those of pure Fe_3O_4 nanoparticles (53.03 emu/g). The decrease in saturation magnetization of $\text{Fe}_3\text{O}_4@\text{GO-Pr-S/IL}$ nanocatalyst might be related to the functionalized GO and the presence of an acid group on the surface of the ionic liquid associated with the support.

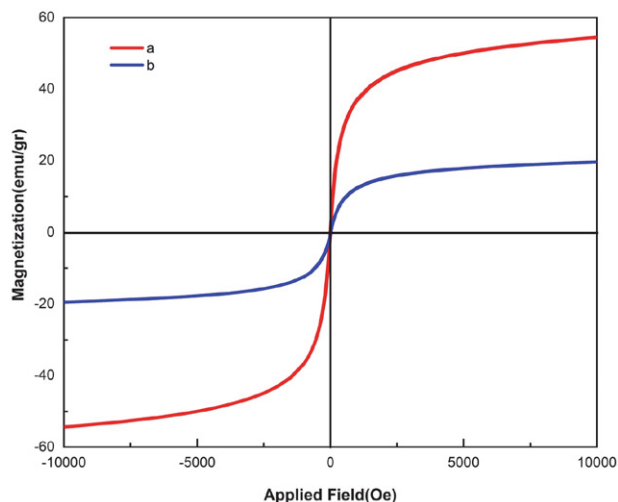


Figure 4. VSM analysis of a) Fe_3O_4 and b) $\text{Fe}_3\text{O}_4@\text{GO-Pr-S/IL}$.

The morphology and size of the nanocatalysts GO and $\text{Fe}_3\text{O}_4@\text{GO-Pr-S/IL}$ were studied using SEM (Figure 5). GO has a 2D structure with a wrinkled edge and a large

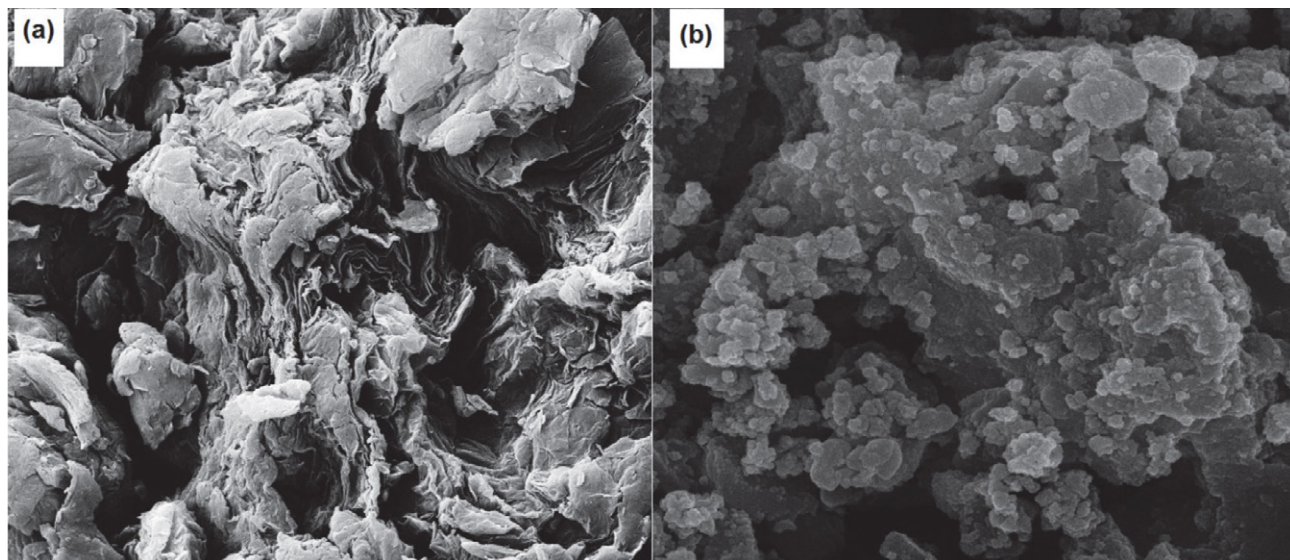
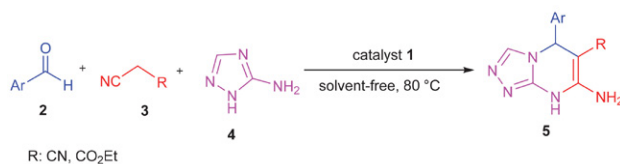


Figure 5. SEM images of a) GO and b) $\text{Fe}_3\text{O}_4@\text{GO-Pr-S/IL}$.

thickness (Figure 5a). However, after immobilization of the ionic liquid, the surface of GO is smooth (Figure 5b). According to this picture, the average particle size is 77–90 nm, and the surface of the nanocatalyst is almost uniform.

The thermal stability of the $\text{Fe}_3\text{O}_4@\text{GO-Pr-S/IL}$ nanocatalyst was also investigated by thermogravimetric analysis (TGA) (Figure 6). The TGA curve of nanocatalyst **1** shows three stages of weight loss between 25 and 900 °C. In this curve, the first weight loss below 220 °C (18%) is due to desorption of chemisorbed and physically adsorbed solvents, organic solvents, and hydroxyl groups. The second weight loss occurs at about 220–550 °C (8%) and is due to decomposition of oxygenated groups into GO, organic groups, acid groups, and amine groups. The final weight losses occur at 550–900 °C (10%). They may be due to the removal of these immobilized organic species on the surface of GO nanosheets and confirm the thermal stability of the prepared nanocatalyst.

In the next step, $\text{Fe}_3\text{O}_4@\text{GO-Pr-S/IL}$ was used as an effective nanocatalyst for the synthesis of triazolo[1,5-*a*]pyrimidine derivatives **5** (Scheme 2).



Scheme 2. Synthesis of triazolo[1,5-*a*]pyrimidine derivatives **5** in the presence of nanocatalyst **1**.

Table 1 shows the effects of catalyst amount, temperature and different solvents on the reaction between benzaldehyde (1 mmol), ethyl cyanoacetate (1 mmol) and 3-amine-1H-1,2,4-triazole (1 mmol) as an example reac-

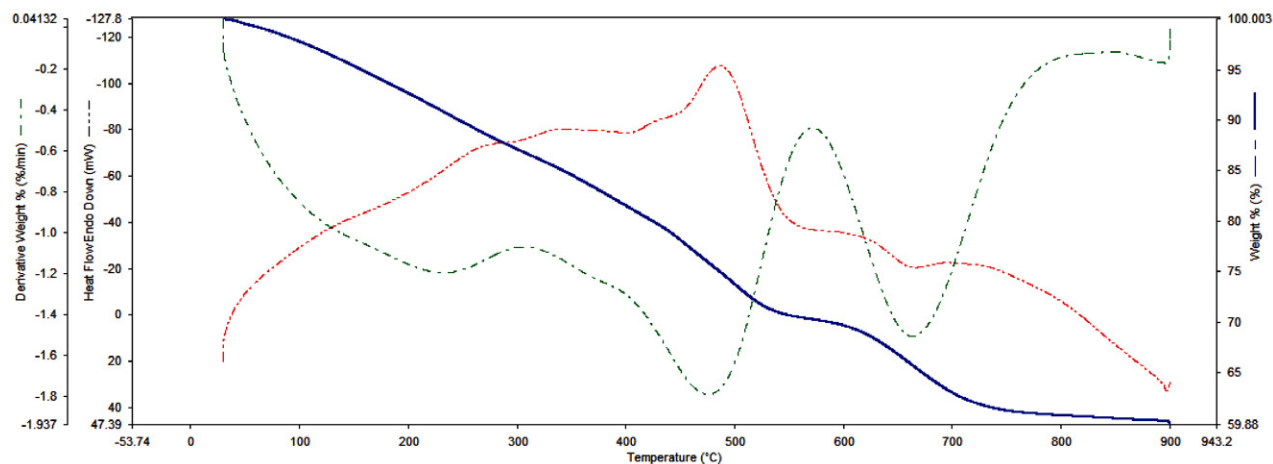


Figure 6. TGA curve of the $\text{Fe}_3\text{O}_4@\text{GO-Pr-S/IL}$ nanocatalyst.

Table 1. The effect of catalyst loading, solvent and temperature in the synthesis of **5a**.^a

Entry	Catalyst 1 (g)	Solvent	Temp. (°C)	Yield ^b (%)
1	0.002	–	25	62
2	0.002	–	60	70
3	0.002	–	80	80
4	0.001	–	80	65
5	0.004	–	80	95
6	0.006	–	80	90
7	0.008	–	80	90
8	0.004	EtOH	80	80
9	0.004	CH ₃ CN	80	82
10	0.004	Toluene	80	70
11	0.004	H ₂ O	80	65
12	0.004	H ₂ O/EtOH (1:1)	reflux	75
13	0.004	GO	80	37
14	0.004	Fe ₃ O ₄	80	45
15	0.004	Fe ₃ O ₄ @GO	80	57
16	–	–	80	trace

^a Reaction conditions: benzaldehyde (1 mmol), ethyl cyanoacetate (1 mmol), 3-amine-1*H*-1,2,4-triazole (1 mmol), time: 20 min. ^b Isolated yields.

tion. The model reaction was carried out at different temperatures, and the best yield was obtained at 80 °C. We optimized the amount of catalyst; the maximum yield of

the product was obtained with 0.004 g of catalyst under solvent-free conditions. The yield of the product was highest when the reaction proceeded under solvent-free conditions, and when EtOH, MeCN, toluene, H₂O, and H₂O/EtOH (1:1) were used as solvents, the yield of the product decreased. When GO, Fe₃O₄ and Fe₃O₄@GO were used as catalysts under solvent-free conditions at 80 °C, the product yield was much lower. The reaction did not proceed without catalyst (Table 1, entry 16), indicating that the catalyst was necessary to promote the reaction. After optimizing the reaction conditions, the efficiency of the Fe₃O₄@GO-Pr-S/IL nanocatalyst was further tested in the synthesis of triazolo[1,5-*a*]pyrimidines using a series of aromatic aldehydes and malononitrile. The results are shown in Table 2, and it was found that almost all substrates gave excellent yields of the desired products in a short reaction time.

A permissible mechanism for the three-component synthesis of triazolo[1,5-*a*]pyrimidines **5** based on previous reports is shown in Scheme 3.^{73,74} First, the aldehyde and active methylene compounds (cyanoacetate or malononitrile) are activated with the acidic surface of the catalyst, and a Knoevenagel condensation to intermediate I occurs. Subsequently, intermediate I reacts with 3-amine-1*H*-1,2,4-triazole to give the intermediate II (via Michael addition). Finally, the desired product was synthesized after intramolecular cyclization and tautomerization.

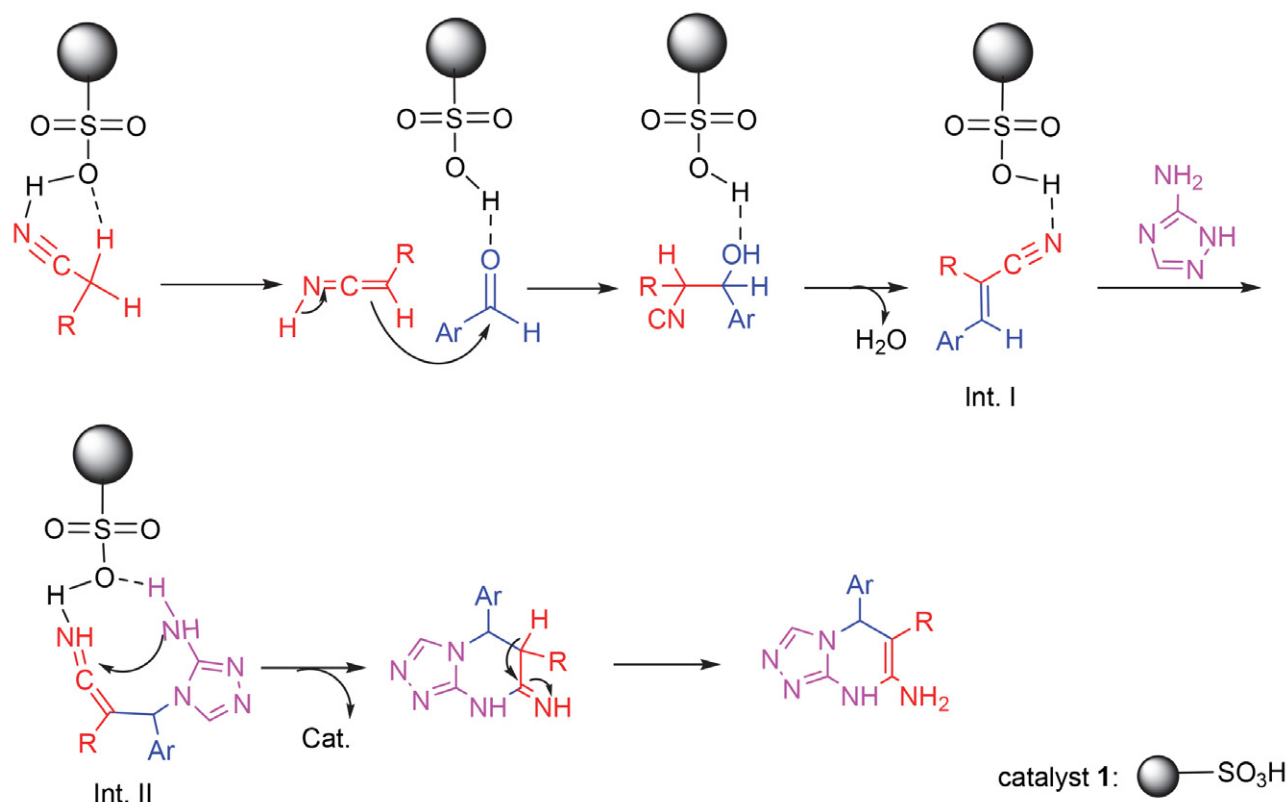
**Scheme 3.** Proposed mechanism for the synthesis of **5** in the presence of Fe₃O₄@GO-Pr-S/IL as catalyst.

Table 2. Synthesis of triazolo[1,5-*a*]pyrimidines in the presence of Fe₃O₄@GO-Pr-S/IL nanocatalyst.^a

Entry	Aldehyde	Product 5	Yield (%) ^b	Mp (°C)
5a	C ₆ H ₄ CHO		95	189–191 ^c
5b	4-Cl C ₆ H ₄ CHO		97	190–191 ⁷⁰
5c	4-Br C ₆ H ₄ CHO		93	184–184 ⁷⁰
5d	4-NO ₂ C ₆ H ₄ CHO		95	194–196 ⁷⁰
5e	3-NO ₂ C ₆ H ₄ CHO		90	190–192 ^c
5f	2,4-Cl ₂ C ₆ H ₃ CHO		88	243–245 ^c
5g	4-CH ₃ C ₆ H ₄ CHO		85	243–245 ⁷¹
5h	4- <i>i</i> -Pr C ₆ H ₄ CHO		84	218–220 ^c
5i	4-NO ₂ C ₆ H ₄ CHO		90	245–247 ⁷¹
5j	2-Cl C ₆ H ₄ CHO		92	263–266 ⁷¹
5k	4-Br C ₆ H ₄ CHO		89	264–266 ⁷¹
5l	4-Cl C ₆ H ₄ CHO		93	257–258 ⁷¹

^a Reaction conditions: aryl aldehyde (1 mmol), ethyl cyanoacetate or malononitrile (1 mmol), 3-amine-1*H*-1,2,4-triazole (1 mmol), catalyst **1** (0.004 g), solvent-free, 80 °C. ^b Isolated yields. ^c New compound.

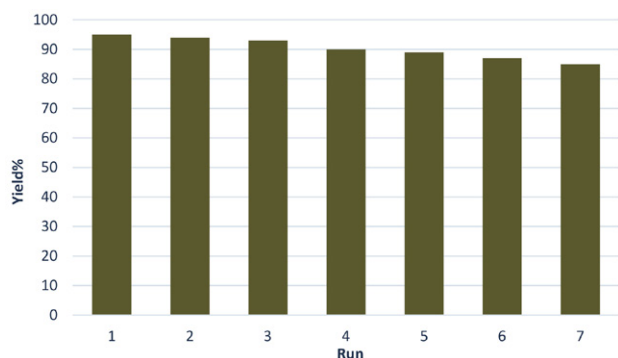


Figure 7. Reusability of the heterogeneous nanocatalyst **1** for the synthesis of **5a**.

A hot filtration test was also performed to study the leaching of the catalyst during the reaction. After about 50% of the process was complete, boiling EtOAc (5 ml) was added and the catalyst was separated with a magnet. The solvent was then removed and the reaction continued under optimized conditions. Nevertheless, no remarkable increase in product conversion was observed during the course of the reaction, indicating that the catalyst func-

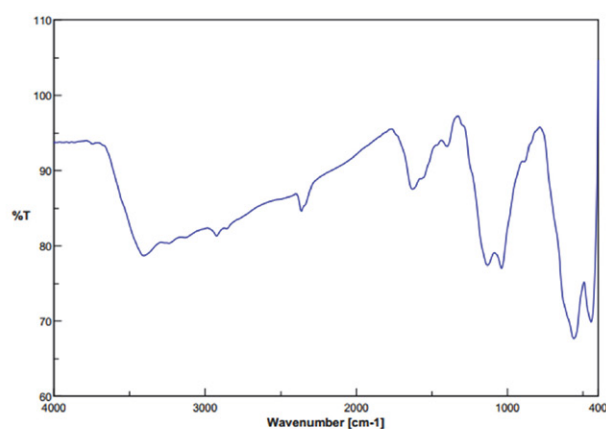


Figure 8. FT-IR spectrum of recycled $\text{Fe}_3\text{O}_4\text{@GO-Pr-S/IL}$.

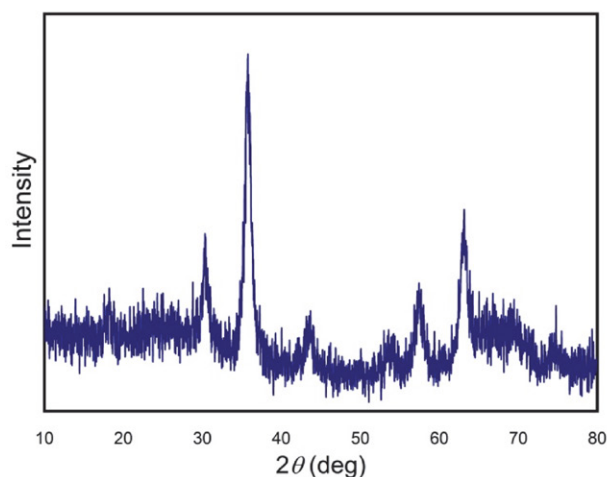


Figure 9. The XRD pattern of recycled nanocatalyst **1**.

tioned as a heterogeneous method and the ionic liquid fraction was kept intact and efficient on the solid support. Moreover, the reusability of $\text{Fe}_3\text{O}_4\text{@GO-Pr-S/IL}$ in the model reaction of benzaldehyde, ethyl cyanoacetate and 3-amine-1*H*-1,2,4-triazole was investigated under optimum conditions. After completion of the reaction, boiling EtOAc was added and the catalyst was separated by an external magnet, washed, and reused in subsequent runs. As shown in Figure 7, the synthesized catalyst can be recovered and reused in at least 7 runs without significant decrease in its efficiency.

In Figure 8, the FT-IR spectrum of the nanocatalyst after seven reaction cycles can be seen. This spectrum also confirms the stability of the structure of the recycled nanocatalyst. The XRD pattern also indicates the structural stability of the catalyst after being reused (Figure 9). The position and relative intensities of all peaks confirm this well.

4. Conclusions

In this work, $\text{Fe}_3\text{O}_4\text{@GO-Pr-S/IL}$ was prepared as a new nanocatalyst and used for the synthesis of triazolo[1,5-*a*]pyrimidine derivatives under green conditions, and the products were obtained in high yield. This magnetic nanocatalyst was characterized by various techniques such as XRD, FT-IR, EDX, SEM, VSM and TGA. $\text{Fe}_3\text{O}_4\text{@GO-Pr-S/IL}$ was used as an efficient catalyst with good durability, high selectivity and stability, mild reaction conditions and short reaction times. The heterogeneous $\text{Fe}_3\text{O}_4\text{@GO-Pr-S/IL}$ catalyst was also successfully recovered seven times, maintaining its activity.

5. References

1. M. Tajbakhsh, H. Alinezhad, M. Norouzi, S. Bagheri, M. Akbari, *J. Mol. Liq.* **2013**, *177*, 44–48. DOI:10.1016/j.molliq.2012.09.017
2. J. Miao, H. Wan, G. Guan, *Catal. Commun.* **2011**, *12*, 353–356. DOI:10.1016/j.catcom.2010.10.014
3. P. Elavarasan, S. Rengadurai, S. Upadhyayula, *Adv. Chem. Eng.* **2020**, *4*, 100045–100053. DOI:10.1016/j.caja.2020.100045
4. J. Miao, H. Wan, Y. Shao, G. Guan, B. Xu, *J. Mol. Catal. A Chem.* **2011**, *348*, 77–82. DOI:10.1016/j.molcata.2011.08.005
5. A. R. Hajipour, F. Rafiee, *Org. Prep. Proced. Int.* **2010**, *42*, 285–362. DOI:10.1080/00304948.2010.490177
6. A. S. Amarasekara, O. S. Owereh, *Catal. Commun.* **2010**, *11*, 1072–1075. DOI:10.1016/j.catcom.2010.05.012
7. Z. M. Li, Y. Zhou, D. J. Tao, W. Huang, X. S. Chen, Z. Yang, *RSC Adv.* **2014**, *4*, 12160–12167. DOI:10.1039/C4RA00092G
8. L. T. Oliveira, R. V. Goncalves, D. V. Goncalves, D. C. S. de Azevedo, S. M. Pereira de Lucena, *J. Chem. Eng. Data* **2019**, *64*, 2221–2228. DOI:10.1021/acs.jced.8b01177
9. Q. Sun, B. Aguila, J. Perman, L. D. Earl, C. W. Abney, Y.

- Cheng, H. Wei, N. Nguyen, L. Wojtas, S. Ma, *J. Am. Chem. Soc.* **2017**, *139*, 2786–2793. DOI:10.1021/jacs.6b12885
10. Q. Wang, S. Zhang, Y. Yu, B. Dai, *Catal. Commun.* **2020**, *147*, 106122–106142. DOI:10.1016/j.catcom.2020.106122
 11. M. A. Zolfigol, R. Ayazi-Nasrabadi, S. Bagheri, V. Khakyzadeh, S. Azizian, *J. Mol. Catal. A: Chem.* **2016**, *418*, 54–67. DOI:10.1016/j.molcata.2016.03.027
 12. M. Sheykhan, L. Ma'mani, A. Ebrahimi, A. Heydari, *J. Mol. Catal. A: Chem.* **2011**, *335*, 253–261. DOI:10.1016/j.molcata.2010.12.004
 13. Q. Zhang, H. Su, J. Luo, Y. Wei, *Green Chem.* **2012**, *14*, 201–208. DOI:10.1039/C1GC16031A
 14. R. Li, Y. Jiang, J. Zhao, D. Ramella, Y. Peng, Y. Luan, *RSC Adv.* **2017**, *7*, 34591–34597. DOI:10.1039/C7RA06201J
 15. M. Khoshnevis, A. Davoodnia, A. Zare-Bidaki, N. Tavakoli-Hoseini, *Synth. React. Inorg. Met.* **2013**, *43*, 1154–1161. DOI:10.1080/15533174.2012.756897
 16. M. L. Testa, V. La Parola, A. M. Venezia, *Catal. Today* **2010**, *158*, 109–113. DOI:10.1016/j.cattod.2010.05.027
 17. K. Niknam, A. Deris, F. Naeimi, F. Majleci, *Tetrahedron Lett.* **2011**, *52*, 4642–4645. DOI:10.1016/j.tetlet.2011.06.105
 18. S. V. Atghia, S. Sarvi-Beigbaghlou, *J. Appl. Organomet. Chem.* **2013**, *745*, 42–49. DOI:10.1016/j.jorganchem.2013.07.033
 19. E. Tabrizian, A. Amoozadeh, S. Rahmani, *RSC Adv.* **2016**, *6*, 21854–21864. DOI:10.1039/C5RA20507G
 20. J. Safari, M. Ahmadizadeh, *J. Taiwan Inst. Chem. Eng.* **2017**, *74*, 14–24. DOI:10.1016/j.jtice.2016.12.010
 21. C. Wang, B. Lin, G. Qiao, L. Wang, L. Zhu, F. Chu, T. Feng, N. Yuan, J. Ding, *Mater. Lett.* **2016**, *173*, 219–222. DOI:10.1016/j.matlet.2016.03.057
 22. B. Yin, X. Zhang, X. Zhang, J. Wang, Y. Wen, H. Jia, Q. Ji, L. Ding, *Polym. Adv. Technol.* **2016**, *28*, 293–302. DOI:10.1002/pat.3886
 23. K. Thakur, B. Kandasubramanian, *J. Chem. Eng. Data* **2019**, *64*, 833–867. DOI:10.1021/acs.jced.8b01057
 24. Y. Zhu, S. Murali, W. Cai, X. Li, J. W. Suk, J. R. Potts, R. S. Ruoff, *Adv. Mater.* **2010**, *22*, 3906–3924. DOI:10.1002/adma.201001068
 25. S. Farhadi, M. Hakimi, M. Maleki, *Acta Chim. Slov.* **2017**, *64*, 1005–1019. DOI:10.17344/acsi.2017.3731
 26. W. Yu, L. Sisi, Y. Haiyana, L. Jie, *RSC Adv.* **2020**, *10*, 15328–15345. DOI:10.1039/D0RA01068E
 27. E. Doustkhah, S. Rostamnia, *J. Colloid Interface Sci.* **2016**, *478*, 280–287. DOI:10.1016/j.jcis.2016.06.020
 28. F. Boorboor-Ajdari, E. Kowsari, A. Ehsani, M. Schorowski, T. Ameri, *Electrochim. Acta* **2018**, *292*, 789–804. DOI:10.1016/j.electacta.2018.09.177
 29. M. Tu, K. Wang, S. Bao, R. Zhang, Q. Tan, X. Kong, L. Yu, G. Wu, B. Xu, *J. Colloid Interface Sci.* **2022**, *608*, 1707–1717. DOI:10.1016/j.jcis.2021.10.068
 30. A. Omidvar, B. Jaleh, M. Nasrollahzadeh, H. RezaDasmeh, *Chem. Eng. Res. Des.* **2017**, *121*, 339–347. DOI:10.1016/j.cherd.2017.03.026
 31. H. Zhou, S. Bai, Y. Zhang, D. Xu, M. Wang, *Int. J. Environ. Res. Public Health.* **2022**, *19*, 7584–7602. DOI:10.3390/ijerph19137584
 32. L. H. Choudhury, T. Parvin, *Tetrahedron* **2011**, *67*, 8213–8228. DOI:10.1016/j.tet.2011.07.020
 33. T. Kaur, P. Wadhwa, S. Bagchi, A. Sharma, *Chem. Commun.* **2016**, *52*, 6958–6976. DOI:10.1039/C6CC01562J
 34. N. Kerru, L. Gummidi, S. Maddila, S. B. Jonnalagadda, *Curr. Org. Chem.* **2021**, *25*, 4–39. DOI:10.2174/1385272824999201020204620
 35. K. Nikoofar, F. M. Yielzoleh, *Curr. Org. Synth.* **2022**, *19*, 115–147. DOI:10.2174/1570179418666210910111208
 36. Y. Xiao, Q. Zhou, Z. Fu, L. Yu, J. Wang, *Macromolecules* **2022**, *55*, 2424–2432. DOI:10.1021/acs.macromol.1c02348
 37. B. Alkan, O. Daglar, S. Luleburgaz, B. Gungor, U. S. Gunay, G. Hizal, U. Tunca, H. Durmaz, *Polym. Chem.* **2022**, *13*, 258–266. DOI:10.1039/D1PY01528A
 38. S. S. Sajadikhah, F. Saeedi, H. Dehghan, *Appl. Chem.* **2022**, *17*, 169–178. DOI: 10.22075/CHEM.2021.23425.1973
 39. Z. Li, K. QIU, X. Yang, W. Zhou, Q. Cai, *Org. Lett.* **2022**, *24*, 2989–2992. DOI:10.1021/acs.orglett.2c00863
 40. S. Yuan, S. Wang, M. Zhao, D. Zhang, J. Chen, J. X. Li, J. Zhang, Y. Song, J. Wang, B. Yu, H. Liu, *Chin. Chem. Lett.* **2020**, *31*, 349–352. DOI:10.1016/j.cclet.2019.07.019
 41. S. Lahmidi, H. Anouar, M. Hafi, M. Boulhaoua, A. Ejoumany, M. Jemli, M. Essassi, J. T. Mague, *J. Mol. Struct.* **2019**, *1177*, 131–142. DOI:10.1016/j.molstruc.2018.09.046
 42. P. N. Kalaria, S. C. Karad, D. K. Raval, *Eur. J. Med. Chem.* **2018**, *158*, 917–936. DOI:10.1016/j.ejmech.2018.08.040
 43. A. Ziyaei-Halimehjani, I. N. N. Namboothiri, S. E. Hooshmand, *RSC Adv.* **2014**, *4*, 48022–48084. DOI:10.1039/C4RA08828J
 44. A. E. M. Abdallah, R. M. Mohareb, M. H. E. Helal, G. J. Mo-feed, *Acta Chim. Slov.* **2021**, *68*, 604–616. DOI:10.17344/acsi.2020.6446
 45. A. Pourkazemi, N. Asaadi, M. Farahi, A. Zarnegaryan, B. Karami, *Acta Chim. Slov.* **2022**, *69*, 30–38. DOI: 10.17344/acsi.2021.6819
 46. Y. Huang, J. Liao, W. Wang, H. Liu, H. Guo, *Chem. Commun.* **2020**, *56*, 15235–15281. DOI:10.1039/D0CC05699E
 47. Y. Zheng, X. Qi, S. Chen, S. Song, Y. Zhang, K. Wang, Q. Zhang, *ACS Appl. Mater. Interfaces* **2021**, *13*, 28390–28397. DOI:10.1021/acsami.1c07558
 48. L. G. do Nascimento, I. M. Dias, G. B. de Souza, L. C. Mourão, M. B. Pereira, J. C. V. Viana, L. M. Lião, G. R. de Oliveira, C. G. Alonso, *New J. Chem.* **2022**, *46*, 6091–6102. DOI:10.1039/D1NJ04686A
 49. S. Prakash, N. Elavarasan, A. Venkatesan, K. Subashini, M. Sowndharya, V. Sujatha, *Adv Powder Technol.* **2018**, *29*, 3315–3326. DOI:10.1016/j.appt.2018.09.009
 50. S. Akrami, B. Karami, M. Farahi, *RSC Adv.* **2017**, *7*, 34315–34320. DOI:10.1039/C7RA06240K
 51. F. Motamedi-Nia, M. Farahi, B. Karami, R. Keshavarz, *Lett. Org. Chem.* **2021**, *18*, 407–414. DOI:10.2174/1570178617999200807214103
 52. K. Fattahi, M. Farahi, B. Karami, R. Keshavarz, *Bulg. Chem. Commun.* **2021**, *53*, 174–179. DOI: 10.34049/bcc.53.2.5307
 53. H. Mohamadi-Tanuraghaj, M. Farahi, *Monatsh. Chem.* **2019**, *150*, 1841–1847. DOI:10.1007/s00706-019-02471-x

54. H. Mohamadi-Tanuraghaj, M. Farahi, *RSC Adv.* **2018**, *8*, 27818–27824. DOI:10.1039/C8RA05501G
55. J. E. Gholtash, M. Farahi, *RSC Adv.* **2018**, *8*, 40962–40967. DOI:10.1039/C8RA06886K
56. H. Mohamadi-Tanuraghaj, M. Farahi, *New J. Chem.* **2019**, *43*, 4823–4829. DOI:10.1039/C8NJ06415F
57. B. Karami, M. Farahi, S. Akrami, D. Elhamifar, *New J. Chem.* **2018**, *42*, 12811–12816. DOI:10.1039/C8NJ02699H
58. B. Karami, M. Farahi, Z. Banaki, *Synlett* **2015**, *26*, 1804–1807. DOI:10.1055/s-0034-1380677
59. M. Farahi, B. Karami, R. Keshavarz, F. Khosravian, *RSC Adv.* **2017**, *7*, 46644–46650. DOI:10.1039/C7RA08253C
60. H. Zhang, X. Wang, Na. Li, J. Xia, Q. Meng, J. Ding, J. Lu, *RSC Adv.* **2018**, *8*, 34241–34251. DOI:10.1039/C8RA06681G
61. O. Metin, S. Aydoğan, K. Meral, *J. Alloys Compd.* **2014**, *585*, 681–688. DOI:10.1016/j.jallcom.2013.09.159
62. G. Vinodha, P. D. Shima, L. Cindrella, *J. Mater. Sci.* **2019**, *54*, 4073–4088. DOI:10.1007/s10853-018-3145-z
63. T. Guo, C. Bulin, B. Li, Z. Zhao, H. Yu, H. Sun, H. B. Zhang, *Adsorpt. Sci. Technol.* **2018**, *36*, 1031–1048. DOI:10.1177/0263617417744402
64. G. He, W. Liu, X. Sun, Q. Chen, X. Wang, H. Chen, *Mater. Res. Bull.* **2013**, *48*, 1885–1890. DOI:10.1016/j.materresbull.2013.01.038
65. S. Feng, Z. Ni, S. Feng, Z. Zhang, S. Liu, R. Wang, J. Hu, *J. Radioanal. Nucl. Chem.* **2019**, *319*, 737–748. DOI:10.1007/s10967-018-6379-y
66. Q. Zhang, H. Su, J. Luo, Y. We, *Green Chem.* **2012**, *14*, 201–208. DOI:10.1039/C1GC16031A
67. H. Zhang, H. Li, H. Pan, A. Wang, S. Souzanchi, C. Xu, S. Yang, *Appl. Energy* **2018**, *223*, 416–429. DOI:10.1016/j.apenergy.2018.04.061
68. K. Qiao, H. Hagiwara, C. Yokoyama, *J. Mol. Catal. A: Chem.* **2006**, *246*, 65–69. DOI:10.1016/j.molcata.2005.07.031
69. M. Yadav, K. Y. Rhee, S. J. Park, D. Hui, *Compos. B. Eng.* **2014**, *66*, 89–96. DOI:10.1016/j.compositesb.2014.04.034
70. S. F. Hojati, A. Amiri, M. Mahamed, *Res. Chem. Intermed.* **2020**, *46*, 1091–1107. DOI:10.1007/s11164-019-04021-w
71. X. Yang, W. Chen, J. Huang, Y. Zhou, Y. Zhu, C. Li, *Sci. Rep.* **2015**, *5*, 1–10. DOI:10.1038/srep10632
72. N. Patel, D. Katheriya, H. Dadhania, A. Dadhania, *Res. Chem. Intermed.* **2019**, *45*, 5595–5607. DOI:10.1007/s11164-019-03922-0
73. L. Zaharani, N. Ghaffari-Khaligh, T. Mihankhah, M. R. Jahan, N. A. Hamizi, *Can. J. Chem.* **2020**, *98*, 630–634. DOI:10.1139/cjc-2020-0145
74. M. Singh, S. Fatma, P. Ankit, S. B. Singh, J. Singh, *Tetrahedron Lett.* **2014**, *55*, 525–527. DOI:10.1016/j.tetlet.2013.11.090

Povzetek

V prispevku je opisana nova, s sulfonsko kislino funkcionalizirana, ionska tekočina, pripravljena z vezavo 1-(propil-3-sulfonato)-vinilimidazolijskega hidrogensulfata ($[(\text{CH}_2)_3\text{SO}_3\text{HVIIm}]\text{HSO}_4$) na $\text{Fe}_3\text{O}_4@\text{GO}$. Pripravljen heterogeni katalizator je okarakteriziran z XRD, FT-IR, EDX, SEM, VSM in TGA analiznimi tehnikami. Rezultati analiz kažejo, da se je $[(\text{CH}_2)_3\text{SO}_3\text{HVIIm}]\text{HSO}_4$ uspešno vezal na površino $\text{Fe}_3\text{O}_4@\text{GO}$ in da pripravljen katalizator kaže dobro termično stabilnost. Avtorji so aktivnost katalizatorja raziskali na primeru sinteze triazolo[1,5-*a*]pirimidinskih derivatov z enostopenjsko trikomponentno reakcijo aktivne metilenske spojine (malononitril ali etil cianoacetat), 3-amin-1*H*-1,2,4-triazola in aril aldehydov, brez uporabe topil. Katalizator je mogoče enostavno in hitro izločiti iz reakcijske zmesi s pomočjo zunanega magneta, ter do sedemkrat reciklirati, brez znatne izgube katalitske aktivnosti.



Except when otherwise noted, articles in this journal are published under the terms and conditions of the Creative Commons Attribution 4.0 International License

Scientific paper

Hybrid Polymer Composite of Prussian Red Doped Polythiophene for Adsorptive Wastewater Treatment Application

Mohd Mustafa,¹ Shabnum Bashir,¹ Syed Kazim Moosvi,² Mohd. Hanief Najar,³ Mubashir Hussain Masoodi^{4,*} and Masood Ahmad Rizvi^{1,*}

¹ Department of Chemistry, University of Kashmir, Hazratbal Srinagar, 190006, J&K, India.

² Department of School Education, Government of Jammu and Kashmir, Srinagar, Jammu and Kashmir, India.

³ Department of Chemistry, Government College of Engineering & Technology, Safapora 193504, Jammu and Kashmir, India.

⁴ Department of Pharmaceutical Sciences, University of Kashmir, Hazratbal Srinagar, 190006, J&K, India.

* Corresponding author: E-mail: masoodku2@gmail.com, mubashir@kashmiruniversity.ac.in

Received: 08-22-2022

Abstract

Coordination compounds as dopants to conducting polymers combine desirable properties of individual components for a synergistic effect. Prussian red (PR) a low spin iron (III) coordination compound was doped in polythiophene (PTP) matrix to explore propensity of this inorganic-organic hybrid composite material towards wastewater treatment. PR doping was observed to improve mechano, thermal, electrical, and photocatalytic attributes of pure PTP. PTP/PR composite characterization was attempted using the powder X-ray diffraction, TEM, TGA, FTIR, BET analysis and UV-Visible spectroscopy. Optimization of adsorption conditions, adsorbent regeneration, adsorption thermodynamics studies of PTP/PR were carried out using malachite green (MG) dye as a model system. Under optimized conditions 92% MG dye adsorption was observed over 20 mg PTP/PR nanocomposite in 20 minutes at pH 7. PTP/PR nanocomposite also demonstrated a complimentary performance with real wastewater samples. Thermodynamic studies indicate spontaneous process with electrostatic attraction as the predominant noncovalent interaction. This study highlights designing catalysts capable of synergistic adsorption and photocatalytic activities for effective wastewater treatment.

Keywords: Adsorption; Malachite Green; Prussian red; Hybrid Material, Nyquist plot; Kinetics; Isotherms

1. Introduction

Water is the most significant substance for living beings, water scarcity is a global problem, and contamination further adds to it. Persistent contaminants from industrial effluents, domestic sewage, and agricultural practices make water unsafe to the aquatic ecosystem as well as human life.^{1,2} Dyes as coloring agents have many applications, limiting their usage is practically impossible, and their eventual disperse in the wastewater/environment is inevitable. Synthetic dyes bring toxicity risks as their intermediate metabolites have been identified to be mutagenic, teratogenic, or carcinogenic, posing serious health threats to ecosystems³ as well as aesthetic concerns. Malachite

green is a triaryl methane cationic dye commonly used in pharmaceuticals, paper, textile and printing industries. Treatment methods based on ozonation, nano-filtration, reverse osmosis, flocculation, electrochemical, photocatalytic and advanced oxidation processes are *in vogue* for discoloration of colored water contaminants.⁴ Among water treatment methods such as advanced-oxidation, filtration, flocculation, coagulation and microbial degradation,^{5,6} adsorption based methods owing to their simplicity, non-invasive reactions, broader scale applicability, lower operational cost, good recyclability are interesting environmentally.^{7,8} Consequently, adsorption based methods are still desirable for safer and cost effective wastewater treatment application.

Designing adsorbents with good adsorption capacity and selectivity is a major concern for effective adsorption processes. Natural adsorbents, although pleasing, have limitations of selectivity with lower adsorption capacity.⁹ Synthetic adsorbents can be desirably tuned for improved results under controlled conditions such as in sewage treatment plants. Among synthetic adsorbents, conducting polymers (CP) having charge distribution over the entire polymeric surface offer many adsorption sites making these attractive materials towards adsorptive removal of water contaminants. CPs are significantly influenced in shape, porosity, charge separation etc. by doping with suitable dopant. A well-engineered conducting polymer composite can desirably improve the adsorption capacity of the pristine conducting polymer.¹⁰ PR was selected as a dopant with the rationale of its good crystallinity, stability over environmental pH range, high charge density, moderate paramagnetism, redox behavior with relatively lower toxicity.¹¹ Thus in continuation of our interests in applications of transition metal complexes,^{12–16} especially as photocatalysts in organic synthesis,^{17,18} and as dopants in conducting polymer matrix for electrical and environmental applications,^{19–21} herein we envisaged the effect of Prussian red (PR) as a transition metal complex dopant to the polythiophene conducting polymer matrix. We synthesized polythiophene (PTP) Prussian red (PR) nanocomposite PTP/PR to envisage the effect of this versatile dopant on its polymer properties. The effect of PR dopant on the polymer properties indicated an enhancement in the mechano, thermal, electrochemical and photocatalytic descriptors of pure PTP. The comparative studies of PR doping to PTP, relative to other organic dopants, revealed an increase in surface area, electrical conductivity, charge separation dynamics, and electrochemical stability as desirable attributes for sensing, photocatalytic activity, and device fabrication. The observed physicochemical properties of synthesized PTP/PR nanocomposite indicate its suitability as material for environmental applications, which was modelled using malachite green (MG) dye adsorption in aqueous phase. PTP/PR nanocomposite displayed significant adsorptive tendency towards decoloration of samples having up to 100 ppm of MG dye concentration under environmentally viable conditions (pH 6–7). The effect of adsorbent dose, dye concentration, temperature, adsorption time and pH effect were optimized for its development as adsorbent in real time water treatment plant application. The experimental data of MG dye adsorption over PTP/PR nanocomposite was also analyzed for parameters such as: kinetics, adsorption isotherms and thermodynamics. PTP/PR signified good propensity as hybrid material towards adsorptive handle of water treatment. The development of PTP/PR nanocomposite as an effective water treatment nanomaterial via synergistic adsorptive and photocatalytic elimination of MG dye was also established and its further extension to other persistent water contaminants is underway in our laboratory.

2. Experimental

2. 1. Materials

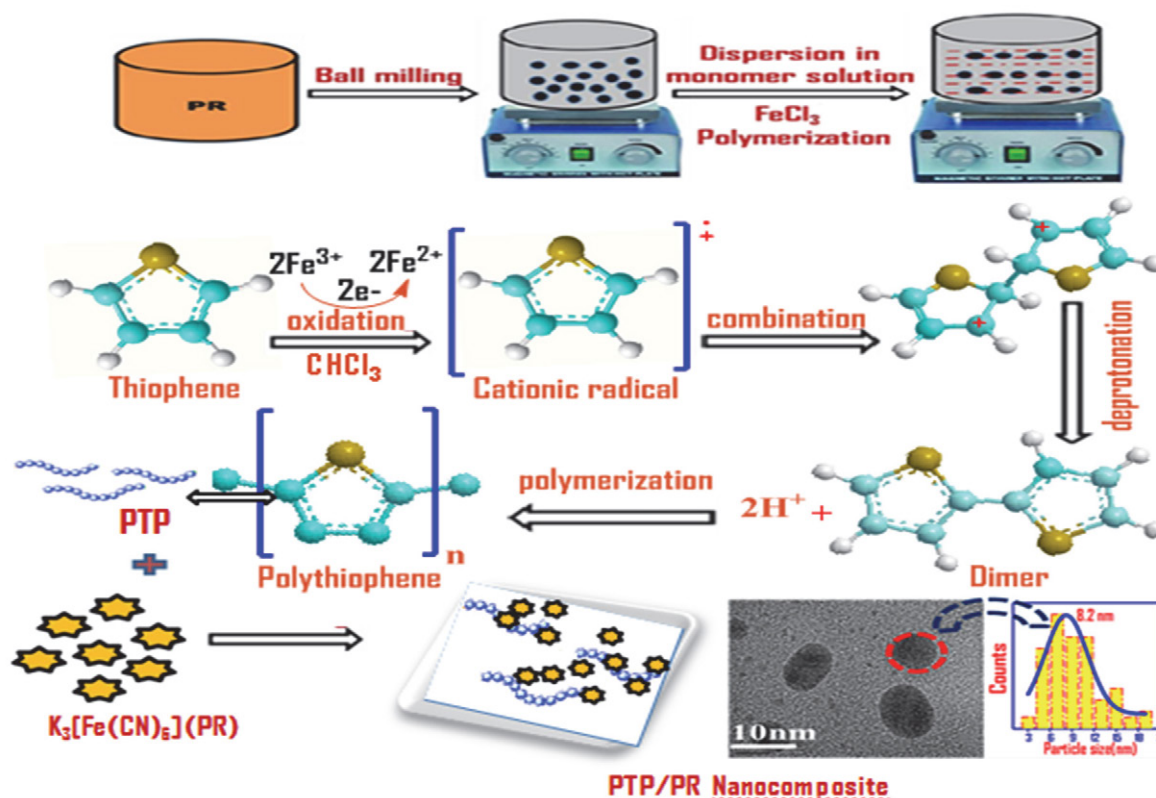
All the reagents used in the study were of analytical grade and procured from Himedia and Merck India. Thiophene was distilled prior to its use. Malachite green (MG), Potassium ferricyanide and anhydrous Ferric chloride were purchased from Merck India. Potassium ferricyanide was ground by ball milling for size reduction to nano dimension (<10 nm).

2. 2. Synthesis of Nanocomposite

The synthesis of PTP/PR nanocomposite was carried out via oxidative polymerization using FeCl_3 as oxidant in a nonaqueous medium.²¹ In the optimized synthetic procedure, 180 mL of 0.05 M FeCl_3 solution in chloroform solvent were added (dropwise) to a magnetically stirred solution of 0.022 M distilled thiophene monomer (in 70 mL of chloroform). The reaction mixture contained about 1 g of ground PR dopant (Scheme1). The polymerization reaction mixture was continuously stirred for 24 h, followed by filtering and washing the product several times with methanol to remove any oligomers and unreacted impurities. After repeated acetone washings and room temperature drying, the polymer composite was obtained as a brown powder which was subjected to structural characterization.

2. 3. Measurements

The characterization of the synthesized composite was done using analytical methods and spectroscopic techniques. Infrared spectra were obtained over a Bruker Alpha FTIR spectrophotometer in range 4000–500 cm^{-1} . The structural characterization of samples was performed by the powder X-ray diffraction (PXRD) method using a PW3050 diffractometer ($\text{CuK}\alpha$ radiations, $\lambda = 1.5418 \text{ \AA}$). The particle shape and size of PTP/PR nanocomposite was analyzed using transmission electron microscopy (TEM) measurements performed on Hitachi SU 8000 microscope at an accelerating voltage of 30 kV. For TEM studies the samples were prepared by spin-casting a THF solution of PTP/PR nanocomposite (3mg/L) on copper grids with carbon coating. The thermogravimetric analysis (TGA) of samples was performed on a SEIKO TG/DTA 6200 instrument. Thermal analysis was done from room temperature to 800°C at a heating rate of 10 °C min^{-1} under nitrogen environment. Adsorption measurements were performed using Double Beam Microprocessor UV-VIS Spectrophotometer (Model:LI-2802). Zeta Potential (surface charge) of the adsorbent particles were determined using an Anton Par Particle Size Analyser (Model:Litesizer 500). BET studies for surface area were attained at 77K using BET instrument, Quantachrome Autosorb IQ Station. The specific surface area and pore size distribution was calcu-



Scheme 1. Schematic depiction of PTP/PR nanocomposite synthesis via FeCl₃ oxidative polymerization.

lated using a multiple point BET method and non-local density functional theory (NLDFT) equilibrium model. Electrochemical experiments were carried out on Bio-Logic SAS Potentiostat (Model SP 150) using three electrode system.

2. 4. Adsorption Experiments

For adsorption studies, 20 mg of PTP/PR nanocomposite was added to a 30 mL solution of 10 ppm MG dye and the suspension was magnetically stirred. Under the optimized reaction conditions, at the regular time intervals aliquots were taken, the adsorbent was separated via centrifugation at 1000 rpm for 20 min and the left-over concentration of dye in the supernatant was measured by a UV-visible spectrophotometer at $\lambda_{\max} = 617$ nm (corresponding to MG dye). The adsorptive capacity of PTP/PR hybrid material was optimized under influencing parameters like, adsorbent dose, contact time, initial MG dye concentration and temperature range of 25–45 °C. The equations 1, 2 were used to calculate adsorption capacity of PTP/PR nanocomposite and % dye removal efficiency.²²

$$\text{Adsorption capacity } q = \frac{C_0 - C_t}{m} V \quad (1)$$

$$\% \text{ Removal} = \frac{C_0 - C_t}{C_0} 100 \quad (2)$$

Where, C_0 and C_t (mg/L) are the initial and final (after adsorption) concentrations of MG dye solution respectively, m (g) is the weight of PTP/PR nanocomposite, and V (L) is the initial volume of dye solution.

2. 5. Adsorption Studies of M.G Dye in Real Water Samples

To test the adsorption efficiency of PTH/PR in real samples, the analysis was performed on collected industrial effluent from local textile dye shop (Hazratbal, Srinagar). The dye sample of (1 mg/mL) concentration was prepared in 100 mL deionised water to which required quantities of fixing agent and mordant were also added. To 30 mL of this prepared dye solution 20 mg of PTP/PR composite was added, samples were magnetically stirred and subjected for left over MG dye estimation over different time intervals using UV-visible spectrophotometry. Furthermore, analysis of MG dye adsorption propensity of samples prepared in different water samples (Tap water and deionised water) was also explored under optimized conditions for comparative studies.

2. 6. Cyclic Voltammetry Experiments

The cyclic voltammetry experiments were carried out using three electrode system with Ag/AgCl as reference,

glassy carbon as working, and platinum wire as a counter electrode with 0.1M KNO₃ as supporting electrolyte. The solid samples of PTP/PR and PR each were dispersed in 0.5mL ethanol solution to which 15 μ L of nafion was added as binder. The suspensions were kept on ultrasonication for about 30 min to make the slurries of each suspension. The obtained slurries were drop-casted onto glassy carbon electrodes and left for open air drying for 40 min.

3. Results and Discussion

A well-planned dopant to the polymer matrix can generate composites with unique properties for aimed applications. PR turned out to be one such interesting dopant to the polythiophene matrix in terms of modulating essential parameters of a polymer composite system for potential applications. These included enhancement in the mechano, thermal, electrochemical, and photocatalytic attributes of pure PTP. The comparative studies of PR doping to PTP relative to organic dopants revealed an increased surface area, conductivity, and electrochemical stability desirable for electrochemical sensing and device fabrication. The shifting of band gap towards visible region and prevention of charge carrier recombination after PR doping were important attributes for its development as photocatalyst. The synergistic effect of adsorption and photocatalysis was also explored for effective degradation of MG dye.

3. 1. Characterization Analysis

3. 1. 1. IR Spectral Analysis

The FT-IR spectra of synthesized composite were compared with pure reactant forms and are as shown in Figure 1. The broad band around 1630 cm⁻¹ and 3300–3400 cm⁻¹ is attributed to O-H stretching vibration of adsorbed water on PTP surface, and the range of 600–1500 cm⁻¹ reflects the fingerprint region of PTP.^{23,24} Furthermore, the C-S stretching vibration of PTP and C-H out of plane deformation modes are designated by weak absorption bands around 690–1300 cm⁻¹. From the Figure 1, the black line corresponding to pure PR shows a specific absorption band around 2100 cm⁻¹ that designates CN stretching and the peak at around 600 cm⁻¹ is due to Fe-CN vibrations. Moreover, the PTP/PR nanocomposite spectrum exhibits peaks from both the constituents (green line). The intensity of pure PR vibrations is shifted and observed at 2078 cm⁻¹ and 497 cm⁻¹ in the nanocomposite FT-IR spectrum. Thus, from the peak pattern analysis (shifting of the major stretching frequencies of PTP and PR) the inclusion of PR nanoparticles particles in PTP matrix can be expected.

3. 1. 2. Thermal Analysis

Thermal stability is an essential parameter for material applications, and thermo-gravimetric analysis (TGA)

is used to examine this important property via % weight change over the programmed heating. TGA curves of pure PTP and PTP/PR nanocomposite are shown in Figure 2. It is evident from TGA plots that incorporation of PR into PTP matrix has enhanced its thermal stability noticeably. The 33% enhancement in thermal stability of PTP/PR composite compared to pristine PTP at higher temperature indicates stronger interaction between PR dopant and PTP matrix possibly via noncovalent supramolecular type forces. The observed initial weight loss at a lower temperature in case of PTP/PR composite can be attributed to the evaporation of the solvent and clinging low molecular mass volatile compounds. Furthermore, the improved mechano strength of PTP post PR doping is evident from the less sharp slope of % weight loss with temperature in the PTP/PR TGA plot. At 600°C the amount of weight loss in the case of PTP/PR composite is only 60% compared to almost 100% for pristine PTP. Thus it can be inferred from the thermograms that PR doping introduces interactions between dopant and polymer matrix which modulates the mechanical strength of pristine PTP polymer leading to its enhanced thermal stability. A comparative analysis of the dopant effect on the thermal stability of PTP composites with varied dopants indicates the improved thermal stability in the presence of PR dopant.^{25,26} The changes in pure PTP structure and function post PR doping were also analyzed using PXRD, Microscopy, and BET analysis.

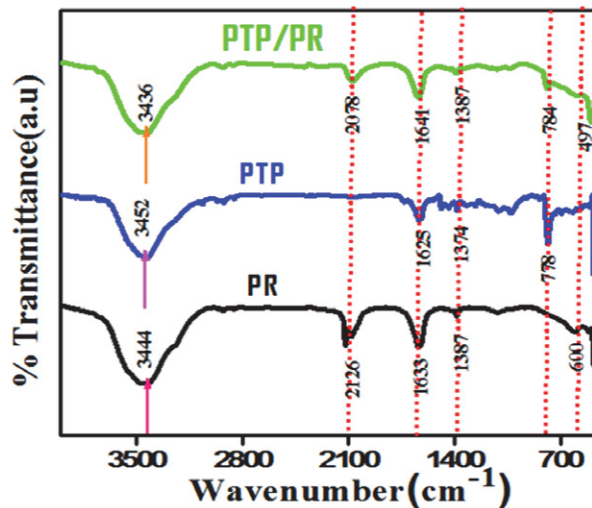


Figure 1. PTP/PR composite characterization (from selected peak picking) using FTIR spectra.

3. 1. 3. XRD Analysis

X-ray Diffraction patterns of PTP and PTP/PR nanocomposite are shown in Figure 3a. Evidently, PTP shows an amorphous halo around Bragg angles of 20–30°, thus exhibiting its amorphous nature.²⁷ However, the X-ray diffraction pattern of PTP/PR nanocomposite clearly revealed strong intense peaks at various Bragg angles, illus-

trating its crystalline nature. The crystallinity developed in nanocomposite can be attributed to the incorporation of PR in PTP matrix. This corroborates the successful synthesis of prepared nanocomposite, which is also evidenced from TEM micrographs. This is expected as polymers, being larger molecules, are capable of stronger Van der Waals and other types of possible non-covalent interactions with dopant molecules. These polymer-dopant supra interactions lead to a fair degree of order and compactness in the nanocomposite material.²⁴ The characteristic peaks were indexed using Powder X software which revealed monoclinic structure with FCC lattice. For crystallite size determination, Scherrer equation (equation 3) has been used.^{28–29}

$$D = \frac{k\lambda}{\beta \cos \theta} \quad (3)$$

Where D is the average crystallite size, k the shape factor (0.94), λ the wavelength used (Cu K α = 1.54 Å), β the FWHM (full width at half maximum) and θ is the Bragg angle. The average crystallite size as determined from above equation has been found to be 7.94 nm. This is almost similar to that obtained from TEM micrographs (8.2 nm), which is indicative of the fact that PR nanoparticle might represent a single grain or crystallite. Thus XRD analysis corroborate with the FT-IR and thermal analysis results.

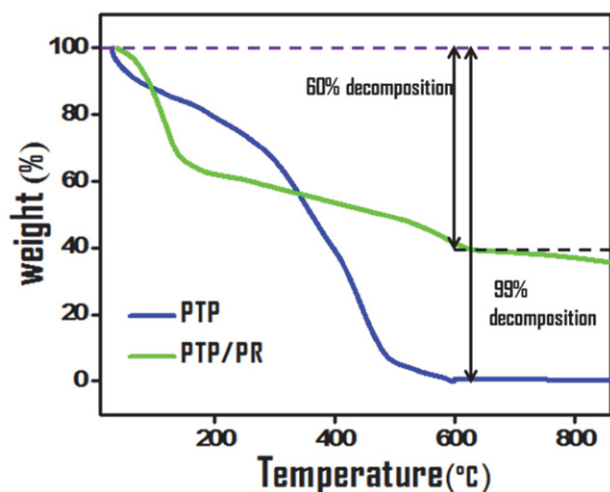


Figure 2. Thermogravimetric analysis plots showing PR enhanced thermal stability of PTP polymer.

3. 1. 4. TEM Analysis

The TEM image of PTP/PR nanocomposite is shown in Figure 3b. The image clearly reveals spherical/granular shape of PR nanoparticles which are dispersed in PTP matrix indicating the formation of nanocomposite. PR nanoparticles are seen to be dispersed in PTP matrix in discrete (inset-1) as well as agglomerated units depending upon

their particle size. The agglomeration might result owing to the Van der Waals interaction of smaller particles for bigger sized particles. The particle size distribution of these nanoparticles has been carried out by Image J software followed by Gaussian fitting that revealed the average particle size of around 8.2 nm (inset-2), revealing a mesoporous character. From TEM results, it is clear that PTP/PR is a nanocomposite. Thus, owing to the presence of small sized particles, the nanocomposite is expected to show enhanced surface area, which is confirmed from BET analysis.

3. 1. 5 Structural and Textural Characterization

Adsorption propensity is greatly influenced by the surface area and pore size of the catalyst, BET analysis was attempted to determine surface characteristics of the synthe-

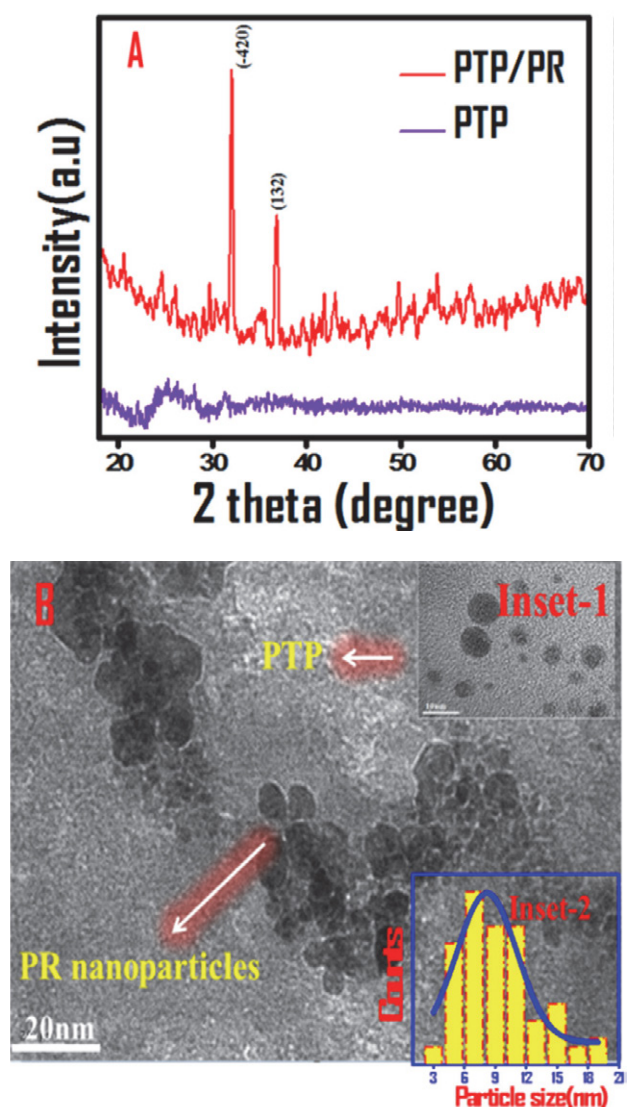


Figure 3. X-ray diffraction pattern of PTP & PTP/PR nanocomposite (A). TEM image of PTP/PR nanocomposite (B) spherical shaped PR nanoparticles of PTP/PR nanocomposite (inset-1). Gaussian histogram fitting plot for particle size distribution (inset-2)

sized PTP/PR nanocomposite. The N_2 adsorption-desorption isotherms and pore diameter distributions of PTP/PR nanocomposite, PR, pure PTP are as shown in Figure 4. The measured surface area for PTP/PR nanocomposite was found to be $81.018 \text{ m}^2 \text{ g}^{-1}$, which is higher than both PTP ($25.560 \text{ m}^2/\text{g}$) and PR ($15.453 \text{ m}^2/\text{g}$) respectively. Besides, the N_2 adsorption-desorption isotherm portrays combined type-II and IV isotherm behavior which is typical of mesoporous structure based on the IUPAC classification.^{30,31} Pure PTP has a granular texture with lesser inter-particle distance, which is evident from its lower porosity and smaller surface area. However, on addition of PR, the inter particle space gets increased, which is evident from increased porosity, in case of PTP/PR nanocomposite. The observed increase in porosity can be the reason for the enhanced surface area of PTP/PR nanocomposite compared to undoped PTP.³² The major pore size distribution of the PTP/PR nanocomposite (2.769 nm) is within the range of $1\text{--}3 \text{ nm}$, which is a characteristic of smaller pore volume systems. Thus, mesoporous structure with enhanced surface area gives PTP/PR nanocomposite a good adsorptive capacity desirable for an adsorption-based wastewater treatment application. The good surface area and visible region bandgap also makes PTP/PR a possible photocatalyst. The comparative analysis of PTP/PR nanocomposite with other closely related PTP nanocomposite systems indicates a significant increase in surface area for adsorption in case of PTP/PR Table 1.

Table 1. Comparative effect of dopants on the surface area of PTP composites

PTP Composite	Surface area (m^2/g)	Reference
PTP/ $\text{Fe}(\text{CN})_3(\text{NO})(\text{bpy}) \cdot 4\text{H}_2\text{O}$	18.9	33
PTP/ Fe_3O_4	19.4	27
PTP/ Cu^{3+}	20.88	34
PTP/ CuFe_2O_4	30.9	35
PTP/PR	81.018	Present work

3. 2. Modeling Adsorptive Propensity of PTP/PR Towards Industrial Dye Malachite Green (MG)

The higher surface area coupled with negative zeta potential value around pH 7 range indicates selectivity of PTP/PR nanocomposite towards cationic water contaminants. With this rationale, we used Malachite green as a model cationic dye for exploring the adsorptive propensity of PTP/PR nanocomposite under environmentally viable conditions.

3. 2. 1. Effects of Contact Time and Initial MG Solution Concentration

The effects of initial MG dye concentration and its contact time on PTP/PR nanocomposite adsorption ca-

capacity were observed around $20^\circ\text{C} \pm 2^\circ\text{C}$ under fixed pH and MG dye concentrations from 10 to 30 mg/L. The adsorption capacity of MG dye on PTP/PR nanocomposite under different initial concentrations with contact time is shown in Figure S1a. At lower dye concentrations, the removal rate was relatively fast and equilibrium was reached within 20 min. which shifted to 25 min. at higher concentrations. The adsorption rate was high for first 20 min. and then progressively saturated with increasing contact time (after 60 min). This observation can be corroborated with the progressive saturation of the available surface sites with increasing contact time. Since many of the adsorption sites get occupied initially and as process proceeds the number of vacant sites gets decreased and occupying remaining sites becomes difficult to occupy due to repulsive forces between the adsorbate molecules on the surface and bulk phases.²² The effect of initial concentration of MG dye on equilibrium adsorption capacity is shown in Figure S1b. From Figure S1b it can be seen that the equilibrium capacities of MG dye under different initial concentrations showed an increasing trend from 14.187 to 34.5 mg/g signifying that MG dye concentration gradient offers a stronger driving force to reduce the mass transfer resistance of the MG dye. The removal efficiency of MG by PTP/PR displayed relatively higher % removal at lower concentrations with decreasing trend towards high concentrations. This can be corroborated with the fixed adsorption capacity of the 20 mg of PTP/PR sample. Thus from adsorption capacities and removal efficiency studies, 10mg/L was observed as optimized concentration of MG dye in the subsequent experiments.

3. 2. 2. Effect of Adsorbent Dosage

The effect of PTP/PR nanocomposite dosage on adsorption properties was studied by adding its increasing amounts (10 to 30 mg) to 30mL of 10 mg/L MG dye solution at 298 K with stirring for 160 min. with the corresponding results presented in Figure S2. The removal efficiency of MG dye increases from 93.8 to 95.94% on increasing adsorbent dosage from 10 to 30 mg. This behavior can be attributed to the fact that there are more accessible active adsorption sites for MG dye over increasing adsorbent dosage, which increases its % removal efficiency. However, the adsorption capacity reduces from 28.2 to 9.59 mg/g with increasing PTP/PR dose which can be attributed to the aggregate formation at high concentration.³⁶ The aggregation of adsorbent particles at their higher concentrations was supported by Dynamic Light Scattering technique. DLS data indicates that with increase in adsorbent dosage, particle diameter increases and is shown in Figure S3. The aggregated particles at higher adsorbent dosage create diffusion resistance for MG dye towards the adsorbent surface, thereby decreasing the adsorption capacity. Thus from adsorbent dosage studies of 10 mg to 30 mg PTP/PR, 20 mg gives 94.58% removal effi-

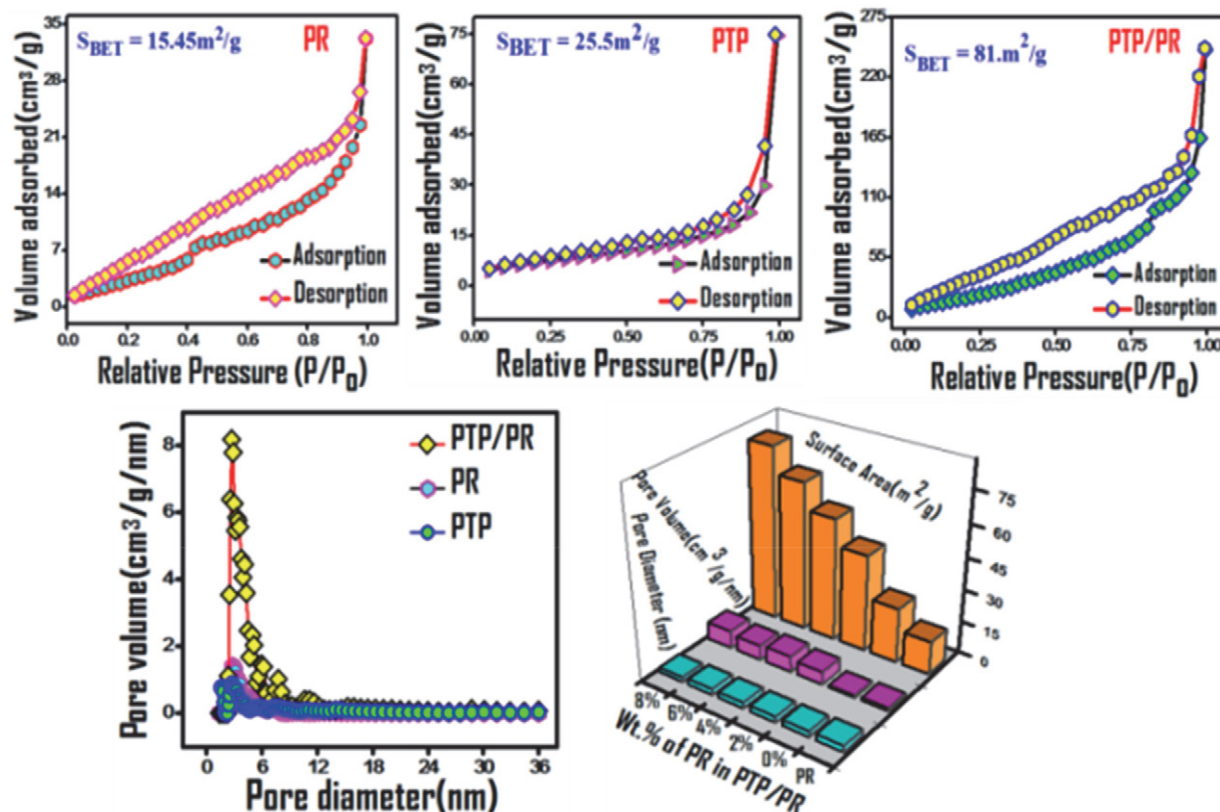


Figure 4. N₂ adsorption-desorption isotherms of PR, PTP and PTP/PR nanocomposite. Pore size distribution curves, Effect of PR wt% on the surface area, pore volume of PTP/PR

ciency under an adsorption capacity of 14.2 mg/g. Further increase in PTP/PR dose was not observed to significantly increase the removal efficiency. Therefore, from the adsorbent dose studies 20 mg was observed as optimum dose for subsequent experiments.

3. 3. Adsorption Kinetic Analysis

Adsorption as a physicochemical process involves the mass transfer of a solute from bulk liquid to the adsorbent surface. Kinetic investigations of such a transfer pave a significant understanding of the adsorption parameters. The kinetics of MG dye adsorption on the PTP/PR nanocomposite was explored by using three kinetic models: pseudo-first-order, pseudo second-order and Elovich models Figure 5 A-C. These kinetic models can be stated in their linear form as equations (4–6).^{37,38}

$$\ln(q_e - q_t) = \ln(q_e) - k_1 t \quad (4)$$

$$\frac{t}{q_t} = \frac{1}{k_2 q_e^2} + \frac{t}{q_e} \quad (5)$$

$$q_t = 1/\beta \ln \alpha \beta + 1/\beta \ln t \quad (6)$$

where, q_t (mg/g) and q_e (mg/g) are the amounts of MG ad-

sorbed at any time t (min) and at equilibrium, respectively; k_1 (min⁻¹) and k_2 (g/mg/min) are the rate constants of pseudo first order and pseudo-second-order kinetic models respectively. The kinetic parameter counting correlation coefficients (R^2), k_1 , k_2 and q_e (cal) values were determined by linear regression. The ' α ' in the equation 6 denotes initial adsorption rate (mg/g/min) and ' β ' is the desorption constant (g/mg). From the plot of q_t vs $\ln t$, Elovich constants (α , β) were determined from slope and intercept values and the values are presented in Table 2. It is seen from table 2, that the R^2 value (0.9999) for the pseudo-second-order kinetic model was much higher than that of pseudo first-order as well as Elovich kinetic models. In addition, the values of $q_{e,cal}$ calculated under pseudo-second-order model were found close to the experimental $q_{e,exp}$. Based on these observations, the pseudo-second-order kinetic model can be predicted to be the suitable to quantify the adsorption kinetics of MG onto PTP/PR nanocomposite. As is evident from calculated descriptors in table 2, the experimental data do not have an acceptable fitting to pseudo first order and Elovich models. The pseudo second order kinetic model better describes adsorption behavior of MG onto PTP/PR nanocomposite. The pseudo second-order kinetic model broadly involves adsorption, including external film diffusion, intraparticle diffusion and surface adsorption.²² Typically, intraparticle diffusion is considered as a possible rate-limiting step for a batch

reaction. To envisage the rate-limiting step of the MG dye adsorption process on PTP/PR nanocomposite, the probability of intraparticle diffusion was tested by using Weber–Morris equation 7.³⁸

$$q_t = K_{id}t^{0.5} + C \quad (7)$$

Here, K_{id} ($\text{mg/g} \cdot \text{min}^{-1/2}$) is the intraparticle diffusion rate constant, C (mg/g) is the intercept related to the thickness of the boundary layer. Figure 5D displays the plot of q_t against $t^{0.5}$, and the corresponding kinetic parameters are listed in table S1. It is seen that the regression of q_t versus $t^{0.5}$ was prompted to be linear, and the plots did not pass through the origin, interpreting that besides intraparticle diffusion, film diffusion may also be involved in the rate-controlling step. The Figure 5D shows two stages, an initial stage showing a faster adsorption rate of MG dye from solution, and flat portion depicting decreased adsorption rate due to unavailability of active sites.^{39,40} The smaller slope of intra-particle stage than that of the film diffusion stage illustrates lower adsorption is occurring at intra-particle stage.⁴¹ Besides the more significant intercept of the second segment, which gives the thickness of the boundary layer indicates that surface adsorption is also involved in the rate limiting step.⁴² Thus, adsorption of MG dye over PTP/PR nanocomposite involves film dispersion and intraparticle diffusion as possible mechanistic

processes, with the intraparticle diffusion as a dominant adsorption mechanism.

3. 4. Adsorption Isotherms

In general, adsorption isotherm marks the relationship between the amount of adsorbate adsorbed per unit mass of an adsorbent at a given temperature. Adsorption isotherms are essential descriptors for analyzing and developing any adsorption system.⁴³ The equilibrium adsorption isotherm unfolds the interaction between the adsorbate and adsorbent. In view of this, MG, PTP/PR system was tested for Langmuir, Freundlich, Temkin isotherm models Figure 6. The Langmuir isotherm model considers monolayer adsorption with all the sorption sites identical and energetically equivalent.⁴⁴ The Freundlich isotherm is based on multilayer adsorption on the heterogeneous surface, and there are interactions between the adsorbed molecules.⁴⁵ Temkin model considers adsorption on heterogeneous surfaces, effects of indirect adsorbate/adsorbent interactions and assumes heat of adsorption of all molecules decreases linearly with an increase in surface coverage.⁴⁴ The linear forms of the three isotherms are given by the following equations (8–10).

$$\frac{1}{q_e} = \frac{1}{q_m} + \frac{1}{K_L q_m C_e} \quad (8)$$

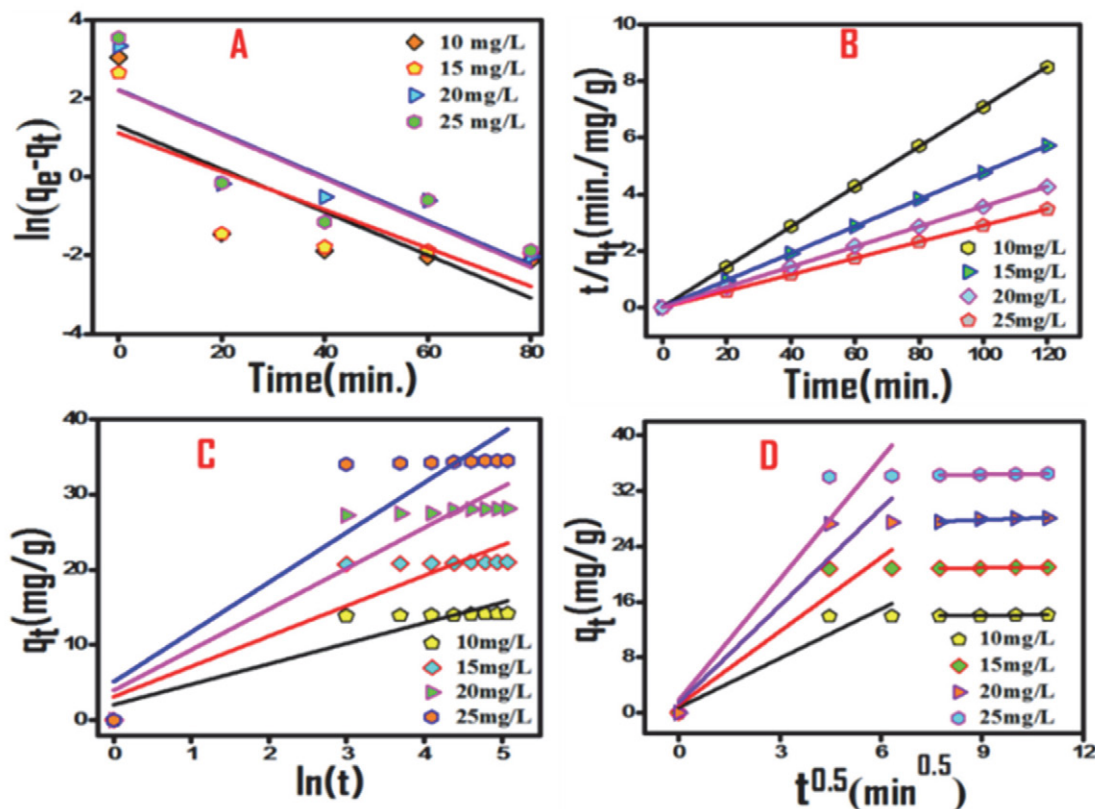


Figure 5. Kinetic models for data fitting of MG (10, 15, 20, 25 mg/L) adsorption onto PTP/PR adsorbent (20mg in 30mL solution at 298K): (A) Pseudo-first order (B) Pseudo-second order (C) Elovich kinetic models (D) Intraparticle diffusion model

Here, q_e (mg/g) is the amount of MG adsorbed at equilibrium time, C_e (mg/L) is equilibrium concentration, q_m (mg/g) is the maximum adsorption capacity and K_L is the Langmuir constant. The parameters of Langmuir model can be calculated from the slope and intercept of the linear plot $1/q_e$ vs $1/C_e$.

$$\log(q_e) = \log(k_f) + \frac{1}{n} \log C_e \quad (9)$$

K_F and n are Freundlich constants

$$q_e = \beta \ln A_T + \beta \ln C_e \quad (10)$$

Where $\beta = RT/b_T$, b_T (kJ/mol) is Temkin constant gives heat of adsorption, T is the absolute temperature (K), R is the universal gas constant (equal to 8.314 J/mol), and A_T is equilibrium binding constant (L/g). The value of Temkin constant indicates the possible mechanism (physical or chemical adsorption) on the adsorbent surface. If $b_T > 40$ kJ/mol, chemisorption occurs and if $b_T < 40$ kJ/mol, physisorption proceeds.⁴⁶ The quantities K_F , K_L , n , q_0 , b and q_t were calculated, and the values are summarized in Table 3. The correlation coefficient for Langmuir isotherm has been found to be higher (0.997) and the adsorption capacity calculated from Langmuir model (34.48 mg/g) is found to be close to the experimental value of 34.5 mg/g. This suggests that the Langmuir isotherm could well explain the adsorption characteristic of PTP/PR nanocomposite. In addition, the separation factor or equilibrium parameter (R_L) of Langmuir adsorption isotherm, which evaluates the feasibility of adsorption on adsorbent was calculated by equation (11).⁴⁷

$$R_L = \frac{1}{1 + K_L C_0} \quad (11)$$

where, K_L was the Langmuir equilibrium constant and C_0 (mg/L) was the initial MG dye concentration. The value of

R_L indicated the type of the isotherm to be either irreversible ($R_L=0$), favorable ($0 < R_L < 1$), unfavorable ($R_L > 1$) or linear ($R_L = 1$). The calculated value of R_L was found in the range of 0.01 – 0.1 in this study,⁴⁸ indicating the adsorption of MG on PTP/PR is favorable, and as such, it can be a good adsorbent material for MG removal from aqueous solution. In addition, the calculated R^2 value of 0.994, for the Freundlich isotherm model signifies a good degree of fit and the heterogeneity factor (n) was calculated to be 1.304. This also confirms a conducive adsorption process as a reaction is classified as favorable if $1 < n < 10$.⁴⁹ The fitting of observed adsorption data with regression values of $R^2 > 0.99$ to both Langmuir and Freundlich isotherms models indicate that adsorption of MG dye over PTP/PR nanocomposite includes combined physical as well as chemical adsorption with monolayer/multilayer adsorption.^{50,51} The possible forces involved in adsorbate adsorbent interaction include π - π stacking, hydrogen-bond interaction, and electrostatic interaction.

3. 5. Effect of Temperature

To assess effect of temperature on adsorption capacity of PTP/PR nanocomposite for MG, batch adsorption experiments in the temperature range of 25–45 °C were carried out. The adsorption propensity of the PTP/PR nanocomposite improved slightly with increase of system temperature^{52,53} (Figure 7A). This can be attributed to increased thermal motion of MG molecules at higher temperature allowing more MG molecules to interact with adsorption sites on PTP/PR nanocomposite. Increasing temperature also decreases viscosity and enhances diffusion of MG dye molecules due to adsorbent surface.⁵⁴ An important observation to note was that adsorption capacities of PTP/PR for MG dye remained at relatively high value of above 14.5 mg/g over the entire investigated temperature range, specifying its ability towards MG dye removal under varied temperature conditions.

Table 2. Kinetic models for the adsorption of MG on PTP/PR nanocomposite at 298 K

Pseudo-1st-order				Pseudo-2nd-order			Elovich model			
C_0 (mg/L)	q_{eexp} (mg/g)	k_1 (min ⁻¹)	q_{ecal} (mg/g)	R^2	k_2 (g /mg/min)	q_{ecal} (mg/g)	R^2	α (mg/g/min)	β (g/mg)	R^2
10	13.92	0.05	1.042	0.50	0.18	14.14	0.99	7.787	0.368	0.821
15	20.81	0.046	1.218	0.51	0.22	21.28	0.99	22.606	0.248	0.813
20	27.45	0.045	17.95	0.78	0.06	28.17	0.99	51.779	0.185	0.831
25	34.15	0.031	6.184	0.86	0.116	34.5	0.99	164.130	0.151	0.814

Table 3. Isotherm parameters for the adsorption of MG onto PTP/PR nanocomposite at 298 K

Langmuir				Freundlich			Temkin		
K_L (L/mg)	q_m (mg/g)	R_L	R^2	K_f (L/g)	n	R^2	b_T (kJ/mol)	A_T	R^2
1.14	34.48	0.08	0.997	18	1.304	0.994	0.145	12.5	0.98

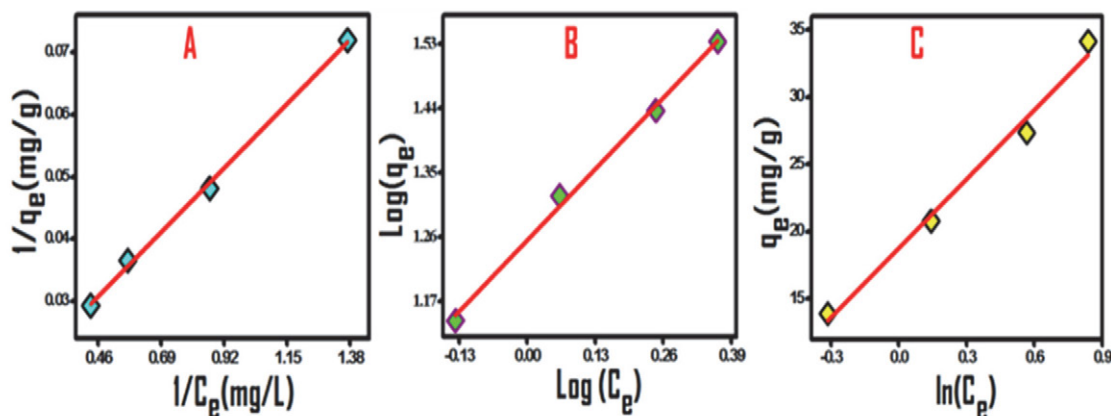


Figure 6. Adsorption isotherms of MG on PTP/PR nanocomposite; (A) Langmuir (B) Freundlich (C) Temkin.

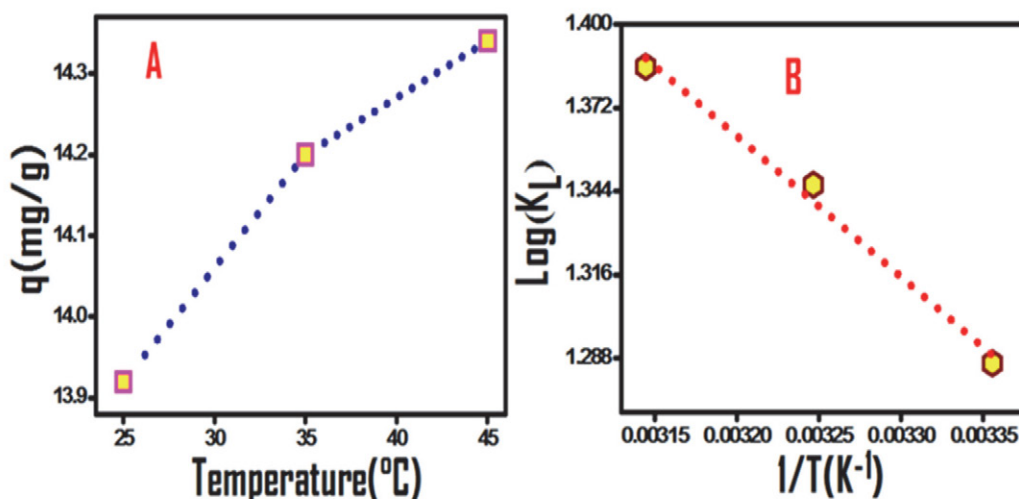


Figure 7 (A) Temperature effect on MG (10 mg/L, 30 mL) adsorption on 20 mg PTP/PR composite (B) Van't Hoff plot

3. 6. Thermodynamic Analysis

The thermodynamic parameters (change in Gibbs free energy (ΔG), enthalpy (ΔH) and entropy (ΔS)) were assessed from the effect of temperature on the adsorption of MG dye onto PTP/PR using the equations (12,13)

$$\Delta G^\circ = -RT \ln(K_L) \quad (12)$$

$$\ln(K_L) = -\Delta H^\circ/RT + \Delta S^\circ/R \quad (13)$$

where, K_L (L/mol) is the Langmuir equilibrium constant; T (K) is system temperature and R (8.314 J/(mol K)) is the molar gas constant. The negative values of ΔG calculated using equation 12 inferred that adsorption of MG onto PTP/PR nanocomposite is thermodynamically feasible. ΔH and ΔS calculated from slope and intercept of the van't Hoff plot $\log(K_L)$ versus $1/T$ shown in Figure 7B. The calculated thermodynamic parameters of MG dye onto PTP/PR are presented in Table 4. Furthermore, the positive value of ΔH (9.03 kJ/mol) specified that the adsorption process is endothermic in nature. Also, the positive value of

ΔS (54.95 J/mol K) means that the randomness increased at the solid–liquid interface during the adsorption of MG dye in the aqueous solution on the PTP/PR nanocomposite.

3. 7. Effect of pH

The pH is a vital parameter to consider adsorptive propensity as it influences surface charge of the adsorbent, degree of ionization of different adsorbates, protonation/deprotonation of functional groups at the adsorbent active sites as well as adsorbate. Moreover, for a significant real time application the adsorption shall occur in the environmentally viable pH range.⁵⁵ Accordingly, pH effect for MG dye adsorption on PTP/PR nanocomposite was studied. Figure 8A depicts comparative pH influence towards MG dye adsorption on PTP/PR nanocomposite. Noticeably, adsorption capacities of PTP/PR nanocomposite for MG were relatively higher at pH 7 (14.187 mg/g) and progressively decreased from pH 7 to 4 from 14.187 to 13.53 mg/g. The higher adsorption of MG dye by PTP/PR nanocom-

posite from the neutral solutions was an encouraging result from the wastewater treatment point of view. Under acidic pH, the surface of the PTP/PR gets positively charged due to protonation of sulphur atom of the thiophene units in the polymer matrix,⁵⁶ thereby repelling the cationic MG dye from polymer matrix. For pH lower than 7.0, MG dye gradually takes positive charge due to protonation on its nitrogen atoms⁵⁷ which decrease adsorption capacities with decreasing solution pH. Around pH 7 deprotonation of sulphur atoms of polymer matrix is complete which attracts cationic MG dye towards PTP/PR surface leading to increased adsorption capacity at environmentally viable neutral pH. The pH effect results were supported by zeta potential studies of PTP/PR nanocomposite over a pH scan Figure 8B. From the zeta potential studies, the pH corresponding to point of zero charge (pHpzc) of pristine PTP⁵⁸ and PTP/PR nanocomposite were calculated to be 4.3 and 3.79 respectively. PTP/PR nanocomposite has a point of zero charge (pHpzc) at pH of 3.79 which also marks its transient pH. Above this pH its surface is negatively charged and below it positively charged. The lowered value of pHpzc corroborates with the presence of negative surface charge in case of PTP/PR nanocomposite above pH 3.8. In pH range 0–3 surface of the nanocomposite is expected to have positive zeta potential, which progressively changes with increasing pH and acquires a maximum negative zeta potential value around pH 7 Figure 8B. From zeta potential studies repulsive interaction at lower pH as well as attractive interaction near neutral pH between cationic MG dye and adsorbent surface can hence be confirmed. The negative surface charge under the environmental pH range of 6 to 8 makes, PTP/PR nanocomposite an excellent adsorbent for cationic contaminants in wastewater. The adsorptive propensity of PTP/PR nanocomposite for cationic MG dye prepared in tap, deionized waters and also with anionic dyes was at-

tempted for comparative analysis. Although pH and zeta potential studies indicate dominance of electrostatic interaction for MG dye adsorption onto PTP/PR nanocomposite but the possibility of other interactional forces such as pi-pi stacking and van der Waals type interactions cannot be ruled out.

Table 4. Thermodynamic parameters for adsorption of MG (10 mg/L, 30 mL) onto (20 mg/L) PTP/PR nanocomposite.

T (K)	ΔG° (kJ/mol)	ΔH° (kJ/mol)	ΔS° (J/mol K)
298	-3.194	9.03	54.95
308	-3.446	9.03	54.95
318	-3.663	9.03	54.95

3. 8. Adsorption Mechanism IR Spectrum

To gain some insights about the adsorption mechanism, FTIR spectral analysis of PTP/PR nanocomposite before and after MG dye adsorption was carried out and are as shown in Fig. S4. The FTIR bands of PTP/PR nanocomposite at 490–498 cm^{-1} corresponding to -C-S-C- ring deformation are decreased in intensity and the absorption bands corresponding to -C-H-, -C-C-, O-H stretch get slightly shifted to lower wave numbers post adsorption with MG dye. These changes indicate role of sulphur site -S- in MG dye adsorption process. A prominent absorption band at 2090 cm^{-1} characteristic of -C-N- stretching frequency due to PR particles also gets decreased in intensity after MG dye adsorption indicates ionic type interaction with -C-N-group. Furthermore, the red shift in absorption frequencies can be attributed to electrostatic attraction resulting from lone pair on -S- and cationic MG dye. In addition, pi-pi stacking interaction could be possi-

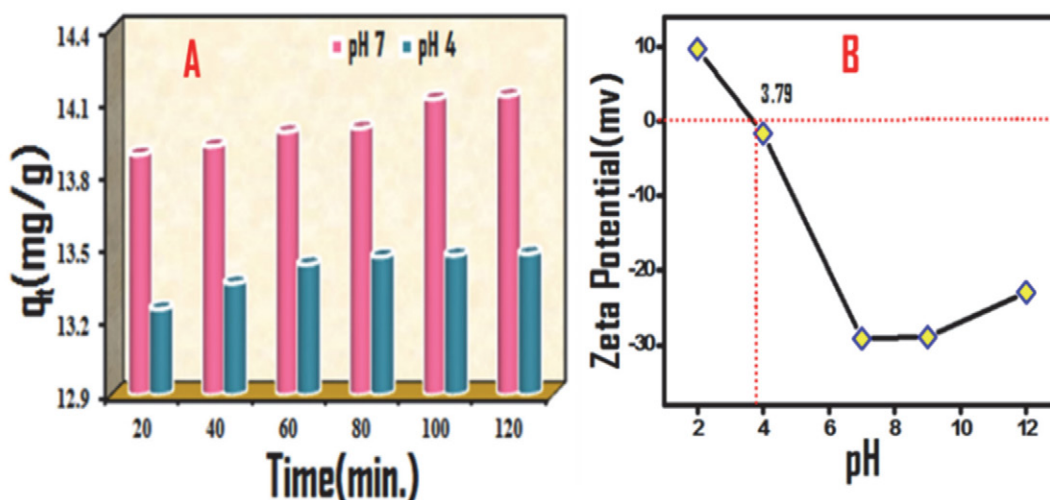


Figure 8. (A) Effects of solution pH on adsorption of MG (10 mg/L, 30 mL) onto the 20 mg of PTP/PR nanocomposite at 298 K. (B) Zeta potential studies of PTP/PR over pH range of 2–12.

ble between aromatic rings of MG dye and polythiophene matrix. The possible adsorption mechanism and probable interactions are shown in Figure S5.

3. 9 Adsorption Studies of MG Dye in Real Time Samples

The real time efficiency of PTP/PR nanocomposite was examined via dye removal efficiency in textile industry wastewater samples. The good adsorptive removal of MG dye from textile industry effluents offers the possibility of using PTP/PR nanocomposite in environmental wastewater treatment application.⁵⁹ The efficacy of PTP/PR nanocomposite towards MG dye removal in samples, prepared in normal tap water and deionized water depicted more or less similar % adsorption under optimized conditions Figure 9A. The viability of selective adsorption using PTP/PR were studied by taking Rhodamine as cationic dye, Congo red and Methyl orange as anionic dyes. It was found that the synthesized PTP/PR exhibited higher adsorption capacity towards cationic dyes than anionic dyes Figure 9B. This can be ascribed to the negative surface charge on the PTP/PR nanocomposite under an environmentally viable pH range.

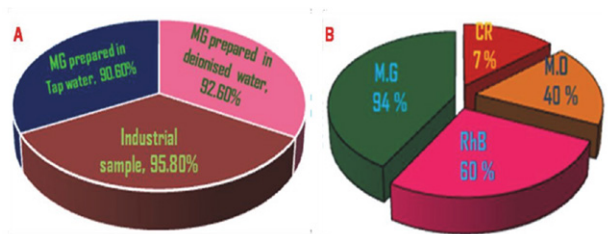


Figure 9. Adsorptive efficiency of PTP/PR towards: (A) real time samples (B) representative dyes from different dye classes.

4. Adsorbent Recovery and Recycling

Adsorption process being a benign and non-invasive method for the widespread wastewater treatment applications is often limited by adsorbent recovery and regeneration post treatment. Regarding regeneration and reusability of adsorbent post treatment, recovery is one of the crucial parameters, magnetic separation is a very helpful method to recover magnetically active adsorbents for an improved economic feasibility. PTP/PR nanocomposite has PR as a magnetic core in the adsorbent nanocomposite, bringing the chances of easy magnetic separation. PTP/PR nanocomposite adsorbent was recovered using magnetic separation any undesired change for better recyclability. In each regeneration cycle, the used adsorbent was suspended in distilled water and magnetically stirred overnight followed by resuspending in 0.1 M HNO₃ and 0.1M NaOH. The adsorption capacity of PTP/PR nano-

composite decreased overall by around 20% after five consecutive cycles post. However, adsorption equilibrium time of 30 minutes progressively increased to 50 minutes after 5 cycles.

4. 1. Synergism of Photocatalysis and Adsorption for Removal of MG Dye by PTP/PR Nanocomposite.

In our attempt to investigate the PR based modulation of the PTP matrix, we calculated the band gap of PTP/PR nanocomposite using Tauc Method.⁶⁰ The calculated band gap of 8 wt% of PTP/PR was found to be 2.4 eV relative to the bandgap of 3.0 eV for pure PTP matrix. This PR lowering of band gap has made the PTP/PR nanocomposite as visible light absorbing semiconductor. The larger surface area of 81m²/g and visible region band gap of PTP/PR nanocomposite are desirable features for the photocatalytic activity. To examine the PR effect on the photo generated hole electron pair recombination of PTP/PR nanocomposite cyclic voltammetry (CV) technique was used. CV experiments in 0.1 M KNO₃ supporting electrolyte at varying scan rates were carried out using PTP/PR nanocomposite and PR modified Glassy carbon electrodes (GCE). The changes in the voltammograms of modified GCE with increasing scan rates from 20 to 100 mV/s can be ascribed to the modified rate of the PR electron transfer in the form of PTP/PR nanocomposite. From Figure 10, it was seen that peak currents increased with scan rate and can be linearly correlated with square root of scan rates suggesting diffusion-controlled process. The shifting of peak potentials on increasing scan rate corroborates with the overall quasi reversibility of redox process. The electrochemical impedance spectroscopy (EIS) analysis of the PTP/PR modified electrode was observed in 0.1M KNO₃. The results of EIS are represented as Nyquist plots depicting semicircular and linear regions. The semicircular part portraying high frequency zone describes electron-transfer resistance (R_{ct}), while the lower frequency linear position indicates diffusion-controlled operation. The higher resistance of PR/GCE electrode can be evidenced from the larger diameter of semicircle which is typically under high R_{ct} condition. The comparatively lower semi-circular arc diameter (Nyquist plot inset of Figure 10) in case of PTP/PR confirms attenuation of R_{ct} on composite formation with PR dopant. The lowering of R_{ct} on composite formation with PTP, indicates that hybrid material (PTP/PR) possesses lower charge transfer resistance indicating that charge carriers (photogenerated electron-hole pairs) are more separated with higher mobility and lower recombination tendency. These attributes are highly desirable for photocatalytic activity.⁶¹ With such desirable properties of PTP/PR nanocomposite towards photocatalytic activity, we envisaged a synergistic effect of photocatalysis and adsorption by PTP/PR nanocomposite towards the MG dye attenuation. The synergistic effect of photocatalysis and

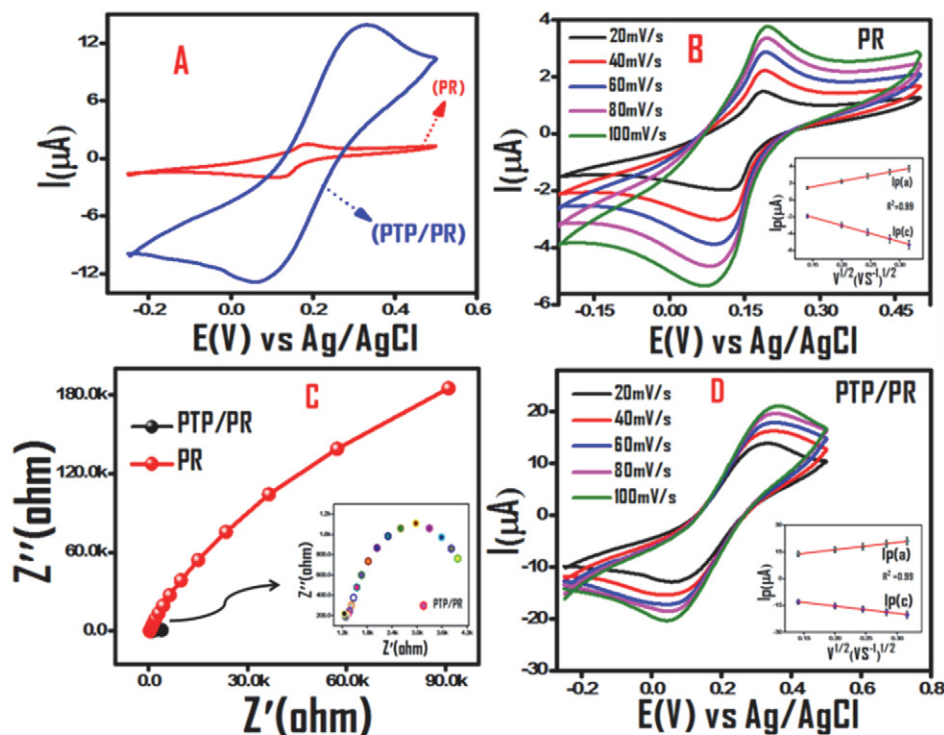


Figure 10. Comparative Cyclic Voltammograms of PR and PTP/PR at constant and increasing scan rates (A, B, D), (C) Comparative Nyquist plots for PR and PTP/PR nanocomposite.

adsorption could be observed within 30 minutes under the irradiation from 150 W CFL. The results of synergistic effect are summarized in the Fig.11.

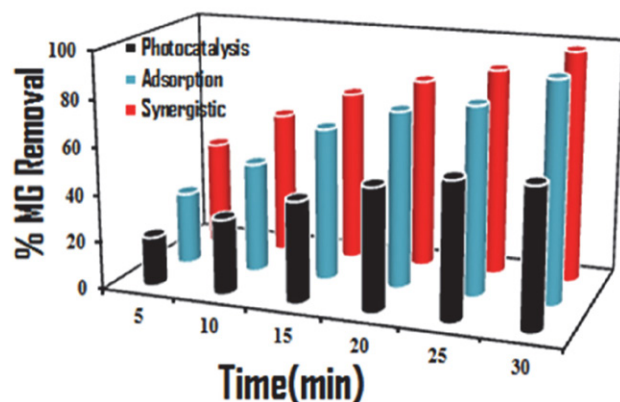


Figure 11. The synergistic effect of photocatalysis and adsorption for MG dye attenuation by PTP/PR nanocomposite

5. Conclusion

Prussian red (PR) on account of its unique properties was envisaged as an inorganic dopant towards polythiophene (PTP) conducting polymer matrix. Oxidative polymerization reaction via solvothermal route was utilized

for incorporating ball milled PR in the polythiophene matrix. The interaction of PR with PTP matrix was observed from the spectral changes in the FTIR and PXRD patterns. TEM imaging data identified PTP/PR hybrid material as a nanocomposite system. The observed thermal, electrochemical and photocatalytic descriptors of PTP/PR over pristine PTP suggested a desirable enhancement in these properties for the possible applications as water treatment nano-material. Zeta potential and pH studies suggest good adsorptive propensity towards cationic dyes under environmental conditions. An adsorption capacity of 35mg/g for removal of cationic dye Malachite Green (MG) was observed in the real time effluents from dye industry. From structural analysis, electrostatic, and pi-pi type interactions have been predicted to be predominant noncovalent forces involved in adsorption of MG dye over PTP/PR nanocomposite. Adsorption data fitted Langmuir and Freundlich adsorption isotherms suggesting monolayer as well as multi-layer adsorption process, besides kinetic studies revealed pseudo-second order model for the adsorption of MG dye over nanocomposite. Negative value of free energy indicated thermodynamic spontaneity, recyclability with good regeneration was observed even after five cycles. Taken together PR as novel dopant in the PTP matrix has desirably enhanced its polymeric properties and as PTP/PR nanocomposite, it has increased the potency of conducting polymer towards wastewater treatment application. Further development of PTP/PR nanocomposite for

a wider water treatment application involving combined effect of adsorptive and photocatalytic elimination of persistent water contaminants is underway in our laboratory.

Acknowledgements

The authors are grateful to Head Dept. of Chemistry NIT Srinagar for allowing the BET studies. MM acknowledges the University Grants Commission GOI, for the award of JRF fellowship.

Conflict of interest

The authors declare that they have no conflict of interest and no competing financial interest.

6. References

1. T. H. Y. Lee, J. Chuah, S. A. Snyder, *ACS EST Water* **2022**, 2, 907–931. **DIO:**10.1021/acsestwater.1c00453
2. W. Ahmad, R. D. Alharthy, M. Zubair, M. Ahmed, A. Hameed, S. Rafque, *Sci. Rep.* **2021**, 11, 17006. **DIO:**10.1038/s41598-021-94616-4
3. A. Tkaczyk, K. Mitrowska, A. Posyniak, *Sci. Total. Environ.* **2020**, 717, 137222. **DIO:**10.1016/j.scitotenv.2020.137222
4. R. Al-Tohamy, S. S. Ali, F. Li, K. M. Okasha, A. G. Mahmoud, T. Elsamahy, H. Jiao, Y. Fu, *J. Sun. Ecotoxicol. Environ. Saf.* **2022**, 231, 113160. **DIO:**10.1016/j.ecoenv.2021.113160
5. Z. Peng, D. Wu, W. Wang, F. Tan, T. Ng, J. Che, X. Qiao, P. Wong, *Appl. Surf. Sci.* **2017**, 396, 19–25. **DIO:**10.1016/j.apsusc.2016.11.026
6. M. Shaban, M. R. Abukhadra, *Environ. Earth Sci.* **2017**, 76, 2–16. **DIO:**10.1007/s12665-017-6636-3
7. S. Dutta, B. Gupta, S. K. Srivastava, A. K. Gupta, *Mater. Adv.* **2021**, 2, 4497. **DIO:**10.1039/D0MA00862A
8. Q. Liu, Y. Li, H. Chen, J. Lu, G. Yu, M. Möslang, J. Y. Zhou, *J. Hazard. Mater.* **2020**, 382, 121040. **DIO:**10.1016/j.jhazmat.2019.121040
9. I. Custodio, M. Candido, I. Carolina, B. Pires, H. P. Oliveira, *CLEAN-SOIL AIR WATER* **2021**, 49, 1863–0650. **DOI:**10.1002/clen.202000189
10. J. Stejskal, M. Kohl, M. Trchova, Z. Kolská, M. Pekárek, I. Křivka, J. Prokeš, *Mater. Adv.* **2021**, 2, 706–717. **DIO:**10.1039/D0MA00730G
11. K. R. Dunbar, R. A. Heintz, *Prog. Inorg. Chem.* **1997**, 45, 283–391
12. M. A. Rizvi, N. Teshima, G. M. Peerzada, *Croat. Chem. Acta.* **2013**, 86, 345–350 **DIO:**10.5562/cca2167
13. M. A. Rizvi, S. A. Akhooon, S. R. Maqsood, G. M. Peerzada, *J. Anal. Chem.* **2015**, 70, 633–638 **DIO:**10.1134/S1061934815050093
14. I. Yousuf, M. Zeeshan, F. Arjmand, M. A. Rizvi, S. Tabassum, *Inorg. Chem. Commun.* **2019**, 106, 48–53. **DIO:**10.1016/j.inoche.2019.05.027
15. Y. Dangat, M. A. Rizvi, P. Pandey, K. Vanka, *J. Organomet. Chem.* **2016**, 801, 30–41. **DIO:**10.1016/j.jorganchem.2015.10.015
16. M. A. Rizvi, M. Mane, M. A. Khuroo, G. M. Peerzada, *Monatsh. Chem.* **2017**, 148, 655–668 **DIO:**10.1007/s00706-016-1813-8
17. M. Kumar, A. Kumar, M. Rizvi, M. Mane, S. C. Taneja, K. Vanka, B. A. Shah, *Eur. J. Org. Chem.* **2014**, 2014, 5247–5255. **DIO:**10.1002/ejoc.201402551
18. S. Devari, M. Kumar, R. Deshidi, M. Rizvi, B. A. Shah, *Beilstein J. Org. Chem.* **2014**, 10, 2649–2653. **DIO:**10.3762/bjoc.10.277
19. M. A. Rizvi, S. K. Moosvi, T. Jan, S. Bashir, P. Kumar, W. D. Roos, H. C. Swart, *Polymer* **2019**, 163, 1–12. **DIO:**10.1016/j.polymer.2018.12.044
20. T. Jan, M. A. Rizvi, S. K. Moosvi, M. H. Najar, S. H. Mir, G. M. Peerzada, *ACS Omega* **2021**, 6, 7413–7421. **DIO:**10.1021/acsomega.0c05799
21. T. Jan, S. K. Moosvi, M. H. Najar, G. M. Peerzada, M. A. Rizvi, *J Mater Sci: Mater Electron* **2022**, 33, 8179–8192. **DIO:**10.1007/s10854-022-07969-5
22. Q. Xin, J. Fu, Z. Chen, S. Liu, Y. Yan, J. Zhang, Q. Xu., *J. Environ. Chem. Eng.* **2015**, 3, 1637–1647. **DIO:**10.1016/j.jece.2015.06.012
23. G. Ma, X. Liang, L. Li, R. Qiao, D. Jiang, Y. Ding, H. Chen, *Chemosphere*, **2014**, 100, 146–151. **DIO:**10.1016/j.chemosphere.2013.11.053
24. M. Faisal, F. A. Harraz, A. E. Al-Salami, S. A. Al-Sayari, A. Al Hajry, M. S. AlAssiri, *Mater. Chem. Phys.* **2018**, 214, 126–134. **DIO:**10.1016/j.matchemphys.2018.04.085
25. M. Sharif, B. Pourabas, *RSC Adv.* **2016**, 6, 93680–93693. **DIO:**10.1039/C6RA16701B
26. K. Namsheer, C. S. Rout, *RSC Adv.* **2021**, 11, 5659–5697. **DIO:**10.1039/D0RA07800J
27. F. Zhanga, Y. Shi, Z. Zhao, W. Song, Y. Cheng, *Appl. Catal. B: Environmental*, **2014**, 150–151, 472–478 **DOI:**10.1016/j.apcatb.2013.12.049.
28. M. H. Najar, K. Majid, M. A. Dar, *J. Mat. Sci. Mat. Electron.* **2017**, 28, 11243–11252. **DIO:**10.1007/s10854-017-6913-7
29. M. H. Najar, K. Majid, *RSC Adv.* **2016**, 6, 25449–25459. **DIO:**10.1039/C6RA00950F
30. F. Rojas, I. Kornhauser, C. Felipe, J. M. Esparza, S. Cordero, A. Dominguez, J. L. Riccardo, *Phys. Chem. Chem. Phys.* **2002**, 4, 2346–2355. **DIO:**10.1039/b108785a
31. M. Thommes, K. Kaneko, A. V. Neimark, J. P. Olivier, F. R. Reinoso, J. Rouquerol, K. S. W. Sing, *Pure Appl. Chem.* **2015**, 87, 1051–1069. **DIO:**10.1515/pac-2014-1117
32. S. P. Takle, S. D. Naik, S. K. Khore, S. A. Ohwal, N. M. Bhujbal, S. L. Landge, B. B. Kale, R. S. Sonawane, *RSC Adv.* **2018**, 8, 20394. **DIO:**10.1039/C8RA02869A
33. M. H. Najar, K. Majid, *RSC Adv.* **2015**, 5, 107209–107221. **DIO:**10.1039/C5RA19992A
34. M. Karegar, M. M. Khodaei, *J. Appl. Polym. Sci.* **2021**, 139, 51489. **DIO:**10.1002/app.51489
35. A. H. Kamel, A. A. Hassan, A. E. E. Amr, H. H. El-Shalakany, M. A. Al-Omar, *Nanomaterials* **2020**, 10, 586. **DIO:**10.3390/nano10030586

36. M. Rajabi, K. Mahanpoor, O. Moradi, *J. Appl. Polym. Sci.* **2019**, *136*, 47495. **DIO:**10.1002/app.47495
37. M. Zhang, L. Chang, Y. Zhao, Z. Yu, *Arab. J. Sci Eng.* **2019**, *44*, 111–121. **DIO:**10.1007/s13369-018-3258-3
38. N. F. Al-Harby, E. F. Albahly, N. A. Mohamed. *Polymers* **2021**, *13*, 4446. **DIO:**10.3390/polym13244446
39. R.-L. Liu, Y. Liu, X.-Y. Zhou, Z.-Q. Zhang, J. Zhang, F. Q. Dang, *Bioresour. Technol.* **2014**, *154*, 138–147. **DIO:**10.1016/j.biortech.2013.12.034
40. N. Rajic, D. Stojakovic, D. Jovanovic, N. Z. Logar, M. Mazaj, V. Kaucic, *Appl. Surf. Sci.* **2010**, *257*, 1524–1532. **DIO:**10.1016/j.apsusc.2010.08.090
41. K. Z. Setshedi, M. Bhaumik, S. Songwane, M. S. Onyango, A. Maity, *Chem. Eng. J.* **2013**, *222*, 186–197. **DIO:**10.1016/j.cej.2013.02.061
42. H. K. Boparai, M. Joseph, D. M. O'Carroll, *J. Hazard. Mater.* **2011**, *186*, 458–465. **DIO:**10.1016/j.jhazmat.2010.11.029
43. M. A. A. Ghouti, D. A. Da'ana, *J. Hazard. Mater.* **2020**, *393*, 122383. **DIO:**10.1016/j.jhazmat.2020.122383
44. J. Wang, X. Guo, *Chemosphere* **2020**, *258*, 127279. **DIO:**10.1016/j.chemosphere.2020.127279
45. R. Saadi, Z. Saadi, R. Fazaeli, N. E. Fard, *Korean J. Chem. Eng.* **2015**, *32*, 787–799. **DIO:**10.1007/s11814-015-0053-7
46. A. L. Taka, E. F. Kankeu, K. Pillay, X. Y. Mbianda, *Environ. Sci. Pollut. Res.* **2018**, *25*, 21752–21767. **DIO:**10.1007/s11356-018-2055-6
47. S. Pandey, S. B. Mishra, *J. Colloid. Interface Sci.* **2011**, *361*, 509–520. **DIO:**10.1016/j.jcis.2011.05.031
48. J. N. Edokpayi, E. Makete, *Phys. Chem. Earth* **2021**, *123*, 103007. **DIO:**10.1016/j.pce.2021.103007
49. K. Parashar, N. Ballav, S. Debnath, K. Pillay, A. Maity, *J. Colloid. Interface Sci.* **2016**, *476*, 103–118. **DIO:**10.1016/j.jcis.2016.05.013
50. Y. Chen, J. Li, F. Wang, H. Yang, L. Liu, *Chemosphere* **2021**, *265*, 129133. **DIO:**10.1016/j.chemosphere.2020.129133
51. K. Y. Foo, B. H. Hameed, *Chem. Eng. J.* **2010**, *156*, 2–10. **DIO:**10.1016/j.cej.2009.09.013
52. D. Robati, M. Rajabi, O. Moradi, F. Najafi, I. Tyagi, S. Agarwal, V. K. Gupta, *J. Mol. Liq.* **2016**, *214*, 259–263. **DIO:**10.1016/j.molliq.2015.12.073
53. K. Gupta, O. P. Khatri, *J. Colloid. Interface Sci.* **2017**, *501*, 11–21. **DIO:**10.1016/j.jcis.2017.04.035
54. C. H. Wu, *J. Hazard. Mater.* **2007**, *144*, 93–100. **DIO:**10.1016/j.jhazmat.2006.09.083
55. M. A. Rizvi, Y. Dangat, T. Shams, K. Z. Khan, *J. Chem. Educ.* **2016**, *93*, 355–361. **DIO:**10.1021/acs.jchemed.5b00499
56. N. C. Joshi, N. Malik, A. Singh, *J. Inorg. Organomet. Polym. Mater.* **2020**, *30*, 1438–1447. **DIO:**10.1007/s10904-019-01252-7
57. G. Y. Abate, A. N. Alene, A. T. Habte, D. M. Getahun, *Environ. Syst. Res.* **2020**, *9*, 29. **DIO:**10.1186/s40068-020-00191-4
58. M. Karegar, M. M. Khodaei, *J. Appl. Polym. Sci.* **2022**, *139*, 51489. **DIO:**10.1002/app.51489
59. S. M. Botsa, K. Basavaiah, *Sci. Rep.* **2020**, *10*, 14080. **DIO:**10.1038/s41598-020-70194-9
60. M. M. Abdi, H. N. M. Ekramul Mahmud, L. C. Abdullah, A. Kassim, M. Z. Ab. Rahman, J. L. Ying Chyi, *Chinese J. Polym. Sci.* **2012**, *30*, 93–100. **DIO:**10.1007/s10118-012-1093-7
61. J. Luo, Y. Ma, H. Wang, J. Chen, *Electrochim. Acta* **2015**, *167*, 119–125. **DIO:**10.1016/j.electacta.2015.03.097

Povzetek

Koordinacijske spojine kot dodatki prevodnim polimerom združujejo zelene lastnosti posameznih komponent za namen sinergističnega učinka. Koordinacijska spojina prusko rdeča (PR) z železom (III) je bila dopirana v matriko politiofena (PTP) z namenom raziskati nagnjenost tega anorgansko-organskega hibridnega kompozitnega materiala k čiščenju odpadne vode. Dopiranje PR izboljša mehanske, toplotne, električne in fotokatalitske lastnosti čistega PTP. Karakterizacija kompozita PTP/PR je bila opravljena z rentgensko difrakcijo prahu, TEM, TGA, FTIR, BET analizo in UV-vidno spektroskopijo. Optimizacija adsorpcijskih pogojev, regeneracija adsorbenta, študije adsorpcijske termodinamike PTP/PR so bile izvedene z uporabo barvila malahitno zeleno (MG). Pri optimiziranih pogojih je bila dosežena 92% adsorpcija barvila MG pri 20 mg nanokompozita PTP/PR v 20 minutah pri pH 7. Nanokompozit PTP/PR je prav tako dokazal komplementarno učinkovitost v primeru realnih vzorcev odpadne vode. Termodinamične študije kažejo na spontan proces z elektrostatično privlačnostjo kot prevladujočo nekovalentno interakcijo. Raziskava poudarja pomembnost oblikovanja katalizatorjev, ki so sposobni sinergistične adsorpcije in fotokatalitskih aktivnosti za učinkovito čiščenje odpadne vode.



Except when otherwise noted, articles in this journal are published under the terms and conditions of the Creative Commons Attribution 4.0 International License

Scientific paper

Synthesis and Biological Evaluation of Some Hydrazide-Hydrazone Derivatives as Anticancer Agents

Kadriye Akdağ,¹ Fatih Tok,¹ Sevgi Karakuş,^{1,*} Ömer Erdoğan,² Özge Çevik² and Bedia Koçyiğit-Kaymakçioğlu¹

¹ Department of Pharmaceutical Chemistry, Faculty of Pharmacy, Marmara University, 34854, Istanbul, Turkey

² Department of Biochemistry, School of Medicine, Aydın Adnan Menderes University, 09010, Aydın, Turkey

* Corresponding author: E-mail: skarakuş@marmara.edu.tr

Received: 10-04-2022

Abstract

In this study, a series of hydrazide-hydrazone derivatives (**3a-3u**) were synthesized and evaluated for their anticancer activities against prostate cancer cell line (PC-3), breast cancer cell line (MCF-7), colon cancer cell line (HT-29) and human umbilical vein endothelial cells (HUVEC) using MTT assay. In particular, compound **3h** having a pyrrole ring was found to be the most potent derivative with $IC_{50} = 1.3, 3.0, 1.7 \mu M$ against PC-3, MCF-7, HT-29 cancer cell lines respectively using paclitaxel as a standard compound. Furthermore, compound **3h** was subjected to further biological studies such as caspase-3 activity and Annexin-V assay to evaluate their inhibitory potentials. The activity results displayed that compound **3h** increased caspase-3 activation and the number of cells to early apoptosis. The additional studies like pharmacokinetics, bioavailability scores and drug-likeness properties were also evaluated. The *in silico* pharmacokinetics predictions displayed that the bioavailability of these compounds may be high.

Keywords: Hydrazone, anticancer, apoptosis, drug-likeness, MCF-7.

1. Introduction

Cancer is a disease characterized by the uncontrolled proliferation and spread of the body's cells. It is the second leading cause of death in developed countries after cardiovascular diseases. It was reported that one out of every two people born after 1960 will get cancer. The distribution of cancer types according to gender differs.¹

While breast cancer is more common in women than other types of cancer, prostate cancer is more common in men. Lung cancer and colorectal cancer highly affect both men and women.² There are different approaches to cancer treatment such as surgery, radiotherapy, chemotherapy and hormone therapy. Despite their severe toxicity, chemotherapy is the main approach for the treatment of cancer worldwide.³ Detailed analyses of pathways and mechanisms and structures of antitumor compounds have led to significant developments in the prevention and treatment of cancer. Therefore, there is still a need for new anticancer compounds with higher potency and less toxicity, as well as less toxic to non-cancerous cells.⁴

Researchers working in the field of discovering new drugs seek to synthesize simple compounds having vari-

ous pharmacological activities such as anticancer, antiviral, antibacterial, antioxidant.⁵ Hydrazide-hydrazone derivatives are molecules containing a highly reactive group (CO-NH-N=CH) and are considered to be a good candidate for the development of a new drug.⁶⁻⁸

There are many studies in the literature that hydrazide-hydrazones have anticancer activity. Saini *et al.* presented useful information about the mechanisms of anticancer activity of hydrazide-hydrazones.⁹ Hydrazone structures can act by inhibiting topoisomerases, protein kinases and induce apoptosis pathways.^{10,11} Abou-Seri *et al.* designed and synthesized potent hydrazones as potential inhibitors of VEGFR2.¹² Taha *et al.* synthesized a new morpholine hydrazone scaffold due to potential anticancer activity.¹³ In addition, the benzothiazole-hydrazone derivatives were reported as potent anticancer agents.¹⁴ In another study, the hydrazone derivatives bearing the pyridine ring synthesized and assessed the anticancer activity against MCF-7. In this study, some of the tested compounds displayed higher anticancer activity than cisplatin.¹⁵ Hydrazone structures play an important role in anticancer-related processes, as mentioned in the examples above.

In light of the above information, we synthesized some hydrazone derivatives and investigated them for their anticancer activity against prostate cancer cell line (PC-3), breast cancer cell line (MCF-7), colon cancer cell line (HT-29) and human umbilical vein endothelial cells (HUVEC).

2. Experimental

All chemicals were purchased from Merck Company and Sigma-Aldrich. Melting points were determined by using a SMP II melting point apparatus. IR spectra were recorded on a Shimadzu FTIR-8400S spectrophotometer. ^1H -NMR and ^{13}C -NMR spectra were obtained on a Bruker Avance DPX-400 spectrometer. Tetramethylsilane as the internal standard and DMSO- d_6 as the solvent was used for NMR spectrums. Elemental analyses were performed with GmbH varioMICRO CHNS.

2. 1. Synthesis

2. 1. 1. General procedure for the synthesis of ethyl 4-[(4-methoxybenzoyl)amino]benzoate (1)

Ethyl 4-aminobenzoate (1mmol) was dissolved in ether (10 mL). 1 mmol of 4-methoxybenzoyl chloride was added dropwise to this solution. It was stirred for 2 hours on a magnetic stirrer. The precipitate was washed with water, filtered and dried.¹⁶

2. 1. 2. General procedure for the synthesis of *N*-[4-(hydrazinylcarbonyl)phenyl]-4-methoxybenzamide (2)

Ethyl 4-[(4-methoxybenzoyl)amino]benzoate (1 mmol) was heated with hydrazine monohydrate (3 mL) in ethanol (15 mL) for 10 hours at 100 °C. After TLC control, the precipitate was filtered and crystallized with ethanol.¹⁶

2. 1. 3. General procedure for the synthesis of hydrazide-hydrazone (3a-3u)

In a solution of *N*-(4-(hydrazinecarbonyl)phenyl)-4-methoxybenzamide (1 mmol) in 10 mL ethanol was added 1 mmol substituted aldehyde derivatives. The mixture was refluxed for 8 hours. After TLC control, the precipitate was filtered and dried. The product was crystallized with ethanol.¹⁷ Compounds **3j**, **3l**, **3m**, **3n**, **3r** and **3u** were reported in the literature.¹⁸⁻²⁰ The other hydrazone derivatives were synthesized for the first time in this article.

N-[4-[2-(2,4-Dichlorobenzylidene)hydrazinecarbonyl]phenyl]-4-methoxybenzamide (3a)

Yield: 68%, M.p. = 298-299 °C, FTIR (ν , cm^{-1}): 3271, 3173 (N-H), 3010 (=C-H), 2983 (C-H), 1641 (C=O), 1606

(C=N), 1589, 1444 (C=C), 852 (=C-H). ^1H -NMR (400 MHz, DMSO- d_6 , ppm): δ 3.85 (s, 3H, OCH₃), 7.07-8.04 (m, 11H, Ar-H), 8.83 (s, 1H, =CH-), 10.37 (s, 1H, -CONH-), 12.08 (s, 1H, -CONHN=). ^{13}C -NMR (100 MHz, DMSO- d_6 , ppm): δ 55.44 (OCH₃), 113.66, 119.42, 126.56, 128.00, 128.48, 129.35, 129.74, 130.80, 133.76, 134.94, 142.09, 142.80, 162.12, 162.59 (C=O), 165.18 (C=O). Anal. Calcd for C₂₂H₁₇Cl₂N₃O₃: C 59.74, H 3.87, N 9.50. Found: C 59.56, H 3.90, N 9.42 %.

N-(4-(2-(3,4-Dichlorobenzylidene)hydrazinecarbonyl)phenyl)-4-methoxybenzamide (3b)

Yield: 63%, M.p. = 280-281 °C, FTIR (ν , cm^{-1}): 3315, 3238 (N-H), 3072 (=C-H), 2935 (C-H), 1641 (C=O), 1602 (C=N), 1589, 1543 (C=C), 840 (=C-H). ^1H -NMR (400 MHz, DMSO- d_6 , ppm): δ 3.83 (s, 3H, OCH₃), 7.05-7.98 (m, 11H, Ar-H), 8.41 (s, 1H, =CH-), 10.34 (s, 1H, -CONH-), 11.95 (s, 1H, -CONHN=). ^{13}C -NMR (100 MHz, DMSO- d_6 , ppm): δ 55.44 (OCH₃), 113.64, 119.41, 126.56, 127.49, 129.74, 131.07, 131.69, 132.09, 135.28, 142.73, 144.52, 162.10, 162.71 (C=O), 165.17 (C=O). Anal. Calcd for C₂₂H₁₇Cl₂N₃O₃: C 59.74, H 3.87, N 9.50. Found: C 59.49, H 3.91, N 9.44 %.

N-[4-[2-(4-Nitrobenzylidene)hydrazinecarbonyl]phenyl]-4-methoxybenzamide (3c)

Yield: 57%, M.p. = 334-335 °C, FTIR (ν , cm^{-1}): 3302, 3213 (N-H), 3068 (=C-H), 2837 (C-H), 1643 (C=O), 1602 (C=N), 1587, 1537 (C=C), 833 (=C-H). ^1H -NMR (400 MHz, DMSO- d_6 , ppm): δ 3.85 (s, 3H, OCH₃), 7.07-8.33 (m, 12H, Ar-H), 8.56 (s, 1H, =CH-), 10.41 (s, 1H, -CONH-), 12.09 (s, 1H, -CONHN=). ^{13}C -NMR (100 MHz, DMSO- d_6 , ppm): δ 55.91 (OCH₃), 114.11, 119.87, 124.52, 127.00, 128.35, 128.99, 130.20, 141.21, 148.21, 162.57 (C=O), 165.63 (C=O). Anal. Calcd for C₂₂H₁₈N₄O₅: C 63.15, H 4.34, N 13.39. Found: C 62.96, H 4.33, N 13.31 %.

N-[4-[2-(3-Nitrobenzylidene)hydrazinecarbonyl]phenyl]-4-methoxybenzamide (3d)

Yield: 58%, M.p. = 294 °C, FTIR (ν , cm^{-1}): 3302, 3228 (N-H), 3074 (=C-H), 2845 (C-H), 1637 (C=O), 1602 (C=N), 1525, 1506 (C=C), 842 (=C-H). ^1H -NMR (400 MHz, DMSO- d_6 , ppm): δ 3.83 (s, 3H, OCH₃), 7.04-8.26 (m, 12H, Ar-H), 8.54 (s, 1H, =CH-), 10.35 (s, 1H, -CONH-), 12.04 (s, 1H, -CONHN=). ^{13}C -NMR (100 MHz, DMSO- d_6 , ppm): δ 55.44 (OCH₃), 113.65, 119.41, 120.80, 124.11, 126.55, 128.51, 129.75, 130.43, 133.32, 136.30, 142.76, 144.83, 148.23, 162.11, 162.77 (C=O), 165.17 (C=O). Anal. Calcd for C₂₂H₁₈N₄O₅: C 63.15, H 4.34, N 13.39. Found: C 62.99, H 4.35, N 13.33 %.

N-[4-[2-(3,5-Dichloro-2-hydroxybenzylidene)hydrazinecarbonyl]phenyl]-4-methoxybenzamide (3e)

Yield: 61%, M.p. = 331-332 °C, FTIR (ν , cm^{-1}): 3340, 3219 (N-H), 3039 (=C-H), 2970 (C-H), 1645 (C=O), 1602 (C=N), 1587, 1500 (C=C), 840 (=C-H). ^1H -NMR

(400 MHz, DMSO- d_6 , ppm): δ 3.86 (s, 3H, OCH₃), 7.08–8.01 (m, 10H, Ar-H), 8.58 (s, 1H, =CH-), 10.40 (s, 1H, -CONH-), 12.26 (s, 1H, -CONHN=), 12.83 (s, 1H, OH). ¹³C-NMR (100 MHz, DMSO- d_6 , ppm): δ 55.44 (OCH₃), 113.66, 119.41, 126.55, 127.37, 128.01, 128.47, 129.74, 130.80, 133.76, 142.09, 142.79, 162.11, 162.57 (C=O), 165.17 (C=O). Anal. Calcd for C₂₂H₁₇Cl₂N₃O₄: C 57.66, H 3.74, N 9.17. Found: C 57.47, H 3.75, N 9.14 %.

N-{4-[2-(Pyridine-4-ylmethylene)hydrazinecarbonyl]phenyl}-4-methoxybenzamide (3f)

Yield: 75%, M.p. = 311–312 °C, FTIR (ν , cm⁻¹): 3327, 3263 (N-H), 3032 (=C-H), 2910 (C-H), 1645 (C=O), 1602 (C=N), 1525, 1496 (C=C), 842 (=C-H). ¹H-NMR (400 MHz, DMSO- d_6 , ppm): δ 3.85 (s, 3H, OCH₃), 7.08–8.65 (m, 12H, Ar-H), 8.67 (s, 1H, =CH-), 10.38 (s, 1H, -CONH-), 12.06 (s, 1H, -CONHN=). ¹³C-NMR (100 MHz, DMSO- d_6 , ppm): δ 55.49 (OCH₃), 113.70, 119.45, 120.98, 126.56, 128.59, 129.80, 141.60, 142.88, 144.85, 150.31, 162.15, 162.82 (C=O), 165.24 (C=O). Anal. Calcd for C₂₁H₁₈N₄O₃: C 67.37, H 4.85, N 14.96. Found: C 67.14, H 4.82, N 14.94 %.

N-{4-[2-(Pyridine-3-ylmethylene)hydrazinecarbonyl]phenyl}-4-methoxybenzamide (3g)

Yield: 65%, M.p. = 287 °C, FTIR (ν , cm⁻¹): 3336, 3273 (N-H), 3043 (=C-H), 2982 (C-H), 1647 (C=O), 1602 (C=N), 1589, 1471 (C=C), 844 (=C-H). ¹H-NMR (400 MHz, DMSO- d_6 , ppm): δ 3.85 (s, 3H, OCH₃), 7.07–8.62 (m, 12H, Ar-H), 8.86 (s, 1H, =CH-), 10.37 (s, 1H, -CONH-), 11.96 (s, 1H, -CONHN=). ¹³C-NMR (100 MHz, DMSO- d_6 , ppm): δ 55.49 (OCH₃), 113.70, 119.46, 124.06, 126.58, 128.49, 129.79, 130.35, 133.41, 142.73, 144.57, 148.73, 150.66, 162.14, 162.67 (C=O), 165.21 (C=O). Anal. Calcd for C₂₁H₁₈N₄O₃: C 67.37, H 4.85, N 14.96. Found: C 67.07, H 4.83, N 14.92 %.

N-{4-[2-(1H-Pyrrol-3-yl-methylene)hydrazinecarbonyl]phenyl}-4-methoxybenzamide (3h)

Yield: 78%, M.p. = 273 °C, FTIR (ν , cm⁻¹): 3308, 3194 (N-H), 3047 (=C-H), 2964 (C-H), 1645 (C=O), 1604 (C=N), 1525, 1500 (C=C), 842 (=C-H). ¹H-NMR (400 MHz, DMSO- d_6 , ppm): δ 3.83 (s, 3H, OCH₃), 4.65 (s, 1H, NH), 7.11–7.87 (m, 11H, Ar-H), 8.33 (s, 1H, =CH-), 10.28 (s, 1H, -CONH-), 11.65 (s, 1H, -CONHN=). ¹³C-NMR (100 MHz, DMSO- d_6 , ppm): δ 55.48 (OCH₃), 113.67, 119.39, 126.69, 127.60, 127.91, 129.74, 141.91, 162.07, 165.15 (C=O), 165.57 (C=O). Anal. Calcd for C₂₀H₁₈N₄O₃: C 66.29, H 5.01, N 15.46. Found: C 66.17, H 5.04, N 15.39 %.

N-{4-[2-(Thiophen-2-ylmethylene)hydrazinecarbonyl]phenyl}-4-methoxybenzamide (3i)

Yield: 70%, M.p. = 250–251 °C, FTIR (ν , cm⁻¹): 3304, 3192 (N-H), 3012 (=C-H), 2966 (C-H), 1645 (C=O), 1604 (C=N), 1581, 1491 (C=C), 842 (=C-H). ¹H-NMR (400 MHz, DMSO- d_6 , ppm): δ 3.82 (s, 3H, OCH₃), 7.04–7.97 (m, 11H, Ar-H), 8.41 (s, 1H, =CH-), 10.32 (s,

1H, -CONH-), 11.79 (s, 1H, -CONHN=). ¹³C-NMR (100 MHz, DMSO- d_6 , ppm): δ 55.36 (OCH₃), 113.56, 119.32, 126.46, 127.75, 128.23, 128.73, 129.65, 130.68, 139.13, 142.37, 161.99, 162.30 (C=O), 165.06 (C=O). Anal. Calcd for C₂₀H₁₇N₃O₃S: C 63.31, H 4.52, N 11.07. Found: C 63.40, H 4.53, N 11.13 %.

N-{4-[2-(5-Nitrofuran-2-yl-methylene)hydrazinecarbonyl]phenyl}-4-methoxybenzamide (3j)

Yield: 64%, M.p. = 297–298 °C. Ref. lit. M.p. = 292 °C.¹⁸

N-{4-[2-(2-Chloroquinolin-3-yl-methylene)hydrazinecarbonyl]phenyl}-4-methoxybenzamide (3k)

Yield: 58%, M.p. = 302 °C, FTIR (ν , cm⁻¹): 3281, 3227 (N-H), 3030 (=C-H), 2989 (C-H), 1641 (C=O), 1604 (C=N), 1591, 1537 (C=C), 840 (=C-H). ¹H-NMR (400 MHz, DMSO- d_6 , ppm): δ 3.86 (s, 3H, OCH₃), 7.08–8.26 (m, 13H, Ar-H), 8.94 (s, 1H, =CH-), 10.39 (s, 1H, -CONH-), 12.21 (s, 1H, -CONHN=). ¹³C-NMR (100 MHz, DMSO- d_6 , ppm): δ 55.36 (OCH₃), 113.57, 119.34, 126.16, 126.44, 126.80, 127.24, 127.53, 127.76, 128.47, 128.92, 129.67, 131.65, 135.49, 142.22, 142.77, 147.01, 148.41, 162.03, 162.55 (C=O), 165.09 (C=O). Anal. Calcd for C₂₅H₁₉ClN₄O₃: C 65.43, H 4.17, N 12.21. Found: C 65.29, H 4.21, N 12.14 %.

N-{4-[2-(2-Benzylidenehydrazinecarbonyl)phenyl]-4-methoxybenzamide (3l)}

Yield: 65%, M.p. = 292–293 °C. Ref. lit. M.p. = 282 °C.¹⁹

N-{4-[2-(4-Hydroxybenzylidene)hydrazinecarbonyl]phenyl}-4-methoxybenzamide (3m)

Yield: 78%, M.p. = 284–285 °C. Ref. lit. M.p. = 289 °C.¹⁹

N-{4-[2-(4-Hydroxy-3-methoxybenzylidene)hydrazinecarbonyl]phenyl}-4-methoxybenzamide (3n)

Yield: 67%, M.p. = 264–265 °C. Ref. lit. M.p. = 270 °C.¹⁹

N-{4-[2-(3-(4-Chlorophenoxybenzylidene)hydrazinecarbonyl]phenyl}-4-methoxybenzamide (3o)

Yield: 74%, M.p. = 252–253 °C, FTIR (ν , cm⁻¹): 3329, 3259 (N-H), 3005 (=C-H), 2837 (C-H), 1641 (C=O), 1604 (C=N), 1573, 1508 (C=C), 839 (=C-H). ¹H-NMR (400 MHz, DMSO- d_6 , ppm): δ 3.82 (s, 3H, OCH₃), 7.04–7.97 (m, 16H, Ar-H), 8.42 (s, 1H, =CH-), 10.33 (s, 1H, -CONH-), 11.81 (s, 1H, -CONHN=). ¹³C-NMR (100 MHz, DMSO- d_6 , ppm): δ 55.35 (OCH₃), 113.56, 115.85, 119.31, 120.44, 122.95, 126.46, 127.44, 128.31, 129.66, 129.92, 130.60, 136.48, 142.56, 146.35, 155.23, 156.71, 162.00, 162.48 (C=O), 165.07 (C=O). Anal. Calcd for C₂₈H₂₂ClN₃O₄: C 67.27, H 4.44, N 8.40. Found: C 67.15, H 4.42, N 8.36 %.

N-{4-[2-(2-Phenylethylidene)hydrazinecarbonyl]phenyl}-4-methoxybenzamide (3p)

Yield: 68%, M.p. = 305–306 °C, FTIR (ν , cm⁻¹): 3296, 3223 (N-H), 3037 (=C-H), 2841 (C-H), 1651 (C=O), 1602 (C=N), 1548, 1504 (C=C), 840 (=C-H). ¹H-NMR

(400 MHz, DMSO- d_6 , ppm): δ 3.60 (d, 2H, $-CH_2-$), 3.82 (s, 3H, OCH₃), 7.04–8.02 (m, 13H, Ar-H), 8.42 (s, 1H, $=CH-$), 10.29 (s, 1H, $-CONH-$), 11.47 (s, 1H, $-CONHN=$). ¹³C-NMR (100 MHz, DMSO- d_6 , ppm): δ 55.37 (OCH₃), 113.55, 119.27, 125.73, 126.52, 127.91, 128.15, 128.60, 128.75, 129.64, 136.83, 142.33, 149.99, 161.99 (C=O), 165.04 (C=O). Anal. Calcd for C₂₃H₂₁N₃O₃: C 71.30, H 5.46, N 10.85. Found: C 71.07, H 5.42, N 10.92 %.

N-{4-[2-(Furan-2-ylmethylene)hydrazinecarbonyl]phenyl}-4-methoxybenzamide (3q)

Yield: 85%, M.p. = 279 °C, FTIR (ν , cm⁻¹): 3304, 3234 (N-H), 3016 ($=C-H$), 2887 (C-H), 1641 (C=O), 1602 (C=N), 1521, 1494 (C=C), 840 ($=C-H$). ¹H-NMR (400 MHz, DMSO- d_6 , ppm): δ 3.85 (s, 3H, OCH₃), 6.64–8.01 (m, 11H, Ar-H), 8.34 (s, 1H, $=CH-$), 10.36 (s, 1H, $-CONH-$), 11.73 (s, 1H, $-CONHN=$). ¹³C-NMR (100 MHz, DMSO- d_6 , ppm): δ 55.36 (OCH₃), 112.09, 113.20, 113.56, 119.32, 126.47, 127.60, 128.27, 129.66, 137.02, 142.51, 145.01, 149.43, 162.01, 162.38 (C=O), 165.08 (C=O). Anal. Calcd for C₂₀H₁₇N₃O₄: C 66.11, H 4.72, N 11.56. Found: C 66.26, H 4.77, N 11.48 %.

N-{4-[2-(4-Methoxybenzylidene)hydrazinecarbonyl]phenyl}-4-methoxybenzamide (3r)

Yield: 74%, M.p. = 295 °C. Ref. lit. M.p. = 298 °C.²⁰

N-{4-[2-(3-Fluorobenzylidene)hydrazinecarbonyl]phenyl}-4-methoxybenzamide (3s)

Yield: 83%, M.p. = 286 °C, FTIR (ν , cm⁻¹): 3333, 3255 (N-H), 3037 ($=C-H$), 2964 (C-H), 1645 (C=O), 1602 (C=N), 1575, 1537 (C=C), 840 ($=C-H$). ¹H-NMR (400 MHz, DMSO- d_6 , ppm): δ 3.82 (s, 3H, OCH₃), 7.04–8.00 (m, 12H, Ar-H), 8.46 (s, 1H, $=CH-$), 10.35 (s, 1H, $-CONH-$), 11.89 (s, 1H, $-CONHN=$). ¹³C-NMR (100 MHz, DMSO- d_6 , ppm): δ 55.36 (OCH₃), 112.74, 112.96, 113.57, 116.52, 119.33, 123.30, 126.48, 127.51, 128.37, 129.67, 130.78, 136.89, 142.61, 145.82, 161.12, 162.02, 162.57, 163.54 (C=O), 165.10 (C=O). Anal. Calcd for C₂₂H₁₈FN₃O₃: C 67.51, H 4.64, N 10.74. Found: C 67.33, H 4.60, N 10.79 %.

N-{4-[2-(4-Cyanobenzylidene)hydrazinecarbonyl]phenyl}-4-methoxybenzamide (3t)

Yield: 68%, M.p. = 306 °C, FTIR (ν , cm⁻¹): 3338, 3253 (N-H), 3070 ($=C-H$), 2978 (C-H), 1645 (C=O), 1600 (C=N), 1539, 1494 (C=C), 839 ($=C-H$). ¹H-NMR (400 MHz, DMSO- d_6 , ppm): δ 3.86 (s, 3H, OCH₃), 7.08–8.02 (m, 12H, Ar-H), 8.52 (s, 1H, $=CH-$), 10.38 (s, 1H, $-CONH-$), 12.04 (s, 1H, $-CONHN=$). ¹³C-NMR (100 MHz, DMSO- d_6 , ppm): δ 55.36 (OCH₃), 111.66, 113.57, 118.59, 119.33, 126.45, 127.47, 128.43, 129.67, 132.66, 138.81, 142.71, 145.18, 162.03, 162.62 (C=O), 165.10 (C=O). Anal. Calcd for C₂₃H₁₈N₄O₃: C 69.34, H 4.55, N 14.06. Found: C 69.15, H 4.53, N 14.19 %.

N-{4-[2-(4-Bromobenzylidene)hydrazinecarbonyl]phenyl}-4-methoxybenzamide (3u)

Yield: 65%, M.p. = 312–313 °C. Ref. lit. M.p. = 316 °C.¹⁸

2. 2. Biological activity

2. 2. 1. MTT assay

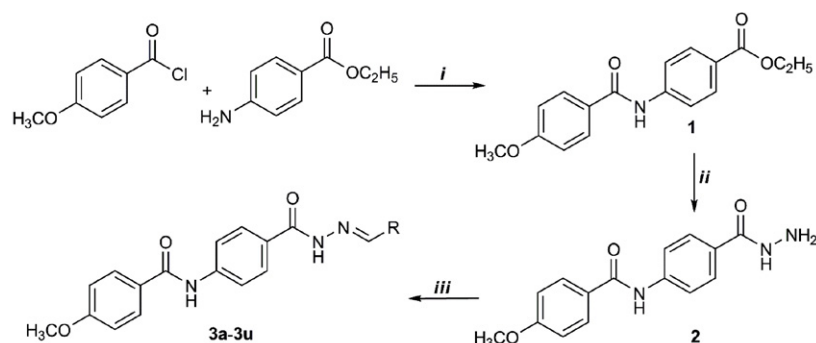
Cytotoxicity tests of the synthesized compounds were performed in a human prostate cancer cell line (PC-3, ATCC CRL-1435), human breast cancer cell line (MCF-7, ATCC-HTB-22), human colon cancer cell line (HT-29, ATCC-HBT-38) and human umbilical vein endothelial cells (HUVEC, ATCC-CRL-1730). MCF-7 and HT-29 cells were cultured in DMEM medium, PC-3 cells were cultured in RPMI-1640 medium and HUVEC cells were cultured in F-12K medium supplemented with 10% fetal bovine serum (FBS), 100 U/mL penicillin and 100 µg/mL streptomycin and 2 mM L-glutamine. The cells were incubated at 37 °C in a humidified atmosphere with 5% CO₂. Cells were seeded in 96 well plates at a density of 1 × 10⁴ and treated with compounds synthesized in different (0.1–1000 µM) concentration ranges. We prepare a 10 mM main stock, dilute them with DMSO and add not exceeding the highest concentration of DMSO (0.5%) (for example, 1 mg compound can be dissolved in about 500 µL DMSO). The compounds we put in the medium are added by dilution in the cell medium when necessary so that they do not exceed the DMSO limit. Paclitaxel was used at the same concentrations as a positive control. The MTT test was performed after the cells were incubated with the synthesized compounds for 24 hours. After incubation, cells were washed once with PBS, and a fresh medium was added. Then, 10 µL of MTT dye (0.5 mg/mL) was placed in each well of the plate and incubated at 37 °C for 4 hours. Finally, DMSO was added and incubated for 30 minutes to dissolve the formazan crystals. Color changes were measured at a wavelength of 570 nm. IC₅₀ values were analyzed using the Graphpad Prism 7.00 program. All experiments were performed with triple biological replicates, and data were given as mean ± standard deviation.

2. 2. 2. AO/EB Staining

MCF-7, PC-3 and HT-29 cells were seeded in 12 well plates and were incubated with the compound **3h** (IC₅₀ concentration) for 24 hours.²¹ After incubation, PBS washed cells and incubated them with AO/EB staining solution (100 µg/mL acridine orange and 100 µg/mL ethidium bromide) in PBS. Images of cells were taken under an inverted fluorescent microscope (Zeiss AxioVert1, Germany). In the analysis, green staining shows viable cells, and red staining shows dead or destructed cells, so the intensity was calculated by taking the green/red ratio. All experiments were performed with triple biological replicates, and data were given as mean ± standard deviation.

2. 2. 3. Annexin-V assay

MCF-7, PC-3 and HT-29 cells were seeded in 6 well plates. After the cells reached a density of 1 × 10⁶, they were incubated with compound **3h** (IC₅₀ concentration) for 24



Scheme 1. The synthetic pathways of target compounds. Reagents: (i) ether, 25 °C, 2h, yield: 75%; (ii) hydrazine monohydrate, ethanol, 100 °C, 10h, yield: 80%; (iii) substituted aldehydes, ethanol, reflux, 8h, yield: 57–85%.

hours.²² After the incubation period was complete, the cells were washed with PBS and removed using trypsin-EDTA. Cells were centrifuged at 600xg for 5 minutes and washed once with PBS. Cells were suspended with a fresh medium containing 10% FBS and performed according to the manufacturer's protocol using the Annexin V & Dead Cell Assay kit (Muse-MCH100105, MilliporeSigma, CA, USA). Cells were incubated in the dark for 30 minutes with the binding buffer and dyes in the kit. Assay results were measured using the Muse Cell Analyzer. All experiments were performed with triple biological replicates, and data were given as mean±standard deviation.

2. 2. 4. Caspase-3 activity

MCF-7, PC-3, and HT-29 cells were seeded in 12 well plates. Cells were incubated with compound **3h** (IC_{50} concentration) for 24 hours and then washed with PBS. Caspase-3 activity in cells was performed using a commercial kit (CASP-3-C, Sigma-Aldrich). After the cells were treated with 100 µl of cell lysis buffer, they were centrifuged at 10.000xg for 10 minutes at 4°C. The supernatant was taken, and measurements were made colorimetrically at a wavelength of 405 nm (Epoch, Biotek) using Ac-DEVD-pNA substrate. The results were calculated as µmol pNA/min/mL, and the protein values of the cells were calculated and used as nmol pNA/min/µg protein. All experiments were performed with triple biological replicates, and data were given as mean±standard deviation.

2. 3. In silico ADME analysis

Physicochemical, pharmacokinetic and drug-likeness properties of all compounds were predicted through SwissAdme online server (<http://www.swissadme.ch/>).

3. Results and Discussion

3. 1. Synthesis

In this study, some hydrazide-hydrazone derivatives were synthesized as given in Scheme 1. Firstly, the amide functional group was prepared from the reaction of *ethyl*

p-aminobenzoate and 4-methoxybenzoyl chloride in ether. In the second step, hydrazide structure was obtained by heating *ethyl 4-(4-methoxybenzamido)benzoate* with hydrazine monohydrate in an ethanolic medium. Finally, hydrazone structures were successfully synthesized by the treatment with hydrazide and different substituted aldehydes in ethanol. The structures of the hydrazone derivatives were elucidated by FTIR, ¹H-NMR, and ¹³C-NMR spectroscopic methods and elemental analysis.

IR spectra of hydrazone compounds (**3a-3u**), the C=O stretching bands of compounds were observed at 1637–1653 cm⁻¹. The NH stretching bands of amide and hydrazone structures were detected at 3173–3340 cm⁻¹. The characteristic strong band in the 1600–1606 cm⁻¹ region, attributed to a C=N stretching, confirmed the hydrazone feature of all derivatives. In the ¹H-NMR spectra, the NH peak of amide structure gave a peak between 10.28 ppm and 10.41 ppm as a singlet. The proton of the imine (–N=CH–) group resonated at 8.33–8.94 ppm as a singlet. The proton of the –CONHN= group was detected at 11.47–12.26 ppm as a singlet. In addition, the disappearance of the proton peaks of the hydrazide amino group is evidence of hydrazone synthesis. In the ¹³C-NMR spectra, carbonyl peaks were observed at 161.99–165.63 ppm. The carbon of the imine (–N=CH–) group was detected at 144.52–149.99 ppm.

3. 2. Biological activity

The cytotoxicity studies of synthesized compounds were performed on prostate cancer cell line (PC-3), breast cancer cell line (MCF-7), colon cancer cell line (HT-29), and human umbilical vein endothelial cells (HUVEC) compared to the Paclitaxel as a standard compound (Table 1).

Compounds carrying 4-nitrophenyl (**3c**), phenyl (**3l**), benzyl (**3p**), 4-bromophenyl (**3u**) and 3-pyrrole (**3h**) against the PC3 cancer cell line; compounds carrying 4-nitrophenyl (**3c**), 5-nitro-2-furyl (**3j**), 4-hydroxyphenyl (**3m**), benzyl (**3p**), 2-furyl (**3q**) and 3-pyrrole (**3h**) against the MCF-7 cancer cell line; compounds carrying 3-nitrophenyl (**3d**), 2-furyl (**3q**) and 3-pyrrole (**3h**) structures against the HT-29 cancer cell line exhibited significant cytotoxic activity.

Table 1. The IC₅₀ values of synthesized compounds.

Comp.	R	PC-3*	MCF-7*	HT-29*	HUVEC*
3a	2,4-dichlorophenyl	137.2±1.2	210.4±12.4	174.2±8.0	218.0±9.1
3b	3,4-(dichloro)phenyl	204.7±0.1	112.3±8.2	102.5±6.7	213.8±8.6
3c	4-nitrophenyl	42.2±1.3	30.1±6.0	54.2±4.0	65.8±5.2
3d	3-nitrophenyl	67.7±2.1	61.0±3.2	36.3±2.9	206.3±1.1
3e	2-hydroxy-3,5-(dichloro)phenyl	81.3±1.1	74.1±2.1	91.0±3.5	154.2±7.3
3f	pyridin-4-yl	178.6±6.3	128.3±7.2	94.2±2.1	302.6±4.1
3g	pyridin-3-yl	321.2±11.0	216.4±9.1	300.1±11.1	314.5±6.1
3h	pyrrol-3-yl	1.3±0.1	3.0±0.1	1.7±0.2	235.3±6.5
3i	thiophen-2-yl	86.4±0.6	165.4±6.0	143.5±3.9	330.3±12.0
3j	5-nitro-2-furyl	88.9±4.1	23.7±3.2	78.2±2.1	538.1±14.7
3k	2-chloroquinolin-3-yl	194.3±3.5	128.2±2.1	205.4±8.7	337.4±4.2
3l	phenyl	46.2±1.0	58.4±5.0	69.1±5.0	84.3±6.0
3m	4-hydroxyphenyl	66.9±6.4	27.1±3.9	86.2±2.2	70.6±3.4
3n	4-hydroxy-3-methoxyphenyl	200.3±8.1	111.1±8.7	170.6±3.1	248.5±8.0
3o	3-(4-chlorophenoxy)phenyl	218.4±9.4	154.1±7.3	204.3±4.6	407.1±11.0
3p	benzyl	14.0±2.0	26.3±2.1	56.1±2.0	67.1±3.3
3q	2-furyl	78.24±8.6	32.2±1.4	44.1±4.2	74.3±2.1
3r	4-methoxyphenyl	103.0±11.1	100.2±5.1	115.4±9.5	233.5±10.9
3s	3-fluorophenyl	258.3±4.0	301.2±12.1	195.3±8.4	374.2±8.7
3t	4-cyanophenyl	145.4±8.0	162.0±4.3	184.1±2.2	388.6±6.2
3u	4-bromophenyl	49.0±5.0	79.2±4.1	62.1±4.3	54.7±1.1
	Paclitaxel	2.4±1.4	5.5±1.1	12.0±2.1	74.4±3.5

*:μM, mean±SD

In particular, the compound having the 3-pyrrole ring (**3h**) was found to have higher cytotoxicity against all cancer cell lines than the standard compound. In addition, the toxicity of this compound against HUVEC is very low. The selectivity index (SI = IC₅₀ for normal cell line HUVEC/IC₅₀ for cancerous cell line) of compound **3h** was found at 181.0 for PC3, 78.4 for MCF-7, and 138.4 for HT-29. As a result, the compound **3h** has been detected that has a selective cytotoxic effect against cancer cell lines.

While synthesizing the hydrazone structure in order to compare the structure-activity relationship; different aromatic and heteroaromatic rings were selected. The ability of electron-donating or electron-withdrawing groups at different positions on these rings to affect the interactions with cancer cells was also investigated. Among the compounds carrying nitro group, compound **3c** showed high cytotoxic effect against PC3 and MCF7, compound **3d** against HT29, and compound **3j** against MCF7 due to the strong electron withdrawing and resonance properties of the nitro group. Moreover, of these compounds, **3j** showed the least cytotoxic activity against HUVEC normal cell. Many studies showed that the nitro group has high antiproliferative activity. Nitro compounds can release NO due to redox reactions inside the cell. For these reasons, cytotoxic effects occur due to disruption of oxidative stress mechanisms. Nitro substituents can also increase the inhibition of target biomolecules such as proteins or enzymes due to its electron withdrawing property favoring interaction with some amino acids such as threonine and glutamine. It has been determined that the nitro group of the

compounds at the para and meta position shows higher efficiency than the ortho position due to the steric effect.^{23, 24}

On the other hand, compound **3h** has a pyrrole ring as a heteroaromatic ring in its structure and showed the highest cytotoxic activity against all cancer cell lines selectively, regardless of the above-mentioned structure-activity relationship.

AO/EB, a dye that allows it to appear under a fluorescent microscope to identify changes in cell membranes during cell death, helps us understand the process of apoptosis. We qualitatively and quantitatively analyzed the changes of compound **3h** (IC₅₀ value) on MCF-7, PC-3, and HT-29 cells using the AO/EB staining method. In AO/EB staining of MCF-7 cells, when compound **3h** was compared with the control group, it was observed that the ratio of live cells to dead cells decreased significantly ($p < 0.001$, Figure 1a-b). In PC3 cells, compound **3h** was compared with the control group, and it was seen that the viable/dead (green/red) ratio of the cells decreased significantly ($p < 0.001$, Figure 2a-b). Finally, in HT-29 cells, the viable/dead ratio of cells in the compound **3h** group was significantly reduced ($p < 0.001$, Figure 3a-b).

Annexin-V is a protein that binds to the cell membrane lipid phosphatidylserine from the onset of apoptosis. Annexin-V binding was measured in MCF-7, PC-3, and HT-29 cells after 24 hours of incubation with compound **3h**. In MCF-7 cells, compound **3h** significantly increased the number of cells to early apoptosis, late apoptosis, and dead cells and decreased the number of live cells compared to the control group ($p < 0.05$, $p < 0.001$, Figure 4a-b). In

PC-3 cells, compound **3h** significantly increased the number of cells going to early apoptosis and late apoptosis, and decreased the number of viable cells compared to the control group ($p < 0.05$, $p < 0.001$, Figure 5a-b). In HT-29 cells, it was observed that compound **3h** significantly increased only the number of cells going to late apoptosis and decreased the number of viable cells compared to the control group ($p < 0.001$, Figure 6a-b).

Caspase-3 is an enzyme that is important in the apoptotic pathway. Caspase-3 is a marker of both intrinsic and extrinsic apoptosis. In the apoptosis of the cell, amino acids in the structure of proteins are targeted by caspase-3 activity, the peptide bonds of the proteins are cut, and the protein that has lost its function cannot perform its function. In this study, caspase-3 activities of compound

3h were measured enzymatically in MCF-7, PC-3, and HT-29 cells. Compound **3h** increased caspase-3 enzyme activity in MCF-7 cells compared to the control group ($p < 0.001$, Figure 4c). In PC-3 cells, compound **3h** increased caspase-3 enzyme activity in 24 hours ($p < 0.001$, Figure 5c). Similarly, compound **3h** increased caspase-3 enzyme activity in HT-29 cells compared to the control group ($p < 0.001$, Figure 6c).

In this study, among the synthesized compounds, **3h** bearing pyrrole ring showed the highest cytotoxic activity against different cancer cell lines such as breast, colon and prostate, it did not show cytotoxic activity against human umbilical vein endothelial cells. Therefore, compound **3h**, which can show selective activity against cancer cell lines in this study, was obtained.

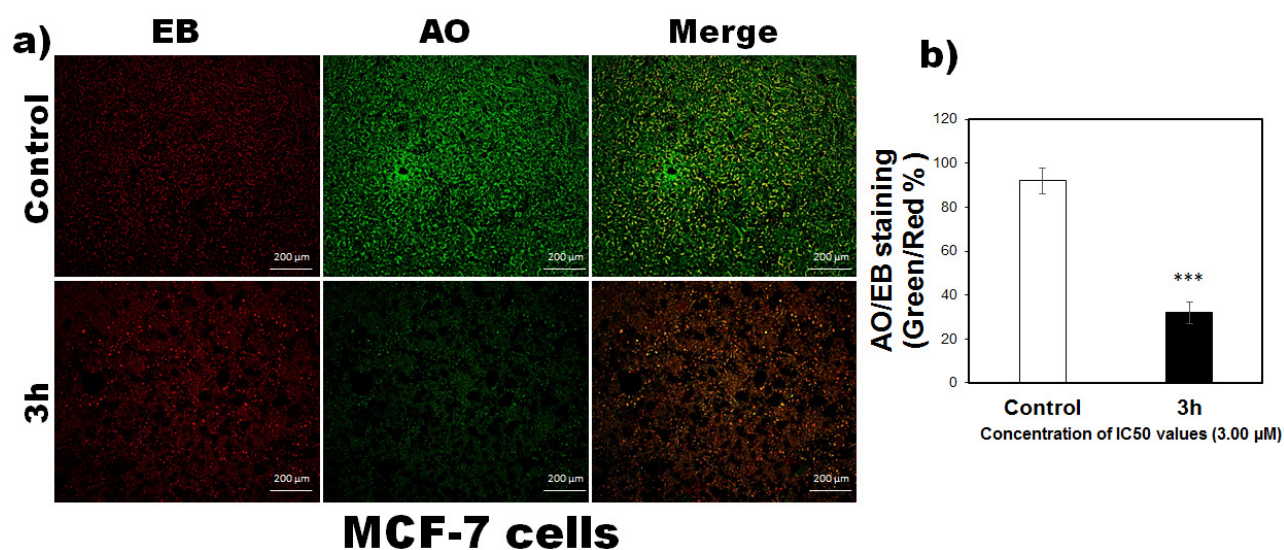


Figure 1. MCF-7 cells treated with 3.00 µM concentration of compound **3h**, a) AO/EB staining in florescence imaging b) AO/EB staining ratio ($*** p < 0.001$ vs control)

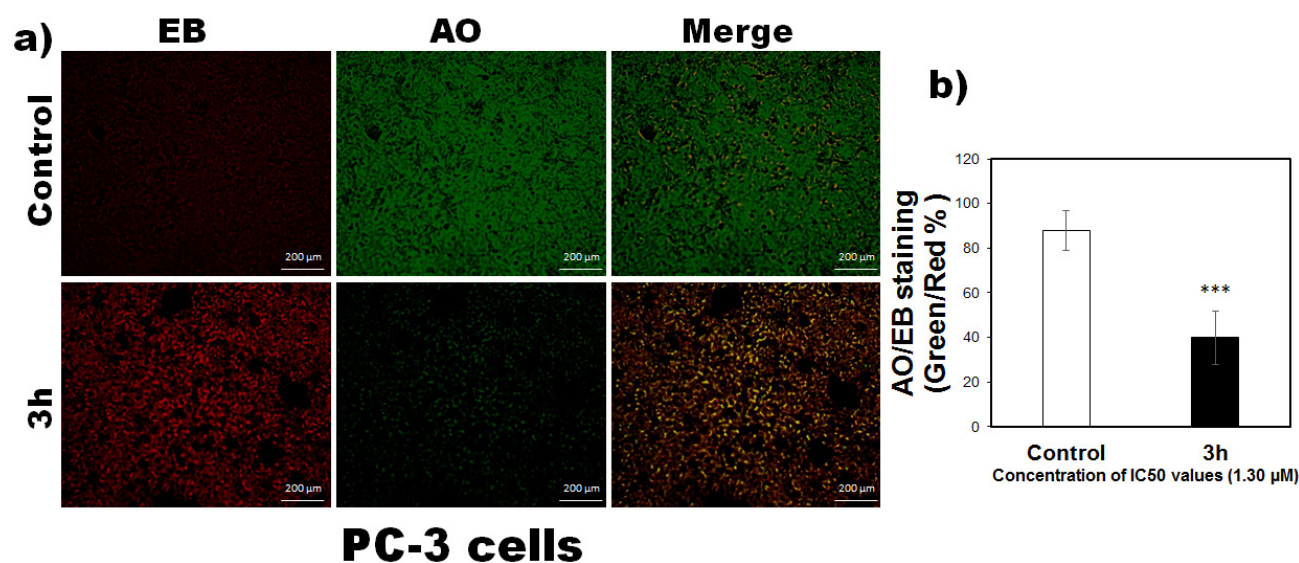


Figure 2. PC-3 cells treated with 1.30 µM concentration of compound **3h**, a) AO/EB staining in florescence imaging b) AO/EB staining ratio ($*** p < 0.001$ vs control)

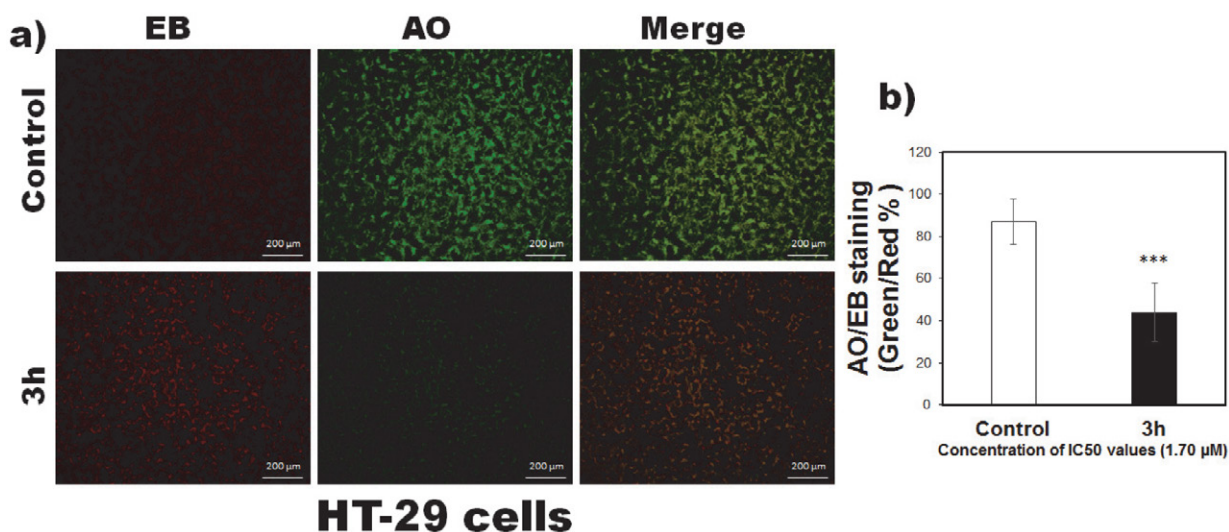


Figure 3. HT-29 cells treated with 1.70 μM concentration of compound **3h**, **a)** AO/EB staining in florescence imaging **b)** AO/EB staining ratio (***p* < 0.001 vs control)

In addition to the effectiveness of a compound in the fight against cancer, it is also very important that it exhibits selective activity. There are many examples in the literature where the non-selective compound showing activity against the cancer cell line was not included in fur-

ther studies.^{25,26} Pena-Moran et al. reported that the compound with an SI value ≥ 10 belongs to a selected potential compound that can be investigated further.²⁷ On the other hand, Weerapreeyakul et al. suggested a lower SI value (≥ 3) for classification of a possible anti-cancer compound.²⁸

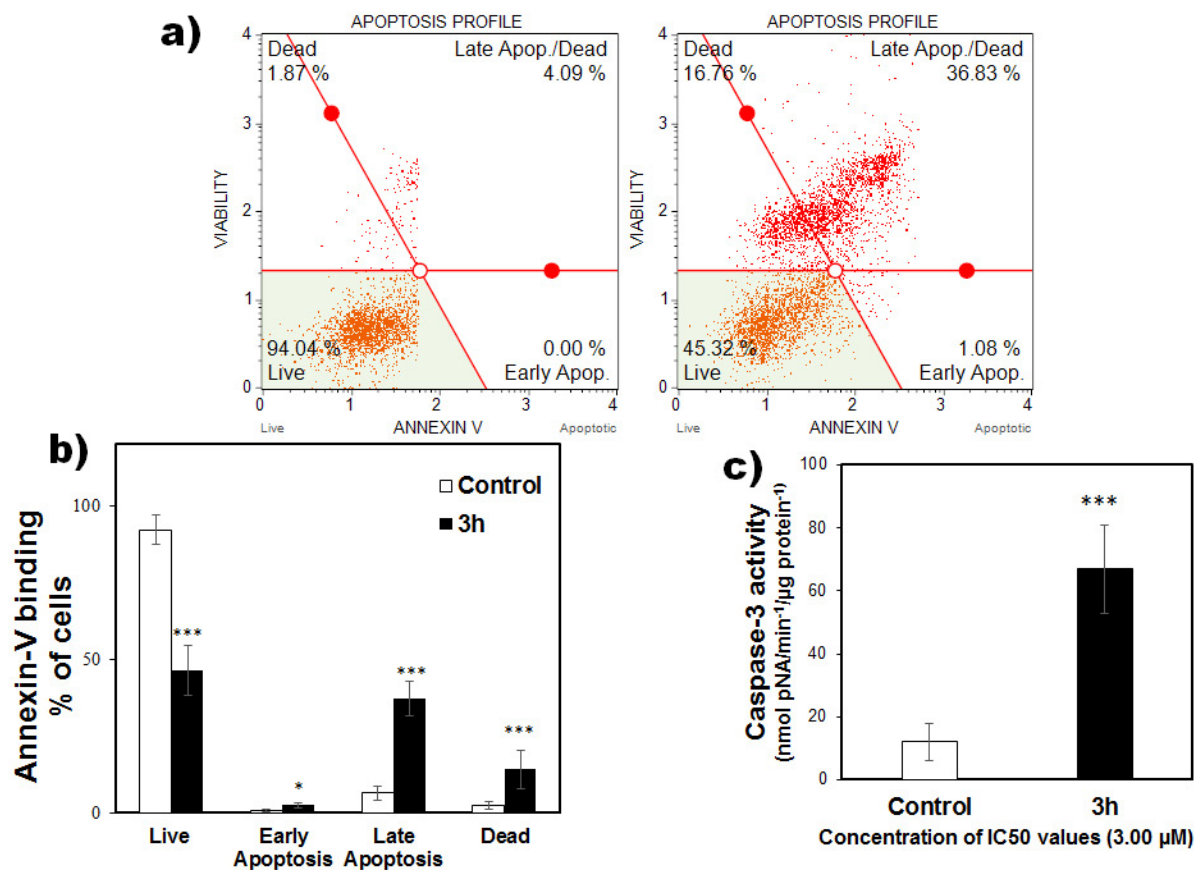


Figure 4. Apoptosis profile for MCF-7 cells treated with compound **3h** (3.00 μM) **a)** Annexin-V binding **b)** The percentage of live, early and late apoptosis/dead cells by MUSE cell analyzer **c)** Caspase-3 activity (* *p* < 0.05, *** *p* < 0.001 vs control)

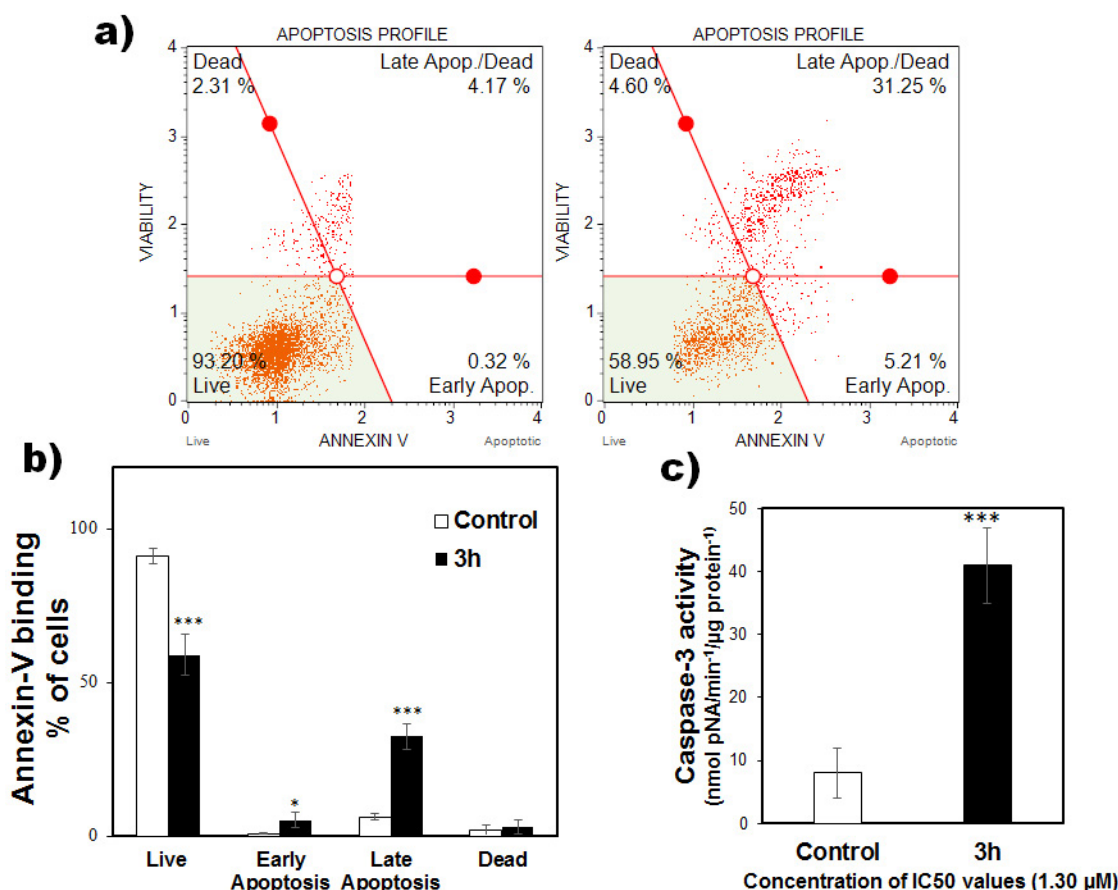


Figure 5. Apoptosis profile for PC-3 cells treated with compound **3h** (1.30 μM) **a**) Annexin-V binding **b**) The percentage of live, early and late apoptosis/dead cells by MUSE cell analyzer **c**) Caspase-3 activity (* $p < 0.05$, *** $p < 0.001$ vs control)

Evaluation of the anti-cancer activity of a compound using only malignant cell lines without SI determination has been reported to be a poor predictor for further (clinical) study.²⁹ For example colchicine exhibits very high cytotoxic effects. Unfortunately, colchicine is too toxic to be used as an antitumor agent.³⁰

As a result, the selectivity index of compound **3h** was found at 181.0 for PC3, 78.4 for MCF-7, and 138.4 for HT-29. The selectivity index of standard drug (Paclitaxel) was found at 31.0 for PC3, 13.5 for MCF-7, and 6.2 for HT-29. The selectivity index of compound **3h** was higher than standard drug. In addition, caspase-3 activity and Annexin-V assay were performed to explain the activity mechanism of compound **3h**. Dose response curves of five compounds (**3c**, **3d**, **3h**, **3l**, **3p** and **3q**) were also added to the Supporting Information (Figure S1).

3. 3. *In silico* ADME analysis

A promising compound must pass *in silico* analysis before it can be taken up for further studies.³¹ Therefore, we evaluated the pharmacokinetics, drug-likeness and physicochemical properties of hydrazone derivatives. The drug-likeness was established based on the physicochemi-

cal properties to obtain oral drug candidates.³² All data for the calculation were shown in Tables 2 and 3.

The SwissAdme web tool allows assessing the probability of a molecule to become an oral drug with respect to bioavailability.

There are five different rule-based filters, also defined below, which can be calculated with the SwissAdme program:³³

- (i) Lipinski's rule of five includes molecular weight ≤ 500 , MLOGP (lipophilicity) ≤ 4.15 , hydrogen bond donors ≤ 5 and hydrogen bond acceptors ≤ 10 .
- (ii) Ghose's filter includes $160 \leq$ molecular weight ≤ 480 , $-0.4 \leq$ WLOGP (lipophilicity) ≤ 5.6 , $40 \leq$ the molar refractivity ≤ 130 , and $20 \leq$ number of atoms ≤ 70 .
- (iii) Veber's rule includes the number of rotatable bonds ≤ 10 and the total polar surface area ≤ 140 .
- (iv) Egan's filter includes WLOGP (Lipophilicity) ≤ 5.88 and the total polar surface area ≤ 131.6 .
- (v) Muegge's filter includes $200 \leq$ molecular weight ≤ 600 , $-2 \leq$ XLOGP (lipophilicity) ≤ 5 , the total polar surface area ≤ 150 , the number of rings ≤ 7 , the number of carbon > 4 , the number of heteroatoms > 1 , the number of rotatable bonds ≤ 15 , the hydrogen bond acceptors ≤ 10 , and the hydrogen bond donors ≤ 5 .

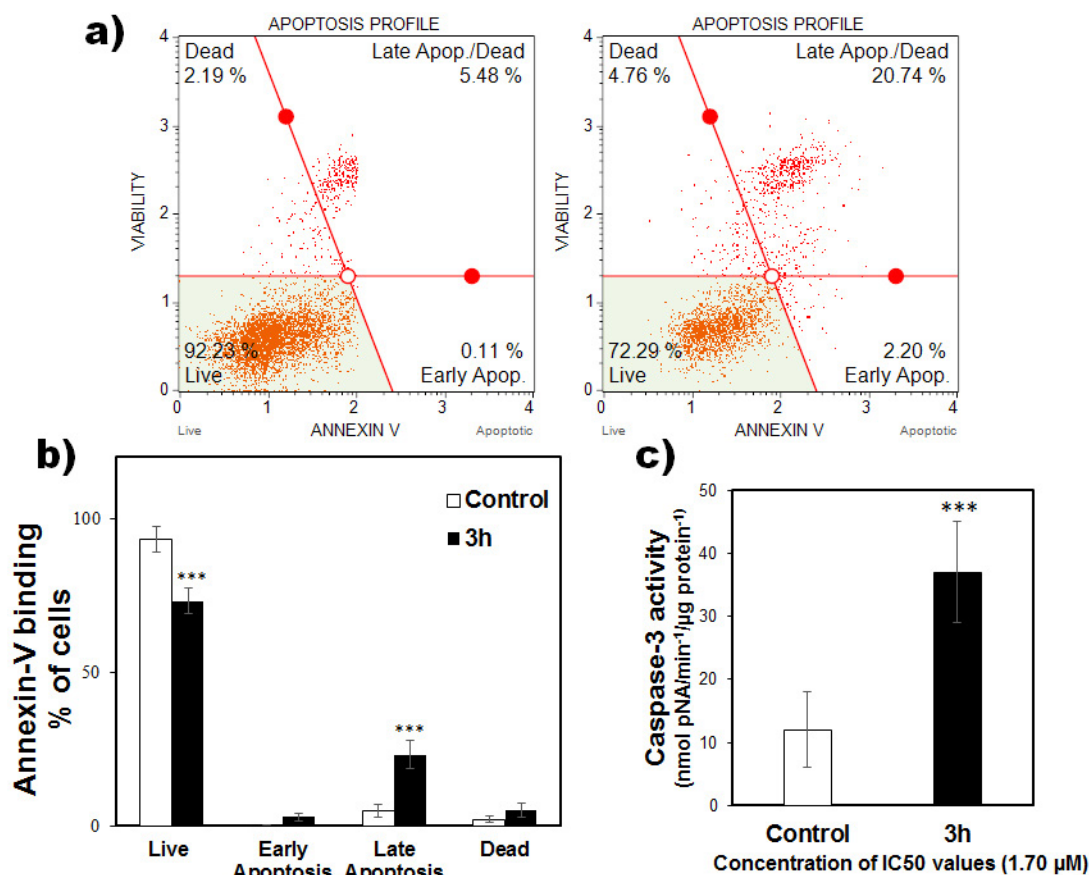


Figure 6. Apoptosis profile for HT-29 cells treated with compound **3h** (1.70 μM) **a)** Annexin-V binding **b)** The percentage of live, early and late apoptosis/dead cells by MUSE cell analyzer **c)** Caspase-3 activity (***) $p < 0.001$ vs control)

The result of the drug-likeness evaluation of hydrazones (**3a–u**) was shown in Table 3, and we can conclude that: (i) Lipinski, Veber, Ghose, Egan and Muegge filters of all compounds were within the accepted range except compounds **3j** and **3o**. (ii) The bioavailability score is 0.55 for all compounds, meaning good bioavailability.

On the other hand, solubility is another important property related to drug absorption by assessing whether the drug is soluble or moderately soluble. Furthermore, one of the prerequisites for the compound to show activity is that it should have good solubility. Solubility class can be estimated according to the following log S scale: insoluble < -10 <poorly < -6 <moderately < -4 <soluble < -2 <very < 0 <highly. Only **3o** of the compounds have poor solubility due to carrying the large lipophilic group (4-chlorophenoxy moiety). It is known that as the number of aromatic rings increases, the solubility decreases.³⁴ All other compounds were detected to have soluble or moderately soluble. In addition, according to Yalkowsky's general solubility equation, the following relationship can be established between solubility, partition coefficient and melting point.³⁵ $[\text{Log } S = 0.5 - 0.01 \times (\text{M.P.} - 25) - \text{Log } P]$. As a matter of fact, the compound **3o** with the highest partition coefficient ($\text{Log } P = 4.40$) has the lowest solubility ($\text{Log } S = -6.42$).

The BOILED-Egg model is used to predict the pharmacokinetic properties of compounds. While molecules in the yellow region easily pass the blood-brain barrier; the white area indicates molecules that pass easily through the gastrointestinal membranes. The absorption of molecules in the gray area is low.³⁶ The BOILED-Egg model showed that all molecules were in the white region except **3j**, so their absorptions through the gastrointestinal membranes were high. The absence of molecules in the yellow region was important to avoid central side effects (Figure 7). Among the compounds **3h**, having the highest activity, showed agreement with all filters and good gastrointestinal absorption.

4. Conclusion

Cancer is an important public health problem globally. In many medical research projects, the aim is related to the discovery of new safer more effective and selective anticancer agents. Therefore, some hydrazide-hydrazone derivatives were synthesized and investigated for their anticancer potency against carcinogenic PC-3, MCF-7, HT-29 and normal HUVEC cell lines. Among these compounds, **3h** having the 3-pyrrole ring showed more cytotoxic effects against three cancer cell lines than the stand-

ard compound paclitaxel. In addition, this compound did not show any cytotoxic effects against normal endothelial cells. The molecular mechanism revealed that compound **3h** increased the activation of caspase-3 cascade and ap-

optosis. Moreover, it has good pharmacokinetics and drug-likeness properties. All results suggest that compound **3h** could be a lead compound for the anticancer drug discovery field.

Table 2. The physicochemical properties of hydrazone derivatives (**3a–u**).

Comp	MW	FCsp3	n-ROTB	n-ON	n-OHNH	MR	TPSA	cLog P	Log S
3a	442.29	0.05	8	4	2	118.34	79.79	4.13	−5.58
3b	442.29	0.05	8	4	2	118.34	79.79	4.13	−5.58
3c	418.40	0.05	9	6	2	117.14	125.61	2.22	−4.46
3d	418.40	0.05	9	6	2	117.14	125.61	2.22	−4.46
3e	458.29	0.05	8	5	3	120.36	100.02	3.60	−5.44
3f	374.39	0.05	8	5	2	106.11	92.68	1.76	−3.73
3g	374.39	0.05	8	5	2	106.11	92.68	1.76	−3.73
3h	362.38	0.05	8	4	3	102.67	95.58	1.58	−3.56
3i	379.43	0.05	8	4	2	106.19	108.03	2.37	−4.43
3j	408.36	0.05	9	7	2	109.40	138.75	1.47	−4.26
3k	458.90	0.04	8	5	2	128.63	92.68	3.18	−5.72
3l	373.40	0.05	8	4	2	108.32	79.79	3.17	−4.23
3m	389.40	0.05	8	5	3	110.34	100.02	2.64	−4.25
3n	419.43	0.09	9	6	3	116.83	109.25	2.34	−4.32
3o	499.94	0.04	10	5	2	139.84	89.02	4.40	−6.42
3p	387.43	0.09	9	4	2	113.12	79.79	3.39	−4.36
3q	363.37	0.05	8	5	2	100.58	92.93	1.58	−4.30
3r	403.43	0.09	9	5	2	114.81	89.02	2.86	−4.47
3s	391.40	0.05	8	5	2	108.27	79.79	3.55	−4.55
3t	398.41	0.04	8	5	2	113.03	103.58	2.52	−4.34
3u	452.30	0.05	8	4	2	116.02	79.79	3.76	−5.30

MW: Molecular weight, FCsp3: Fraction Csp3, n-ROTB: Number of rotatable bonds, n-ON: Number of hydrogen bond acceptors, n-OHNH: Number of hydrogen bond donors, MR: Molar Refractivity, TPSA: Topological polar surface area, cLog P: Partition coefficient and Log S: Water solubility.

Table 3. The drug-likeness and pharmacokinetic properties of target compounds (**3a–u**).

Comp	Pharmacokinetics		Druglikeness					
	GI abs.	BBB per.	Lipinski	Veber	Ghose	Egan	Muegge	Bio. score
3a	High	No	✓	✓	✓	✓	✓	0.55
3b	High	No	✓	✓	✓	✓	✓	0.55
3c	High	No	✓	✓	✓	✓	✓	0.55
3d	High	No	✓	✓	✓	✓	✓	0.55
3e	High	No	✓	✓	✓	✓	✓	0.55
3f	High	No	✓	✓	✓	✓	✓	0.55
3g	High	No	✓	✓	✓	✓	✓	0.55
3h	High	No	✓	✓	✓	✓	✓	0.55
3i	High	No	✓	✓	✓	✓	✓	0.55
3j	Low	No	✓	✓	✓	–	✓	0.55
3k	High	No	✓	✓	✓	✓	✓	0.55
3l	High	No	✓	✓	✓	✓	✓	0.55
3m	High	No	✓	✓	✓	✓	✓	0.55
3n	High	No	✓	✓	✓	✓	✓	0.55
3o	High	No	✓	✓	–	–	–	0.55
3p	High	No	✓	✓	✓	✓	✓	0.55
3q	High	No	✓	✓	✓	✓	✓	0.55
3r	High	No	✓	✓	✓	✓	✓	0.55
3s	High	No	✓	✓	✓	✓	✓	0.55
3t	High	No	✓	✓	✓	✓	✓	0.55
3u	High	No	✓	✓	✓	✓	✓	0.55

GI abs.: Gastrointestinal absorption, BBB per.: Blood-brain barrier permeation, Bio.: Bioavailability

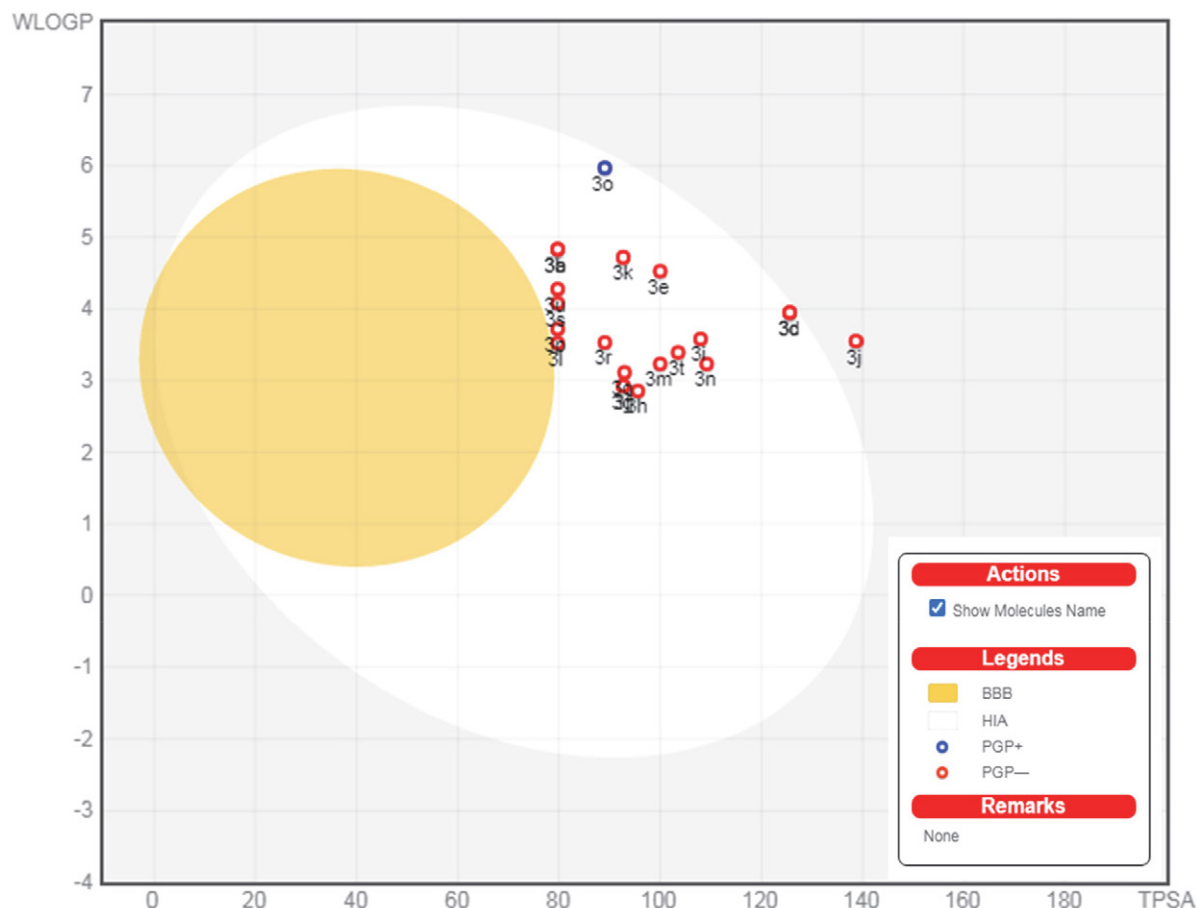


Figure 7. The BOILED-Egg model of target compounds (3a-u).

Conflict of interest

The authors declare that they have no known competing financial interests.

5. References

- J. M. Ritter, R. J. Flower, G. Henderson, Y. K. Loke, D. MacEwan, H. P. Rang, Rang & Dale's Pharmacology, 9th edn. Elsevier, China, **2020**.
- R. Ali, Z. Mirza, G. M. D. Ashraf, M. A. Kamal, S. A. Ansari, G. A. Damanhouri, A. M. Abuzenadah, A. G. Chaudhary, I. A. Sheikh, *Anticancer Res.* **2012**, 32(7), 2999–3005. ISSN: 0250–7005
- V. Hanusova, L. Skalova, V. Kralova, P. Matouskova, *Curr. Cancer Drug Targets.* **2015**, 15(1), 35–52. DOI:10.2174/1568009615666141229152812
- J. Nath, R. Paul, S. K. Ghosh, J. Paul, B. Singha, N. Debnath, *Life Sci.* **2020**, 258, 1–16. DOI:10.1016/j.lfs.2020.118189
- H. H. Amer, S. H. Alotaibi, A. H. Trawneh, A. M. Metwaly, I. H. Eissa, *Arab. J. Chem.* **2021**, 14, 1–18. DOI:10.1016/j.arabjc.2021.103348
- A. El-Faham, M. Farooq, S. N. Khattab, N. Abutaha, M. A. Wadaan, H. A. Ghabbour, H. K. Fun, *Molecules.* **2015**, 20, 14638–14655. DOI:10.3390/molecules200814638
- U. Acar-Çevik, B. N. Sağlık, C. M. Ardic, Y. Özkay, Ö. Ath, *Turk. J. Biochem.* **2018**, 43(2), 151–158. DOI:10.1515/tjb-2017-0167
- F. Tok, B. N. Sağlık, Y. Özkay, S. Ilgin, Z. A. Kaplancıklı, B. Koçyiğit-Kaymakçioğlu, *Bioorg. Chem.* **2021**, 114, 1–11. DOI:10.1016/j.bioorg.2021.105038
- D. Saini, M. Gupta, *Asian J. Pharm. Sci.* **2018**, 4(2), 116–122. DOI:10.31024/ajpp.2018.4.2.4
- R. Islam, F. Koizumi, Y. Koderu, K. Inoue, T. Okowara, M. Masutani, *Bioorg. Med. Chem. Lett.* **2014**, 24, 3802–3806. DOI:10.1016/j.bmcl.2014.06.065
- T. Damghani, F. Moosavi, M. Khoshneviszadeh, M. Mortazavi, S. Pirhadi, Z. Kayani, L. Saso, N. Edraki, O. Firuzi, *Sci. Rep.* **2021**, 11, 1–20. DOI:10.1038/s41598-021-83069-4
- S. M. Abou-Seri, A. A. M. Eissa, M. G. M. Behery, F. A. Omar, *Bioorg. Chem.* **2021**, 116, 1–19. DOI:10.1016/j.bioorg.2021.105334
- M. Taha, S. A. A. Shah, M. Afifi, M. Zulkeflee, S. Sultan, A. Wadood, F. Rahim, N. H. Ismail, *Chin. Chem. Lett.* **2017**, 28, 607–611. DOI:10.1016/j.ccl.2016.10.020
- S. Govindaiah, S. Naha, T. M. Rao, B. C. Revanasiddappa, S. M. Srinivasa, L. Parashuram, S. Velmathi, S. Sreenivasa, *Bioorg. Chem.* **2021**, 3, 1–14. DOI:10.1016/j.rechem.2021.100197

15. S. A. A. Noma, M. Erzengin, T. Tunç, S. Balçioğlu, *J. Mol. Struct.* **2020**, 1205, 1–8. DOI:10.1016/j.molstruc.2019.127550
16. S. Karakuş, S. Rollas, *J. Res. Pharm.* **2016**, 20(2), 199–206. DOI:10.12991/mpj.20162013533
17. B. Koçyiğit-Kaymakçioğlu, S. S. Yazıcı, F. Tok, M. Dikmen, S. Engür, E. E. Oruç-Emre, A. İyidoğan, *Lett. Drug Des. Discov.* **2019**, 16(5), 522–532. DOI:10.2174/1570180815666180816124102
18. S. G. Kucukguzel, E. E. Oruç, S. Rollas, F. Şahin, A. Özbek, *Eur. J. Med. Chem.* **2002**, 37, 197–206. DOI:10.1016/S0223-5234(01)01326-5
19. N. S. Habib, A. S. Issa, S. M. Rida, F. A. Ashour, G. G. Tawil, *Pharmazie*. **1986**, 41, 761–764.
20. M. I. Husain, M. Amir, *Curr. Sci.* **1985**, 54(22), 1159–1161.
21. Ö. Çevik, D. Li, E. Baljinnyam, D. Manvar, E. M. Pimenta, G. Waris, B. J. Barnes, N. Kaushik-Basu, *J. Biol. Chem. Dec.* **2017**, 292(52), 21676–21689. DOI:10.1074/jbc.M117.792721
22. Ö. Erdoğan, S. Paşa, G. M. Demirbolat, Ö. Çevik Ö, *Turk. J. Chem.* **2021**, 45(4), 1086–1096. DOI:10.3906/kim-2102-2
23. S. Noriega, J. Cardoso-Ortiz, A. Lopez-Luna, M. D. R. Cuevas-Flores, J. A. F. D. L. Torre, *Pharmaceuticals*. **2022**, 15(717), 1–14. DOI:10.3390/ph15060717
24. T. Kauerova, J. Kos, T. Gonce, J. Jampilek, P. Kollar, *Int. J. Mol. Sci.* **2016**, 17(1219), 1–14. DOI:10.3390/ijms17081219
25. M. Lopez-Lazaro, *Oncoscience*. **2015**, 2(2), 91–98. DOI:10.18632/oncoscience.132
26. G. Indrayanto, G. S. Putra, F. Suhud, *Profiles Drug Subst. Ex-cip. Relat. Methodol.* **2021**, 46, 273–307. DOI:10.1016/bs.podrm.2020.07.005
27. O. A. Pena-Moran, M. L. Villarreal, L. Alvarez-Berber, A. Meneses-Acosta, V. Rodriguez-Lop, *Molecules*. **2016**, 21(1013), 1–15. DOI:10.3390/molecules21081013
28. N. Weerapreeyakul, A. Nonpunya, S. Barusrux, T. Thitimeth-aroch, B. Sripanidkulchai, *Chin. Med.* **2012**, 7(15), 1–7. DOI:10.1186/1749-8546-7-15
29. M. Lopez-Lazaro, *Drug Discov. Today*. **2015**, 20, 167–169. DOI:10.1016/j.drudis.2014.12.006
30. J. Krzywik, W. Mozga, M. Aminpour, J. Janczak, E. Maj, J. Wietrzyk, J. A. Tuszyński, A. Huczynski, *Molecules*. **2020**, 25(1789), 1–33. DOI:10.3390/molecules25081789
31. B. N. Sağlık, B. Kaya-Çavuşoğlu, U. Acar-Çevik, D. Osmani-ye, S. Levent, Y. Özkay, Z. A. Kaplancıklı, *RSC Med. Chem.* **2020**, 11, 1063–1074. DOI:10.1039/D0MD00150C
32. A. S. Hassan, *J. Iran. Chem. Soc.* **2022**, Accepted paper. DOI:10.1007/s13738-022-02551-6
33. S. Pathania, P. K. Singh, *Expert Opin. Drug Metab. Toxicol.* **2021**, 17, 351–354. DOI:10.1080/17425255.2021.1865309
34. S. B. Bunally, C. N. Luscombe, R. J. Young, *SLAS Discov.* **2019**, 24, 791–801. DOI:10.1177/2472555219859845
35. C. P. Tinworth, R. J. Young, *J. Med. Chem.* **2020**, 63, 10091–10108. DOI:10.1021/acs.jmedchem.9b01596
36. F. Tok, B. I. Abas, Ö. Çevik, B. Koçyiğit-Kaymakçioğlu, *Bioorg. Chem.* **2020**, 102, 1–10. DOI:10.1016/j.bioorg.2020.104063

Povzetek

V raziskavi smo sintetizirali serijo hidrazid-hidrazonskih derivatov (3a–3u) in ocenili njihovo protirakavo delovanje na celično linijo raka prostate (PC-3), celično linijo raka dojke (MCF-7), celično linijo raka debelega črevesa (HT-29) in endotelijske celice človeške popkovnične vene (HUVEC) z uporabo testa MTT. Spojina 3h s pirolnim obročem je predstavljala najmočnejši derivat z IC₅₀ = 1,3; 3,0 in 1,7 µM proti rakavim celicam PC-3, MCF-7 in HT-29, pri čemer je bil kot standardna spojina uporabljen paklitaksel. Poleg tega smo spojino 3h vključili v nadaljnje biološke študije, kot sta aktivnost kaspaze-3 in test aneksina-V, da bi ocenili njen inhibični potencial. Rezultati aktivnosti so pokazali, da spojina 3h poveča aktivacijo kaspaze-3 in število celic v zgodnji apoptozi. Izvedene so bile tudi dodatne študije, kot so farmakokinetika, ocena biološke razpoložljivosti in podobnost učinkovinam. Farmakokinetične napovedi *in silico* so pokazale, da bi biološka razpoložljivost teh spojin lahko bila visoka.



Except when otherwise noted, articles in this journal are published under the terms and conditions of the Creative Commons Attribution 4.0 International License

Preparation and Characterization of NiCoFe₂O₄ Nanoparticles as an Effective Catalyst for the Synthesis of Trisubstituted Imidazole Derivatives Under Solvent-free Conditions

Leila Hemmesi and Hossein Naeimi*

Department of Organic Chemistry, Faculty of Chemistry, University of Kashan, Kashan, 873117-51167, I.R. Iran

* Corresponding author: E-mail: Naeimi@kashanu.ac.ir

Tel: 0983155912388, Fax No: 983155912397

Received: 06-23-2022

Abstract

In this study, NiCoFe₂O₄ nanoparticles were prepared and used as a reactive catalyst for the synthesis of trisubstituted imidazoles. The multicomponent reactions of aromatic aldehydes, benzil and ammonium acetate were carried out under solvent-free and conventional heating conditions. In this reaction, some imidazole derivatives with high purity, short reaction times and high yields were obtained. The prepared nanocatalyst was characterized by FT-IR, XRD, EDX, VSM and SEM techniques. Moreover, the organic products were identified by melting point, FT-IR and ¹H NMR analyzes.

Keywords: Ammonium acetate, Aromatic aldehydes, NiCoFe₂O₄ nanoparticles, Benzil, Imidazoles

1. Introduction

Imidazoles are the largest and most diverse group of heterocyclic compounds used for environmental and biological purposes.¹ In recent years, research has received special attention due to their industrial and medical applications. For example, imidazoles are used in the photographic industry as photosensitive materials² and in combustion. Biochemical properties include histidine, histamine, and biotin, which are found in pharmaceuticals.³ Other medical uses include antiallergic,⁴ antiparasitic,⁵ analgesic,⁶ plant growth regulating,⁷ enzyme activity inhibiting,⁸ cardiovascular,^{9,10} antitumor,¹¹ anticancer,¹² antifungal,¹³ antibacterial, and antiviral,¹⁴ enzyme inhibitors.^{15–17} Originally, imidazoles were synthesized by Debus in 1858, but low yield was one of the problems of his proposed reaction.¹⁸

Imidazoles have also been synthesized using several methods and different catalysts.^{19,20} Other catalysts that have been used for the synthesis of imidazoles include sulfuric acid on silicate supports,²¹ InCl₃·3H₂O,²² BaMnO₄,²³ H₂SO₄/EtOH/reflux,²⁴ Al₂O₃-ZrCl₄, NiCl₂·6H₂O zeolite,^{25,26} BF₃SiO₂,²⁷ L-proline,²⁸ NaNO₂,²⁹ ZrOCl₂,³⁰ CH₃CO₂NH₄/CH₃COOH/reflux,^{31,32} glutamic acid,³³ ZrCl₄,³⁴ Fe₃O₄@SiO₂, HM.SO₃H,³⁵ K₅CoW₁₂O₄₀,³⁶

n-Bu₄NBr,³⁷ acetic acid,³⁸ zeolite HY/silica gel³⁹ and Zr(acac).⁴⁰ Recently, some of the nanoparticles have been used as catalysts for the synthesis of heterocyclic compounds.^{41–45}

Continuing our work on catalytic reactions,^{46–49} we would like to report here on the preparation of NiCoFe₂O₄ NPs as nanocatalysts for the four-component synthesis of tri-substituted imidazoles from benzil and aromatic aldehydes with ammonium acetate under solvent-free conditions.

2. Experimental Section

2.1. Apparatus

Chemicals were purchased from Fluka and Merck Chemical Companies and used without purification. The FT-IR spectra were recorded as KBr pellets using a Perkin Elmer 781 spectrophotometer and an Impact 400 Nicolet FT-IR spectrophotometer. The ¹H NMR spectra were recorded in DMSO-*d*₆ using a Broker DRX-400 spectrometer with tetramethylsilane (TMS) as an internal reference. Nanostructures were characterized using a Holland Philips Xpert X-ray powder diffraction (XRD) diffractom-

eter (CuK, radiation, $\lambda = 0.154056$ nm) at a scan speed of 20/min from 100 to 1000 (2 θ). Energy dispersive X-ray (EDX) analysis of nanoparticles was performed using a Zeiss PL GMA vp. Magnetic properties of nanoparticles were measured using a vibrating magnetometer (VSM, PPMS-9T) at 300 K (University of Kashan, Iran). Scanning electron microscopy (SEM) of nanoparticles was performed using a KYKYEM-3200. The melting point of the products was determined using a Yanagimoto micromelting point and was not corrected. Substrate determination and reaction monitoring were performed by TLC (thin layer chromatography) on silica gel polygram SILG UV 254 plates (Merck Company).

2. 2. General Procedure for the Preparation of NiCoFe₂O₄ Nanoparticles

FeCl₃·6H₂O (1 mmol), NiCl₂ (0.025 mmol) and CoCl₂ (0.025 mmol) were added to 100 ml HCl (1.2 M) under ultrasonic sonication for 30 minutes, then 150 ml NaOH (1.25 M) was added and nitrogen gas was added for 5 minutes. The mixture was heated at 80 °C for 2 hours, the black precipitate was washed several times with water and dried in an oven at 80 °C.

2. 3. General Procedure for the Synthesis of Imidazoles

Aromatic aldehyde (1 mmol), benzil (1 mmol), ammonium acetate (2 mmol) were mixed as powder and NiCoFe₂O₄ (0.004 g) nanoparticles were added and stirred in paraffin bath at 110 °C under solvent-free conditions for an appropriate time. After completion of the reaction, the progress of the reaction was monitored by TLC using petroleum ether/ethyl acetate (70:30 ratio) as eluent. The reaction mixture was cooled to room temperature and acetone was added. The nanoparticles were separated with an external magnet, washed with acetone and dried a few times in an oven at 100 °C for 5 hours. Then a few drops of water were added and cooled in ice. After filtration of the solution, the products were purified by recrystallization from ethanol and water. The pure products were characterized by spectroscopic data such as IR and ¹H NMR, and the melting points of the known compounds were compared with those of the authentic samples.

2,4,5-Triphenyl-1H-imidazole (4a): White solid; m.p. 272–273 °C (lit.⁵⁰ 275); IR (KBr, cm⁻¹) ν 3444 (NH), 3061 (C=C–H), 1487 (CN), 1451, 1592 (C=C aromatic); ¹H NMR (400 MHz, DMSO-*d*₆) δ 7.37–8.09 (m, 15 H, Ar-H), 12.76 (s, 1H, NH).

2-(3-Methoxyphenyl)-4,5-diphenyl-1H-imidazole (4b): White solid; m.p. 250–251 °C (lit.⁴⁰ 253–256); IR (KBr, cm⁻¹) ν 3448 (NH), 3063 (C=C–H), 2924 (C–C–H), 1487 (CN), 1451, 1592 (C=C aromatic), 1211 (C–O); ¹H NMR

(400 MHz, DMSO-*d*₆) δ 3.51 (s, 3H, OMe), 7.50 (s, 1H, ArH), 7.60–7.97 (m, 13H, ArH), 12.75 (s, 1H, NH).

2-(4-Methoxyphenyl)-4,5-diphenyl-1H-imidazole (4c): Yellow solid; m.p. 226–228 °C (lit.⁵¹ 230–232); IR (KBr, cm⁻¹) ν 3464 (NH), 3060 (C=C–H), 2932 (C–C–H), 1502 (C=N), 1446, 1657 (C=C aromatic), 1255 (C=O); ¹H NMR (400 MHz, DMSO-*d*₆) δ 3.84 (s, 3H, OCH₃), 7.13–7.15 (d, 2H, *J*=8.0 Hz, Ar), 7.13–7.61 (m, 10 H, Ar), 7.92–8.07 (d, 2H, *J*=8.0 Hz, Ar), 12.85 (s, 1H, NH).

2-(2,3-Dimethoxy phenyl)-4,5-diphenyl-1H-imidazole (4d): White solid; m.p. 322–323 °C (lit.⁵² 325–326); IR (KBr, cm⁻¹) ν 3241 (NH), 3063 (C=C–H), 2837 (C–C–H), 1473 (C=N), 1447, 1591 (C=C aromatic), 1298 (C=O); ¹H NMR (400 MHz, DMSO-*d*₆) δ 3.53 (s, 3H, OMe), 3.99 (s, 3H, OMe), 7.30–7.99 (m, 13H, Ar), 12.49 (s, 1H, NH).

2-(4-Methylphenyl phenyl)-4,5-diphenyl-1H-imidazole (4e): White solid; m.p. 230–231 °C (lit.⁵³ 232–235); IR (KBr, cm⁻¹) ν 3447 (NH), 3032 (C=C–H), 2854 (C–C–H), 1493 (C=N), 1446, 1596 (C=C aromatic); ¹H NMR (400 MHz, DMSO-*d*₆) δ 2.83 (s, 3H, Me), 7.27–7.29 (d, 2H, *J*=8.0 Hz, ArH), 7.30–7.58 (d, 2H, *J*=8.0 Hz, ArH), 12.64 (s, 1H, NH).

2-(2-Hydroxyphenyl)-4,5-diphenyl-1H-imidazole (4f): White solid; m.p. 112–114 °C (lit.⁵³ 117–119); IR (KBr, cm⁻¹) ν 3316 (NH), 3063 (C=C–H), 3023 (OH), 2331 (C–C–H), 1489 (C=N), 1448, 1592 (C=C aromatic); ¹H NMR (400 MHz, DMSO-*d*₆) δ 7.1–7.81 (m, 14H, Ar), 11.96 (s, 1H, OH), 12.36 (s, 1H, NH).

2-(4-Hydroxyphenyl)-4,5-diphenyl-1H-imidazole (4g): Yellow solid; m.p. 231–232 °C (lit.⁵⁴ 233); IR (KBr, cm⁻¹) ν 3134 (NH), 3005 (C=C–H), 2924 (OH), 2790 (C–C–H), 1508 (C=N), 1447, 1608 (C=C aromatic), 1238 (C–O); ¹H NMR (400 MHz, DMSO-*d*₆) δ 7.26–7.28 (d, 2H, *J*=8.3 Hz), 7.65–7.67.96 (d, 2H, *J*=8.3 Hz), 7.87–7.99 (m, 10H, ArH), (s, 1H, NH), 9.73 (s, 1H, OH), 12.39 (s, 1H, NH).

2-(2,3 Dichlorophenyl)-4,5-diphenyl-1H-imidazole (4h): White solid; m.p. 192–193 °C (lit.⁴⁰ 194–197); IR (KBr, cm⁻¹) ν 3433 (NH), 3062 (C=C–H), 1593 (C=N), 1448, 1661 (C=C aromatic), 1048 (C–Cl); ¹H NMR (400 MHz, DMSO-*d*₆) δ 7.32–7.54 (m, 12H, ArH), 12.76 (s, 1H, NH).

2-(4-Chlorophenyl)-4,5-diphenyl-1H-imidazole (4i): White solid; m.p. 257–258 °C (lit.⁵⁵ 258–260); IR (KBr, cm⁻¹) ν 3316 (NH), 3063 (C=C–H), 1482 (C=N), 1447, 1592 (C=C aromatic), 1091 (C–Cl); ¹H NMR (400 MHz, DMSO-*d*₆) δ 7.04–7.91 (m, 12H, ArH), 7.65–7.81 (m, 2H, Ar), 12.76 (s, 1H, NH).

2-(2,4-Dichlorophenyl)-4,5-diphenyl-1H-imidazole (4j): Yellow solid; m.p. 170–172 °C (lit.⁵⁶ 176–177); IR (KBr,

cm^{-1}) ν 3430 (NH), 3062 (C=C-H), 2966 (C-C-H), 1475 (C=N), 1447, 1668 (C=C aromatic); ^1H NMR (400 MHz, DMSO- d_6) δ 7.40–8.08 (m, 13H, ArH), 11.56 (s, 1H, NH).

2-(3-Chlorophenyl)-4,5-diphenyl-1H-imidazole (4k): Yellow solid; m.p. 283–284 °C (lit.⁵⁵ 285–287); IR (KBr, cm^{-1}) ν 3429 (NH), 3062 (C=C-H), 2968 (C-C-H), 1503 (C=N), 1447, 1650 (C=C aromatic), 1029 (C-Cl); ^1H NMR (400 MHz, DMSO- d_6) δ 7.26–7.52 (m, 12H, ArH), 7.91 (d, 1H, $J=7.0$ Hz, ArH), 12.78 (s, 1H, NH).

2-(4-Bromophenyl)-4,5-diphenyl-1H-imidazole (4l): White solid; m.p. 260–264 °C (lit.⁵⁵ 262); IR (KBr, cm^{-1}) ν 3443 (NH), 3063 (C=C-H), 1592 (C=N), 1447, 1661 (C=C aromatic), 1069 (C-Br). ^1H NMR (400 MHz, DMSO- d_6) δ 7.27–7.47 (m, 12H, ArH), 7.74–7.76 (m, 2H, ArH), 11.59 (s, 1H, NH).

2-(4-Fluorophenyl)-4,5-diphenyl-1H-imidazole (4m): White solid; m.p. 193–194 °C (lit.⁵⁶ 190); IR (KBr, cm^{-1}) ν 3379 (NH), 3064 (C=C-H), 1517 (C=N), 1448, 1665 (C=C aromatic), 1173 (C-F); ^1H NMR (400 MHz, DMSO- d_6) δ 7.08–7.28 (m, 12H, ArH), 7.97–7.99 (m, 2H, ArH), 12.76 (s, 1H, NH).

2-(4-Nitrophenyl)-4,5-diphenyl-1H-imidazole (4n): White solid; m.p. 202–204 °C (lit.⁵⁷ 199–201); IR (KBr, cm^{-1}) ν 3379 (NH), 3064 (C=C-H), 1599 (C=N), 1448, 1665 (C=C aromatic), 1517 (N=O), 1336 (N-O); ^1H NMR (400 MHz, DMSO- d_6) δ 7.65–7.87 (m, 12H, ArH), 8.23–8.25 (m, 2H, ArH), 11.59 (s, 1H, NH).

3. Results and Discussion

3. 1. Preparation and Characterization of the Catalyst

NiCoFe₂O₄ NPs nanoparticles were prepared by the reaction of FeCl₃·6H₂O, NiCl₂, and CoCl₂ in the presence of NaOH and HCl under N₂ atmosphere according to the procedure described in a previous work (Figure 1).³⁴ The prepared nanocatalyst was investigated by various analyses such as FT-IR, XRD, SEM, EDX and VSM.

The FT-IR spectrum of NiCoFe₂O₄ is shown in Figure 2. In general, the stretching vibration of the O–H bond corresponding to the hydroxyl group was observed at 3200–3600 cm^{-1} . In the IR spectrum of NiCoFe₂O₄ catalyst, the stretching vibration of OH appeared at 3358 cm^{-1} .

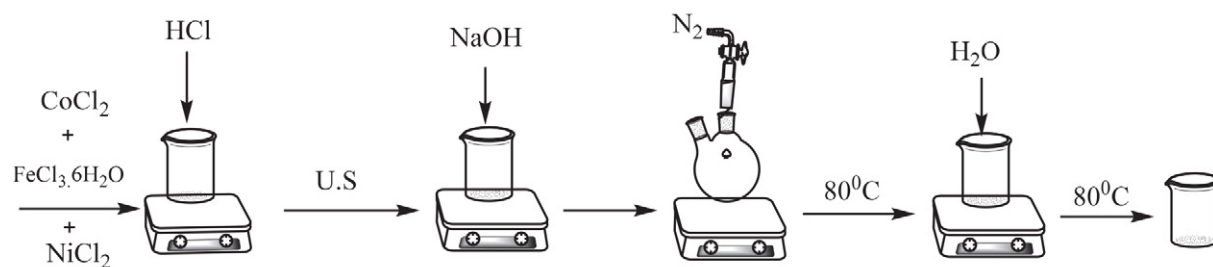


Figure 1. Preparation of NiCoFe₂O₄ NPs.

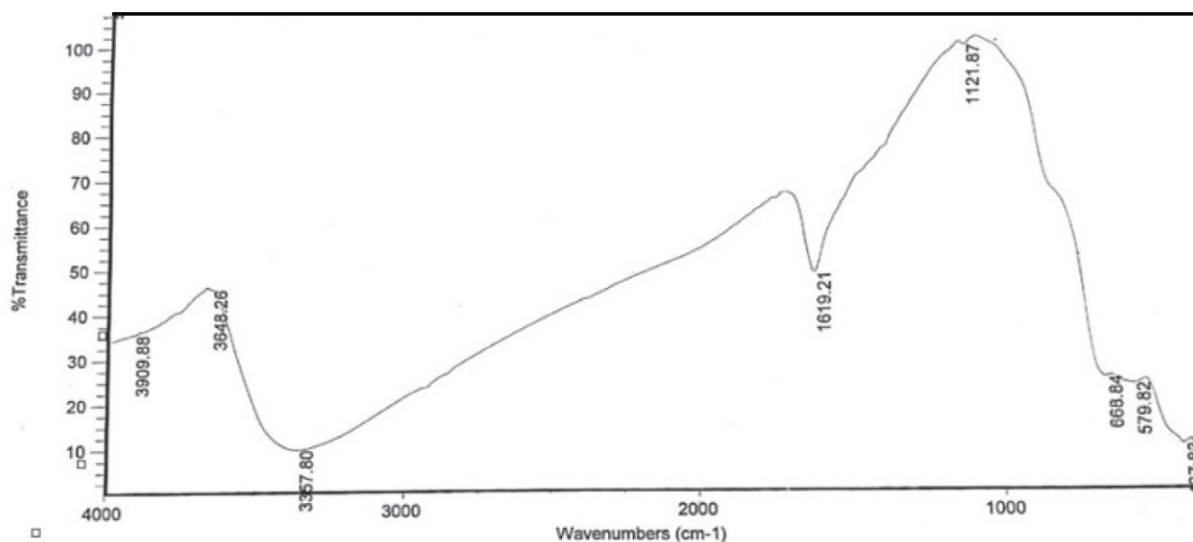


Figure 2. The FT-IR spectrum of NiCoFe₂O₄ catalyst.

Two very weak peaks related to the metal bonds of Fe–O and Co–O showed broad bands in the range of 669 and 580 cm^{-1} .

The XRD patterns of $\text{NiCoFe}_2\text{O}_4$ nanoparticles are shown in Figure 3. The position and relative intensity of the peaks are consistent with the standard XRD pattern of $\text{NiCoFe}_2\text{O}_4$. The average crystallite size was calculated according to the Scherer equation and was 34 nm.

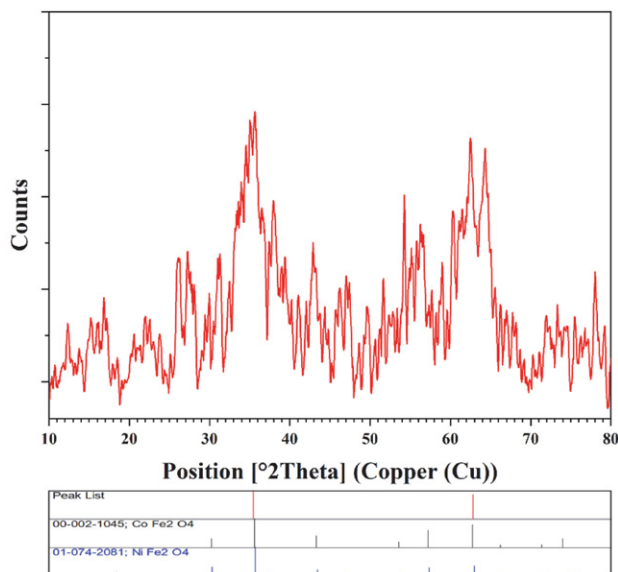


Figure 3. The XRD patterns of $\text{NiCoFe}_2\text{O}_4$ catalyst.

The morphology of the $\text{NiCoFe}_2\text{O}_4$ NPs was determined by scanning electron microscopy (SEM) analysis (Figure 4). The average size of the precipitated spherical particles was about 35 nm.

Energy diffraction X-ray (EDX) analysis of the $\text{NiCoFe}_2\text{O}_4$ NPs was performed (Figure 5) and confirmed the structure of the prepared catalyst.

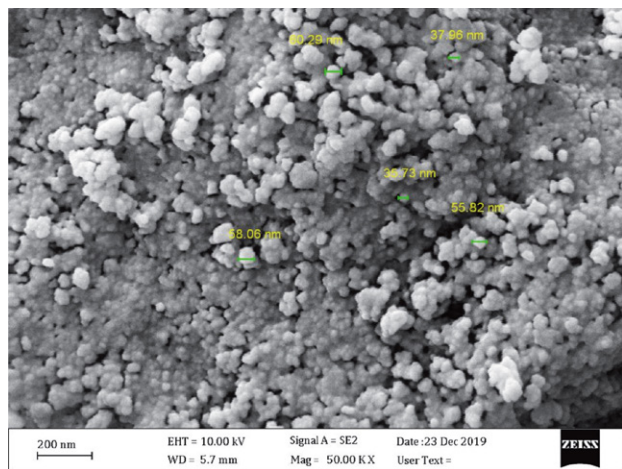


Figure 4. The SEM of $\text{NiCoFe}_2\text{O}_4$ catalyst

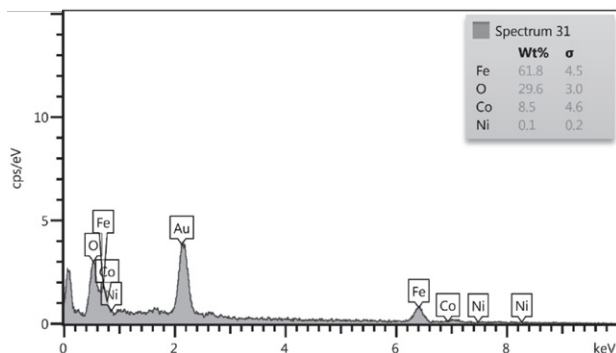


Figure 5. Energy diffraction X-ray (EDX) analysis of $\text{NiCoFe}_2\text{O}_4$ NPs.

The results of the vibration of magnetization (VSM) for the $\text{NiCoFe}_2\text{O}_4$ NPs are shown in Figure 6 and shows that the magnetization increased after the furnace was turned on.

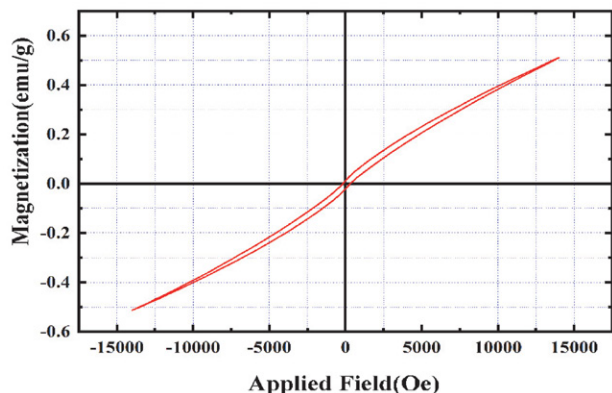
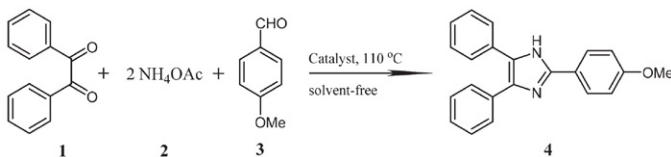


Figure 6. The vibration of magnetization (VSM) for $\text{NiCoFe}_2\text{O}_4$ NPs.

3. 2. Investigation of Catalytic Activity

3. 2. 1. Optimization of the Catalyst Amount

To determine the amount of catalyst, the reaction with benzil, 4-methoxybenzaldehyde and ammonium acetate was carried out in the presence of different amounts of catalyst under solvent-free conditions as a model reaction (Scheme 1). The corresponding results are listed in Table 1.



Scheme 1. Synthesis of 2-(4-methoxyphenyl)-4,5-diphenyl-1H-imidazole.

Table 1. Effect of different amounts of catalyst on reaction yield.^a

Entry	Catalyst loading (g)	Time (min)	Yield (%) ^b
1	0.001	15	65
2	0.002	10	80
3	0.003	10	90
4	0.004	5	95
5	0.005	5	95

a) General reaction conditions: 4-methoxybenzaldehyde (**3**, 1 mmol), benzil (**1**, 1 mmol), ammonium acetate (**2**, 2 mmol) at 110 °C under solvent-free condition. b) Isolated yield.

As shown in Table 1, the reaction was carried out using 4 mg of the catalyst under solvent-free conditions. The product was obtained in high yield and short reaction time (Table 1, entry 4). Then, the effect of different temperatures on the reaction was investigated (Table 2). As can be seen from this table, the reaction at 110 °C gave the product with the highest yield and the shortest reaction time among the different temperatures used for the reaction (Table 2, entry 5).

Table 2. Influence of different temperatures on the reaction.^a

Entry	Time (min)	Temp. (°C)	Yield (%) ^b
1	35	60	55
2	25	70	65
3	15	80	72
4	15	90	85
5	5	110	95
6	5	120	95

a) General reaction conditions: 4-methoxybenzaldehyde (**3**, 1 mmol), benzil (**1**, 1 mmol), ammonium acetate (**2**, 2 mmol) with 0.004 g catalyst under solvent-free condition. b) Isolated yield.

The course of the reaction was studied, and the present work with the prepared catalyst was compared with previously reported work with various other catalysts (Table 3). From this table, it can be seen that NiCoFe₂O₄ NPs as nanocatalyst was the best catalyst in terms of product yield and reaction times among the catalysts used in other works (Table 3, entry 10 versus entries 1–9).

After optimizing the reaction conditions with different amounts of catalyst and temperatures, the optimal state of a reaction was determined (Scheme 2). The NiCoFe₂O₄ NPs (4 mg) were selected as catalyst for the synthesis of tri-substituted imidazoles from aromatic aldehyde (1 mmol), benzil (1 mmol) and ammonium acetate (2 mmol) under solvent-free conditions. The various imidazole derivatives were synthesized at a temperature of 110 °C with a yield of 73–95% and a reaction time of 5–25 min. The corresponding results are summarized in Table 4.

As shown in Table 4, the various aromatic aldehydes with electron-withdrawing and electron-donating groups reacted well and gave the corresponding products in high yield and short reaction time. These results indicate that the present method is an efficient approach for the one-pot four-component synthesis of triaryl imidazole derivatives. The structure of the products was characterized by spectroscopic data such as IR, ¹H NMR and melting point, and these compounds agreed with those of the authentic samples.^{40,50–57}

In the FT-IR spectrum of 2(4-methoxyphenyl)-4,5-diphenyl-1H-imidazole, the peak observed at 3464 cm⁻¹ is associated with the N-H stretching bond of the amine group. The C=N peak with average intensity appears in the region of 1503 cm⁻¹. The peaks observed at 1408 and 1608 cm⁻¹ are related to the C=C bond and the C–O bond

Table 3. The synthesis of trisubstituted imidazoles catalyzed by various catalysts.

Entry	Catalyst	Ref.	Time (min)	Yield (%)
1	L-Proline	9	87	25
2	InCl ₃ ·H ₂ O	8.2	76	28
3	Fe ₃ O ₄ @SiO ₂ /HM.SO ₃ H	0.5	85	35
4	DEP	7200	81–92	34
5	DABCO	720	92	58
6	[EMMOAc]	4	70	59
7	CAN	600	75	60
8	Silica gel/NaHSO ₄	150	80	61
9	High surface SiO ₂	150	69	62
10	NiCoFe ₂ O ₄ NPs, Solvent-free	5	95	This work

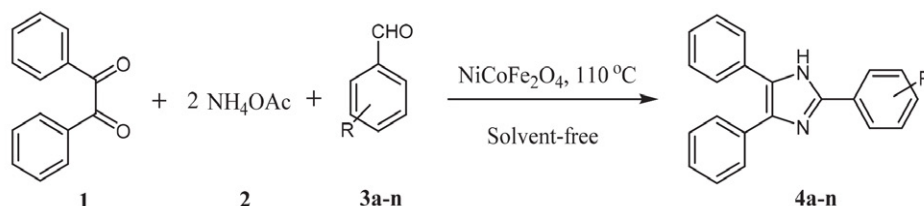
**Scheme 2.** Synthesis of triaryl imidazoles catalyzed by NiCoFe₂O₄ NPs.

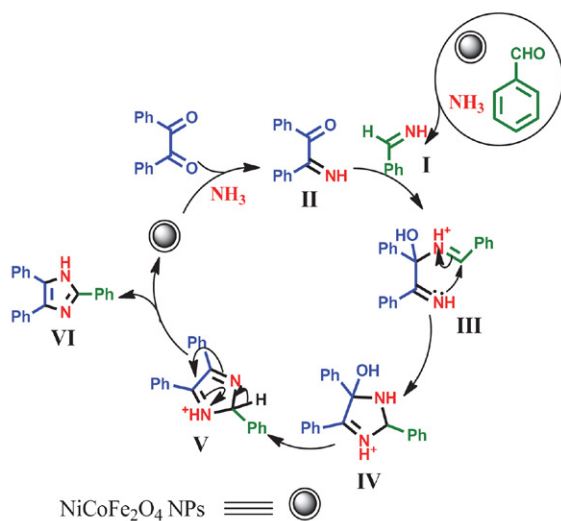
Table 4. Synthesis of various triaryl imidazoles using NiCoFe₂O₄ NPs as nanocatalysts.^a

Entry	R	Product	Time (min)	Yield (%) ^b	M.p. (°C) Found (Lit.) ^{Ref.}
1	H	4a	8	85	272–273 (275) ⁵⁰
2	3-OMe	4b	15	92	250–251 (253–256) ⁴⁰
3	4-OMe	4c	5	95	226–228 (230–232) ⁵¹
4	2,3-diOMe	4d	7	91	322–323 (325–326) ⁵²
5	4-Me	4e	6	93	230–231 (232–235) ⁵³
6	2-OH	4f	20	80	112–114 (117–119) ⁵³
7	4-OH	4g	14	90	231–232 (233) ⁵⁴
8	2,3-diCl	4h	19	83	192–193 (194–197) ⁴⁰
9	4-Cl	4i	10	90	257–258 (258–260) ⁵⁵
10	2,4-diCl	4j	17	85	170–172 (176–177) ⁵⁶
11	3-Cl	4k	13	85	283–284 (285–287) ⁵⁵
12	4-Br	4l	17	78	260–264 (262) ⁵⁵
13	4-F	4m	25	76	193–194 (190) ⁵⁶
14	4-NO ₂	4n	20	73	202–204 (199–201) ⁵⁷

^a General reaction conditions: Aromatic aldehyde (1 mmol), benzil (1 mmol), ammonium acetate (2 mmol) in the presence of 4 mg catalyst at 110 °C under solvent-free conditions ^b Isolated yield

stretching at 1073 cm⁻¹. The strong absorption band at 697 cm⁻¹ is related to the out-of-plane (=C–H) bending vibration. The relatively weak absorption at 769 cm⁻¹ indicates the =C–H bending vibration in para position of the aromatic ring. The aliphatic =C–H absorption peak appears at 240 cm⁻¹.

In the ¹H NMR spectrum, the N–H peak appears at δ 12.73 ppm. The peak associated with OCH₃ group is observed at δ 3.90 ppm. The aromatic hydrogens appear at δ 7.13 and 7.92 ppm. The hydrogen in *ortho*- position associated with methoxy group is observed at δ 8.07 and 8.09 ppm. In the ¹³C NMR spectrum, the peak in the range of δ 20–60 ppm relates to the saturated carbon atoms and the peak observed at δ 120–170 ppm relates to the aromatic carbon atoms.



Scheme 3. Proposed mechanism of the reaction.

3. 2. 2. Proposed Reaction Mechanism

In a proposed reaction mechanism for the formation of imidazoles, first aldehyde and benzil are activated by the nanocatalyst, and then intermediates **I** and **II** are formed by the reaction with ammonia. In the next step, imine from intermediate **I** attacks the carbonyl group of intermediate **II** and forms the intermediate **III**. Then an intramolecular nucleophilic attack occurs at **III**, followed by cyclization to form the intermediate **IV**. Finally, elimination of an H₂O molecule from **IV** occurs to form intermediate **V**, which tautomerizes to give the target product **VI** (Scheme 3).

3. 2. 3. Reusability of the Catalyst

To investigate the reusability of the catalyst, the NiCoFe₂O₄ catalyst was easily separated from the reaction medium by an external magnetic field after the model reaction was completed. The separated catalyst was washed several times with ethanol and acetone, dried at 50 °C for

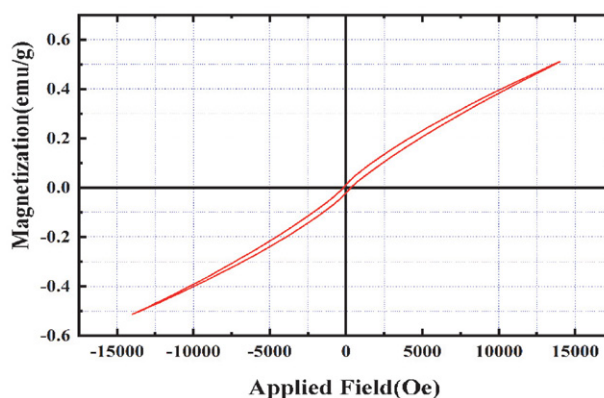


Figure 7. Reusability of the catalyst for the synthesis of triarylimidazoles.

8 hours, and reused for the next run. It was found that the catalyst could be reused at least six times without any noticeable decrease in its catalytic performance (Figure 7).

4. Conclusion

In the present work, NiCoFe₂O₄ nanoparticles were prepared, characterized by different techniques and used for the synthesis of imidazole derivatives. Pure products with high yields and short reaction times were obtained. The catalyst was easily separated from the reaction and recovered a few times without loss of its activity.

Acknowledgement

The authors gratefully acknowledge the support of this work by the University of Kashan under grant No. 159148/71.

Conflict of interest

The authors declare that they have no conflict of interest.

5. References

1. A. Teimouri, A. N. Chermahini, *J. Mol. Catal. A: Chem.* **2011**, 349, 39–45. DOI:10.1021/cs200495s
2. I. Satorno, *Chem. Abstr.* **1989**, 117, 8617. DOI:10.1039/ca92528fp003
3. T. L. Gilchrist, *J. Chem. Soc., Perkin Trans. 1*, **1999**, 2849–2866. DOI:10.1039/a808162j
4. J. W. Black, G. J. Durant, J. C. Emmet, C. R. Ganellin, *Nature*, **1974**, 248, 65–67. DOI:10.1038/248065a0
5. O. S. Adeyemi, A. O. Eseola, W. Plass, K. Kato, C. A. Otuechere, O. J. Awakan, O. Atolani, D. A. Othiniyi, T. C. Elebiyo, I. O. Evbuomwan, *Chem. Biol. Interact.* **2021**, 349, 109676–109678. DOI:10.1016/j.cbi.2021.109676
6. U. Ucucu, N. G. Karaburun, I. Isikdag, *Farmaco*, **2001**, 56, 285–290. DOI:10.1016/S0014-827X(01)01076-X
7. R. Schmierer, H. Mildenberg, H. Buerstell, *German Patent* 1987, 3614364.
8. J. C. Lee, J. T. Laydon, P. C. McDonnmar, T. F. Gallagher, S. Kumar, D. Green, D. McNulty, M. J. Blumenthal, J. R. Keys, S. W. Landvatter, *Nature*, **1994**, 368, 720–739. DOI:10.1186/1742-4682-3-17
9. D. W. Roberston, E. Beedle, J. H. Krushinski, G. D. Pollock, H. Wilson, V. L. Wyss, J. S. Hayes, *J. Med. Chem.* **1985**, 28, 717–727. DOI:10.1021/jm00383a006
10. P. W. Erhardt, A. A. Hagedorn, D. Davey, C. A. Pease, B. R. Venepalli, C. W. Griffin, R. P. Gomez, J. R. Wiggins, W. R. Ingebresten, *J. Med. Chem.*, **1989**, 32, 1173–1176. DOI:10.1021/jm00126a005
11. H. M. Refaat, *Eur. J. Med. Chem.*, **2010**, 45, 2949–2956. DOI:10.1016/j.ejmech.2010.03.022
12. Y. Ozkay, L. Istikdag, Z. Incesu, G. Akalin, *Eur. J. Med. Chem.*, **2010**, 45, 3320–3328. DOI:10.1016/j.ejmech.2009.10.044
13. M. D. Brewer, R. J. Dorgan, B. R. Maneger, P. Mamalis, R. A. Webster, *J. Med. Chem.*, **1987**, 1848–1853. DOI:10.1021/jm970467t
14. M. Shaker, A. Davoodnia, H. Vahedi, *J. Heterocycl. Chem.*, **2017**, 54, 313–317. DOI:10.1021/jm970467t
15. J. A. Nathanson, *Proc. Nat. Acad. Sci. USA*, **1985**, 82, 599–603. DOI:10.1073/pnas.82.2.599
16. L. I. Kruse, C. Kaiser, W. E. DeWolf, J. S. Frazee, E. Garvey, E. L. Hilbert, W. A. Faulkner, K. E. Flaim, J. L. Sawyer, B. A. Berkowitz, *J. Med. Chem.*, **1968**, 29, 2272–2465. DOI:10.1021/jm00307a028
17. K. H. Liyk, H. S. Hsu, M. Segawa, *J. Biochem.* **1998**, 23, 416–422. DOI:10.1097/00004669-199811000-00010
18. H. Debus, *Liebigs Ann. Chem.*, **1858**, 107, 199–208. DOI:10.1039/D0RA01408G
19. F. Mostaghni, H. Shafiekhani, N. M. Mahani, *Acta Chim. Slov.* **2022**, 69, 91–97. DOI: 10.17344/acsi.2021.7021
20. F. Mostaghni, *Acta Chim. Slov.* **2021**, 68, 170–177. DOI:10.17344/acsi.2020.6299
21. A. Shabani, A. Ramati, *J. Mol. Catal. A: Chem.* **2006**, 249, 246–248. DOI: 10.1016/j.molcata.2006.01.006
22. S. D. Sharma, P. Hazarika, D. Kondwar, *Tetrahedron Lett.* **2008**, 49, 2216–2220. DOI:10.4236/mrc.2014.32008
23. C. R. Elderfield, *Heterocycl. Compound*, **1957**, 5. DOI:10.1021/ed034p418.3
24. L. A. Paquette, In *Principles of Modern Heterocyclic Chemistry*, New York, Benjamin, 1968, pp 173–183.
25. M. Heravi, K. Bakhtiari, H. A. Oskooie, S. Taheri, *J. Mol. Catal. A: Chem.*, **2007**, 263, 279–281. DOI:10.1016/j.molcata.2006.08.070
26. S. Balalaei, A. Arabanian, *Green Chem.*, **2000**, 2, 274–276. DOI:10.1039/b006201o
27. B. Sadeghi, B. F. Mirjalili, M. M. Hashemi, *Tetrahedron Lett.*, **2008**, 49, 2575–2577. DOI:10.1016/j.tetlet.2008.02.100
28. S. Samai, G. C. Nandi, P. Singh, M. S. Singh, *Tetrahedron*, **2009**, 65, 49, 10155–10161. DOI:10.1016/j.tet.2009.10.019
29. S. Yugandar, S. Konda, G. Parameshwarappa, H. Ha, *J. Org. Chem.* **2016**, 81, 5606–5622. DOI:10.1021/acs.chemrev.5b00360
30. K. F. Shelke, S. Sapkal, M. S. Shingare, *Chin. Chem. Lett.*, **2009**, 20, 283–287. DOI:10.1016/j.cclet.2008.11.033
31. Y. N. Yana, D. Y. Lina, W. L. Panb, X. L. Li, Y. Q. Wana, Y. L. Mai, H. C. Songa, *Spectrochim. Acta, Part A*, **2009**, 74, 233–242. DOI:10.1016/j.saa.2009.06.020
32. Y. N. Yan, W. L. Pan, H. C. Song, *Dyes. Pig.* **2010**, 86, 249–258. DOI:10.1038/s41598-020-62029-4
33. F. K. Fezabad, K. Khandan-Barani, A. Hassanabadi, *J. Chem. Res.*, **2017**, 41, 673–675. DOI:10.3184/174751917X15105690662854
34. G. V. M. Sharma, Y. Jyuthi, P. S. Lankshmi, *Synth. Commun.*, **2006**, 36, 2991–3000. DOI:10.1080/00397910600773825
35. H. Naeimi, D. Aghaseydkarimi, *New J. Chem.* **2015**, 39, 9415–9421. DOI:10.1039/C5NJ01273B

36. L. Nagarapu, S. Apuri, S. Kantevari, *J. Mol. Catal. A: Chem.* **2007**, 266, 104–108. DOI:10.1016/j.jscs.2013.01.005
37. M. V. Chary, N. C. Keerthysri, S. V. N. Vupallapati, N. Lingai-ah, S. Kantevari, *Catal. Commun.* **2008**, 9, 2013–2017. DOI:10.1016/j.catcom.2008.03.037
38. B. Sadeghi, B. B. F. Mirjalili, M. M. Hashemi, *Tetrahedron Lett.* **2008**, 49, 2575–2577. DOI:10.1016/j.tetlet.2008.02.100
39. S. Balalaei, A. Arbanian, *Green Chem.* **2000**, 2, 274–276. DOI:10.1024//1016-264X.11.4.274b
40. A. R. Khosropour, *Ultrason. Sonochem.* **2008**, 15, 659–664. DOI:10.1016/j.ultsonch.2007.12.005
41. C. Liu, *Acta Chim. Slov.* **2021**, 68, 983–989. DOI:10.17344/acsi.2021.6979
42. F. Belferdi, F. Bouremmad, S. Shawuti, M. A. Gulgun, *Acta Chim. Slov.* **2021**, 68, 355–362. DOI:10.17344/acsi.2020.6300
43. A. Pourkazemi, N. Asaadi, M. Farahi, A. Zarnegaryan, B. Kar-ami, *Acta Chim. Slov.* **2022**, 69, 30–38. DOI: 10.17344/acsi.2021.6819
44. R. Mahadevaiah, L. S. Haralur, L. H. K. Eshwaraiah, *Acta Chim. Slov.* **2022**, 69, 116–124. DOI: 10.17344/acsi.2021.7055
45. M. Moradian, M. Nazarabi, *Acta Chim. Slov.* **2021**, 68, 594–604. DOI:10.17344/acsi.2020.6412
46. H. Naeimi, S. Rahmatinejad, *Polycyclic Aromatic Compounds*, **2016**, 36, 773–788. DOI:10.1080/10406638.2015.1053503
47. H. Naeimi, M. F. Zarabi, *RSC Adv.*, **2019**, 9, 7400–7410. DOI:10.1039/C8RA10180A
48. J. M. Racicot, T. L. Mako, A. Healey, B. Hos, M. Levine, *ChemPlusChem*, **2020**, 85, 1730–1736. DOI:10.1002/cplu.202000410
49. S. Moradi, M. Moradian, H. Naeimi, *Acta Chim. Slov.* **2022**, 69, 2, 349–358. DOI:10.17344/acsi.2021.7238
50. S. A. Siddiqui, U. C. Narkhede, S. S. Palimkar, T. Daniel, R. J. Lahoti, K. V. Sinivasan, *Tetrahedron*, **2005**, 61, 3539–3546. DOI:10.1016/j.tet.2005.01.116
51. D. M. White, J. Sonnenberg, *J. Org. Chem.* **1964**, 29, 1673–1676. DOI:10.1021/jo01030a700
52. T. Heinze, T. Liebert, *Progress in Polymer Sci.* **2001**, 26, 1689–1762. DOI:10.1016/S0079-6700(01)00022-3
53. B. P. Bandgar, B. S. Hote, B. L. Kobad, S. A. Patil, *J. Chem.*, **2011**, 8, 1339–1345. DOI:10.1155/2011/759706
54. M. Kidwai, P. Mothsra, V. Bansal, R. K. Somvanshi, *J. Mol. Catal. A: Chem.*, **2007**, 265, 177–182. DOI:10.1016/j.molcata.2006.10.009
55. J. G. Lombardino, “Anti-flamatory imidazole” U.S. Patent, **1973**, 377244
56. J. A. Marshal, W. I. Fenta, *J. Org. Chem.* **1964**, 29, 2501–2505. DOI:10.1021/jo01032a004
57. K. R. Babu, S. Maripi, S. Madasu, N. R. Appna, *Chem. Sci. Trans.*, **2017**, 6, 3, 428–436. DOI:10.7598/cst2017.1382
58. S. N. Mourthy, B. Madhav, Y. V. D. Nageswar, *Tetrahedron Lett.* **2010**, 51, 5252–5257. DOI:10.1016/j.tetlet.2010.07.128
59. H. Zang, Q. Su, Y. Mo, B. V. Cheng, S. Jan, *Ultrason. Sonochem.* **2010**, 17, 749–751. DOI:10.1016/j.ultsonch.2010.01.015
60. F. Nemati, M. M. Hosseini, H. Kiani, *J. Saudi. Chem. Soc.*, **2016**, 20, 503–508. DOI: 10.1016/j.jscs.2013.02.004
61. A. R. Karimi, Z. Alimohammadi, J. Azizian, A. A. Moham-madi, P. R. Mohammadzadeh, *Catal. Commun.*, **2006**, 7, 728–732. DOI:10.1016/j.catcom.2006.04.004
62. R. A. Mekheirmer, A. M. Abdel Hammeed, S. A. A. Mansour, K. U. Sadek, *Chin. Chem. Lett.*, **2009**, 20, 812–814. DOI:10.1016/j.cclet.2009.02.017

Povzetek

V tej študiji so NiCoFe₂O₄ nanodelce pripravili in uporabili kot reaktivni katalizator za sintezo trisubstituiranih imidazolov. Večkomponentne reakcije aromatskih aldehydov, benzila in amonijevega acetata so bile izvedene v pogojih brez topil in pri običajnih pogojih segrevanja. V reakciji so bili pripravljene derivati imidazola z visoko čistostjo, kratkimi reakcijskimi časi in visokimi izkoristki. Pripravljen nanokatalizator je bil karakteriziran s FT-IR, XRD, EDX, VSM in SEM tehnikami. Poleg tega so bili produkti reakcij identificirani in okarakterizirani z določitvijo temperature tališča, ter FT-IR in ¹H NMR spektroskopijo.



Except when otherwise noted, articles in this journal are published under the terms and conditions of the Creative Commons Attribution 4.0 International License

Cost-Effective Control of Molecular Weight in Ultrasound-Assisted Emulsion Polymerization of Styrene

Ibrahim Korkut,¹ Fuat Erden² and Salih Ozbay^{1,*}

¹ Department of Chemical Engineering, Sivas University of Science and Technology, 58000, Sivas, Turkey

² Department of Aeronautical Engineering, Sivas University of Science and Technology, 58000, Sivas, Turkey

* Corresponding author: E-mail: salihozbay86@gmail.com, salihozbay@sivas.edu.tr

Phone: +90 (346) 219 1398

Received: 07-04-2022

Abstract

This paper focuses on the determination of economically most feasible conditions to obtain polystyrene with various target molecular weights through ultrasound-assisted emulsion polymerization. Briefly, batch polymerizations of styrene have been performed by ultrasound-assisted emulsion polymerization process using different reaction feed compositions. Polymerization rates were calculated using the monomer conversions at various reaction times. Also, molecular weights of the synthesized polymers, as well as the Mark-Houwink constants, were determined by intrinsic viscosity and gel permeation chromatography measurements. It was found that the polydispersity index of the polymers is ranging from 1.2 to 1.5, and the viscosity average molecular weights are in between 100000–1500000 g/mol depending on the reaction conditions. Finally, model equations were also developed for response variables, and the most economical ways of reaching various target molecular weights were interpreted by response surface methodology based multi objective optimization.

Keywords: Ultrasound, polystyrene, emulsion polymerization, molecular weight, cost performance

1. Introduction

Emulsion polymerization process is widely used in industry to polymerize various monomers in a continuous heterogeneous phase due to its economic advantages. Besides, water is used as a solvent in emulsion polymerization, making it environmentally friendly.^{1,2} Upon introducing appropriate amounts of monomer, water, emulsifier, and initiator to a suitable reactor, a milky fluid called latex is obtained at the end of the reaction.^{2,3} Among unsaturated organic compounds, the research activities related to styrene are increasing drastically since polystyrene (PS) has widespread applications in various fields such as automotive, electronics, food packaging, construction, and medical industries.⁴ In fact, conventional emulsion polymerization of styrene has been systematically handled in many research articles with a particular focus on kinetic examinations.^{3,5–16} For example, Smith-Ewart kinetic theory was developed for the polymerization of styrene and is still widely used in the field.^{2,3,5,6} Likewise, rate of emulsion polymerization of styrene was investigated in numerous previous studies.^{7–18} According to the examinations in

means of mechanism and kinetics, emulsion polymerization follows the free radical addition polymerization by the reaction of free radicals with relatively hydrophobic monomers within submicron polymer particles.^{2,18} Yet, it is important to note that polymerization mechanism is slightly different in US-assisted polymerization. Thanks to US-assistance, it is possible to conduct polymerization or achieve high polymerization yields at a lower surfactant amount than critical micelle concentration (CMC).

Apart from rate of polymerization, the molecular weight distribution of a polymer synthesized in an emulsion polymerization has also a significant influence on the processability, as well as the mechanical, and application properties of the final product.^{18,19} For instance, various applications of emulsion polymerization products such as adhesives, paper coatings, paints, varnishes, carpet backings require the formation of a continuous film with high mechanical strength that directly depends on the molecular weight of the polymer.²⁰ Thus, controlling of the molecular weight in polymers synthesized by emulsion polymerization is critical to obtain a desired product. Intensive efforts have been made to control molecular weight of pol-

ystyrene thoroughly by emulsion polymerization method in the literature.^{19,21–29} For example, Salazar et al. investigated the effect of commercial mercaptans on the molecular weight distribution of PS in a starved emulsion polymerization by developing a mathematical model.¹⁹ Vicente et al. developed a calorimetric method for the on-line control of the molecular weight distribution for linear emulsion polymers by synthesizing polystyrene latexes.²⁴ Herrera-Ordóñez et al. investigated the effect of initial monomer concentration on the molecular weight of polystyrene obtained by emulsion polymerization process above the critical micelle concentration.²⁵ A recent study conducted by Patrocínio et al. shows that high molecular weight polystyrene (above 1000 kDa) can be obtained at ~70% conversion and reaction times of longer than 12 hours by cationic emulsion polymerization catalyzed with imidazolium based ionic liquid.²⁸ All of these studies indicate that controlling of the molecular weight for linear emulsion polymers is a challenging topic and an effective control is a very important issue even in a highly studied monomer type such as styrene.

Although conventional emulsion polymerization is a useful method to polymerize many industrial monomers, ultrasound-assisted emulsion polymerization has some advantages over the conventional one, due to the improved reaction rate, suitability for obtaining polymers with a narrow molecular weight distribution, even in relatively mild reaction conditions.^{29–31} In fact, ultrasonic waves could be applied to various chemical reactions, improving reaction rates. This is because, extreme temperatures and pressures could be reached through acoustic cavitation, and hence, the mass transport could be enhanced.^{32,33} Besides, ultrasonication could also boost formation of various radicals depending on the liquid medium through transient implosive collapse of ultrasound associated bubbles.³⁴ During the conventional emulsion polymerization, monomer droplets coalesce due to the insufficient monomer dispersion, causing phase separation, and thus deceleration of the reaction rate.³⁵ Whereas, stable and uniform droplets can be obtained in ultrasound-assisted emulsion polymerization thanks to the acoustic cavitation activity at the interface of immiscible organic liquid phase.^{29–37} For mentioned reasons, ultrasound-assisted polymerization of styrene has been investigated many times.^{35,38–43} For example, Cheung and Gaddam carried out ultrasound-assisted emulsion polymerization of styrene and methyl methacrylate using AIBN, KPS and ferrous sulphate initiators.³⁸ Ooi and Biggs reported that the ultrasound-assisted emulsion polymerization of styrene could be performed with ~90% monomer conversion in the absence of initiator after 3 hours of irradiation time.³⁹ Zhang et al. performed the ultrasonically irradiated emulsion polymerization of styrene in the presence of carboxymethyl cellulose and alkyl poly(ethoxy) acrylate based polymeric surfactants.⁴¹ Qiu et al. used Fe^{2+} in ultrasound-assisted emulsion polymerization of styrene to increase the reac-

tion rate by increasing the sonochemical efficiency.⁴³ On the other hand, although there are many emulsion polymerization studies stating the positive effects of ultrasound, there are also some drawbacks such as energy consumption, contamination, probe erosion, and possibility of side reactions, particularly when ultrasound is irradiated for prolonged times.⁴⁴ Thus, accomplishing an emulsion polymerization where the desired products can be obtained with the use of short-term ultrasound is critical. In this context, Nagatomo et al. investigated the effect of ultrasonic pre-treatment on the emulsion polymerization of styrene to reach higher monomer conversions.³⁵ To sum up, many studies have been conducted to advance the ultrasound-assisted emulsion polymerization process. However, additional studies are still necessary, particularly on the molecular weight control at high monomer conversions to make this process more feasible.

In addition to this, such molecular weight control should be evaluated in accordance with economic considerations, because PS is widely used in industrial applications. However, to the best of our knowledge, there are no previous reports on the cost-molecular weight performance relationship of the emulsion polymerization of styrene. Accordingly, the main aim of this work is to determine the economically most feasible conditions to obtain PS with various target molecular weights through ultrasound-assisted emulsion polymerization. For this purpose, we performed ultrasound assisted emulsion polymerizations of styrene using different reaction feed compositions and correlate conversion efficiency, molecular weight and cost through a statistical approach.

2. Experimental Section

2.1. Materials

Styrene (Reagent Plus ≥99%) was purchased from Sigma Aldrich and pre-distilled in a rotary evaporator to remove the inhibitor (hydroquinone). Sodium dodecyl sulfate (SDS), ammonium persulfate (APS), sodium bisulfite (SBS), toluene and methanol were also purchased from Sigma Aldrich at ACS reagent grade and used as-received. Double distilled water was used throughout the experiments to prepare necessary solutions, and all glassware's were cleaned with copious amounts of double distilled water after the reactions.

2.2. Experimental Set-up

Bandelin® HD 2070 (frequency: 20 kHz, maximum power output: 70 W) ultrasonic homogenizer, equipped with a horn type probe (probe diameter: 13 mm) was used to deliver pulsed ultrasound. The pulse ratio was adjusted as 7 s on and 3 s off. The ultrasound power delivered to the reactor was calculated by calorimetric method. The details of calorimetric method and calorimetric results were given

in the supporting information section. Polymerization experiments were carried out at 11.1, 14.6, 18.2 and 22.1 W calorimetric powers. Three necked round bottom glass reactor which equipped with a reflux condenser was put on a hot plate to ensure constant temperature within ± 1 °C. In a typical synthesis, a mixture of styrene, APS, SBS, SDS, and double distilled water were added to the reactor, and degassed by bubbling nitrogen gas at 25 °C. The reactor temperature was set to 60 °C and the experiments were conducted for a total of 3 hours. Ultrasound was applied at various ultrasonic calorimetric powers only for 1 hour in all experiments. After 1 hour of ultrasound exposure, experiments were continued for 2 hours in the absence of ultrasound. The experiment temperature was chosen as 60 °C since the decomposition of APS is faster at higher temperatures.^{45,46} To calculate the monomer conversions, 1 ml of samples were taken from the reactor at 30 min time intervals throughout the experiments. The samples, were then dried in a vacuum oven at 80 °C until constant weight was attained, and the monomer conversions were determined gravimetrically.

2. 3. Polymerization Experiments and Characterizations

All of the polymerizations were conducted using the same reaction volume (200 ml) to ensure replicable acoustic power density dissipation. We first studied the effect of the APS/SBS molar ratio on the monomer conversion. The best APS/SBS molar ratio was determined as 1:1.2 in terms of obtaining higher monomer conversions. Therefore, the rest of the experiments were conducted by keeping APS/SBS ratio constant at 1:1.2 by mole and the effect of various initial monomer concentrations, initiator concentrations, emulsifier concentrations and ultrasound powers were studied accordingly. After 3 hours of polymerization reactions, the latex mixtures were dried at room temperature. Following this, the reaction products were washed with methanol for further purification. Finally, the polymers were vacuum filtered and dried at room temperature. Table 1 shows the polymerization conditions and the monomer conversions after 3 hours. It is important to note that CMC of SDS is 9.2 mM at 60 °C.⁴⁷ This means that in a total reaction volume of 200 ml, 0.531 g of SDS is required to achieve the CMC, and thus, the present work focuses US-assisted polymerization of styrene below CMC.

Intrinsic viscosities of the synthesized polymers were determined in toluene by an Ubbelohde-type viscometer at 25 °C using Huggins' viscosity equation given below⁴⁸:

$$\frac{\eta_{sp}}{c} = [\eta] + k_H[\eta]^2 c \quad (1)$$

In a typical measurement, the efflux time of toluene was recorded as a reference. Then, a certain amount of PS was dissolved in 20 mL of toluene, and the efflux time was recorded again. Following this, the PS solution was diluted

multiple times, and efflux times were recorded for various concentrations. Overall, specific viscosity (η_{sp}) and reduced viscosity (η_{sp}/c) values were calculated, which is followed by the determination of intrinsic viscosities by extrapolation of the reduced viscosity values to zero concentration procedure.

The weight average (M_w) and number average (M_n) molecular weight of the polymers were determined in ultra-pure THF using gel permeation chromatography (GPC) where the calibration was done using polystyrene standards, and the passage time of solvent was 1.0 ml/min. The glass transition temperature (T_g) values of the polymers were obtained by using DSC where the heating rate was 10 °C/min between 0 and 150 °C. Before the measurements, samples were preheated to 150 °C in order to eliminate thermal affects and then the measurements were started after they were cooled to 0 °C.

Table 1. Polymerization conditions and the final monomer conversions.

Poly- mer	Ultrasound calorimetric power (W)	[M] ₀ (mol/L) ^a	APS (wt. %) ^b	SDS (wt. %) ^c	Conver- sion (%)
	(A)	(B)	(C)	(D)	
PS-1	14.6	0.50	0.50	0.5	85.7
PS-2	14.6	0.50	1.00	0.5	88.3
PS-3	14.6	0.50	1.25	0.5	89.4
PS-4	14.6	0.50	1.50	0.5	90.7
PS-5	14.6	0.50	2.00	0.5	93.9
PS-6	0	0.50	2.00	0.5	40.7
PS-7	11.1	0.50	2.00	0.5	94.1
PS-8	18.2	0.50	2.00	0.5	93.1
PS-9	22.1	0.50	2.00	0.5	91.7
PS-10	11.1	0.50	2.00	0.0	85.8
PS-11	11.1	0.50	2.00	1.0	93.6
PS-12	11.1	0.60	2.00	0.5	95.3
PS-13	11.1	0.75	2.00	0.5	97.8
PS-14	11.1	1.00	2.00	0.5	99.2

^a Initial monomer concentration. Typically, (mole amount of styrene in the feed)/(total volume of the reaction solution) is 0.5 mol/L for PS-1.

^b Based on the weight amount of monomer in the feed. Typically, (APS/Styrene)×100 is 0.5 for PS-1.

^c Based on the weight amount of monomer in the feed. Typically, (SDS/Styrene)×100 is 0.5 for PS-1.

3. Results and Discussion

3. 1. Effect of Process Parameters on Monomer Conversion and Rate of Polymerization

PS has very broad application areas as explained previously, and thus it can be regarded as one of the in-

dustrialized polymers. Most manufacturers synthesize PS by emulsion polymerization since it allows high polymer yields at affordable prices. In this regard, monomer conversion could possibly be considered as the most significant parameter by the manufacturers as it dictates economic feasibility. In the present work, we prepared PS by ultrasound-assisted emulsion polymerization, which will decrease reaction time to reach high monomer conversions, and thus will directly reduce the cost. However, the power necessity of the ultrasound assistance will inevitably raise the costs in this case, and there should be a trade-off between ultrasound power and reduction in reaction time. In anyway, one should control monomer conversion to comment more on the effectiveness of ultrasound-assisted emulsion polymerization in terms of economic feasibility. In other words, the costs associated with the power necessity to reach high reaction yields in ultrasound-assisted polymerization should be compared with the costs associated with the extra reaction time to reach the same level of monomer conversion in the absence of ultrasound. This is why we first focused on to maximize monomer conversion in the present work.

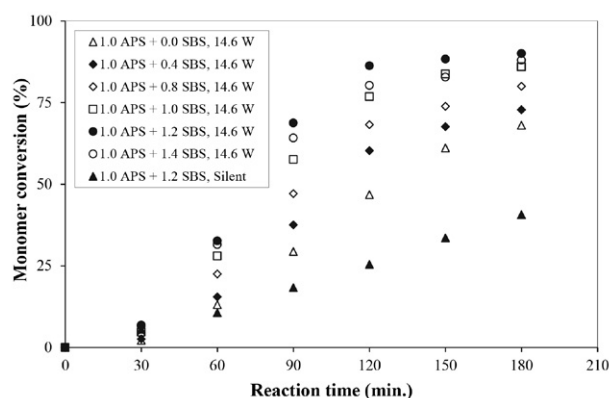


Fig. 1. The effect of molar APS/SBS ratios on the monomer conversion.

In preliminary experiments, we studied the effect of APS/SBS ratio on the outcome of emulsion polymerization. In fact, APS and SBS are expected to enter the polymerization reaction with a molar ratio of 1:1 in a typical synthesis. However, there might be some deviations in practice due to the hygroscopic nature of both APS and SBS. Accordingly, we first focused on to optimize the APS/SBS ratio, and Fig. 1 shows the effect of APS/SBS on the monomer conversion at various reaction times. The results show that the monomer conversion is higher when SBS is introduced together with APS, since persulfate ions are now expected to react with bisulfite ions to produce radicals for redox initiation, and thus, decreasing activation energy of bond scission.² In line with this, increasing the SBS concentration resulted in higher monomer conversions until reaching a molar APS/SBS ratio of 1:1.2. When

APS/SBS ratio is increased to 1:1.4, monomer conversion decreased due to possible unexpected side reactions of excess radicals.

Accordingly, the optimum APS/SBS ratio in terms of best monomer conversion was found to be 1:1.2, and the rest of the tests were conducted at this concentration. However, it is important to note that the redox systems are known to be effective only at sub-ambient temperatures in general.² Interestingly, our results suggest that such temperature requirement might not be necessary in ultrasound-assisted emulsion polymerization. This was ascribed to the generation of acoustic waves, which might provide more activation energy through acoustic cavitation and allowing use of redox systems at relatively higher temperatures. To check this idea, another set of experiments were conducted at optimum APS/SBS ratio (1:1.2) in the absence of ultrasound (Fig. 1). In this case, a monomer conversion of only ~41% was achieved after 3h, adding credibility to the afore-mentioned claim. The difference between both processes, lies in the polymer particle nucleation mechanism. Based on Smith-Ewart kinetic theory, nucleation occurs in micelles, and surfactant concentration should be above the CMC of the surfactant in conventional emulsion polymerization. The monomer droplets act as reservoir and monomer is transported to the growing polymer particles. In miniemulsion polymerization, the reaction starts with substantially smaller droplets (in the range 50–500 nm) that are stabilized with the surfactant available and hence monomer swollen micelles are not present. Therefore, nucleation occurs in monomer droplets.^{49,50} In the experiments reported in this work, the concentration of SDS is below the CMC (9.2 mM for SDS at 60°C)⁴⁷ in all the cases, which means that no micelles are present. Thus, in the polymerizations carried out without ultrasound, polymer particles can only be formed by the so-called homogeneous nucleation and in this case, the number of particles should be small and the size relatively large (couple of hundreds of nanometers). As a result, polymerization rate is slow in our conditions. When ultrasound is applied the polymerization system, size of the droplets changes to the nanometer scale, and therefore polymerization rate increases.

Fig. 2 shows the effects of initiator concentration, ultrasound calorimetric power, SDS amount and initial monomer concentration on the monomer conversion. As seen in Fig. 2a, monomer conversion increased with the increase of APS concentration for the ultrasound-assisted polymerization having ultrasound calorimetric power of 14.6 W. As the amount of initiator increases, there will be more radicals per monomer in the system, and thus time-dependent polymerization rates increase.² At the end of the reaction, over 85% monomer conversions were obtained at all initiator concentrations studied in this work when the ultrasonic calorimetric power was 14.6 W. On the other hand, the effect of ultrasound power on the monomer conversion was shown in Fig. 2b. As expected,

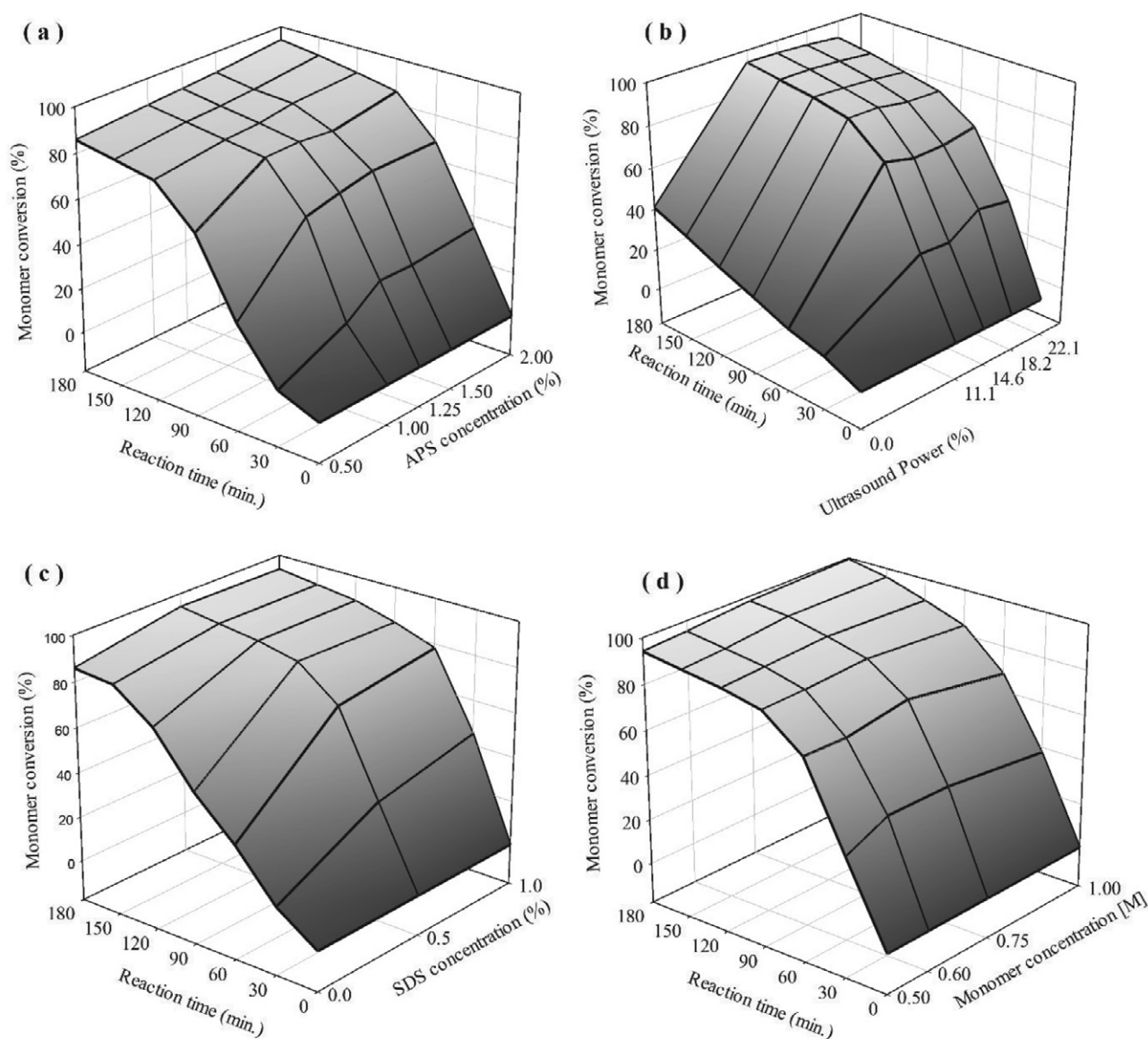


Fig. 2. (a) Effects of initiator concentration, (b) ultrasound calorimetric power, (c) SDS amount and (d) initial monomer concentration on the monomer conversion.

presence of ultrasound in the reaction medium increases the monomer conversion, accordingly. Acoustic cavitation associated with the ultrasound contributes to the dispersion of monomer droplets. Besides, with the application of ultrasound to the polymerization reaction, the initiator produces more radicals due to its further degradation.⁴⁵ The primary radicals that originated by the decomposition of the initiator, might directly enter a monomer droplet through acoustic cavitation, and generate monomeric radicals at the bubble/solution interface, and hence contribute to the polymerization.³¹ The results show that while we reached a monomer conversion of higher than 80% after 90 mins for the ultrasound-assisted polymerization even at 11.1 W ultrasonic calorimetric power, the monomer conversion was only ~41% in the absence of ultrasound even

after 3 hours. In fact, sonication should be conducted with a power above the acoustic threshold to create cavitation bubbles.³⁶ Yet, we found that the effect of ultrasound power on the monomer conversion is negligible between ultrasonic calorimetric powers of 11.1 W and 22.1 W. This means that 11.1 W ultrasonic calorimetric power is sufficient to improve reaction rate considerably, and it seems that it won't be feasible to further increase ultrasound power beyond this point. This might be due to the choice of the appropriate reaction volume and geometry that fits with the appropriate probe diameter in our system, which might provide better dispersion even at low ultrasound powers.³⁶

In order to make clarify the effect of ultrasound, rate of polymerization (R_p) for our system was also studied. As

known, suitable numerical differentiation formulas can be used to evaluate the rate of a reaction in a batch reactor when the data points in the independent variable are equally spaced.⁵¹ Thus, the rate of polymerization as a function of reaction time was calculated from conversion values using below equations (Equation 2 is given for intermediate data points and Equation 3 is given for last data points)^{51,52}:

$$-\left(\frac{dC_A}{dt}\right)_{t_i} = \frac{1}{2\Delta t}(C_{A(i+1)} - C_{A(i-1)}) \quad (2)$$

$$-\left(\frac{dC_A}{dt}\right)_{t_i} = \frac{C_{A(i-2)} - 4C_{A(i-1)} + 3C_{A(i)}}{2\Delta t} \quad (3)$$

where C_A is the monomer concentration in mol/L, i is equally spaced intermediate data points (from $i = 1$ to $i = 6$, i.e., C_{A0} means the data at 0 min, C_{A1} means data at 30 min, etc.), and Δt ($t_1 - t_0 = t_2 - t_1 = 30$ min) is time interval, respectively.

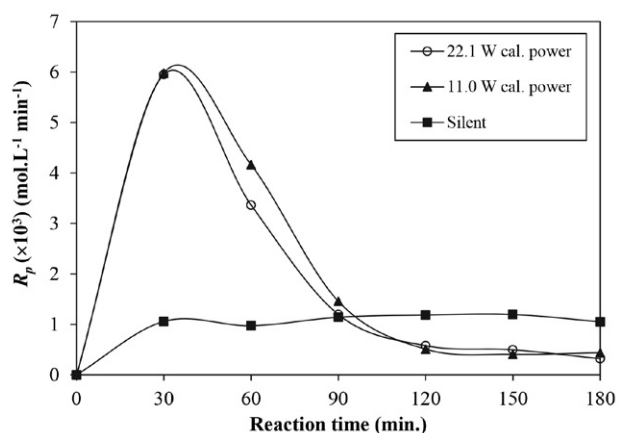


Fig. 3. Rate of polymerization versus reaction time at different ultrasound calorimetric powers (APS: wt. % 2, SDS: wt. % 0.5).

Fig. 3 shows the R_p (mol L⁻¹ min⁻¹) as a function of reaction time at different ultrasonic power conditions. As can be seen in this figure, R_p attains maximum level in the first 30 minutes of the reaction and then reduces with reaction time, indicating that ultrasound assisted mini-emulsion polymerization proceeds in two intervals,^{23,30,49,50} whereas conventional emulsion polymerization proceeds in three intervals.^{2,14,18,49} Observation of faster reaction rate in the early stage of ultrasound-assisted mini-emulsion polymerization can be attributed to the fact that the cavitation jets facilitate transporting of free radicals to monomer droplets in this process.²⁹ Briefly, the presence of ultrasonic cavitation in reaction medium improves the polymerization rate considerably.

The effect of surfactant concentration on the monomer conversion was also investigated between 0% and 1%, while keeping other parameters constant (APS concentration: 2 wt. % of styrene feed, ultrasound calorimetric power: 11.1 W, and initial monomer concentration: 0.5 M). Fig. 2c shows that monomer conversions were increased

with the increase of the SDS concentration. With the aid of ultrasound, it can easily perform mini-emulsion polymerizations without the use of surfactant or below the critical micellar concentration. Also, ultrasound prevents agglomerations that may occur during the polymerization reaction. In conventional emulsion polymerization, particles tend to collide and agglomerate due to Brownian and bulk fluid motion.¹⁵ Considering that SDS is an ionic surfactant, it could stabilize particles and solve the agglomeration problem through electrostatic repulsion that could counteract van der Waals interactions.^{53,54} Therefore, there might be a certain amount of SDS to effectively counteract the van der Waals interactions, and above this point the importance of SDS might tend to vanish in terms of monomer conversion as there is already enough SDS to overcome agglomeration.

The effect of initial monomer concentration on the monomer conversion is also studied between 0.5 M and 1.0 M, while keeping other parameters constant (Ultrasound calorimetric power: 11.1 W, APS concentration: 2 wt. % of styrene feed, and SDS concentration: 0.5 wt. %). It can be seen from Fig. 2d and Fig. 4 that the increase in the initial monomer concentration also increases the monomer conversion and reaction rate to some extent. In fact, the effect of monomer/water ratio on the rate of polymerization should have no influence according to the Smith-Ewart kinetic model for conventional emulsion polymerization.^{2,3,49} However, in practice, rate of polymerization is affected from the solubility of the monomer in water and polymer phases.² Thus, the increase in the reaction rate with the increase of monomer concentration can be explained by the enhancement of solubility of the monomer in the water phase and reduction in the size of monomer droplets under the influence of ultrasonic cavitation.

In the present study, we focused on a narrow monomer concentration region and didn't increase the initial monomer concentration above 1.0 M to further increase

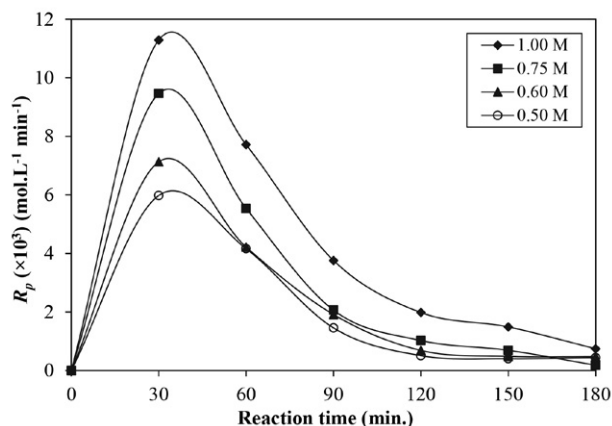


Fig. 4. Rate of polymerization versus reaction time at different initial monomer concentrations (Ultrasound calorimetric power: 11.1 W, APS: wt. % 2, SDS: wt. % 0.5).

the monomer conversion. Because, when we tried to increase the initial monomer concentration, monomer particles tended to adhere on the ultrasound probe, eventually halting the process. Thus, 1 M initial monomer concentration seems to be the highest allowable concentration at this SDS amount to apply ultrasound in our system effectively.

3. 2. Evaluation of Molecular Weight, Intrinsic Viscosity, and Cost of Synthesized Polymers

Regarding molecular weight, we first focused on intrinsic viscosity $[\eta]$ values of the synthesized polymers. In general, intrinsic viscosity value of a polymer is a measure of the capacity of a polymer molecule to improve the viscosity of a polymer solution, and it reflects the chain length of a polymer in a specific solvent.^{48,55–57} Thus, it can be said that intrinsic viscosity of polymers is highly correlated with their molecular weight. On the other hand, it is already known that molecular weight of a polymer can be calculated from intrinsic viscosity values by Mark-Houwink equation, as given below:

$$[\eta] = KM_v^\alpha \quad (4)$$

where $[\eta]$ is intrinsic viscosity values of polymer, M_v is viscosity average molecular weight, and K and α are Mark-Houwink constants for polymer-solvent combinations. However, this necessitates knowledge of the Mark-Houwink parameters. Although these constants are available in the literature, most of the previously reported values are only valid in definite molecular weight regions.⁵⁷ In order to find more suitable Mark-Houwink constants for our system, we determined the M_w of some representative samples through GPC (Table 2). Then, the K and α values that could be used for our polymers were calculated as 0.0116 ml/g and 0.687, respectively, by using a logarithmic plot of $[\eta]$ versus M_w as given in Fig. 5. Finally, the viscosity average molecular weight (M_v) values were calculated using the determined Mark-Houwink constants. Glass transition temperature (T_g) of synthesized polymers are also given in Table 2. The T_g of polystyrene increases with molecular weight until it reaches about 107 °C at molecular weight values of above 100000, which results are in good accordance with previous reports.^{58–60} Also, particle size analysis was conducted by using Malvern laser diffraction particle size analyser to further comment on the microstructure of the resultant polymers and the results are given in Table 2. In general, particle sizes on the latex samples are naturally much smaller.³⁵ However, we conducted particle size analysis on dried polymers since the aim of this work is to perform cost-target molecular weight optimization for commercial applications, and the particle size results on Table 2 are actually comparable with commercial PS.⁶¹ Table 3 shows the $[\eta]$ and M_v values of all polymers synthesized in this work.

Table 2. Representative GPC, thermal analysis and particle size analysis results of synthesized polymers.

Polymer	M_w (g/mol)	M_n (g/mol)	PDI	T_g (°C)	D_{50} (µm)
PS-1	1353000	1027000	1.32	106.6	292
PS-5	392000	291200	1.35	107.1	92
PS-6	101600	78900	1.29	100.4	225
PS-12	532800	392400	1.36	106.8	88
PS-14	605000	407900	1.48	107.4	170

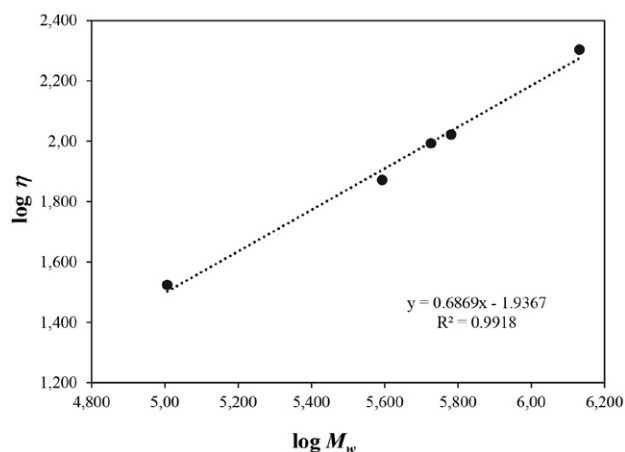


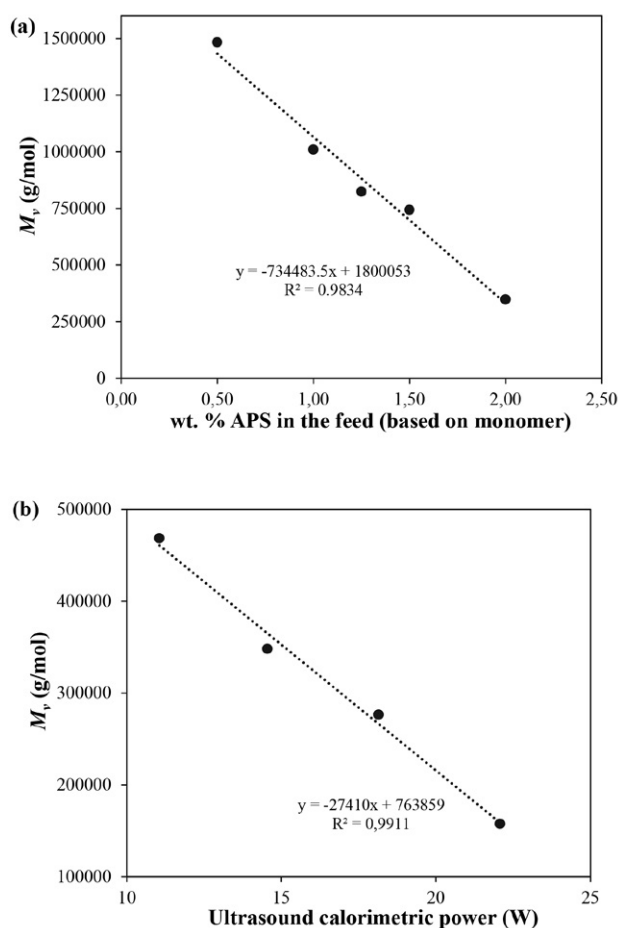
Fig. 5. Change of $\log M_w$ of the polymers with the change of $\log \eta$.

Overall, the results show that the molecular weight is decreasing with APS, SDS and ultrasound power, while increasing with initial monomer concentration. When more and more APS and SDS are introduced to the system, more radicals can be formed to initiate the polymerization, but with the expense of chain length (Table 3). For example, the M_v of the PS decreased sharply from 1483600 to 348200 g/mol with the increase of APS concentration as seen in Fig. 6a. This is because, more monomers might be reacting with these radicals in this case rather than attaching to the active monomer chains, and thus resulting in shorter polymer chains in the final structure, yielding a lower molecular weight. Similar situation could also be persistent for the ultrasound power as seen in Fig. 6b. It might be easier for the radicals to decompose due to acoustic cavitation under higher applied ultrasound power, and thus causing shorter polymer chains in the final structure, similar as explained for the effect of APS and SDS. Moreover, the polydispersity index (PDI) values of the synthesized polymers were ranged between 1.28 and 1.48 (Table 2) and were actually relatively lower, particularly considering free radical polymerization.^{2,55} This is expected, because the acoustic cavitation might break down the longer polymer chains, further decreasing the molecular weight and causing all polymer chains to a similar length.^{29,31,39,41} However, Kojima et al. reported that sonication for 3 h at 92 kHz in polymerization of styrene gives very high polydispersity (5.0) indicating that sonication time is very important to

Table 3. Molecular weight of synthesized polymers, and cost-molecular weight relationship.

Polymer	Actual Results			Model Predictions		
	$[\eta]$ (ml/g)	M_v (g/mol)	Cost (\$/ton PS)	$[\eta]$ (ml/g)	M_v (g/mol)	Cost (\$/ton PS)
PS-1	201.2	1483600	44518.9	199.4	1420100	44457.2
PS-2	154.5	1010000	44271.1	158.4	1068100	44321.7
PS-3	134.3	824200	44224.7	137.9	892100	44254.0
PS-4	125.2	743700	44146.5	117.4	716100	44186.3
PS-5	74.3	348200	43622.5	76.4	364100	44050.8
PS-6	33.4	108800	100295.4	NA*	NA*	NA*
PS-7	91.2	468800	43496.7	91.5	465300	43913.9
PS-8	63.4	276500	44028.9	60.9	259900	44191.5
PS-9	43.1	157600	44739.9	44.1	147100	44343.0
PS-10	95.8	504000	34530.0	97.6	510900	33283.1
PS-11	83.5	412800	55791.6	85.3	419700	54544.7
PS-12	98.5	524500	42941.6	94.8	492500	43303.3
PS-13	104.0	567700	41844.4	99.8	533340	42387.4
PS-14	105.3	577800	41204.7	108.1	601400	40860.9

* Outside the validity region of the developed models.

**Fig. 6.** (a) Change of viscosity average molecular weight with the change of weight fraction of APS in the feed (Ultrasound calorimetric power: 14.6 W, SDS: wt. % 0.5, $[M]_0 = 0.5$ M), (b) Change of viscosity average molecular weight with the change of ultrasound power (APS: wt. % 2, SDS: wt. % 0.5, $[M]_0 = 0.5$ M).

prevent undesired effects of ultrasound.⁴⁰ These results show that ultrasound assisted emulsion polymerization of styrene in our conditions is suitable for obtaining narrow molecular weight distributions. On the other hand, we ascribed the slightly positive effect of initial monomer concentration on the molecular weight to the possible increase of the biradical coupling ratio to the disproportionation in the termination step, which might be occurring due to the very low APS concentration (2 wt. % of initial monomer concentration) in our system.²

3. 3. Statistical Analysis

We used a statistical approach to interpret the economic feasibility of the ultrasound-assisted emulsion polymerization of styrene through Design Expert (trial version). Statistical optimization tools are widely used nowadays in various fields to converge scientific studies to industrial applications.^{62–65} Considering that polystyrene is an industrialized polymer, economic considerations are important for manufacturers as mentioned before. Therefore, a multi objective optimization procedure, which is particularly focusing on to determine the minimum cost to reach a PS with any desirable molecular weight would be beneficial. For this purpose, we assigned ultrasound power, initial monomer concentration, APS concentration, and SDS concentration as independent variables (factors), while defining molecular weight, intrinsic viscosity, and cost as the response variables in Design Expert (trial version). Then, a cost equation (Equation 5) was established to determine the expenses in PS synthesis at the experimental conditions of this work. It is important to note that although cost of SBS was added to the cost equation, the amount of SBS was not introduced as a factor, since we used a definite APS:SBS ratio of 1.2, and thus, SBS is not an independent variable.

$$\text{Cost (per ton of PS)} = \frac{(C_{elec} + C_{styrene} + C_{APS} + C_{SDS} + C_{SBS}) \times 1000000}{W_{PS}} \quad (5)$$

where C_{elec} represents the expenses associated with the electricity consumption of the ultrasonic homogenizer. The power consumption in our system was measured and recorded by Unit UT 71E True RMS digital multimeter in Watts. Then, C_{elec} was calculated by converting the measured W to kWh for 1 hour of ultrasound assistance during the polymerization and multiplying with the tariffs in Turkey as retrieved from the Turkish Electricity Distribution Corporation. Other expenses include the prices of styrene ($C_{styrene}$), APS (C_{APS}), SDS (C_{SDS}), and SBS (C_{SBS}), which were calculated for their respective amounts in our polymerization reactions using their base prices retrieved from Sigma Aldrich. Simply, we used the price tags of 2.5 L reagent plus grade styrene, 2.5 kg ACS reagent grade APS, 2.5 kg ACS reagent grade SBS, and 100 g ACS reagent grade SDS from the official website of Sigma Aldrich/Merck (accessed on 1 January 2022) as the base prices, to determine the values of $C_{styrene}$, C_{APS} , C_{SDS} , and C_{SBS} , which were calculated for the actual amounts introduced to our system. In order to introduce the effect of conversion to the cost calculations, the equation is divided by $W_{polystyrene}$, which is the total weight of the synthesized polystyrene after each experiment. Also, the equation is multiplied by 1000000 to reflect the cost per ton of synthesized PS. Following the necessary cost calculations, experimental intrinsic viscosity and molecular weight results were inputted to Design Expert (trial version), together with the as-calculated cost results to formulate mathematical models for the afore-mentioned response variables. The model estimations are listed in Table 3 and the validity regions of these models are given in Table 4. Simply, the developed models are only valid between these lower and higher levels of the factors in Table 4. The corresponding models that developed in this work are given below:

$$\text{Intrinsic viscosity} = +133.72 - 32.33A + 8.36B - 61.50C - 6.15D \text{ (codec equation)} \quad (6)$$

$$\text{Intrinsic viscosity} = +292.01 - 4.24A + 32.88B - 82.02C - 12.30D \quad (7)$$

$$\text{Mol. weight} = +8.76e^5 - 2.17e^5A + 6.80e^4B - 5.28e^5C - 4.56e^4D \text{ (codec equation)} \quad (8)$$

$$\text{Mol. weight} = +2.10e^6 - 28.54e^3A + 2.67e^5B - 7.03e^5C - 9.12e^4D \quad (9)$$

$$\text{Cost} = +4.28e^4 + 293.24A - 1.53e^3B - 2.03e^2C + 10.63e^4D \text{ (codec equation)} \quad (10)$$

$$\text{Cost} = +3.64e^4 + 39.09A - 6.11e^3B - 2.71e^2C + 2.13e^4D \quad (11)$$

Table 4. The validity regions of the developed models.

Factors	Levels	
	−1	+1
Ultrasound calorimetric power (A) (W)	10.0	25.0
Monomer concentration (B) ([M])	0.5	1
APS concentration (C) (%)	0.5	2
SDS concentration (D) (%)	0	1

Considering the coefficients of the factors in the developed models and their respective higher and lower levels, we could conclude that while APS concentration is the most significant term for both intrinsic viscosity and molecular weight, SDS concentration is the most significant term for cost, which result is in good accordance with the experimental observations. Besides, comparison of the experimental results with the theoretical predictions in Table 3 indeed suggest that the developed models have high accuracy in estimating the actual results. In addition to this, analysis of variance (ANOVA) was also conducted as given in Table 5 to further verify the validity of the developed models.

The effectiveness of statistical models could be identified by the F values, p values, R^2 values and adequate precision, since F values correspond to the ratio of mean square of factors to error mean square, and should be as high as possible to signify greater dispersion, p-values represent the possibility of null hypothesis and should be less than 0.05, R^2 shows the variations between the predicted and actual data, and should be close to 1 in acceptable fittings, while adequate precision corresponds the signal to noise ratio, and should be higher than 4 in valid models.⁶⁶ Therefore, ANOVA results in Table 5 further confirms that all of the developed models are statistically significant as they all possess high F-values, low p-values, high adequate precision, and R^2 , R^2_{adj} , and R^2_{pred} values of close to 1. Besides, the R^2_{adj} and R^2_{pred} values are within 0.2 of each other.

Finally, we used multi objective optimization to prepare PS at various targeted molecular weights and also to

Table 5. Statistical indicators of the intrinsic viscosity, molecular weight and cost models.

Model	F-value	p-value	R ²	R ² _{adj.}	R ² _{pred.}	Adequate precision
η	378.68	< 0.0001	0.9928	0.9902	0.9791	74.14
M_v	252.75	< 0.0001	0.9892	0.9853	0.9652	58.68
Cost	138.57	< 0.0001	0.9805	0.9735	0.8726	57.97

Table 6. Multi objective optimization results.

Target M_v (g/mol)	Most feasible conditions to reach target M_v				Cost predictions at optimum conditions		Desirability
	A	B	C	D	Cost (\$/ton PS)	Std Error	
250000±34800	20.12	0.52	2.00	0.06	34799.9	588.3	0.995
500000±22480	13.17	0.61	1.95	0.14	35759.3	379.9	0.971
750000±22500	12.69	0.60	1.62	0.15	35928.1	380.3	0.967
1000000±23600	12.11	0.61	1.28	0.19	36937.4	398.9	0.942
1250000±27510	12.09	0.59	0.92	0.22	37770.8	465.0	0.921

A: Ultrasound calorimetric power (W), B: Initial monomer concentration (mol/L), C: wt. % of APS, D: wt. % of SDS. Cost to prepare PS ($M_v=108800$) without ultrasound assistance is 100295.4 USD per ton of PS.

minimize the cost simultaneously. In fact, various ways might be used to reach a desired molecular weight in the final polymer such as by changing the initial monomer concentration, ultrasound power, initiator concentration, etc. considering the afore-mentioned effects of these individual factors. However, only one of these condition sets will become the most economical solution and the multi objective optimization was conducted to find this optimum point. The economically most feasible solutions with highest desirability values to reach polystyrene with target viscosity average molecular weights of 250000, 500000, 750000, 1000000 and 1250000 are given in Table 6 for illustration. The standard errors are lower than 35000 for molecular weight and 600 USD per ton of PS for cost in all of these optimization studies, increasing the reliability. In addition to these, the cost of preparing a ton of PS in the absence of ultrasound (based on sample PS-6) is also given as a dip note of Table 6 for better comparison. The results clearly show that ultrasound-assisted emulsion polymerization is economically more feasible comparing to conventional emulsion polymerization of styrene. Besides, the most feasible conditions are differing depending on the target molecular weight, and manufacturers should keep this into account in designing their processes to reach higher profits.

4. Conclusions

The present work involves preparation of polystyrene via ultrasound assisted emulsion polymerization of styrene. We first studied the effects of ultrasound power,

initial monomer concentration, initiator concentration and surfactant concentration on the monomer conversion, intrinsic viscosity and viscosity average molecular weight. The viscosity average molecular weights were determined through intrinsic viscosity measurements and calculation of Mark-Houwink constants using GPC results. Briefly, we found that increasing the amount of initial monomer and initiator concentrations increase the polymerization rate and monomer conversion. However, SDS amount is found to be having only a slight effect on the monomer conversion. In addition to this, the results also suggest that while application of ultrasound increases the polymerization rate and monomer conversion at first, upon increasing the ultrasound calorimetric power above 11.1 W, its effect starts to vanish, and instead, higher ultrasound powers tended to provide lower conversions due possibly to the breakdown of longer polymer chains under extreme acoustic cavitation. Regarding molecular weight, we report a strong negative correlation between molecular weights of polymers and the amount of initiator and ultrasound power. On the other hand, initial monomer concentration and SDS amount have only a slight influence on the viscosity average molecular weight. Finally, we opted a statistical approach to comment on the economic feasibility of the ultrasound assistance. For this purpose, we developed theoretical models for intrinsic viscosity, molecular weight and overall expenses during the synthesis of polystyrene. Then, the most economical solutions were found to reach a polystyrene with various target molecular weights through multi objective optimization. The results show that ultrasound-assisted emulsion polymerization is much more economical comparing to conventional emul-

sion polymerization, and the economically most feasible reaction conditions could vary based on the targeted molecular weight. We believe that our methodology can be used to control the molecular weight of polymers obtained from styrene-like monomers in the future.

Acknowledgements

The authors acknowledge the financial support of Siyas University of Science and Technology under the grant no: 2021-GENL-MUH-0006.

5. References

- W. D. Harkins, *J Am Chem Soc*, **1947**, 69, 1428–1444. DOI:10.1021/ja01198a053
- H. Y. Erbil, Vinyl acetate emulsion polymerization and copolymerization with acrylic monomers, CRC Press, Boca Raton, **2000**. DOI:10.1201/9781420038804
- W. V. Smith, R. H. Ewart, *J Chem Phys*, **1948**, 16, 592–599. DOI:10.1063/1.1746951
- T. Arfin, F. Mohammad, N. A. Yusof, in: C. Lynwood (Ed.): Polystyrene: synthesis, characteristics and applications, Applications of polystyrene and its role as a base in industrial chemistry, Nova Publishers, New York, **2014**, pp. 269–280.
- W. V. Smith, *J Am Chem Soc*, **1948**, 70, 3695–3702. DOI:10.1021/ja01191a045
- W. V. Smith, *J Am Chem Soc*, **1949**, 71, 4077–4082. DOI:10.1021/ja01180a058
- M. Harada, M. Nomura, H. Kojima, W. Eguchi, S. Nagata, *J Appl Polym Sci*, **1972**, 16, 811–833. DOI:10.1002/app.1972.070160402
- M. Nomura, M. Harada, W. Eguchi, S. Nagata, *J Appl Polym Sci*, **1972**, 16, 835–847. DOI:10.1002/app.1972.070160403
- L. V. de la Rosa, E. D. Sudol, M. S. El-Aasser, A. Klein, *J Polym Sci Part A Polym Chem*, **1996**, 34, 461–473. DOI:10.1002/(SICI)1099-0518(199602)34:3<461::AID-POLA15>3.0.CO;2-N
- X. Wang, E. D. Sudol, M. S. El-Aasser, *J Polym Sci Part A Polym Chem*, **2001**, 39, 3093–3105. DOI:10.1002/pola.1290
- X. Wang, E. D. Sudol, M. S. El-Aasser, *Langmuir*, **2001**, 17, 6865–6870. DOI:10.1021/la010641n
- S. Y. Lin, C. S. Chern, T. J. Hsu, C. T. Hsu, I. Capek, *Polymer*, **2001**, 42, 1481–1491. DOI:10.1016/S0032-3861(00)00526-7
- M. F. Kemmere, J. Meuldijk, A. A. H. Drinkenburg, A. L. German, *J Appl Polym Sci*, **2001**, 79, 944–957. DOI:10.1002/1097-4628(20010131)79:5<944::AID-APP180>3.0.CO;2-5
- C. S. Chern, *Prog Polym Sci*, **2006**, 31, 443–486. DOI:10.1016/j.progpolymsci.2006.02.001
- S. Feiz, A. H. Navarchian, *Chem Eng Sci*, **2012**, 69, 431–439. DOI:10.1016/j.ces.2011.10.063
- T. Sirirat, T. Vatanatham, N. Hansupalak, G. L. Rempel, W. Arayaprane, *J Polym Res*, **2015**, 22, 16. DOI:10.1007/s10965-014-0643-9
- E. S. Schultz, N. Sheibat-Othman, A. Mitsos, A. Mhamdi, *Ind Eng Chem Res*, **2020**, 59, 16368–16379. DOI:10.1021/acs.iecr.0c02771
- C. S. Chern, Principles and applications of emulsion polymerization, John Wiley & Sons, New Jersey, **2008**. DOI:10.1002/9780470377949
- A. Salazar, L. M. Gugliotta, J. R. Vega, G. R. Meira, *Ind Eng Chem Res*, **1998**, 37, 3582–3591. DOI:10.1021/ie980009y
- A. Echevarria, J. R. Leiza, J. C. De La Cal, J. M. Asua, *AIChE J*, **1998**, 44, 1667–1679. DOI:10.1002/aic.690440718
- Z. F. M. Said, *Die Makromol Chemie*, **1991**, 192, 405–414. DOI:10.1002/macp.1991.021920220
- C. M. Miller, P. A. Clay, R. G. Gilbert, M. S. El-Aasser, *J Polym Sci Part A Polym Chem*, **1997**, 35, 989–1006. DOI:10.1002/(SICI)1099-0518(19970430)35:6<989::AID-POLA2>3.0.CO;2-C
- L. M. Gugliotta, A. Salazar, J. R. Vega, G. R. Meira, *Polymer*, **2001**, 42, 2719–2726. DOI:10.1016/S0032-3861(00)00730-8
- M. Vicente, S. Benamor, L. M. Gugliotta, J. R. Leiza, J. M. Asua, *Ind Eng Chem Res*, **2001**, 40, 218–227. DOI:10.1021/ie000387e
- J. Herrera-Ordóñez, O. Rivera, H. Maldonado-Textle, J. C. Ramirez, *J Polym Sci Part A Polym Chem*, **2005**, 43, 1963–1972. DOI:10.1002/pola.20661
- Y. Kim, K. Kim, B. H. Lee, S. Choe, *Macromol Res*, **2012**, 20, 977–984. DOI:10.1007/s13233-012-0144-9
- K. Yan, X. Gao, Y. Luo, *Macromol Rapid Commun*, **2015**, 36, 1277–1282. DOI:10.1002/marc.201500052
- V. M. B. Patrocínio, T. Agner, G. V. S. Dutra, F. Machado, B. A. D. Neto, P. H. H. Araújo, C. Sayer, *Macromol React Eng*, **2019**, 13, 1800061. DOI:10.1002/mren.201800061
- B. A. Bhanvase, D. V. Pinjari, S. H. Sonawane, P. R. Gogate, A. B. Pandit, *Ultrason Sonochem*, **2012**, 19, 97–103. DOI:10.1016/j.ultsonch.2011.05.016
- B. A. Bhanvase, S. H. Sonawane, D. V. Pinjari, P. R. Gogate, A. B. Pandit, *Chem Eng Process Process Intensif*, **2014**, 85, 168–177. DOI:10.1016/j.cep.2014.08.014
- B. M. Teo, S. W. Prescott, M. Ashokkumar, F. Grieser, *Ultrason Sonochem*, **2008**, 15, 89–94. DOI:10.1016/j.ultsonch.2007.01.009
- L. A. Crum, T. J. Mason, J. L. Reisse, K. S. Suslick, *Sonochemistry and sonoluminescence* Springer Science & Business Media, Washington, **1998**.
- Y. Liao, Q. Wang, H. Xia, X. Xu, S. M. Baxter, R. V. Slone, S. Wu, G. Swift, D. G. Westmoreland, *J Polym Sci Part A Polym Chem*, **2001**, 39, 3356–3364. DOI:10.1002/pola.1318
- V. L. Gole, P. R. Gogate, *Chem Eng Process Process Intensif*, **2012**, 53, 1–9. DOI:10.1016/j.cep.2011.12.008
- D. Nagatomo, T. Horie, C. Hongo, N. Ohmura, *Ultrason Sonochem*, **2016**, 31, 337–341. DOI:10.1016/j.ultsonch.2016.01.010
- I. Korkut, M. Bayramoglu, *Ultrason Sonochem*, **2014**, 21, 1592–1599. DOI:10.1016/j.ultsonch.2013.12.028
- T. G. Leighton, *Prog Biophys Mol Biol*, **2007**, 93, 3–83. DOI:10.1016/j.pbiomolbio.2006.07.026
- H. M. Cheung, K. Gaddam, *J Appl Polym Sci*, **2000**, 76, 101–104.

- DOI:10.1002/(SICI)1097-4628(20000404)76:1<101::AID-APP13>3.0.CO;2-F
39. S. K. Ooi, S. Biggs, *Ultrason Sonochem*, **2000**, 7, 125–133.
DOI:10.1016/S1350-4177(99)00040-1
40. Y. Kojima, S. Koda, H. Nomura, *Ultrason Sonochem*, **2001**, 8, 75–79. DOI:10.1016/S1350-4177(00)00064-X
41. J. Zhang, Y. Cao, Y. He, *J Appl Polym Sci*, **2004**, 94, 763–768.
DOI:10.1002/app.20948
42. D. Kobayashi, H. Matsumoto, C. Kuroda, *Chem Eng J*, **2008**, 135, 43–48. DOI:10.1016/j.cej.2007.05.015
43. G. Qiu, M. Nie, Q. Wang, *Ultrason Sonochem*, **2008**, 15, 269–273. DOI:10.1016/j.ultsonch.2007.12.003
44. T. J. Mason, D. Peters D, *Practical sonochemistry: Power ultrasound uses and applications*. Woodhead Publishing, Cambridge, 2002.
45. G. J. Price, A. A. Clifton, *Polymer*, **1996**, 37, 3971–3973.
DOI:10.1016/0032-3861(96)00197-8
46. I. M. Borisov, R. S. Luksha, S. T. Rashidova, *Russ Chem Bull*, **2015**, 64, 2512–2513. DOI:10.1007/s11172-015-1185-y
47. J. P. Marcolongo, M. Miranda, *J Chem Educ*, **2011**, 88, 629–633. DOI:10.1021/ed900019u
48. M. L. Huggins, *J Am Chem Soc*, **1942**, 64, 2716–2718.
DOI:10.1021/ja01263a056
49. P. A. Lovell, F. J. Schork, *Biomacromolecules*, **2020**, 21, 4396–4441. DOI:10.1021/acs.biomac.0c00769
50. J. M. Asua, *Prog Polym Sci*, **2002**, 27, 1283–1346.
DOI:10.1016/S0079-6700(02)00010-2
51. H. F. Scott, *Elements of chemical reaction engineering*. Prentice Hall International Series in the Physical and Chemical Engineering Sciences, New Jersey, **2016**.
52. B. Carnahan, H. A. Luther, J. O. Wilkes, *Applied Numerical Methods*. John Wiley & Sons, New York, **1969**.
53. C. D. Immanuel, F. J. Doyle III, C. F. Cordeiro, S. S. Sundaram, *AIChE J*, **2003**, 49, 1392–1404.
DOI:10.1002/aic.690490606
54. N. Vogel, S. Goerres, K. Landfester, C. K. Weiss, *Macromol Chem Phys*, **2011**, 212, 1719–1734.
DOI:10.1002/macp.201100187
55. S. Ozbay, H. Y. Erbil, *Colloids Surfaces A Physicochem Eng Asp*, **2014**, 452, 9–17. DOI:10.1016/j.colsurfa.2014.03.054
56. S. Ozbay, H. Y. Erbil, *Colloids Surfaces A Physicochem Eng Asp*, **2015**, 481, 537–546. DOI:10.1016/j.colsurfa.2015.05.049
57. J. Brandrup, E. H. Immergut, E. A. Grulke, A. Abe, D. R. Bloch, *Polymer Handbook*. John Wiley and Sons, New York, **1999**.
58. R. Claudy, J. M. L  toff  , Y. Camberlain, J. P. Pascault, *Polym Bull*, **1983**, 9, 208–215. DOI:10.1007/BF00283709
59. L. Singh, P. J. Ludovice, C. L. Henderson, *Thin Solid Films*, **2003**, 449, 231–241. DOI:10.1016/S0040-6090(03)01353-1
60. L. P. Blanchard, J. Hesse, S. L. Malhatro, *Can J Chem*, **1974**, 52, 3170–3175. DOI:10.1139/v74-465
61. Y. Li, M. Li, Z. Li, L. Yang, X. Liu, *Chemosphere*, **2019**, 231, 308–314. DOI:10.1016/j.chemosphere.2019.05.116
62. B. Akgul, F. Erden, S. Ozbay, *Powder Technology*, **2021**, 391, 11–19. DOI:10.1016/j.powtec.2021.06.007
63. G. E. P. Box, K. B. Wilson, *J R Stat Soc Series B Stat Methodol*, **1951**, 13, 1–45.
64. M. H. Esfe, H. Hajmohammad, R. Moradi, A. A. A. Arani, *Appl Therm Eng*, **2017**, 112, 1648–1657.
DOI:10.1016/j.applthermaleng.2016.10.129
65. M. H. Esfe, S. Esfandeh, M. Rejvani, *J Therm Anal Calorim*, **2018**, 131, 1437–1447. DOI:10.1007/s10973-017-6680-y
66. M. Kul, F. Erden, K. O. Oskay, O. Karasungur, M. Simsir, L. C. Kumruoglu, I. Karakaya, *J Sustain Metall*, **2021**, 7, 1224–1240.
DOI:10.1007/s40831-021-00406-7

Povzetek

Raziskava se osredoto  a na dolo  itev ekonomsko najbolj optimalnih pogojev za pridobitev polistirena z razli  nimi ciljnimi molekulskimi masami z ultrazvo  no podprto emulzijsko polimerizacijo.   ar  ne polimerizacije stirena z ultrazvo  no podprtim postopkom emulzijske polimerizacije so bile izvedene pri razli  nih sestavah reakcijskih komponent. Hitrost polimerizacije je bila izra  unana na osnovi pretvorbe monomera pri razli  nih reakcijskih   asih. Molekulske mase sintetiziranih polimerov in Mark-Houwinkove konstante so bile dolo  ene z meritvami intrinzi  ne viskoznosti in gelske izklju  itvene kromatografije. Ugotovljeno je bilo, da je indeks polidisperznosti polimerov v razponu od 1,2 do 1,5, povpre  ne molekulske mase viskoznosti pa so med 100.000–1.500.000 g/mol, odvisno od reakcijskih pogojev. Na koncu so bile razvite tudi modelne ena  be za dolo  itev glavnih spremenljivk, najbolj ekonomski na  ini za doseganje razli  nih ciljnih molekulskih mas pa so bili razlo  eni z metodologijo odzivne povr  ine, ki temelji na optimizaciji ve   ciljev.



Except when otherwise noted, articles in this journal are published under the terms and conditions of the Creative Commons Attribution 4.0 International License

The Paramagnetic or Spin Crossover Iron(III) Complexes Based-on Pentadentate Schiff Base Ligand: Crystal Structure, and Magnetic Property Investigation

Zhijie Xu, Shuo Meng, Tong Cao, Yu Xin, Mingjian Zhang, Xiaoyi Duan, Zhen Zhou and Daopeng Zhang*

College of Chemical and Chemical Engineering, Shandong University of Technology, Zibo 255049, PR China

* Corresponding author: E-mail: dpzhang73@126.com

Received: 07-12-2022

Abstract

A series of bi- or mononuclear hexacoordinate iron(III) complexes, $[\text{Fe}(\text{L})][\text{Fe}(\text{bpb})(\text{CN})_2] \cdot \text{CH}_3\text{OH} \cdot 0.5\text{H}_2\text{O}$ (**1**), $[\text{Fe}(\text{L})][\text{Co}(\text{bpb})(\text{CN})_2] \cdot \text{CH}_3\text{OH}$ (**2**), $[(\text{Fe}(\text{L}))_2(4,4'\text{-bipy})](\text{BPh}_4)_2$ (**3**), $[\text{Fe}(\text{L})(\text{py})](\text{BPh}_4)$ (**4**) and $[\text{Fe}(\text{L})(\text{dmap})](\text{BPh}_4)$ (**5**) (bpb = 1,2-bis(pyridine-2-carboxamido)benzenate, L = *N,N'*-bis(2-hydroxybenzyliden)-1,7-diamino-4-azaheptane, dmap = 4-dimethylaminopyridine), have been prepared with the pentadentate Schiff base iron(III) compound as assemble precursor and characterized by element analysis, IR and X-ray diffraction. Single crystal structural determination revealed the neutral cyanide-bridged binuclear entity for complexes **1** and **2** and the cationic di- or mononuclear structure for complexes **3–5** with the positive charge(s) balanced by BPh_4^- ion(s). The experimental study and theoretical simulation of the magnetic property discovered the ferromagnetic coupling between the Fe(III) ions bridged by cyanide group in complex **1** and the always high spin state of the Fe(III) ion coordinated to the Schiff base ligand in both complexes **1** and **2**. The temperature dependent magnetic susceptibility investigation over complexes **3–5** showed the occurrence of the thermo-induced gradual complete spin crossover (SCO) property at about 115, 170 and 200 K, respectively.

Keywords: Cyanide-bridged, Crystal structure, Ferromagnetic coupling, Spin crossover

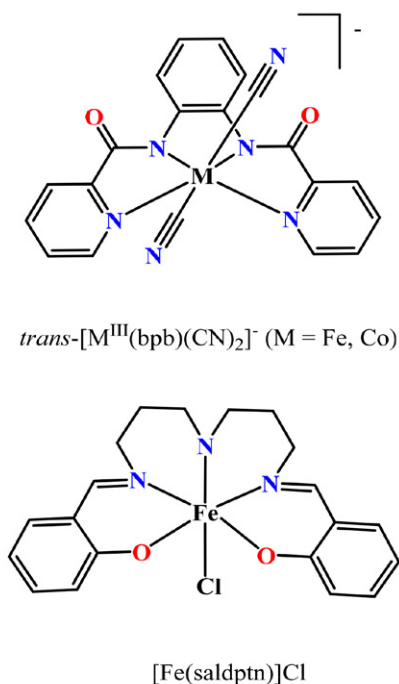
Introduction

Since the 21st century, the synthesis of materials with special functions and applications based on the coordination chemistry has been one of the important directions of current chemical research.^{1–10} Molecular materials with spin crossover behavior have broad application prospects in the fields of nano device, spintronics, information storage, sensors, digital display, and so on.^{11–18} The use of spin crossover complexes as switches or sensors depend on spin transition distinguished by different magnetic, optical and structural characteristics, which included structural changes between two different spin states and could be realized under the suitable coordination field by external stimuli such as temperature, light irradiation and the guest solvent molecules.^{19–25} It was generally found that the metal centers with the $3d^4$ – $3d^7$ electronic configurations and involved in octahedral coordination surroundings could readily occur spin transition between the different spin states.^{26–28}

Among $3d^4$ – $3d^7$ metal ions, the strong interest has always been devoted to the switchable molecular materials

centered with iron(II) ion. During the past several decades, a great deal of the Fe(II)-based complexes with various structure types from 0D clusters, 1D infinite chains to 2–3D networks and interesting SCO properties have been reported. However, with comparison to the intensely studied divalent Fe(II) in SCO field, research on Fe(III) ion-based SCO material is comparatively limited,^{29–33} as is also with the SCO possibility between the high spin $S = 5/2$ and low spin $S = 1/2$. The pentadentate Schiff base ligands (Scheme 1), which can encapsulate the hexa-coordinated metal with sixth position weakly bonded to other ligand, are a type of precursor for preparation function complexes.^{34–36} In fact, some previous reports have proven that the above pentadentate Schiff base based iron(III) compounds are suitable candidates for assembling SCO materials under the help of the pyridine-like ligands^{37,38} and some of the obtained complexes have been structurally characterized and experimentally magnetic investigated. Taking into account that the cyanometallic precursors with tunable coordination field, such as $[\text{M}(\text{CN})_4]^{2-}$ ($\text{M} = \text{Ni}, \text{Pd}$,

Pt), $[M'(CN)_2]^-$ ($M' = Cu, Ag, Au$) and other polycyano-metallates, have been widely employed to construct SCO materials, especially for those ones with Hoffman topologic structures,^{39–42} the reactions of the pentadentate Schiff base iron(III) compound with the *trans*-dicyanoiron(III)/cobalt(III) building blocks (Scheme 1), for the latter which has been extensively used to prepare cyanide-bridged molecular magnetic materials by our group,^{43–46} were investigated, resulting in two new binuclear homo- or heterometallic complexes formulated as $[Fe(L)][Fe(bpb)(CN)_2]$ $CH_3OH \cdot 0.5H_2O$ (1), $[Fe(L)][Co(bpb)(CN)_2]$ CH_3OH (2) ($bpb = 1,2$ -bis(pyridine-2-carboxamido)benzenate, $L = saldptn = N,N'$ -bis(2-hydroxybenzyliden)-1,7-diamino-4-azaheptane).^{47,48} At the same time, by using 4,4'-bipy,⁴⁹ py or *dmap* (*dmap* = 4-dimethylaminopyridine) as ancillary ligand, three monometallic Fe(III) complexes with the formula $[(Fe(L))_2(4,4'-bipy)](BPh_4)_2$ (3), $[Fe(L)(py)](BPh_4)$ (4) and $[Fe(L)(dmap)](BPh_4)$ (5) have been successfully obtained. The synthesis, crystal structures and magnetic properties for the reported complexes will be detailed described in this paper.



Scheme 1. Structure of the Schiff base iron(III) precursor and the *trans*-dicyano building blocks.

2. Experimental Section

Elemental analyses (C, H and N) were carried out with a VarioEl element analyser. IR spectroscopic analysis on KBr pellets was performed on a Magna-IR 750 spectrophotometer in the 4000–400 cm^{-1} region. Variable-temperature magnetic susceptibility and field-dependent magnetization measurements were performed on a Quan-

tum Design MPMS SQUID magnetometer. The experimental susceptibilities were corrected for the diamagnetism of the constituent atoms (Pascal's tables).

General procedures and materials. All the reactions were carried out under air atmosphere and all chemicals and solvents used were reagent grade without further purification. H_2L , $[Fe(L)]Cl$, $K[Fe(bpb)(CN)_2]$ and $K[Co(bpb)(CN)_2]$ were prepared to accord to experimental methods already described.^{50–52}

Caution! KCN is hypertoxic and should be handled in small quantities with great care.

2. 1. The Preparation of the Complexes 1 and 2

A solution containing $K[Fe(bpb)(CN)_2]$ (0.10 mmol, 46.5 mg) or $K[Co(bpb)(CN)_2]$ (0.10 mmol, 46.7 mg) dissolved in methanol (10 mL) was slowly added into the methanol-water (10 mL, 4:1 v/v) solution of $[Fe(L)]Cl$ (43 mg, 0.10 mmol) under the stirring. The mixture was stirred at room temperature for several minutes and filtered to remove any insoluble substances. Then, the filtrate was allowed for slow evaporation without interference for about two weeks. Dark brown crystals suitable for X-ray diffraction were collected by filtration, washed with cold methanol and dried in air.

Complex 1: Yield: 52.9 mg, 61.7%. Anal. Calcd. For $C_{41}H_{40}Fe_2N_9O_5$: C, 57.36; H, 4.70; N, 14.68. Found: C, 57.47; H, 4.62; N, 14.79. Main IR bands (cm^{-1}): 2160, 2120 (s, $\nu C-N$), 1630 (vs $\nu C=N$), 3056, 2846, 2660 (w, $\nu C-H$), 1444, 1401, 1279 (s, $\nu C-O$).

Complex 2: Yield 53.9 mg, 63.3%. Anal. Calcd. For $C_{41}H_{39}CoFeN_9O_5$: C, 57.76; H, 4.61; N, 14.79. Found: C, 57.87; H, 4.52; N, 14.89. Main IR bands (cm^{-1}): 2158, 2122 (s, $\nu C-N$), 1630 (vs $\nu C=N$), 3059, 2855, 2656 (w, $\nu C-H$), 1458, 1387, 1275 (s, $\nu C-O$).

2. 2. The Preparation of Complexes 3–5

To a methanol solution of $[Fe(L)]Cl$ (43 mg, 0.10 mmol) was added 4,4'-bipy (7 mg, 0.05 mmol) or py (8 mg, 0.1 mmol) or *dmap* (12 mg, 0.1 mmol). The mixture was stirred for about ten minutes at 60 °C before an excess of sodium tetraphenylborate (855 mg, 2.5 mmol) was added. After the insoluble substances were filtered out, the filtrate was partial evaporated and the crystals obtained was collected and washed with methanol and ether.

Complex 3: Yield 48.0 mg, 60.7 %. Anal. Calcd. for $C_{98}H_{94}B_2Fe_2N_8O_4$: C, 74.44; H, 5.99; N, 7.09. Found: C, 74.52; H, 5.93; N, 7.15. Main IR bands (cm^{-1}): 1633 (vs $\nu C=N$), 732, 708 ($\nu B-C$), 3057, 2978 (w, $\nu C-H$), 1251 (s, $\nu C-O$). Anal.

Complex 4: Yield 42.0 mg, 53.1 %. Anal. Calcd. for $C_{49}H_{48}BFeN_4O_2$: C, 74.34; H, 6.11; N, 7.08. Found: C, 74.44; H, 6.01; N, 7.15. Main IR bands (cm^{-1}): 1628 (vs $\nu C=N$), 735, 706 ($\nu B-C$), 3054, 2977 (w, $\nu C-H$), 1252 (s, $\nu C-O$). Anal.

Complex 5: Yield 42.6 mg, 51.2 %. Anal. Calcd. for $C_{51}H_{52}BFeN_5O_2$: C, 73.48; H, 6.29; N, 8.40. Found: C, 73.54; H, 6.19; N, 8.54. Main IR bands (cm^{-1}): 1630 (vs $\nu C=N$), 733, 707 ($\nu B-C$), 3050, 2975 (w, $\nu C-H$), 1245 (s, $\nu C-O$). Anal.

2. 3. X-ray Data Collection and Structure Refinement

Single crystals of all the complexes for X-ray diffraction analyses with suitable dimensions were mounted on a glass rod and the crystal data were collected on a Bruker SMART CCD diffractometer with a Mo K α sealed tube ($\lambda = 0.71073 \text{ \AA}$) at 293 K, using a ω scan mode. For complexes 3 and 4, their structures have been further measured at about 120 K. The structures were solved by direct methods and expanded to use Fourier difference techniques with

the SHELXTL-97 program package. The non-hydrogen atoms were refined anisotropically, while hydrogens were introduced as fixed contributors. All non-hydrogen atoms were refined with anisotropic displacement coefficients. Hydrogens were assigned isotropic displacement coefficients $U(H) = 1.2U(C)$ or $1.5U(C)$, and their coordinates were allowed riding on their respective carbons using SHELXL-2018, except some hydrogens of solvent molecules, which were refined isotropically with fixed U values and the DFIX command was used to rationalize the bond parameters. CCDC 2169018–2169022 for complexes 1–5 contain the supplementary crystallographic data for this paper. These data can be obtained free of charge from the Cambridge Crystallographic Data Centre via www.ccdc.cam.ac.uk/data_request/cif. Details of the crystal parameters, data collection, and refinement are summarized in tables 1 and 2.

Table 1. Crystallographic data for complexes 1, 2 and 5.

	1 (293k)	2 (293k)	5 (293k)
Chemical formula	$C_{41}H_{40}Fe_2N_9O_{5.5}$	$C_{41}H_{39}CoFeN_9O_5$	$C_{51}H_{53}BFeN_5O_2$
Fw	858.52	852.59	834.64
Crystal system	Monoclinic	Monoclinic	Monoclinic
Space group	$P2_1/c$	$P2_1$	$P2_1/n$
$a/\text{\AA}$	10.8753(10)	10.875(7)	18.3588(16)
$b/\text{\AA}$	10.0446(9)	10.065(6)	14.5766(13)
$c/\text{\AA}$	36.595(3)	18.331(11)	18.5738(16)
α/deg	90.0	90.0	90
β/deg	92.349(2)	95.586(11)	117.698(2)
γ/deg	90.0	90.0	90
Z	2	2	4
$V/\text{\AA}^3$	3994.2(6)	1997(2)	4400.9(7)
$F(000)$	1780.0	882.0	1764.0
GOF	1.030	1.028	1.024
$R_1 [I > 2\sigma(I)]$	0.1241	0.073	0.1180
wR_2 (all data)	0.1435	0.1901	0.1455

Table 2. Crystallographic data for complexes 3 and 4.

	3 (293k)	3 (120k)	4 (293k)	4 (120k)
Chemical formula	$C_{49}H_{48}BFeN_4O_2$	$C_{49}H_{48}BFeN_4O_2$	$C_{98}H_{94}B_2Fe_2N_8O_4$	$C_{98}H_{94}B_2Fe_2N_8O_4$
Fw	791.57	791.57	1581.13	1581.13
Crystal system	Monoclinic	Monoclinic	Monoclinic	Monoclinic
Space group	$P2_1/c$	$P2_1/c$	$C2/c$	$C2/c$
$a/\text{\AA}$	18.373(2)	18.295(4)	33.480(2)	33.1757(16)
$b/\text{\AA}$	11.9535(13)	11.880(2)	16.7773(11)	16.7010(6)
$c/\text{\AA}$	21.064(2)	20.678(4)	16.3933(11)	16.0077(6)
α/deg	90.0	90.0	90.0	90.0
β/deg	114.530(2)	114.60(3)	117.094(1)	116.567(5)
γ/deg	90.0	90.0	90.0	90.0
Z	4	4	4	4
$V/\text{\AA}^3$	4208.6(8)	4086.5(4)	8197.6(10)	7932.9(6)
$F(000)$	1668.0	1668.0	3328.0	3328.0
GOF	1.006	1.028	1.005	1.027
$R_1 [I > 2\sigma(I)]$	0.0415	0.0462	0.1159	0.0607
wR_2 (all data)	0.1086	0.0793	0.1394	0.1503

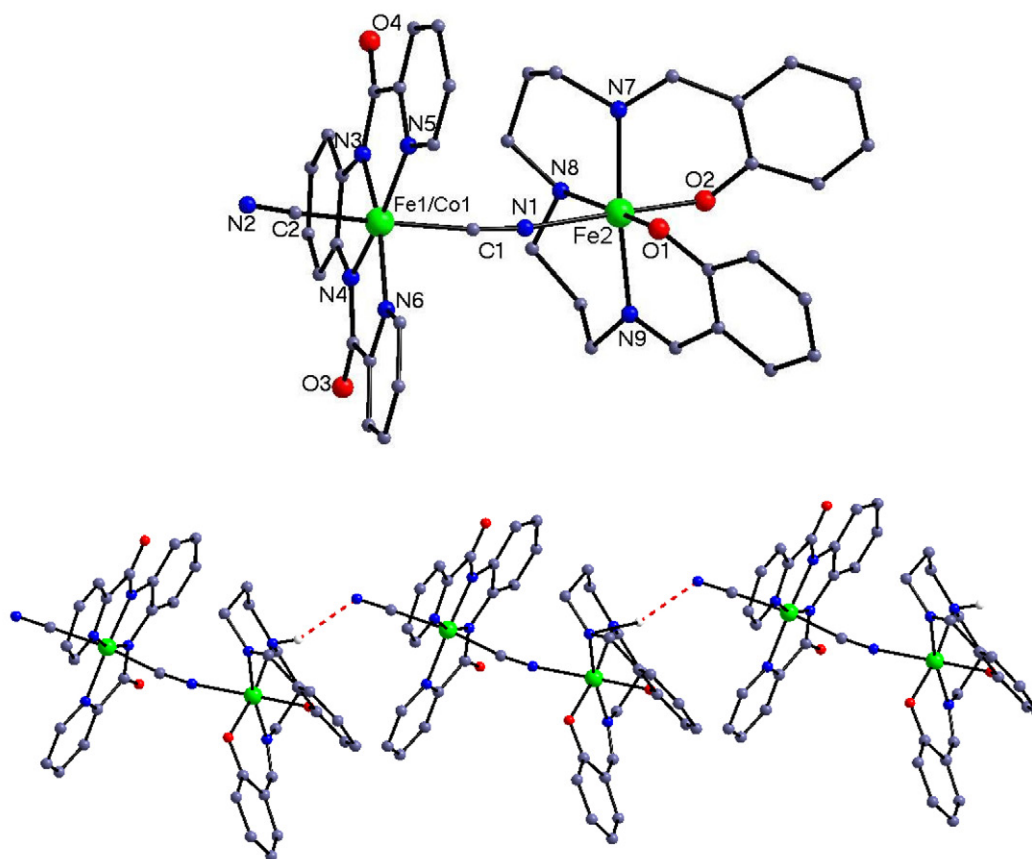


Figure 1. The neutral binuclear structures of complexes **1** and **2** (top) and the 1D supramolecular chain constructed by H-bond interactions (bottom). All the H atoms except one used to form H-bond and the solvent content have been omitted for clarity.

3 Results and Discussion

3. 1. Crystal Structure Description

3. 1. 1 Crystal Structures of Complexes 1 and 2

The selected important structural parameters for complexes **1** and **2** are collected in Table 3. The neutral binuclear and the 1D supramolecular single chain structure constructed by the hydrogen bond interactions for these two complexes are shown in Figure 1.

The structures of complexes **1** and **2**, crystallizing in space group $P2_1/c$ and $P2_1$ containing four and two independent units in the unit cell, respectively, belong to neutral binuclear entity. The $[\text{Fe/Co}(\text{bpb})(\text{CN})_2]^-$ anion acting as monodentate ligand connects the $[\text{Fe}(\text{L})]^+$ cation through one cyanide group with the other *trans* one terminal, therefore forming neutral binuclear dimer. The $\text{Fe}^{\text{III}}/\text{Co}^{\text{III}}$ in the cyano precursors with low spin state is coordinated by an equatorial N_4 unit from bpb and two carbons of cyanide groups in the *trans* position. The $\text{Fe}^{\text{III}}/\text{Co}^{\text{III}}-\text{N}$ bond lengths were slightly longer than the $\text{Fe}^{\text{III}}/\text{Co}^{\text{III}}-\text{C}_{\text{cyanide}}$ ones (1.923(8)–1.976(5) Å), revealing a slightly distorted octahedral geometry around the metal ions. As listed in Table 3, the bond angles of $\text{Fe}^{\text{III}}/\text{Co}^{\text{III}}-\text{C}-\text{N}$ very close to

Table 3. Selected bond lengths (Å) and angles (°) for complexes **1** and **2**.

Complexes	Fe	Co1
Fe2–O1	1.911(3)	1.918(5)
Fe2–O2	1.927(3)	1.900(5)
Fe2–N1	2.134(4)	2.141(7)
Fe2–N7	2.098(4)	2.087(7)
Fe2–N8	2.201(4)	2.202(7)
Fe2–N9	2.108(4)	2.115(8)
Fe1/Co1–C1	1.976(5)	1.923(8)
Fe1/Co1–C2	1.951(5)	1.893(8)
Fe1/Co1–N3	1.879(4)	1.894(6)
Fe1/Co1–N4	1.891(4)	1.885(6)
Fe1/Co1–N5	1.933(4)	1.960(5)
Fe1/Co1–N6	2.004(4)	1.963(6)
C1–Fe1/Co1–N6	90.56(16)	88.0(3)
O1–Fe2–N9	89.66(14)	95.1(3)
N1–C1–Fe1/Co1	172.5(4)	173.9(6)
C2–Fe1/Co1–C1	168.93(19)	174.3(3)
O2–Fe2–N1	179.01(15)	179.2(3)
N2–C2–Fe1/Co1	175.2(5)	174.1(7)
N3–Fe1/Co1–N4	83.26(19)	82.4(3)
N4–Fe1/Co1–C1	91.47(11)	90.0(3)

180° clearly indicated that the three atoms were with perfect linear conformation.

The coordination sphere of Fe^{III} ion in [Fe(L)]⁺ is six-coordinated octahedron, in which the four equatorial positions are occupied by three N atoms and one O atom from the Schiff base ligand and the two axial ones coordinated by one O atom of the Schiff base ligand and one N atom of the bridge cyanide group. The averaged Fe–N_{cyanide} and Fe–N_{Schiff base} bond lengths in complexes **1** and **2** are 2.134(4), 2.141(7), 2.136(4) and 2.147(7) Å, respectively, longer than the averaged Fe–O_{Schiff base} bond with the values of 1.919(3) and 1.909(5) Å, demonstrating the obviously distorted octahedral geometry around the Fe(III) ion in [Fe(L)]⁺ unit. These bond lengths are in good agree-

ment with the corresponding bond lengths around the high spin Fe(III) ion found in the reported complexes,⁵³ indicative of the high spin state of Fe(III) ions involved in the Schiff base precursor in these two complexes. Different from the perfect linear Fe^{III}/Co^{III}–C–N unit, the C–N–Fe^{I-II}/Co^{III} bond angles are some bent with the values of 172.2(5) and 169.7(6)°, respectively. With the help of the intermolecular N–H...N hydrogen bond interactions, the binuclear entity can be further constructed into supramolecular 1D infinite structure.

3. 1. 2 Crystal Structures of Complexes 3–5

Some important bond parameters for complexes **3–5** are given in Table 4. The cationic bi- or mononuclear

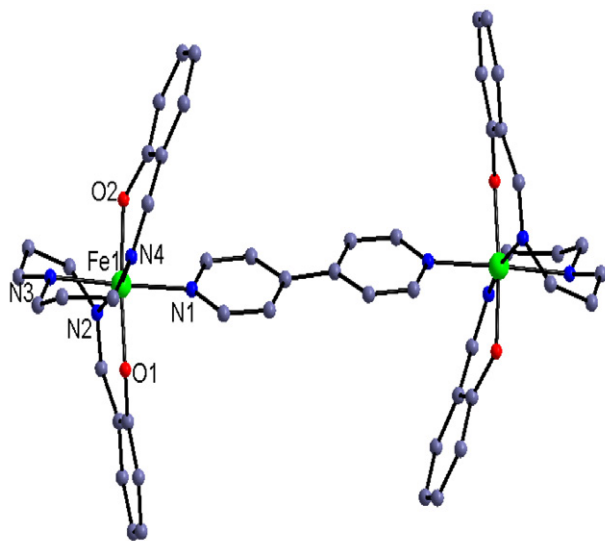


Figure 2. The cationic binuclear structure of complex **3**. All the H atoms and the balanced anions have been omitted for clarity.

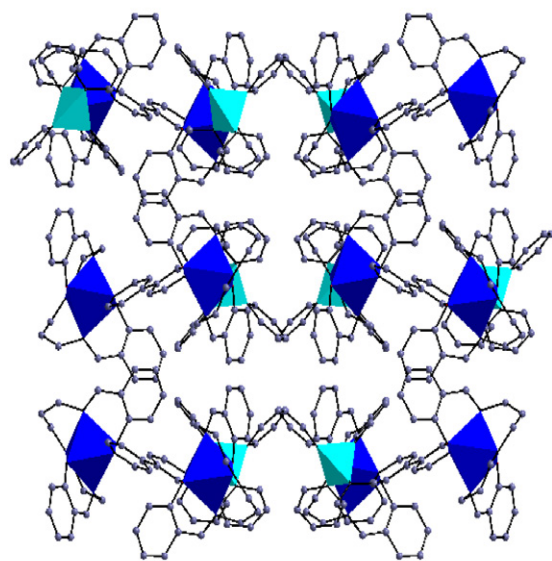


Figure 3. The cell packing diagram of complex **3** along b axial. All the H atoms have been omitted for clarity.

Table 4. Selected bond lengths (Å) and angles (°) for complexes **3–5** at room and low temperature

Complex 3	(293K)	(120K)	
Fe1–O1	1.889(5)	1.8725(5)	
Fe1–O2	1.895(5)	1.8827(5)	
Fe1–N1	2.094(7)	2.012(7)	
Fe1–N2	1.999(7)	1.952(7)	
Fe1–N3	2.083(6)	2.01(6)	
Fe1–N4	2.007(6)	1.961(6)	
O1–Fe1–N1	88.34(9)	87.42(11)	
O1–Fe1–O2	174.20(10)	175.91(11)	
O2–Fe1–N2	92.72(11)	87.87(13)	
O2–Fe1–N3	91.66(11)	93.16(12)	
O2–Fe1–N4	88.58(12)	91.57(13)	
N2–Fe1–N4	168.15(12)	173.79(13)	
N3–Fe1–N1	177.43(10)	178.29(13)	
Complex 4	(293K)	(120K)	
Fe1–O1	1.889(5)	1.8725(17)	
Fe1–O2	1.895(5)	1.8827(18)	
Fe1–N1	2.094(7)	2.012(2)	
Fe1–N2	1.999(7)	1.961(2)	
Fe1–N3	2.083(6)	2.020(2)	
Fe1–N4	2.007(6)	1.952(2)	
O1–Fe1–N1	88.2(3)	88.77(8)	
O2–Fe1–O1	175.3(2)	176.04(8)	
O2–Fe1–N2	92.2(3)	91.26(8)	
O2–Fe1–N3	90.7(2)	90.53(8)	
O2–Fe1–N4	89.3(2)	89.47(8)	
N3–Fe1–N1	177.6(3)	177.42(9)	
N4–Fe1–N1	94.3(3)	91.27(8)	
Complex 5 (293K)			
Fe1–O1	1.883(2)	Fe1–O2	1.901(2)
Fe1–N1	2.011(3)	Fe1–N3	1.996(3)
Fe1–N4	2.060(4)	Fe1–N5	1.985(3)
O1–Fe1–N1	92.09(11)	O1–Fe1–N5	90.63(12)
O1–Fe1–O2	179.06	N1–Fe1–N4	179.95(19)
O2–Fe1–N3	91.31(12)	O2–Fe1–N4	91.30(13)
N3–Fe1–N1	91.52(12)	N3–Fe1–N5	176.01(13)
C24–N4–Fe1	116.8(4)	C25–N4–Fe1	117.6(4)

structures are presented in Figure 2 and the cell packing diagram with complex 3 as representative is shown in Figure 3. As can be found, the three complexes, which crystallizes in $C2/c$, $P2_1/c$ and $P2_1/n$ space group, respectively, are composed by cationic bi- or mononuclear entity and the balanced BPh_4^- anion(s). For complex 3, the asymmetric unit contains only half the dinuclear molecule. In complexes 3–5, the coordination geometry of the Fe(III) ion is octahedron, in which the equatorial plane is connected by the N_2O_2 unit from the Schiff base ligand, different from that in complexes 1 and 2, and the two axial positions are occupied by the N atom of the Schiff base ligand and the N atom of the pyridine ligand. It should be pointed out that the configuration of the Schiff base ligand in these three complexes are obviously different from that in complexes 1 and 2, implying maybe the different spin state of the Fe(III) ion. Additionally, there exist weak π - π stacking interactions in complex 3 between the pyridine ring and the ben-

zene ring of the BPh_4^- with center-center distance of 3.74(7) Å.

To further confirm the spin transition, the structures of complexes 3 and 4 have been measured at low temperature (120 K). As tabulated in Table 4, the cell volume of these two complexes in the low temperature contracted obviously from 8197.68 to 7932.85 Å³ for 3 and 4208.58 to 4086.34 Å³ for 4, respectively. The averaged Fe–N and Fe–O bond lengths at low temperature are 1.984(7) Å, 1.993(5) Å, 1.878(5) Å, 1.867(7) Å, which are conspicuously shorter than the room temperature ones with the values 2.045(7) and 2.099(2) Å, indicating different spin state of the Fe(III) ion in these complexes. The comparatively smaller difference for complex 4 can be attributed to the mixed spin state of Fe(III) ion at room temperature, proved also by the magnetic property (*vide infra*).

3.2 Magnetic Properties of Complexes 1–5.

The temperature dependent magnetic susceptibilities of the five complexes were measured by using the corresponding single crystal with quality about 10–20 mg in the range of 2–300 K under an external magnetic field of 2000 Oe. The room temperature $\chi_m T$ values of complexes 1 and 2 (Figure 5) are 4.78 and 4.29 emu K mol^{−1}, respectively, which are basically consistent with the spin only value 4.75 and 4.375 emu K mol^{−1} for the free low spin Fe(III) and high spin Fe(III) ion or the only high spin Fe(III) ion (the cyanide precursor in complex 2 is diamagnetic), respectively. For complex 1, the $\chi_m T$ value increases with very low speed and attain the highest peak about 5.23 emu K mol^{−1} with the temperature decreasing to about 10 K, and then decreases at a high speed and reaches the value of about 3.85 emu K mol^{−1} at 2 K. The $\chi_m T$ - T change tendency can preliminarily confirm the ferromagnetic coupling between the high spin and low spin Fe(III) ion through the cyanide bridge. For complex 2, with temperature decreasing from 300 K, the $\chi_m T$ value keeps always constant until the sample is cooled to about 20 K, and since then the $\chi_m T$ began to decrease obviously and reaches the lowest value about 3.23 emu K mol^{−1} at 2 K, demonstrating the always high spin state of the Fe(III) ion in this complex.

The ferromagnetic coupling observed in complex 1 can be understood by the orthogonality between the t_{2g} and e_g magnetic orbital of high and low spin Fe(III) ions through the bridging cyanide group. On the basis of the binuclear model, the magnetic susceptibility of complex 1 can be fitted accordingly by the following expression derived from the exchange spin Hamiltonian $\hat{H} = -J\hat{S}_{Fe(HS)}\hat{S}_{Fe(LS)}$:

$$\chi_m = \frac{Ng^2\beta^2}{kT} \cdot \frac{10\exp(-3J/kT) + 28}{5\exp(-3J/kT) + 7} \quad (1)$$

By using the above model, the susceptibility over the temperature range of 10–300 K was simulated, giving the best-fit parameters $J = 1.47(1)$, $g = 2.01(2)$, $R = \sum(c_{\text{obsd}} T -$

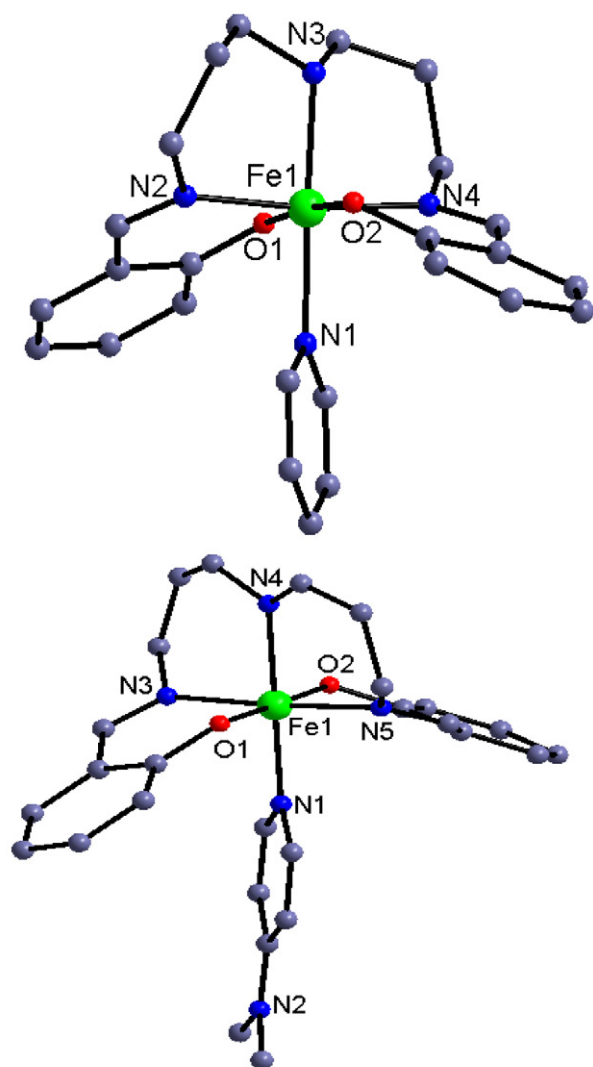


Figure 4. The cationic mononuclear structure of complexes 4 (top) and 5 (bottom). All the H atoms and the balanced anion have been omitted for clarity.

$c_{\text{calcd}}T)^2/\Sigma(c_{\text{obsd}}T)^2 = 4.37 \times 10^{-5}$. The small positive J value indicates also the ferromagnetic interaction in complex **1**. To further confirm the magnetic coupling nature in complex **1**, the field-dependent magnetization measured up to 50 kOe at 2 K was carried out. The experimental M-H curve (Inset of Figure 5) are basically consistent with the calculated Brillouin function corresponding to the ferromagnetic coupled low spin Fe(III) ($S = 1/2$) ion and high spin Fe(III) ($S = 5/2$) ion with $g = 2.0$ at 2 K. The saturated magnetization value is about $5.89 N\beta$, which is very close to the expected theoretical value ($6.0 N\beta$), indicating further the existed overall weak ferromagnetic interactions between the adjacent Fe(III) ions.

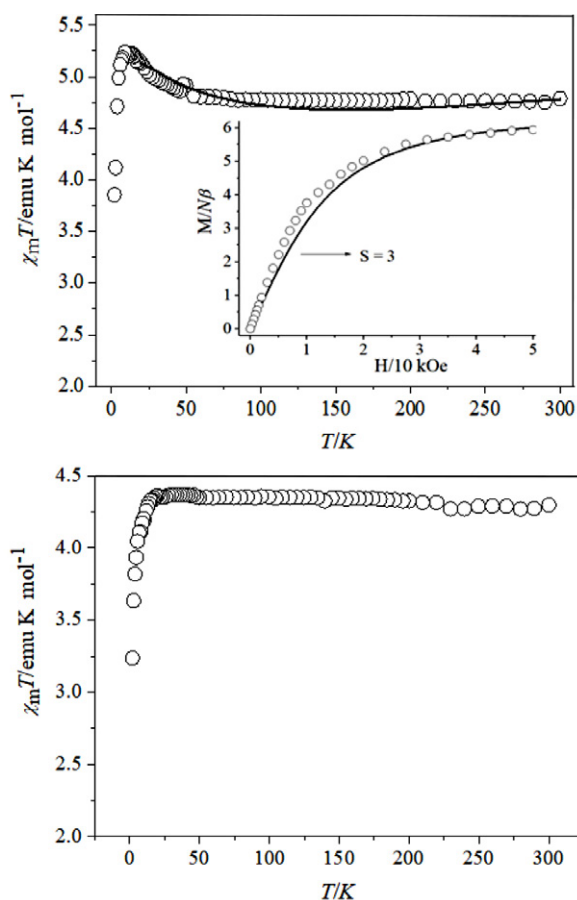


Figure 5. Temperature dependence of $\chi_m T$ of **1** (top) and **2** (bottom). Inset: Field dependence of magnetization at 2 K of complex **1** (the solid Brillouin curve is the ferromagnetic coupled one low spin Fe(III) ion and one high spin Fe(III) ion for complex **1**).

The $\chi_m T$ - T curves of complexes **3–5** are shown in Figure 6 and Figure S1 (Support Information). The room temperature $\chi_m T$ value for complex **3** is about $7.4 \text{ emu K mol}^{-1}$, indicating the two Fe(III) ions bridged by the bipyridine ligand are with almost complete high spin state. For complexes **4** and **5**, the $\chi_m T$ values at 300 K are only 1.82 and $1.41 \text{ emu K mol}^{-1}$, providing clear information that the stable high spin state of the Fe(III) ions in these

two complexes outclass the room temperature. With the temperature lowering, the $\chi_m T$ for all the three complexes decreases with a rapid speed to about 1.33, 0.61 and $0.55 \text{ cm}^3 \text{ K mol}^{-1}$ at about 115, 170 and 200 K, respectively, showing the occurrence of a gradually almost complete spin transition. After that, the $\chi_m T$ values keep almost constant with the temperature cooling to 2 K, indicating the stable low spin state at low temperature for these three complexes. Such types of the $\chi_m T$ - T change tendency can also be found in the reported examples based on the similar pentadentate Schiff base Fe(III) precursor and pyridine-like ligands.

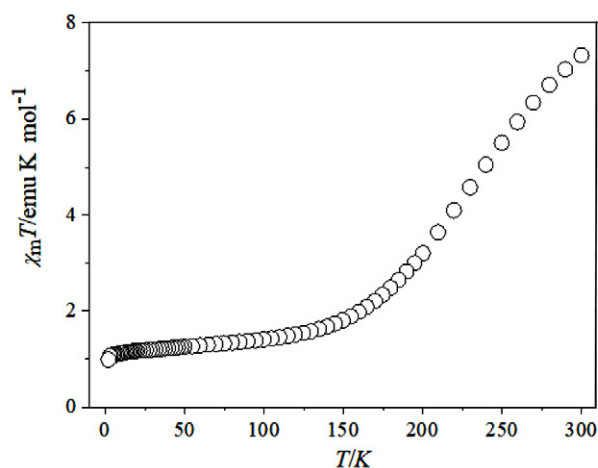


Figure 6. Temperature dependence of $\chi_m T$ of **3**

4. Conclusion

In summary, for the purpose of preparation of Fe(I–II)-based spin crossover molecular magnetic materials, the reactions of pentadentate Schiff base based Fe(III) compounds with the *trans*-dicyanometallates or the pyridine-type ligands were investigated, leading to cyano precursor or 4,4'-bipy bridged binuclear and pyridine coordinated mononuclear complexes. The study over the temperature dependence of the magnetic susceptibility and the field-dependent magnetization revealed the ferromagnetic coupling in cyanide-bridged Fe(III)(low spin)-Fe(III)(high spin) complex. For the pyridine-like ligand involved mono- or binuclear Fe(III) complexes, the thermo-induced gradual complete spin crossover behavior occurring at different temperatures could be found, revealed the important role of the auxiliary ligand with different coordination fields, which provided meaningful information for the future design of SCO magnetic material.

Acknowledgement

This work was supported by the Natural Science Foundation of China (22171166). All authors disclosed no relevant relationships.

5. References

- P. Wang, Y. Xu, Q. Lin and M. Lu, *Chem. Soc. Rev.* **2018**, *20*, 7522–7538. DOI:10.1039/C8CS00372F
- P. He, J. G. Zhang, X. Yin, J. T. Wu, L. Wu, Z. N. Zhou and T. L. Zhang, *Chem. Eur. J.* **2016**, *22*, 7670–7685. DOI:10.1002/chem.201600257
- D. K. Mahapatra, S. K. Bharti, V. Asati and S. K. Singh, *Eur. J. Med. Chem.* **2019**, *174*, 142–158. DOI:10.1016/j.ejmech.2019.04.032
- J. K. Sun, X. D. Yang, G. Y. Yang and J. Zhang, *Coord. Chem. Rev.* **2019**, *378*, 533–560. DOI:10.1016/j.ccr.2017.10.029
- J. G. Haasnoot, *Coord. Chem. Rev.* **2000**, *200*, 131–185. DOI:10.1016/S0010-8545(00)00266-6
- G. N. Liu, W. J. Zhu, Y. N. Chu and C. Li, *Inorg. Chim. Acta.* **2015**, *425*, 28–35. DOI:10.1016/j.ica.2014.10.024
- R. Mukherjee, *Coord. Chem. Rev.* **2000**, *203*, 151–218. DOI:10.1016/S0010-8545(99)00144-7
- M. B. Bushuev, Y. V. Gatilov, V. P. Krivopalov and O. P. Shkurko, *Inorg. Chim. Acta.* **2015**, *425*, 182–188. DOI:10.1016/j.ica.2014.10.017
- C. Gao, J. Wang, H. Xu and Y. Xiong, *Chem. Soc. Rev.* **2017**, *46*, 2799–2823. DOI:10.1039/C6CS00727A
- R. D. Antonio, J. M. Antonio, C. Joan, R. José, D. C. L. Duane and C. Enrique, *Dalton Trans.* **2009**, *32*, 6335–6344.
- J. S. Miller and D. Gatteschi, *Chem. Soc. Rev.* **2011**, *40*, 3065–3066. DOI:10.1039/c1cs90019f
- T. K. Ekanayaka, G. Hao, A. Mosey, A. S. Dale, X. Jiang, A. J. Yost, K. R. Sapkota, G. T. Wang, J. Zhang, A. T. N'Diaye, A. Marshall, R. Cheng, A. Naeemi, X. Xu and P. A. Dowben, *Magnetochemistry*. **2021**, *7*, 37. DOI:10.3390/magnetochemistry7030037
- Y. Chen, J. G. Ma, J. J. Zhang, W. Shi, P. Cheng, D. Z. Liao and S. P. Yan, *Chem. Commun.* **2010**, *46*, 5073–5075. DOI:10.1039/b927191k
- M.-L. Hu, A. Morsali and L. Aboutorabi, *Coord. Chem. Rev.* **2011**, *255*, 2821–2859. DOI:10.1016/j.ccr.2011.05.019
- B. Brizet, A. Eggenspieler, C. P. Gros, J. M. Barbe, C. Goze, F. Denat and P. D. Harvey, *J. Org. Chem.* **2012**, *77*, 3646–3650. DOI:10.1021/jo3000833
- D. Tanaka, N. Aketa, H. Tanaka, T. Tamaki, T. Inose, T. Akai, H. Toyama, O. Sakata, H. Tajiri and T. Ogawa, *Chem. Commun.* **2014**, *50*, 10074–10077. DOI:10.1039/C4CC04123B
- M. A. Halcrow, *Chem. Lett.* **2014**, *43*, 1178–1188. DOI:10.1246/cl.140464
- A. Bousseksou, G. Molnár, L. Salmon and W. Nicolazzi, *Chem. Soc. Rev.* **2011**, *40*, 3313–3335. DOI:10.1039/c1cs15042a
- A. Tissot, X. Kesse, S. Giannopoulou, I. Stenger, L. Binet, E. Rivière and C. Serre, *Chem. Commun.* **2019**, *55*, 194–197. DOI:10.1039/C8CC07573E
- D. Gao, Y. Liu, B. Miao, C. Wei, J. G. Ma, P. Cheng and G. M. Yang, *Inorg. Chem.* **2018**, *57*, 12475–12479. DOI:10.1021/acs.inorgchem.8b02408
- A. B. Gaspar, V. Ksenofontov, M. Seredyuk and P. Gülich, *Coord. Chem. Rev.* **2005**, *249*, 2661–2676. DOI:10.1016/j.ccr.2005.04.028
- B. Benaicha, K. Van. Do, A. Yangui, A. Yangui, N. Pittala, A. Lusson, M. Sy, G. Bouchez, H. Fourati, C. J. Gómez-García, S. Triki and K. Boukheddaden, *Chem. Sci.* **2019**, *10*, 6791–6798. DOI:10.1039/C9SC02331C
- R. Ohtani and S. Hayami, *Chem. Eur. J.* **2017**, *23*, 2236–2248. DOI:10.1002/chem.201601880
- Z. P. Ni, J. L. Liu, M. N. Hoque, W. Liu, J. Y. Li, Y. C. Chen and M. L. Tong, *Coord. Chem. Rev.* **2017**, *335*, 28–43. DOI:10.1016/j.ccr.2016.12.002
- J. L. Wang, Q. Liu, Y. S. Meng, X. Liu, H. Zheng, Q. Shi, C. Y. Duan and T. Liu, *Chem. Sci.* **2018**, *9*, 2892–2897. DOI:10.1039/C7SC05221A
- S. Soleymani-Babadi, A. Beheshti, M. Bahrani-Pour, P. Mayer, H. Motamedi, D. Trzybinski and K. Wozniak, *Cryst. Growth. Des.* **2019**, *19*, 4934–4948. DOI:10.1021/acs.cgd.9b00038
- A. Beheshti, E. S. M. Fard, M. Kubicki, P. Mayer, C. T. Abrahams and S. E. Razatofighi, *Cryst. Eng. Comm.* **2019**, *21*, 251–262. DOI:10.1039/C8CE01348A
- M. A. Halcrow, *Chem. Soc. Rev.* **2011**, *40*, 4119–4142. DOI:10.1039/c1cs15046d
- I. Nemec, R. Boča, R. Herchel, Z. Trávníček, M. Gembický and W. Linert, *Monats. Chem.* **2009**, *140*, 815–828. DOI:10.1007/s00706-008-0096-0
- Y. Komatsumaru, M. Nakaya, F. Kobayashi, R. Ohtani, M. Nakamura, L. F. Lindoy and S. Hayami, *Z. Anorg. Allg. Chem.* **2018**, *644*, 729–734. DOI:10.1002/zaac.201800087
- S. Vela, M. Fumanal, J. Cirera and J. Ribas-Arino, *Phys. Chem. Chem. Phys.* **2020**, *22*, 4938–4945. DOI:10.1039/D0CP00162G
- T. Fujinami, K. Nishi, R. Kitashima, K. Murakami, N. Matsumoto, S. Iijima and K. Toriumi, *Inorg. Chim. Acta.* **2011**, *376*, 136–143. DOI:10.1016/j.ica.2011.06.004
- D. J. Harding, P. Harding and W. Phonsri, *Coord. Chem. Rev.* **2016**, *313*, 38–61. DOI:10.1016/j.ccr.2016.01.006
- S. Mukherjee, T. Weyhermüller, E. Bill, K. Wieghardt and P. Chaudhuri, *Inorg. Chem.* **2005**, *44*, 7099–7108. DOI:10.1021/ic050885l
- H. Chun, C. N. Verani, P. Chaudhuri, E. Bothe, E. Bill, T. Weyhermüller and K. Wieghardt, *Inorg. Chem.* **2001**, *40*, 4157–4166. DOI:10.1021/ic010106a
- M. Arai, W. Kosaka, T. Matsuda and S. Ohkoshi, *Chem. Int. Ed.* **2008**, *47*, 6885–6887. DOI:10.1002/anie.200802266
- K. Tanimura, R. Kitashima, N. Brefuel, M. Nakamura, N. Matsumoto, S. Shova and J. P. Tuchagues, *Bull. Chem. Soc. Jpn.* **2005**, *78*, 1279–1282. DOI:10.1246/bcsj.78.1279
- R. Kitashima, S. Imatomi, M. Yamada, N. Matsumoto and Y. Maeda, *Chem. Lett.* **2005**, *34*, 1388–1389. DOI:10.1246/cl.2005.1388
- W. Phonsri, L. C. Darveniza, S. R. Batten and K. S. Murray, *Inorganics*. **2017**, *5*, 51. DOI:10.3390/inorganics5030051
- W. Phonsri, D. Macedo, B. A. Lewis, D. F. Wain and K. S. Murray, *Magnetochemistry*. **2019**, *5*, 37. DOI:10.3390/magnetochemistry5020037
- W. Phonsri, B. A. I. Lewis, G. N. L. Jameson and K. S. Murray, *Chem. Commun.* **2019**, *55*, 14031–14034.

- DOI:10.1039/C9CC07416C
42. O. I. Kucheriv, I. O. Fritsky and I. A. Gural'skiy, *Inorg. Chim. Acta*. **2021**, 521, 120303. DOI:10.1016/j.ica.2021.120303
43. Z. H. Ni, L. F. Zhang, C. H. Ge, A. L. Cui, H. Z. Kou and J. Jiang, *Transit. Metal. Chem.* **2008**, 11, 94–96. DOI:10.1016/j.inoche.2007.10.017
44. D. Zhang and H. Zhang, *Polyhedron*. **2015**, 100, 36–42. DOI:10.1016/j.poly.2015.07.024
45. D. Zhang, L. Kong, P. Wang and X. Chen, *Synth. Ynth. React. Inorg. M.* **2016**, 46, 828–831. DOI:10.1080/15533174.2014.989597
46. J. Shi, Q. Meng, C. Xue, Q. Liu and D. Zhang, *Transit. Metal. Chem.* **2018**, 43, 45–52. DOI:10.1007/s11243-017-0192-2
47. Z. H. Ni, H. Z. Kou, L. F. Zhang, C. Ge, R. J. Wang and A. L. Cui, *J. Chem. Crystallog.* **2006**, 36, 465–472.
48. D. Zhang, P. Wang, Z. Zhao and X. Chen, *J. Coord. Chem.* **2014**, 67, 1664–1672. DOI:10.1080/00958972.2014.918266
49. R. Boča, Y. Fukuda, M. Gembický, R. Herchel, R. Jaroščík, W. Linert, F. Renz and J. Yuzurihara, *Chem. Phys. Lett.* **2000**, 325, 411–419. DOI:10.1016/S0009-2614(00)00701-6
50. R. Kitashima, S. Imatomi, M. Yamada, N. Matsumoto and Y. Maeda, *Chem. Lett.* **2005**, 34, 1388–1389. DOI:10.1246/cl.2005.1388
51. N. Matsumoto, S. Ohta, C. Yoshimura, A. Ohyoshi, S. Kohata, H. Okawa and Y. Maeda, *J. Chem. Soc. Dalton Trans.* **1985**, 12, 2575–2584. DOI:10.1039/dt9850002575
52. H. Z. Kou, Z. H. Ni, C. M. Liu, D. Q. Zhang and A. L. Cui, *New J. Chem.* **2009**, 33, 2296–2299. DOI:10.1039/b9nj00316a
53. T. Senapati, C. Pichon, R. Ababei, C. Mathonier and R. Clérac, *Inorg. Chem.* **2012**, 51, 3796–3812. DOI:10.1021/ic2027708

Povzetek

Serijska dvo- ali enojedernih heksakoordiniranih kompleksov železa(III), $[\text{Fe}(\text{L})][\text{Fe}(\text{bpb})(\text{CN})_2] \cdot \text{CH}_3\text{OH} \cdot 0.5\text{H}_2\text{O}$ (**1**), $[\text{Fe}(\text{L})][\text{Co}(\text{bpb})(\text{CN})_2] \cdot \text{CH}_3\text{OH}$ (**2**), $[(\text{Fe}(\text{L}))_2(4,4'\text{-bipy})](\text{BPh}_4)_2$ (**3**), $[\text{Fe}(\text{L})(\text{py})](\text{BPh}_4)$ (**4**) in $[\text{Fe}(\text{L})(\text{dmap})](\text{BPh}_4)$ (**5**) (bpb = 1,2-bis(piridin-2-karboksamido)benzenat, L = N,N'-bis(2-hidroksibenziliden)-1, 7-diamino-4-azaheptan, dmap = 4-dimetilaminopiridin), je bila pripravljena iz železovega(III) kompleksa s pentadentatno Schiffovo bazo kot prekursorjem ter okarakterizirana z elementno analizo, IR in rentgensko difrakcijo. Strukturna analiza monokristalov je razkrila nevtralno cianidno vezano dvojedrno zvrst za kompleksa **1** in **2** ter kationsko dvo- ali enojedrno strukturo za komplekse **3–5** s pozitivnim nabojem ter BPh_4^- protiionom. Eksperimenti in teoretične simulacije magnetnih lastnosti razkrijejo feromagnetno sklopitev med Fe(III) ioni, ki jih povezuje cianidna skupina v kompleksu **1**, in visokospinsko stanje Fe(III) iona, koordiniranega z ligandom Schiffove baze v kompleksih **1** in **2**. Raziskava magnetne susceptibilnosti kompleksov **3–5** v odvisnosti od temperature je pokazala, da se pri približno 115, 170 in 200 K pojavi toplotno-induciran popoln spinski prehod.



Except when otherwise noted, articles in this journal are published under the terms and conditions of the Creative Commons Attribution 4.0 International License

Scientific paper

Zinc(II) Complex Containing Oxazole Ring: Synthesis, Crystal Structure, Characterization, DFT Calculations, and Hirshfeld Surface Analysis

Karwan Omer Ali,^{1,*} Hikmat Ali Mohamad,² Thomas Gerber³ and Eric Hosten³¹ Department of Physics, College of Science, University of Halabja, Halabja 46018, Iraq² Department of Chemistry, College of Education, Salahaddin University, Erbil 44001, Iraq³ Department of Chemistry, Faculty of Science, Nelson Mandela University, Port Elizabeth 6031, South Africa

* Corresponding author: E-mail: karwan.ali@uoh.edu.iq

Phone No. 009647503849284

Received: 07-12-2022

Abstract

A new complex of Zn(II), with 5-chloro-2-methylbenzoxazole ligand (L), has been synthesized by the reaction of zinc dichloride with the ligand (L= C₈H₆ClNO) in ethanol solution: dichloridobis(5-chloro-2-methyl-1,3-benzoxazole)-zinc(II), C₁₆H₁₂Cl₄N₂O₂Zn. The synthesized complex has been fully characterized by elemental analysis, molar conductivity, FT-IR, UV-Vis, and single-crystal X-ray diffraction (XRD). The XRD analysis reveals that the complex has a 1:2 metal-to-ligand ratio. The zinc(II) complex has a distorted tetrahedral geometry with two coordinated nitrogen atoms from the ligand. Density Functional Theory (DFT) calculations were performed at the B3LYP level of theory using the LANL2DZ basis set for metal complex and the 6-31G(d) basis set for non-metal elements to determine the optimum geometry structure of the complex, and the calculated HOMO and LUMO orbital energies were presented. A natural bond orbital (NBO) analysis was carried out on the molecules to analyze the atomic charge distribution before and after the complexation of the ligand. The Hirshfeld surface mapped over d_{norm} , shape index, and curvature exhibited strong H...Cl/Cl...H and H...H intermolecular interactions as the principal contributors to crystal packing.

Keywords: Zn(II), Benzoxazole, Distorted tetrahedral geometry, Hirshfeld surface analysis, NBO analysis, DFT calculations

1. Introduction

Benzoxazole is a bicyclic heterocyclic compound containing both oxygen and nitrogen atoms in which the benzene ring is fused to a 1,3-oxazole ring at positions 4 and 5.¹ It is one of the most common heterocyclics in industry and scientific research.² Transition metal ions have different binding forces with N and O atoms.³ Commonly, N-donor oxazole groups have demonstrated excellent coordination ability with the first-row transition metal ions.⁴ Due to the variety of coordination modes and configurations, N-heterocyclic ligands are typically used as neutral ligands in the synthesis of metal complexes.^{5,6} Counterions are used to balance the total charge when studying the neutral ligand, which not only affects the coordination modes of the metal ions but also the entire geometry of the met-

al complex.^{7,8} Most Zn(II) complexes show tetrahedral and distorted tetrahedral coordination geometries, in agreement with a d^{10} electronic configuration.^{9,10} Thus, the strategy of using neutral mono and bidentate ligands with metal halides to force tetrahedral geometry has been widely used for stabilizing Zn(II) complexes. Similarly, benzoxazole derivatives have also been used to stabilize zinc in a +2 oxidation state.¹¹ Because of their good emission properties and inexpensive cost compared to other d^{10} metal complexes, zinc (II) complexes have been shown to be important candidates for electroluminescent applications. For example, the Zinc(II) complex of [(2-(2-hydroxyphenyl)benzoxazole)(2-methyl-8-hydroxyquinoline)] has been recognized as a blue-emitting zinc complex to fabricate stacked organic light-emitting diodes.¹² Changes in the intermolecular interactions between metal ions and ligands that are

studied by the Hirshfeld surface analysis and DFT calculations can be seen in a series of Zinc(II) complexes with 2-(4-imidazolyl)-4-methyl-1,2-quinazoline- N^3 -oxide,¹³ 2-cetylpyridinenicotinichydrazone,¹⁴ and sulfamethoxazole,¹⁵ etc. Nonetheless, data on X-ray crystal structures and theoretical studies of related complexes containing an oxazole ring are scarce. The current work reports the synthesis and characterization of a new zinc(II) complex based on a 5-chloro-2-methylbenzoxazole ligand (L), which was characterized by elemental analysis, molar conductivity, FT-IR, UV-Vis, and X-ray analysis. Furthermore, the crystal structure was verified using Hirshfeld surface analysis, and it is helpful for understanding the intermolecular forces in crystal packing. In addition, DFT calculations were done to predict the electronic and geometrical structure of the complex.

2. Experimental

2.1. Materials and General Methods

The solvents used in this study (Ethanol 99% and dimethyl sulfoxide 99.8%) were purchased from Alfa Aesar and used without further purification. 5-Chloro-2-methylbenzoxazole produced by Sigma Aldrich was used without purification. Single-crystal X-ray structure measurement was performed at 200 K using a Bruker Kappa Apex II diffractometer with a radiation wavelength of ($\lambda = 0.71073 \text{ \AA}$). C, H, N, and O percentages were determined by EURO EA 300 CHNS analyzer. A Shimadzu FT-IR-8400S spectrophotometer was used to record infrared spectra in the 4000–400 cm^{-1} range as KBr discs and the 600–200 cm^{-1} range as CsI discs. The UV-visible spectra in DMSO were measured on the AEUV1609 LTD Shimadzu spectrophotometer. The molar conductivities were measured on Meter CON 700 Benchtop conductivity meter using 10^{-3} M solutions of the complex and ligands in DMSO at room temperature. The melting point was measured using scientific Stuart SMP3 melting point equipment.

2.2. Synthesis of $[\text{Zn}(\text{L})_2\text{Cl}_2]$

A solution of ZnCl_2 (0.284 g, 2.0 mmol) in ethanol (25 mL) was added dropwise under stirring to a solution of 5-chloro-2-methylbenzoxazole ($\text{L}=\text{C}_8\text{H}_6\text{ClNO}$) ligand (0.670 g, 4.0 mmol) in ethanol (25 mL). Subsequently, the mixture was stirred for 5 hrs. at room temperature with the formation of a clear solution, which was then evaporated slowly at room temperature to yield pale-yellow crystalline products within one week. m.p. 208–209 °C. Yield: 0.915 g (96%). Anal. Calcd. for $\text{C}_{16}\text{H}_{12}\text{Cl}_4\text{N}_2\text{O}_2\text{Zn}$: C 41.10, H 2.56, N 5.94, O 6.78. Found: C 41.05, H 2.70, N 5.97, O 6.79. Molar conductivity: $9.11 \times 10^{-5} \text{ S cm}^2 \text{ mol}^{-1}$. FT-IR (KBr) 3091, 3062, 1600, 1562, 1452, 1303, 445, 343 cm^{-1} . UV-Vis data in DMSO [λ/nm , (cm^{-1}): 426(23474), 287(34843), 280(35714).

2.3. X-ray Crystal Structure Determination

X-ray diffraction measurement for the Zn(II) complex was performed on a Bruker Kappa Apex II X-ray diffractometer equipped with graphite monochromated Mo-K α radiation ($\lambda = 0.71073 \text{ \AA}$) at 200 K. The structure was solved by a dual-space algorithm using SHELXT-2018 and refined by least-squares procedures using the SHELXL-2018/3 crystallographic software.^{16,17} All C, N, Cl, O, and Zn atoms were anisotropically resolved. The hydrogen atoms attached to C atoms were allowed to rotate geometrically and treated as a riding model with a C-H distance of 0.95 \AA (aromatic) and 0.98 \AA ($-\text{CH}_3$ group) with $U_{\text{iso}}(\text{H}) = 1.2 U_{\text{eq}}(\text{C})$.¹⁸ The crystal data and structure refinement details for the complex are summarized in (Table 1).

Table 1. Crystal data and structure refinement of the complex

Formula	$\text{C}_{16}\text{H}_{12}\text{Cl}_4\text{N}_2\text{O}_2\text{Zn}$
Formula weight	471.47
Temperature, K	200
Wavelength, nm	0.71073
Crystal system	Monoclinic
Space group	$\text{P2}_1/\text{n}$
Crystal size, mm	$0.52 \times 0.53 \times 0.67$
$a / \text{\AA}$	7.5590(5)
$b / \text{\AA}$	7.1873(5)
$c / \text{\AA}$	33.842(2)
$\alpha / ^\circ$	90
$\beta / ^\circ$	95.101(3)
$\gamma / ^\circ$	90
$V / \text{\AA}^3$	1831.3(2)
Z	4
$D_c / \text{g cm}^{-3}$	1.710
Absorption coefficient, mm^{-1}	1.937
θ range for data collection, $^\circ$	2.4, 28.3
Dataset	–10:9; –9:9; –43:45
F_{000}	944
No. of reflections	4539
No. of parameters	228
R_{int}	0.027
R_1, wR_2	0.0405, 0.0921
S	1.28
$[I > 2\sigma(I)]$	4325
$\Delta\rho_{\text{min}}, \Delta\rho_{\text{max}} / \text{e \AA}^{-3}$	–0.83, 0.47

2.4. Computational Details

To better understand the structure of the zinc complex, the Gaussian 09 software package was used for density functional theory (DFT) calculations. The frontier molecular orbitals of the ligand and the Zn(II) complex were helped by the Gauss View 6.0 software at the B3LYP level of theory. In particular, the LANL2DZ basis set for the zinc metal atom¹⁹ and the 6-31G(d)²⁰ basis set for

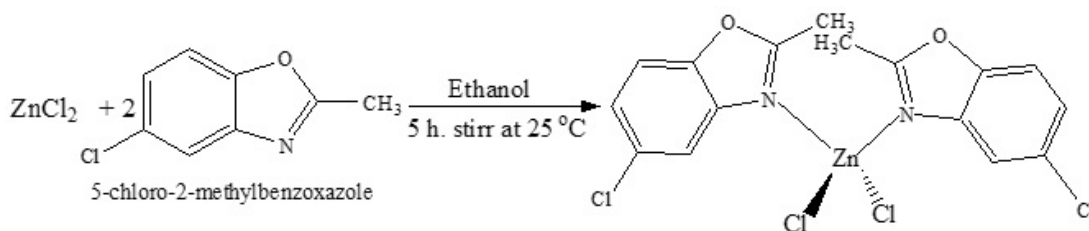
non-metal elements (C, H, N, O, and Cl) were both treated. The neutral bond orbital (NBO) analysis of the complex was done using the Gaussian 09 program at the same level of theory.²¹

2. 5. Hirshfeld Surface

A crystallographic information file (CIF) obtained from single-crystal X-ray diffraction analysis was used as an input file for Hirshfeld surface visualization of the zinc complex. To generate the Hirshfeld surface analysis and a better understanding of the intermolecular interactions in the complex crystal structure, the program Crystal Explorer 21.5 was used.²² Hirshfeld surface visualization, presentation of results as d_{norm} , shape index, and curvedness, and calculation of 2D fingerprint plots with deans d_e and d_i distances were produced using the same software.²³

4. Results and Discussion

The zinc (II) complex is formed by the complexation of Zn(II) chloride with the 5-chloro-2-methylbenzoxazole ligand, as shown in (Scheme 1). The complex is stable under atmospheric conditions. The complex was produced as pale-yellow crystals at a good yield suitable for single-crystal X-ray structure analysis. At room temperature, the complex is soluble in common organic solvents such as dimethyl sulfoxide, dimethylformamide, and chloroform, but not in ethanol, acetone, methanol, and petroleum ether.



Scheme 1. Synthetic route of the Zn(II) complex.

3. 1. The Crystal Structure Description of the Zn(II) Complex

The crystal molecular structure of the $[\text{Zn}(\text{L})_2(\text{Cl})_2]$ complex was depicted in (Figure 1). Relevant bond lengths and bond angles from X-ray diffraction are summarized in (Table 2). Through two nitrogen atoms from the oxazole ring and two chlorine atoms, the Zn(II) metal is located on a crystal lattice center and achieves a slightly distorted tetrahedral coordination geometry. Bond angles of the internal coordination sphere of the complex, which are different from the ideal angle of 109° for a perfect tetrahedral geometry, are $[(\text{Cl}3-\text{Zn}1-\text{Cl}4) 120.52(3)^\circ, (\text{Cl}3-\text{Zn}1-\text{N}1)$

$108.88(7)^\circ, (\text{Cl}3-\text{Zn}1-\text{N}2) 104.79(7)^\circ, (\text{Cl}4-\text{Zn}1-\text{N}2) 109.70(8)^\circ$, and $(\text{Cl}4-\text{Zn}1-\text{N}1) 104.99(7)^\circ]$. The Zn-Cl bond distances range between $2.1986(7)$ and $2.2799(14)$ Å, and the bond angles involving the Zn(II) atom range between $97.5(13)^\circ$ and $114.87(11)^\circ$ are comparable to those found in the literature.^{24,25} The bond distances between Zn1-N1 ($2.068(3)$) and Zn1-N2 ($2.042(3)$) are shorter than those between Zn1-Cl3 ($2.2154(9)$) and (Zn-Cl4 $2.2227(9)$), indicating that the interaction between Zn(II) metal center and N atom is stronger than that between Zn(II) and Cl atom. The Torsion/Dihedral Angles of N2-Zn1-N1-C17, N1-Zn1-N2-C27, Cl4-Zn1-N1-C11, and Zn1-N2-C21-C26 are $63.0(3)^\circ, 48.9(3)^\circ, 111.0(2)^\circ$, and $6.7(5)^\circ$ respectively, which results in a steric interaction between methyl groups on the benzoxazole rings and electron repulsion of chlorine atoms.²⁶ Consequently, crystallographically generated centroids Cg(1) to Cg(4) were related to the various aromatic rings around the Zn(II) centers. The distance between the adjacent ring centroids for Cg(1)...

Table 2. Selected bond distances (Å) and bond angles ($^\circ$) of the complex.

Zn1-Cl3	2.2154(9)	Cl3-Zn1-Cl4	120.52(3)
Zn1-Cl4	2.2227(9)	Cl3-Zn1-N1	108.88(7)
Zn1-N1	2.068(3)	Cl3-Zn1-N2	104.79(7)
Zn1-N2	2.042(3)	Cl4-Zn1-N1	104.99(7)
N1-C11	1.421(4)	Cl4-Zn1-N2	109.70(8)
N1-C17	1.302(4)	N1-Zn1-N2	107.41(11)
N2-C21	1.412(4)	C12-O1-C17	105.0(2)

Cg(1), Cg(2)---Cg(2), Cg(3)---Cg(3), and Cg(4)---Cg(4) are $4.7676(17), 4.5328(18), 5.4387(19)$, and $3.7652(18)$ Å respectively. As shown in Figure 1, the electron density around C18 clearly shows that this methyl group has the rotational disorder, whereas C28 has not. Each hydrogen for the C18 group has half occupancy, so the total number of hydrogens is three.

3. 2. FT-IR Spectra

In the free ligand (Fig. S1), the bands at 3093 cm^{-1} and 1166 cm^{-1} are attributed to C-H and C-Cl stretching vibrations, respectively.²⁷ Free 5-chloro-2-methylbenzoxazole shows strong intensity bands at 1608 cm^{-1} and 1253 cm^{-1} , with the two bands being assigned to the C=N and

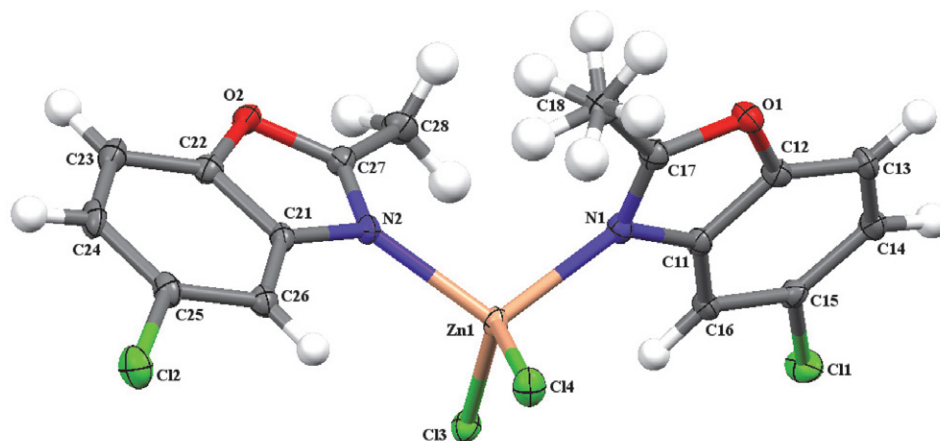


Figure 1. Single-crystal x-ray molecular structure of the complex. ellipsoids with a 30% of probability

C-O stretching vibrations of the oxazole group, respectively.^{28,29} The C=N band in the Zn(II) complex (Fig. S2) is shifted to lower wavenumber (1600 cm^{-1}) indicating the participation of benzoxazole nitrogen in coordination with the Zn(II) ion.³⁰ The presence of a new weak band at 445 cm^{-1} in the spectrum of the complex corresponding to the (Zn-N) vibration band also confirms the bonding between ligand and Zinc metal.³¹ In the IR spectrum of the zinc complex (Fig. S3), the weak band at 343 cm^{-1} was matching to Zn-Cl vibration.³²

3. 3. Electronic Spectra and Conductivity Properties

The electronic absorption spectra of 5-chloro-2-methylbenzoxazole (L) Ligand and their complex were measured at room temperature in $10^{-3}\text{ mol. L}^{-1}$ DMSO solution (Figure 2). The free ligand 5-chloro-2-methylbenzoxazole shows high energy absorption bands at 280 and 287 nm, which are attributed to ligand $\pi-\pi^*$ transitions of the benzene ring and C=N bond respectively.^{33,34} These absorption bands that remain unchanged in the spectrum of the complex indicate the coordination of the ligand to the Zn(II) metal center. Additionally, a new absorption

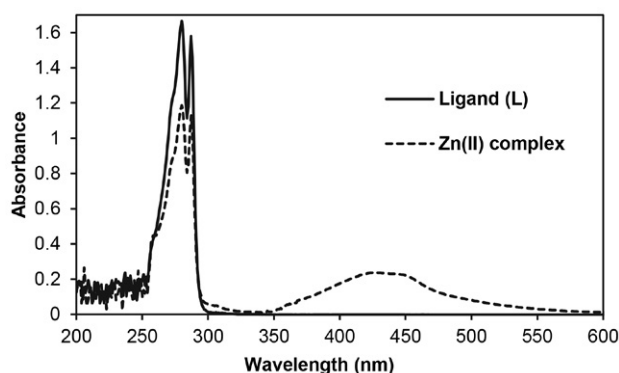


Figure 2. Electronic absorption spectra of ligand (L) and Zn(II) complex

peak in the complex was observed at 426 nm (23474 cm^{-1}), which is attributed to the ligand-to-metal charge transfer (LMCT) that is characteristic of the zinc metal complex.³⁵ The synthesized complex containing chlorinated ligand had a very low molar conductivity value in DMSO ($9.11 \times 10^{-5}\text{ S. cm}^2.\text{ mol}^{-1}$), showing that it is non-electrolyte in nature.³⁶

3. 4. DFT Studies

The frontier molecular orbitals were used to investigate the electronic properties of the ligand (L) and complex. The energies of the highest occupied molecular orbital (E_{HOMO}) and the lowest unoccupied molecular orbital (E_{LUMO}) are used to estimate the HOMO-LUMO energy gap ($\Delta E = E_{\text{LUMO}} - E_{\text{HOMO}}$). The E_{HOMO} , E_{LUMO} , and ΔE energy gaps of the ligand and Zn(II) complex are shown in (Table 3) and (Figure 3). The free 5-chloro-2-methylbenzoxazole ligand has an energy gap (ΔE) of 3.526 eV, while the Zn(II) complex has an ΔE of 2.423 eV. According to DFT calculations, Beheshti et al. reported the synthesis of a pyrazolyl-based mononuclear zinc(II) complex with a 4.59 eV HOMO-LUMO energy gap.³⁷ The HOMO-LUMO energy gap value of the zinc(II) complex based on the benzoyl hydrazone ligand was calculated by the DFT method to be 3.76 eV in 2017.³⁸ As a result, the synthesized zinc(II) complex in this study is less stable than those that have been previously described. The HOMO orbital primarily acts as an electron donor, whereas the LUMO orbital mainly acts as an electron acceptor. A metal complex that has a large HOMO-LUMO energy gap is more stable than one that has a small HOMO-LUMO energy gap. The calculated NBO atomic charges of atoms for the free ligand and its complex are collected in Table 3. The calculated charge on the zinc metal (+0.993) is lower than the formal charge of the zinc ion (+2), suggesting electron transfer from the ligand to the metal center.³⁹ The NBO data shows that the N2 atom in the complex has a greater negative charge than the N1 atom. This result supports X-ray results showing

the Zn1-N2 bond distance is shorter than the Zn1-N1 bond distance and suggests that N2 is coordinated to the metal center more strongly than N1.⁴⁰

Table 3. HOMO-LUMO orbital energies (eV) and NBO Charges (e) of ligand (L) and its complex

Parameter	Ligand	Zn complex	
E_{HOMO}	-5.672	-6.381	
E_{LUMO}	-2.146	-3.958	
ΔE	3.526	2.423	

The NBO charge of ligand and Zn(II) complex			
Atom	Ligand	Atom	Zn complex
Cl	0.009	Zn	0.993
N	-0.541	Cl4	-0.608
O	-0.505	Cl3	-0.605
		N1	-0.697
		N2	-0.737

3. 5. Hirshfeld Surfaces Analysis (HAS)

The Hirshfeld surface analyses (HSA) and the fingerprints of the zinc complex were achieved with Crystal

Explorer 21.5 program.²² Fingerprint plots of the complex is displayed in (Figure 4). Similarly, Hirshfeld surface (HS) of the complex is shown in (Figure 5). Figure 5 exposes surfaces that were mapped across d_{norm} , shape index, and curvature. The d_{norm} surface has been mapped over a range of -0.0490 to 1.3232 Å while shape index and curvedness are mapped over the ranges -1.0000 to 1.0000 Å and -4.0000 to 0.4000 Å, respectively. As illustrated in (Figure 4), the 2D fingerprint plots reveal that the major intermolecular interactions in the zinc complex are H...Cl/Cl...H, H...H, H...C/C...H, C...Cl/Cl...C, C...O/O...C, C...C, H...O/O...H, and O...Cl/Cl...O. The highest contribution to the overall Hirshfeld surface occurs due to H...Cl/Cl...H close contacts with 39.1%. The percentages of H...H, H...C/C...H, C...Cl/Cl...C, C...O/O...C, C...C, H...O/O...H, O...Cl/Cl...O, Cl...Cl, H...N/N...H, C...N/N...C, Zn...H/H...Zn, and Cl...N/N...Cl interactions are 21.7, 7.7, 7.0, 5.7, 4.7, 4.8, 3.4, 3.4, 1.8, 0.3, 0.3, and 0.1 % of the complex surface, respectively. The d_{norm} Hirshfeld surface of the complex shows red and white spots, which indicate the presence of C-H...Cl and C-H...H intermolecular interaction in the crystal structure of the zinc complex respectively. The shape index and curvedness of HS can be used to investigate π ... π stacking interaction, where blue triangles represent convex regions of the compound inside the surface and red triangles represent concave regions above the

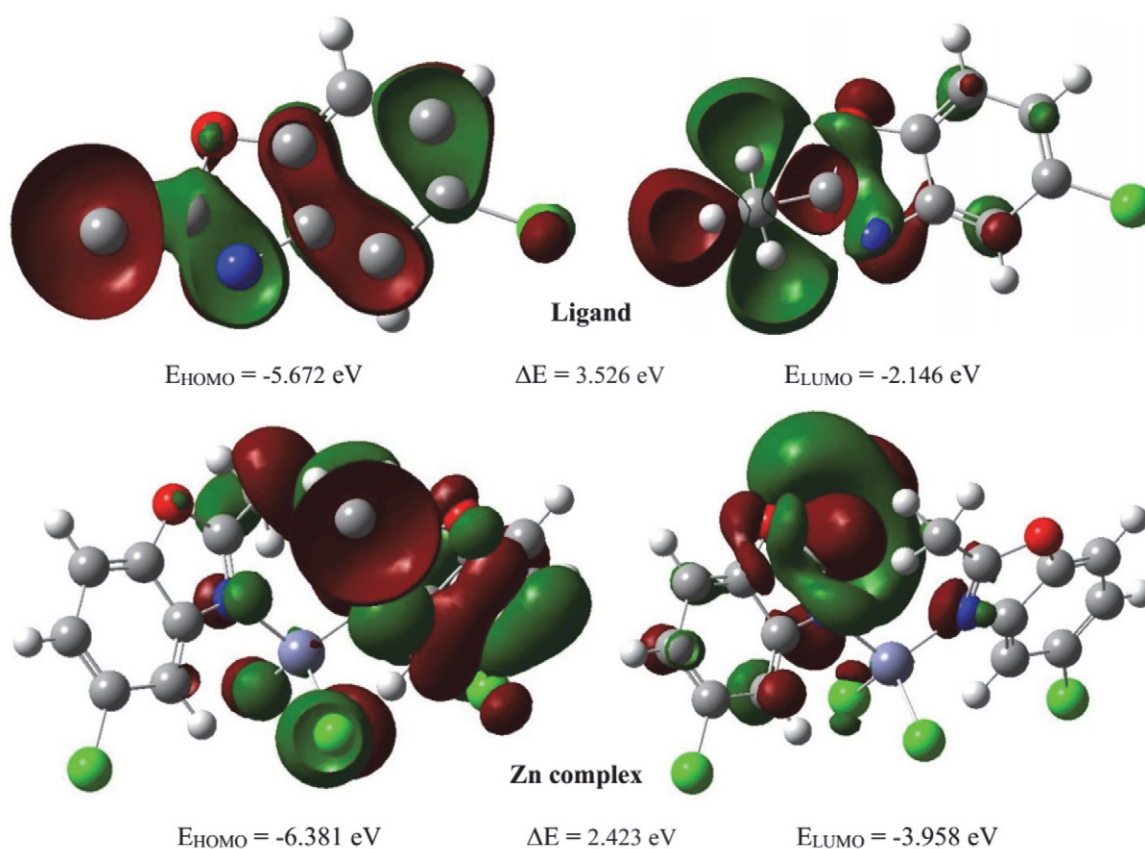


Figure 3. Surface plots of HOMO and LUMO orbitals of ligand (L) and zinc complex

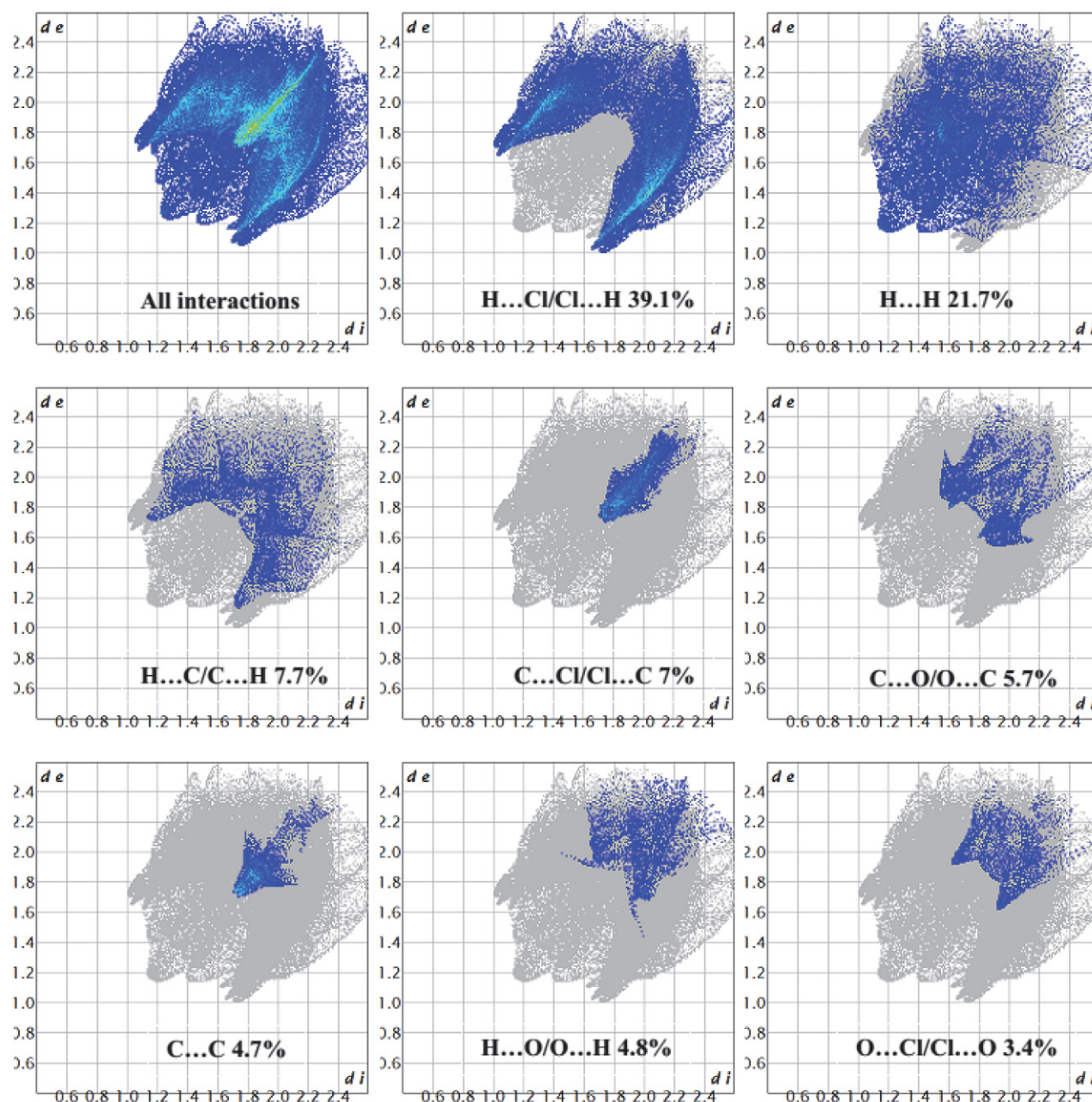


Figure 4: Fingerprint plots for the zinc(II) complex show the percentages of major contacts contributed to the total Hirshfeld surface analysis (HAS).

surface due to the $\pi\cdots\pi$ stacked compound's phenyl carbon atoms.⁴¹ Green flat regions on the curvedness surface also indicate the presence of $\pi\cdots\pi$ interaction in the complex.

4. Conclusion

In summary, a new zinc(II) complex was synthesized with a 5-chloro-2-methylbenzoxazole ligand. The spectroscopic method and crystallographic data indicated the formation of a mononuclear zinc complex with a ben-

zoxazole ligand acting as a monodentate ligand in neutral form. Structural analysis showed a tetracoordinate environment via two nitrogen and two chloride anions of the complex with distorted tetrahedral geometry. The electronic spectrum of the complex displayed a peak at 23474 cm^{-1} , which corresponded to the ligand-to-metal charge transfer (LMCT). The DFT study reveals that the zinc complex was less stable and more reactive than the ligand. The NBO analysis showed that the charge on the zinc metal surrounded by the nitrogen atoms of the ligand is 0.993 e found to be lower than the formal charge of the zinc ion

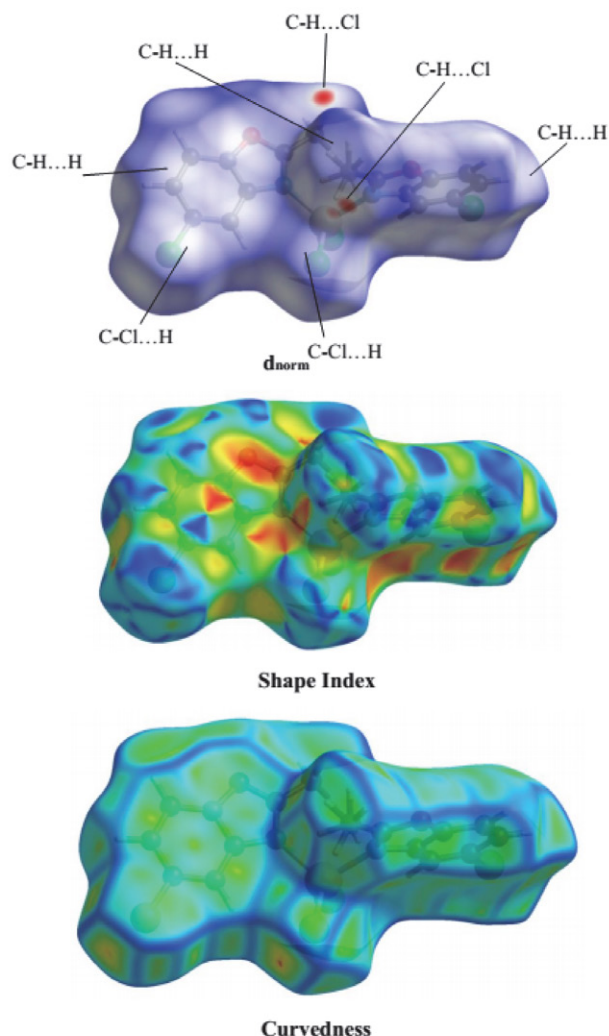


Figure 5: Hirshfeld surfaces mapped with d_{norm} , shape index, and curvedness of zinc(II) complex

(+2). The Hirshfeld surface and 2D fingerprint plots analysis showed various H... Cl/Cl ...H (39.1%), H ... H (21.7%), and H...C/C... H (7.7%) noncovalent interactions are the driving force in stable crystal packing.

Supplementary material

Crystallographic data for the Zn(II) complex have been deposited with the Cambridge crystallographic data Center (CCDC), with the deposit number 2097040. The data can be obtained free of charge via <http://www.ccdc.cam.ac.uk/conts/retrieving.html>.

Acknowledgments

The authors would like to acknowledge the department of chemistry, college of education, University of Salahaddin and the department of physics, college of science, University of Halabja for providing the required assistance

to complete the present study. We acknowledge Nelson Mandela University for single-crystal X-ray diffraction analysis. The authors would also like to thank Mr. Mzgin Ayoob for assisting us with the FT-IR measurement.

Funding

The authors would like to acknowledge the college of science, University of Halabja in Kurdistan region, Iraq for providing the financial funding throughout this study.

5. References

1. D. F. Back, G. M. de Oliveira, M. A. Ballin, V. A. Corbellini, *Inorg. Chim. Acta.* **2010**, 363, 807–812. DOI:10.1016/j.ica.2009.11.033
2. Y. Xu, S. Mao, K. Shen, X. Shi, H. Wu, X. Tang, *Inorg. Chim. Acta.* **2018**, 471, 17–22. DOI:10.1016/j.ica.2017.10.023
3. A. Altun, S. Dursun, N. M. Aghatabay, *Vib. Spectrosc.* **2015**, 81, 1–12. DOI:10.1016/j.vibspec.2015.09.001
4. L. Wang, H. Zhou, J. Wu, Y. Tian, *Dalton Trans.* **2015**, 44, 9921–9926. DOI:10.1039/C5DT01090J
5. Y. X. Sun, W. Y. Sun, *Cryst. Eng. Comm.* **2015**, 17, 4045–4063. DOI:10.1039/C5CE00372E
6. H. Wu, J. Zhang, C. Chen, H. Zhang, H. Peng, F. Wang, Z. Yang, *New J. Chem.* **2015**, 39, 7172–7181. DOI:10.1039/C5NJ01684C
7. M. M. Kimani, D. Watts, L. A. Graham, D. Rabinovich, G. P. Yap, J. L. Brumaghim, *Dalton Trans.* **2015**, 44, 16313–16324. DOI:10.1039/C5DT02232K
8. H. Wu, H. Wang, X. Wang, G. Pan, F. Shi, Y. Zhang, Y. Bai, J. Kong, *New J. Chem.* **2014**, 38, 1052–1061. DOI:10.1039/c3nj01145c
9. K. Zhao, Y. Qu, Y. Wu, C. Wang, K. Shen, C. Li, H. Wu, *Transit. Met. Chem.* **2019**, 44, 713–720. DOI:10.1007/s11243-019-00340-4
10. I. B. Lozada, T. Murray, D. E. Herbert, *Polyhedron.* **2019**, 161, 261–267. DOI:10.1016/j.poly.2019.01.023
11. S. E. Korolenko, K. P. Zhuravlev, V. I. Tsaryuk, A. S. Kubasov, V. V. Avdeeva, E. A. Malinina, A. S. Burlov, L. N. Divaeva, K. Y. Zhizhin, N. T. Kuznetsov, *J. Lumin.* **2021**, 237, 118156–118169. DOI:10.1016/j.jlumin.2021.118156
12. P. Tyagi, R. Srivastava, A. Kumar, V. K. Rai, R. Grover, M. N. Kamalasanan, *Synth. Met.* **2010**, 160, 756–761. DOI:10.1016/j.synthmet.2010.01.016
13. H. B. Zhang, X. F. Zhang, L. Q. Chai, L. J. Tang, H. S. Zhang, *Inorg. Chim. Acta.* **2020**, 507, 119610–119621. DOI:10.1016/j.ica.2020.119610
14. P. H. Santiago, M. B. Santiago, C. H. Martins, C. C. Gatto, *Inorg. Chim. Acta.* **2020**, 508, 119632–119641. DOI:10.1016/j.ica.2020.119632
15. I. Habila, M. Saoudi, F. Berrah, B. Benmerad, M. Boudraa, H. Merazig, S. Bouacida, *J. Mol. Struct.* **2021**, 1244, 130903–130913. DOI:10.1016/j.molstruc.2021.130903
16. G. M. Sheldrick, *Acta Crystallogr. A: Found. Adv.* **2015**, 71,

- 3–8. DOI:10.1107/S2053273314026370
17. C. B. Hübschle, G. M. Sheldrick, B. Dittrich, *J. Appl. Crystallogr.* **2011**, *44*, 1281–1284. DOI:10.1107/S0021889811043202
18. L. Krause, R. Herbst-Irmer, G. M. Sheldrick, D. Stalke, *J. Appl. Crystallogr.* **2015**, *48*, 3–10. DOI:10.1107/S1600576714022985
19. T. Li, Y. Hu, *Opt. Mater.* **2020**, *109*, 110260–110264. DOI:10.1016/j.optmat.2020.110260
20. L. Q. Chai, Q. Hu, K. Y. Zhang, L. Zhou, J. J. Huang, *J. Lumin.* **2018**, *203*, 234–246. DOI:10.1016/j.jlumin.2018.06.058
21. N. S. Abdel-Kader, S. A. Abdel-Latif, A. L. El-Ansary, A. G. Sayed, *J. Mol. Struct.* **2021**, *1223*, 129203. DOI:10.1016/j.molstruc.2020.129203
22. E. Al-Masri, M. Al-Refai, H. T. Al-Masri, B. F. Ali, A. Geyer, S. I. Ivlev, N. Aljaar, *Chem. Data Collect.* **2021**, *36*, 100786. DOI:10.1016/j.cdc.2021.100786
23. P. Van Thong, N. T. T. Chi, M. Azam, C. H. Hanh, M. Alam, S. I. Al-Resayes, N. Van Hai, *Polyhedron.* **2022**, *212*, 115612. DOI:10.1016/j.poly.2021.115612
24. S. V. Larionov, T. F. Kokina, V. F. Plyusnin, L. A. Glinskaya, A. V. Tkachev, Y. A. Bryleva, N. V. Kuratieva, M. I. Rakhmanova, E. S. Vasilyev, *Polyhedron.* **2014**, *77*, 75–80. DOI:10.1016/j.poly.2014.04.011
25. N. Ling, X. Wang, D. Zeng, Y. W. Zhang, X. Fang, H. X. Yang, *J. Mol. Struct.* **2020**, *1206*, 127641. DOI:10.1016/j.molstruc.2019.127641
26. V. P. Singh, P. Singh, A. K. Singh, *Inorg. Chim. Acta.* **2011**, *379*, 56–63. DOI:10.1016/j.ica.2011.09.037
27. K. A. M. I. A. R. Zomorodian, S. O. G. H. R. A. Khabnadideh, *Farmacia.* **2020**, *68*, 155–163. DOI:10.31925/farmacia.2020.1.22
28. L. H. Wang, X. Y. Qiu, S. J. Liu, *Acta Chim. Slov.* **2019**, *66*, 675–680. DOI:10.17344/acsi.2019.5117
29. R. V. Chikhale, A. M. Pant, S. S. Menghani, P. G. Wadibhasme, P. B. Khedekar, *Arab. J. Chem.* **2017**, *10*, 715–725. DOI:10.1016/j.arabj.2014.06.011
30. A. Jana, B. Das, S. K. Mandal, S. Mabhai, A. R. Khuda-Bukhsh, *New J. Chem.* **2016**, *40*, 5976–5984. DOI:10.1039/C6NJ00234J
31. M. Shebl, A. A. Saleh, S. M. Khalil, M. Dawy, A. A. Ali, *Inorg. Nano-Met. Chem.* **2021**, *51*, 195–209. DOI:10.1080/24701556.2020.1770794
32. F. Sameri, M. A. Bodaghifard, A. Mobinikhaledi, *Appl. Organomet. Chem.* **2021**, *35*, e6394. DOI:10.1002/aoc.6394
33. L. H. Wang, X. Y. Qiu, S. J. Liu, *J. Coord. Chem.* **2019**, *72*, 962–971. DOI:10.1080/00958972.2019.1590561
34. Y. Tan, *Acta Chim. Slov.* **2019**, *66*, 1002–1009. DOI:10.17344/acsi.2019.5297
35. S. M. Khalil, M. Shebl, F. S. Al-Gohani, *Acta Chim. Slov.* **2010**, *57*, 716–725.
36. P. Singh, D. P. Singh, K. Tiwari, M. Mishra, A. K. Singh, V. P. Singh, *RSC Adv.* **2015**, *5*, 45217–45230. DOI:10.1039/C4RA11929K
37. A. Beheshti, M. Bahrani-Pour, M. Kolahi, E. Shakerzadeh, H. Motamedi, P. Mayer, *Appl. Organomet. Chem.* **2021**, *35*, e6173. DOI:10.1002/aoc.6173
38. Y. Li, Z. Yang, B. Song, H. Xia, Z. Wang, *Inorg. Nano-Met. Chem.* **2017**, *47*, 966–972. DOI:10.1080/24701556.2016.1278554
39. L. Saghatforoush, K. Moeini, S. A. Hosseini-Yazdi, Z. Mardani, A. Bakhtiari, A. Hajabbas-Farshchi, S. Honarvar, M. S. Abdelbaky, *Polyhedron.* **2019**, *170*, 312–324. DOI:10.1016/j.poly.2019.05.057
40. L. Saghatforoush, K. Moeini, S. A. Hosseini-Yazdi, Z. Mardani, A. Hajabbas-Farshchi, H. T. Jameson, S. G. Telfer, J. D. Woollins, *RSC adv.* **2018**, *8*, 35625–35639. DOI:10.1039/C8RA07463A
41. Y. Zhang, Y. Q. Pan, M. Yu, X. Xu, W. K. Dong, *Appl. Organomet. Chem.* **2019**, *33*, e5240. DOI:10.1002/aoc.5368

Povzetek

Z reakcijo med cinkovim dikloridom in ligandom 5-kloro-2-metilbenzoksazol ($L = C_8H_6ClNO$) v etanolni raztopini smo sintetizirali nov kompleks $Zn(II)$: dikloridobis(5-kloro-2-metil-1,3-benzoksazol)-cink(II), $C_{16}H_{12}Cl_4N_2O_2Zn$. Spojino smo karakterizirali z elementno analizo, meritvami molarne prevodnosti, FTIR, UVVis in monokristalno rentgensko analizo (XRD). Rentgenska analiza je pokazala, da se v kompleksu kovina in ligand povezuje v razmerju 1 : 2. Spojina ima popačeno tetraedrično geometrijo z dvema vezanima dušikovima atomoma iz liganda. Izvedli smo izračune z DFT metodo in uporabo B3LYP funkcije z naborom osnov LANL2DZ za kovinski kompleks in 6-31G(d) za nekovinske elemente. Izračunali in predstavili smo optimalno geometrijsko strukturo kompleksa in orbitalne energije HOMO in LUMO. Opravili smo analizo naravnih veznih orbital (NBO) z namenom analize razporeditve naboja pred in po kompleksaciji liganda. Hirshfeldova analiza opravljena na d_{norm} je pokazala da močne medmolekulske interakcije $H...Cl/Cl...H$ in $H...H$ predstavljajo glavni prispevek k pakiranju kristalov.



Except when otherwise noted, articles in this journal are published under the terms and conditions of the Creative Commons Attribution 4.0 International License

Synthesis, Crystal Structures and Antibacterial Activities of *N,N'*-Ethylene-bis(3-bromosalicylaldehyde) and Its Copper(II) and Cobalt(III) Complexes

Xue-Song Lin,*Yong-Gang Huang, Rui-Fa Jin and Ya-Li Sang

College of Chemistry and Life Science, Chifeng University, Chifeng 024000, P.R. China

* Corresponding author: E-mail: xuesong_lin@126.com

Received: 08-17-2022

Abstract

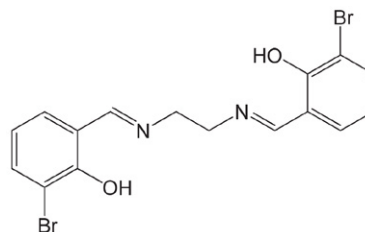
A bis-Schiff base *N,N'*-ethylene-bis(3-bromosalicylaldehyde) (H_2L) was prepared from 3-bromosalicylaldehyde and ethane-1,2-diamine. With H_2L as ligand, a new copper(II) complex $[CuL]$ (**1**) and a new cobalt(III) complex $[CoL(NCS)(DMF)]$ (**2**) were prepared and characterized by physico-chemical methods and single crystal X-ray analysis. X-ray analysis indicates that the Cu atom in complex **1** is in square planar coordination, and the Co atom in complex **2** is in octahedral coordination. The compounds were tested *in vitro* for their antibacterial activities on *Bacillus subtilis*, *Staphylococcus aureus*, *Escherichia coli* and *Pseudomonas fluorescens*. Both complexes have effective activities on the bacteria.

Keywords: Schiff base; copper complex; cobalt complex; crystal structure; antibacterial activity

1. Introduction

Schiff bases bearing typical group $C=N$ are important ligands in coordination chemistry, which are readily prepared by the condensation reaction of carbonyl containing compounds with organic amines. Schiff bases with donor atoms (N, O, S) have structure similarities with natural biological systems and due to the presence of imine group, are utilized in biological systems.¹ A great number of literature reported that they have interesting antibacterial, antifungal and antitumor activities.² It is well known that some biological activities, when administered as metal complexes, are being increased.³ Bis-Schiff bases derived from ethane-1,2-diamine, propane-1,3-diamine, propane-1,2-diamine and cyclohexyl-1,2-diamine with salicylaldehyde and its analogues are widely used tetradentate ligands.⁴ It was reported that salicylaldehyde derivatives with halo atoms in the aromatic ring showed variety of biological activities, especially antibacterial activities.⁵ Schiff base copper and cobalt complexes have shown remarkable antibacterial properties.⁶ In addition, thiocyanate anion is a co-ligand in most Schiff base cobalt complexes.⁷ In the present work, two new copper(II) and cobalt(III) complexes, $[CuL]$ (**1**) and $[CoL(NCS)(DMF)]$ (**2**), where L is the dianionic form of *N,N'*-ethylene-bis(3-bromosalicylaldehyde) (H_2L), are prepared and characterized. The an-

tibacterial activities against *Bacillus subtilis*, *Staphylococcus aureus*, *Escherichia coli* and *Pseudomonas fluorescens*, were studied.



Scheme 1. The bis-Schiff base H_2L

2. Experimental

2. 1. Materials and Measurements

3-Bromosalicylaldehyde and ethane-1,2-diamine with AR grade were obtained from Aldrich and used as received. Copper nitrate and cobalt nitrate were purchased from TCI. Ammonium thiocyanate was purchased from Aladin Chemical Co. Ltd. Elemental analyses were performed using a Perkin-Elmer 240C analytical instrument. Infrared spectra were recorded on a Nicolet 5DX FT-IR spectrophotometer with KBr pellets. UV-Vis spectra were

recorded on a Lambda 35 spectrometer. Molar conductance was measured with a Shanghai DDS-11A conductometer.

2. 2. Synthesis of H₂L

3-Bromosalicylaldehyde (0.40 g, 2.0 mmol) dissolved in methanol (30 mL) was reacted with ethane-1,2-diamine (0.030 g, 1.0 mmol) diluted by methanol (10 mL). The mixture was stirred at reflux for 1 h and with three quarter of the solvent removed by distillation, to give yellow product. Yield: 0.37 g (88%). Anal. Calcd. for C₁₆H₁₄Br₂N₂O₂ (%): C, 45.10; H, 3.31; N, 6.57. Found: C, 44.92; H, 3.40; N, 6.71. IR data (KBr, cm⁻¹): 3438 (OH), 1628 (C=N), 1217 (Ar–O). UV-Vis data in methanol [λ_{\max} (nm), ϵ (L mol⁻¹ cm⁻¹): 215, 22350; 260, 8940; 328, 2980; 415, 1935.

Diffraction quality yellow single crystals were obtained by slow evaporation of the methanol solution of the product.

2. 3. Synthesis of [CuL] (1)

H₂L (42 mg, 0.10 mmol) and copper nitrate trihydrate (24 mg, 0.10 mmol) were dissolved in methanol (20 mL). A brown solution was formed immediately. After 30 min stirring, the solution was filtered and the filtrate was kept for slow evaporation. The diffraction quality brown single crystals that deposited over a period of 5 days were collected by filtration and washed with methanol. Yield: 22 mg (45%). Anal. Calcd. for C₁₆H₁₂Br₂CuN₂O₂ (%): C, 39.41; H, 2.48; N, 5.74. Found: C, 39.26; H, 2.37; N, 5.85. IR data (KBr, cm⁻¹): 1632 (C=N), 1180 (Ar–O). UV-Vis data

in methanol [λ_{\max} (nm), ϵ (L mol⁻¹ cm⁻¹): 270, 16720; 368, 6270. Λ_M (10⁻³ mol L⁻¹ in DMSO/H₂O): 41 Ω^{-1} cm² mol⁻¹.

2. 4. Synthesis of [CoL(NCS)(DMF)] (2)

H₂L (42 mg, 0.10 mmol) and cobalt nitrate hexahydrate (29 mg, 0.10 mmol) were dissolved in methanol (20 mL) and DMF (5 mL). A deep red solution was formed immediately. After 30 min stirring, the solution was filtered and the filtrate was kept for slow evaporation. The diffraction quality red single crystals that deposited over a period of 27 days were collected by filtration and washed with methanol. Yield: 18 mg (29%). Anal. Calcd. for C₂₀H₁₉Br₂CoN₄O₃S (%): C, 39.11; H, 3.12; N, 9.12. Found: C, 39.27; H, 3.21; N, 9.03. IR data (KBr, cm⁻¹): 1641 (C=O), 1633 (C=N), 1183 (Ar–O). UV-Vis data in methanol [λ_{\max} (nm), ϵ (L mol⁻¹ cm⁻¹): 267, 15560; 380, 3315. Λ_M (10⁻³ mol L⁻¹ in DMSO/H₂O): 33 Ω^{-1} cm² mol⁻¹.

2. 5. X-Ray Crystallography

Suitable single crystals of the complexes were selected and mounted on a Bruker Smart 1000 CCD area-detector diffractometer with graphite monochromatized Mo-K α radiation (λ = 0.71073 Å). Diffraction data for the compounds were collected by ω scan mode at 298(2) K. Data reduction and cell refinement were performed by the SMART and SAINT programs.⁸ Empirical absorption correction was applied by using SADABS.⁹ The structures were solved by direct methods and refined with the full-matrix least-squares technique using SHELXL.¹⁰ The non-H atoms in the structures were subjected to refined anisotropic refinement. The hydrogen atoms were located

Table 1. Crystallographic data and refinement details for the compounds

	H ₂ L	1	2
Molecular formula	C ₁₆ H ₁₄ Br ₂ N ₂ O ₂	C ₁₆ H ₁₂ Br ₂ CuN ₂ O ₂	C ₂₀ H ₁₉ Br ₂ CoN ₄ O ₃ S
Molecular weight	426.11	487.64	614.20
Crystal system	Monoclinic	Orthorhombic	Monoclinic
Space group	<i>P</i> 2 ₁ / <i>n</i>	<i>Pbca</i>	<i>P</i> 2 ₁ / <i>c</i>
<i>a</i> , Å	8.3320(5)	10.6159(8)	11.1597(6)
<i>b</i> , Å	10.1997(7)	12.6984(9)	16.6043(8)
<i>c</i> , Å	9.5717(7)	24.0006(12)	13.3480(7)
β , °	101.332(2)	90	109.9890(10)
<i>V</i> , Å ³	797.58(9)	3235.4(4)	2324.4(2)
<i>Z</i>	2	8	4
ρ_{calcd} , g cm ⁻³	1.774	2.002	1.755
μ , mm ⁻¹	5.090	6.299	4.295
Reflections collected	7634	16247	26163
Unique reflections	1730	3009	4330
Observed reflections ($I \geq 2\sigma(I)$)	1344	2320	3243
Data/restraints/parameters	1730/0/101	3009/0/208	4330/0/282
<i>R</i> _{int}	0.0329	0.0538	0.0365
GOOF on <i>F</i> ²	1.055	1.035	1.015
<i>R</i> ₁ , <i>wR</i> ₂ ($I \geq 2\sigma(I)$)	0.0328, 0.0724	0.0272, 0.0552	0.0360, 0.0766
<i>R</i> ₁ , <i>wR</i> ₂ (all data)	0.0496, 0.0812	0.0446, 0.0605	0.0571, 0.0861

in geometrically and treated with the riding mode. Crystallographic data and experimental details for the compounds are summarized in Table 1.

2. 6. Antibacterial Assay

Antibacterial activities of the compounds were tested *in vitro* against *Bacillus subtilis*, *Staphylococcus aureus*, *Escherichia coli* and *Pseudomonas fluorescens* using MH medium (Mueller–Hinton medium: casein hydrolysate 17.5 g, soluble starch 1.5 g, beef extract 1000 mL). The minimum inhibitory concentrations (MIC) of the test compounds were determined by a colorimetric method using the dye MTT (3-(4,5-dimethylthiazol-2-yl)-2,5-diphenyltetrazolium bromide).¹¹ A solution of the compound (50 $\mu\text{g mL}^{-1}$) in DMSO was prepared and graded quantities of the assayed compounds were incorporated in specified quantity of sterilized liquid MH medium. A specified quantity of the medium containing the compound was poured into microtitration plates. Suspension of the microorganism was prepared to contain about 10^5 colony forming units cfu mL^{-1} and applied to micro-titration plates with serially diluted compounds in DMSO to be tested and incubated at 37 °C for 24 h. After the MICs were visually determined on each of the micro-titration plates, 50 μL of PBS (Phosphate Buffered Saline 0.01 mol L^{-1} , pH 7.4: $\text{Na}_2\text{HPO}_4 \cdot 12\text{H}_2\text{O}$ 2.9 g, KH_2PO_4 0.2 g, NaCl 8.0 g, KCl 0.2 g, distilled water 1000 mL) containing 2 mg of MTT was added to each well. Incubation was continued at room temperature for 4–5 h. The content of each well was removed, and 100 μL of isopropyl alcohol containing 5% 1.0 mol L^{-1} HCl was added to extract the dye. After 12 h of incubation at room temperature, the optical density (OD) was measured with a micro-plate reader at 550 nm.

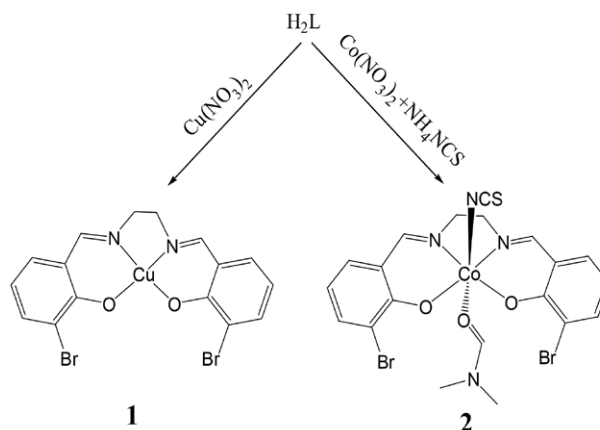
3. Results and Discussion

3. 1. Chemistry

The bis-Schiff base H_2L was prepared by 2:1 condensation reaction of 3-bromosalicylaldehyde with ethane-1,2-diamine in methanol (Scheme 2). Complexes **1** and **2** were facile prepared by the reaction of the bis-Schiff base with copper nitrate trihydrate and cobalt nitrate hexahydrate, respectively, in methanol. As usually observed for the preparation of cobalt complexes, Co^{II} in complex **2** underwent aerial oxidation to Co^{III} in the synthetic route. The molar conductivities of the complexes **1** and **2** measured in $\text{DMF}/\text{H}_2\text{O}$ (V:V = 1:9) at concentration of 10^{-3} mol L^{-1} are 41 and 33 $\Omega^{-1} \text{cm}^2 \text{mol}^{-1}$, respectively, indicating the non-electrolytic nature of both complexes in such solution.¹²

3. 2. IR and Electronic Spectra

In the infrared spectrum of H_2L , the weak absorption at 3438 cm^{-1} is assigned to the O–H vibration of the phenol



Scheme 2. The synthetic procedure of the complexes

group, and the characteristic imine stretching is observed at 1628 cm^{-1} as a strong signal.¹³ The spectra of complexes **1** and **2** show imine stretching at $1632\text{--}1633 \text{ cm}^{-1}$. The Schiff base ligands coordination is substantiated by the phenolic C–O stretching bands at 1217 cm^{-1} for H_2L , while $1180\text{--}1183 \text{ cm}^{-1}$ for the complexes.¹⁴ The intense absorption band at 2117 cm^{-1} in the spectrum of complex **2** can be assigned to the thiocyanate ligand.¹⁵ Coordination of the Schiff base ligands is further confirmed by the appearance of weak bands in the low wave numbers $400\text{--}600 \text{ cm}^{-1}$, corresponding to $\nu(\text{Cu/Co-N})$ and $\nu(\text{Cu/Co-O})$.

In the electronic spectra of H_2L and the complexes, the bands at 260–270 nm and 328 nm are attributed to the $n\text{--}\pi^*$ transitions.¹⁶ The bands at 360–380 nm in the complexes can be attributed to the ligand to metal charge transfer transition (LMCT).¹⁷

3. 3. Crystal Structure Description of H_2L

Molecular structure of H_2L is shown in Fig. 1. Selected bond lengths and angles for the compound are listed in Table 2. All the bond lengths in the compound are within normal ranges,¹⁸ and comparable to those of the similar bis-Schiff bases.¹⁹ The bond length of C7–N1 confirms it as a double bond. The two benzene rings form a dihedral angle of 0° due to the centrosymmetric symmetry. In the crystal structure of the compound, the molecules are linked through intermolecular hydrogen bonds of C–H...O (C7–H7 = 0.93 Å, H7...O1ⁱ = 2.41 Å, C7...O1ⁱ =

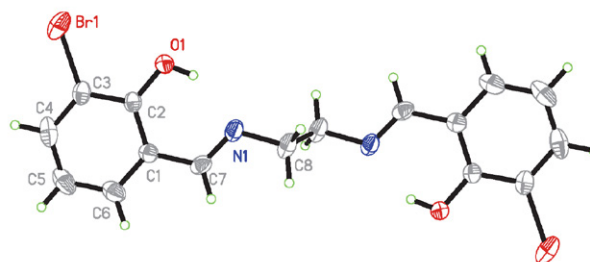


Fig. 1. Molecular structure of H_2L with thermal ellipsoids of 30% probability level.

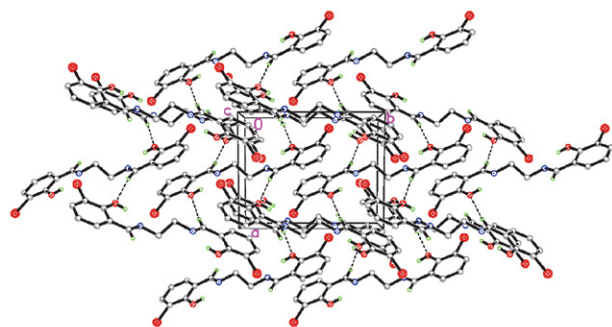


Fig. 2. Molecular packing diagram of H_2L , viewed along the c axis. Hydrogen bonds are shown as dashed lines.

3.328(3) Å, $C7-H7\cdots O1^i = 170^\circ$; symmetry code for i : $\frac{1}{2} + x, \frac{1}{2} - y, \frac{1}{2} + z$, to form two-dimensional sheets parallel to the bc plane (Fig. 2). Moreover, there are π -electron ring– π -electron ring interactions (4.209(3) Å) in the packing structure of the compound.

3. 4. Crystal Structure Description of Complex 1

Molecular structure of the mononuclear copper(II) complex **1** is shown in Fig. 3. Selected bond lengths and angles for the compound are listed in Table 2. The Cu atom is coordinated by two phenolate oxygen and two imino nitrogen of the bis-Schiff base ligand, forming square planar coordination. The square planar geometry is slightly distorted from ideal model, as evidenced by the bond angles. The angles in the coordination are in the ranges of $84.78(11)$ – $92.96(10)^\circ$ and $176.27(10)$ – $177.64(10)^\circ$, respectively. The Cu–O and Cu–N bond lengths are comparable to those observed in Schiff base copper complexes.²⁰ The two benzene rings form a dihedral angle of $5.7(5)^\circ$.

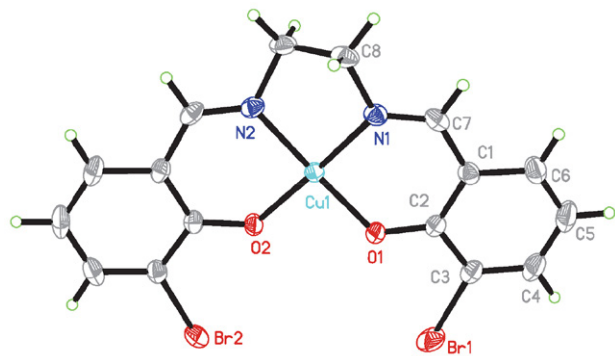


Fig. 3. Molecular structure of complex **1** with thermal ellipsoids of 30% probability level.

3. 5. Crystal Structure Description of Complex 2

Molecular structure of the mononuclear cobalt(III) complex **2** is shown in Fig. 4. Selected bond lengths and angles for the compound are listed in Table 2. The Co atom is coordinated by two phenolate oxygen and two imino ni-

Table 2. Selected bond distances (Å) and angles ($^\circ$) for the compounds

Bond	Å	Bond	Å
H_2L			
C7–N1	1.269(4)	C8–N1	1.463(3)
C2–O1	1.319(3)		
1			
C7–N1	1.279(4)	C8–N1	1.474(4)
C10–N2	1.279(4)	C9–N2	1.471(4)
C2–O1	1.301(3)	C12–O2	1.312(3)
Cu1–N1	1.940(2)	Cu1–N2	1.930(2)
Cu1–O1	1.896(2)	Cu1–O2	1.908(2)
O1–Cu1–N1	92.96(10)	O1–Cu1–N2	177.64(10)
O1–Cu1–O2	89.74(8)	N1–Cu1–N2	84.78(11)
N1–Cu1–O2	176.27(10)	N2–Cu1–O2	92.49(10)
2			
C7–N1	1.271(5)	C8–N1	1.474(5)
C10–N2	1.276(5)	C9–N2	1.464(5)
C2–O1	1.302(4)	C12–O2	1.297(4)
Co1–O1	1.887(2)	Co1–N1	1.889(3)
Co1–N2	1.891(3)	Co1–O2	1.896(2)
Co1–N3	1.893(3)	Co1–O3	1.937(3)
O1–Co1–N1	94.70(12)	O1–Co1–N2	176.99(12)
O1–Co1–O2	87.30(11)	N1–Co1–N2	85.47(13)
N1–Co1–O2	177.45(12)	N2–Co1–O2	92.45(12)
N3–Co1–O1	92.68(13)	N3–Co1–O2	92.28(13)
N3–Co1–N1	89.21(13)	N3–Co1–N2	90.32(14)
O3–Co1–O1	87.40(11)	O3–Co1–O2	89.96(11)
O3–Co1–N1	88.56(12)	O3–Co1–N2	89.60(12)
N3–Co1–O3	177.76(13)		

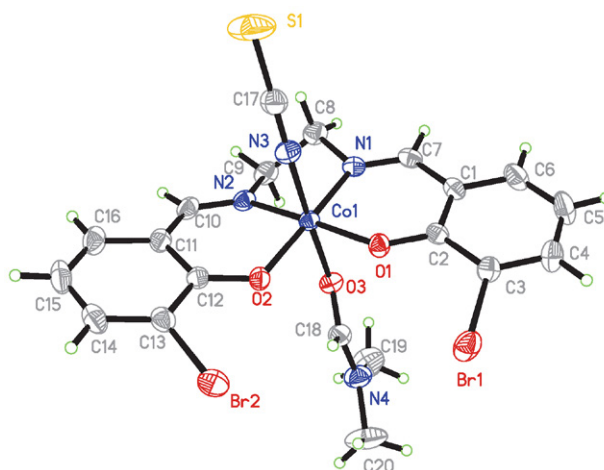


Fig. 4. Molecular structure of complex **2** with thermal ellipsoids of 30% probability level.

trogen of the bis-Schiff base ligand, one thiocyanate nitrogen and one oxygen of a DMF ligand, forming octahedral coordination. The equatorial plane of the octahedral coordination is defined by the four donor atoms of the Schiff base ligand, and the axial positions are occupied by the donor atoms of thiocyanate and DMF ligands. The octahe-

dral geometry is distorted from ideal model, as evidenced by the bond angles. The bond angles in the coordination are in the ranges of 85.47(13)–94.70(12)° and 176.99(12)–177.76(13)°, respectively. The Co–O and Co–N bond lengths are comparable to those observed in Schiff base cobalt complexes.²¹

3. 6. Antibacterial Activities

The compounds were screened *in vitro* for antibacterial activities against *Bacillus subtilis*, *Staphylococcus aureus*, *Escherichia coli* and *Pseudomonas fluorescens* by the MTT method. The MICs of the compounds against the bacteria are presented in Table 3. Penicillin was used as a reference.

Table 3. Antibacterial activities (MIC (μg mL⁻¹))

	<i>Bacillus subtilis</i>	<i>Escherichia coli</i>	<i>Pseudomonas fluorescens</i>	<i>Staphylococcus aureus</i>
H ₂ L	12.5	25	25	6.25
1	0.78	3.12	12.5	1.56
2	6.25	6.25	3.12	3.12
Penicillin	1.3	> 100	> 100	2.1

The bis-Schiff base H₂L shows medium to weak activities against the bacteria. In general, both complexes have stronger activities against the bacteria than H₂L. Complex **1** showed strong activity against *Bacillus subtilis*, *Escherichia coli* and *Staphylococcus aureus*, and medium activity against *Pseudomonas fluorescens*. The complex has better activity against *Bacillus subtilis* than the polynuclear copper complex with the Schiff base ligand 2-hydroxy-5-methylbenzaldehyde oxime.²² Complex **2** showed strong activity against *Pseudomonas fluorescens* and *Staphylococcus aureus*, and medium activity against *Bacillus subtilis* and *Escherichia coli*. Complex **1** has stronger activities against the bacteria than complex **2**, except for *Pseudomonas fluorescens*. Interestingly, complex **1** has stronger activities against the bacteria than Penicillin. The trends in the present work are in accordance with those in the literatures that metal complexes usually have stronger antibacterial activities than their corresponding ligands.²³ The copper complex has stronger activity against *Bacillus subtilis*, *Staphylococcus aureus* and *Escherichia coli* than the copper complex with the Schiff base 2-(2-(2,4-dinitrophenyl)hydrazono)-1,2-diphenylethanone.²⁴ The cobalt complex has stronger activity against *Staphylococcus aureus* than the cobalt complexes with the Schiff bases 4-X-2-[(2-(2-pyridine-2-yl-ethylsulfanyl)ethylimino)methyl]phenol (X = methoxy, phenylazo, bromo, nitro).²⁵ This enhanced antibacterial activity of the complexes can be explained by the coordination of the metal ions with the azomethine groups of the Schiff base ligands.²⁶ According to chelating

theory,²⁷ chelation could enhance the lipophilic character of the central metal ions, which subsequently favor their permeation through the lipid layers of the cell membrane and blocking the metal binding sites on enzymes of micro-organism. On chelation, the polarity of the metal ions decreases to a greater extent, due to the overlap of the ligand orbital and partial sharing of their positive charge with donor groups. In addition, it improves the π -electron delocalization on the whole chelating ring which affects the lipophilicity of the complexes.²⁸

4. Conclusion

Two new copper(II) and cobalt(III) complexes have been prepared and characterized. The bis-Schiff base ligand coordinates to the metal atoms through phenolate oxygen and imino nitrogen. Structures of H₂L and the complexes were characterized by spectroscopic methods and confirmed by single crystal X-ray determination. The antibacterial activities of the bis-Schiff base and the complexes were assayed. The results indicated that both complexes are potential antibacterial agents.

Supplementary Material

CCDC reference numbers 969428 (H₂L), 2195359 (**1**) and 2195360 (**2**) contain the supplementary crystallographic data for this paper. These data can be obtained free of charge at www.ccdc.cam.ac.uk, or from Cambridge Crystallographic Data Center, 12, Union Road, Cambridge CB2 1EZ, UK; Fax: +44 1223 336 033; e-mail: deposit@ccdc.cam.ac.uk.

Acknowledgments

We gratefully acknowledge the financial support by the Natural Science Research Project of Chifeng City (SZR2022015), the Research Program of Science and Technology at Universities of Inner Mongolia Autonomous Region (NJZY21139), and Inner Mongolia Key Laboratory of Photoelectric Functional Materials.

5. References

- (a) E. Keskioglu, A.B. Gunduzalp, S. Cete, F. Hamurcu, B. Erk, *Spectrochim. Acta A*, **2008**, 70, 634–640. DOI:10.1016/j.saa.2007.08.011
(b) J.Z. Wu, L. Yuan, *J. Inorg. Biochem.* **2004**, 98, 41–45. DOI:10.1016/j.jinorgbio.2003.08.011
- (a) H. Liu, Z.-W. Chu, D.-G. Xia, H.-Q. Cao, X.-H. Lv, *Bioorg. Chem.* **2020**, 99, 103807. DOI:10.1016/j.bioorg.2020.103807
(b) N. Caliskan, A. Usta, F.S. Beris, N. Baltas, E. Celik, *Lett. Org. Chem.* **2020**, 17, 631–638. DOI:10.2174/1570178617666200108111211

- (c) A.S. Hassan, H.M. Awad, A.A. Magd-El-Din, T.S. Hafez, *Med. Chem. Res.* **2018**, 27, 915–927. DOI:10.1007/s00044-017-2113-5
- (d) Y.M. Hao, *Acta Chim. Slov.* **2021**, 68, 102–108. DOI:10.17344/acsi.2020.6205
3. D. N. Akbayeva, L. Gonsalvi, W. Oberhauser, M. Peruzzini, F. Vizza, P. Bruggeller, A. Romerosa, G. Sava, A. Bergamo, *Chem. Commun.* **2003**, 264–265. DOI:10.1039/b210102e
4. (a) E.C. Constable, G.Q. Zhang, C.E. Housecroft, M. Neuburger, J.A. Zampese, *CrystEngComm* **2010**, 12, 1764–1773. DOI:10.1039/b922929a
- (b) M.A. Vazquez-Fernandez, M.I. Fernandez-Garcia, A. M. Gonzalez-Noya, M. Maneiro, M. R. Bermejo, M. J. Rodriguez-Douton, *Polyhedron* **2012**, 31, 379–385. DOI:10.1016/j.poly.2011.09.031
- (c) G. Bhargavi, M.V. Rajasekharan, J.-P. Costes, J.-P. Tuchagues, *Polyhedron* **2009**, 28, 1253–1260. DOI:10.1016/j.poly.2009.02.024
- (d) M. Sarwar, A.M. Madalan, F. Lloret, M. Julve, M. Andruh, *Polyhedron* **2011**, 30, 2414–2420. DOI:10.1016/j.poly.2011.06.011
5. (a) L. Shi, H.M. Ge, S. H. Tan, H.Q. Li, Y.C. Song, H.L. Zhu, R.X. Tan, *Eur. J. Med. Chem.* **2007**, 42, 558–564. DOI:10.1016/j.ejmech.2006.11.010
- (b) J. Lv, T. Liu, S. Cai, X. Wang, L. Lu, Y. Wang, *J. Inorg. Biochem.* **2006**, 100, 1888–1896. DOI:10.1016/j.jinorgbio.2006.07.014
- (c) M. Salehi, F. Ghasemi, M. Kubicki, A. Asadi, M. Behzad, M.H. Ghasemi, A. Gholizadeh, *Inorg. Chim. Acta* **2016**, 453, 238–246. DOI:10.1016/j.ica.2016.07.028
- (d) H.-Y. Qian, *Acta Chim. Slov.* **2021**, 68, 700–708. DOI:10.17344/acsi.2021.6721
- (e) M. Ghosh, M. Layek, M. Fleck, R. Saha, D. Bandyopadhyay, *Polyhedron* **2015**, 85, 312–319. DOI:10.1016/j.poly.2014.08.014
- (f) M. Zhang, D.-M. Xian, H.-H. Li, J.-C. Zhang, Z.-L. You, *Aust. J. Chem.* **2012**, 65, 343–350. DOI:10.1071/CH11424
6. (a) S.H. Sumrra, W. Zafar, S.A. Malik, K. Mahmood, S.S. Shafqat, S. Arif, *Acta Chim. Slov.* **2022**, 69, 200–216. DOI: 10.17344/acsi.2021.7182
- (b) H.-Y. Qian, N. Sun, *Transition Met. Chem.* **2019**, 44, 501–506. DOI:10.1007/s11243-018-00296-x
7. (a) S. Banerjee, J.-T. Chen, C.-Z. Lu, *Polyhedron* **2007**, 26, 686–694. DOI:10.1016/j.poly.2006.08.035
- (b) S. Chattopadhyay, G. Bocelli, A. Musatti, A. Ghosh, *Inorg. Chem. Commun.* **2006**, 9, 1053–1057. DOI:10.1016/j.inoche.2006.06.017
- (c) M. Sarkar, R. Clerac, C. Mathoniere, N. G. R. Hearn, V. Bertolasi, D. Ray, *Eur. J. Inorg. Chem.* **2009**, 4675–4685. DOI:10.1002/ejic.200900577
- (d) M. Fleck, D. Karmakar, M. Ghosh, A. Ghosh, R. Saha, D. Bandyopadhyay, *Polyhedron* **2012**, 34, 157–162. DOI:10.1016/j.poly.2011.12.019
8. SMART and SAINT. Area Detector Control and Integration Software, Siemens Analytical X-Ray Systems, Inc., Madison, Wisconsin, USA, **1996**
9. G. M. Sheldrick, SADABS, Program for Empirical Absorption Correction of Area Detector Data, University of Göttingen, Germany, **1996**
10. G.M. Sheldrick, SHELXTL V5.1 Software Reference Manual, Bruker AXS, Inc., Madison, Wisconsin, USA, **1997**
11. J. Meletiadis, J. F. G. M. Meis, J. W. Mouton, J.P. Donnelly, P.E. Verweij, *J. Clin. Microbiol.* **2000**, 38, 2949–2954. DOI:10.1128/JCM.38.8.2949-2954.2000
12. W.J. Geary, *Coord. Chem. Rev.* **1971**, 7, 81–122. DOI:10.1016/S0010-8545(00)80009-0
13. Y. Luo, J. Wang, X. Ding, R. Ni, M. Li, T. Yang, J. Wang, C. Jing, Z. You, *Inorg. Chim. Acta* **2021**, 516, 120146. DOI:10.1016/j.ica.2020.120146
14. Y. Luo, J. Wang, B. Zhang, Y. Guan, T. Yang, X. Li, L. Xu, J. Wang, Z. You, *J. Coord. Chem.* **2020**, 73, 1765–1777. DOI:10.1080/00958972.2020.1795645
15. M. Sarwar, A.M. Madalan, F. Lloret, M. Julve, M. Andruh, *Polyhedron* **2011**, 30, 2414–2420. DOI:10.1016/j.poly.2011.06.011
16. Y.-M. Zhou, X.-R. Ye, F.-B. Xin, X.-Q. Xin, *Transition Met. Chem.* **1999**, 24, 118–120. DOI:10.1023/A:1006989707001
17. I. Banerjee, J. Marek, R. Herchel, M. Ali, *Polyhedron* **2010**, 29, 1201–1208. DOI:10.1016/j.poly.2009.12.023
18. F. H. Allen, O. Kennard, D.G. Watson, L. Brammer, A.G. Orphen, R. Taylor, *J. Chem. Soc. Perkin Trans.* **1987**, 2:S1–S19. DOI:10.1039/p2987000000s1
19. (a) A. Elmali, *J. Chem. Crystallogr.* **2000**, 30, 473–477. DOI:10.1023/A:1011355601133
- (b) S.S. Tandon, V. McKee, *J. Chem. Soc. Dalton Trans.* **1989**, 1, 19–24. DOI:10.1039/dt9890000019
- (c) A. Aguiari, E. Bullita, U. Casellato, P. Guerriero, S. Tamburini, P.A. Vigato, *Inorg. Chim. Acta* **1992**, 202, 157–171. DOI:10.1016/S0020-1693(00)86831-0
20. (a) S. Mukherjee, C.K. Pal, M. Kotakonda, M. Joshi, M. Shit, P. Ghosh, A.R. Choudhury, B. Biswas, *J. Mol. Struct.* **2021**, 1245, 131057. DOI:10.1016/j.molstruc.2021.131057
- (b) S. Parvarinezhad, M. Salehi, M. Kubicki, A. Khaleghian, *Appl. Org. Chem.* **2021**, 35, e6443. DOI:10.1002/aoc.6443
21. (a) X.-Q. Luo, Q.-R. Liu, Y.-J. Han, L.-W. Xue, *Acta Chim. Slov.* **2020**, 67, 159–166. DOI:10.17344/acsi.2019.5303
- (b) N.C. Jana, M. Patra, P. Brandao, A. Panja, *Polyhedron* **2019**, 164, 23–34. DOI:10.1016/j.poly.2019.02.024
22. Y.-L. Sang, X.-S. Lin, *Acta Chim. Slov.* **2019**, 66, 168–172. DOI:10.17344/acsi.2018.4749
23. (a) Y.-L. Sang, L.-F. Zou, R.-F. Jin, Y.-H. Liu, X.-S. Lin, X.-H. Zhang, *J. Coord. Chem.* **2021**, 74, 1929–1946. DOI:10.1080/00958972.2021.1938015
- (b) Y.-L. Sang, X.-S. Lin, *Transition Met. Chem.* **2009**, 34, 931–936. DOI:10.1007/s11243-009-9283-z
- (c) L.-W. Xue, C. Chen, G.-Q. Zhao, W.-C. Yang, *Acta Chim. Slov.* **2020**, 67, 189–194. DOI:10.17344/acsi.2019.5327
24. P. Gull, A.A. Hashmi, *J. Mol. Struct.* **2017**, 1139, 264–268. DOI:10.1016/j.molstruc.2017.03.053
25. L. A. Saghatforoush, F. Chalabian, A. Aminkhani, G. Karimnezhad, S. Ershad, *Eur. J. Med. Chem.* **2009**, 44, 4490–4495. DOI:10.1016/j.ejmech.2009.06.015

26. A. A. El-Sherif, M. M. Shoukry, M. M. A. Abd-Elgawad, *Spectrochim. Acta A Mol. Biomol. Spectrosc.* **2012**, 98, 307–321. DOI:10.1016/j.saa.2012.08.034
27. J. W. Searl, R.C. Smith, S. Wyard, *J. Proc. Phys. Soc.* **1961**, 78, 1174–1181; DOI: 10.1088/0370-1328/78/6/311
28. P. Gull, M.A. Malik, O.A. Dar, A.A. Hashmi, *J. Mol. Struct.* **2017**, 1134, 734–741. DOI:10.1088/0370-1328/78/6/311

Povzetek

Iz 3-bromosalicilaldehida in etan-1,2-diamina smo pripravili bis-Schiffovo bazo N,N' -etilen-bis(3-bromosalicilaldimin) (H_2L). Z H_2L kot ligandom smo pripravili nova kompleksa bakra(II) $[CuL]$ (**1**) in kobalta(III) $[CoL(NCS)(DMF)]$ (**2**), ki smo ju okarakterizirali s fizikalno-kemijskimi metodami in monokristalno rentgensko analizo. Rentgenska analiza kaže, da je atom Cu v kompleksu **1** v kvadratni planarni koordinaciji, atom Co v kompleksu **2** pa v oktaedrični koordinaciji. Spojine so bile testirane *in vitro* na antibakterijsko delovanje na *Bacillus subtilis*, *Staphylococcus aureus*, *Escherichia coli* in *Pseudomonas fluorescens*. Oba kompleksa izkazujeta učinkovito delovanje na bakterije.



Except when otherwise noted, articles in this journal are published under the terms and conditions of the Creative Commons Attribution 4.0 International License

Synthesis and *In Vitro* Cytotoxicity of Novel Halogenated Dihydropyrano[3,2-*b*]Chromene Derivatives

Salehe Sabouri,^{1,2} Ehsan Faghih-Mirzaei³ and Mehdi Abaszadeh^{*,4}

¹ Herbal & Traditional Medicine Research Center, Kerman University of Medical Sciences, Kerman, Iran.

² Department of Pharmaceutical Biotechnology, Faculty of Pharmacy, Kerman University of Medical Sciences, Kerman, Iran.

³ Department of Medicinal Chemistry, Faculty of Pharmacy, Kerman University of Medical Sciences, Kerman, Iran

⁴ Pharmaceutics Research Center, Institute of Neuropharmacology, Kerman University of Medical Sciences, Kerman, Iran.

* Corresponding author: E-mail: abaszadeh@kmu.ac.ir

Received: 08-20-2022

Abstract

Lung and breast cancers are among the most common cancers. In the present work, initially, 6-bromo-; and 6-chloro-3-hydroxychromone compounds were prepared. In the next step, a series of 8-bromo-; and 8-chloro-dihydropyrano[3,2-*b*]chromene derivatives were synthesized by one-pot three component reaction of these two compounds, aromatic aldehydes, and ethyl cyanoacetate in the presence of triethylamine in EtOH at reflux conditions. The synthesized compounds were tested for their *in vitro* cytotoxic activity against A549 (lung cancer) and MCF-7 (breast cancer) cell lines. It was found that some compounds have high to moderate cytotoxicity, which makes them potential candidates for further studies. This study can be the basis for further studies to design and synthesis potent anticancer compounds and investigating their mechanism of action.

Keywords: Chromone derivatives; 6-bromo-3-hydroxychromone; 6-chloro-3-hydroxychromone; Three-component reactions; Cytotoxicity; Cancer cell line

1. Introduction

Compounds with a fused benzene and 4-pyrone ring are called 4*H*-1-benzopyran-4-one, 4*H*-chromen-4-one or chromone. Chromones are a group of naturally occurring compounds that are ubiquitous in nature, especially in plants.^{1,2} They are present in various flavonoids as a core structure. For instance, 3-hydroxyflavone (a type of hydroxyflavone) is a compound with a phenyl group in the 2-position and a hydroxyl group in the 3-position in the pyrone ring of chromone scaffold. Moreover, the chromone derivatives with a hydroxyl group in the 3-position in the pyrone ring are called 3-hydroxychromone. Chromone derivatives display a wide range of biological activities including antifungal,³ antimicrobial,⁴ antiobesity,⁵ antiviral,^{6,7} anti-inflammatory,⁸ anticancer,^{9,10} antioxidant,¹¹ and protein kinase inhibitory.¹² In addition, chromones are good bidentate ligands able to coordinate metal ions. These compounds are widely investigated as fluorescent membrane probes and fluorescent chelators.^{13,14}

Cancer, a worldwide health problem, is the second cause of death. Lung cancer is the leading cause of cancer death in males and females. Breast cancer is also one of the most common cancers that ranks as the second cause of deaths from cancer among females.¹⁵ In spite of the existence of several strategies for cancer therapy, searching for new chemotherapeutic agents continues. It is because of the complex nature of cancer and occurring drug resistance in cancerous cells.¹⁶

Herein, we have synthesized 6-bromo-; and 6-chloro-3-hydroxychromone (**3a,b**) at first step. Then, we prepared 8-halopyrano[3,2-*b*]chromen-10(4*H*)-one derivatives (**6a-j**) by one-pot three component reactions of (**3a,b**), aromatic aldehydes, and ethyl cyanoacetate in the presence of triethylamine in ethanol as solvent and at reflux conditions. Biological evaluation was also carried out for screening the potential cytotoxic activity of the compounds by MTT assay.

2. Experimental

2. 1. General Methods

All chemicals and reagents used in current study were obtained from commercial sources and used without further purification. All melting points were determined on Electrothermal-9100 apparatus and are uncorrected. IR spectra were recorded on a Bruker FTIR (Alpha model) spectrophotometer using KBr pellets. ^1H NMR (300 MHz) and ^{13}C NMR (75 MHz) spectra were recorded on a Bruker AVANCE III 300 MHz spectrometer in $\text{DMSO}-d_6$, with TMS as an internal standard. Chemical shifts (δ) are given in parts per million (ppm) and coupling constants (J) are given in Hertz (Hz). Reactions were monitored by thin layer chromatography (TLC) on the Aluminium-backed silica gel sheets (GF254) and visualized in UV light (254 nm). Elemental analyses were performed using a Heraeus CHN-O-Rapid analyzer.

2. 2. Preparation of 6-bromo-; and 6-chloro-3-hydroxychromone (3a,b)

These compounds were prepared according to literature procedures which presented by Spadafora and et al. and represented in Scheme 1.¹³ The isolated products were crystallised from ethanol.

6-Bromo-3-hydroxy-4H-chromen-4-one (3a)

Pale yellow powders; yield: 88%; mp 205–206 °C; IR (KBr) ν 3101 (OH), 1623 (C=O), 1601 cm^{-1} (C=C); ^1H NMR (300 MHz, $\text{DMSO}-d_6$) δ_{ppm} : 9.35 (br, 1H, OH), 8.27 (s, 1H, CH), 8.17 (d, 1H, $J=3$ Hz, ArH), 7.89 (dd, 1H, $J=9$ Hz, 3 Hz, ArH), 7.62 (d, 1H, $J=9$ Hz, ArH); ^{13}C NMR (75 MHz, $\text{DMSO}-d_6$) δ_{ppm} : 171.96 (C=O), 154.60 (C3), 142.50 (C2), 141.70, 136.38, 127.40, 124.72, 121.59, 117.35; Anal. calcd. for $\text{C}_9\text{H}_5\text{BrO}_3$: C, 44.85; H, 2.09%. Found: C, 44.64; H, 1.96%.

6-Chloro-3-hydroxy-4H-chromen-4-one (3b).

White powders; yield: 91%; mp 218–219 °C (lit.¹⁷ 216 °C); IR (KBr) ν 3296 (OH), 1629 (C=O), 1605 cm^{-1} (C=C); ^1H NMR (300 MHz, $\text{DMSO}-d_6$) δ_{ppm} : 9.36 (br, 1H, OH), 8.26 (s, 1H, CH), 8.05 (d, 1H, $J=3$ Hz, ArH), 7.80 (dd, 1H, $J=9$ Hz, 3 Hz, ArH), 7.71 (d, 1H, $J=9$ Hz, ArH); ^{13}C NMR (75 MHz, $\text{DMSO}-d_6$) δ_{ppm} : 172.10 (C=O), 154.26 (C3), 142.45 (C2), 141.73, 133.74, 129.49, 124.29, 124.25, 121.44; Anal. calcd. for $\text{C}_9\text{H}_5\text{ClO}_3$: C, 54.99; H, 2.56%. Found: C, 54.83; H, 2.41%.

2. 3. General Procedure for the Preparation of Dihydropyrano[3,2-*b*]chromene derivatives (6a-j)

A mixture of 6-bromo-; or 6-chloro-3-hydroxychromone (3a,b) (2 mmol), aromatic aldehydes (4a-j) (2 mmol) and ethyl cyanoacetate (5) (2.1 mmol), and three

drops of triethylamine in ethanol (10 mL) were added to a 50 mL round bottomed flask equipped with a magnetic stirring bar and a reflux condenser. It was stirred and refluxed for 1 h. The progress of the reaction was monitored by TLC using hexane/ethyl acetate as an eluent. After completion of the reaction, the mixture was cooled and the obtained crude product was filtered, washed with ethanol and crystallized from ethanol to give the pure solid sample for analysis.

Ethyl 2-amino-8-bromo-10-oxo-4-phenyl-4,10-dihydropyrano[3,2-*b*]chromene-3-carboxylate (6a)

white powders; yield: 90%; mp 200–201 °C; IR (KBr) ν 3431, 3315 (NH_2), 3027 (CH, aromatic), 2982 (CH, aliphatic), 1686, 1650 (2C=O), 1611 (C=C), 1193 cm^{-1} (C-O); ^1H NMR (300 MHz, $\text{DMSO}-d_6$) δ_{ppm} : 8.13 (d, 1H, $J=3$ Hz, ArH), 7.89 (br, 2H, NH_2), 7.85 (dd, 1H, $J=9$ Hz, 3 Hz, ArH), 7.50 (d, 1H, $J=9$ Hz, ArH), 7.36–7.21 (m, 5H, ArH), 4.93 (s, 1H, CH), 3.97 (q, 2H, $J=6$ Hz, OCH_2CH_3), 1.04 (t, 3H, $J=6$ Hz, OCH_2CH_3); ^{13}C NMR (75 MHz, $\text{DMSO}-d_6$) δ_{ppm} : 167.99 (C-10, CO), 167.75 (ester CO), 160.04 (C-2), 153.95, 153.51, 143.36, 137.28, 133.35, 129.01, 128.22, 127.71, 125.23, 121.31 (C-8), 118.21, 75.38 (C-3), 59.42 (OCH_2CH_3), 41.03 (C-4), 14.57 (OCH_2CH_3); Anal. calcd. for $\text{C}_{21}\text{H}_{16}\text{BrNO}_5$: C, 57.03; H, 3.65; N, 3.17%. Found: C, 56.79; H, 3.49; N, 3.21%.

Ethyl 2-amino-8-bromo-4-(4-chlorophenyl)-10-oxo-4,10-dihydropyrano[3,2-*b*]chromene-3-carboxylate (6b)

white powders; yield: 92%; mp 239–241 °C; IR (KBr) ν 3468, 3333 (NH_2), 3062 (CH, aromatic), 2984 (CH, aliphatic), 1708, 1671 (2C=O), 1622 (C=C), 1192 cm^{-1} (C-O); ^1H NMR (300 MHz, $\text{DMSO}-d_6$) δ_{ppm} : 8.13 (d, 1H, $J=3$ Hz, ArH), 7.93 (br, 2H, NH_2), 7.87 (dd, 1H, $J=6$ Hz, 3 Hz, ArH), 7.52 (d, 1H, $J=9$ Hz, ArH), 7.40–7.33 (m, 4H, ArH), 4.96 (s, 1H, CH), 3.97 (q, 2H, $J=6$ Hz, OCH_2CH_3), 1.04 (t, 3H, $J=6$ Hz, OCH_2CH_3); ^{13}C NMR (75 MHz, $\text{DMSO}-d_6$) δ_{ppm} : 167.87 (C-10, CO), 167.80 (ester CO), 159.99 (C-2), 153.97, 152.81, 142.34, 137.34, 133.40, 132.29, 130.14, 128.96, 127.73, 125.24, 121.32 (C-8), 118.24, 74.99 (C-3), 59.48 (OCH_2CH_3), 40.48 (C-4), 14.60 (OCH_2CH_3); Anal. calcd. for $\text{C}_{21}\text{H}_{15}\text{BrClNO}_5$: C, 52.19; H, 3.17; N, 2.94%. Found: C, 52.22; H, 2.98; N, 2.69%.

Ethyl 2-amino-8-bromo-10-oxo-4-(*p*-tolyl)-4,10-dihydropyrano[3,2-*b*]chromene-3-carboxylate (6c)

white powders; yield: 87%; mp 209–210 °C; IR (KBr) ν 3396, 3291 (NH_2), 3023 (CH, aromatic), 2984 (CH, aliphatic), 1680, 1661 (2C=O), 1615 (C=C), 1196 cm^{-1} (C-O); ^1H NMR (300 MHz, $\text{DMSO}-d_6$) δ_{ppm} : 8.14 (d, 1H, $J=3$ Hz, ArH), 7.90–7.86 (m, 3H, NH_2 , ArH), 7.53 (d, 1H, $J=9$ Hz, ArH), 7.16 (q, 4H, $J=9$ Hz, ArH), 4.89 (s, 1H, CH), 3.97 (q, 2H, $J=6$ Hz, OCH_2CH_3), 2.24 (s, 3H, CH_3), 1.07 (t, 3H, $J=6$ Hz, OCH_2CH_3); ^{13}C NMR (75 MHz, $\text{DMSO}-d_6$) δ_{ppm} : 168.02 (C-10, CO), 167.76 (ester CO), 160.01 (C-2), 153.96, 153.78, 140.42, 137.29, 136.88, 133.29, 129.59,

128.06, 127.73, 125.24, 121.34 (C-8), 118.21, 75.49 (C-3), 59.44 (OCH_2CH_3), 40.61 (C-4), 21.07 (CH_3), 14.62 (OCH_2CH_3); Anal. calcd. for $\text{C}_{22}\text{H}_{18}\text{BrNO}_5$: C, 57.91; H, 3.98; N, 3.07%. Found: C, 58.02; H, 3.71; N, 2.89%.

Ethyl 2-amino-8-bromo-4-(4-fluorophenyl)-10-oxo-4,10-dihydropyrano[3,2-b]chromene-3-carboxylate (6d)

cream powders; yield: 90%; mp 214–215 °C; IR (KBr) ν 3466, 3381 (NH_2), 3044 (CH, aromatic), 2991 (CH, aliphatic), 1707, 1684 ($2\text{C}=\text{O}$), 1659 ($\text{C}=\text{C}$), 1194 cm^{-1} (C-O); ^1H NMR (300 MHz, $\text{DMSO}-d_6$) δ_{ppm} : 8.13 (d, 1H, $J=3$ Hz, ArH), 7.91–7.86 (m, 3H, NH_2 , ArH), 7.52 (d, 1H, $J=9$ Hz, ArH), 7.38–7.34 (m, 2H, ArH), 7.15 (t, 2H, $J=9$ Hz, ArH), 4.96 (s, 1H, CH), 3.97 (q, 2H, $J=6$ Hz, OCH_2CH_3), 1.04 (t, 3H, $J=6$ Hz, OCH_2CH_3); ^{13}C NMR (75 MHz, $\text{DMSO}-d_6$) δ_{ppm} : 167.92 (C-10, CO), 167.80 (ester CO), 163.33 (C-2), 160.12, 159.97, 153.97, 153.11, 139.52, 137.32, 133.33, 130.22, 130.11, 127.73, 125.24, 121.32 (C-8), 118.22, 115.89, 115.61, 75.26 (C3), 59.44 (OCH_2CH_3), 40.55 (C-4), 14.58 (OCH_2CH_3); Anal. calcd. for $\text{C}_{21}\text{H}_{15}\text{BrFNO}_5$: C, 54.80; H, 3.29; N, 3.04%. Found: C, 54.59; H, 2.98; N, 3.11%.

Ethyl 2-amino-8-bromo-4-(4-methoxyphenyl)-10-oxo-4,10-dihydropyrano[3,2-b]chromene-3-carboxylate (6e)

yellow powders; yield: 86%; mp 211–213 °C; IR (KBr) ν 3423, 3297 (NH_2), 3069 (CH, aromatic), 2983 (CH, aliphatic), 1686, 1656 ($2\text{C}=\text{O}$), 1632 ($\text{C}=\text{C}$), 1189 cm^{-1} (C-O); ^1H NMR (300 MHz, $\text{DMSO}-d_6$) δ_{ppm} : 8.13 (d, 1H, $J=3$ Hz, ArH), 7.89–7.85 (m, 3H, NH_2 , ArH), 7.52 (d, 1H, $J=9$ Hz, ArH), 7.21 (d, 2H, $J=9$ Hz, ArH), 6.87 (d, 2H, $J=9$ Hz, ArH), 4.87 (s, 1H, CH), 3.98 (q, 2H, $J=6$ Hz, OCH_2CH_3), 3.71 (s, 3H, OCH_3), 1.07 (t, 3H, $J=6$ Hz, OCH_2CH_3); ^{13}C NMR (75 MHz, $\text{DMSO}-d_6$) δ_{ppm} : 168.05 (C-10, CO), 167.75 (ester CO), 159.98 (C-2), 158.84, 153.96, 153.85, 137.26, 135.39, 133.22, 129.22, 127.72, 125.24, 121.31 (C-8), 118.19, 114.38, 75.64 (C-3), 59.42 (OCH_2CH_3), 55.48 (OCH_3), 40.17 (C-4), 14.64 (OCH_2CH_3); Anal. calcd. for $\text{C}_{22}\text{H}_{18}\text{BrNO}_6$: C, 55.95; H, 3.84; N, 2.97%. Found: C, 55.98; H, 3.56; N, 2.73%.

Ethyl 2-amino-8-chloro-10-oxo-4-phenyl-4,10-dihydropyrano[3,2-b]chromene-3-carboxylate (6f)

white powders; yield: 91%; mp 190–192 °C; IR (KBr) ν 3466, 3411 (NH_2), 3028 (CH, aromatic), 2982 (CH, aliphatic), 1687, 1662 ($2\text{C}=\text{O}$), 1612 ($\text{C}=\text{C}$), 1193 cm^{-1} (C-O); ^1H NMR (300 MHz, $\text{DMSO}-d_6$) δ_{ppm} : 8.03 (t, 1H, $J=3$ Hz, ArH), 7.90 (br, 2H, NH_2), 7.82–7.77 (m, 1H, ArH), 7.63 (q, 1H, $J=3$ Hz, ArH), 7.37–7.22 (m, 5H, ArH), 4.95 (s, 1H, CH), 3.97 (q, 2H, $J=6$ Hz, CH_2), 1.05 (t, 3H, $J=6$ Hz, CH_3); ^{13}C NMR (75 MHz, $\text{DMSO}-d_6$) δ_{ppm} : 168.00 (C-10, CO), 167.92 (ester CO), 160.06 (C-2), 153.61, 143.38, 134.63, 133.35, 130.34, 129.04 (C-8), 128.22, 127.71, 124.89, 124.64, 121.22, 75.41 (C-3), 59.43 (OCH_2CH_3), 41.03 (C-4), 14.58 (OCH_2CH_3); Anal. calcd. for $\text{C}_{21}\text{H}_{16}\text{ClNO}_5$: C, 63.40; H, 4.05; N, 3.52%. Found: C, 63.27; H, 3.85; N, 3.49%.

Ethyl 2-amino-8-chloro-4-(4-chlorophenyl)-10-oxo-4,10-dihydropyrano[3,2-b]chromene-3-carboxylate (6g)

cream powders; yield: 93%; mp 238–240 °C; IR (KBr) ν 3470, 3335 (NH_2), 3065 (CH, aromatic), 2984 (CH, aliphatic), 1706, 1672 ($2\text{C}=\text{O}$), 1654 ($\text{C}=\text{C}$), 1194 cm^{-1} (C-O); ^1H NMR (300 MHz, $\text{DMSO}-d_6$) δ_{ppm} : 8.01 (d, 1H, $J=3$ Hz, ArH), 7.93 (br, 2H, NH_2), 7.79 (dd, 1H, $J=9$ Hz, 3 Hz, ArH), 7.62 (d, 1H, $J=9$ Hz, ArH), 7.41–7.33 (m, 4H, ArH), 4.97 (s, 1H, CH), 3.97 (q, 2H, $J=6$ Hz, OCH_2CH_3), 1.05 (t, 3H, $J=6$ Hz, OCH_2CH_3); ^{13}C NMR (75 MHz, $\text{DMSO}-d_6$) δ_{ppm} : 167.93 (C-10, CO), 167.88 (ester CO), 159.99 (C-2), 153.60, 152.83, 142.35, 134.66, 133.38, 132.29, 130.36, 130.16, 128.97 (C-8), 124.86, 124.62, 121.18, 75.00 (C-3), 59.48 (OCH_2CH_3), 40.47 (C-4), 14.60 (OCH_2CH_3); Anal. calcd. for $\text{C}_{21}\text{H}_{15}\text{Cl}_2\text{NO}_5$: C, 58.35; H, 3.50; N, 3.24%. Found: C, 58.11; H, 3.37; N, 3.19%.

Ethyl 2-amino-8-chloro-10-oxo-4-(p-tolyl)-4,10-dihydropyrano[3,2-b]chromene-3-carboxylate (6h)

yellow powders; yield: 88%; mp 196–197 °C; IR (KBr) ν 3460, 3313 (NH_2), 3049 (CH, aromatic), 2995 (CH, aliphatic), 1687, 1660 ($2\text{C}=\text{O}$), 1607 ($\text{C}=\text{C}$), 1191 cm^{-1} (C-O); ^1H NMR (300 MHz, $\text{DMSO}-d_6$) δ_{ppm} : 8.00 (d, 1H, $J=3$ Hz, ArH), 7.87 (br, 2H, NH_2), 7.74 (dd, 1H, $J=9$ Hz, 3 Hz, ArH), 7.57 (d, 1H, $J=9$ Hz, ArH), 7.15 (q, 4H, $J=9$ Hz, ArH), 4.87 (s, 1H, CH), 3.97 (q, $J=6$ Hz, 2H, OCH_2CH_3), 2.23 (s, 3H, CH_3), 1.06 (t, $J=6$ Hz, 3H, OCH_2CH_3); ^{13}C NMR (75 MHz, $\text{DMSO}-d_6$) δ_{ppm} : 168.02 (C-10, CO), 167.85 (ester CO), 160.01 (C-2), 153.73, 153.55, 140.42, 136.87, 134.55, 133.26, 130.31, 129.57 (C-8), 128.05, 124.82, 124.59, 121.12, 75.47 (C-3), 59.43 (OCH_2CH_3), 40.61 (C-4), 21.05 (CH_3), 14.60 (OCH_2CH_3); Anal. calcd. for $\text{C}_{22}\text{H}_{18}\text{ClNO}_5$: C, 64.16; H, 4.41; N, 3.40%. Found: C, 64.23; H, 4.17; N, 3.39%.

Ethyl 2-amino-8-chloro-4-(4-fluorophenyl)-10-oxo-4,10-dihydropyrano[3,2-b]chromene-3-carboxylate (6i)

white powders; yield: 89%; mp 208–210 °C; IR (KBr) ν 3469, 3334 (NH_2), 3068 (CH, aromatic), 2985 (CH, aliphatic), 1707, 1672 ($2\text{C}=\text{O}$), 1653 ($\text{C}=\text{C}$), 1194 cm^{-1} (C-O); ^1H NMR (300 MHz, $\text{DMSO}-d_6$) δ_{ppm} : 7.98 (d, 1H, $J=3$ Hz, ArH), 7.91 (br, 2H, NH_2), 7.75 (dd, 1H, $J=9$ Hz, 3 Hz, ArH), 7.58 (d, 1H, $J=9$ Hz, ArH), 7.38–7.33 (m, 2H, ArH), 7.19–7.12 (m, 2H, ArH), 4.95 (s, 1H, CH), 3.96 (q, 2H, $J=6$ Hz, OCH_2CH_3), 1.04 (t, 3H, $J=6$ Hz, OCH_2CH_3); ^{13}C NMR (75 MHz, $\text{DMSO}-d_6$) δ_{ppm} : 167.92 (C-10, CO), 167.89 (ester CO), 163.34 (C-2), 160.12, 159.98, 153.57, 153.08, 139.56, 139.52, 134.59, 133.30, 130.21 (C-8), 124.83, 124.60, 121.11, 115.88, 115.60, 75.25 (C-3), 59.43 (OCH_2CH_3), 40.55 (C-4), 14.57 (OCH_2CH_3); Anal. calcd. for $\text{C}_{21}\text{H}_{15}\text{ClFNO}_5$: C, 60.66; H, 3.64; N, 3.37%. Found: C, 60.39; H, 3.67; N, 3.13%.

Ethyl 2-amino-8-chloro-4-(4-methoxyphenyl)-10-oxo-4,10-dihydropyrano[3,2-b]chromene-3-carboxylate (6j)

yellow powders; yield: 87%; mp 207–208 °C; IR (KBr) ν 3419, 3295 (NH_2), 3072 (CH, aromatic), 2984 (CH, ali-

phatic), 1686, 1656 (C=O), 1632 (C=C), 1192 cm^{-1} (C-O); ^1H NMR (300 MHz, DMSO- d_6) δ_{ppm} : 8.00 (d, 1H, $J=3$ Hz, ArH), 7.86 (brs, 2H, NH_2), 7.76 (dd, 1H, $J=9$ Hz, 3 Hz, ArH), 7.59 (d, 1H, $J=9$ Hz, ArH), 7.22 (d, 2H, $J=9$ Hz, ArH), 6.88 (d, 2H, $J=9$ Hz, ArH), 4.87 (s, 1H, CH), 3.98 (q, 2H, $J=6$ Hz, OCH_2CH_3), 3.70 (s, 3H, OCH_3), 1.07 (t, 3H, $J=6$ Hz, OCH_2CH_3); ^{13}C NMR (75 MHz, DMSO- d_6) δ_{ppm} : 168.05 (C-10, CO), 167.86 (ester CO), 159.98 (C-2), 158.84, 153.84, 153.57, 135.40, 134.55, 133.19, 130.30, 129.22 (C-8), 124.84, 124.60, 121.13, 114.37, 75.63 (C-3), 59.42 (OCH_2CH_3), 55.47 (OCH_3), 40.17 (C-4), 14.63 (OCH_2CH_3); Anal. calcd. for $\text{C}_{22}\text{H}_{18}\text{ClNO}_6$: C, 61.76; H, 4.24; N, 3.27%. Found: C, 61.51; H, 4.29; N, 3.01%.

2. 4. Cell Culture

All the cell lines were purchased from the Iranian Biological Resource Center (IBRC, Tehran, Iran) and cultured in Dulbecco's modified Eagle's medium (DMEM, Biosera, France) supplemented with 10% heat-inactivated fetal bovine serum (FBS, Gibco, USA) and antibiotics (100 U/ml penicillin and 100 $\mu\text{g}/\text{ml}$ streptomycin, Biosera, France). The cells were incubated at 37 $^\circ\text{C}$, 5% CO_2 , and 95% relative humidity.

2. 4. 1. The Cytotoxic Assay

The synthesized compounds were dissolved in DMSO to prepare stock solutions. Afterwards, different concentrations (from 0.2 to 1000 μM) were prepared by diluting the appropriate amounts of the stock solutions in DMEM (without FBS). The final amounts of DMSO were kept below 1%.

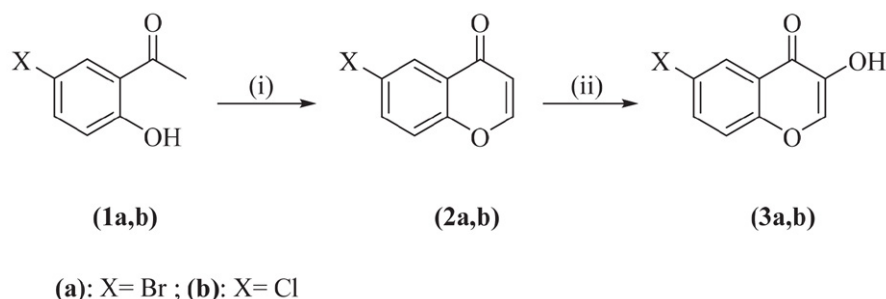
The cells with a confluency of about 80% were harvested with trypsin-EDTA (Biosera, France); and 1×10^4 cells were cultured in each well of a 96-well culture microplate. The microplates were then incubated in the same conditions mentioned above for 24 h. The next day, the media was removed from the wells and replaced with 100 μL of the prepared concentrations of the synthesized compounds or doxorubicin (as the standard). At least 3 wells of the microplate were used for each concentration. The cell controls were treated with DMEM containing the same percent of DMSO without the compounds. The microplates were further incubated for 24 h. Finally, 10 μL of the MTT

solution (5 mg/ml, Melford, England) was added to the wells, the microplates were incubated for 3 h protected from light, formed formazan crystals were solubilized in 100 μL DMSO, and the absorbance was measured at 570 nm in a multiplate reader. The experiment was repeated 3 times. GraphPad® Prism version 5 was used to calculate the IC_{50} values from the mean percent of viable cells.¹⁶

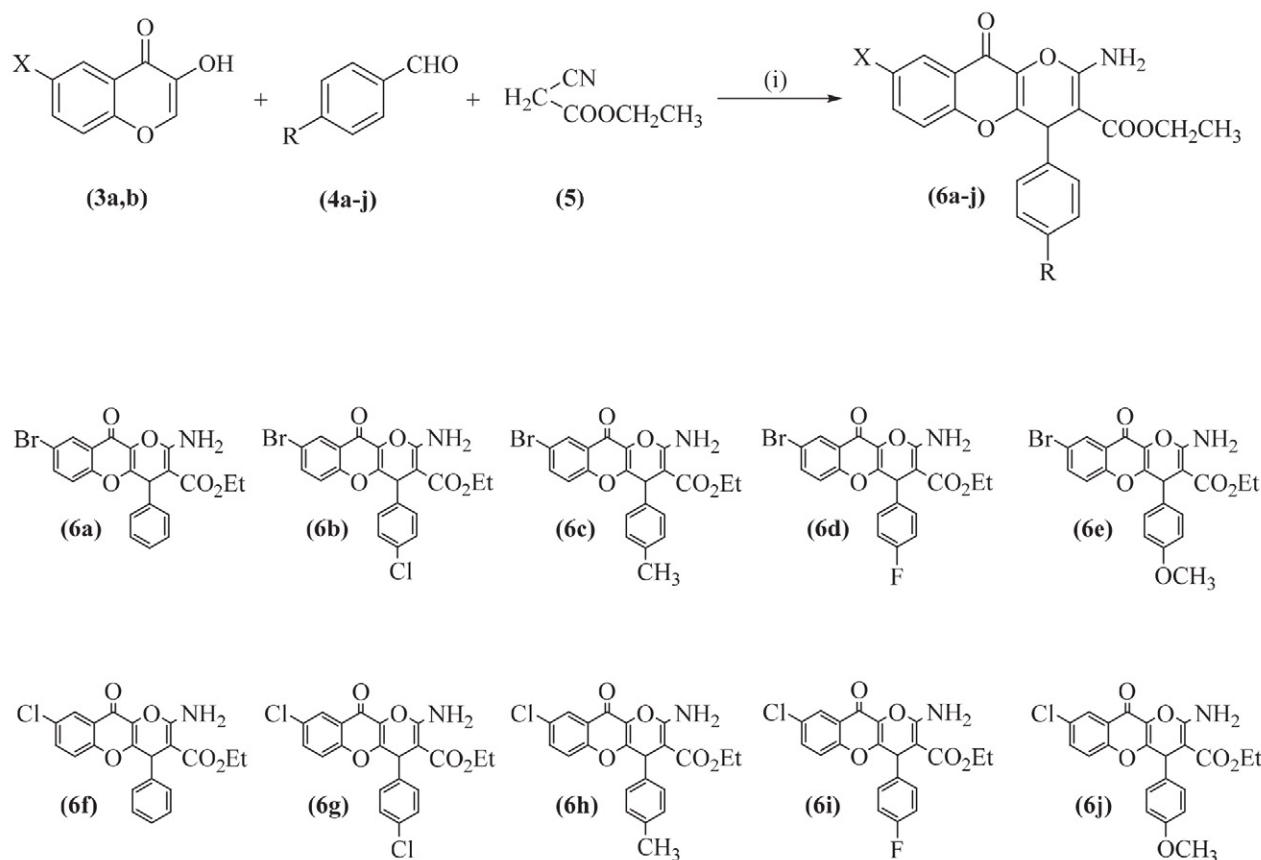
3. Results and Discussions

To prepare (6a-j) derivatives, 3-hydroxychromone derivatives were used as substrates (Scheme 1). The condensation of 5'-bromo-; or 5'-chloro-2'-hydroxyacetophenone (**1a,b**) with N,N-dimethylformamide-dimethylacetal (DMF-DMA) was irradiated under microwave conditions, then refluxed with concentrated HCl. This reaction led to the production of 6-bromo-; and 6-chloro-chromone derivatives (**2a,b**), which formed epoxy chromones upon treatment with $\text{H}_2\text{O}_2/\text{NaOH}$ in methylene chloride. This undergoes ring opening with concentrated HCl afforded 6-bromo-; and 6-chloro-3-hydroxychromones (**3a,b**) in good yields.¹³ These compounds were fully characterized by standard spectroscopic techniques (IR, ^1H and ^{13}C NMR) and elemental analyses.

Following our previous works on multi-component reactions to reach potentially bioactive scaffolds,^{18,19} we have synthesized a novel one-pot three component reaction for the synthesis of 8-halopyrano[3,2-*b*]chromen-10(4*H*)-one (**6a-j**) including 6-bromo-; and 6-chloro-3-hydroxychromones (**3a,b**), aromatic aldehydes (**4a-j**), and ethyl cyanoacetate (**5**) in the presence of three drops of Et_3N in ethanol as the solvent and at reflux conditions. After completion of the reaction, the crude product was purified by recrystallization and a series of ethyl 8-halo-4,10-dihydropyrano[3,2-*b*]chromene-3-carboxylate derivatives (**6a-j**) were prepared in 86–93% yields (Scheme 2). The structures of compounds (**6a-j**) were determined on the basis of their elemental analyses, ^1H and ^{13}C NMR and IR spectroscopic data. In similar studies heteroannulation of cyclic ketones were conducted by use of catalysts like sodium carbonate, sodium saccharine and poly(4-vinylpyridine);^{20–22} however in the present study we man-



Scheme 1. Synthesis of 6-bromo-; and 6-chloro-3-hydroxychromone. Reagents and conditions: (i): 1) DMF-DMA/ MW; 2) HCl (con.), CH_2Cl_2 , reflux; (ii): 1) H_2O_2 , NaOH, CH_2Cl_2 , ice-bath; 2) HCl (con.), reflux.



Scheme 2. Synthesis of dihydropyrano[3,2-*b*]chromene derivatives. Reagents and conditions: (i): triethylamine, EtOH, reflux.

aged to synthesized halogenated dihydropyranochromene by one pot three component reaction without any catalyst in good yields.

3. 1. The Cytotoxic Assay

To evaluate the cytotoxic activity of the synthesized compounds, MTT assay was used after treating MCF-7 (breast cancer) and A549 (lung cancer) cell lines. The compounds had three or four aromatic rings, and based on Nagai et. al, having more than two aromatic rings leads to a higher tumor specificity.⁹ The IC₅₀ values range from 36 μM (compound **6f**) to 631 μM (compound **6j**) for MCF-7 and 56 μM (compound **6f**) to 558 μM (compound **6j**) for A549 cells (Table 1). The most potent compound is compound **6f** (Fig.1). Compared to compound **6a**, which has a Br atom in C8, **6f** (the compound with a Cl atom in this position) is about 11 and 7 times stronger on MCF-7 and A549, respectively. Placing any moiety on para position of aromatic aldehydes (R) leads to a decrease in the cytotoxicity when X is a chlorine atom, however, when X is a bromine atom, adding an R moiety results in a more potent compound especially when the R group is a chlorine atom (compound **6b**). In our previous study, a halogen group substitution on the carbon 4 of the phenyl ring decreased

the cytotoxic activity of the compound except when it was Cl, interestingly it is also understood that chromenes bearing chlorine and bromine have quite much cytotoxic effect in comparison with ones that lack Cl and Br.¹⁹ Since compound **6f** can be a promising candidate as a cytotoxic agent, it was tested on SW480 (a colorectal cancer cell line) and HUVEC (Human Umbilical Vein Endothelial Cells). The IC₅₀ values were 10.8 ± 1.5 and 57.2 ± 3.2 μM, respectively. By comparison of our compounds with benzo[*h*]chromene derivatives, it is revealed that fused ring at 2,3-position may boost antitumor activity of compound.²³ So a rationale in our future work is to fuse ring at 2,3 position and making new compounds which may have stronger cytotoxic activity. One study showed that inclusion of thienyl group next to chromene ring make these compounds more potent and also selective against prostate cancer.²² In another study it is found that a chlorophenyl moiety on central dihyrobenzo[*h*]pyrano[3,2-*c*]chromene ring has a positive impact on cytotoxicity, which is also effective in our compounds.²⁴ It is also revealed that electron withdrawing group at the four position of the phenyl ring at the 1-position of 1*H*-benzo[*f*]chromene enhance the antitumor activity of the compounds.²⁵ This trend is also in accordance with our finding. Generally, it seems that modifications at the C-4 and C-6 positions of

Table 1. The IC_{50} (μM) values of the compounds on two cancer cell lines measured by MTT assay method (mean \pm standard error of mean).

Compd. NO.	A549	MCF-7
6a	414.8 \pm 2.1	389.0 \pm 18
6b	120.5 \pm 0.3	115.5 \pm 1.2
6c	155 \pm 1.2	169.1 \pm 0.5
6d	142.3 \pm 0.5	168.5 \pm 1.5
6e	150.5 \pm 8.9	175.8 \pm 1.9
6f	56 \pm 0.3	35.8 \pm 3.8
6g	107.8 \pm 6.4	179.8 \pm 5.8
6h	272.3 \pm 8.9	232.1 \pm 3
6i	230.6 \pm 4.8	328.8 \pm 16.6
6j	558.2 \pm 8.7	631.2 \pm 8.5
Doxorubicin	7.9 \pm 0.2	6.4 \pm 0.1

chromenes have impacts on anticancer activity of these compounds.²⁶

4. Conclusion

The present study describes the synthesis and investigation of cytotoxic activities of a series of novel halopyranochromene derivatives. We have synthesized some derivatives by one-pot three component reactions of 6-bromo-; or 6-chloro-3-hydroxychromone, aromatic aldehydes, and ethyl cyanoacetate in the presence of triethylamine in ethanol as solvent and at reflux conditions. Some of the compounds showed moderate cytotoxicity on the two cancer cell lines (A549 and MCF-7). The best com-

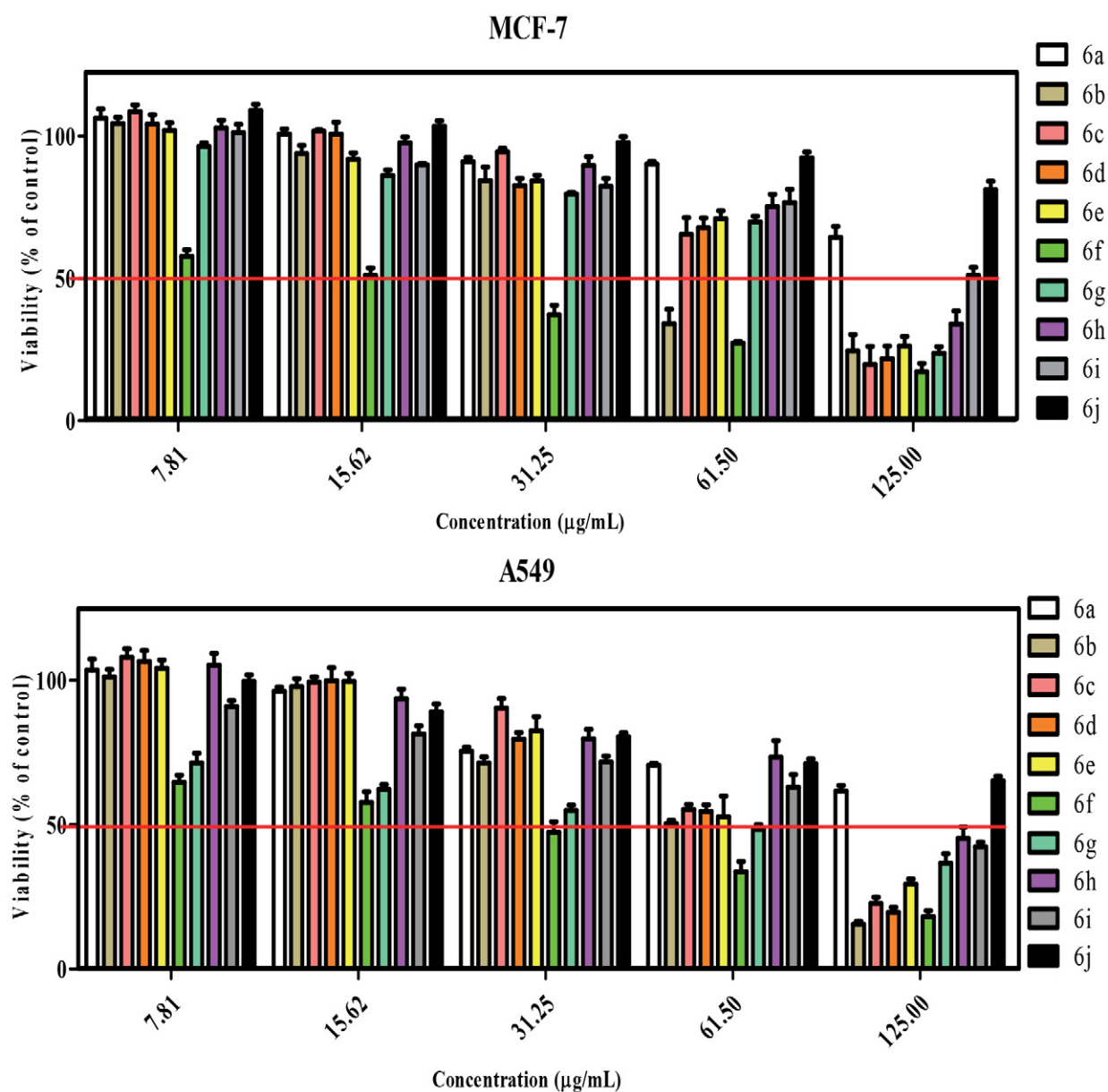


Fig. 1. The viability percent of the cells (MCF-7 and A549) after 24 hours treatment with different concentrations of the synthesized compounds.

pound had a Cl atom (C8) and a phenyl ring (C4) of pyranochromene scaffold (compound **6f**). It is concluded that these compounds can be lead compounds for synthesizing anticancer agents.

Abbreviations

EtOH: ethanol; MTT: (3-(4,5-dimethylthiazol-2-yl)-2,5-diphenyltetrazolium bromide; DMF-DMA: N,N-dimethylformamide-dimethylacetal; HUVEC: Human Umbilical Vein Endothelial Cells; IC₅₀: 50% Inhibition concentration; KBr: Potassium bromide; ppm: parts per million; TLC: thin layer chromatography.

Supplementary Information

The online version contains supplementary material available at <https://doi....>

Acknowledgements

The authors express their great appreciation to Pharmaceutics Research Center, Institute of Neuropharmacology, Kerman University of Medical Sciences for supporting this investigation.

Authors' contributions

Ehsan Faghih-Mirzaei and Mehdi Abaszadeh, designed, synthesized and performed experiments, analysed data and wrote the paper. Salehe Sabouri, designed and performed the biologic assay and data analysis and contributed in writing the manuscript. All authors were involved in revising the content, agree to take accountability for the integrity and accuracy of the work, and have read and approved the final manuscript.

Funding

This research was supported by a grant from Kerman University of Medical Sciences [No.97000675]. The funders had no role in the research design, data collection, analysis, and the decision to publish.

Disclosure statement

No potential conflict of interest was reported by the authors.

5. References

1. G. P. Ellis. Chemistry of Heterocyclic Compounds: Chromenes, Chromanones, and Chromones, vol. 31. New York: John Wiley & Sons, Inc.; 1977, pp. 1–10. DOI:10.1002/9780470187012.ch1
2. A. Gaspar, M. J. Matos, J. Garrido, E. Uriarte, F. Borges. *Chem Rev.* **2014**, 114, 4960–92. DOI:10.1021/cr400265z
3. S. Yang, J. Zhou, D. Li, C. Shang, L. Peng, S. Pan. *Food Chem.* **2017**, 224, 26–31. DOI:10.1016/j.foodchem.2016.12.001
4. T. P. Cushnie, A. J. Lamb. *Int J Antimicrob Agents.* **2005**, 26, 343–56. DOI:10.1016/j.ijantimicag.2005.09.002
5. S. Lee, W. K. Yang, J. H. Song, Y. M. Ra, J. H. Jeong, W. Choe, I. Kang, S. S. Kim, J. Ha. *Biochem Pharmacol.* **2013**, 85, 965–76. DOI:10.1016/j.bcp.2012.12.023
6. H. Zakaryan, E. Arabyan, A. Oo, K. Zandi. *Arch Virol.* **2017**, 162, 2539–51. DOI:10.1007/s00705-017-3417-y
7. P. Ninfali, A. Antonelli, M. Magnani, E. S. Scarpa. *Nutrients.* **2020**, 12, 2534. DOI:10.3390/nu12092534
8. H. P. Kim, K. H. Son, H. W. Chang, S. S. Kang. *J Pharmacol Sci.* **2004**, 96, 229–45. DOI:10.1254/jphs.CRJ04003X
9. J. Nagai, H. Shi, N. Sezaki, N. Yoshida, K. Bandow, Y. Uesawa, H. Sakagami, M. Tomomura, A. Tomomura, K. Takao, Y. Sugita. *Anticancer Res.* **2019**, 39, 6479–88. DOI:10.21873/anticancer.13862
10. J. Baby, A. R. Devan, A. R. Kumar, J. N. Gorantla, B. Nair, T. S. Aishwarya, L. R. Nath. *J Food Biochem.* **2021**, 45, e13761 (1–23).
11. N. Phosrithong, W. Samee, P. Nunthanavanit, J. Ungwitayatorn. *Chem Biol Drug Des.* **2012**, 79, 981–89. DOI:10.1111/j.1747-0285.2012.01368.x
12. J. Lee, T. Park, S. Jeong, K. Kim, C. Hong. *Bioorg Med Chem Lett.* **2007**, 17, 1284–87. DOI:10.1016/j.bmcl.2006.12.011
13. M. Spadafora, V. Y. Postupalenko, V. V. Shvadchak, A. S. Klymchenko, Y. Mély, A. Burger, R. Benhida. *Tetrahedron.* **2009**, 65, 7809–16. DOI:10.1016/j.tet.2009.07.021
14. A. M. Verdan, H. C. Wang, C. R. Garcia, W. P. Henry, J. L. Brumaghim. *J Inorg Biochem.* **2011**, 105, 1314–22. DOI:10.1016/j.jinorgbio.2011.07.006
15. R. L. Siegel, K. D. Miller, H. E. Fuchs, A. Jemal. *Cancer J Clin.* **2021**, 71, 7–33. DOI:10.3322/caac.21654
16. M. Abaszadeh, A. Ebrahimi, S. Sabouri. *Biointerface Res Appl Chem.* **2021**, 11, 10987–95. DOI:10.33263/BRIAC113.1098710995
17. P. Rao, G. Srimannarayana. *Synth Commun.* **1987**, 17, 1507–12. DOI:10.1080/00397918708057776
18. M. Abaszadeh, M. Seifi. *Lett Org Chem.* **2015**, 12, 271–76. DOI:10.2174/1570178612666150203004727
19. S. Sabouri, M. Abaszadeh. *Polycyclic Aromat. Compd.* **2021**, 41, 467–77. DOI:10.1080/10406638.2019.1597381
20. R. Keshavarz, M. Farahi, B. Karami. *Acta Chim. Slov.* **2021**, 68, 332–340. DOI:10.17344/acsi.2020.6266
21. L. Moradi, M. Aghamohammad Sadegh. *Acta Chim. Slov.* **2017**, 64, 506–512. DOI:10.17344/acsi.2017.3417
22. J. Albadi, A. Mansourneshad, F. Akbari Balout-Bangan. *Acta Chim. Slov.* **2014**, 61, 185–190.
23. R. M. Okasha, F. F. Alblewi, T. H. Afifi, A. Naqvi, A. M. Fouda, A. A. M. Al-Dies, A. M. El-Agrody. *Molecules.* **2017**, 22, 479. DOI:10.3390/molecules22030479
24. N. Esmati, M. Foroughian, M. Saeedi, M. Mahdavi, M. Khoshneviszadeh, O. Firuzi, N. Tanideh et al. *J. Heterocycl. Chem.* **2015**, 52, 97–104. DOI:10.1002/jhet.1991

25. H. M. Mohamed, A. M. Fouda, E. S. Khattab, A. M. El-Agrody, and T. H. Afifi. *Zeitschrift für Naturforschung C*. **2017**, 72, 161–71.
26. V. Raj, J. Lee. *Front. Chem.* **2020**, 8, 623. DOI:10.3389/fchem.2020.00623

Povzetek

Pljučni rak in rak dojke sta med najpogostejšimi raki. V okviru dela smo najprej pripravili 6-bromo- in 6-kloro-3-hidroksikromonske spojine. V naslednjem koraku je bila sintetizirana serija derivatov 8-bromo- in 8-kloro-dihidropirano[3,2-b] kromena s hkratno trikomponentno reakcijo teh dveh spojin, aromatskih aldehydov in etil cianoacetata v prisotnosti trietilamina v EtOH pri pogojih povratnega toka. Sintetizirane spojine so bile testirane za *in vitro* citotoksično delovanje na celičnih linijah A549 (pljučni rak) in MCF-7 (rak dojke). Ugotovljeno je bilo, da imajo nekatere spojine visoko do zmerno citotoksičnost, zato so potencialni kandidati za nadaljnje študije. Ta študija je lahko podlaga za nadaljnje študije za načrtovanje in sintezo močnih proti-rakavih spojin ter raziskovanje njihovega mehanizma delovanja.



Except when otherwise noted, articles in this journal are published under the terms and conditions of the Creative Commons Attribution 4.0 International License

Syntheses, Crystal Structures and Xanthine Oxidase Inhibitory Activity of Aroylhydrazones

Yong-Jun Han,¹ Xue-Yao Guo² and Ling-Wei Xue^{1,*}

¹ School of Chemical and Environmental Engineering, Pingdingshan University, Pingdingshan Henan 467000, P.R. China

² Pingdingshan Ecological Environment Monitoring Center, Henan 467000, P.R. China

* Corresponding author: E-mail: pdsuchemistry@163.com

Received: 09-21-2022

Abstract

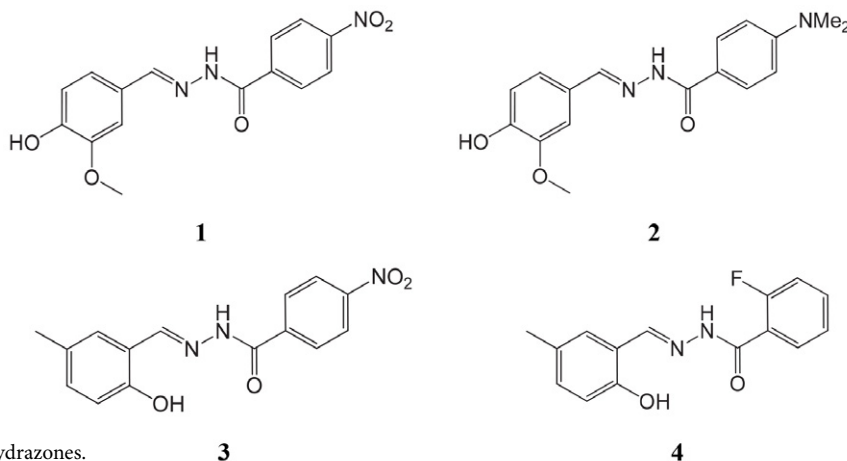
A series of hydrazones, (*E*)-*N'*-(4-hydroxy-3-methoxybenzylidene)-4-nitrobenzohydrazide (1), (*E*)-4-(dimethylamino)-*N'*-(4-hydroxy-3-methoxybenzylidene)benzohydrazide (2), *N'*-(2-hydroxy-5-methylbenzylidene)-4-nitrobenzohydrazide (3) and 2-fluoro-*N'*-(2-hydroxy-5-methylbenzylidene)benzohydrazide (4), were prepared and structurally characterized by elemental analysis, IR and ¹H NMR spectra, and X-ray single crystal determination. The xanthine oxidase inhibitory activities of the compounds were investigated. Among the compounds, *N'*-(3-methoxybenzylidene)-4-nitrobenzohydrazide (1) showed the strongest activity. Docking simulations were performed to insert the compounds into the crystal structure of xanthine oxidase at the active site and to investigate the probable binding modes.

Keywords: Hydrazone; xanthine oxidase; inhibition; crystal structure; molecular docking study.

1. Introduction

Xanthine oxidase (XO; EC 1.17.3.2), a molybdenum hydroxylase, catalyzes the hydroxylation of hypoxanthine and xanthine to form uric acid and superoxide anions. These superoxide anions are associated with postischemic tissue damage and edema, as well as vascular permeability.¹ XO can oxidize the synthetic purine drug 6-mercaptopurine, causing it to lose its pharmacologic properties. XO is also associated with diseases such as liver and kidney

damage, atherosclerosis, chronic heart failure, hypertension, and sickle cell anemia because it produces reactive oxygen species (ROS) in addition to uric acid.² Therefore, control of XO activity may be helpful in the therapy of some diseases. Allopurinol is a widely recognized XO inhibitor used to treat gout.³ However, given its side effects, toxicity, and inability to prevent free radical formation by the enzyme,⁴ there is a need to investigate new and efficient XO inhibitors. A number of compounds of different



Scheme 1. The aroylhydrazones.

types, such as carboxylic acids and pyrimidines,⁵ pyrimidinones and 3-cyanoindoles,⁶ amides,⁷ pyrazoles,⁸ thiobarbiturates,⁹ hydrozingerones,¹⁰ have been described with XO inhibitory activities. Schiff bases have long been of great interest in biological chemistry.¹¹ Leigh and coworkers have described some Schiff bases as novel XO inhibitors.¹² However, studies on hydrazones are limited, and rational structure-activity relationships have not yet been established. As an extension of work exploring effective XO inhibitors in conjunction with Schiff bases, a series of hydrazone-like Schiff bases, (*E*)-*N'*-(4-hydroxy-3-methoxybenzylidene)-4-nitrobenzohydrazide (**1**), (*E*)-4-(dimethylamino)-*N'*-(4-hydroxy-3-methoxybenzylidene)benzohydrazide (**2**), *N'*-(2-hydroxy-5-methylbenzylidene)-4-nitrobenzohydrazide (**3**), and 2-fluoro-*N'*-(2-hydroxy-5-methylbenzylidene)benzohydrazide (**4**), were synthesized and structurally characterized. The XO inhibitory activities of the compounds were investigated by both experimental and molecular docking studies.

2. Experimental

2.1. Materials and Methods

Starting materials, reagents, and solvents of AR grade were purchased from commercial suppliers and used without further purification. Elemental analyses were performed using a Perkin-Elmer 240C elemental analyzer. IR spectra were recorded as KBr pellets in the 4000–400 cm^{-1} range using a Jasco FT/IR-4000 spectrometer. ^1H NMR data were recorded using a Bruker 300 MHz instrument and X-ray diffraction was performed with a Bruker SMART 1000 CCD area diffractometer.

2.2. General Method for the Synthesis of the Compounds

The compounds were prepared according to the literature method.¹³ Equimolar amounts (1.0 mmol each) of the hydrazides and aldehydes were dissolved in methanol (30 ml) and stirred at room temperature for 30 minutes to give a clear solution. X-ray quality single crystals were formed by slowly evaporating the solution in air over several days.

2.2.1. *N'*-(3-Methoxybenzylidene)-4-nitrobenzohydrazide (**1**)

4-Hydroxy-3-methoxybenzaldehyde and 4-nitrobenzohydrazide. Yield: 87%. Anal. calcd. for $\text{C}_{11}\text{H}_{10}\text{N}_2\text{O}_6$: C, 54.7; H, 4.7; N, 12.3; Found: C, 54.5; H, 4.8; N, 12.4%. IR (KBr, cm^{-1}) ν 3318 (m, O-H), 3217 (m, N-H), 1653 (s, C=O), 1621 (s, C=N). ^1H NMR (300 MHz, CDCl_3) δ 12.07 (s, 1H, -NH), 10.12 (s, 1H, -OH), 8.57 (s, 1H, CH=N), 8.08–8.50 (m, 4H, ArH), 6.87–7.53 (m, 3H, ArH), 3.79 (s, 3H, -OCH₃).

2.2.2. *N'*-(4-Hydroxy-3-methoxybenzylidene)-4-dimethylaminobenzohydrazide (**2**)

4-Hydroxy-3-methoxybenzaldehyde and 4-dimethylaminobenzohydrazide. Yield: 91%. Anal. calcd. for $\text{C}_{17}\text{H}_{21}\text{N}_3\text{O}_4$: C, 61.6; H, 6.4; N, 12.7; Found: C, 61.5; H, 6.4; N, 12.6%. IR data (KBr, cm^{-1}) ν 3351 (m, O-H), 3208 (m, N-H), 1649 (s, C=O), 1623 (s, C=N). ^1H NMR (300 MHz, CDCl_3) δ 12.23 (s, 1H, -NH), 10.10 (s, 1H, -OH), 8.56 (s, 1H, CH=N), 6.90–7.63 (m, 7H, ArH), 3.79 (s, 3H, -OCH₃), 3.02 (s, 6H, -N(CH₃)₂).

2.2.3. *N'*-(2-Hydroxy-5-methylbenzylidene)-4-nitrobenzohydrazide (**3**)

5-Methylsalicylaldehyde and 4-nitrobenzohydrazide. Yield: 89%. Anal. calcd. for $\text{C}_{15}\text{H}_{13}\text{N}_3\text{O}_4$: C, 60.2; H, 4.4; N, 14.0. Found: C, 60.1; H, 4.5; N, 14.2%. IR data (KBr, cm^{-1}) ν 3403 (w, O-H), 3186 (w, N-H), 1650 (s, C=O), 1606 (s, C=N), 1565 (m, NO₂), 1334 (s, NO₂). ^1H NMR (300 MHz, CDCl_3) δ 12.17 (s, 1H, -NH), 11.23 (s, 1H, -OH), 8.75 (s, 1H, CH=N), 8.39 (d, 2H, ArH), 8.15 (d, 2H, ArH), 7.51 (s, 1H, ArH), 7.12 (d, 1H, ArH), 6.89 (d, 1H, ArH), 2.32 (s, 3H, CH₃).

2.2.4. 2-Fluoro-*N'*-(2-hydroxy-5-methylbenzylidene)benzohydrazide (**4**)

5-Methylsalicylaldehyde and 2-fluorobenzohydrazide. Yield: 92%. Anal. calcd. for $\text{C}_{15}\text{H}_{13}\text{FN}_2\text{O}_2$: C, 66.2; H, 4.8; N, 10.3. Found: C, 66.0; H, 4.7; N, 10.2%. IR data (KBr, cm^{-1}) ν 3411 (w, O-H), 3183 (w, N-H), 1653 (s, C=O), 1608 (s, C=N). ^1H NMR (300 MHz, CDCl_3) δ 12.21 (s, 1H, -NH), 11.16 (s, 1H, -OH), 8.75 (s, 1H, CH=N), 8.01 (m, 2H, ArH), 7.50 (s, 1H, ArH), 7.41 (m, 2H, ArH), 7.12 (d, 1H, ArH), 6.89 (d, 1H, ArH), 2.32 (s, 3H, CH₃).

2.3. Measurement of the XO Inhibitory Activity

XO activities with xanthine as substrate were measured spectrophotometrically, based on the procedure reported by L. D. Kong et al (with modifications).¹⁴ Xanthine oxidase activity is measured by the formation of uric acid at 295 nm. The assay was performed in a final volume of 1 mL 50 mmol L⁻¹ K₂HPO₄ pH 7.8 in a quartz cuvette. The reaction mixture contains 200 μL of 84.8 $\mu\text{g}\cdot\text{mL}^{-1}$ xanthine in 50 mmol L⁻¹ K₂HPO₄, 50 μL of the tested compounds at various concentrations. The reaction is started by adding 66 μL 37.7 mU mL⁻¹ xanthine oxidase. The reaction is monitored at 295 nm for 6 min, and the product is expressed as μmol of uric acid per minute. The reaction kinetics were linear during this 6-minute monitoring.

2.4. Docking Simulations

The molecular docking study of the compounds to the 3D X-ray structure of XO (entry 1FIQ in the Protein Data

Bank) was performed using AutoDock version 4.2. First, the AutoGrid component of the program precomputes a 3D grid with interaction energies based on the macromolecular target using the force field AMBER. The cubic grid box with $60 \times 80 \times 66 \text{ \AA}^3$ points in x, y, and z directions with a spacing of 0.375 \AA and grid maps were created representing the catalytically active target region in which the native ligand was embedded. Automated docking studies were then performed to determine the free energy of the inhibitor within the macromolecules. The search algorithm GALS (genetic algorithm with local search) was chosen to search for the best conformers. Parameters were set using ADT software (AutoDock-Tools package, version 1.5.4) at PC in conjunction with AutoDock 4.2. Default settings were used with an initial population of 100 randomly placed individuals, a maximum number of 2.5×10^6 energy ratings, and a maximum number of 2.7×10^4 generations. A mutation rate of 0.02 and a crossover rate of 0.8 were chosen. Considering the most favorable free energy of the bidding and majority clusters, the results were selected as the most likely complex structures.

2. 5. Data Collection, Structural Determination and Refinement

Diffraction intensities for the compounds were recorded at 298(2) K using a Bruker D8 VENTURE PHO-

TON diffractometer with Mo K α radiation ($\lambda = 0.71073 \text{ \AA}$). Collected data were reduced using SAINT,¹⁵ and multi-scan absorption corrections were performed using SADABS.¹⁶ Structures were solved using direct methods and refined against F² using full matrix least squares methods with SHELXTL.¹⁷ All non-hydrogen atoms were refined anisotropically. The amino, hydroxyl, and water H atoms were localized using Fourier difference maps and refined isotropically, with N-H, O-H, and H...H distances constrained to 0.90(1), 0.85(1), and 1.37(2) \AA , respectively. All other H atoms were placed in idealized positions and confined to their parent atoms. Crystallographic data for the compounds are summarized in Table 1. Information on the hydrogen bonds can be found in Table 2.

3. Results and Discussion

3. 1. Chemistry

The compounds were readily synthesized by reacting aldehydes in a 1:1 molar ratio with hydrazides in methanol at room temperature with high yield and purity. Single crystals suitable for X-ray diffraction were obtained by slowly evaporating the solutions containing the compounds in air. The compounds were characterized by elemental analyses and IR spectra. The structures of the compounds were also confirmed by single crystal X-ray crystallography.

Table 1. Crystallographic and experimental data for the compounds.

Compound	1 $\times \frac{1}{2} \text{H}_2\text{O}$ $\times \frac{1}{2} \text{CH}_3\text{OH}$	2	3 $\times \text{H}_2\text{O}$	4
Formula	$\text{C}_{31}\text{H}_{32}\text{N}_6\text{O}_{12}$	$\text{C}_{17}\text{H}_{21}\text{N}_3\text{O}_4$	$\text{C}_{15}\text{H}_{13}\text{N}_3\text{O}_4$	$\text{C}_{15}\text{H}_{10}\text{F}_3\text{N}_3\text{O}_5$
<i>Mr</i>	680.6	331.4	299.3	369.3
<i>T</i> (K)	298(2)	298(2)	298(2)	298(2)
Crystal system	Triclinic	Monoclinic	Monoclinic	Monoclinic
Space group	<i>P</i> -1	<i>P</i> ₂ / <i>n</i>	<i>P</i> ₂ / <i>c</i>	<i>P</i> ₂ / <i>c</i>
<i>a</i> (\AA)	7.655(1)	8.243(1)	10.257(2)	9.753(2)
<i>b</i> (\AA)	12.638(2)	21.573(2)	15.190(2)	10.505(2)
<i>c</i> (\AA)	17.213(1)	10.106(2)	9.181(3)	14.251(30)
α ($^\circ$)	77.350(2)	90	90	71.257(2)
β ($^\circ$)	80.122(2)	106.749(2)	94.912(2)	84.879(3)
γ ($^\circ$)	88.953(2)	90	90	81.267(3)
<i>V</i> (\AA^3)	1600.4(3)	1720.8(5)	1425.2(6)	1365.5(5)
<i>Z</i>	2	4	4	4
<i>D_c</i> (g cm^{-3})	1.412	1.279	1.395	1.324
μ (Mo-K α) (mm^{-1})	0.110	0.092	0.104	0.099
<i>F</i> (000)	712	704	624	568
Reflections collected	11674	8178	5818	10030
Unique reflections	5874	3178	2597	4990
Observed reflections ($I \geq 2\sigma(I)$)	2665	1655	1315	4077
Parameters	458	230	205	371
Restraints	36	4	2	2
Goodness-of-fit on <i>F</i> ²	0.988	0.993	0.941	1.069
<i>R</i> ₁ , <i>wR</i> ₂ [$I \geq 2\sigma(I)$] ^a	0.0679, 0.1664	0.0586, 0.1236	0.0618, 0.1111	0.0482, 0.1460
<i>R</i> ₁ , <i>wR</i> ₂ (all data) ^a	0.1516, 0.2129	0.1261, 0.1543	0.1313, 0.1334	0.0614, 0.1718
Large diff. peak and hole (e \AA^{-3})	0.244, −0.528	0.186, −0.177	0.157, −0.203	0.509, −0.329

^a $R_1 = F_o - F_c/F_o$, $wR_2 = [w(F_o^2 - F_c^2)/\sum w(F_o^2)^{1/2}]^{1/2}$

Table 2. Hydrogen bond distances (Å) and bond angles (°) for the compounds.

<i>D</i> – <i>H</i> ... <i>A</i>	<i>d</i> (<i>D</i> – <i>H</i>)	<i>d</i> (<i>H</i> ... <i>A</i>)	<i>d</i> (<i>D</i> ... <i>A</i>)	Angle(<i>D</i> – <i>H</i> ... <i>A</i>)
1				
O11–H11A...N1	0.85(1)	2.32(2)	3.092(5)	153(4)
O11–H11A...O1	0.85(1)	2.31(3)	2.861(5)	124(3)
O11–H11B...O7 ^{#1}	0.85(1)	2.25(3)	3.011(5)	150(4)
N5–H5A...O4 ^{#2}	0.90(1)	2.13(2)	3.003(4)	165(4)
N2–H2A...O12	0.90(1)	1.99(2)	2.870(5)	168(4)
O12–H12A...O11 ^{#3}	0.82	1.89	2.709(7)	177
O8–H8...O1 ^{#1}	0.82	2.04	2.813(4)	156
O3–H3...O6 ^{#4}	0.82	1.91	2.718(4)	169
2				
O1–H1...O4 ^{#5}	0.82	1.79	2.608(3)	172
N2–H2...O1 ^{#6}	0.90(1)	2.25(1)	3.141(3)	173(3)
O4–H4A...O3 ^{#7}	0.85(1)	1.88(1)	2.734(3)	175(3)
O4–H4B...O3 ^{#6}	0.85(1)	2.07(2)	2.850(3)	152(3)
O4–H4B...N1 ^{#6}	0.85(1)	2.49(2)	3.170(3)	137(2)
3				
O1–H1...N1	0.85(1)	1.90(2)	2.655(3)	147(3)
N2–H2...O2 ^{#8}	0.90(1)	2.04(2)	2.911(3)	163(3)
4				
N4–H4...O2 ^{#9}	0.90(1)	2.05(1)	2.920(2)	163(2)
N2–H2...O4	0.90(1)	1.99(1)	2.872(2)	168(2)
O3–H3...N3	0.82	1.89	2.609(2)	145
O1–H1...N1	0.82	1.92	2.619(2)	143

Symmetry codes: #1: $1-x, 1-y, 1-z$; #2: $x, y, -1+z$; #3: $x, 1-y, 1-z$; #4: $-1+x, 1+y, z$; #5: $x, y, -1+z$; #6: $-1/2+x, 1/2-y, -1/2+z$; #7: $3/2-x, -1/2+y, 1/2-z$; #8: $x, 1/2-y, -1/2+z$; #9: $1+x, y, z$.

3. 2. Structure Description of the Compounds 1 and 2

The structures of compounds **1** and **2** and the numbering scheme of the atoms are shown in Figures 1 and 2, respectively. The asymmetric unit of **1** contains two carbohydrazone molecules, one methanol molecule, and one water molecule. The asymmetric unit of **2** contains one carbohydrazone molecule and one water molecule. The carbohydrazone molecules adopt an *E* configuration around the C=N bonds. The dihedral angles between the C1–C6 and C9–C14 in benzene rings, and C16–C21 and C24–C29 in **1**, and C1–C6 and C9–C14 in **2** are 5.8(3), 5.2(3), and 10.4(3)°, respectively. The bond distances C7–N1 (1.285(4) Å) and C22–N4 (1.258(4) Å) in **1** and C7–N1 (1.259(3) Å) in **2** correspond to C=N double bonds and are comparable to the previously reported analogs of carbohydrazones.¹⁸ The bond distances C8–N2 (1.330(5) Å) and C23–N5 (1.339(4) Å) in **1** and C8–N2 (1.339(4) Å) in **2** are shorter than the typical values for C–N single bonds, indicating the presence of conjugation in the carbohydrazone molecules.

In the crystal structures of the two compounds, the carbohydrazone molecules and the solvent molecules are connected *via* N–H...O, O–H...N, and O–H...O intermolecular hydrogen bonds to form 3D networks (Figure 3

for **1** and Figure 4 for **2**). The water and methanol molecules in the compounds act as both acceptors and donors in the hydrogen bonds. In addition, weak π ... π interactions are observed in **1**, ranging from 3.6461 to 3.9636 Å. In **2**, the centroid to centroid distances are in the range of 4.8621–5.5703 Å, which are far from the π ... π interactions.

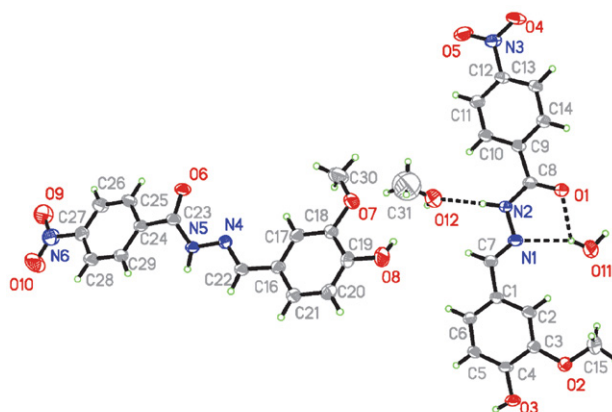


Figure 1. A perspective view of the molecular structure of **1** showing the atomic labeling scheme. The thermal ellipsoids are drawn at the 30% probability level. The hydrogen bonds are shown as a dashed line.

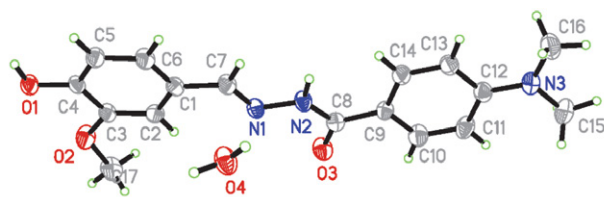


Figure 2. A perspective view of the molecular structure of **2** showing the atomic labeling scheme. The thermal ellipsoids are drawn at the 30% probability level.

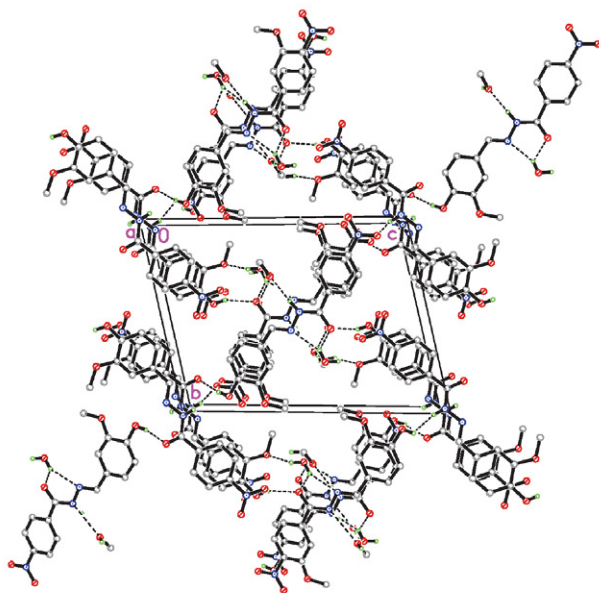


Figure 3. The packing diagram of **1**. Hydrogen bonding interactions are shown as dashed lines.

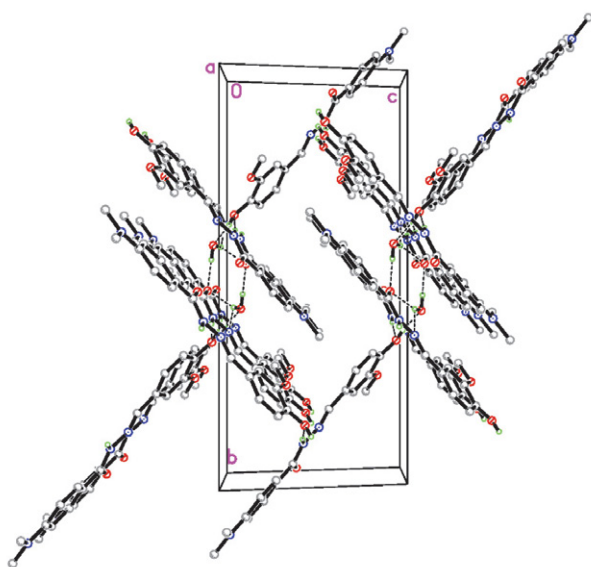


Figure 4. The packing diagram of **2**. Hydrogen bonding interactions are shown as dashed lines.

3. 3. Structure Description of the Compounds **3** and **4**

The structures of compounds **3** and **4** are shown in Figures 5 and 6, respectively, along with the atom numbering scheme. The asymmetric unit of compound **3** consists of two independent molecules. All molecules of the compounds adopt the *trans* configuration with respect to the C=N methylidene units. The distances of the methylidene bonds, ranging from 1.26 to 1.28 Å, confirm that they are typical double bonds. The shorter than usual distances of the C–N bonds and the longer than usual distances of the C=O bonds for the –C(O)–NH units indicate the presence of conjugation effects in the molecules. It is noteworthy that the C8=N1 bond in **3** is much shorter than that of the C=N double bonds in **4**, which could be due to the electron-withdrawing effects of the nitro groups. The other bond lengths in the compounds are comparable with each other and are within normal values.¹⁸ The dihedral angles between the two aromatic rings are 4.8(3)° for **3** and 31.1(3)° and 52.4(3)° for **4**. In each of the compounds, an intramolecular O–H...N hydrogen bond (Table 2) forms an S(6) ring motif.¹⁹

In the crystal structure of **3**, the molecules are linked by intermolecular N–H...O hydrogen bonds (Table 2) and form 1D chains running along the *c* axis (Figure 7). In the crystal structure of **4**, the molecules are linked by intermolecular N–H...O hydrogen bonds (Table 2) and form 1D chains running along the *c*-axis (Figure 8). In addition, weak π ... π interactions are observed in the compounds, ranging from 3.692 to 4.025 Å for **3** and from 4.018 to 4.833 Å for **4**.

3. 4. Infrared and ¹H NMR Spectra

The broad and intermediate bands at 3318 cm^{−1} (**1**) and 3351 cm^{−1} (**2**) are due to the O–H stretching vibrations of the water and hydroxyl groups. The sharp bands at 3217 cm^{−1} (**1**), 3208 cm^{−1} (**2**), 3186 cm^{−1} (**3**) and 3183 cm^{−1} (**4**) are due to the N–H stretching vibrations. The compounds exhibit strong absorptions at 1621–1623 cm^{−1} for **1** and **2**, and 1606–1608 cm^{−1} for **3** and **4**, which can be attributed to the C=N vibrations.²⁰ The bands originating from the stretching vibrations of the C=O groups are observed at 1649–1653 cm^{−1} for the compounds. The bands

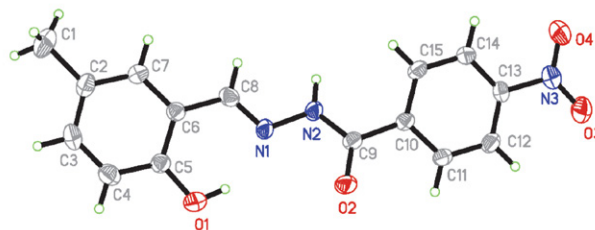


Figure 5. A perspective view of the molecular structure of **3** showing the atomic labeling scheme. The thermal ellipsoids are drawn at the 30% probability level.

indicative of the $\nu_{as}(\text{NO}_2)$ and $\nu_s(\text{NO}_2)$ vibrations are observed at 1565 and 1334 cm^{-1} for compound **1**.²⁰

In ^1H NMR, the absence of NH_2 signals and the appearance of peaks for NH protons in the range $\delta = 12.07$ –12.23 ppm and imine CH protons in the range $\delta = 8.56$ –8.75 ppm confirm the synthesis of the hydrazine compounds. The signals of aromatic protons were found in their respective ranges with different multiplicities, confirming their relevant substitution pattern.

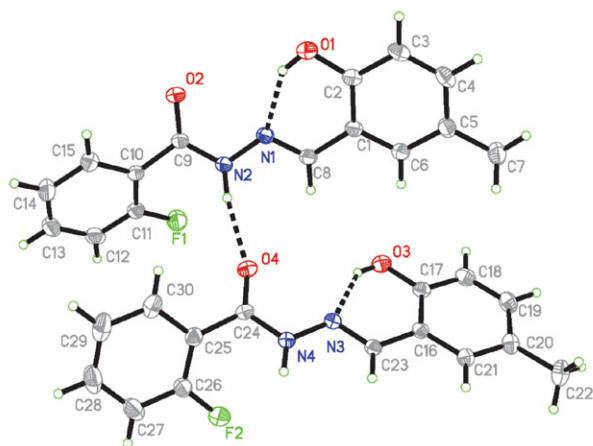


Figure 6. A perspective view of the molecular structure of **4** showing the atomic labeling scheme. The thermal ellipsoids are drawn at the 30% probability level. Hydrogen bonds are shown as dashed lines.

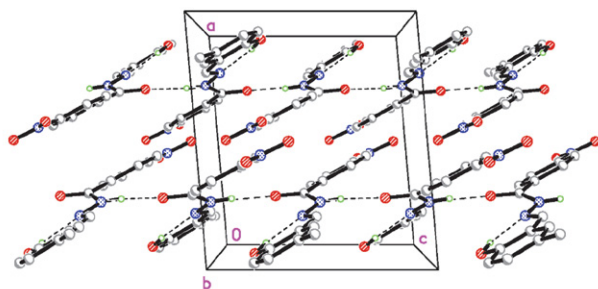


Figure 7. Molecular packing diagram of **3**, viewed along the *b* axis. Hydrogen bonds are shown as dashed lines.

3. 5. Pharmacology

Measurement of XO inhibitory activity was performed for three parallel time points. The percentages of inhibition at a concentration of 100 $\mu\text{mol}\cdot\text{L}^{-1}$ and the IC_{50} values for the compounds against XO are summarized in Table 3.

Allopurinol served as a reference with a percent inhibition of 80.7 ± 4.3 and an IC_{50} value of 8.7 ± 2.3 $\mu\text{mol}\cdot\text{L}^{-1}$. Compound **1** showed the strongest activity with a percent inhibition of 82.3 ± 3.0 and an IC_{50} value of 7.6 ± 1.8 $\mu\text{mol}\cdot\text{L}^{-1}$, which is better than allopurinol. The other three compounds showed intermediate activity with a per-

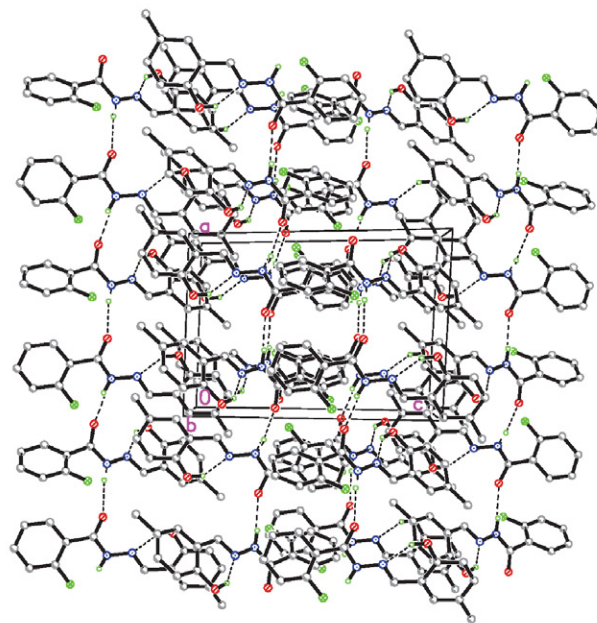


Figure 8. Molecular packing diagram of **4**, viewed along the *b* axis. Hydrogen bonds are shown as dashed lines.

Table 3. Inhibition of XO by the compounds tested.

Compounds	Percent of Inhibition ^b	IC_{50} ($\mu\text{mol}\cdot\text{L}^{-1}$)
1	82.3 ± 3.0	7.6 ± 1.8
2	45.4 ± 2.7	–
3	39.5 ± 2.6	–
4	35.7 ± 2.2	–
Allopurinol	80.7 ± 4.3	8.7 ± 2.3

^b The concentration of the tested material is 100 $\mu\text{mol}\cdot\text{L}^{-1}$.

cent inhibition value of less than 50%. Although the number of compounds tested is limited, some structural features important for the inhibitory effect on xanthine oxidase can be deduced. Compound **1** containing NO_2 group has significantly higher activity than compound **2** containing an NMe_2 group, suggesting that NO_2 is a preferred group for the inhibition process. Comparing compounds **1** and **2** with compound **3**, it can be seen that the other substituent groups such as OH and OMe also contribute to the inhibition. And interestingly, it is not difficult to find out from the results of compounds **3** and **4** that NO_2 is a better group than F for XO inhibition. These results are consistent with reports in the literature that the presence of electron-withdrawing groups in the benzene rings can enhance the activities²¹ and are also similar to the fact that the presence of a bulky ethyl group has a stronger activity than a methyl group.²²

3. 6. Molecular Docking Study

To explain and understand the strong inhibitory effect observed in the experiment, a molecular docking

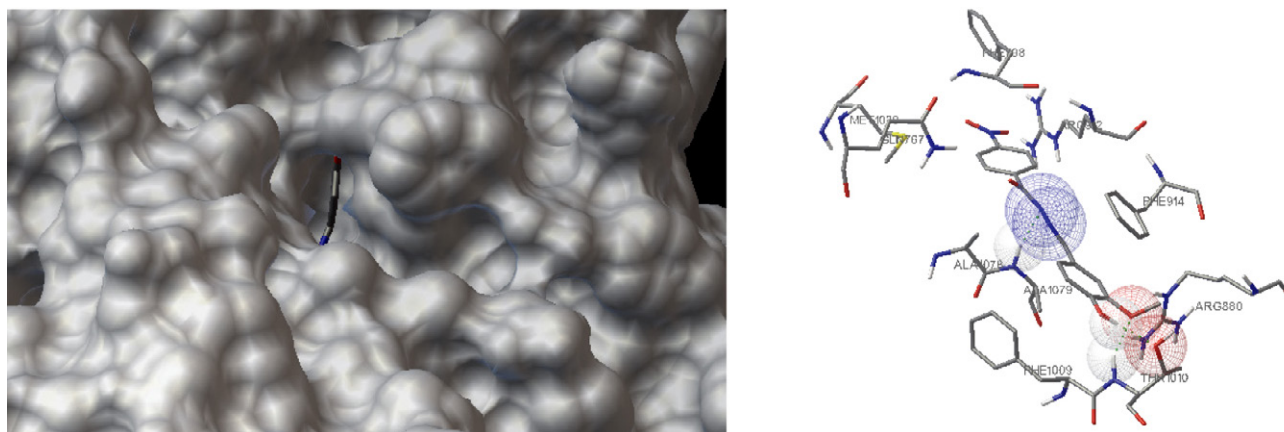


Figure 9. 3D (left) and 2D (right) binding modes of compound **1** with the active site of XO. Hydrogen bonds are shown as dashed lines.

study was performed to investigate the binding effects between compound **1** and the active sites of XO (entry 1FIQ in the Protein Data Bank). Allopurinol was used to test the docking model, which gave satisfactory results. Figure 9 shows the binding model for compound **1** at the active site of enzyme XO. The docking score is -9.83 . In comparison, the docking score for allopurinol is -6.27 .

From the docking results, the molecule of compound **1** fits well into the active pocket of XO. The molecule of **1** is attached to the enzyme via four hydrogen bonds with ALA1079, PHE1008, THR1010, and ARG880. In addition, there are hydrophobic interactions between the compounds and the active sites of the enzyme. The results of the molecular docking study may explain the effective inhibitory effect of compound **1** on XO.

4. Conclusion

The present study reports the synthesis, crystal structures, and XO inhibitory activities of a series of hydrazones. The compounds were characterized by elemental analysis, IR and ^1H NMR spectra, as well as single crystal X-ray diffraction. Among the compounds, N' -(3-methoxybenzylidene)-4-nitrobenzohydrazide (**1**) has effective XO inhibition with an IC_{50} value of $7.6 \pm 1.8 \mu\text{mol}\cdot\text{L}^{-1}$, which can be used as a potential XO inhibitor and deserves further investigation. The molecule can be well filled and combined with hydrogen bonds in the active pocket of XO.

Supplementary Material

CCDC – 859725 for **1**, 859726 for **2**, 902484 for **3**, and 902485 for **4** contain the supplemental crystallographic data for this article. These data are available free of charge at <http://www.ccdc.cam.ac.uk/const/retrieving.html> or from the Cambridge Crystallographic Data Center (CCDC), 12 Union Road, Cambridge CB2 1EZ, UK; fax: +44(0)1223-336033 or e-mail: deposit@ccdc.cam.ac.uk.

5. References

- (a) L. Tiano, R. Belardinelli, P. Carnevali, F. Principi, G. Seddaiu, G. P. Littarru, *Eur. Heart J.* **2007**, 28, 2249–2255 DOI:10.1093/eurheartj/ehm267
(b) A. Pinto, M. Kornfeld, H. Aubin, P. Akhyari, A. Lichtenberg, *Free Rad. Biol. Med.* **2014**, 76, S52–S52 DOI:10.1016/j.freeradbiomed.2014.10.420
(c) P. H. Chan, J. W. Schimidley, R. A. Fishman, S. M. Longar, *Neurology* **1984**, 34, 315–320. DOI:10.1212/WNL.34.3.315
- (a) A. A. Fatokun, T. W. Stone, R. A. Smith, *Neurosci. Lett.* **2007**, 416, 34–38; DOI:10.1016/j.neulet.2007.01.078
(b) X. Yu, L. Zhang, P. Zhang, J. Zhi, R. N. Xing, L. Q. He, *Pharm. Biol.* **2020**, 58, 944–949. DOI:10.1080/13880209.2020.1817951
(c) E. O. Dangana, T. E. Omolekulo, E. D. Areola, K. S. Olaniyi, A. O. Soladoye, L. A. Olatunji, *Chem. Biol. Interact.* **2020**, 316, 108929. DOI:10.1016/j.cbi.2019.108929
(d) J. Nomura, N. Busso, A. Ives, C. Matsui, S. Tsujimoto, T. Shirakura, M. Tamura, T. Kobayashi, A. So, Y. Yamanaka, *Sci. Rep.* **2014**, 4, 4554. DOI:10.1038/srep04554
(e) B. Butts, D. A. Calhoun, T. S. Denney, S. G. Lloyd, H. Gupta, K. K. Gaddam, I. Aban, S. Oparil, P. W. Sanders, R. Patel, J. F. Collawn, L. J. Dellitalia, *Free Rad. Biol. Med.* **2019**, 134, 343–349. DOI:10.1016/j.freeradbiomed.2019.01.029
(f) P. Pacher, A. Nivorozhkin, C. Szabo, *Pharmacol. Rev.* **2006**, 58, 87–114. DOI:10.1124/pr.58.1.6
- (a) C. A. Hay, J. A. Prior, J. Belcher, C. D. Mallen, E. Roddy, *Arthr. Care Res.* **2021**, 73, 1049–1054. DOI:10.1002/acr.24205
(b) P. C. Robinson, N. Dalbeth, P. Donovan, *Arthr. Care Res.* **2021**, 73, 1537–1543. DOI:10.1002/acr.24357
(c) S. Z. Zhang, T. Xu, Q. Y. Shi, S. Y. Li, L. Wang, Z. M. An, N. Su, *Front. Med.* **2021**, 8, 698437. DOI:10.3389/fmed.2021.698437
(d) A. Jeyaruban, W. Hoy, A. Cameron, H. Healy, Z. Wang, J. Zhang, A. Mallett, *J. Nephrol.* **2021**, 34, 753–762. DOI:10.1007/s40620-020-00937-4
(e) L. G. Gao, B. Wang, Y. Pan, Y. Lu, R. Cheng, *Clin. Cardiol.*

- 2021, 44, 907–916. DOI:10.1002/clc.23643
4. (a) G. Beyer, M. F. Melzig, *Biol. Pharm. Bull.* **2005**, 28, 1183–1186. DOI:10.1248/bpb.28.1183
(b) A. Smelcerovic, K. Tomovic, Z. Smelcerovic, Z. Petronijevic, G. Kocic, T. Tomasic, Z. Jakopin, M. Anderluh, *Eur. J. Med. Chem.* **2017**, 135, 491–516. DOI:10.1016/j.ejmech.2017.04.031
 5. (a) J. X. Zhao, Q. Mao, F. W. Lin, B. Zhang, M. Sun, T. J. Zhang, S. J. Wang, *Eur. J. Med. Chem.* **2022**, 229, 114086. DOI:10.1016/j.ejmech.2021.114086
(b) N. Zhai, C. C. Wang, F. S. Wu, L. W. Xiong, X. G. Luo, X. L. Ju, G. Y. Liu, *Inter. J. Mol. Sci.* **2021**, 22, 8122. DOI:10.3390/ijms22158122
 6. (a) T.-J. Zhang, S. Tu, X. Zhang, Q.-Y. Wang, S.-S. Hu, Y. Zhang, Z.-H. Zhang, Z.-R. Wang, F.-H. Meng, *Bioorg. Chem.* **2021**, 117, 105417. DOI:10.1016/j.bioorg.2021.105417
(b) B. Zhang, Y. L. Duan, Y. W. Yang, Q. Mao, F. W. Lin, J. Gao, X. W. Dai, P. Zhang, Q. H. Li, J. X. Li, R. H. Dai, S. J. Wang, *Eur. J. Med. Chem.* **2022**, 227, 113928. DOI:10.1016/j.ejmech.2021.113928
 7. S. Tu, T.-J. Zhang, Y. Zhang, X. Zhang, Z.-H. Zhang, F.-H. Meng, *Bioorg. Chem.* **2021**, 115, 105181. DOI:10.1016/j.bioorg.2021.105181
 8. A. Alsayari, M. Z. Hassan, Y. I. Asiri, A. Bin Muhsinah, M. Kamal, M. S. Akhtar, *Indian J. Heterocycl. Chem.* **2021**, 31, 635–640. DOI:10.3390/biomedicines9101443
 9. J. L. Serrano, D. Lopes, M. J. A. Reis, R. E. F. Boto, S. Silvestre, P. Almeida, *Biomedicines* **2021**, 9, 1443. DOI:10.3390/biomedicines9101443
 10. H. Hayun, R. Hanifati, A. D. Pratiwik, *Indian J. Pharm. Sci.* **2021**, 83, 1074–1080. DOI:10.36468/pharmaceutical-sciences.863
 11. (a) G.-X. He, L.-W. Xue, Q.-L. Peng, P.-P. Wang, H.-J. Zhang, *Acta Chim. Slov.* **2019**, 66, 570–575. DOI:10.17344/acsi.2018.4868
(b) C.-L. Zhang, X.-Y. Qiu, S.-J. Liu, *Acta Chim. Slov.* **2019**, 66, 484–489. DOI:10.17344/acsi.2019.5019
(c) J. Qin, Q. Yin, S.-S. Zhao, J.-Z. Wang, S.-S. Qian, *Acta Chim. Slov.* **2016**, 53, 55–61; DOI:10.17344/acsi.2015.1918
(d) F. Qureshi, M. Y. Khuhawar, T. M. Jahangir, A. H. Channar, *Acta Chim. Slov.* **2016**, 63, 113–120. DOI:10.17344/acsi.2015.1994
(e) X.-Q. Luo, Q.-R. Liu, Y.-J. Han, L.-W. Xue, *Acta Chim. Slov.* **2020**, 67, 159–166. DOI:10.17344/acsi.2019.5303
(f) K. M. El-Mahdy, A. M. E.-Kazak, M. Abdel-Megid, M. Seada, O. Farouk, *Acta Chim. Slov.* **2016**, 67, 18–25. DOI:10.17344/acsi.2015.1555
(g) M. Kaur, S. Kumar, M. Yusuf, J. Lee, R. J. C. Brown, K. H. Kim, A. K. Malik, *Coord. Chem. Rev.* **2021**, 449, 214214. DOI:10.1016/j.ccr.2021.214214
 12. (a) N. Choudhary, D. L. Hughes, U. Kleinkes, L. F. Larkworthy, G. J. Leigh, M. Maiwald, C. J. Marmion, J. R. Sanders, G. W. Smith, C. Sudbrake, *Polyhedron* **1997**, 16, 1517–1528. DOI:10.1016/S0277-5387(96)00436-6
(b) M. Leigh, C. E. Castillo, D. J. Raines, A. K. Duhme-Klair, *ChemMedChem* **2011**, 6, 612–616. DOI:10.1002/cmdc.201000429
 13. (a) Y. Lu, D.-H. Shi, Z.-L. You, X.-S. Zhou, K. Li, *J. Coord. Chem.* **2012**, 65, 339–352. DOI:10.1080/00958972.2011.653785
(b) D. Qu, F. Niu, X. Zhao, K.-X. Yan, Y.-T. Ye, J. Wang, M. Zhang, Z. You, *Bioorg. Med. Chem.* **2015**, 23, 1944–1949. DOI:10.1016/j.bmc.2015.03.036
 14. L. D. Kong, Y. Zhang, X. Pan, R. X. Tan, C. H. K. Cheng, *Cell Mol. Life Sci.* **2000**, 57, 500–505. DOI:10.1007/PL00000710
 15. Bruker, SMART and SAINT. Bruker AXS Inc., Madison, Wisconsin, USA (2002).
 16. G. M. Sheldrick, SADABS. Program for Empirical Absorption Correction of Area Detector, University of Göttingen, Germany (1996).
 17. G. M. Sheldrick, *Acta Crystallogr.* **2008**, A64, 112–122. DOI:10.1107/S0108767307043930
 18. (a) F. H. Allen, O. Kennard, D. G. Watson, L. Brammer, A. G. Orpen, R. Taylor, *J. Chem. Soc. Perkin Trans.* **1987**, 12, S1–S19. DOI:10.1039/p2987000000s1
(b) L.-W. Xue, S.-T. Li, Y.-J. Han, X.-Q. Luo, *Acta Chim. Slov.* **2022**, 69, 385–392. DOI:10.17344/acsi.2021.7252
(c) F.-M. Wang, L.-J. Li, G.-W. Zang, T.-T. Deng, Z.-L. You, *Acta Chim. Slov.* **2021**, 68, 541–547. DOI:10.17344/acsi.2020.6051
(d) G.-X. He, L.-W. Xue, *Acta Chim. Slov.* **2021**, 68, 567–574. DOI:10.17344/acsi.2020.6333
(e) H.-Y. Zhu, *Acta Chim. Slov.* **2021**, 68, 65–71. DOI:10.17344/acsi.2020.6333
(f) C. R. Bhimapaka, N. R. Rayala, R. Kommera, D. Cherupally, R. M. Thampunuri, V. K. Shasi, *Acta Chim. Slov.* **2018**, 65, 34–49. DOI:10.17344/acsi.2017.3453
 19. J. Bernstein, R. E. Davis, L. Shimoni, N.-L. Chang, *Angew. Chem. Int. Ed. Engl.* **1995**, 34, 1555–1573. DOI:10.1002/anie.199515551
 20. M. Zhang, D.-M. Xian, H.-H. Li, J.-C. Zhang, Z.-L. You, *Aust. J. Chem.* **2012**, 65, 343–350. DOI:10.1071/CH11424
 21. S. Gupta, L. M. Rodrigues, A. P. Esteves, A. M. F. Oliveira-Campos, M. S. J. Nascimento, N. Nazareth, H. Cidade, M. P. Neves, E. Fernandes, M. Pinto, N. M. F. S. A. Cerqueira, N. Bras, *Eur. J. Med. Chem.* **2008**, 43, 771–780. DOI:10.1016/j.ejmech.2007.06.002
 22. S. Wang, J. Yan, J. Wang, J. Chen, T. Zhang, Y. Zhao, M. Xue, *Eur. J. Med. Chem.* **2010**, 45, 2663–2670. DOI:10.1016/j.ejmech.2010.02.013

Povzetek

V prispevku je opisana priprava štirih hidrazonov: (*E*)-*N'*-(4-hidroksi-3-metoksibenziliden)-4-nitrobenzohidrazida (**1**), (*E*)-4-(dimetilamino)-*N'*-(4-hidroksi-3-metoksibenziliden)benzo-hidrazida (**2**), *N'*-(2-hidroksi-5-metilbenziliden)-4-nitrobenzohidrazida (**3**) in 2-fluoro-*N'*-(2-hidroksi-5-metilbenziliden)benzohidrazida (**4**), ter njihova strukturna karakterizacija z elementarno analizo, IR in ¹H NMR spektroskopijo, ter rentgensko analizo monokristalov. Raziskane so bile tudi inhibitorne aktivnosti pripravljenih spojin na ksantin oksidazo. Med njimi je *N'*-(3-metoksibenziliden)-4-nitrobenzohidrazid (**1**) pokazal največjo aktivnost. Izvedene so bile tudi simulacije prileganja spojin v kristalno strukturo aktivnega mesta ksantin oksidaze, ter verjetni načini njihove vezave.



Except when otherwise noted, articles in this journal are published under the terms and conditions of the Creative Commons Attribution 4.0 International License

Scientific paper

In vitro Assessment of Antiprotozoal and Antimicrobial Activities of Fractions and Isolated Compounds from *Pallenis hierochuntica*

Vincent O. Imieje,¹ Abiodun Falodun¹ and Ahmed A. Zaki²¹ Department of Pharmaceutical Chemistry, Faculty of Pharmacy, University of Benin, Benin City, 300001, Nigeria.² Pharmacognosy Department, Faculty of Pharmacy, Mansoura University, Mansoura 35516, Egypt.* Corresponding author: E-mail: vincent.imieje@uniben.edu;
+2348024118853

Received: 08-23-2022

Abstract

The antiprotozoal and antimicrobial properties of the extract and fractions of the whole plant of *Pallenis hierochuntica* were investigated against a panel of pathogenic organisms. Fractionation of the methanol extract of the whole plant of *P. hierochuntica* using reverse-phase chromatography gave 28 fractions and led to the isolation of 2 new bisabolone hydroperoxides, 6,10 β ,11-trihydroxybisabol-2-ene-1-one (**1a**), 6,10 α ,11-trihydroxybisabol-2-ene-1-one (**1b**) and also 6,10 β -dihydroxybisabol-2,11-diene-1-one (**2**). They were characterised by extensive spectrometric analysis. Anti-infective investigations of the fractions revealed that fractions 22 to 26 possessed significant antimalarial activity against the D6 and W2 strains of *Plasmodium falciparum* with IC₅₀ = 7.62–9.91 μ g/mL and 5.49–6.08 μ g/mL, respectively, and SI > 6.0 on average. Fractions 7, 16 to 24 exhibited good activity against *Leishmania donovani* promastigotes (IC₅₀ = 6.71–18.77 μ g/mL). Fractions 25 to 28 were active against *Trypanosoma brucei* trypomastigotes, fraction 25 being the most potent (IC₅₀ = 4.13 μ g/mL). Only fractions 11 to 13 were active against *Aspergillus fumigatus* (IC₅₀ = 13.406 μ g/mL). Compounds **1a** and **2** were not promising against the organisms tested. **1a** and **1b** were characterised for the first time.

Keywords: *Pallenis hierochuntica*, leishmaniasis, antimalarial, characterization, spectrometry

1. Introduction

Medicinal plants have been a major reservoir of unique and chemically diverse molecules and a large pool of novel drug leads. Plants are known to synthesise potent molecules that exhibit anticancer, anti-infective, anti-inflammatory, antiviral and antiprotozoal activities. Today, many drugs in clinical use are either directly obtained from natural sources or natural products derived. A study conducted by Newman *et al.* revealed that over 35% of drugs approved by the United States in the past four decades are either natural products or their derivatives.¹

The genus *Pallenis* (synonym: *Asteriscus*) is known to express biologically valuable compounds, especially those with humulene and bisabolone skeletons. Extracts, fractions and isolated compounds from members of this genus have been shown to exhibit different pharmacological

activities: antibacterial and antileishmanial,^{2,3} anticancer and phytotoxicity,⁴ and antioxidant activity.⁵ Phytochemical studies of some species of this genus have resulted in the isolation and characterisation of bioactive humulene skeleton sesquiterpene lactones: asteriscunolides A–D^{6–9}, steriscanolide and aquatolide sesquiterpene lactones,⁹ flavonoids, bisabolone hydroperoxides and farsenol derivatives.^{10,3,11} Others include sesquiterpene alcohol, germacrane and deoxygenated germacrane,^{12,13} and naupliolide, having a novel tetracyclic skeleton.¹⁴

This study investigated the antiprotozoal and antimicrobial activity of fractions of *Pallenis hierochuntica* (Michon) Greuter, family Asteraceae. Herein we report the isolation, characterisation, and structure elucidation of three compounds (two of these are new) from the methanol extract of the whole plant and their antiprotozoal and antimicrobial activities.

2. Materials and Methods

2. 1. General

Experimental

The acquisition of the 1D and 2D NMR spectra were done on Bruker Avance III 500 and 400 MHz spectrometer. The compounds were dissolved in CD₃OD (¹³C and ¹H NMR data at 125 and 500 MHz, respectively). Chemical shift values are reported in ppm and referenced to the residual protons of the solvent (CD₃OD). Mass spectra were acquired on an Agilent Technologies 6200 series mass spectrometer. Isolations and purifications of all compounds were performed by column chromatography (CC), over normal silica gel (32–63 μ, Dynamic adsorbents Inc.), and reversed-phase C-18 silica Polar Plus (J. T. Baker®). Analytical TLC was conducted on precoated silica gel F₂₅₄ aluminum sheets (0.25 mm, Sorbtent Tech.) or Silica 60 RP-18 F₂₅₄ aluminum sheets (20 × 20 cm, Merck). Spots were visualized by observing under UV at 254 nm and 365 nm light and by spraying with 1% vanillin (Sigma) in conc. H₂SO₄/EtOH mixture (1:9) followed by heating with a heat gun. All isolation and purification procedures were done by using analytical grade solvents (Fisher chemicals). Pentamidine and amphotericin B (Sigma-Aldrich, St Louis, MO) were used as standard antileishmanial agents. Chloroquine and artemisinin (Sigma-Aldrich, MO) were used as drug controls in the antimalarial assay. Fluconazole, amphotericin B, ciprofloxacin, vancomycin, methicillin, cefotaxime and meropenem were used as positive control antibacterial and antifungi agents.

2. 2. Plant Material

The whole plant of *Pallenis hierochuntica* was collected from the Mediterranean coastal area of Egypt in 2015, and the plant was identified at the Pharmacognosy Department, Mansoura University, Egypt, where a voucher specimen (AH-14-PD) was deposited.

2. 3. Extraction and Isolation

The dried whole plant of *Pallenis hierochuntica* was grounded to powder. The powdered plant material (500 g) was macerated with methanol (98%) by percolation (4 L × 4) for 48 h at room temperature. The solvent was removed with a rotary evaporator at 40 °C to give 35 g of crude extract (7% as yield). The extract (33 g) was mixed with 30 g RP-18 silica gel and applied to a VLC over RP-18 silica (30 cm × 3.5 cm, 500 g) and eluted with gradients of H₂O/MeOH (90:10–0:100) and acetone to give 28 fractions (AH-1 to AH-28). Fraction AH-25 (1.8 g) was subjected to column chromatography (SiO₂, EtOAc:CHCl₃:MeOH:H₂O (15:8:4:1; 10:6:4:1; 8:2:0.25; 7:3:0.5; MeOH 100%)) to give 45 sub-fractions AH1A–AH45A. Fractions with similar *R_f* were pooled to get 7 fractions (H1–H7). Fraction H6 (200 mg) was processed over column chromatography with

normal silica gel (3 × 65 cm) eluted with hexane:EtOAc (4:1, 7:3, 3:2) to give 8 fractions (G1–G8). Repeated column chromatographic purification of fraction G8 (40 mg) with hexane:EtOAc (4:1–3:2) yielded AH6 (2.4 mg) as fine needles. Compounds **1a** (0.8 mg) and **1b** (0.7 mg) were purified from AH6, and **2** was purified from PTLC (20 × 20 cm, 500 μm pore size) of AH5 (14.9 mg) with elution system of hexane:chloroform (1:4) (50 mL) to give 0.8 mg of white solid.

2. 4. Antiprotozoal and Antimicrobial Assays

2. 4. 1. Antileishmanial Assay

The fractions and isolated compounds **1a** and **2** were evaluated against *Leishmania donovani* promastigote, *L. donovani* axenic amastigote, and *L. donovani* amastigote in THP1 according to the protocol described by Jain *et al.*¹⁵ which uses the Alamar Blue colourimetric assay method.¹⁶ Pentamidine and amphotericin B standard antileishmanial drugs were used as positive controls. The IC₅₀ and IC₉₀ values were computed from response curves using XLFit®.

2. 4. 2. Antimalarial Assay

The *in vitro* antiplasmodial activity of the fractions and compounds **1a** and **2** was measured by a colourimetric assay that determines the parasites lactate dehydrogenase (pLDH) activity.^{17,18} Included in this assay are two strains of *Plasmodium falciparum* (Sierra Leone D6 (chloroquine-sensitive) and Indochina W2 (chloroquine resistant) obtained from the Walter Reed Army Institute of Research, Silver Spring, MD. The effects of the fractions and test compounds on plasmodial LDH activity were determined using Malstat reagent (Flow Inc, Portland, OR). DMSO (0.25%) and chloroquine/artemisinin were included in each assay which serves as vehicle and positive control drugs, respectively.

2. 4. 3. Cytotoxicity Assay

The cytotoxicity of the test samples was determined against transformed human monocytic (THP1) cells. The assay method previously described by Jain *et al.* was adopted. This experiment used a 4 days old culture of THP1 cells in the experimental phase diluted with RPMI medium to 2.5 · 10⁵ cells/mL. To achieve the parasite cells transformation to the adherent macrophages, Phorbol 12-myristate 13-acetate (PMA) was added to the culture at a concentration of 25 ng/mL. The THP1 cell culture treated with PMA was seeded into 96 well plates with 200 μL culture (2.5 · 10⁵ cells/mL) in each well and incubated overnight at 37 °C in a 5% CO₂ incubator. The medium in plates with THP1 cells was replaced with a fresh medium. The test samples (fractions and compounds) and standards diluted with RPMI medium in separate plates were added to these plates and then incubated in a 5% CO₂ incubator at 37 °C

for 48 h. After the incubation period, each well received 10 μ L of Alamar Blue solution (AbDSerotec, catalogue number BUF012B), and the plates were incubated further overnight. Again, standard fluorescence was measured on a Fluostar Galaxy fluorometer (BMG LabTechnologies) at 544 nm excitation, 590 nm emission wavelengths. The half-maximal concentration IC_{50} and IC_{90} values were computed from the dose-response growth inhibition curve by XLfit version 5.2.2.¹⁵ The selectivity indices (SI) were computed by measuring the cytotoxicity of the test compounds against Vero cell lines (monkey fibroblast).¹⁵

2. 4. 4. *In vitro* Antimicrobial Activity

Extracts, fractions, and isolated compounds of *P. hi-erochuntica* were subjected to *in vitro* susceptibility testing against a panel of pathogenic organisms: the fungi include *Candida albicans* (ATCC 90028), *Candida krusei* (ATCC 6258), *Candida glabrata* (ATCC 90030), *Cryptococcus neoformans* (ATCC 90113), *Aspergillus fumigatus* (ATCC 204305); while the bacteria include methicillin-resistant bacterium *Staphylococcus aureus* (MRSA; ATCC 33591), *Escherichia coli* (ATCC 35218), *Klebsiella pneumonia* (ATCC 43816), vancomycin-resistance *Enterococcus faecium* (49532) and *Mycobacterium intracellulare* (ATCC 23068) using a modified version of the NCCLS methods.¹⁹ On the other hand, that against *M. intracellulare* was done using the modified Alamar Blue procedure previously described.²⁰ The fungi and bacteria used in this experiment were obtained from the American Type Culture Collection (ATCC), Manassas, VA. All the test samples were dissolved in DMSO (0.25%), which also acted as a negative control agent. They were all diluted with 0.9% saline serially and transferred in duplicate to the 96-well microtitre plates. The final microbial inoculums were prepared after comparison of the absorbance at 630 nm of cell suspensions to the 0.5 McFarland standard and diluting the suspensions in broth (Sabouraud dextrose and cation-adjusted Müller–Hinton (Difco) for the fungi and bacteria, respectively, and 5% Alamar Blue (BioSource International) in Middlebrook 7H9 broth to afford recommended inocula. Microbial inocula were added to the diluted samples to realize a final volume of 200 μ L. The microtitre plates were read at either 630 nm or 544ex/590em before and after incubation. IC_{50} values relative to controls were obtained using XL fit 4.2 software (IDBS, Alameda, CA).

3. Results and Discussion

3. 1. Characterisation of Compounds 1a and 1b

Compounds **1a** and **1b** were purified from compound **1** (2.4 mg) which showed a clear molecular ion peak $[M+Na]^+$ at m/z 293.1696, corresponding to the molecular

formula $C_{15}H_{26}O_4Na$ (calcd 293.1729) from its HRESIMS spectrum. However, careful examination of the 1H and ^{13}C NMR spectra of **1** (Figure S18), revealed the presence of double peaks, suggesting a mixture of two bisabolone-type sesquiterpenoids³, a feature usually associated with closely related compounds (mixtures).

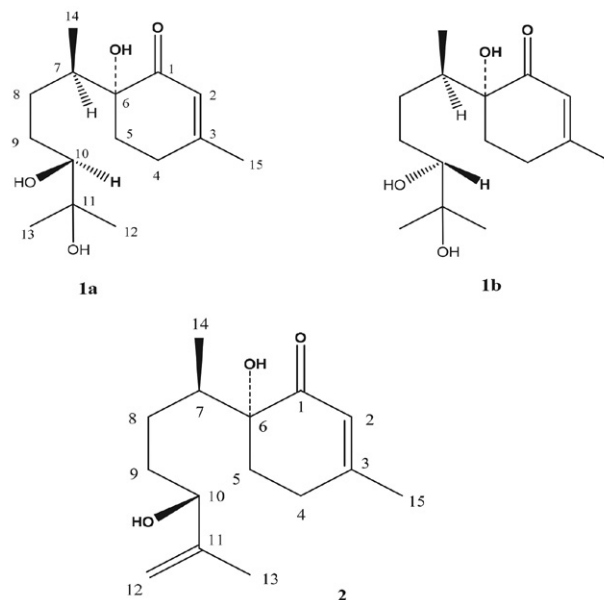


Figure 1. Molecular structures of compounds **1a**, **1b** and **2**

As such, compound **1** was subjected to further purification to give two compounds of the same molecular weight, **1a** (0.8 mg) and **1b** (0.7 mg). Compound **1a** (6,10 β ,11-trihydroxybisabol-2-ene-1-one), white needles from sub-fraction AH6 (0.8 mg), HRESIMS $[M+Na]^+$ at m/z 293.1694, corresponding to the molecular formula $C_{15}H_{26}O_4Na$ (calcd 293.1729). The 1H NMR spectrum of **1a** in CD_3OD (Table 1) displayed an olefinic proton signal at δ 5.84 (1H, dq , $J = 2.4, 1.1$ Hz), a doublet at δ 1.01 (3H, d , $J = 6.7$ Hz), a singlet at δ (6H, s , 1.12), a singlet at δ 1.99 (3H, s) and a methine proton at δ 3.15 (dd , $J = 9.3, 2.4$ Hz). The ^{13}C NMR spectrum (Figure S2) revealed the presence of characteristic signals: a carbonyl carbon at δ 204.1, olefinic methine at δ 124.5 and quaternary olefinic carbon at δ 165.5, together with the olefinic proton signal at δ 5.84 (1H, dq , $J = 2.4, 1.1$ Hz), indicated the presence of a mono-substituted α,β -unsaturated carbonyl groups. The DEPT experiment (Supplementary material, Figure S4) showed the presence of four methylene carbons at δ 31.6, 29.1, 28.9 and 29.3. The HMQC (Supplementary material, Figure S6) revealed their connectivities with the proton signals at δ (2.24, 2.28), (1.29, 1.40), (1.06, 1.27), and (2.42, 2.44), respectively. The correlations observed in HMBC spectrum (Supplementary material, Figure S7) between the proton at δ 2.36 with carbon signals at δ 125.0, 165.5, 32.9, and 78.1 (quaternary carbon), together with the correlations be-

tween the protons at δ 2.24 with 78.1 (quaternary carbon), 202.6 and 29.1, and between the proton at δ 5.84 with 78.1 and 29.1, are consistent with the cyclic (six-carbon ring) unsaturated ketone with branching at the oxygenated quaternary carbon (δ 78.1). The side chain consists of eight carbon atoms discriminated by DEPT experiment into three methyls (δ 24.3, 23.5 and 12.6), two methylene (δ 28.7.0 and 27.4), one quaternary (δ 72.4), and one methine (δ 78.8). Careful examination of all correlations in ^1H – ^1H COSY, HMQC and HMBC confirmed the proposed identity of the structure, which is a bisabolone-skeleton with an OH at C-10 (δ 78.8) and C-11 (δ 72.4) (Figure 1). The relative configuration of **1a** was established through the analysis of cross-peaks observed in the NOESY spectrum (Supplementary material, Figure S8), which displayed a correlation of H-15 (*s*, 1.99, 3H) with both H-14 (*d*, 1.01, 3H) and H-4 (2.44), correlation of H-10 (*dd*, 3.16) with H-14 (*d*, 1.01, 3H), indicated the β -oriented H-14 and H-10. Therefore, the structure of compound **1a** was determined to be 6,10 β ,11-trihydroxybisabol-2-ene-1-one. The other compound **1b** (6,10 α ,11-trihydroxybisabol-2-ene-1-one), white needles from sub-fraction AH6 (0.7 mg), HRESIMS $[\text{M}+\text{Na}]^+$ at m/z 293.1694, corresponding to the molecular formula $\text{C}_{15}\text{H}_{26}\text{O}_4\text{Na}$ (calcd 293.1729), was of the same structure as **1a** with a slight deviation in the NMR signals (Table 1, supplemental material, Figures S11–S17). The differences resulted from the hydroxy group orientation at C-10. Upon careful analysis of the NOESY (Supplementary material, Figure S16) spectrum of **1b**, the correlation of H-15 (*s*, 1.99, 3H) with both H-14 (*d*, 1.02) and H-4 (2.44), and the correlation of H-10 (*dd*, 3.15) with H-7 (*m*, 1.91), indicated that the 10-OH is α -oriented. The structure of **1b** was concluded to be 6,10 α ,11-trihydroxybisabol-2-ene-1-one.

3. 2. Characterisation of Compound 2

Compound **2** (Figure 1) was obtained as fine white needles. HRESIMS showed a clear molecular ion peak $[\text{M}+\text{Na}]^+$ at m/z 275.1594 (calcd $\text{C}_{15}\text{H}_{24}\text{O}_3\text{Na}$, 275.1623). The ^1H and ^{13}C NMR spectra of **2** revealed the same skeleton as compound **1a**, a bisabolone-type sesquiterpene, with the disappearance of the one methyl and oxygenated quaternary carbon at δ 72.5 which was assigned for C-11 of **1a** and **1b**, and the appearance of one olefinic methylene group and quaternary olefinic carbon. The ^1H NMR spectrum of **2** showed two olefinic protons at δ 4.86 (*p*, $J = 1.6$ Hz) and 4.87 (*dt*, $J = 1.9, 0.9$ Hz) (Table S1) assigned to C-12 explaining the absence of a methyl group. The ^{13}C NMR displayed a hydroxylation at C-10, the same as compound **1a**, and the H-10 chemical shift at δ 3.94 together with the coupling value (*t*, $J = 6.7$ Hz) is in full agreement with the β -oriented C-10 hydroxyl group. The chemical structure of **2** was deduced as 6,10 β -dihydroxybisabol-2,11-diene-1-one (Figure 1). Compound **2** was previously reported as a reduction product of 10-peroxy

derivatives,³ but this is the first time it was isolated directly from a natural source.

3. 3. In vitro Antiparasitic Screening of Fractions and Isolated Compounds

The results of the antimalarial screening of the fractions against the two strains of *Plasmodium falciparum* (D6 and W2) are shown in Table S2 (Supplementary material). Similarly, the antileishmanial and antitrypanosomal results of the fractions are shown in Table S3 (Supplementary material), and the antimicrobial activity of the fractions is reported in Table S4. Results of the *in vitro* antimalarial, antileishmanial, antitrypanosomal and antimicrobial activities of compounds **1a** and **2** are presented in Tables S5 to S7 (Supplementary material).

According to the WHO report of 2019, it was estimated that there were 229 million cases of malaria worldwide, resulting in 409,000 deaths, most of whom are children under five, especially in Sub-Saharan Africa, making malaria a major global health problem.²¹ Several researchers have reported the antimalarial effects of plant extracts and fractions.^{22–24} According to the WHO, about 80% of people depend on herbal products as their primary health-care source(s).²¹

The result of the antimalarial screening of the fractions of *Pallenis hierochuntica* is shown in Table S2 (Supplementary material). In the primary screening experiment, the two strains (D6 and W2) of *P. falciparum* were tested against the fractions at concentrations range of 47.6–5.28 $\mu\text{g/mL}$. Only fractions that showed antimalarial activity ($\geq 50\%$) in this screening were investigated in the secondary antimalarial screening to determine their IC_{50} values. From the table, fractions AH11–AH12 and AH14–AH28 exhibited significant antimalarial activity against the chloroquine-sensitive (D6) and resistant (W2) strains of *P. falciparum* with IC_{50} values ranging from 7.62–30.33 $\mu\text{g/mL}$ and 5.49–25.49 $\mu\text{g/mL}$, respectively. Fractions AH23–AH27 were particularly effective against the two strains of PF with $\text{IC}_{50} = 5.49$ –9.19 $\mu\text{g/mL}$. As such, these fractions are classified as having promising antimalarial activity. Their IC_{50} values were, however, higher than those obtained for artemisinin and chloroquine ($\text{IC}_{50} < 0.026$ –0.202 $\mu\text{g/mL}$), standard antimalarial drugs used as positive control drugs. They also showed better selectivity indices ($\text{SI} = > 5.2$ – > 8.7). Our report is the first on the *in vitro* antimalarial activity of this plant. There is a lack of information on the antimalarial activity of the *Pallenis* genus representatives in general.

Similarly, leishmaniasis and trypanosomiasis (sleeping sickness) affect humans and livestock in the tropical and subtropical countries of Africa, Asia and South America. It has been estimated that over 70 million and 350 million people worldwide are at risk of trypanosomiasis and leishmaniasis, respectively, with attendant annual deaths of 14,000 to 70,000.²⁵ In our continued investigation of

Table 1. ^{13}C and ^1H NMR data for compound **1a** and **1b** (CD_3OD at 125 and 400 MHz, respectively).

Carbon No.	1a δ_{H} (ppm), Multiplicity, J (Hz)	^{13}C	DEPT	1b δ_{H} (ppm), Multiplicity, J (Hz)	^{13}C	DEPT
1	--	204.1	C	--	204.0	C
2	5.84 (dq , $J = 2.4, 1.1$ Hz)	123.2	CH	5.83 (dq , $J = 2.4, 1.1$ Hz)	124.6	CH
3	--	163.9	C	--	165.2	C
4	2.42 2.44	29.3	CH_2	2.36 2.44	30.5	CH_2
5	2.24(ddd , $J = 5.0, 3.3, 1.7$ Hz) 2.28	31.6	CH_2	2.23(ddd , $J = 5.0, 3.3, 1.7$ Hz) 2.28	33.1	CH_2
6	--	78.1	C	--	78.5	C
7	1.91, m	35.4	CH	1.91, m	37.3	CH
8	1.06 1.27	28.9	CH_2	1.07 1.26	29.0	CH_2
9	1.29 1.40	29.1	CH_2	1.29 1.40	30.8	CH_2
10	3.15 (dd , $J = 9.3, 2.4$ Hz)	78.8	CH	3.15 (dd , $J = 9.3, 2.4$ Hz)	80.3	CH
11	--	72.5	C	--	74.0	C
12	1.12, s	24.3	CH_3	1.14, s	25.9	CH_3
13			CH_3		14.1	CH_3
14	1.01(d , $J = 6.7$ Hz)	12.5	CH_3	1.02 (d , $J = 6.7$ Hz)	23.9	CH_3
15	1.99, s	23.5	CH_3	1.97, s		CH_3

medicinal plants for antiprotozoal metabolites, fractions of *Pallenis hierochuntica* were subjected to *in vitro* screening against *Leishmania donovani* (promastigotes, axenic amastigotes, and intracellular amastigotes in THP1 cells) and blood-stage promastigotes of *Trypanosoma brucei*. The result of this screening is shown in Table S3 (Supplementary material). From the result, fractions AH-1 and AH-3 showed activity against *T. brucei*, $\text{IC}_{50} = 11.33$ and 12.50 $\mu\text{g/mL}$, respectively. Fraction AH-7 was active against *L. donovani* promastigotes and axenic amastigotes with IC_{50} and IC_{90} values of 12.03 – 19.47 $\mu\text{g/mL}$ and also against *T. brucei* ($\text{IC}_{50} = 13.6$ $\mu\text{g/mL}$). Fractions AH-12, AH-16 to AH-18, and AH-24 were also effective against the promastigotes of *L. donovani*. While fractions AH-25 to AH-28 were active against *T. brucei* blood-stage trypomastigotes with IC_{50} values of 4.13 – 13.48 $\mu\text{g/mL}$ and IC_{90} values of 11.46 – 19.28 $\mu\text{g/mL}$. All the fractions at 20 – 8 $\mu\text{g/mL}$ test concentrations did not show activity against intracellular amastigotes in THP1 cells. The positive control drugs, pentamidine and DMFO, possess better activity against these protozoa except fraction AH-25, which showed better activity ($\text{IC}_{50} = 4.13$ $\mu\text{g/mL}$) than DMFO ($\text{IC}_{50} = 6.25$ $\mu\text{g/mL}$) against *T. brucei*. Several studies have highlighted the activity of plant extracts and fractions against leishmaniasis and trypanosomiasis.^{26,25,27} Further purification of these extracts and fractions has led to the isolation of

potent compounds exhibiting significant leishmanicidal and trypanocidal effects against these pathogenic protozoal.^{28–30} In a related study, the ethyl acetate extract of *Asteriscus graveolens* exhibited potent activity against both promastigote and amastigote forms of *L. infantum* and *L. major* with IC_{50} value of 22.93 ± 0.39 $\mu\text{g/mL}$ and 131.6 ± 0.21 $\mu\text{g/mL}$ against *L. infantum*. Also, the hydroethanolic extract of the plant inhibited *L. major* and *L. infantum* parasites with $\text{IC}_{50} = 33.64 \pm 0.46$ $\mu\text{g/mL}$ and 143.4 ± 0.28 $\mu\text{g/mL}$, respectively.² An *in vitro* antiprotozoal activity of crude methanol extract of *Pallenis hierochuntica* (*Asteriscus hierochuntica*) was reported by Zaki *et al.*,³¹ in which the extract showed promising and good antitrypanosomal activity against the promastigotes of *T. brucei* with IC_{50} and IC_{90} values being 1.18 and 1.89 $\mu\text{g/mL}$, respectively. Our study is the first report of the antileishmanial and antitrypanosomal activity of the fractions of *Pallenis hierochuntica*.

In the antimicrobial screening experiment, 28 fractions (AH-1 to AH-28) were subjected to *in vitro* antimicrobial evaluation against a panel of pathogenic microorganisms (fungi and bacteria) (Table S4). The fractions were tested at a 200 – 8 $\mu\text{g/mL}$ concentration range. From the results of our study, only fractions AH-11 to AH-13 exhibited significant activity against *Aspergillus fumigatus* with IC_{50} values of 13.406 (AH-11), 88.607 (AH-12)

and 130.228 µg/mL (AH-13), respectively. Other studies reported the antimicrobial activities of members of the genus *Asteriscus*. Ramdane *et al.* reported the antimicrobial activity of the ethyl acetate fractions of *A. graveolens* against *L. monocytogenes* (MIC = 0.312 mg/mL), *S. aureus* and *B. cereus* (MIC = 0.625 mg/mL), but the fractions show no activity against *E. coli* (ATCC 35214) and *P. aeruginosa* (ATCC 27853).² Also, Medimagh *et al.* evaluated the root oil of *Asteriscus maritimus* (L.) for antimicrobial activity against some pathogenic fungi, including *Aspergillus flavus*, *A. niger*, *Botrytis cinerea* and *Penicillium* sp. The zones of inhibition range from 8.3 mm to 10.3 mm. However, the oil was not active against the bacteria isolates tested.³² The oil of *A. graveolens* was also reported to significantly ($p < 0.05$) inhibit the mycelial growth of some pathogenic fungi (*Alternaria* sp., *P. expansum*, and *R. stolonifer*) at different concentrations.³³

3. 4. *In vitro* Antimalarial and Antimicrobial Activities of Compounds 1a and 2

The *in vitro* antimalarial, antileishmanial, antitrypanosomal and antimicrobial screening of compounds **1a** and **2** are reported in Tables S5–S7 (Supplementary material). They were screened against the different pathogenic organisms mentioned in section 2.4 above. The study results showed that the compounds exhibited no significant activity against tested organisms at the concentrations tested.

4. Conclusion

In the present study, two new compounds with bisabolone skeleton and a known compound were isolated and identified as 6,10β,11-trihydroxybisabol-2-ene-1-one, 6,10α,11-trihydroxybisabol-2-ene-1-one, and 6,10β-dihydroxybisabol-2,11-diene-1-one, respectively. These compounds hold no promising antiprotozoal and antimicrobial activities. The fractions of *Pallenis hierochuntica* show significant activity against *Plasmodium falciparum*, *Leishmania donovani* promastigotes, axenic amastigotes and trypomastigotes of *Trypanosoma brucei*. This plant holds potential for further investigation for lead compounds as antiprotozoal agents.

Acknowledgements

This work was in part supported by USAID/HED grant 153 – 6200BF A15 – 01 to one of the authors. We also acknowledge the University of Benin as a shared cost partner in this grant, and the National Center for Natural Product Research (NCNPR), School of Pharmacy, University of Mississippi, for the use of their laboratory for part of this work.

5. References

1. D. J. Newman, G. M. Cragg, K. M. Snader. *Nat. Prod. Rep.* **2000**, 17, 215–234. DOI:10.1039/a902202c
2. F. Ramdane, R. Essid, K. Mkadmini, M. Hammami, N. Fares, M. H. Mahammed, D. El Ouassiss, O. Tabbene, F. Limam, M. D. O Hadj. *Process Biochem.* **2017**, 56, 186–192. DOI:10.1016/j.procbio.2017.03.004
3. T. Sarg, S. El-Dahmy, A. Ateya, H. Abdel-Fattah. *Fitoterapia (Milano)*. **1994**, 65, 241–244.
4. A. P. Rauter, I. Branco, J. Bermejo, A. G. González, M. D. García-Grávalos, A. San Feliciano. *Phytochemistry*. **2001**, 56, 167–171. DOI:10.1016/S0031-9422(00)00304-6
5. H. Alilou, A. Asdadi, L. I. Hassani, C. González-Mas, M. A. Blázquez, M. Akssira. *J. Nat. Sci. Res.* **2014**, 4, 1–10. DOI:10.1007/s13596-018-0315-0.
6. J. Jakupovic, L. Lehmann, F. Bohlmann, A. A. Hogdson. *Phytochemistry*. **1987**, 26, 2854–2855. DOI:10.1016/S0031-9422(00)83606-7
7. A. San Feliciano, A. Barrero, J. M. del Corral, E. Ledesma, F. Sánchez-Ferrando. *Tetrahedron Lett.* **1982**, 23, 3097–3100. DOI:10.1016/S0040-4039(00)87542-5
8. A. San Feliciano, A. Barrero, M. Medarde, J. M. del Corral, A. A. Aizpiri, F. Sánchez-Ferrando. *1984. Tetrahedron. Lett.* **1984**, 40, 873–878. DOI:10.1016/S0040-4020(01)91476-0
9. A. San Feliciano, A. Barrero, M. Medarde, J. M. del Corral, A. Aramburu, A. Perales, J. Fayos, F. Sanchez-Ferrando. *Tetrahedron*. **1985**, 41, 5711–5717. DOI:10.1016/S0040-4020(01)91377-8
10. A. A. Ahmed, M. Ishak, H. Micheal, M. El-Ansari, H. El-Sissi. *J. Nat. Prod.* **1991**, 54, 1092–1093. DOI:10.1021/np50076a027
11. S. Youssef, Z. Ibraheim, A. Attia. *Bull. Pharm. Sci.* **1995**, 18, 33–38. DOI:10.21608/bfsa.1995.69671
12. G. Appendino, G. Cravotto, P. Gariboldi, F. Claudi, V. Picci. *Phytochemistry*. **1989**, 28, 849–850. DOI:10.1016/0031-9422(89)80127-X
13. G. Appendino, J. Jakupovic, S. Jakupovic. *Phytochemistry*. **1997**, 46, 1039–1043. DOI:10.1016/S0031-9422(97)00386-5
14. M. Akssira, F. Mellouki, A. Salhi, H. Alilou, A. Saouf, F. El Hanbali, J. F. Arteaga, A. F. Barrero. *Tetrahedron Lett.* **2006**, 47, 6719–6721. DOI:10.1016/j.tetlet.2006.07.094
15. S. K. Jain, R. Sahu, L. A. Walker, B. L. Tekwani. *J. Vis. Ex.* **2012**, 30, 4054. DOI: 10.3791/4054.
16. J. Mikus, D. Steverding. *Parasitol. Int.* **2000**, 48, 265–269. DOI:10.1016/S1383-5769(99)00020-3
17. M. T. Makler, J. M. Ries, J. A. Williams, J. E. Bancroft, R. C. Piper, B. L. Gibbins, D. J. Hinrichs. *Am. J. Trop. Med. Hyg.* **1993**, 48, 739–741. DOI:10.4269/ajtmh.1993.48.739
18. V. Samoylenko, M. K. Ashfaq, M. R. Jacob, B. L. Tekwani, S. I. Khan, S. P. Manly, V. C. Joshi, L. A. Walker, I. Muhammad. *J. Nat. Prod.* **2009**, 72, 92–98. DOI:10.1021/np800653z
19. CLSI. 2008. Reference method for broth dilution, *Reference method for broth dilution antifungal susceptibility testing of yeasts. Approved standard, 3th ed.*, 28(14): 0–13.
20. S. G. Franzblau, R. S. Witzig, J. C. McLaughlin, P. Torres,

- G. Madico, A. Hernandez, M. T. Degnan, M. B. Cook, V. K. Quenzer, R. M. Ferguson, R. H. Gilman. *J. Clin. Microbiol.* **1998**, 36, 362–366. DOI:10.1128/JCM.36.2.362-366.1998
21. WHO. 2019. <https://www.who.int/publications/i/item/9789241565721>. Accessed 8th August, 2022
22. A. Bagavan, A. A. Rahuman, N. K. Kaushik, D. Sahal. *Parasitol. Res.* **2011**, 108, 15–22. DOI:10.1007/s00436-010-2034-4
23. W. Berthi, A. González, A. Rios, S. Blair, A. Cogollo, A. Pabón. *Malar. J.* **2018**, 17, 1–12. DOI:10.1186/s12936-018-2301-x
24. S. Gebrehiwot, M. Shumbahri, A. Eyado, T. Yohannes. *J. Parasitol. Res.* **2019**, 1–8.
25. C. J. D. Obbo, S. Kariuki, J. Gathirwa, W. Olaho-Mukani, P. Cheplogoi, E. Mwangi. *J. Ethnopharmacol.* **2019**, 229, 127–136. DOI:10.1155/2019/4519298
26. S. Jain, M. Jacob, L. Walker, B. Tekwani. *BMC Complement Altern. Med.* **2016**, 16, 1–6. DOI:10.1186/s12906-016-1122-0
27. E. O. Ogbadoyi, A. O. Abdulganiy, T. Z. Adama, J. I. Okogun. *J. Ethnopharmacol.* **2007**, 112, 85–89. DOI:10.1016/j.jep.2007.02.015
28. V. Imieje, A. A. Zaki, P. S. Fasinu, Z. Ali, I. A. Khan, B. Tekwani, S. I. Khan, E. O. Nosa, A. Falodun. *Trop. J. Nat. Prod. Res.* **2017**, 1, 89–94. DOI:10.26538/tjnpr/v1i2.8
29. H. M. Malebo, T. Wenzler, M. Cal, S. M. Swaleh, M. O. Omoilo, A. Hassanali, U. Séquin, D. Häussinger, P. Dalsgaard, M. Hamburger. *BMC Complement Altern. Med.* **2013**, 13, 1–10. DOI:10.1186/1472-6882-13-48
30. A.M. Nour, S. A. Khalid, M. Kaiser, R. Brun, E. A. Wai'l, T. J. Schmidt. *J. Ethnopharmacol.* **2010**, 129, 127–130. DOI:10.1016/j.jep.2010.02.015
31. A. Zaki, Z. Ali, Y. El-Amier, A. Ashour, B. Oluwasesan, S. Jain, B. Tekwani, I. Khan. *Planta Med.* **2016**, 82, PC85. DOI:10.1055/s-0036-1578787
32. S. Medimagh, M. Daami-Remadi, H. Jabnoun-Khiareddine, M. Naffati, H. Ben Jannet, & M. H. A. Hamza. *J. Essent. Oil-Bear. Plants*, **2013**, 16, 4, 443–450. DOI:10.1080/0972060X.2013.813272
33. M. Znini, G. Cristofari, L. Majidi, H. Mazouz, P. Tomi, J. Paoilini, J. Costa. *Nat Prod Commun.* **2011**, 6, 1763–1768. DOI:10.1177/1934578X1100601147

Povzetek

Za ekstrakte iz celotne rastline *Pallenis hierochuntica* in njegove frakcije smo s serijo testov preverili morebitno aktivnosti proti patogenim organizmom (delovanje proti protozoam in proti mikrobom). Frakcioniranje metanolnega ekstrakta iz rastline *P. hierochuntica* s pomočjo reverznofazne kromatografije je dalo 28 frakcij in omogočilo izolacijo dveh novih bisabolonskih hidroperoksidov: 6,10 β ,11-trihidroksibisabol-2-en-1-ona (**1a**) ter 6,10 α ,11-trihidroksibisabol-2-en-1-ona (**1b**) in tudi 6,10 β -dihidroksibisabol-2,11-dien-1-ona (**2**). Vse tri spojine smo karakterizirali z obširno spektroskopsko analizo. Izkazalo se je, da imajo frakcije 22 do 26 občutno antimalarijsko delovanje proti sevoma *Plasmodium falciparum* D6 (z IC₅₀ vrednostmi 7.62–9.91 μ g/mL) in W2 (z IC₅₀ vrednostmi 5.49–6.08 μ g/mL); indeks selektivnosti je bil v povprečju večji od 6.0. Frakcije 7 in 16 do 24 so izkazale dobro aktivnost proti *Leishmania donovani* promastigotom (IC₅₀ = 6.71–18.77 μ g/mL). Frakcije 25 do 28 so bile aktivne proti *Trypanosoma brucei* tripomastigotom, od katerih se je frakcija 25 izkazala kot najbolj učinkovita (IC₅₀ = 4.13 μ g/mL). Proti *Aspergillus fumigatus* so bile učinkovite zgolj frakcije 11 do 13 (IC₅₀ = 13.406 μ g/mL). Izkazalo se je, da spojini **1a** in **2** nista obojavni učinkovini proti testiranim organizmom. Karakterizaciji spojin **1a** in **1b** v literaturi še nista bili opisani.



Except when otherwise noted, articles in this journal are published under the terms and conditions of the Creative Commons Attribution 4.0 International License

AUTHOR INDEX

Acta Chimica Slovenica
Year 2022, Vol. 69 No. 1–4

Abaszadeh Mehdi	920	Cao Tong.....	896
Abdassalam Aesha FSH	187	Carmona-Alvarado Idalia Francisca.....	49
Abdo Nadia Y. Megally	700	Cavazos-Rocha Norma.....	49
Aghajani Yeganeh	837	Çelik İsmail	419
Akdağ Kadriye	863	Cerc Korošec Romana	217
Akyıldız Hasan.....	39	Česko Cengiz	665
Al-Asafi Omar Jamal Mahdi	519	Çetinkaya Zeynep.....	39
Al-Dhalemi Dhuha Mohsin	681	Çevik Özge	293
Aldulaim Ahmed Kareem Obaid	681	Çevik Özge	863
Ali Karwan Omer	905	Chen Ruo-nan.....	227
Ali Saqib.....	405	Chtita Samir	489
Alimuddin	681	Ciuffreda Pierangela.....	571
Alkan Leman.....	316	Coskun Demet	73
Alruwaili Nabil K.....	483	Coskun Mehmet Fatih	73
Ambrož Ana.....	806	Černič Tina	448
Arenas Luis Andres Barboza.....	681	Dalvand Kolsoum.....	322
Arif Saira.....	200	Dascalu Izabella	331
Asaadi Negin.....	30	de Torres Noemi Waksman.....	49
Asiltürk Erol.....	60	Deniz Nahide Gulsah.....	187
Aslan Nazife	638	Dere Nurşen	108
Atakol Orhan	147	Dilmaghani Karim Akbari	619
Ayad Magda Mohamed.....	507	Dinçer Barbaros.....	604
Aydogdu Seyda	647	Doğan Hacer	281
Azam Mohammed Afzal	393	Dolničar Danica.....	167
Azizi Seyed Naser	458	Drtil Miloslav.....	657
Bahar Mehmet Refik	281	Duan Xiaoyi	896
Bai Su-Zhen.....	787	Duc Ha Danh.....	811
Bakhouch Mohamed.....	489	Dural Turan.....	604
Bálint Erika.....	735	Elmetwally Amira Mohamed.....	13
Ban Irena	826	El-Sayed kh.....	722
Bano Saeeda	405	Elshoky Hisham Ali	722
Barka Nouredine	536	ElZorkany Heba Elsayed	722
Bártová Iveta	371	Emirik Mustafa	604
Basha Mubarak Ali Muhamath	1	Enache Mirela	331
Bashir Shabnum.....	848	Erden Fuat	884
Bavec Aljoša	478	Erdoğan Ömer	293, 863
Baviskar Shweta	437	Erol Rabia	81
Belaidi Salah.....	489	Eryılmaz Müjde	419
Boh Podgornik Bojana.....	167	Eshwaraiah Latha Haraluru Kamamma	116
Božnar Alič Elizabeta.....	564	Fabjan Teja.....	564
Bren Urban	378	Faghih-Mirzaei Ehsan.....	920
Brontowiyono Widodo	681		
Cai Zhi-qiang	227		
Çalışkan Eray	281		

Falodun Abiodun	937	Imieje O. Vincent.....	937
Farah Mahnaz	837	İnal Emine Kübra	147
Farahi Mahnaz	30	Iqbal Sadaf	405
Farajian Fereshte.....	714	Iqbal Samina.....	405
Fatima Nasreen	405	Ishfaq Shazia	405
Fei-fei Li.....	227	Islas Jose Francisco	49
Feng Xinhui.....	674	Ivanova Iliana A.....	722
Ferk Savec Vesna.....	167	Izzat Samar Emad.....	681
Findik Serap	336, 552		
Fırat Özge	81	Jahanbakhshi Azar	837
Fırat Özgür	81	Jamil Waqas.....	772
Frlan Rok	261	Jayaram Unni	393
Fuchs Godec Regina.....	378	Jeran Marko	S95
		Jereb Matjaž.....	564
Gaál Enikő Éva.....	796	Jiang Jian.....	629
Gamaan Marwa Soliman	13	Jin Rui-Fa.....	913
Garza-Juarez Aurora de Jesús	49		
Gerber Thomas	905	Karakoyun Gülen Önal.....	60
Ghiasvand Alireza	322	Karakuş Sevgi.....	863
Gilani Neda Salek	458	Karami Bahador.....	30
Glamočlija Una	243	Karlovska Ines	657
Gökmen Uğur	638	Kešelj Dragana	803
Golični Marko.....	478	Khieu Dinh Quang.....	811
Görgülü Ahmet Orhan	281	Kilcigil Gülgün.....	419
Gruden Evelin	S95	Kızıl Demet	604
Gu Yuqing.....	674	Klečková Marta.....	371
Gunduz Bayram.....	73	Kobliha Zbyněk	125
Guo Xue-Yao	928	Koca Murat.....	466
Gürpınar Kübra	147	Koçyiğit-Kaymakçioğlu Bedia.....	293, 863
Gürpınar Suna Sibel	419	Koran Kenan	281
		Koraqi Hyrije.....	665
Halenova Tetiana	584	Koren Monika	448
Hamdi Amin	322	Korkut Ibrahim.....	884
Hamrahjou Nasrin	98	Kostadinova Anelyia s.....	722
Han Yong-Jun.....	385, 928	Kožárová Bibiána.....	657
Hanuljaková Hana.....	657	Kshash Abdullah Hussein	519
Haraluru Lalithamba Shankraiah.....	116	Kucukguzel Sukriye Guniz	526
Hashemi Payman.....	714	Kulabas Necla.....	526
Hassan Mohamed A.....	722	Kumer Kristina	564
Hatipoglu Arzu	647	Kurt Adnan.....	466
Heidari Nahid	322	Kuzmič Samo	261
Hemmesi Leila	876		
Hosny Mervat Mohamed.....	507	Lazarevic Jelena S	571
Hosten Eric.....	905	Lazić Dragica.....	803
Hrast Martina.....	261	Lei Yan.....	235
Hu Yanhong.....	133	Leng Xinyu	779
Hu Ze	133	Li Fen-Fang	596
Huang Qiu-chen.....	227	Li Shi-Tong.....	385
Huang Yong-Gang.....	913	Li Wei	227
Hung Nguyen Van	811	Li Xiaoyan	674
Hussein Shaymaa Abed	681	Liang Peng	629
Hussien Emad Mohamed	507	Lin Xue-Song	913
		Lisjak Darja	448
Ibrahim Rehab Ali.....	13	Liu Cheng	157
Imad Saima.....	405	Liu Chengguo.....	779
Imreová Zuzana	657	Liu Peng.....	133

Liu Shu-Juan.....	694	Petrič Boštjan	478
Liu Zhaogang	133	Petrović Zoran	803
Ljubijankić Nevzeta.....	243	Pitschmann Vladimír.....	125
Lobotka Martin.....	125	Ponikvar-Svet Maja	448
Lukić Milica.....	564	Popovics-Tóth Nóra	735
Luo Xiao-Qiang.....	385	Pourali Ali Reza	271
Luxbacher Thomas	826	Pourkazemi Arezoo.....	30
		Pucko Sara	564
Mahadevaiah Raghavendra.....	116		
Mahani Nosrat Madadi.....	91	Qais Faizan Abul.....	489
Mahdi Ahmed B.	681	Qazimi Bujar	665
Mahmood Khalid	200	Qiu Xiao-Yang	694
Majaron Boris	448		
Makovec Darko.....	756	Reli Martin	217
Malik Sabaahatul Ain.....	200	Riverón Aymara Ricardo	536
Markovic Ana.....	571	Rizvi Masood Ahmad	848
Masoodi Mubashir Hussain	848	Rodriguez Maria Martin	564
Matoh Lev.....	217	Roškar Robert	796
Meng Shuo.....	896	Rusek Martin.....	359, 371
Metias Youstina Mekhail	507		
Mihovec Katja	796	Sabouri Salehe.....	920
Mohamad Hikmat Ali.....	905	Sadat-Mansouri Seyedeh Nazanin	98
Mohamed Ahmed Said	489	Salazar-Cavazos Maria de la Luz	49
Mohareb Rafat Milad	13, 700	Salih Hanaa Kaen	519
Molčanov Krešimir.....	243	Salihoglu Huseyin.....	187
Moosvi Syed Kazim.....	848	Salihović Mirsada	243
Moradi Somayeh.....	349	Sandal Süleyman.....	281
Moradian Mohsen	349	Sang Ya-Li	913
Mostaghni Fatemeh.....	91	Santaniello Enzo	571
Mustafa Mohd.....	848	Sarveahrabi Yasin	619
Mustafa Yasser Fakri	681	Savchuk Olexii	584
		Sayil Cigdem	187
Naeimi Hossein	349, 876	Şen Hasan Tahsin	419
Najar Mohd. Hanief	848	Senkardes Sevil	526
Nangare Sopan.....	437	Serbest Kerim.....	604
Nath Kaushik	304	Shafiekhani Homa	91
Nazir Hasan.....	147	Shafqat Syed Salman	200
Nghi Nguyen Huu	811	Shahzaman Muhammad.....	405
Nguyet Bui Thi Minh	811	Shuai Xiao-min	227
Nisar Shazia.....	405	Siirilä Joonas.....	251
		Sirka Lütfiye.....	281
Ocak Sema Bilge	638	Sirotek Vladimír	371
Osmanović Amar	243	Smelcerovic Andrija.....	571
Osredkar Joško.....	564	Solangi Sorath	772
Ouassaf Mebarka	489	Srinivasan Sathiya.....	1
Ozbay Salih.....	884	Stasevych Maryna.....	584
Ozyurek Mustafa	187	Stojanovic Gordana.....	571
		Sumrra Sajjad Hussain.....	200
Panda Dibya Sundar.....	483	Sun Deyun	133
Parra Rosario Mireya Romero.....	681	Sun Tao	227
Patil Ashwini.....	437	Svoboda Ingrid.....	147
Patil Pravin	437	Swain Kalpana.....	483
Patra Indrajit	681		
Pattnaik Satyanarayan.....	483	Škapin Andrijana Sever Škapin	217
Pavlova Elitsa L.....	722	Špirtović-Halilović Selma.....	243
Penedo Medina Margarita.....	536	Štrofová Jitka	371

Štukovnik Zala	378	Yang Ting.....	674
Tabari Sonia.....	271	Yaqoob Muhammad.....	772
Taghvaei-Ganjali Saeed.....	98	Yaremkevych Olena.....	584
Taha Muhammad	772	Ye Fei	779
Tang Mao	133	Yesil Emin Ahmet.....	187
Tekin Suat	281	Yeşilçayır Elif.....	419
Temova Rakuša Žane	796	Yıldırım Şeküre	39
Tenhu Heikki.....	251	Yılmaz Nurdane	147
Tien Nguyen Anh.....	811	Yocheva Lyubomira D.....	722
Tilami Salma Ehsani	458	Yolcu Murat.....	108
Toader Ana Maria	331	Yolcu Zuhail	108
Tok Fatih	293, 863	You Zhonglu.....	629, 674
Torres Lidia Naccha	49	Yu Huiyuan.....	629
Toshkovska Radostina D.	722	Zadmard Reza.....	98
Trajkovska Petkoska Anka	665	Zafar Wardha	200
Tramšek Melita	S95	Zahid Kanwal.....	405
Tuncer Yaprak Gürsoy	147	Zahmatkesh Karim.....	619
Uslu Harun	281	Zakhar Ronald	657
Vaghela Naresh R.....	304	Zaki A. Ahmed	937
Vargas Armando Rojas	536	Zang Qi-qi	227
Vaskevych Alla.....	584	Zare Ehsan Nazarzadeh	271
Veljović Elma	243	Zarnegaryan Ali.....	30
Vives Alba González	536	Zengin Ali.....	604
Vojtř Karel	359, 371	Zhang Daopeng	896
Vovk Mykhaylo	584	Zhang Li.....	674
Wang Chu-Yi.....	694	Zhang Mingjian	896
Wang Jing.....	674	Zhang Wei	227
Wu Jinxiu	133	Zhao Xiao-Jun.....	787
Xin Yu	896	Zhou Gao-Qi.....	694
Xu Zhijie	896	Zhou Zhen.....	896
Xue Ling-Wei	928, 385, 787	Zvarych Viktor	584
		Žener Boštjan.....	217

DRUŠTVENE VESTI IN DRUGE AKTIVNOSTI

SOCIETY NEWS, ANNOUNCEMENTS, ACTIVITIES

Vsebina

Trideset let delovanja Šole eksperimentalne kemije na Institutu »Jožef Stefan«:	
trideset let motiviranja mladih generacij in utrjevanja poti naravoslovnega	
izobraževanja	S95
Slavnostna akademija ob 70-letnici Slovenskega kemijskega društva	S98
Koledar važnejših znanstvenih srečanj s področja kemije in kemijske tehnologije	S107
Navodila za avtorje	S110

Contents

Thirty years of the School of Experimental Chemistry at the "Jožef Stefan" Institute:	
thirty years of motivating young generations and strengthening the path	
of scientific education	S95
Ceremonial Academy on the Occasion of the 70 th Anniversary	
of the Slovenian Chemical Society	S98
Scientific meetings – Chemistry and chemical engineering.....	S107
Instructions for authors	S110

Trideset let delovanja Šole eksperimentalne kemije na Institutu »Jožef Stefan«: trideset let motiviranja mladih generacij in utrjevanja poti naravoslovnega izobraževanja

Melita Tramšek, Evelin Gruden in Marko Jeran*

Odsek za anorgansko kemijo in tehnologijo, Institut »Jožef Stefan«, Jamova cesta 39, Ljubljana, Slovenija

* Corresponding author: E-mail: marko.jeran@ijs.si

Tel.: +386 1 477 33 28

Received: 11-01-2022

Abstract

Pred 30. leti, natančneje spomladi leta 1992, je bila, v okviru Odseka za anorgansko kemijo in tehnologijo Instituta »Jožef Stefan«, ustanovljena Šola eksperimentalne kemije. Zaradi razvoja znanosti in interdisciplinarnih pristopov, je njen glavni namen približevanje kemije mladim generacijam in prikazovanje njene širše uporabe v vsakdanjem življenju. Šola eksperimentalne kemije tako ustvarja pomemben most med raziskovanjem in izobraževanjem ter aktivno prispeva k popularizaciji predmetnega področja v šolah.

Gljučne besede: Šola eksperimentalne kemije; izobraževanje; raziskovanje; povezovanje; popularizacija; kemija

Kemija se v modernem času ukvarja z odgovori na pomembna vprašanja, kot so na primer kemijske osnove mišljenja, razvoj procesov življenja, okoljska problematika, sinteza različnih materialov in na vse zadnje tudi z odkrivanjem novih (alternativnih) virov energije¹. Omenjena področja zajemajo izrazit interdisciplinarni pristop, zato je potreba po povezovanju ključna. Kemija prav tako predstavlja gonilno silo različnih panog industrije, kjer se morajo strokovnjaki prav tako spoprijemati z najrazličnejšimi praktičnimi izzivi. Če pomislimo, je kemija postala del našega življenja¹. Zaradi omenjenih razlogov in razvoja interdisciplinarnih pristopov v znanosti, je vselej nujno mlajše generacije opremiti z znanjem in veščinami, ki jih bodo lahko tekom študija in razvoja profesionalne poti tudi oplemenitili. Še kako pomembno je navduševati mlade generacije učencev in dijakov za povezovanje v naravoslovju skozi različne dogodke in vsebine, in nenazadnje tudi za komunikacijo znanstvenih vsebin s splošno javnostjo.

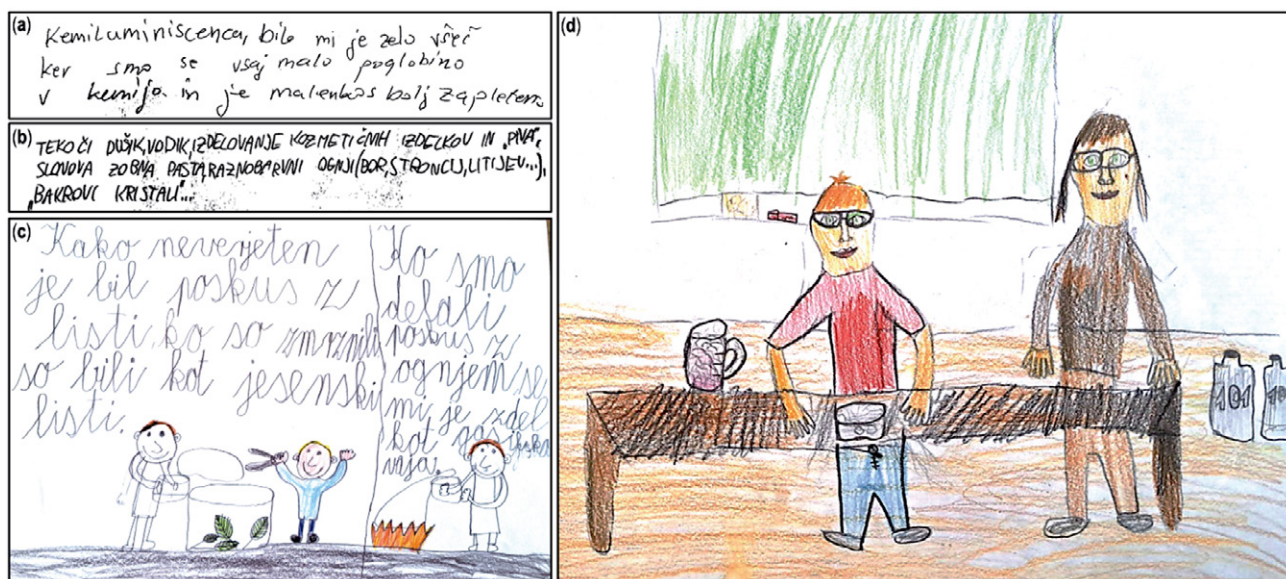
Ker je kemija nekoč veljala za splošno pust in težak predmet, kar je posledično vplivalo tudi na njeno priljubljenost, je bila pred 30. leti, natančneje spomladi leta 1992, v okviru Odseka za anorgansko kemijo in tehnologijo Instituta »Jožef Stefan«, ustanovljena Šola eksperimentalne kemije^{2,3,4}. Njen začetnik, prof. dr. Andrej Šmalc, je že ob njeni 15. obletnici poudaril, da so kemijski eksperimenti tisto, s čimer je mogoče pouk kemije bistveno pope-

striti, ga narediti zanimivega in privlačnega². V izvedbenem pogledu so prav kemijski poskusi, v primerjavi s fizikalnimi, bolj zahtevni in potrebujejo posebej za to urejene prostore. Po večini se v šolskih kemijskih učilnicah izvajajo zgolj demonstracijski tipi poskusov, med tem ko so možnosti za individualno eksperimentalno delo učencev dokaj omejene².

Šola eksperimentalne kemije je namenjena učencem in dijakom, ki želijo znanja kemije poglobiti še na eksperimentalni ravni, predvsem takim, ki jih veseli samostojno eksperimentiranje.

Poskusi, ki so zanimivi, zabavni in postavljeni v kontekstualni okvir vsakdanjega življenja, se hkrati skladajo z vsebinami temeljnega kurikulumu in udeležence spodbujajo k poglobljenemu razmišljanju². Pri eksperimentiranju udeleženci na primer spoznajo naravne pojave in jih na preprost način razložijo s kemijskimi poskusi (primer nastanek in oddajanje svetlobe)^{5,6}, pojasnjujejo vlogo in uporabo naravnih barvil⁷, povezujejo kemijo z drugimi tehniškimi disciplinami, kot sta elektrotehnika in razvoj senzorjev⁸, in podobno (Slika 1).

Med delom v laboratoriju si udeleženci pridobijo osnovne eksperimentalne veščine in spoznajo ukrepe za varno delo. Skozi delo v skupinah se učijo medsebojnega sodelovanja ter skozi predstavitve in demonstracije poskusov urijo svoje govorniške spretnosti.

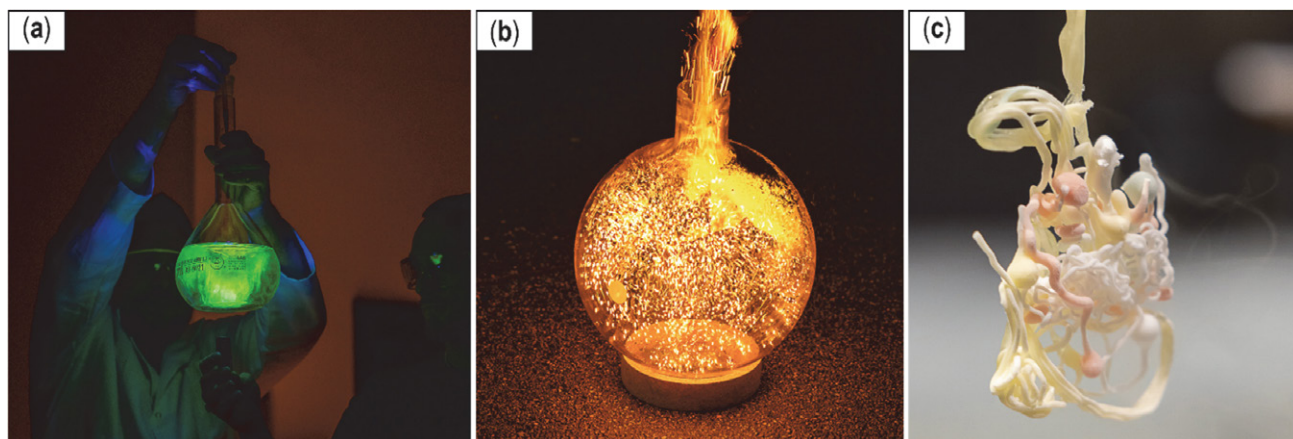


Slika 1: Odzivi udeležencev poletne Šole eksperimentalne kemije (a, b) in primera umetniških vtisov po obisku delavnice Šole eksperimentalne kemije na eni izmed šol (c, d) (Vir: osebni arhiv M. Tramšek).

Obiski učencev in dijakov se lahko povežejo tudi z ogledom laboratorijev Odseka za anorgansko kemijo in tehnologijo. Posamezniki se tako seznani z dejansko uporabo nekaterih metod pri raziskovalnem delu, katerih osnove so spoznali pri poskusih. V tem primeru lahko v živo vidijo in vsaj na kratko občutijo utrip raziskovalnega okolja.

Šola eksperimentalne kemije je bila sprva zasnovana v obliki enotedenskih tečajev v skupnem trajanju 32 šolskih ur, ki potekajo v t.i. šolskem laboratoriju inštitutskega odseka. Tečaj vodi mentor, ki udeležencem pripravi ustrezen program, gradivo in udeležence seznani z varnostno kulturo ter z ravnanjem z odpadki po izvedenem poskusu². Skozi leta je Šola eksperimentalne kemije postala pomemben akter promocije znanosti na različnih dogodkih. Predvsem je bila dobro sprejeta na vsakoletnih dogodkih Festivala znanosti, ki poteka pod okriljem Slo-

venske znanstvene fundacije (SZF)⁹. Člani ekipe vsako leto aktivno promoviramo znanost z različnimi demonstracijskimi nastopi po osnovnih in srednjih šolah ter vrtcih. Od leta 2018, izvajalci delavnice Šola eksperimentalne kemije v okviru Evropske noči raziskovalcev, aktivno sodelujemo pri projektu »Noč ima svojo moč«, kjer skupaj s partnerji (poleg Instituta »Jožef Stefan« še: Ustanova Hiša eksperimentov, Kemijski inštitut, Tehniški muzej Slovenije, Geološki zavod Slovenije ter Botanični vrt Univerze v Ljubljani) poudarjamo pomen znanosti za širšo družbo¹⁰. Evropski dogodek noči raziskovalcev med drugim, preko različnih predavanj in delavnic, omogoča neposredno komunikacijo raziskovalcev s posamezniki. Na ta dan sodelavci Instituta »Jožef Stefan« sodelujemo pri večeru odprtih vrat z najrazličnejšimi delavnicami, in dogajanje popestrimo s »showi« eksperimentov (Slika 2).



Slika 2: »Show« eksperimentov, ki je potekal v okviru dogodka »Noč ima svojo moč 2022«, na Institutu »Jožefa Stefana« (Foto: M. Verč, Institut »Jožef Stefan«). (a) Difuzija in fluorescenca barvila fluorescein v vodnem stolpcu (angl. vortex); (b) s kromovim(III) oksidom katalizirana oksidacija amonijaka, pri kateri nastanejo iskre oz. t.i. »kresničke«; (c) vključevanje naravnih barvil v natrijev alginat in preučevanje lastnosti gela v tekočem dušiku. (Foto: M. Verč, Institut »Jožef Stefan«)

Glavni namen Šole eksperimentalne kemije temelji na približevanju kemije mladim generacijam in prikazovanju njene širše uporabe v vsakdanjem življenju ter s tem prispevati k njeni popularizaciji. Ob enem pa naj bi šola tistim učencem, ki čutijo večje nagnjenje do naravoslovja, ustvarila željo po študiju kemije in morda tudi po raziskovalnem delu na tem področju.

»Življenje je potovanje, ne cilj.«

Ralph Waldo Emerson

Izvajalci programa Šole eksperimentalne kemije smo počaščeni, da smo lahko del programa s trideset letno tradicijo. Nadvse nas navdušuje, da lahko svoje poslanstvo širimo med mlade in jih tako motiviramo za raziskovanje naravoslovnih znanosti.

Zahvala

Avtorji prispevka se iskreno zahvaljujemo začetnikom Šole eksperimentalne kemije: prof. dr. Andreju Šmalcu, prof. dr. Borisu Žemvi in mag. Tomažu Ogrinu, ter njihovim sodelavcem in prostovoljcem, ki so s svojim entuziazmom in predanostjo pripomogli k častitljivi obletnici. Prav tako hvala tudi doc. dr. Gašperju Tavčarju, vodji Odseka za anorgansko kemijo in tehnologijo Instituta »Jožef Stefan«, za podporo in motivacijo pri nadaljnjih korakih. Velika zahvala gre tudi Javni agenciji za raziskovalno dejavnost Republike Slovenije (ARRS) in raziskovalnemu

programu P1-0045 za podporo pri ohranjanju povezav instituta s celotno izobraževalno vertikalo.

Literatura

1. A. Godec, *Kemija v šoli in družbi* **2007**, 19, 4, 27–33.
2. A. Šmalc, M. Tramšek, *Novice IJS* **2007**, januar, 129, 20–22.
3. T. Ogrin, *Novice IJS* **2002**, april, 95, 14–15.
4. E. Gruden, M. Tramšek, *Novice IJS* **2022**, 202, 12–14.
5. M. Jeran, S. Cvar, A. Podgoršek Berke, *Kemija v šoli in družbi* **2012**, 24, 4, 10–16.
6. M. Jeran, *Proteus* **2016**, 78, 5, 205–214.
7. M. Orel (ur.), M. Jeran (ur.); Skozi mavrico kemijskih sprememb: kemijski poskusi, Gimnazija Moste in Mako R, Ljubljana, **2017**. https://www.gimoste.si/images/datoteke/Skozi_mavrico_kemijskih_sprememb.pdf (obiskano: 13. 10. 2022)
8. M. Kovačič, Telefoncek.si, Šola eksperimentalne kemije, Ljubljana, **2018**. <https://telefoncek.si/2018/07/04/sola-eksperimentalne-kemije/> (obiskano: 10. 10. 2022)
9. Ustanova Slovenska znanstvena fundacija; Evropski festival znanosti, Ljubljana, **2021**. <https://www.u-szf.si/evropski-festival-znanosti/> (obiskano: 15. 10. 2022)
10. Evropska noč raziskovalcev; Noč ima svojo moč, Konzorcij partnerjev: Ustanova Hiša eksperimentov, Institut »Jožef Stefan«, Kemijski inštitut, Tehniški muzej Slovenije, Geološki zavod Slovenije ter Botanični vrt Univerze v Ljubljani, Ljubljana, **2022**. <https://www.nocmoc.eu/#predstavitev> (obiskano: 15. 10. 2022)



Except when otherwise noted, articles in this journal are published under the terms and conditions of the Creative Commons Attribution 4.0 International License



V letu 2021 je Slovensko kemijsko društvo praznovalo 70 –letnico ustanovitve. Zaradi epidemiološke situacije smo bili primorani Slavnostno akademijo preložiti na letošnje leto- potekala je 22. 9. 2022 v Grand Hotelu Bernardin v Portorožu. Dogodka se je udeležilo več kot 310 povabljenih gostov iz 13 držav, med drugim tudi predsednika hrvaškega in slovaškega kemijskega društva ter predstavniki ECTN in EuChemS.

Slavnostni govorniki so bili prof. dr. Tamara Lah Turnšek, akad. prof. dr. Branko Stanovnik in prof. dr. Venčeslav Kaučič, katerih govore si lahko preberete v nadaljevanju.

Slovensko kemijsko društvo je podelilo priznanja 8 častnim članom, 9 zaslužnim članom, 11 zaslužnim inštitucijam; priznanja za sodelovanje pri uredništvu znanstvene revije Acta Chimica Slovenica pa je prejelo 30 sodelavcev. Vsem se želim še enkrat zahvaliti za odlično delo v Slovenskem kemijskem društvu.

Na koncu gre zahvala tudi sponzorjem Slavnostne akademije, ki so omogočili proslavo ob tako pomembni obletnici- hvala torej podjetjem Cinkarna Celje, Salonit Anhovo, Knauf Insulation, Melamin, Aquafil, Novartis, Belinka Perkemija, Krka, Kemomed, Mettler Toledo in Primalab za podporo in sodelovanje.

Dr. Peter Venturini,
predsednik Slovenskega kemijskega društva

Dr. Peter Venturini, predsednik SKD:

Spoštovani visoki gostje, dragi prijatelji!

Biti kemik je velik privilegij in hkrati odgovornost. Je poslanstvo, ki ga z veseljem izpolnjujemo. Pri raziskovalnem delu odkrivamo nova znanja, ki so osnova za razvoj novih izdelkov in tehnologij, ki vodijo v napredek industrije in družbe kot celote ter smo pri tem zavezani varovanju okolja in zdravja ljudi. Prav nova spoznanja kemikov, kemijskih tehnologov in kemijskih inženirjev so bistveno prispevala k vse boljši kvaliteti življenja v Sloveniji in po svetu.

Prvi namen ustanovitve Slovenskega kemijskega društva je pospeševanje napredka kemije v najširšem pomenu besede. Zavedanje, da je za razvoj stroke ključnega pomena dobro sodelovanje med strokovnjaki v Sloveniji in tesna vpetost v mednarodno okolje, vodi delo članov društva in vse naše aktivnosti. Člani društva aktivno sodelujemo pri mnogih mednarodnih znanstvenih in strokovnih pobudah- na primer pri organizaciji konferenc, kot uredniki pri mednarodnih publikacijah in smo aktivni člani mnogih sorodnih mednarodnih združenj.

Ob mnogih aktivnostih našega društva tokrat izpostavljam dve:

- Vsakoletno srečanje poimenovano Slovenski kemijski dnevi in
- Izdajanje revije Acta Chimica Slovenica.

Dr. Peter Venturini, SCS President:

Distinguished guests, dear friends!

Being a chemist is both a privilege and a responsibility. It is a mission that we are happy to fulfil. Our research work uncovers new knowledge that forms the basis for the development of new products and technologies that lead to progress in industry and society as a whole, with a commitment to protecting the environment and human health. It is the new discoveries of chemists, chemical technologists and chemical engineers that have contributed significantly to the increasing quality of life in Slovenia and around the world.

The initial purpose of the founding of the Slovenian Chemical Society was to promote the progress of chemistry in the broadest sense of the word. The understanding that good cooperation between experts in Slovenia and close involvement in the international environment are crucial for the development of the profession guides the work of the members of the Society and all our activities. Members of the Society actively participate in many international scientific and professional initiatives – for example, in the organisation of conferences, as editors of international publications and as active members of many related international associations.

Among the many activities of our Society, I would like to highlight two:

Velika zahvala gre vsem članom in prijateljem Slovenskega kemijskega društva, ki ste pripomogli k odlični kakovosti in mednarodni prepoznavnosti obeh. V zadnjih letih je Kemijske dneve zelo uspešno razvijal organizacijski odbor pod vodstvom profesorja Albina Pintarja s Kemijskega inštituta. Zelo smo ponosni tudi na visoko odmevnost naše revije *Acta Chimica Slovenica*. Revija sledi sodobnim trendom odprte znanosti pri objavi znanstvenih člankov s prostim dostopom do vseh objav. Uredniški odbor revije že vrsto let uspešno vodi glavna urednica profesorica Ksenija Kogej s Fakultete za kemijo in kemijsko tehnologijo, Univerze v Ljubljani. Lepa hvala spoštovana Ksenija in Albin za izjemno opravljeno delo.

Že daljši čas je pomembna usmeritev pri našem delu trajnostni razvoj in ponosen sem, da bomo v okviru tokratnih Slovenskih kemijskih dni prvič podelili tudi nagrade študentom za najboljša dela s tega področja.

Pomembno delo za navduševanje mladih za kemijo ter njihovo ozaveščanje za okoljsko odgovorno obnašanje opravijo naši kolegi učitelji v osnovnih, srednji šolah in na univerzah za kar jim gre vse priznanje.

V Sloveniji smo lahko ponosni na izredno visok interes in nivo znanja na različnih področjih kemije na vseh stopnjah šolanja. Odličen je tudi nivo znanosti v visokošolskih ustanovah in na raziskovalnih inštitutih. Mnogi slovenski strokovnjaki sodijo med vodilne v svetu, kar je temelj za to, da so tudi mnoga slovenka podjetja zelo uspešna v mednarodnem okolju.

V Slovenskem kemijskem društvu se bomo tudi v prihodnje trudili za pospeševanje napredka kemije, kemijske tehnologije in kemijskega inženirstva s ciljem pridobivanja ključnih znanj za naslednje korake pri trajnostnem razvoju in dvigu kvalitete življenja v Sloveniji in širše.

Na koncu se želim zahvaliti vsem članom društva, predstavnikom podjetij, raziskovalnih in izobraževalnih ustanov ter javne uprave za odlično sodelovanje in partnerstvo ter tudi finančno podporo, ki nam omogoča izvedbo vseh naših aktivnosti.

Iskrene čestitke in velika zahvala gre vsem današnjim nagrajencem, ki ste pomembno prispevali k razvoju Slovenskega kemijskega društva.

Vsem želim prijetno in zanimivo druženje, ter veliko novih poznanstev in izmenjav znanj v okviru konference Slovenski kemijski dnevi.

- the annual meeting known as Slovenian Chemical Days and
- the publication of *Acta Chimica Slovenica*.

A very special thank you to all the members and friends of the Slovenian Chemical Society who have contributed to the excellent quality and international visibility of both. In recent years, the Chemical Days have been developed very successfully by the organising committee led by Professor Albin Pintar from the National Institute of Chemistry. We are also very proud of the high visibility of our journal *Acta Chimica Slovenica*. The journal follows the current trends of open science in publishing scientific articles with open access to all publications. The Editorial Board of the journal has been successfully led for a number of years by the Editor-in-Chief, Professor Ksenija Kogej from the Faculty of Chemistry and Chemical Technology, University of Ljubljana. Thank you very much, Ksenija and Albin, for your outstanding work.

Sustainable development has been an important focus of our work for quite some time and I am proud that for the first time at this year's Slovenian Chemical Days, we will also be awarding prizes for the best work in this field to students.

The work our fellow teachers in primary and secondary schools and at universities are doing is essential for getting young people excited about chemistry and to raise their awareness of environmentally responsible behaviour, for which they are to be commended.

Slovenia can be proud of the extremely high level of interest and knowledge in various areas of chemistry at all levels of education. The level of science in higher education institutions and research institutes is also excellent. Many Slovenian experts are among the leading in the world, which is why a number of Slovenian companies are also highly successful in the international environment.

The Slovenian Chemical Society will continue its efforts to promote the advancement of chemistry, chemical technology and chemical engineering in order to accumulate key competencies for the next steps in sustainable development and improving the quality of life in Slovenia and beyond.

Finally, I would like to thank all the members of the Society, representatives of companies, research and educational institutions and public administration for their excellent cooperation and partnership, as well as the financial support that makes all our activities possible.

Heartfelt congratulations and a big thank you to all of today's award winners who have made a significant contribution to the development of the Slovenian Chemical Society!

I wish you an enjoyable and eventful time and I hope that you form many new acquaintances and knowledge exchanges during the Slovenian Chemical Days.

Prof. dr. Tamara Lah Turnšek, Predsednica znanstveno- raziskovalnega razreda IAS:

»Spoštovanim tovarišem kemikom spročamo, da je bil dne 15. februarja 1951 ustanovni občni zbor »Slovenskega kemijskega društva« ki bo združevalo vse kemike v LR Sloveniji. S tem se je spremenila dosedanja organizacijska oblika kemične sekcije Društva inženirjev in tehnikov LRS in razširila v samostojno strokovno in znanstveno društvo«.

Tako je bil oznanjen zgodovinski dogodek ustanovitve Slovenskega Kemijskega Društva - SKD pred dobrim stoletjem.

Seveda segajo začetki kemije na slovenskem kar precej dlje! V različnih oblikah se je kemija poučevala na srednjih, višjih in visokih šolah in predhodnih formalnih oblik današnje Fakulte za kemijo in kemijski tehnologijo Univerze v Ljubljani

Iz tega (zgodovinskega) prepleta znanj je izšel tudi prvi slovenski Nobelov nagrajenec, dr. Friderik Fritz Pregl, rojen v Ljubljani in leta 1894 promoviran za doktorja vsega zdravilstva (medicum universum) na univerzi v Gradcu. Njegovo delo bi danes sodilo na področje biokemije, saj so njegova temeljna spoznanja v organski kemiji obravnavala predvsem aminokisline, ogljikove hidrate in purine, kar bi sodilo danes na področje biokemije! Nobelovo nagrado je prejel 1923 za razvoj, na milijoninko grama natančne, tehtnice za kvantitativno organsko mikroanalizo v sodelovanju s podjetjem Kuhlmane in je omogočil hiter napredek organske kemije v 20. stoletju. V svoji raziskovalni vni se že kot priznani znanstvenik udinjal kot vajenec pri nekem mizarju, pri ključavničarju in steklopihaču. Tako je sam zaradi svoje »dodatne izobrazbe« izdelal zamišljene aparature od prvega grobega osnutka do zadnje fine obdelave. S tem pa je postavil tudi enega pomembnih temeljnih kamnov slovenskega inženirstva!

To dejstvo se dotika drugega pomembnega dogodka leta 1995, ko je na podlagi več kot stoletja inženirskega dela Skupina slovenskih znanstvenikov s področja tehniških in naravoslovnih znanosti ter uglednih inženirjev, članov društva SATENA, ustanovilo Inženirsko akademijo Slovenije (IAS) z namenom, da se ustvari platforma za politiko in formiranje razvojnih perspektiv proizvodnih industrij, znanstvenih in tehnoloških raziskav ter kvalitetnega inženirskega in poslovnega študija v Sloveniji, v letu 2006 je bila IAS tudi zakonsko ustanovljena na državni ravni.

Trdimo lahko, da prav edina »slovenska« Nobelova nagrada kaže na tesno povezanost med poslanstvom Slovenskega kemijskega društva in IAS. Na to smo lahko prav na današnji slavnosti ponosni!

Ob tem se zavedam globokih korenin znanj, inovativnega

Prof. Dr. Tamara Lah Turnšek, President of the Scientific-Research Group of the IAS:

“Esteemed fellow chemists, we would like to inform you that the founding general assembly of the ‘Slovenian Chemical Society’, which will unite all the chemists in the People’s Republic of Slovenia, was held on 15 February 1951. The current organisational form of the Chemical Section of the Society of Engineers and Technicians of the PRS has thus been changed and expanded to form an independent professional and scientific society”.

This was how the historic event of the founding of the Slovenian Chemical Society (SCS) was announced nearly a century ago.

Of course, the beginnings of chemistry in Slovenia go back much further! Chemistry was taught in various forms at secondary and higher education institutions, and at the previous organisational forms of today’s Faculty of Chemistry and Chemical Technology of the University of Ljubljana.

This (historical) intertwining of knowledge produced the first Slovenian Nobel Prize winner, Dr. Friderik Fritz Pregl, born in Ljubljana and promoted to Doctor of Medicine (medicum universum) at the University of Graz in 1894. His work would today be a part of biochemistry, as his fundamental findings in organic chemistry mainly dealt with amino acids, carbohydrates and purines! He won the 1923 Nobel Prize for developing a balance, precise to the millionth of a gram, for quantitative organic microanalysis in collaboration with the company Kuhlmann, and thereby enabled the rapid progress of organic chemistry in the 20th century. In his eagerness for research, he served, when he was already a renowned scientist, as an apprentice to a carpenter, a locksmith and a glass-blower. Thanks to his “additional education”, he could make the envisaged apparatus for himself from the first rough draft to the last finishing touches. In doing so, he also laid one of the most important cornerstones of Slovenian engineering!

This fact touches upon another significant event in 1995, when, on the basis of more than a century of engineering work, a group of Slovenian scientists, working in technical and natural sciences, and prominent engineers, members of the SATENA association, founded the Slovenian Academy of Engineering (IAS) with the aim of creating a platform for policies and shaping the development perspectives of the manufacturing industries, scientific and technological research, and quality engineering and business studies in Slovenia; in 2006, the IAS was also established by law at the national level.

It could be argued that the only “Slovenian” Nobel Prize

duha in stremljenj vseh mojih predhodnikov v slovenski zgodovni slovenske kemijske znanosti in inženirstva, ki so danes pripeljali obe vеди do uspehov, ki jih naši raziskovalci dosegajo doma in v svetu! S ponosom sem in smo danes lahko hvaležni, da smo imeli priložnost vskravati vse te dobrine tekom svojega učenja in delovanja. Danes imam torej čast, da kot članica, in obenem inženirka organske oz biokemijske smeri, v imenu predsednika in vseh članov IAS čestitam SKD o jubileju društva.

Obenem bi želela poudariti, da imata obe instituciji zelo podobna strmljenja in poslanstva:

da pospešujeta napredek kemije, kemijske tehnologije in kemijskega inženirstva v najširšem pomenu; da skrbita za rast strokovnega znanja svojega članstva in da sodelujeta z vsemi organizacijami, ki se ukvarjajo s kemijsko, tudi biokemijski stroko in bioinženirstvom, z njimi izmenjujeta izkušnje in jim pomagata

Nadalje pa si članice in čani IAS želimo tesnejšega sodelovanja, da skupaj z SKD opažamo pereče probleme stroke, jih rešujemo in odločevalcem skupaj predlagamo aktivnosti in najbolj kakovostne rešitve; tudi za relevante širše družbene probleme, ki vključujejo in potrebujejo naša znanja in izkušnje.

Čisto nazadnje in sploh ne najmanj pomembno, je omeniti prispevek ženskih kolegic k delu, uspehu in ugledu obeh institucij. Čeprav je danes diplomantk in doktorandk na področju kemije in kemijskega inženirstva v Sloveniji vsaj enako ali celo več, kar se delno odseva tudi članstvu SKD, so ženske dokaj slabo, le z nekaj odstotki zastopane v akademijah in med dobitniki najvišjih strokovnih priznanj. Če se vrnem na začetek nagovora – k Nobelovi nagradi – je bilo nagrajenk v 121. letih je samo pet, začenši z Marie Skłodowskiej Curie v letu 1911 in Jennifer Doudna v letu 2021!

Zato seveda potrebujemo podporo skupnosti in tudi kolegov!

shows how closely linked the missions of the Slovenian Chemical Society and the IAS really are. This is truly something we can be proud of at today's celebration!

I am also aware of the deep roots of knowledge, the innovative spirit and the ambitions of all my predecessors in the history of Slovenian chemical science and engineering, which have led both sciences to the successes that our researchers are today achieving at home and around the world. I, and we, can be proud and thankful today that we have had the opportunity to absorb all these benefits in the course of our studies and work. Today, therefore, I have the honour, as a member and as an organic chemistry or biochemical engineer, to congratulate the SCS on its anniversary on behalf of the President and all the members of the IAS.

At the same time, I would like to point out that both institutions have very similar ambitions and missions:

to promote the advancement of chemistry, chemical technology and chemical engineering in the broadest sense; to foster the professional development of its members and to work with all the organisations involved in the chemical and biochemical profession and bioengineering by sharing experience and assisting them.

Furthermore, IAS members would like to work more closely together with the SCS to identify pressing problems in the profession, solve them and jointly propose actions and the best solutions to decision makers; including for any relevant broader societal problems that involve and need our knowledge and experience.

Last but by no means least, it is important to note the contribution of female colleagues to the work, success and reputation of both institutions. Although the number of female graduates and PhD students in chemistry and chemical engineering in Slovenia today is at least equal or even higher, which is partly reflected in the membership of the SCS, women are rather poorly represented, i.e. only a few percent, in academies and among the winners of the highest professional awards. If I may return to the beginning of my address – to the Nobel Prize – there have been only five female Nobel Prize winners in 121 years, starting with Marie Skłodowska-Curie in 1911 and Jennifer Doudna in 2021!

So we obviously need the support of the community and also of our male colleagues!

Akad. prof. dr. Branko Stanovnik, predstavnik Slovenske akademije znanosti in umetnosti:

Spoštovani gospod predsednik SKD Dr. Peter Venturini,
Spoštovani ugledni gostje, kolegice in kolegi, dragi
prijatelji

V prijetno dolžnost mi je, da vas najprej pozdravim v imenu predsednika Slovenske akademije znanosti in umetnosti akademika Petra Štiha, ki se zaradi drugih obveznosti ni mogel udležiti današnje slovesnosti, in izročim njegove pozdrave in čestitke SKD in vam ob tem pomembnem jubileju za vse imenitne dosežke, ki jih je društvo doseglo v svoji zgodovini. Obenem želi SKD še naprej veliko uspehov, predsedniku pa uspešno vodenje društva še naprej. Slovenska akademija znanosti in umetnosti je ponosna, da je bil prvi predsednik SKD član akademije in v mednarodnem svetu ugledni znanstveni Maks Samec.

2. 9. 1945 je bil Samec odstranjen z univerze. Njegovo nadaljnje delovanje je povezano z gradnjo instituta za kemijo, ki je bil ustanovljen hkrati s fizikalnim inštitutom Jožef Stefan in elektroinštitutom Milana Vidmarja v okviru Slovenske akademije znanosti in umetnosti. Od 1. 10. 1946 do 1959 je bil upravnik kemijskega laboratorija AZU (pozneje SAZU), ki se je 12. 6. 1953 preimenoval v Kemični inštitut Borisa Kidriča. Maks Samec je odigral pionirsko vlogo na področju organiziranja Slovenskega kemijskega društva, ki je bilo ustanovljeno 15. 12. 1951. Bil je njegov prvi predsednik 1951–1962 in častni predsednik 1963/64.

Ker je Komite za šolstvo in znanost Federativne republike Jugoslavije v Beogradu zahteval, da se naj znanstvena dela najprej objavijo v domačih strokovnih revijah, šele nato v tujini je Samec ustanovil najprej Zbornik in nato Vestnik Slovenskega kemijskega društva.

Zgodovina SKD na spletni strani je razmeroma skromna. Zato naj dodam še nekaj glede tega.

1. Uredništvo Vestnika Slovenskega kemijskega društva in preimenovaje v Acta Chimica Slovenica

Prof. Dušan Hadži me je kot predsednik SKD 1976 zaprosil, da bi prevzel uredništvo Vestnika, ki je do takrat zelo neredno izhajal. Kot novi urednik sem si zadal dve nalogi: 1. da bo Vestnik izhajal redno štirikrat na leto in 2. predlagal sem, da bi Vestnik preimenovali v Acta Chimica Slovenica. Glede rednega izhajanja mi je stvar uspela ob izdatni pomoči Marka Razingerja kot tehničnega urednika. Vestniku je bil kmalu priznan faktor vpliva. Glede preimenovanja pa je moj predlog leta 1976 popolnoma pogorel. Eksplicitno sta bila proti prof. Hadži in prof. Dolar. Nisem se hotel prepirati, sklenil sem počakati na ugodnejše čase. Počakal sem do razglasitve samostojne države. Potem, ko

Akad. prof. dr. Branko Stanovnik, representative of the Slovenian Academy of Sciences and Arts:

Honourable President of the SCS, Dr. Peter Venturini,
distinguished guests, colleagues, dear friends,

It is my pleasant duty first of all to greet you on behalf of the President of the Slovenian Academy of Sciences and Arts, Academician Peter Štih, who was unable to attend today's ceremony due to other commitments, and to convey his greetings and congratulations to the SCS and to you on this special anniversary for all the outstanding achievements that the Society has accomplished in its history. He also wishes the SCS many successes in the future and the President continued successful leadership of the Society. The Slovenian Academy of Sciences and Arts is proud that the first President of the SCS was a member of the Academy and internationally renowned scientist Maks Samec.

On 2 September 1945 Samec was removed from the university. His further activities were linked to the construction of the Institute of Chemistry, which was founded at the same time as the Jožef Stefan Institute and the Milan Vidmar Electric Power Research Institute under the auspices of the Slovenian Academy of Sciences and Arts. From 1 October 1946 to 1959, he was the manager of the chemical laboratory of the Academy of Sciences and Arts (later the Slovenian Academy of Sciences and Arts), which was renamed the Boris Kidrič Institute of Chemistry on 12 June 1953. Maks Samec had a pioneering role in the organisation of the Slovenian Chemical Society, which was founded on 15 December 1951. He was its first President from 1951 to 1962 and Honorary President in 1963/64.

Because the Committee for Education and Science of the Federal Republic of Yugoslavia in Belgrade demanded that scientific works should first be published in domestic professional journals, and then abroad, Samec founded first the Zbornik and then the Vestnik Slovenskega kemijskega društva.

There is relatively little written about the history of the SCS on its website. Allow me to add something to this topic.

1. The Editorial Board of the Vestnik Slovenskega kemijskega društva and the renaming to Acta Chimica Slovenica.

In 1976, Prof. Dušan Hadži, then President of the SCS, asked me to take over the editorship of the Vestnik, which until then had been published very irregularly. As the new editor, I set myself two tasks: 1. that the Vestnik would be published regularly four times a year, and 2. I proposed that the Vestnik be renamed Acta Chimica Slovenica. As regards regular publication, I succeeded with the substan-

je bilo SKD sprejeto 1992 v Federacijo evropskih kemijskih društev, sem kot urednik Vestnika predlagal spremembo naslova. Tokrat je bil predlog brez pripomb soglasno sprejet in leta 1993 je začel izhajati kot Acta Chimica Slovenica. Uredništvo so prevzeli mlajši ljudje, ki so ga ustrezno preoblikovali in digitalizirali in že v nekaj letih so Acta Chimica Slovenica postala mednarodno prepoznaven časopis.

2. Sprejem Slovenskega kemijskega društva v Federacijo evropskih kemijskih društev. Prvo mednarodno priznanje strokovnega društva v mednarodni organizaciji v samostojni Sloveniji.

V osemdesetih in devetdesetih letih prejšnjega stoletja sem bil najprej kot predstavnik Unije jugoslovanskih kemijskih društev, pozneje pa kot predstavnik Slovenskega kemijskega društva član Sveta Federacije evropskih kemijskih društev. Seja Sveta Federacije EKD je bila v Londonu 24. in 25. junija 1991. Ker je bilo takrat že jasno, kakšna bo usoda Jugoslavije, sem situacijo pojasnil in se dogovoril s predsednikom Sveta Federacije evropskih kemijskih društev dr. Gowom, generalnim sekretarjem Royal Society of Chemistry in drugimi člani Sveta za sprejem Slovenskega kemijskega društva v Federacijo evropskih kemijskih društev. To ustno soglasje je bilo sprejeto nekaj ur pred razglasitvijo samostojne Slovenije. Ko sem zgodaj popoldne prišel na letališče v Londonu in sem se hotel prijaviti za let v Ljubljano, mi povedo, da je Adria let odpovedan, namesto tega pa leti letalo Air France. Izkazalo se je, da je Adria no letalo letelo pod francosko zastavo in tako smo varno pristali v Ljubljani na predvečer razglasitve samostojne Slovenije. To je bilo zadnje letalo, ki je pristalo v Ljubljani pred desetdnevno vojno za Slovenijo. Tisto noč so tanki odpeljali iz vrhniške kasarne proti Brniku. Letališče je bilo nato nekaj mesecev zaprto.

Glede na to, da sem prinesel iz London ustno zagotovilo o priznanju Slov. kem. društva, je prof. Ljubo Golič, tedanji predsednik Slovenskega kemijskega društva, pripravil pisno vlogo na Federacijo, ki je bila obravnavana na Seji Sveta Federacije evr. kem. društev v Varšavi na sedežu Polske akademije znanosti 22. junija 1992. Slovenija je bila sprejeta z aplavzom brez kakršne koli pripombe ali komentarja. To je prvo mednarodno priznanje nekega strokovnega društva v mednarodni asociaciji.

Hvala lepa

tial support of Marko Razinger as technical editor. The Vestnik was soon recognised as having an impact factor. As for the renaming, my proposal in 1976 was completely rejected. Prof. Hadži and Prof. Dolar were explicitly against it. As I did not want to argue, I decided to wait for better times. I waited until the country declared independence. After the SCS was admitted to the Federation of European Chemical Societies in 1992, I, as editor of the Vestnik, proposed a change of its name. This time the proposal was unanimously adopted without objections and in 1993 the journal started to be published as Acta Chimica Slovenica. The Editorial Board was taken over by younger people, who reorganised and digitised it accordingly, and within a few years, Acta Chimica Slovenica became an internationally renowned journal.

2. The admission of the Slovenian Chemical Society to the Federation of European Chemical Societies. The first international recognition of a professional society by an international organisation in independent Slovenia.

In the 1980s and 1990s, I was a member of the Council of the Federation of European Chemical Societies, first as a representative of the Union of Yugoslav Chemical Societies, and later as a representative of the Slovenian Chemical Society. The Council of the Federation of European Chemical Societies met in London on 24 and 25 June 1991. At the time, it was already clear what the fate of Yugoslavia would be, so I explained the situation and agreed with the President of the Council of the Federation of European Chemical Societies, Dr. Gow, the General Secretary of the Royal Society of Chemistry and other members of the Council that we would admit the Slovenian Chemical Society to the Federation of European Chemical Societies. This oral consent was given a few hours before the declaration of Slovenia's independence. When I arrived at the airport in London in the early afternoon to check in for my flight to Ljubljana, I was told that Adria's flight had been cancelled and that Air France was flying instead. It turned out that Adria's plane was flying under the French flag, which allowed us to land safely in Ljubljana on the eve of Slovenia's declaration of independence. This was the last plane to land in Ljubljana before the Ten-Day War for Slovenia. That night, tanks started rolling out of the Vrhnika barracks towards Brnik. The airport was closed for several months after that.

As I had brought from London a verbal assurance that the Slovenian Chemical Society would be recognised, Prof. Ljubo Golič, then President of the Slovenian Chemical Society, prepared a written application for the Federation, which was discussed at the Warsaw meeting of the Council of the Federation of European Chemical Societies at the headquarters of the Polish Academy of Sciences on 22 June 1992. Slovenia was admitted with applause and without any remarks or comments. This is the first international recognition of a professional society by an international association.

Thank you.

Prof. dr. Venčeslav Kaučič, častni predsednik SKD:

Spoštovane in drage kolegice in kolegi, prisrčno pozdravljeni.

Posebej želim pozdraviti, jim čestitati in se jim zahvaliti za njihov doprinos k delovanju in uspehom društva današnjim slavljenecem, novim častnim in novim zaslužnim članom društva.

I also warmly welcome our dear guests from abroad, with whom we were meeting and cooperated closely for many years. Today we thank them for their contribution to the professional growth of our society and for their help in integrating our society into international professional organizations and international connections by awarding them the title of honorary member of the Slovenian Chemical Society.

Zelo na kratko želim navesti nekaj utrinkov o razvoju in delovanju društva v preteklih sedemdesetih letih. Kot smo že slišali je bil pobudnik ustanovitve in prvi predsednik Prof. Maks Samec. Za njim so ga vodili izjemni, svetovno znani znanstveniki in inženirji: prof. Roman Modic (od 1963 do 1974), akad. prof. Dušan Hadži (od 1974 do 1986), akad. prof. Ljubo Golič (od 1986 do 1996) in v novejšem času prof. Venčeslav Kaučič (od 1996 do 2017), prof. Albin Pintar (od 2017 do 2021) in od 2021 ga vodi dr. Peter Venturini.

Zanimiva je bila moja včlanitev in nato 50 let delovanja v društvu in v mednarodnih združenjih kemikov. Na podelitvi visokošolske diplome leta 1973 sem dobil vabilo za včlanitev v SKD. Še isti dan sem šel v pisarno društva na Kemijskem inštitutu, kjer sem srečal takratnega tajnika društva prof. Marcela Žorgo, ki me je vpisal v društvo pod vpisno št. 305. Kupil sem še Laboratorijski priročnik, ki ga je izdalo društvo in mi je bil v tistem času, ko je bilo na razpolago malo strokovnih knjig v slovenskem in v tujih jezikih, v veliko pomoč.

Leta 1986 sem bil izvoljen za tajnika društva in v tem svojstvu deloval do leta 1996, ko sem bil na občnem zboru, ki je potekal na konferenci Slovenski kemijski dnevi v Mariboru, izvoljen za predsednika društva.

To je bilo na dan, ko se je Prof. Miha Japelj veselil rojstva svoje prve vnučke in sva imela razlog več za proslavljanje. Prof. Japelj se tega zagotovo dobro spominja.

Funkcijo predsednika društva sem z veseljem in spoštovanjem opravljal do leta 2017. Posebej sem si prizadeval za članstvo društva v uglednih mednarodnih strokovnih združenjih in aktivno delovanje naših članov v njih. Prepričan sem, da so naši člani s svojim strokovnim delovanjem primerno promovirali slovensko znanost v mednarodni znanstveni srenji.

Prof. dr. Venčeslav Kaučič, Honorary President of the SCS:

Ladies and gentlemen, dear colleagues, a warm welcome.

I would also like to extend a special welcome, congratulations and thanks for their contribution to the operation and success of the Society to today's honorees, the new Honorary Members and the new Emeritus Members of the Society.

I also warmly welcome our dear guests from abroad, with whom we have been meeting and cooperating closely for many years. Today, we thank them for their contribution to the professional growth of our Society and for their help in integrating our Society into international professional organisations and international connections by awarding them the title of Honorary Member of the Slovenian Chemical Society.

I would like to give you, very briefly, some highlights from the development and activities of the Society over the past 70 years. As we have already heard, the initiator and first President was Professor Maks Samec. After him, the Society was led by outstanding, world-renowned scientists and engineers: Prof. Roman Modic (from 1963 to 1974), Acad. Prof. Dušan Hadži (from 1974 to 1986), Acad. Prof. Ljubo Golič (from 1986 to 1996) and more recently Prof. Venčeslav Kaučič (from 1996 to 2017), Prof. Albin Pintar (from 2017 to 2021), and since 2021 it has been led by Dr. Peter Venturini.

My becoming a member and then 50 years of service in the Society and in international associations of chemists was interesting. I received an invitation to join the SCS at my university graduation ceremony in 1973. On the same day, I went to the Society's office at the National Institute of Chemistry, where I met the then Secretary of the Society, Prof. Marcel Žorga, who enrolled me in the Society under registration number 305. I also bought the Laboratory Manual published by the Society, which was a great help to me at that time, because there were few scientific books available in Slovenian or in foreign languages.

In 1986, I was elected Secretary of the Society and served in this capacity until 1996, when I was elected President at the general assembly held at the Slovenian Chemical Days in Maribor.

This was on the day Prof. Miha Japelj was celebrating the birth of his first granddaughter and we had an additional reason to celebrate. I am sure Prof. Japelj remembers this well.

I have served as President of the Society with pleasure and respect until 2017. It was always my goal that the Society would become a member of renowned international professional associations and that our members would be

Društvo aktivno sodeluje tudi s številnimi društvi na bilateralni ravni, z društvi iz naše bližnje okolice, v evropskem prostoru in tudi z društvi iz drugih kontinentov.

Leta 2017 sem bil izvoljen za častnega predsednika Slovenskega kemijskega društva, na kar sem ponosen. Od 1986 do 2017 (mandat tajnika in nato predsednika) je več kot 30 let in prof. Pejovnik mi je večkrat rekel, da zanj priimek Kaučič hkrati pomeni kemijsko društvo in obratno, da kemijsko društvo hkrati pomeni Kaučič. Hvala ti, Stane.

Morda omenim še, da sem bil preko 30 let aktiven v IUPAC-u. Letos je izšel IUPAC-ov periodni sistem, preveden v 26 svetovnih jezikov. Na svetu obstaja med 6000 in 7000 jezikov. Ponosno povem, da je izšel tudi v slovenskem jeziku (eden od 26 prevodov).

Zahvaljujem se za vsestransko podporo društvu s strani pomembnih industrijskih partnerjev, univerz, znanstvenih in strokovnih inštitutov ter ministrstva za šolstvo, znanost in šport in Javne agencije za raziskovalno dejavnost Republike Slovenije.

Hkrati si želim, da društvo strokovno raste še naprej in da z dejavnostmi aktivno nadaljuje v naslednjih letih ter jih tudi nadgrajuje.

Hvala za vašo pozornost, po koncu te slovesnosti pa vam želim veselo, prijazno in sproščujoče druženje.

active in them. I am confident that our members have adequately promoted Slovenian science in the international scientific community through their professional activities.

The Society also actively and bilaterally cooperates with a number of societies, with societies in our immediate surroundings, in the European area and also with societies from other continents.

In 2017, I was elected Honorary President of the Slovenian Chemical Society, which I am proud of. The period from 1986 to 2017 (my service as Secretary and then President) was longer than 30 years, and Prof. Pejovnik told me several times that, for him, the surname Kaučič is synonymous with the Chemical Society and vice versa, that the Chemical Society also means Kaučič. Thank you for that, Stane.

I would also like to mention that I have been active in the IUPAC for over 30 years. This year, the IUPAC Periodic Table was published, translated into 26 world languages. There are between 6000 and 7000 languages in the world. I am proud to say that it has also been published in Slovenian (one of 26 translations).

For their comprehensive support provided to the Society, I would like to extend my thanks to the important industrial partners, universities, scientific and professional institutes, the Ministry of Education, Science and Sport and the Slovenian Research Agency.

At the same time, I would like to see the Society continue to grow professionally and to actively continue and build on its activities in the coming years.

Thank you for your attention and have a happy, pleasant and relaxing time after this ceremony.

Seznam nagrajencev

Častni člani:

1. Prof. dr. Peter Glavič
2. Akademik prof. dr. Branko Stanovnik
3. Zasl. prof. dr. Marjan Veber
4. Prof. dr. Jean Marie Lehn
5. Prof. dr. Wolfram Koch
6. Prof. dr. Pavel Drašar
7. Prof. dr. Andrej Šmalc
8. Prof. dr. Leiv K. Sydnes

Zaslužni člani:

1. Dr. Vida Hudnik
2. Prof. dr. Darinka Brodnjak Vončina
3. Prof. dr. Majda Žigon
4. Mag. Alenka Gogala
5. Mija Marin, dipl. inž. kem. tehnologije
6. Prof. dr. Miha Japelj
7. Zasl. prof. dr. Stane Pejovnik
8. Prof. dr. Aleksander Pavko
9. Prof. dr. Lucija Zupančič Kralj

Zaslužne institucije:

1. Kemijski inštitut
2. Institut „Jožef Stefan“
3. Fakulteta za kemijo in kemijsko tehnologijo, UL
4. Fakulteta za kemijo in kemijsko tehnologijo, UM
5. Cinkarna Celje, d.d.
6. Krka, d.d., Novo mesto
7. Kemomed, d.o.o.
8. AquafilSLO d.o.o.
9. Mettler Toledo d.o.o.
10. MIKRO+POLO d.o.o.
11. DONAU Lab d.o.o.

Priznanja za delo v uredništvu

Acta Chimica Slovenica:

1. Janez Košmrlj
2. Aleksander Pavko
3. Ksenija Kogej
4. Marija Bešter-Rogač
5. Matija Strlič
6. Mladen Franko
7. Alojz Demšar
8. Andrej Petrič
9. Bert VW Maes
10. Janez Cerkovnik
11. Barbara Malič
12. Krištof Kranjc
13. Damjana Rozman
14. Primož Šegedin
15. Boris Pihlar
16. Johannes T. Van Elteren
17. Michael Beeston
18. Irena Vovk
19. Helena Prosen
20. Melita Tramšek
21. Franc Perdih
22. Aleš Podgornik
23. Alen Albreht
24. Aleš Berlec
25. Mirela Dragomir
26. Matjaž Kristl
27. Vinko Vovk
28. Stanislav Oražem
29. Olga Gorše
30. Marjana Gantar Albreht

KOLEDAR VAŽNEJŠIH ZNANSTVENIH SREČANJ S PODROČJA KEMIJE IN KEMIJSKE TEHNOLOGIJE

SCIENTIFIC MEETINGS – CHEMISTRY AND CHEMICAL ENGINEERING

2023

January 2023

- 1 EUROPEAN FOOD CHEMISTRY CONGRESS XXI – EuroFoodChem XXI
Belgrade, Serbia
Information: <http://horizon2020foodentwin.rs/eurofoodchemxxi/>

February 2023

- 8 – 11 EMBO WORKSHOP IN SITU STRUCTURAL BIOLOGY: FROM CRYO-EM TO MULTI-
SCALE MODELLING
Heidelberg, Germany
Information: <https://www.embl.org/about/info/course-and-conference-office/events/iss23-01/>

March 2023

- 20 – 23 VIII INTERNATIONAL CONGRESS “ENGINEERING, ENVIRONMENT AND MATERIALS
IN PROCESS INDUSTRY
Jahorina, Bosnia and Hercegovina
Information: <https://eem.tfzv.ues.rs.ba/>

April 2023

- 16 – 21 HTCC 5
Dubrovnik, Croatia
Information: <https://htcc5.org/>

May 2023

- 16 – 17 EUROPEAN CONFERENCE ON CO₂ CAPTURE, STORAGE & REUSE 2023
Copenhagen, Denmark
- 21 – 25 PPEPPD 2023
Tarragona, Spain
Information: <https://ppeppd.org/ppeppd2023/>
- 29 – June 2 15TH MEDITERRANEAN CONGRESS OF CHEMICAL ENGINEERING – MECCE
Barcelona, Spain
Information: <https://www.mecce.org/>
- 31 – June 2 8TH EUROPEAN PROCESS INTENSIFICATION CONFERENCE
Warsaw, Poland
Information: <https://www.epic2023.pw.edu.pl/index/>

July 2023

- 2 – 6 FEZA 2023 – 9TH CONFERENCE OF THE FEDERATION OF THE EUROPEAN ZEOLITE ASSOCIATIONS
Portorož-Portorose, Slovenia
Information: <https://feza2023.org/en/>
- 2 – 7 XV POSTGRADUATE SUMMER SCHOOL ON GREEN CHEMISTRY
Venice, Italy
Information: <https://www.greenchemistry.school/>
- 9 – 14 38TH INTERNATIONAL CONFERENCE ON SOLUTION CHEMISTRY
Belgrade, Serbia
Information: <https://isc2023.pmf.uns.ac.rs/>
- 7 – 11 9TH EUCHEMS CHEMISTRY CONGRESS (ECC9)
Dublin, Ireland

Acta Chimica Slovenica

Author Guidelines

Submissions

Submission to ACSi is made with the implicit understanding that neither the manuscript nor the essence of its content has been published in whole or in part and that it is not being considered for publication elsewhere. All the listed authors should have agreed on the content and the corresponding (submitting) author is responsible for having ensured that this agreement has been reached. The acceptance of an article is based entirely on its scientific merit, as judged by peer review. There are no page charges for publishing articles in ACSi. The authors are asked to read the Author Guidelines carefully to gain an overview and assess if their manuscript is suitable for ACSi.

Additional information

- Citing spectral and analytical data
- Depositing X-ray data

Submission material

Typical submission consists of:

- full manuscript (PDF file, with title, authors, abstract, keywords, figures and tables embedded, and references)
- supplementary files
 - **Full manuscript** (original Word file)
 - **Statement of novelty** (Word file)
 - **List of suggested reviewers** (Word file)
 - **ZIP file containing graphics** (figures, illustrations, images, photographs)
 - **Graphical abstract** (single graphics file)
 - **Proposed cover picture** (optional, single graphics file)
 - **Appendices** (optional, Word files, graphics files)

Incomplete or not properly prepared submissions will be rejected.

Submission process

Before submission, authors should go through the checklist at the bottom of the page and prepare for submission.

Submission process consists of 5 steps.

Step 1: Starting the submission

- Choose one of the journal sections.
- Confirm all the requirements of the **checklist**.
- Additional plain text comments for the editor can be provided in the relevant text field.

Step 2: Upload submission

- Upload full manuscript in the form of a Word file (with title, authors, abstract, keywords, figures and tables embedded, and references).

Step 3: Enter metadata

- First name, last name, contact email and affiliation for all authors, in relevant order, must be provided. Corresponding author has to be selected. Full postal address and phone number of the corresponding author has to be provided.

- **Title and abstract** must be provided in plain text.
- Keywords must be provided (max. 6, separated by semicolons).
- Data about contributors and supporting agencies may be entered.
- **References** in plain text must be provided in the relevant text field.

Step 4: Upload supplementary files

- Original Word file (original of the PDF uploaded in the step 2)
- **List of suggested reviewers** with at least five reviewers with two recent references from the field of submitted manuscript must be uploaded as a Word file. At the same time, authors should declare (i) that they have no conflict of interest with suggested reviewers and (ii) that suggested reviewers are experts in the field of the submitted manuscript.
- All **graphics** have to be uploaded in a single ZIP file. Graphics should be named Figure 1.jpg, Figure 2.eps, etc.
- **Graphical abstract image** must be uploaded separately
- **Proposed cover picture** (optional) should be uploaded separately.
- Any additional **appendices** (optional) to the paper may be uploaded. Appendices may be published as a supplementary material to the paper, if accepted.
- For each uploaded file the author is asked for additional metadata which may be provided. Depending of the type of the file please provide the relevant title (Statement of novelty, List of suggested reviewers, Figures, Graphical abstract, Proposed cover picture, Appendix).

Step 5: Confirmation

- Final confirmation is required.

Article Types

Feature Articles are contributions that are written on Editor's invitation. They should be clear and concise summaries of the author's most recent work written with the broad scope of ACSi in mind. They are intended to be general overviews of the authors' subfield of research but should be written in a way that engages and informs scientists in other areas. They should contain the following (see also general guidelines for article structure below): (1) an introduction that acquaints readers with the authors' research field and outlines the important questions for which answers are being sought; (2) interesting, novel, and recent contributions of the author(s) to the field; and (3) a summary that presents possible future directions. Manuscripts should normally not exceed 40 pages of one column format (font size 12, 33 lines per page). Generally, experts who have made an important contribution to a specific field in recent years will be invited by the Editor to contribute a **Feature Article**. Individuals may, however, send a proposal (of no more than one page) for a **Feature Article** to the Editor-in-Chief for consideration.

Scientific articles should report significant and innovative achievements in chemistry and related sciences and should exhibit a high level of originality. They should have the following structure:

1. Title (max. 150 characters),
2. Authors and affiliations,
3. Abstract (max. 1000 characters),
4. Keywords (max. 6),
5. Introduction,
6. Experimental,
7. Results and Discussion,
8. Conclusions,
9. Acknowledgements,
10. References.

The sections should be arranged in the sequence generally accepted for publications in the respective fields and should be successively numbered.

Short communications generally follow the same order of sections as Scientific articles, but should be short (max. 2500 words) and report a significant aspect of research work meriting separate publication. Editors may decide that a Scientific paper is categorized as a Short Communication if its length is short.

Technical articles report applications of an already described innovation. Typically, technical articles are not based on new experiments.

Preparation of Submissions

Text of the submitted articles must be prepared with Microsoft Word. Normal style set to single column, 1.5 line spacing, and 12 pt Times New Roman font is recommended. Line numbering (continuous, for the whole document) must be enabled to simplify the reviewing process. For any other format, please consult the editor. Articles should be written in English. Correct spelling and grammar are the sole responsibility of the author(s). Papers should be written in a concise and succinct manner. The authors shall respect the ISO 80000 standard [1], and IUPAC Green Book [2] rules on the names and symbols of quantities and units. The Système International d'Unités (SI) must be used for all dimensional quantities.

Graphics (figures, graphs, illustrations, digital images, photographs) should be inserted in the text where appropriate. The captions should be self-explanatory. Lettering should be readable (suggested 8 point Arial font) with equal size in all figures. Use common programs such as MS Excel or similar to prepare figures (graphs) and ChemDraw to prepare structures in their final size. Width of graphs in the manuscript should be 8 cm. Only in special cases (in case of numerous data, visibility issues) graphs can be 17 cm wide. All graphs in the manuscript should be inserted in relevant places and **aligned left**. The same graphs should be provided separately as images of appropriate resolution (see below) and submitted together in a ZIP file (Graphics ZIP). Please do not submit figures as a Word file. In **graphs**, only the graph area determined by both axes should be in the frame, while a frame around the whole graph should be omitted. The graph area should be white. The legend should be inside the graph area. The style of all graphs should be the same. **Figures and illustrations** should be of sufficient quality for the printed version, i.e. 300 dpi minimum. **Digital images and photographs** should be of high quality (minimum

250 dpi resolution). On submission, figures should be of good enough resolution to be assessed by the referees, ideally as JPEGs. High-resolution figures (in JPEG, TIFF, or EPS format) might be required if the paper is accepted for publication.

Tables should be prepared in the Word file of the paper as usual Word tables. The captions should appear above the table and should be self-explanatory.

References should be numbered and ordered sequentially as they appear in the text, likewise methods, tables, figure captions. When cited in the text, reference numbers should be superscripted, following punctuation marks. It is the sole responsibility of authors to cite articles that have been submitted to a journal or were in print at the time of submission to ACSi. Formatting of references to published work should follow the journal style; please also consult a recent issue:

1. J. W. Smith, A. G. White, *Acta Chim. Slov.* **2008**, *55*, 1055–1059.
2. M. F. Kemmere, T. F. Keurentjes, in: S. P. Nunes, K. V. Peinemann (Ed.): *Membrane Technology in the Chemical Industry*, Wiley-VCH, Weinheim, Germany, **2008**, pp. 229–255.
3. J. Levec, Arrangement and process for oxidizing an aqueous medium, US Patent Number 5,928,521, date of patent July 27, **1999**.
4. L. A. Bursill, J. M. Thomas, in: R. Sersale, C. Collola, R. Aiello (Eds.), *Recent Progress Report and Discussions: 5th International Zeolite Conference*, Naples, Italy, 1980, Gianini, Naples, **1981**, pp. 25–30.
5. J. Szegezdi, F. Csizmadia, Prediction of dissociation constant using microconstants, http://www.chemaxon.com/conf/Prediction_of_dissociation_constant_using_microconstants.pdf, (assessed: March 31, 2008)

Titles of journals should be abbreviated according to Chemical Abstracts Service Source Index (CASSI).

Special Notes

- Complete characterization, **including crystal structure**, should be given when the synthesis of new compounds in crystal form is reported.
- Numerical **data should be reported with the number of significant digits corresponding to the magnitude** of experimental uncertainty.
- **The SI system of units and IUPAC recommendations** for nomenclature, symbols and abbreviations should be followed closely. Additionally, the authors should follow the general guidelines when citing spectral and analytical data, and depositing crystallographic data.
- **Characters** should be correctly represented throughout the manuscript: for example, 1 (one) and l (ell), 0 (zero) and O (oh), x (ex), D7 (times sign), B0 (degree sign). Use Symbol font for all Greek letters and mathematical symbols.
- The rules and recommendations of the **IUBMB** and the **International Union of Pure and Applied Chemistry (IUPAC)** should be used for abbreviation of chemical names, nomenclature of chemical compounds, enzyme nomenclature, isotopic compounds, optically active isomers, and spectroscopic data.
- **A conflict of interest** occurs when an individual (author, reviewer, editor) or its organization is in-

volved in multiple interests, one of which could possibly corrupt the motivation for an act in the other. Financial relationships are the most easily identifiable conflicts of interest, while conflicts can occur also as personal relationships, academic competition, etc. **The Editors** will make effort to ensure that conflicts of interest will not compromise the evaluation process; potential editors and reviewers will be asked to exempt themselves from review process when such conflict of interest exists. When the manuscript is submitted for publication, **the authors** are expected to disclose any relationships that might pose potential conflict of interest with respect to results reported in that manuscript. In the Acknowledgement section the source of funding support should be mentioned. The statement of disclosure must be provided as Comments to Editor during the submission process.

- **Published statement of Informed Consent.** Research described in papers submitted to ACSi must adhere to the principles of the Declaration of Helsinki (<http://www.wma.net/e/policy/b3.htm>). These studies must be approved by an appropriate institutional review board or committee, and informed consent must be obtained from subjects. The Methods section of the paper must include: 1) a statement of protocol approval from an institutional review board or committee and 2), a statement that informed consent was obtained from the human subjects or their representatives.
- **Published Statement of Human and Animal Rights.** When reporting experiments on human subjects, authors should indicate whether the procedures followed were in accordance with the ethical standards of the responsible committee on human experimentation (institutional and national) and with the Helsinki Declaration of 1975, as revised in 2008. If doubt exists whether the research was conducted in accordance with the Helsinki Declaration, the authors must explain the rationale for their approach and demonstrate that the institutional review body explicitly approved the doubtful aspects of the study. When reporting experiments on animals, authors should indicate whether the institutional and national guide for the care and use of laboratory animals was followed.
- To avoid conflict of interest between authors and referees we expect that not more than one referee is from the same country as the corresponding author(s), however, not from the same institution.
- Contributions authored by **Slovenian scientists** are evaluated by non-Slovenian referees.
- Papers describing **microwave-assisted reactions** performed in domestic microwave ovens are not considered for publication in *Acta Chimica Slovenica*.
- *Manuscripts that are **not prepared and submitted** in accord with the instructions for authors are not considered for publication.*

Appendices

Authors are encouraged to make use of supporting information for publication, which is supplementary material (appendices) that is submitted at the same time as the manuscript. It is made available on the Journal's

web site and is linked to the article in the Journal's Web edition. The use of supporting information is particularly appropriate for presenting additional graphs, spectra, tables and discussion and is more likely to be of interest to specialists than to general readers. When preparing supporting information, authors should keep in mind that the supporting information files will not be edited by the editorial staff. In addition, the files should be not too large (upper limit 10 MB) and should be provided in common widely known file formats to be accessible to readers without difficulty. All files of supplementary materials are loaded separately during the submission process as supplementary files.

Proposed Cover Picture and Graphical Abstract Image

Graphical content: an ideally full-colour illustration of resolution 300 dpi from the manuscript must be proposed with the submission. Graphical abstract pictures are printed in size 6.5 x 4 cm (hence minimal resolution of 770 x 470 pixels). Cover picture is printed in size 11 x 9.5 cm (hence minimal resolution of 1300 x 1130 pixels)

Authors are encouraged to submit illustrations as candidates for the journal Cover Picture*. The illustration must be related to the subject matter of the paper. Usually both proposed cover picture and graphical abstract are the same, but authors may provide different pictures as well.

* The authors will be asked to contribute to the costs of the cover picture production.

Statement of novelty

Statement of novelty is provided in a Word file and submitted as a supplementary file in step 4 of submission process. Authors should in no more than 100 words emphasize the scientific novelty of the presented research. Do not repeat for this purpose the content of your abstract.

List of suggested reviewers

List of suggested reviewers is a Word file submitted as a supplementary file in step 4 of submission process. Authors should propose the names, full affiliation (department, institution, city and country) and e-mail addresses of five potential referees. Field of expertise and at least two references relevant to the scientific field of the submitted manuscript must be provided for each of the suggested reviewers. The referees should be knowledgeable about the subject but have no close connection with any of the authors. In addition, referees should be from institutions other than (and countries other than) those of any of the authors. Authors declare no conflict of interest with suggested reviewers. Authors declare that suggested reviewers are experts in the field of submitted manuscript.

How to Submit

Users registered in the role of author can start submission by choosing USER HOME link on the top of the page, then choosing the role of the Author and follow the relevant link for starting the submission process. Prior to submission we strongly recommend that you familiarize yourself with the ACSi style by browsing the journal, particularly if you have not submitted to the ACSi before or recently.

Correspondence

All correspondence with the ACSi editor regarding the paper goes through this web site and emails. Emails are sent and recorded in the web site database. In the correspondence with the editorial office please provide ID number of your manuscript. All emails you receive from the system contain relevant links. **Please do not answer the emails directly but use the embedded links in the emails for carrying out relevant actions.** Alternatively, you can carry out all the actions and correspondence through the online system by logging in and selecting relevant options.

Proofs

Proofs will be dispatched via e-mail and corrections should be returned to the editor by e-mail as quickly as possible, normally within 48 hours of receipt. Typing errors should be corrected; other changes of contents will be treated as new submissions.

Submission Preparation Checklist

As part of the submission process, authors are required to check off their submission's compliance with all of the following items, and submissions may be returned to authors that do not adhere to these guidelines.

1. The submission has not been previously published, nor is it under consideration for publication in any other journal (or an explanation has been provided in Comments to the Editor).
2. All the listed authors have agreed on the content and the corresponding (submitting) author is responsible for having ensured that this agreement has been reached.
3. The submission files are in the correct format: manuscript is created in MS Word but will be **submitted in PDF** (for reviewers) as well as in original MS Word format (as a supplementary file for technical editing); diagrams and graphs are created in Excel and saved in one of the file formats: TIFF, EPS or JPG; illustrations are also saved in one of these formats. The preferred position of graphic files in a document is to embed them close to the place where they are mentioned in the text (See **Author guidelines** for details).
4. The manuscript has been examined for spelling and grammar (spell checked).
5. The **title** (maximum 150 characters) briefly explains the contents of the manuscript.
6. Full names (first and last) of all authors together with the affiliation address are provided. Name of author(s) denoted as the corresponding author(s), together with their e-mail address, full postal address and telephone/fax numbers are given.
7. The **abstract** states the objective and conclusions of the research concisely in no more than 150 words.
8. Keywords (minimum three, maximum six) are provided.
9. **Statement of novelty** (maximum 100 words) clearly explaining new findings reported in the manuscript should be prepared as a separate Word file.
10. The text adheres to the stylistic and bibliographic requirements outlined in the **Author guidelines**.
11. Text in normal style is set to single column, 1.5 line spacing, and 12 pt. Times New Roman font is

recommended. All tables, figures and illustrations have appropriate captions and are placed within the text at the appropriate points.

12. Mathematical and chemical equations are provided in separate lines and numbered (Arabic numbers) consecutively in parenthesis at the end of the line. All equation numbers are (if necessary) appropriately included in the text. Corresponding numbers are checked.
13. Tables, Figures, illustrations, are prepared in correct format and resolution (see **Author guidelines**).
14. The lettering used in the figures and graphs do not vary greatly in size. The recommended lettering size is 8 point Arial.
15. Separate files for each figure and illustration are prepared. The names (numbers) of the separate files are the same as they appear in the text. All the figure files are packed for uploading in a single ZIP file.
16. Authors have read **special notes** and have accordingly prepared their manuscript (if necessary).
17. References in the text and in the References are correctly cited. (see **Author guidelines**). All references mentioned in the Reference list are cited in the text, and vice versa.
18. Permission has been obtained for use of copyrighted material from other sources (including the Web).
19. The names, full affiliation (department, institution, city and country), e-mail addresses and references of five potential referees from institutions other than (and countries other than) those of any of the authors are prepared in the word file. At least two relevant references (important recent papers with high impact factor, head positions of departments, labs, research groups, etc.) for each suggested reviewer must be provided. Authors declare no conflict of interest with suggested reviewers. Authors declare that suggested reviewers are experts in the field of submitted manuscript.
20. Full-colour illustration or graph from the manuscript is proposed for graphical abstract.
21. **Appendices** (if appropriate) as supplementary material are prepared and will be submitted at the same time as the manuscript.

Privacy Statement

The names and email addresses entered in this journal site will be used exclusively for the stated purposes of this journal and will not be made available for any other purpose or to any other party.

ISSN: 1580-3155

Koristni naslovi

Slovensko kemijsko društvo
Slovenian Chemical Society



Slovensko kemijsko društvo

www.chem-soc.si

e-mail: chem.soc@ki.si



Wessex Institute of Technology

www.wessex.ac.uk



SETAC

www.setac.org



European Water Association

<http://www.ewa-online.eu/>



European Science Foundation

www.esf.org



European Federation of Chemical Engineering

<https://efce.info/>



IUPAC

INTERNATIONAL UNION OF
PURE AND APPLIED CHEMISTRY

International Union of Pure and Applied Chemistry

<https://iupac.org/>

Novice evropske zveze kemijskih društev EuChemS najdete na:

 **EuChemS**
European Chemical Society

Brussels News Updates

<http://www.euchems.eu/newsletters/>



DONAU LAB Ljubljana
Member of LPPgroup

 **BINDER**

Best conditions for your success



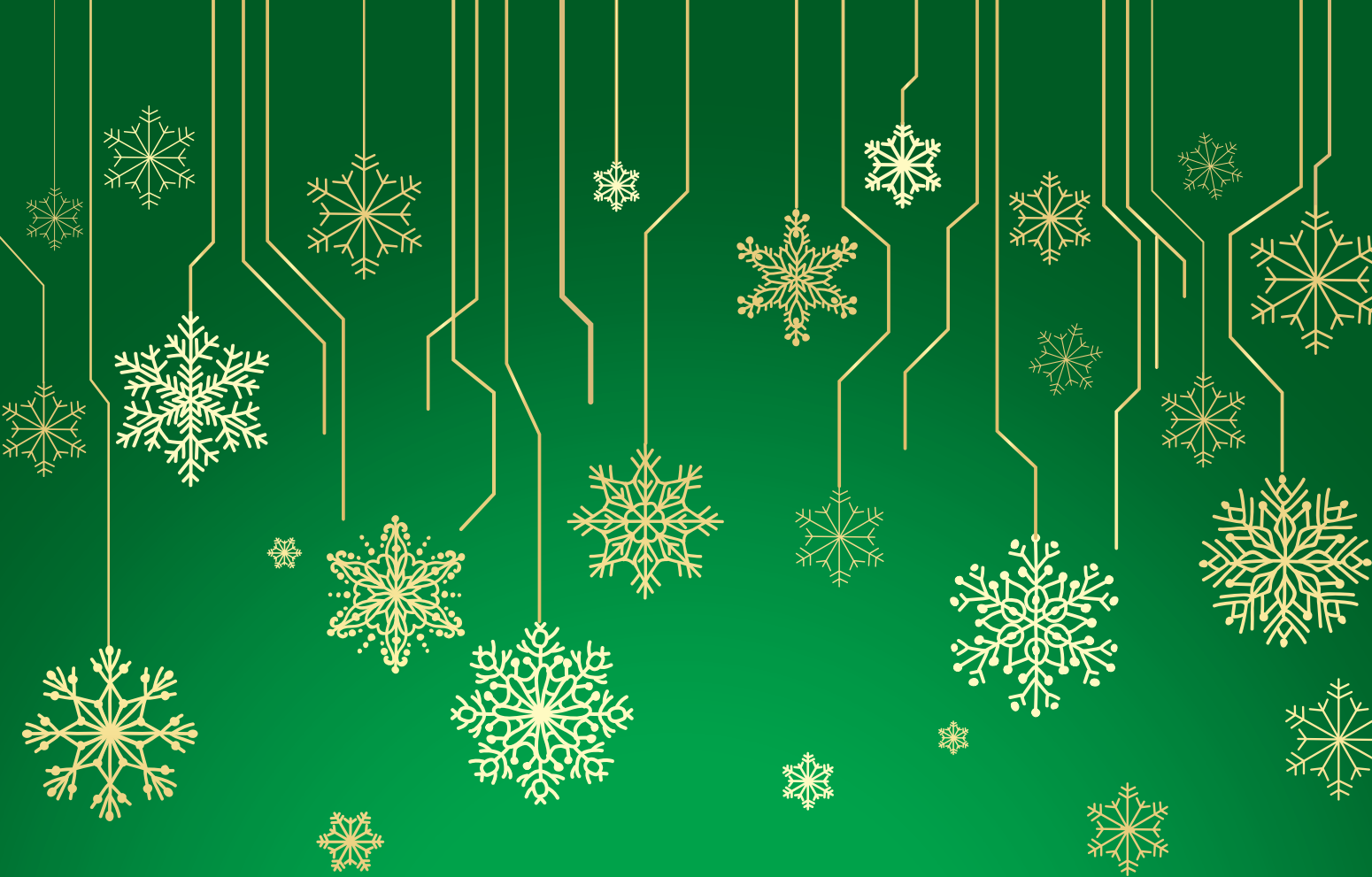
Komore za testiranje baterij

Vakuumski sušilniki

Klimatske komore



Donau Lab d.o.o., Ljubljana
Tbilisijska 85
SI-1000 Ljubljana
www.donaulab.si
office-si@donaulab.com



*We will ensure top results and
good interpersonal relationships
by following our mission and
taking responsible steps.*

Happy 2023!

Razvoj in inovacije za globalno uspešnost

Znanje, kreativnost zaposlenih in inovacije so ključnega pomena v okolju, kjer nastajajo pametni premazi skupine KANSAI HELIOS. Z rešitvami, ki zadostijo široki paleti potreb, kontinuiranim razvojem ter s kakovostnimi izdelki, Helios predstavlja evropski center za inovacije in poslovni razvoj skupine Kansai Paint.

Part of  **KANSAI
PAINT**

www.helios-group.eu

 **KANSAI
HELIOS**
Designing Excellence

Acta Chimica Slovenica

Acta Chimica Slovenica

The significance of nitrogen- and oxygen-heterocycles in many areas of life is well-known, however, the preparation of new derivatives remains important. The multicomponent synthesis of potentially biologically active heterocycles containing a phosphonate or a phosphine oxide moiety was performed (page 735).



Year 2022, Vol. 69, No. 4

